Springer Series in Geomechanics and Geoengineering

Alessio Ferrari · Lyesse Laloui *Editors*

Energy Geotechnics

SEG-2018

Springer

Springer Series in Geomechanics and Geoengineering

Series editor

Wei Wu, Universität für Bodenkultur, Vienna, Austria
e-mail: wei.wu@boku.ac.at

Geomechanics deals with the application of the principle of mechanics to geomaterials including experimental, analytical and numerical investigations into the mechanical, physical, hydraulic and thermal properties of geomaterials as multiphase media. Geoengineering covers a wide range of engineering disciplines related to geomaterials from traditional to emerging areas.

The objective of the book series is to publish monographs, handbooks, workshop proceedings and textbooks. The book series is intended to cover both the state-of-the-art and the recent developments in geomechanics and geoengineering. Besides researchers, the series provides valuable references for engineering practitioners and graduate students.

More information about this series at http://www.springer.com/series/8069

Alessio Ferrari · Lyesse Laloui
Editors

Energy Geotechnics

SEG-2018

Springer

Editors
Alessio Ferrari
École Polytechnique Fédérale de Lausanne
Lausanne, Switzerland

Lyesse Laloui
École Polytechnique Fédérale de Lausanne
Lausanne, Switzerland

and

Unviversità degli Studi di Palermo
Palermo, Italy

ISSN 1866-8755 ISSN 1866-8763 (electronic)
Springer Series in Geomechanics and Geoengineering
ISBN 978-3-319-99669-1 ISBN 978-3-319-99670-7 (eBook)
https://doi.org/10.1007/978-3-319-99670-7

Library of Congress Control Number: 2018952059

This Springer imprint is published by the registered company Springer Nature Switzerland AG
The registered company address is: Gewerbestrasse 11, 6330 Cham, Switzerland

Preface

Geomechanics and geotechnical engineering are at the core of the energy scientific and technological challenges of this century. Most of new and conventional technologies for energy production, transportation, storage and use require in fact a specialized understanding of the mechanical behaviour of geomaterials.

The International Symposium on Energy Geotechnics 2018 (SEG-2018) has been organized recognizing the strong need for shared knowledge in innovative and challenging geomechanical and geotechnical applications related to energy. SEG-2018 was held on the 25–28 of September 2018, at the Swiss Federal Institute of Technology in Lausanne (EPFL). The symposium has been organized under the auspices of the Technical Committee TC-308 "Energy Geotechnics" of the International Society of Soil Mechanics and Geotechnical Engineering.

About two hundred researchers and practitioners working on Energy Geotechnics topics were invited to present their most recent advances in more than thirty technical sessions. Twelve keynote and feature lectures from the most prominent scientists in the field completed the technical programme.

This book collects the full papers accompanying about sixty of the oral presentations delivered at SEG-2018. The papers cover a wide range of themes in Energy Geotechnics, including energy geostructures, energy geostorage, thermo-hydro-chemo-mechanical behaviour of geomaterials, unconventional resources, hydraulic stimulation, induced seismicity, CO_2 geological storage, nuclear waste disposal and other energy-related topics such as tower and offshore foundations.

We would like to express our thanks to all the authors for their outstanding contributions. We are especially grateful to Dr. Melis Sutman and Dr. Patrycja Baryla for their assistance with the preparation of this book.

Alessio Ferrari
Lyesse Laloui

Contents

Energy Geostructures and Energy Geostorage

Evaluating the Applicability of the Radial Approximation for Pile Heat Exchangers

Nick Woodman[1(✉)], F. A. Loveridge[2], Saqib Javed[3], and Johan Claesson[3]

[1] University of Southampton, Southampton, UK
n.d.woodman@soton.ac.uk
[2] University of Leeds, Leeds, UK
[3] Lund University, Lund, Sweden

Abstract. This paper appraises the efficacy of using an analytical radial approximation for different thermal pile heat exchanger geometries. Unsteady radial heat-flow from fluid in a pipe set within a grouted borehole into the external ground is well-documented and can be solved analytically very rapidly using Laplace Transforms (Javed and Claesson 2011). By comparing the radial model with finite-element simulations including explicit pile geometries, this paper provides a provisional analysis of the accuracy of this approach. Initial findings suggest that the radial model may provide an appropriate approximation to pile behaviour for certain pipe configurations, albeit with small 'mid-time' error.

1 Introduction

Energy piles are an alternative to classical borehole exchangers to provide energy-saving for newly constructed buildings. The primary heat-exchange circuit is embedded within the concrete building piles. This saves on embodied energy and has the ability to place the ground-source heat exchanger close to the building where it is needed. The contrast between the thermal properties of the concrete and the surrounding ground means that the typical assumptions used for designing borehole heat exchangers may not necessarily apply; in particular the transient heat transport due to heat storage within the pile itself may cause pile heat exchangers to perform significantly differently to ordinary boreholes.

Various arrangements of exchanger pipes are engineered, typically relating to the underlying construction method of the pile. Where piles are constructed using a Continuous Flight Auger (CFA), the fluid pipes tend to be located towards the centre of the pile, arranged around reinforcement bar for stability. Where there is rotary pile construction, the fluid pipes are located closer to the outside edge of the pile. Both arrangements are summarised in Fig. 1. These differences give rise to different thermal response characteristics.

There have been numerous studies on how best to capture different arrangements in terms of a step response (or 'G-function'), without the computational cost of explicitly modelling the detailed geometry of the borehole (Loveridge and Powrie 2013). Here we build on this general approach, making use of an elegant semi-analytical solution

A. Ferrari and L. Laloui (Eds.): SEG 2018, SSGG, pp. 3–10, 2019.
https://doi.org/10.1007/978-3-319-99670-7_1

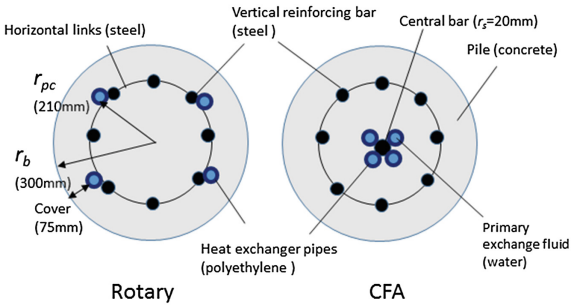

Fig. 1. Cartoon of typical thermal pile construction arrangements assumed here

which exploits radial symmetry. The specific models used here we call the Claesson-Javed Radial model (CJRM) and the Claesson-Javed Radial model with Storage (CJRMS). These are detailed in Javed and Claesson (2011) and Claesson (2017, Personal communication) and are implemented here in Matlab R2017a.

The radial models and their equivalence to typical geometries are summarised in Fig. 2. The radial models are consistent with the explicit models in solving unsteady-state Fourier conduction in the ground and concrete borehole, and in treating the fluid as an isothermal unit. The models differ in geometry, but also in that the pipes in the radial model are modelled as steady-state resistances. For the CJRMS model, the inner store is considered to be a further isothermal unit, which is connected to the fluid via a pipe resistance. The total pipe resistance is divided by an empirical weighting factor between the transfer to the store and the transfer to the concrete pile.

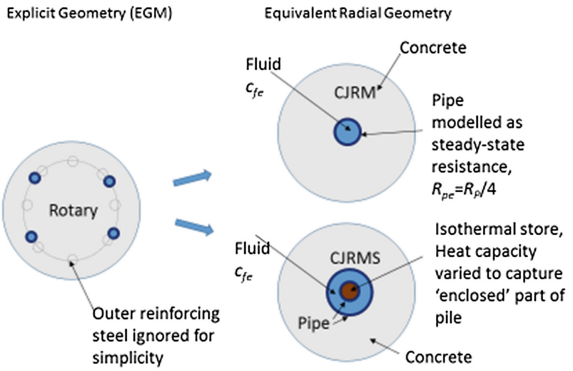

Fig. 2. Radial models to represent explicit geometry (rotary case given as example)

To scope the issues we keep to two different arrangements, here short-handed by the construction method (i.e. 'CFA' or 'Rotary'), both times with four pipes (N_p = 4). The steel is modelled for the CFA, since it is surrounded by the pipes, but we neglect it in the Rotary case.

The CJRM and CJRSM models are a geometric simplification of the true underlying geometry of a typical borehole pile arrangement, so it is prudent to examine the potential inaccuracies. Before making this analysis we conjectured that the CJRMS may improve the CJRM, which would be anticipated to be less accurate in the instance where the borehole pipes are significantly offset from the centre of the pile (including where they are set around concrete reinforcement bar).

This paper presents examines the nature of this simplification, focusing on a 600 mm diameter concrete pile. A wider analysis is to follow.

2 Explicit Geometry Simulations

We generate synthetic data in our 'Explicit Geometry Model' (EGM), which is a 2D solid conductive heat-flow pile model in COMSOL. The assumptions are summarised in Table 1. A key assumption is that there is no heat-flow out of plane (i.e. we simulate a unit depth with no effects from the end of the borehole, the ground surface or due to different fluid temperatures in the pipes). Each thermal unit (i.e. ground, concrete, pipe and fluid) is considered to be a homogeneous uniform continuum each characterised by thermal parameters constant in time and temperature.

Table 1. Input assumptions. Two generic pile types are simulated: 'CFA' and 'Rotary'. The thermal conductivities of the concrete and ground (λ_c, λ_g) are permuted as (1, 1); (1, 2); (2, 1) and (2, 2).

Item	Geometry	Properties	Comments
Fluid	$N_p = 4$, $r_{pi} = 0.0123$ m	$\rho_f = 1000$ kg/m^3 $c_f = 4217$ J/kgK $C_f = \rho_f c_f$ $\pi r_{pi}^2 = 8017.2$ J/mK	Isothermal. Constant heating of 50 W/m applied to the fluid (i.e. 12.5 W/m/pipe)
Pipes	$r_{po} = 0.015$ m $N_p = 4$, at 90° separation *CFA:* $r_{pc} = 0.035$ m *Rotary*: $r_{pc} = 0.21$ m	$\rho_p = 950$ kg/m^3 $c_p = 1900$ J/kgK $\lambda_p = 0.45$ W/mK	High density polyethylene (Cecinato and Loveridge 2015)
Concrete pile	Circular $r_b = 0.3$ m	$\rho_c = 2000$ kg/m^3 $c_c = 800$ J/kgK $\lambda_c = 1$ or 2 W/mK	
Ground	Circular outer model domain ($r_o = 25$ m)	$\rho_g = 2000$ kg/m^3 $c_g = 2000$ J/kgK $\lambda_g = 1$ or 2 W/mK	
Steel	$r_s = 0.02$ m at the centre of the pile	$\rho_s = 7801$ kg/m^3 $c_s = 473$ J/kgK $\lambda_s = 43$ W/mK	Only for CFA Loveridge and Cecinato (2016)

Four fluid pipes per borehole are modelled. The thermal properties of the fluid in these pipes are of water, which is assumed to be of equal temperature throughout the pipe (i.e. well-mixed). For simplicity we neglect to include a wall heat-transfer coefficient, which could be added to the pipe resistance if necessary.

The assumed initial condition is for uniform, equilibrated temperatures. At the start of modelling period, there is a step-change in input power to the fluid. The model is run for 1×10^7 s (i.e. $\sim$116 days), outputting ten times per logarithmic interval starting at for 1×10^{-5} s. The early end of the range is of course substantially shorter than the timescales of practical interest and are included to enable validation of early-time asymptotic behaviour.

A typical duty might crudely be summarised as a square-wave (on-off) cycle of period one day, being sustained for months or years at a time. Therefore, in practice the daily timescale (i.e. from $\sim 1 \times 10^3$ to $\sim 1 \times 10^5$ s) is of particular interest for optimisation purposes.

3 Matching to Radially-Symmetric Model

The method for matching the radially-symmetric models (CJRM and CJRMS) to the synthetic explicit model simulations (EGM) are summarised in Fig. 2. The philosophy of the matching is to preserve the true geomey and physics whenever possible. Therefore, the concrete and ground thermal properties and geometry (i.e. r_b = 0.3 m) are kept unchanged from the EGM. In theory these could be varied to give additional degrees of freedom thereby potentially improving the fit.

The effective radius of the single effective pipe (r_{pe}) is set so as to provide the identical fluid temperature drop over the concrete pile during quasi steady-state conduction at the end of the simulation as occurs for the EGM (i.e. at $t = 1 \times 10^7$ s). This is achieved by computing the averages of T_{po} and T_b around the borehole and pipe boundaries and rearranging the steady-state heat-flow Eq. [1] to find r_{pe}:

$$\overline{T}_{po} - \overline{T}_b = qR_b = \frac{q}{2\pi\lambda_c} \ln\left(\frac{r_b}{r_{pe}}\right) \tag{1}$$

By doing this we remove the issue of how to estimate R_b given a particular borehole geometry; this is discussed very comprehensively by Javed and Spitler (2017). The thermal capacity of the fluid C_f is kept equal to the capacity in the EGM. Since the effective area of fluid has changed, this is achieved by using a scaled specific heat of fluid, c_{fe}.

The characteristic time for thermal diffusion within the pipe wall is $c_{pp}(r_{po} - r_{pi})^2/\lambda_p$, which is relatively short ($\sim$30 s). This is the basis for the assumption made in the radial model of steady-state heat transfer in the pipe. Thus, in a similar manner for R_b, the thermal resistance is estimated as:

$$R_p = \frac{1}{2\pi\lambda_p} \ln\left(\frac{r_{po}}{r_{pi}}\right) \tag{2}$$

The equivalent pipe resistance for the EGM is a quarter since there is only one pipe in the CRM dispersing the same total power, i.e. $R_{pe} = R_p/4$.

The above matching via R_p, R_b, (or r_{pe}) and c_{fe} ensures long- and short- time asymptotic matching. However, between these times the models may diverge. For the CRM, there is no obviously sensible adjustment to the parameters that can be made to improve the mid-time. We test the conjecture that the CJRMS may instead provide some adjustment, and with a physically-logical basis. For the CJRMS different values may be appropriate for the thermal capacity of the central store. For CFA geometry the thermal capacity of the store is set equal to the capacity of the steel. For the radial geometry a reasonable upper bound for the capacity of the store C_{ST} is to lump the capacity of the concrete at $r < r_{pc}$.

4 Results

Figure 3 illustrates the comparison, plotted in real temperatures and times. The solutions converge to the asymptotic solutions for short and long times, albeit there is numerical error appearing at the very earliest part of the EGM simulation. At mid-time, there is a departure which reaches a maximum of 0.6 °K at 2511 s before declining. This is a small absolute error when compared to the temperature at the end of the period (18.7 °K), but is a 17% relative error at that point in time. The matching departure can be seen to occur within the approximate range 20–20,000 s (Table 2).

The pattern from Fig. 3 is repeated in Fig. 4a relatively small error occurs at mid-time in all the plots. CJRMS cannot remedy the discrepancy between the models; it lowers the mid-time temperatures as the store capacity C_s increases, and thereby worsening the match.

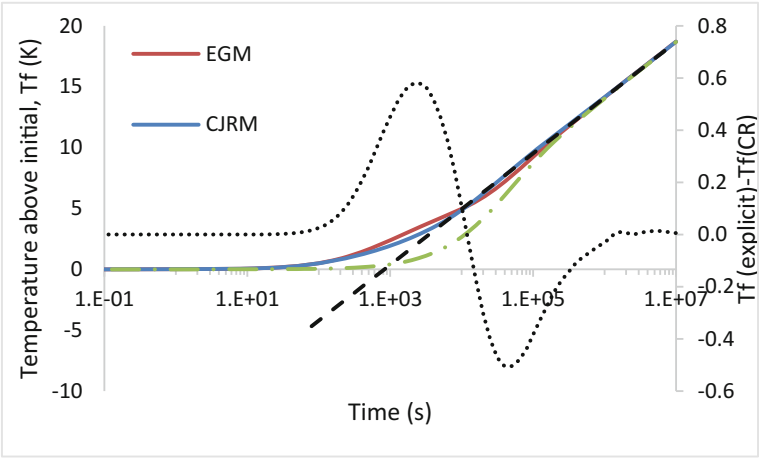

Fig. 3. EGM and CJRM compared for rotary case (r_b = 300 mm) for (λ_c, λ_g,) = (1,2) W/mK $T_f \sim \frac{q}{4\pi\lambda_g}\left[\ln\left(\frac{4\lambda_g t}{c_g\rho_g r_b^2}\right) - 0.5772\right] + q\left[R_p + R_b\right]$ at long time (dashed line). $C_{ST} = 100,000$ J/(Km) in the CJRMS.

Table 2. Summary parameters. Note R_p calculated via Eq. [2] is 0.0702. So, R_{pe} = 0.0175. This is confirmed in the EGM at 1×10^7 s.

Case	λ_c, λ_g (W/mK)	c_{fe} (J/kgK)	R_{be} (Km/W)	$\left\|\text{Max}\left(T_f\|_{EGM} - T_f\|_{CJRM}\right)\right\|$
CFA1-2	1, 2	1471.0	0.31	0.66
CFA2-1	2, 1	1556.9	0.16	0.24
CFA2-2	2, 2	1560.1	0.16	0.24
Rot1-1	1, 2	141.3	0.13	0.58
Rot2-1	2, 1	142.2	0.06	0.38
Rot2-2	2, 2	142.1	0.06	0.47

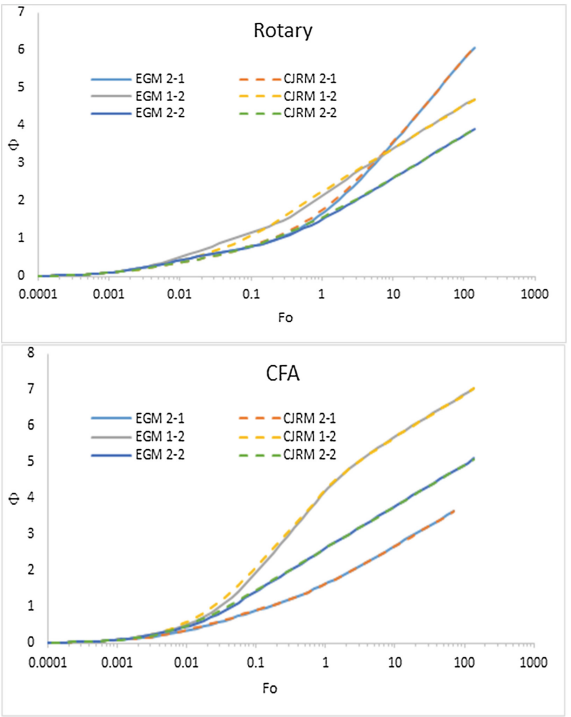

Fig. 4. Comparison of step response behaviour between geometries for dimensionless temperature $\Phi = 2\pi\lambda_g \Delta T_f / q$ against dimensionless time $Fo = \alpha_g t / r_b^2$. λ_c–λ_g in legend.

5 Discussion

Figure 3 shows that the addition of the store in CJRMS doesn't improve the fit; the effect of the store is to lower the mid-time temperature. Simulating the store as a fully diffusive cylinder also provides no improvement (numerically or analytically via block-geometry functions provided by Barker 1985). The departure from the idealised radial

solution is due to the fact that the pipes are not centred on the borehole, which can be illustrated qualitatively at the simplest level by varying the location of a single pipe. Thus, despite the intuitive nature of the CJRMS, it does not correctly capture the physics of the situation. The dominant cause of the discrepancy away from a purely radially-symmetric case is due to the asymmetry of the location of the pipes. This can be demonstrated by comparing the response for a single-pipe as it is moved out from the centre.

In terms of the CJRM simplification applied to non-centred pipes set within a large-pile situation where there is contrasting ground-concrete thermal conductivities, it is notable how close the radial approximation is. The step response is dominated by the fluid thermal capacity at early time and by the ground resistance at late-time, transitioning between these, via a period dominated by borehole resistance at mid-time.

By computing R_b in the EGM, asymptotic late-time matching was guaranteed. In practise, since the point of the radial models is to avoid building EGMs, R_b requires estimation. As is demonstrated in Javed and Spitler (2017), the multi-pole method is an accurate means of doing this.

A more generalised analysis over a wider geometry range is the logical next step to build on these provisional findings. In particular it will be useful to quantify the accuracy of the CRM over a wider range of geometries and parameters (including number of pipes).

6 Conclusions

For the parameter ranges and geometries assumed in the paper (which we believe to be reasonably typical) the CJRM is demonstrated to be reasonably accurate, given the geometric simplification. There are, nonetheless, differences that arise primarily due to the asymmetry. The radial (CJRM) and the radial-store model (CJRMS) although able to match the asymptotic behaviour at both early and late time, develops discrepancy during the mid-time. The CJRMS worsens CJRM fit, since it is not introducing the correct physical behaviour relating to this asymmetry.

Acknowledgements. This work was supported under the EPSRC grant EP/P001351/1, 'Non Steady Analytical Models for Energy Pile Testing and Design'.

References

Barker, J.A.: Block-Geometry functions characterising transport in densely fissured media. J. Hydrol. **77**, 263–279 (1985)

Cecinato, F., Loveridge, F.A.: Influences on the thermal efficiency of energy piles. Energy **82**, 1021–1033 (2015)

Javed, S., Claesson, J.: New analytical and numerical solutions for the short-term analysis of thermal response tests used to measure ground thermal properties. ASHRAE Trans. **117**(1), 13–21 (2011)

Javed, S., Spitler, J.: Accuracy of borehole thermal resistance calculation methods for grouted single U-tube ground heat exchangers. Appl. Energy **187**, 790–806 (2017)

Loveridge, F., Cecinato, F.: Thermal performance of thermoactive continuous flight auger piles. Environ. Geotech. **3**(4), 265–279 (2016)

Loveridge, F., Powrie, W.: Temperature response functions (G-functions) for single pile heat exchangers. Energy **57**, 554–564 (2013)

Numerical Assessment of Thermal Performance and Heat Storage Capacity of Thermoactive Geostructures

Yvon Delerablee[1(✉)], Sebastien Burlon[2], Philippe Reiffsteck[2], and Eric Antoinet[1]

[1] Antea Group, 92160 Antony, France
yvon.delerablee@anteagroup.com
[2] University of Paris-Est, The French Institute of Science and Technology for Transport, Development, and Networks (IFSTTAR), 77447 Marne La Vallée, France

Abstract. Thermoactive geostructures represent an original technique to fulfil energy demand of buildings and infrastructure. The thermal performance of such structure depends on several parameters as the thermal solicitation, the hydro-geological context and the thermal characteristics. To improve the design of the thermoactives geostructures, an original approach based on the analysis of thermal flux and volumetric thermal power has been developed. This method permits to assess the temperature variation of a volume and the potential thermal drift of the system. Moreover, this method is used to analyse the thermal behaviour of thermoactive diaphragm walls.

1 Introduction

Thermoactives geostructures aim at the production of heating during winter and cooling during summer and include various geotechnical structures with embedded heat exchanger tubes. This technology can also be implemented in deep foundations, retaining walls, base slab and tunnels (CFMS and SYNTEC 2017). Since its development during the years 1980 (Brandl 2006), the complexity of the structures equipped with heat exchanger tubes increases continuously and now one of the current challenge concerns the installation of these tubes in more complex structures as metro stations and tunnels (Barla et al. 2016).

The design of geotechnical structures requires to consider thermal stress and strain and the interactions between mechanical and thermal effects. Many studies have been carried out to study the thermo-mechanical behaviour of ground (Campanella and Mitchell 1968; Laloui and Cekerevac 2008) and thermal piles (Bourne-Webb et al. 2009; Adam and Markiewicz 2009; Di Donna et al. 2016). From the thermal point of view, two study scales can be defined: the heat exchanger scale and the structure scale in its environment. The first issue has mobilized many research efforts from decades for the development of vertical borehole heat exchanger (Pahud et al. 1999). The second issue is related to the long-term behaviour of thermoactive geostructure and ground in terms of temperature variations and heat exchanges. The influence of the groundwater

A. Ferrari and L. Laloui (Eds.): SEG 2018, SSGG, pp. 11–18, 2019.
https://doi.org/10.1007/978-3-319-99670-7_2

flow is of major importance to assess the potential thermal plume and the natural thermal recharge. At this scale, the heat exchanges are governed by (i) the thermal conductivity through the concrete and the ground, (ii) the groundwater flow velocity that affects the thermal recharge and the heat exchange by advection (Fromentin and Pahud 1997; Barla et al. 2016), (iii) the temperature variation of the external air and (iv) the 3D shape of the structure that has an influence on the groundwater flow.

Some approaches considering the building scale have been developed to simulate thermal response tests (Signorelli et al. 2007; Zarella et al. 2017) and can be applied to thermoactives geostructures (Xia et al. 2012). Based on these studies, three main issues in terms of design can be dealt with: what are the long-term effects on the ground and on the groundwater? What is the real heat exchange between the ground and the structure? What are the contributions of conduction and advection in term of heat exchange related to the groundwater flow velocity?

In this paper, an original approach based on the study of the heat fluxes induced by conduction and advection and their contributions to volumetric thermal power is developed to assess the long-term behaviour of such structure and especially thermoactive diaphragm walls. It is illustrated with an example of Paris metro stations.

2 Assessment of Thermal Exchanges by Conduction and Advection

2.1 Analysis of the Energy Balance Equation

The energy balance equation governing the heat exchange between the ground and the structure includes the contributions of conduction and advection:

$$C_{eff}\frac{\partial T}{\partial t} + div\left(\vec{j}_{cond}\right) + div\left(\vec{j}_{adv}\right) - j_{int} = 0 \tag{1}$$

where C_{eff} is the effective specific heat (J/m^3.K), T the temperature (K), j_{cond} the conductive heat flux (W/m^2) j_{adv} the advective heat flux and j_{int} the production of intern volumetric heat (W/m^3) which is usually neglected regarding the low depth of the structures.

The theorem of Green-Ostrogradski links the flux to the divergence of the heat fluxes:

$$\oiint_{\partial v} \vec{j} \cdot dS = \iiint_{v} \vec{\nabla} \cdot \vec{j} dV \tag{2}$$

The direct calculation of the different component of the heat fluxes in 3D is complex. From the divergence calculation, the inlet and the outlet fluxes are calculated to characterise the heat exchange across a volume. It is also a way to analyse the temperature variations. Indeed, when the sign of the divergence is negative, resp. positive, the temperature increase, resp. decrease. The higher the divergence is, the faster the increase/decrease is. Moreover, at steady state, the sum of the divergence is null which implies that the inlet heat flux is equal to the outlet heat flux. It means

that, at null divergence, the energy of the system does not vary anymore and cannot gain or lose energy.

2.2 Application to the Thermoactives Geostructures

The divergence approach provides the thermal fluxes through a control volume defined by the first meter of ground close to the walls of the metro station (see Fig. 1). The control volume is defined to consider the heat exchange in every direction. The integration of the divergence on the control volume correspond to the thermal exchange at the time t between the ground and the structure $P_{tot}(t)$:

$$div\left(\vec{j}_{tot,i}(t)\right) = div\left(\vec{j}_{cond,i}(t)\right) + div\left(\vec{j}_{adv,i}(t)\right) \text{ at any point} \quad (3)$$

$$P_{tot}(t) = \sum_{i=1}^{n} V_i div\left(\vec{j}_{tot,i}(t)\right) \text{ for the control volume} \quad (4)$$

where n is the number of subdivisions of the volume and V_i the volume of the subdivision i (m^3).

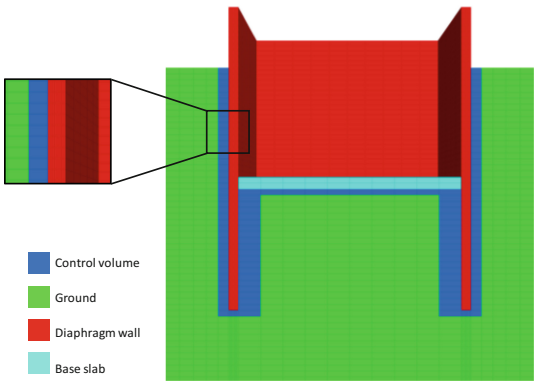

Fig. 1. Example of control volume around diaphragm wall

It is also possible to define a volume to assess the energy balance and predict a thermal drift.

3 Numerical Analysis

3.1 Methodology

3.1.1 Introduction

Within the framework of the diaphragm wall, it is essential to consider 3D effects. Indeed, the geometry of the underground structure can modify the initial characteristics of the groundwater flow (intensity and direction). It is called the dam effect. As the heat

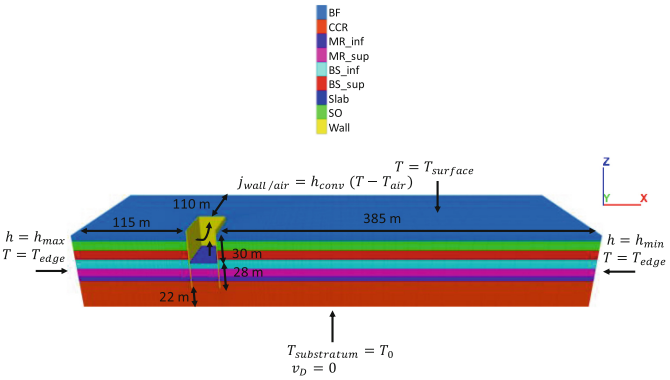

Fig. 2. Cross-section of the metro station 3D model

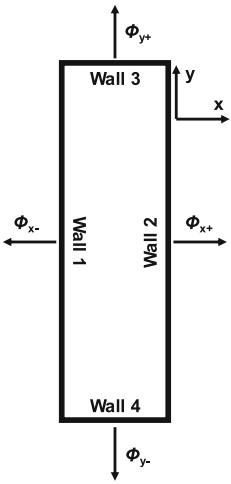

Fig. 3. Position of the walls and heat fluxes

flux by advection is proportional to the groundwater flow velocity, the heat fluxes at the interface ground/structure are function of the dam effect. Therefore, the heat exchange can vary for each diaphragm wall.

In the model, some local variables can be calculated: heat fluxes $\vec{j}(x,t)$ (W/m^2), divergence of the heat fluxes $div\left(\vec{j}(x,t)\right)$ (W/m^3), temperature $T(x, t)$ (K), groundwater flow velocity $\vec{v}_D(x,t)$ (m/s), heat exchange $P(x, t)$ (W), etc. Moreover, some global variables at the structure scale can be computed: global heat exchange $P_{tot}(t)$ (W), global mean heat flux $\Phi(t)$ (W/m^2) or by wall (see Fig. 3), thermal drift, etc. To represent the results of the simulations, it is also possible to define temporal means values, as the daily annual mean of global heat exchange $\overline{P}_{tot,year}$ ($W_{day/year}$) and the seasonal annual mean of heat fluxes $\overline{\Phi}_{year}$ $\left(W/m^2_{3month/year}\right)$.

It is essential to note that the main input data of the thermal solicitation of the thermoactive geostructure is the heating and cooling demand of the building. Indeed, the main goal is to determine how the ground reacts when this demand is satisfied partially or not. It is why the peak of demand and the global quantity of energy shall be considered. Indeed, a high peak demand is possible on a short period if the heat reservoir allows it. Within the framework of the thermoactives geostructures, the heat reservoir is the ground and the heat exchanges between the geostructure, the heat pump and the ground are only efficient if the ground can provide the right amount of heat. If it is not the case, the heat pump compensates with electric energy, decreasing its coefficient of performance.

3.1.2 Initial Conditions

The calculations are performed with the FLAC3D software (ITASCA 2013). The main assumptions considered are the following: the variation of the external air temperature, a desaturated zone in the subsurface and a convective heat flux between the internal air

of the structure and the walls. In a first step, the groundwater flow is initialised to simulate the dam effect. In a second step, the temperature in the ground is initialised according to the groundwater flow, the external air temperature variations and the heat exchanges between the internal air and the wall, before thermal activation of the structure. In this case, the external air temperature variations are governed by a sinusoidal signal.

Thereby, the temperature is equal to 14 °C from about ten-meter depth. However, in the first meters, the ground temperature is function of the depth. Regarding the classical geometry of diaphragm walls (<60 m depth), a non-negligible part of the structure is influenced by the external air temperature variations.

The thermal solicitation is applied as a nodal power in the plan of the heat exchanger tubes.

3.2 Typical Metro Station of the Grand Paris Express Project

3.2.1 Geometry, Boundary Conditions and Ground Parameters

Table 1 and Fig. 2 show the geometry and the boundary conditions of the model. Table 2 gives the geology and the thermo-hydraulic parameters used. The mesh is refined close to the diaphragm walls and it includes 411 450 nodes and 398 800 zones.

Table 1. Geometry and boundary conditions

Properties	Diaphragm wall	Base slab	Boundaries
Length [m]	100	100	+115 from diaphragm wall downstream/+385 from diaphragm wall upstream
Width [m]	30	30	+110 from diaphragm wall
Depth [m]	58	30	+22 from diaphragm wall
Thickness [m]	0.8	1	–

Boundary conditions		Symbol	Unity	Value
Thermal	Initial temperature	T_{ave}	[°C]	14
	Seasonal variation of temperature	$T_{surface}$	[°C]	2 (winter) – 26 (summer)
	Temperature of the substratum	$T_{substratum}$	[°C]	14
	Temperature of the edges	T_{edge}	[°C]	–
	Heat exchange convective coefficient	h_{conv}	[$W/m^2.K$]	1
	Inside air temperature	T_{air}	[°C]	20
	Damping depth	d	[m]	3
Hydraulic	Minimal water head	h_{min}	[m]	75
	Maximal water head	h_{max}	[m]	77

Table 2. Geology and thermo-hydraulic parameters

Geology*	BF	SO	BS_{sup}	BF_{inf}	MR_{sup}	MR_{inf}	CCR
Thickness [m]	6	10	10	11	5	15	> 10
Hydraulic conductivity [m/s]	$1{\cdot}10^{-5}$	$2{\cdot}10^{-5}$	$1{\cdot}10^{-5}$	$3{\cdot}10^{-6}$	$1{\cdot}10^{-3}$	$1{\cdot}10^{-3}$	$2{\cdot}10^{-4}$
Thermal conductivity [W/m/K]	1.7	2.1	2.3	2.3	2.1	2.1	2.4
Volumetric heat capacity [$MJ/m^3/K$]	2.2	2.2	2.3	2.3	2.2	2.2	2.2

**BF*: Backfill, *SO*: Saint-Ouen calcareous rock, *BS*: Beauchamp sands, *MR*: Marls and Rocks, *CCR*: Coarse Calcareous Rocks

4 Results

After the initialisation of the groundwater flow and the temperature field, a thermal solicitation is applied to the diaphragm walls at 20 cm from the interface ground/structure for ten years (see Fig. 4). Two signals are tested: a sinusoid perfectly balanced and a real solicitation with more heating than cooling on one year and with thermal rest during the night and the week-end.

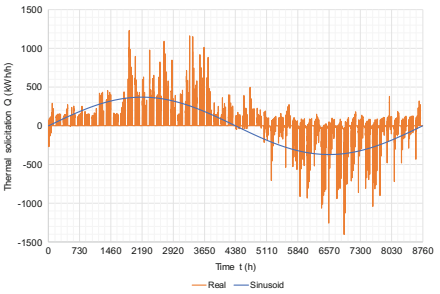

Fig. 4. Thermal solicitations apply to the diaphragm walls

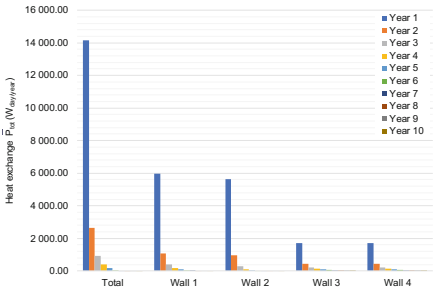

Fig. 5. Heat exchange based on the divergence approach – sinusoidal solicitation

Figure 5 presents the mean daily heat exchange calculated on one year $\overline{P}_{tot,year}$ ($W_{day/year}$) for the overall metro station and the four diaphragm walls for the sinusoidal solicitation. For the first year, the values are positive showing a decrease of temperature in the control volume. The values tend to decrease year after year until it reached zero at the fifth year. It can be concluded that there is no thermal drift in this control volume and consequently, at the scale of the structure. Indeed, the heat injected in the ground is stored during the cooling period (the first six month of the sinusoid) before its use during winter. As a result, the ground reaches the steady state after few cycles. Moreover, the temperature of the system is in the right range (+1/+35 °C) and the heat exchanges are mainly conductive due to the hydraulic context.

However, locally, in the zones where the groundwater flow velocity is the highest (on the corner), the advection is non-negligible, counting for 30% of the heat exchanges. In these zones, the heat cannot be stored and is dissipated by the groundwater flow leading to extreme temperature. Indeed, as there is no more reserve, the ground has to provide more heating or cooling.

Figure 6 presents the mean daily heat exchange calculated on one year $\overline{P}_{tot,year}$ ($W_{day/year}$) for the overall metro station and the four diaphragm walls for the real solicitation. Year after year, the values increased leading to a progressive cooling of the control volume. The steady state is not reached after ten years. However, the cooling decreased slowly. Furthermore, the thermal drift is higher at the wall 1 (upstream) and 2 (downstream) where the groundwater flow is the lowest due to the dam effect of the structure. Figure 7 presents the ratio between the mean seasonal heat flux on one year $\overline{\Phi}_{year}\left(W/m^2_{3month/year}\right)$ and the maximum mean seasonal heat flux on one year $\overline{\Phi}_{max,year}\left(W/m^2_{3month/year}\right)$ or the wall 1. It highlights the decrease of the performance related to the thermal drift. After ten years, the decrease of the performance of the system reached 10% for the autumn. These results are dependant of the thermal solicitation and of the wall.

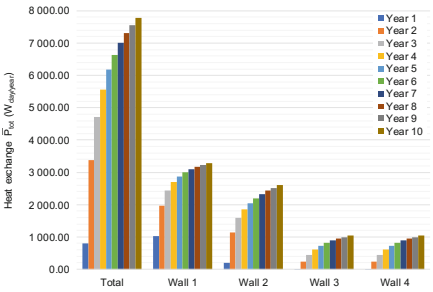

Fig. 6. Heat exchange based on the divergence approach – real solicitation

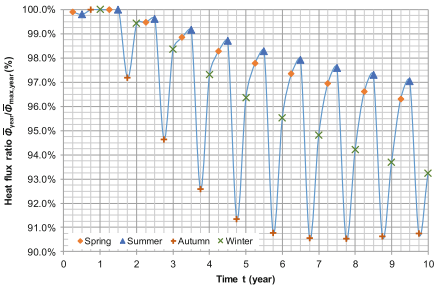

Fig. 7. Decreasing of the thermal performance related to the thermal drift – wall 1

5 Conclusion

The methodology developed in this paper aims at the assessment of the heat exchange between a thermoactive geostructure and the ground considering the heat conductive flux and the advective flux due to the groundwater flow velocity. The results highlight the zones and the conditions where the thermal drift is likely. Thereby, in the case of a perfectly balanced energy demand, the system does not drift and the steady-state is reached after few years. In the case of an unbalanced thermal solicitation, the temperature around the structure increases or decreases along the years, leading to lower and lower performances of the system. In each case, the heat exchange is function of the depth and of the diaphragm wall.

References

Adam, D., Markiewicz, R.: Energy from earth-coupled structures, foundations, tunnels and sewers. Géotechnique **59**(3), 229–236 (2009)

Barla, M., Di Donna, A., Perino, A.: Application of energy tunnels to an urban environment. Geothermics **61**, 104–113 (2016)

Brandl, H.: Energy foundations and other thermo-active ground structures. Géotechnique **56**(2), 81–122 (2006)

Bourne-Webb, P.J., Amatya, B., Soga, K., Amis, T., Davidson, C., Payne, P.: Energy pile test at Lambeth College, London: geotechnical and thermodynamic aspects of pile response to heat cycles. Géotechnique, **59**(3), 237–248 (2009)

Campanella, R.G., Mitchell, J.K.: Influence of temperature variations on soil behavior. J. Soil Mech. Found. Div. ASCE **94**(3), 709–734 (1968)

CFMS et SYNTEC.: Recommandations pour la conception, le dimensionnement et la mise en oeuvre des géostructures thermiques. Revue Française de Géotechnique **149**, 120 (2017)

Di Donna, A., Rotta, A.F., Laloui, L.: Numerical study of the response of a group of energy piles under different combinations of thermo-mechanical loads. Comput. Geotech. **72**, 126–142 (2016)

ITASCA.: FLAC3D Version 5.01 User's guide. Minnesota, USA: ITASCA Consulting Group, Inc. (2013)

Fromentin A., Pahud, D.: Recommandations pour la réalisation d'installations avec pieux échangeurs. Rapport final. Rapport d'étude n°120.104. Office fédéral de l'énergie, Lausanne, Suisse, 79 p. (1997)

Laloui, L., Cekerevac, C.: Numerical simulation of the non-isothermal mechanical behavior of soils. Comput. Geotech. **35**, 729–745 (2008)

Pahud, D., Fromentin. A., Hubbuch, M.: Heat exchanger pile system of the dock midfield at the Zürich Airport. Detailed simulation and optimization of the installation. Rapport final. Rapport d'étude n°120.110. Office fédéral de l'énergie, Lausanne, Suisse, 49 p. (1999)

Signorelli, S., Bassetti, S., Pahud, D., Kohl, T.: Numerical evaluation of thermal response tests. Geothermics **36**, 141–166 (2007)

Xia, C., Sun, M., Zhang, G., Xiao, S., Zou, Y.: Experimental study on geothermal heat exchangers buried in diaphragm walls. Energy Build. **52**, 50–55 (2012)

Zarella, A., Emmi, G., Zecchin, R., De Carli, M.: An appropriate use of thermal response test for the design of energy foundation piles with U-tube circuits. Energy Build. **134**, 259–270 (2017)

Analysis of Groundwater Advection and Ground-Heat Exchanger Spacing on Intermittent Ground-Source Heat Pump Operation

Scott Harold Lines(✉), Marcelo A. Llano-Serna, and David J. Williams

University of Queensland, Brisbane, Australia
s.lines@uq.edu.au

Abstract. Shallow geothermal systems allow both heating and cooling of structures by using the ground as a renewable energy source. These systems have received significant attention in recent decades and careful design consideration is necessary to ensure maximum efficiency. In this paper, the authors examine the impact of spacing between ground heat exchangers (GHE) and groundwater advection on a 5 × 5 array using a transient numerical model. The conditions chosen represent those experienced in Brisbane, Australia. The energy load used represents four months of cooling and three months of heating annually, a simplification based on local conditions. The spacing explored ranged from 4–10 m between GHEs and the groundwater flow examined included 0.1, 10, 30 and 50 m/year. The results show increasing spacing reduces thermal interference and increases the sustainability over the lifetime of the system, represented as 25 years in this study. In these conditions, a GHE spacing of 4 m can experience temperatures 8.5 °C larger then when the spacing is 10 m. While increasing spacing increased sustainability, this did not prevent an imbalanced load reducing efficiency overtime. Furthermore, it was found groundwater flow had a positive impact on sustainability, over the lifetime of the system a temperature 3.1 °C lower was experienced when a groundwater flow of 0.1 m/year was compared to 50 m/year. Such an impact should be taken into consideration during the design phase due to the reduced GHE length required.

1 Introduction

The use of shallow geothermal energy has been growing rapidly in recent decades as a source for renewable energy. Part of the reason for increased popularity has been a pronounced push to switch to cleaner forms of energy as a method of both lowering electricity bills and reducing pollution. Ground source heat pump (GSHP) systems have seen the largest increase in usage as the most popular shallow geothermal technology (Lund et al. 2015). GSHPs utilize the steady surface temperatures of ground throughout the year in the order of tens of meters deep. Providing heating for winter by using the ground as a heat source and cooling for summer by using the ground as a heat sink. The advantage of GSHP systems is the high efficiency that can be obtained when

A. Ferrari and L. Laloui (Eds.): SEG 2018, SSGG, pp. 19–26, 2019.
https://doi.org/10.1007/978-3-319-99670-7_3

compared to more traditional heating and cooling technologies (Self et al. 2013), furthermore a reduction in CO_2 emissions makes the technology more attractive as an alternative energy option (Blum et al. 2009).

Often in practice, a GSHP system experiences a load imbalance and thermal recovery is required to take place to ensure the system can be sustainable. An imbalance occurs when more energy is put in the ground then taken out, or *vice versa*. Over time this reduces efficiency and can eventually lead to a complete termination of operations, to allow thermal recovery to take place (Qian and Wang 2014; Yang et al. 2013). This process of thermal recovery can take years in extreme cases (Epstein and Sowers 2006; Ryback and Mongillo 2006). Such events outline why ensuring a sustainable system is imperative during the design stage; further refurbishments after installation are often a costly prospect. If natural recovery is not possible then other methods can be employed in order to correct the balance. Techniques to help with ensuring sustainability may include installation of a cooling tower, water-chilled cooler or using cool night air through an integrated soil cold storage system (Wan et al. 2017; Zhou et al. 2016). Alternatively installation of a supplemental heat rejecter, an extra loop designed to dispel excess heat has been shown to increase efficiency by up to 21% (Park et al. 2012). These methods help ensure a sustainable system, however add extra costs, while increasing complexity and maintenance.

Local conditions will dictate the recovery time, for closed systems in unconsolidated materials, with little or no groundwater flow, the surrounding temperature influence will not reach a steady state in one cycle. However, with larger groundwater flows in material such as sand or gravel, steady state conditions could be reached within one cycle (Hähnlein et al. 2013). Furthermore, an additional element to take into consideration is the local ecosystem and environment, decreasing or increasing the soil temperature can influence chemical, biological and physical properties of the ground and groundwater (Brielmann et al. 2009; Brons et al. 1991; Griffioen and Appelo 1993; Hall et al. 2008). When designing GSHP systems it is vital that the heat transfer process through soil based on local conditions is analyzed during the design phase for the expected lifetime of any system.

The main objective of this paper was to investigate the effects of GHE spacing and groundwater flow on the intermittent operation of a GSHP system in a cooling dominated environment such as Brisbane, Australia. The soil and climate conditions used were representative of local conditions. By studying 25 years' of intermittent operation, the ground temperature in the immediate vicinity of the GHE was analyzed. This paper provides a reference for utilization in GSHP design for cooling dominated climates.

2 Numerical Model

In this study the commercial software COMSOL (COMSOL Multiphysics 2013) has been utilized to develop a numerical model for vertical GSHP to calculate the 2D transient heat and mass transport processes with satisfactory accuracy and minimal computational effort. The proposed model simplifies the borehole as a cylindrical heat source to compute the thermal long-term behavior. The diameter for the GHEs is 0.3 m and the far field uses the formula 15 L_b (see Fig. 1a). The mesh surrounding the GHEs

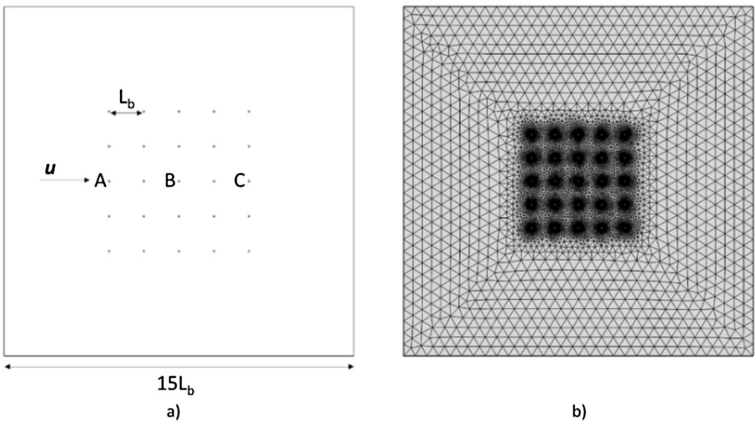

Fig. 1. (a) Drawing of GHE field, (b) Mesh used for modelling purposes.

has a much higher density and becomes coarser based on proximity from the center (see Fig. 1b). The GHE using notation A represents the upstream, B is the center GHE and C the downstream GHE.

Heat transfer surrounding the GHEs is primarily by conduction in the soil, with advection occurring when sufficient groundwater flow is present. The pure conductive heat transfer is governed by:

$$\rho c_p \frac{\partial T}{\partial t} + \nabla \cdot (-\boldsymbol{k} \nabla T) = 0 \tag{1}$$

Equation 1 is solved for temperature, T (°C), ρ represents density (kg/m^3) and c_p specific heat capacity (J/kg K). This model has been validated in numerous conditions (Gashti et al. 2014; Wei et al. 2016). In porous soil, a groundwater flux can occur and has the potential to transfer heat at a faster rate than conduction. This heat transfer occurs through advection and is calculated using Darcy's Law:

$$\nabla \cdot (\rho \boldsymbol{u}) = Q_m \tag{2}$$

$$\boldsymbol{u} = -\frac{\kappa}{\mu} \nabla p \tag{3}$$

Equation 2 involves the density, ρ, (kg/m^3) and Darcy velocity, $\boldsymbol{u}$, (m/s) is equal to the mass flow, Q_m, (kg/m^3 s). Equation 3 states that the Darcy velocity is equal to the porous medium, κ, (m^2), divided by the dynamic viscosity of the fluid, u, (Pa s), and multiplied by the unit vector of pressure, p, (Pa), which is used when the flux is driven by gradients in hydraulic conductivity, this formula ignores the gravity effects of the elevation. As the simulation is being run in Brisbane, Australia, the geothermal system is operated with four months of cooling (heat injection), representing the months November to February in the summer and three months of heating (heat extraction), representing the winter from June until August. The initial ground temperature is taken

as 22.5 °C (Lines et al. 2017). The operation period is 25 years and uses a heat transfer rate of 30 Wm^{-2}, a positive value is used to represent heat injected into the ground and a negative value is used to represent heat extracted from the ground.

2.1 Site Characterization

Investigation of a site in Brisbane, Australia was undertaken and a number of thermal response tests were performed on a three U-loop energy pile with a depth of 13.5 m using water as the heat carrying fluid. This site was used as the basis for numerical investigation carried out in this study. The geological-geotechnical environment may be classified as estuary deposits comprising of a significant amount of shells and organic matter. Laboratory classification testing showed the soil profile as silty clays for the initial 3 m, followed by clayey sands until 8 m and further silty clays from then onwards. An averaged density of 1700 kg/m^3 was used for this study and is based on laboratory results. Groundwater was present from 1.7 m and the thermal conductivity was approximately 1.88 W/m K with a specific heat capacity of 2800 J/kg K.

3 Results and Discussion

The 2D model was used to evaluate the long-term effects of a temperature imbalance on the operation of GSHP over 25 years. One method to increase sustainability is to increase the spacing (represented by L_b) and hence the volume of soil that is used for heat injection and extraction. As the space increases the interference between GHE decreases and the heat recovery improves. The temperature increase based on different spacing (from 4 to 10 m) without groundwater flow is shown in Figs. 3 and 4 (moving average). Spacing of 4 m results in the largest heat increase over the lifetime, the soil around the borehole has increased to a maximum of 42.6 °C by the 25th year of operation and continues to increase each year. Increasing the space to 6 m, results in a maximum temperature of 38.1 °C, a substantial decrease from the high temperatures reach using a spacing of 4 m. Further increasing spacing to 8 m drops the maximum to 35.6 °C and a spacing of 10 m to 34.1 °C, illustrating the diminishing returns from

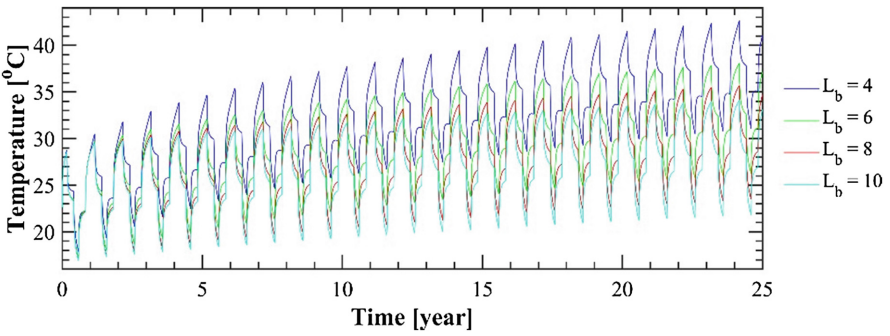

Fig. 2. Long-term temperature response with varying GHE spacing

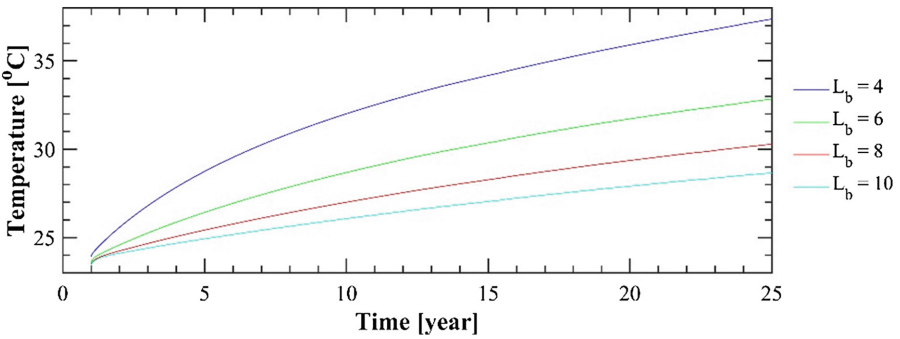

Fig. 3. Moving average of temperature with varying GHE spacing

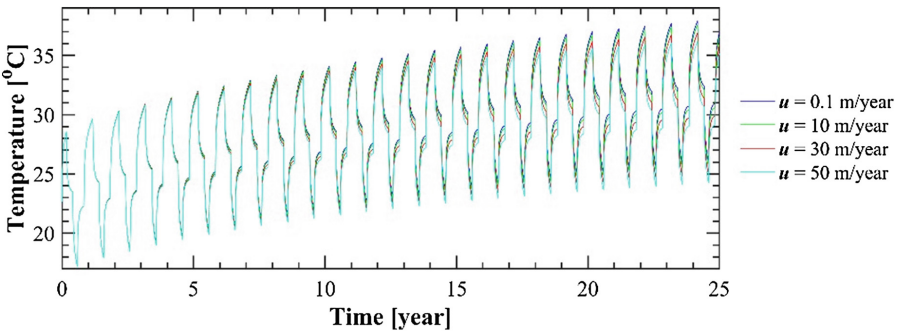

Fig. 4. Temperature from intermittent operation with varying groundwater flow

increased spacing. A GHE spacing of 10 m is significant and the temperature continues increasing from a maximum of 28.6 °C in the 1st year of operation to 34.1 °C in the 25th year without reaching a steady state. Such a significant increase in temperature, despite a large distance between each GHE, displays the need to investigate further methods of ensuring sustainability when a load imbalance is present (Fig. 2).

Groundwater flow, influenced by hydraulic gradient and hydraulic conductivity can significantly enhance the heat transfer properties of soil through the addition of advection. Therefore, it is vital to examine groundwater flow during the design phase, as it can potentially save on capital costs (i.e. drilling). For the purposes of examining the impact of groundwater flow a GHE spacing of 6 m is chosen, and the groundwater flows 0.1, 10, 30 and 50 m/year are investigated. This flow range is representative of soil varying from a clay to coarse sand; however, for the purposes of this example the thermal properties used are those aforementioned despite the soils having differing thermal properties in practice.

Figure 4 displays the temperature increase over a period of 25 years comparing the center GHE (B), demonstrating that even with a large flow at 50 m/year there is still a temperature increase over time due to the energy load imbalance. However, it is

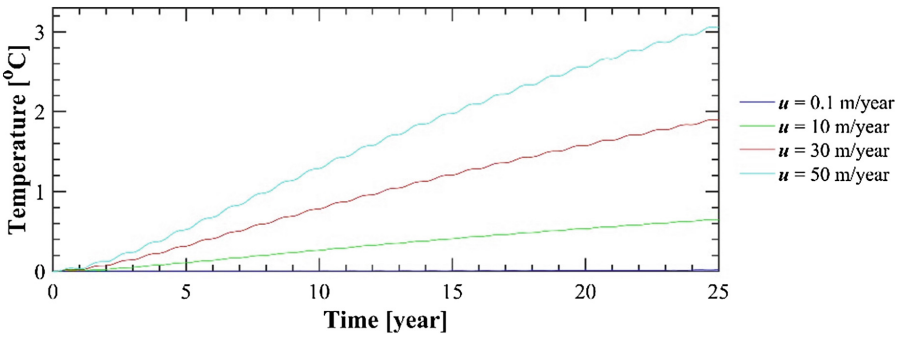

Fig. 5. Difference between upstream and downstream GHE temperature over time

important to consider that the edge GHEs will be impacted differently. The upstream GHE (A) will lose heat at a faster rate than the downstream GHE (C).

Figure 5 displays the temperature difference between the upstream GHE and the downstream GHE for the various groundwater flows. When the flow is very minor at 0.1 m/year, the difference between the upstream and downstream GHEs is approaching zero. However, once the flow is 50 m/year is reached the difference between GHE over the lifetime increases to approximately 3.1 °C.

4 Summary and Conclusions

This paper examines the long-term effects of an energy load imbalance investigating both GHE spacing and groundwater flow using soil conditions and example intermittent energy loads found in Brisbane, Australia. This study aims to quantify the impact of an imbalance over a 25-year period to determine the overall impact this has on sustainability and feasibility of a GSHP. Several conclusions were drawn from this study, as follows:

1. Increasing the GHE spacing reduces the thermal interference between GHEs, this reduces the maximum temperatures reached and increases the sustainability and lifetime of the GHSP system. However, an imbalanced energy load still had a detrimental impact on operations despite significantly large spacing being examined. Due consideration of spacing is essential when an imbalanced load is generated through local energy requirements.
2. Groundwater flow can significantly accelerate the diffusion of heat downstream. This aspect should be taken into consideration at the earliest opportune time in order to ensure the GHE field is arranged to maximum the efficiency gains and minimize the potential negative consequences. Over the lifetime of the GSHP system this impact becomes extremely beneficial.
3. Groundwater flow and increased GHE spacing does not completely eliminate the impact of an imbalanced energy load and over time this will result in a decrease in efficiency if thermal recovery is not allowed to take place.

Acknowledgements. The authors gratefully acknowledge the support provided by John Wagstaff and his company Wagstaff Pty Ltd for his assistance in constructing and installing the energy pile and for the use the location for further testing.

References

Blum, P., Campillo, G., Münch, W., Kölbel, T.: CO2 savings of ground source heat pump systems – a regional analysis. Renew. Energy **35**, 122–127 (2009). https://doi.org/10.1016/j.renene.2009.03.034

Brielmann, H., Griebler, C., Schmidt, S.I., Michel, R., Lueders, T.: Effects of thermal energy discharge on shallow groundwater ecosystems. FEMS Microbiol. Ecol. **68**(3), 273–286 (2009). https://doi.org/10.1111/j.1574-6941.2009.00674.x

Brons, H.J., Griffioen, J., Appelo, C.A.J., Zehnder, A.J.B.: (Bio)geochemical reactions in aquifer material from a thermal energy storage site. Water Res. **25**(6), 729–736 (1991). https://doi.org/10.1016/0043-1354(91)90048-U

COMSOL Multiphysics.: Comsol Multiphysics Reference Manual (2013)

Epstein, C.M., Sowers, L.S.: The continued warming of the stockton geothermal well field. In: Proceedings of the ECOSTOCK Symposium: Galloway, pp. 1–5. Richard Stockton College of New Jersey, New Yersey (2006)

Gashti, E.H.N., Uotinen, V.-M., Kujala, K.: Numerical modelling of thermal regimes in steel energy pile foundations: a case study. Energy Build. **69**, 165–174 (2014). https://doi.org/10.1016/j.enbuild.2013.10.028

Griffioen, J., Appelo, C.A.J.: Nature and extent of carbonate precipitation during aquifer thermal energy storage. Appl. Geochem. **8**(2), 161–176 (1993). https://doi.org/10.1016/0883-2927(93)90032-C

Hähnlein, S., Bayer, P., Ferguson, G., Blum, P.: Sustainability and policy for the thermal use of shallow geothermal energy. Energy Policy **59**, 914–925 (2013). https://doi.org/10.1016/j.enpol.2013.04.040

Hall, E.K., Neuhauser, C., Cotner, J.B.: Toward a mechanistic understanding of how natural bacterial communities respond to changes in temperature in aquatic ecosystems. ISME J. **2**(5), 471–481 (2008). https://doi.org/10.1038/ismej.2008.9

Lines, S., Williams, D.J., Galindo-Torres, S.A.: Determination of thermal conductivity of soil using standard cone penetration test. Energy Procedia **118**, 172–178 (2017). https://doi.org/10.1016/j.egypro.2017.07.036

Lund, J.W., Freeston, D.H., Boyd, T.L.: Direct utilization of geothermal energy 2015 worldwide review. Geothermics **40**(3), 159–180 (2015). https://doi.org/10.1016/j.geothermics.2011.07.004

Park, H., Lee, J.S., Kim, W., Kim, Y.: Performance optimization of a hybrid ground source heat pump with the parallel configuration of a ground heat exchanger and a supplemental heat rejecter in the cooling mode. Int. J. Refrig. **35**(6), 1537–1546 (2012). https://doi.org/10.1016/j.ijrefrig.2012.05.002

Qian, H., Wang, Y.: Modeling the interactions between the performance of ground source heat pumps and soil temperature variations. Energy. Sustain. Dev. **23**, 115–121 (2014). https://doi.org/10.1016/j.esd.2014.08.004

Ryback, L., Mongillo, M.: Geothermal sustainability-a review with identified research needs. GRC Trans. **30**, 1083–1090 (2006). https://doi.org/10.1177/0146167200268006

Self, S.J., Reddy, B.V., Rosen, M.A.: Geothermal heat pump systems: Status review and comparison with other heating options. Appl. Energy **101**, 341–348 (2013). https://doi.org/10.1016/j.apenergy.2012.01.048

Wan, H., Xu, X., Li, A., Yan, T., Gang, W.: A wet-bulb temperature-based control method for controlling the heat balance of the ground soil of a hybrid ground-source heat pump system. Adv. Mech. Eng. **9**(6), 168781401770170 (2017). https://doi.org/10.1177/1687814017701705

Wei, J., Wang, L., Jia, L., Cai, W.: A new method for calculation of short time-step g-functions of vertical ground heat exchangers. Appl. Therm. Eng. **99**, 776–783 (2016). https://doi.org/10.1016/j.applthermaleng.2016.01.105

Yang, W., Chen, Y., Shi, M., Spitler, J.D.: Numerical investigation on the underground thermal imbalance of ground-coupled heat pump operated in cooling-dominated district. Appl. Therm. Eng. **58**(1–2), 626–637 (2013). https://doi.org/10.1016/j.applthermaleng.2013.04.061

Zhou, S., Cui, W., Li, Z., Liu, X.: Feasibility study on two schemes for alleviating the underground heat accumulation of the ground source heat pump. Sustain. Cities Soc. **24**, 1–9 (2016). https://doi.org/10.1016/j.scs.2016.03.014

Smart Ground-Source Borehole Heat Exchanger Backfills: A Numerical Study

Douglas D. Cortes[1(✉)], Ali Nasirian[1], and Sheng Dai[2]

[1] New Mexico State University, Las Cruces, USA
dcortes@nmsu.edu
[2] Georgia Institute of Technology, Atlanta, USA

Abstract. Geothermal heat pump borehole heat exchangers rely on sensible heat for energy storage and low thermal conductivity materials for heat transfer. This paper examines numerically the potential benefits of an engineered backfill on the performance of a borehole heat exchanger. The results show that improving the thermal conductivity of the backfill and introducing a phase change material for energy storage can alter the thermal radius of influence of the borehole, improve the system efficiency, and reduce long-term changes in ground temperature.

1 Introduction

Ground-source Heat Pump (GHP) systems use heat exchangers buried into the ground to extract (heating) or inject (cooling) heat. Heat exchangers (HE) come in vertical or horizontal arrays, and in some cases may double as structural elements. In all cases, the HEs rely on the soil sensible heat storage capacity. That is, heat extraction or injection results in temperature changes within the soil. The magnitude and extent of these temperature changes depend on the heating/cooling demand and on the properties of the soil (thermal conductivity, heat capacity, density, degree of saturation, etc.). Daily extraction/injection of heat dominate the thermal radius of influence of a heat exchanger and dictate the minimum spacing required between neighboring HEs to avoid mutual interference. Under a balanced thermal load, the heat extracted from the soil for heating is later replenished by the heat injected during cooling. However, seasonal imbalances between the thermal energy extracted and injected will result in progressive changes in the ground temperature. Since the original design of a GHP system is predicated on the ground maintaining a constant mean temperature, the progressive temperature change negatively impacts the system's efficiency which can diminish to the point of making it economically unviable (Rybach and Mongillo 2006).

Thermal energy can also be stored in the form of latent heat. The energy storage, in this case, is given by $Q = m \cdot \Delta HPC$, where ΔHPC is the latent heat or enthalpy of transformation. Unlike sensible heat, latent heat storage takes place at constant temperature. Thermal energy is stored in or released from the molecular structure of a material when its temperature reaches the phase transformation temperature and does not result in a temperature change. Thus, latent heat storage provides an increase in the heat storage capacity at a constant temperature. In the last decade, biodegradable

A. Ferrari and L. Laloui (Eds.): SEG 2018, SSGG, pp. 27–34, 2019.
https://doi.org/10.1007/978-3-319-99670-7_4

non-toxic phase-change-materials (PCMs) have been developed to target a range of phase transition temperatures between −40 and 150 °C The technology has matured to the point of industrial production and PCMs of tailored thermal properties are readily available in the form of solids, encapsulated particles, and slurries (Farid et al. 2004; Khudhair and Farid 2004; Zalba et al. 2003).

In this paper, the authors explore numerically the effects of incorporating a phase change material into the backfill of a borehole heat exchanger to limit the temperature changes induced in the ground and improve the overall efficiency of GHP systems.

2 Numerical Model

Typical BHEs are constructed by drilling 10.6 cm diameter boreholes to depths between 50 and 150 m. The piping consists of a 2.54 cm diameter plastic U-loop, and the borehole is backfilled with bentonite grout (Lund 1988), see Fig. 1a. The backfill is intended to provide: mechanical support for the borehole during construction, a medium for heat conduction from the pipe to the ground, and a low hydraulic conductivity seal around the pipes to prevent loss of cooling fluid. The thermal conductivity, λ_T, of soils varies between 0.07 $W{\cdot}m^{-1}{\cdot}K^{-1}$, for dry clays under low effective stress, to 4.2 $W{\cdot}m^{-1}{\cdot}K^{-1}$, for saturated sands at high confining stress. The large variation in thermal conductivity results from its dependency on particle size, d_p, void ratio, e, effective stress, σ', stiffness, E, and moisture content, w (Andersland and Ladanyi 2004; Cortes et al. 2009; Farouki 1985; Nasirian et al. 2015). The effective stress dependency of thermal conductivity in granular media dictates that, even in a homogeneous soil deposit, λ_T varies with depth. The specific heat capacity, C_p, depends primarily on e and w, which are also expected to change as a function of the soil type and depths.

Previous attempts to alter the thermal properties of backfills have concentrated on the thermal conductivity of the grout yet very little work has been done in trying to engineer the backfill thermal storage capacity to improve the overall efficiency of the GHP system. The following sections present a numerical study of the potential effects of altering the thermal properties of the backfill, in particular, the incorporation of a phase change material.

2.1 Description of the Numerical Model

In all simulations, the soil is assumed to be initially in equilibrium at 15 °C, and to have a thermal conductivity of 0.2 $W{\cdot}m^{-1}{\cdot}K^{-1}$, a specific heat capacity of 828J $kg^{-1}{\cdot}K^{-1}$, and a density of 1390 $kg{\cdot}m^{-3}$, typical values for dry sands. The model uses the axisymmetric geometry depicted in Fig. 1b. In the interest of simplifying the simulations and concentrating on the response of the backfill, the model uses a line source for heat injection and extraction. The thermal dampening effect of fluid flow and the PVC pipe are not considered in this model. A line source 10 cm in length is used as input, establishing a uniform temperature along the heat source that varies as a function of time according to the equation:

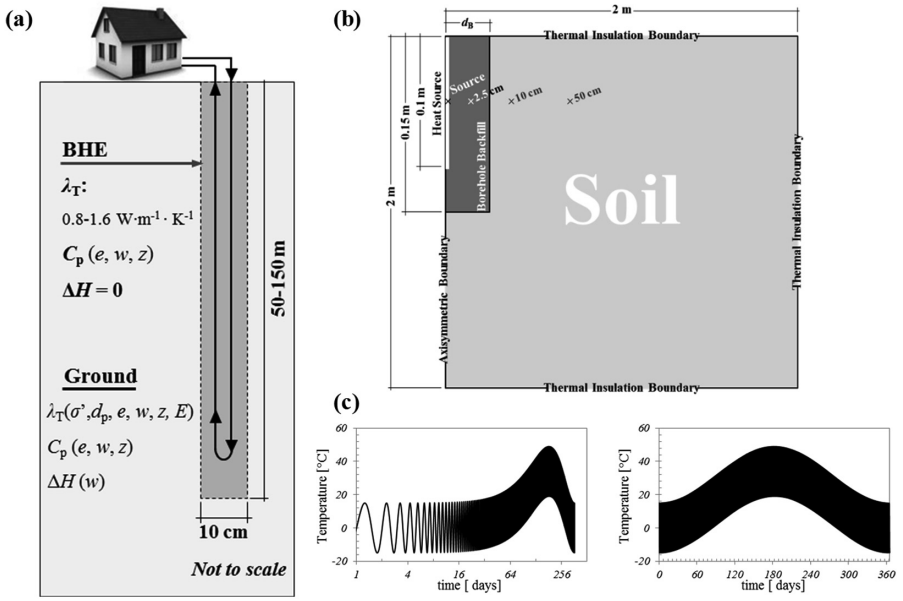

Fig. 1. Model descriptions. (a) Schematic of a typical Borehole Heat Exchanger (BHE). (b) Numerical model geometry. The underlined points are located at the following radial distances from the source: Source = 0 cm, 2.5 cm, 10 cm, and 50 cm. (c) Input temperature signal as a function of time. The semi-logarithmic plot (left) shows detail on the daily and yearly variations in temperature, which appear as a thick sinusoidal wave in linear-scale (right). Thus, the thickness of the line captures daily fluctuations in temperature.

$$T = 17 - 17\cos\left(\frac{2\pi t}{3.15 \times 10^7}\right) + 15\sin\left(\frac{2\pi t}{8.64 \times 10^4}\right). \quad (1)$$

The selected $T_{(t)}$ function approximates the daily and seasonal variation in temperature for Las Cruces, NM, USA. Time t is in units of seconds. The input temperature function is presented in Fig. 1c. The numerical model was developed using COMSOL Multiphysics®.

3 Simulations

The BHE can be engineered by altering the thermal conductivity and heat capacity of the backfill. While these changes alter heat transfer and storage within the BHE, the nature of heat injection and extraction remains the same, i.e., sensible heat. Thus, the borehole and the ground experience a change in temperature in response to a change in thermal energy. Numerical models of an embedded line heat source for the following cases are presented:

(a) Base case: ground in direct contact with the heat source.
(b) BHE: the heat source is embedded in a 10 cm-diameter conventional backfill.
(c) High thermal conductivity BHE: 10 cm-diameter backfill modeled with high thermal conductivity.
(d) Large BHE: the heat source is embedded in a 1 m-diameter conventional backfill.

3.1 Latent Heat

Latent heat is the thermal energy absorbed or released by a material undergoing phase change. The key difference between sensible and latent heat is that the latter occurs at constant temperature. Latent heat storage is not currently used in geothermal systems because the only Phase Changing Material (PCM) naturally available in the attainable temperature range is water (0 °C). Since the temperature difference between the ground and phase change (typically 18 °C) is large, the ground will experience extensive temperature difference ΔT before heat can be stored as latent heat. Furthermore, the volumetric expansion associated with the phase change of water could lead to undesirable ground volume changes (Loveridge et al. 2012). Thus, an effort is made to avoid freezing temperatures in the ground.

Latent heat storage provides an increase in the heat storage capacity at a constant temperature. Thus, incorporating PCMs as part of an engineered borehole backfill could result in: a reduction in the required BHE depth (i.e., improved operating efficiency), a reduction in the BHE radius of influence (i.e., feasibility in urban areas) and a reduction in the long-term temperature change (i.e., improved sustainability). Numerical simulations of latent heat enabled BHEs are presented for the following three cases: (e) Ground TPC: The phase transformation temperature matches the initial ground temperature (15 °C); (f) Summer savings I: The phase transformation temperature matches the summer hottest day mean temperature (25 °C); (g) Winter savings I: The phase transformation temperature matches the winter coldest day mean temperature (7 °C); (h) Summer savings II: The phase transformation temperature is closer to the summer hottest day minimum temperature (20 °C); (i) Winter savings II: The phase transformation temperature is closer to the winter coldest day maximum temperature (12 °C). The material properties used in the simulations are summarized in Table 1.

Table 1. Material properties used in the numerical simulations

Case	Borehole thermal properties					
	d_B [cm]	λ_T [W $m^{-1}{\cdot}K^{-1}$]	C_p [J $kg^{-1}{\cdot}K^{-1}$]	ρ [kg·m^{-3}]	ΔH_{PC} [J·gr^{-1}]	T_{PC} [°C]
(a)	0	-NA-	-NA-	-NA-	-NA-	-NA-
(b)	10	0.2	2000	1390	0	-NA-
(c)	10	5	2000	1390	0	-NA-
(d)	100	0.2	2000	1390	0	-NA-
(e)	10	0.2	2000	1390	205	15
(f)	10	0.2	2000	1390	205	25
(g)	10	0.2	2000	1390	205	7
(h)	10	0.2	2000	1390	205	20
(i)	10	0.2	2000	1390	205	12

4 Results and Discussions

The results of the first four simulations, case (a) through (d), are presented in Fig. 2. Each plot presents the input temperature signal at the source, $T_{(t)}$, and the induced temperature changes within the BHE at radial distances of 2.5 cm and in the ground at radial distances of 10 cm and 50 cm from the source. Minor differences between the Base case (a) and the BHE case (b) are to be expected based on the small size of the borehole and the selection of material properties. An increase in the thermal conductivity of the backfill (c) results in a significant increase in the amplitude of the temperature variation both within the BHE and in the ground. This indicates an improvement in heat conduction which comes at the cost of an increase in the thermal radius of influence (thicker lines at 2.5 cm and 10 cm radial distances from the source). Finally, a large BHE (d) increases the sensible heat storage capacity in the vicinity of the source, leading to a very modest reduction in the radius of influence (slightly thinner line in 10 cm radial distances from the source).

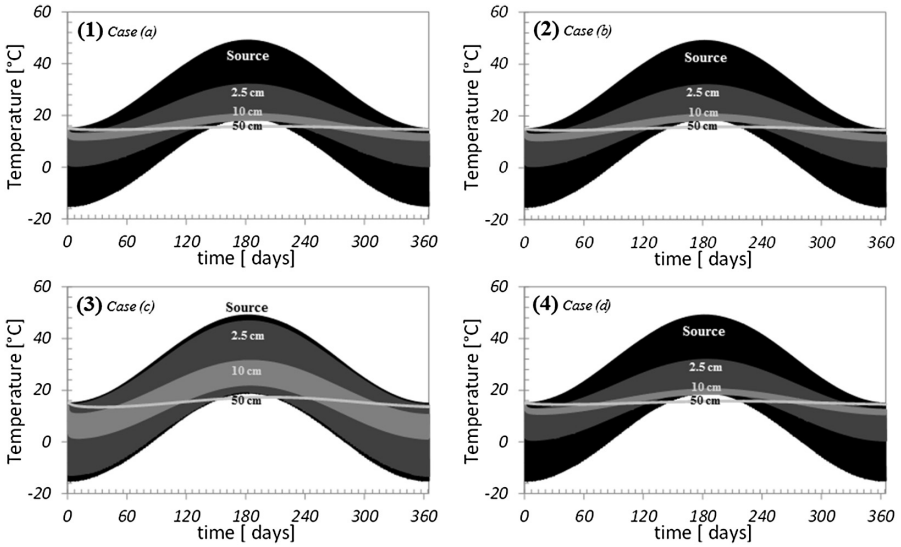

Fig. 2. Input temperature with time. The semi-logarithmic plot (left) shows detail on the daily and yearly variations in temperature, which appear as a thick sinusoidal wave in linear-scale (right). Thus, the thickness of the line captures daily temperature fluctuations.

The only significant changes in the ground thermal response under sensible heat thermal energy storage are observed by increasing the thermal conductivity of the backfill. Note that while increasing the backfill λ_T can lead to more efficient heat transfer and reductions in the required BHE depth, the increase in the thermal radius of influence could lead to interference with neighboring BHEs and/or unintended depletion of neighboring geothermal reservoirs.

Results for the cases (e), (f) and (g) are presented in Fig. 3 along with that of case (a) for comparison. Selected phase transformation temperature and latent heat values correspond to commercially available PCM materials (Entropy Solutions Inc.). Latent heat thermal energy storage in the backfill causes the thermal field in both the BHE and the ground to change for temperatures in the vicinity of TPC. Latent heat storage causes a reduction in the daily temperature variation (line thickness). The effect is more pronounced when the mean input temperature is close to TPC, spring and fall for case (e) simulations and summer and winter for cases (f) and (g) respectively. However, observed changes in daily temperature variation cannot adequately assess the overall effect of the PCM on the system efficiency.

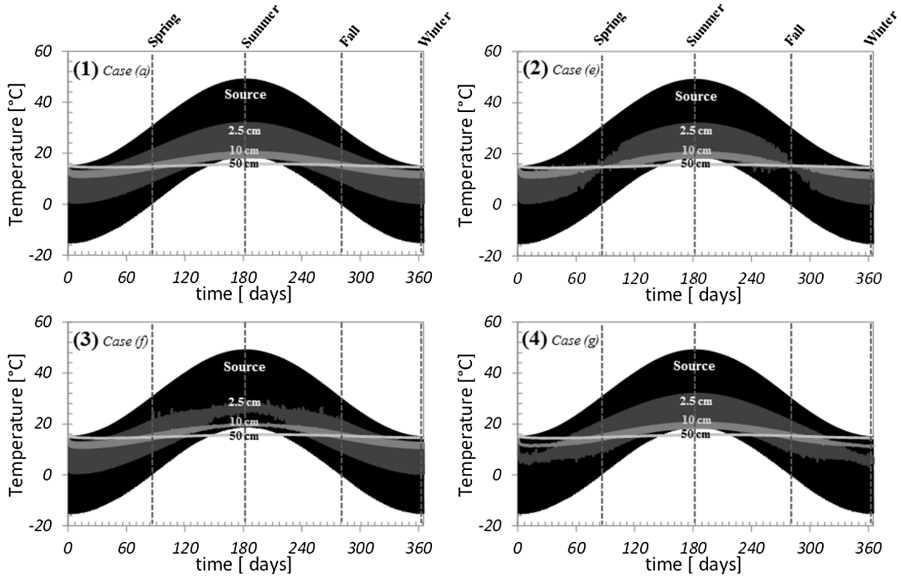

Fig. 3. Numerical modelling results for latent and sensible heat thermal energy storage. (a) Base case, (e) Ground TPC, (f) Summer savings, and (g) Winter savings. Each plot presents the input temperature signal at the source, $T_{(t)}$, and the induced temperature changes within the BHE at 2.5 cm from the source and in the ground at radial distances of 10 cm and 50 cm. The line thickness captures daily fluctuation in temperature.

Figure 4 shows the average daily temperature as a function of time at a radial distance of 2.5 cm from the line source for cases (e), (f) and (g) compared to the case (a) for reference. The figure shows that despite the reduction in the amplitude of the thermal oscillation observed in Fig. 3-4, the average daily temperatures in the winter (Fig. 4-1) decrease when $T_{pc} = 7$ °C. This implies that the presence of the PCM ($T_{pc} = 7$ °C) actually reduces the efficiency of the system. Similar results are observed for summer temperatures when $T_{pc} = 25$ °C (Figs. 3-3, 4-3). The only substantial improvement in system efficiency is observed in spring and fall when $T_{pc} = 15$ °C, see Fig. 4-2.

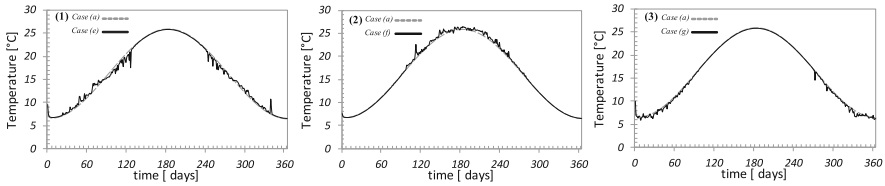

Fig. 4. Average daily temperature changes, Case (a) base case, Case (g) T_{pc} = 7 °C, Case (e) T_{pc} = 15 °C, Case (f) T_{pc} = 25 °C.

Further simulations conducted at T_{pc} = 12 °C and Tpc = 20 °C show an increase in winter average daily temperature (Fig. 5-1) and a decrease in summer average daily temperature (Fig. 5-2). These results indicate that in order to increase the system efficiency in the winter months, the appropriate T_{PC} should be above the minimum average daily temperature of the year. Similarly, an improvement in efficiency in the summer months requires the use of a PCM with T_{pc} below the maximum average daily temperature of the year.

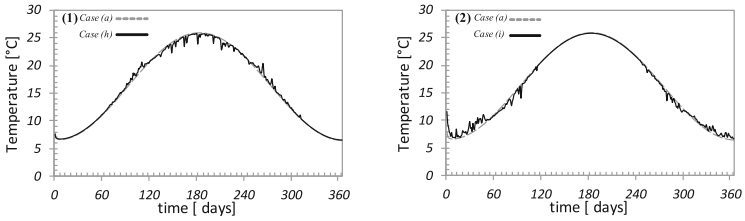

Fig. 5. Average daily temperature changes, Case (i) T_{pc} = 12 °C, Case (h) T_{pc} = 20 °C.

5 Conclusions

The results of this study demonstrate that the performance of a ground source borehole heat exchanger can be altered by modifying the thermal properties of the backfill, mainly the thermal conductivity and latent heat storage capacity. Numerical simulations show that an increase in thermal conductivity improves heat transfer leading to shorter boreholes but with a larger radius of influence. The results also show that the introduction of a PCM as part of the backfill in a geothermal BHE can, despite the relatively small size of the BHE, effectively alter its thermal radius of influence and overall system efficiency. The partial storage and release of thermal energy from changes in the molecular structure of the PCM reduce the change in sensible heat in the ground.

Furthermore, our simulations also show that the phase transformation temperature can be tailored to improve the system efficiency along the year. Reductions in the average daily temperatures during the summer can be attained by selecting a PCM with a phase transformation temperature below the maximum average temperature in the

summer. Similarly, increments in the average daily temperatures during the winter can be attained by selecting a PCM with a phase transformation temperature above the minimum average daily temperature in the winter.

Acknowledgements. Support for this work was provided by the Engineering Research Center Program of the National Science Foundation under NSF Cooperative Agreement Number EEC-1449501. Any opinions, findings and conclusions, or recommendations expressed in this material are those of the author(s), and do not necessarily reflect those of the NSF.

References

Andersland, O.B., Ladanyi, B.: Frozen Ground Engineering. Wiley, London (2004)

Cortes, D.D., Martin, A.I., Yun, T.S., Francisca, F.M., Santamarina, J.C., Ruppel, C.: Thermal conductivity of hydrate-bearing sediments. J. Geophys. Res. Solid Earth **114**, 11103 (2009)

Farid, M.M., Khudhair, A.M., Razack, S.A.K., Al-Hallaj, S.: A review on phase change energy storage: materials and applications. Energy Convers. Manag. **45**(9), 1597–1615 (2004)

Farouki, O.T.: Ground thermal properties: thermal design considerations. In: Frozen Ground Engineering, pp. 186–202 (1985)

Khudhair, A.M., Farid, M.M.: A review on energy conservation in building applications with thermal storage by latent heat using phase change materials. Energy Convers. Manag. **45**(2), 263–275 (2004)

Loveridge, F., Amis, T., Powrie, W.: Energy pile performance and preventing ground freezing. In: Choi, C.K. (ed.) 2012 World Congress on Advances in Civil, Environmental, and Materials Research, pp. 2419–2432. Techno-Press, Seoul (2012)

Lund, J.W.: Geothermal heat pump utilization in the United States. GHC Q. Bull. **11**(1), 5–7 (1988)

Nasirian, A., Cortes, D., Dai, S.: The physical nature of thermal conduction in dry granular media. Géotech. Lett. **5**, 1–5 (2015)

Rybach, L., Mongillo, M.: Geothermal sustainability: a review with identified research needs. Geotherm. Resour. Counc. Trans. **30**, 1083–1090 (2006)

Zalba, B., Marín, J.M., Mehling, L.F., Marín, H.: Review on thermal energy storage with phase change: materials, heat transfer analysis and applications. Appl. Therm. Eng. **23**(3), 251–283 (2003)

Impact of Temperature Cycles at Soil – Concrete Interface for Energy Piles

Andreea Roxana Vasilescu[1,2(✉)], Anne-Laure Fauchille[1], Christophe Dano[3], Panagiotis Kotronis[1], Richard Manirakiza[2], and Philippe Gotteland[4]

[1] Ecole Centrale de Nantes, Université de Nantes, CNRS, Institut de Recherche en Génie Civil et Mécanique (GeM), 1 rue de la Noë, 44000 Nantes, France
andreea-roxana.vasilescu@ec-nantes.fr
[2] PINTO SAS, 48 Rue Jules Verne, 35300 Fougères, France
[3] Univ. Grenoble Alpes, CNRS, Grenoble INP*, 3SR, 38000 Grenoble, France
[4] Fédération Nationale des Travaux Publics, 3 rue de Berri, 75008 Paris, France

Abstract. Energy piles are double purpose foundation elements used both for transferring loads to the soil and temperature regulation in buildings. The response of the pile-soil interface is influenced by daily and seasonal temperature variations. In order to assess the impact of the thermal cycles on the mobilization of shear strength, in-situ and laboratory experiments were performed. Three energy piles were instrumented with vibrating cord sensors in the foundation of a waste water treatment plant in the North East (NE) part of Paris (at Sept Sorts, Seine et Marne), France. The deformation of these sensors has been recorded for more than one year and the impact of temperature cycles was assessed. In addition the impact of cyclic thermal loading on soil deformation at the soil-pile interface was also studied in the laboratory using an interface direct shear device equipped with a temperature control system. The preliminary results show that the undisturbed soil temperature below 5 m deep remains constant, around 13 °C and that the response of sand-concrete interface at different temperatures and temperature cycles consists in the overall low contraction of the sand.

1 Introduction

The global energy demand increase has stimulated the research for new sustainable and cost effective energy sources. Geothermal energy pile foundations are such an alternative solution for heating and/or cooling needs. The technique consists in encasing heat exchanging pipes in pile foundation, connected to a ground source heat pump in order to extract/inject heat from/into the ground (Laloui et al. 2003; Brandl 2006; Bourne-Webb et al. 2009; McCartney and Murphy 2012; Sutman et al. 2015; You et al. 2016). Although this solution has been used for some time in Europe, the information concerning the long term thermo-mechanical behaviour of the foundation and of the surrounding soil is still limited (Amatya et al. 2012). During the operation of the ground source system energy piles experience temperature changes which can have an impact on the pile deformation (expansion during heating, contraction during cooling)

A. Ferrari and L. Laloui (Eds.): SEG 2018, SSGG, pp. 35–42, 2019.
https://doi.org/10.1007/978-3-319-99670-7_5

as well as on the soil-pile interface (Bourne-Webb et al. 2009; Amatya et al. 2012; Bourne-Webb et al. 2015; Di Donna et al. 2015; Yavari et al. 2016).

To better understand the behaviour of energy piles during building operation, three piles (two energy piles and a conventional pile) were instrumented during the construction of a building in a water treatment plant at Sept Sorts, in the NE of Paris. Additionally, a second experimental campaign was performed in laboratory, to focus on the effect of temperature changes on the soil-concrete interface. An interface direct shear device adapted for thermo-mechanical loading was used.

In a first step, experimental instrumentation and preliminary results are presented for the in-situ study at Sept-Sorts, and in a second step for the laboratory investigation.

2 Sept Sorts Full Scale Test

2.1 Experimental Setup

Two energy piles (P18 and P29) and a conventional pile (P15) were instrumented during the construction of the pretreatment building of the Sept Sorts water treatment plant in Seine-et-Marne department, in France (Fig. 1) and their behaviour under exploitation conditions was recorded.

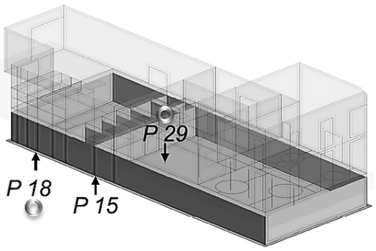

Fig. 1. Location of the instrumented conventional pile P15 and energy piles P18 and P29 on the 3D plot of the pretreatment building in the water treatment plant.

This building is supported by 100 continuous flight auger piles (0.420 m diameter, 9 m length) out of which 45 are energy piles. The mechanical properties of soils under the pretreatment building are presented in Table 1 (Sémofi 2013). For this project, the energy extracted by the abovementioned foundation is used for heating/cooling of the water treatment plant's administrative building located next to the pretreatment building.

The energy piles P29 and P18 are located under the slab and a wall, respectively while P18 is located under a wall (Fig. 1). These locations were chosen in order to assess the effect of the pile head constraint. The conventional instrumented pile, P15, is located at the equal distance of 4 m to the two energy piles.

Seven vibrating wire sensors were incorporated inside the energy piles P18 and P29 (Fig. 2a) in order to monitor the distribution of axial strain as a function of depth. The sensors were oriented longitudinally and attached to the transversal reinforcement bars

Table 1. Soil properties.

Soil	E_M(MPa)*	c′ (kPa)*	φ′ (°)*
Modern colluvial soil	5	0	30
Marls and altered gravels	11	5	25
Marls and gravels	30	10	25
Coarse limestone	100	50	30

*E_M - Menard pressuremeter modulus, c′ - effective cohesion and φ′ - effective friction angle

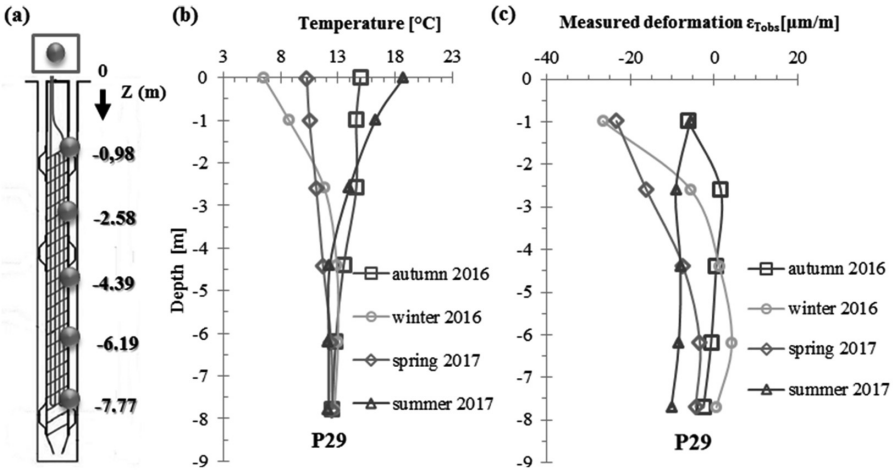

Fig. 2. (a) Temperature and deformation sensors positions (b) Seasonal evolution of temperature in pile P29 and (c) Measured strain change in pile P29.

then cast in fresh concrete during pile installation. Each vibrating wire sensor is equipped with a thermistor to monitor the temperature variations at each sensor location (Fig. 2a).

Five vibrating wire sensors were installed in the conventional pile P15 to quantify the effect of geothermal activation of the foundation on non-geothermal piles. The conventional pile P15 is therefore considered as the reference pile.

The atmospheric temperature variations are recorded with a temperature sensor installed in the data acquisition box, next to the station. From September 2016 to September 2017 temperatures and strains were recorded every 60 min with a precision of 2 °C and 10 µm/m, respectively.

2.2 Preliminary In-situ Results

Seasonal temperature variations recorded in October 2016, January 2016, April 2017 and July 2017 (representing autumn, winter, spring and summer respectively) in each sensor installed in P29 are depicted in Fig. 2b.

Below 5 m deep, the pile temperature is around 13 °C and remains constant along the acquisition time. This temperature is higher than the recorded winter and spring temperatures and lower than the summer and autumn temperatures, thus confirming that ground can be used as a source of heat during winter and conversely it can be used as a heat sink during summer.

The ground temperature measured in our test is similar to previous observations found in the literature (Laloui et al. 2003; Brandl 2006; McCartney and Murphy 2012; Loveridge et al. 2016; Minh Tang et al. 2017). Note here that a seasonal cyclic thermal loading is observed even before the geothermal activation of the foundation.

The mechanical load (the weight of the superstructure) for this study is considered constant and only the effect of the thermal loads (temperature changes) is presented. Between 0 and 5 m deep, temperature variations in P29 are accompanied by small but not negligible strain changes ($\varepsilon_{T\text{-}obs}$) in the range of 40 μm/m (Fig. 2c). From autumn 2016 to winter 2016, the temperatures are decreasing and the pile is contracting.

3 Laboratory Soil-Concrete Interface Tests

Temperature changes encountered in energy foundations also have an influence on the soil-structure interface. Heating-cooling cycles result in expansion-contraction of the pile (Laloui et al. 2003; Brandl 2006; Bourne-Webb et al. 2009) thus changing the normal pressure at the soil-pile interface which may lead to changes in the soil-pile shear resistance (Xiao et al. 2014; Di Donna et al. 2015; Yavari et al. 2016; Xiao et al. 2017). The in-situ instrumentation described above is only suitable for assessing the temperature and deformations evolution in piles but does not provide information of the soil changes at the soil-pile interface.

For a better understanding of the interactions between temperature and deformations of soil at the soil-concrete interface, a new direct shear device adapted for thermo-mechanical loading was employed at Centrale Nantes.

3.1 Experimental Setup

The new direct shear device is composed of a square shear box divided in two parts (upper part and bottom part). The box is installed in a container filled with water to consider saturated conditions. The upper part accommodates samples of 100 mm × 100 mm soil specimens with an initial height of 25 mm. The bottom part accommodates a 140 mm × 100 mm × 11 mm concrete plate.

A temperature sensor (precision of ±0.2 °C) is situated in the lower part. The thermal loading is applied through a closed loop circuit, that passes through a system installed under the container accommodating the shear box and that is connected to a refrigerated heating circulator bath with air-cooled cooling machine. The thermoregulation system is equipped with one Pt100 internal temperature sensor and one Pt100 temperature sensor external connection, in which the bottom temperature sensor is plugged-in. The temperature in the tested specimen is measured through the above mentioned Pt100 temperature sensor installed in the bottom of the lower shear box which is also used for running the temperature tests.

A load cell is installed on each actuator to measure both the vertical and horizontal loads applied on the sample. Two linear variable differential transducers (LVDTs) are used to measure the horizontal and vertical displacements with a precision of ±10 μm.

In the present work direct shear tests on Fontainebleau sand NE34 (Sibelco company, 99% quartz) in contact with a concrete structural element are presented. The literature review shows that the temperature effect on this sand is negligible (Di Donna et al. 2016; Yavari et al. 2016), this choice of soil was made in order to evaluate the performance of the testing device and the repeatability of the testing procedure. The physical properties of this sand are presented in Table 2.

Table 2. Fontainebleau sand properties (Pra-ai 2013).

d_{50}* (mm)	Gs* (g/cm^3)	e_{max}* (−)	e_{min}* (−)	$C_u = d_{60}/d_{10}$* (−)
0.23	2.65	0.866	0.545	1.72

*d_{50} - mean diameter, G_s - particle density, e_{max} - maximum void ratio, e_{min} -minimum void ratio, C_u - coefficient of uniformity

The same concrete plate was used for all experiments. Roughness measurements performed with a superior surface roughness tester were acquired before and after the tests. The value of the arithmetic mean roughness Ra was 10 to 12 μm before and after the tests. Therefore no significant changes of Ra after the direct shear tests were recorded in the study conditions.

Dry Fontainebleau sand was poured directly into the box and compacted by tamping. The sample was then placed in the loading frame and a vertical load was applied (consolidation) and kept constant during the entire test (constant normal load CNL test). Distilled water was added in the container in order to perform the test in almost saturated conditions. Temperature was then set to 13 °C.

A series of monotonic displacement-controlled direct shear tests were performed at 13 °C (in-situ soil temperature below 5 m deep, Fig. 2(b)), under constant normal stress equal to 50 kPa, 100 kPa and 150 kPa (corresponding to the effective lateral pressure at 5 m, 10 m and 15 m deep, respectively). The rate of applied horizontal displacement was 0.5 mm/min. Tests at 13 °C were used as references. A series of monotonic displacement controlled direct shear tests were also performed at 8 °C and 18 °C. In that case, the temperature was imposed at 13 °C in a first step and then imposed to 8 °C or 18 °C in a second step. Then the sample was subjected to shearing conditions.

A series of displacement controlled direct shear tests after 10 thermal cycles was done for the three temperatures and the three vertical loading cited above. The procedure for a cycle between 8 and 18 °C is given as example: (1) the temperature was decreased from 13 °C to 8 °C; (2) 10 temperatures cycles between 8 °C–18 °C cycles were imposed, (3) shearing.

3.2 Preliminary Laboratory Results

The interface friction angle was calculated from the three monotonic tests at 8 °C, 13 °C and 18 °C and for the cyclic test 8–18 °C (Fig. 3a). The calculated interface friction

angle for all of the tests is equal to 24.5° ± 0.7°. This value is lower than the soil internal friction angle (36°) which confirms that the shearing occurs at the interface rather than in the soil. A standard variation of 0.7° of the interface friction angle indicates that there is no influence of temperature on the shear strength mobilization for the sand concrete interface.

During the thermal cyclic test (8–18 °C), the volumetric strain ε_v shows cycles with an amplitude in the range of 0.25% which qualitatively highlight a thermo-elastic behavior. However, an accumulation of negative strains is registered (Fig. 3b). This result was interpreted by small grain rearrangement and gradual volume reduction (a dilating phase during heating is followed by a contracting phase during cooling for each cycle) leading to an overall contraction of the sample. It may explain the slightly higher interface friction angle obtained for this series of tests.

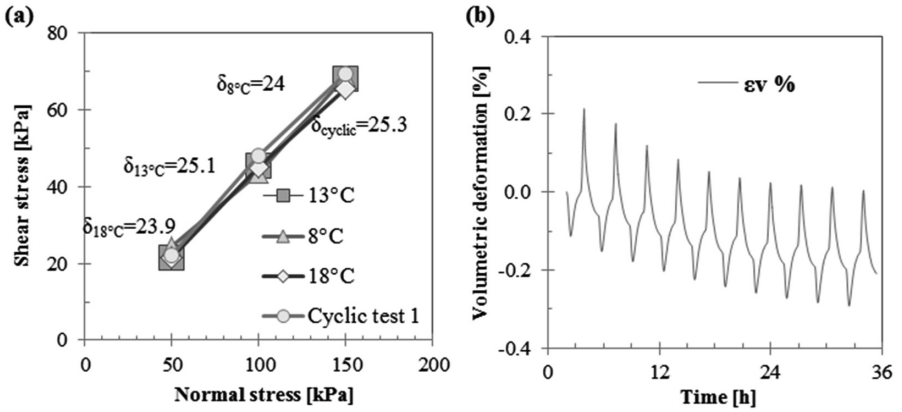

Fig. 3. (a) Interface friction angle; (b) Volumetric deformation during cyclic thermal loading for a normal stress of 50 kPa.

4 Conclusions and Perspectives

Energy piles represent an economic and sustainable energy source for space heating/cooling. The preliminary experimental results available for the 3 instrumented piles from Sept Sorts show that seasonal temperature variation is limited to the first 5 m of soil after which the temperature remains constant, around 13 °C. This temperature is higher than the air temperature in winter and lower than the air temperature in summer and the temperature difference can be used as a heat source/sink (depending on the season) thus providing proof of concept. Additionally the, effect of cyclic temperature changes on the soil-pile (sand-concrete) interface was studied in the laboratory using an interface direct shear device adapted for thermo-mechanical loading. The effect of temperature on shear strength is low and the temperature cycles result in an overall low contraction of the sand.

In perspectives, data acquisition in Sept-Sorts is still running and the heat pump has been activated in the water treatment plan in December 2017. The evolution of

temperatures and strains, in the 3 instrumented piles in Sept Sorts, are now being monitored in geothermal conditions. Moreover, interface direct shear experiments are programmed on various clayey and sandy soils, and especially soils from Sept-Sorts, at different temperatures and loading conditions in the laboratory. This new series of experiments will help to understand the relationships between the temperature and shearing behaviour of a large panel of natural soils. Future in-situ and laboratory tests will participate to improve the design of more efficient energy piles.

References

Amatya, B.L., Soga, K., Bourne-Webb, P.J., Amis, T., Laloui, L.: Thermo-mechanical behaviour of energy piles. Géotechnique **62**, 503–519 (2012). https://doi.org/10.1680/geot.10.P.116

Bourne-Webb, P.J., Amatya, B., Soga, K., Amis, T., Davidson, C., Payne, P.: Energy pile test at Lambeth College, London: geotechnical and thermodynamic aspects of pile response to heat cycles. Géotechnique **59**, 237–248 (2009). https://doi.org/10.1680/geot.2009.59.3.237

Bourne-Webb, P.J., Freitas, T.M.B., Assunção, R.M.F.: Soil: pile thermal interactions in energy foundations. Géotechnique **66**, 167–171 (2015). https://doi.org/10.1680/jgeot.15.T.017

Brandl, H.: Energy foundations and other thermo-active ground structures. Géotechnique **56**, 81–122 (2006). https://doi.org/10.1680/geot.2006.56.2.81

Di Donna, A., Ferrari, A., Laloui, L.: Experimental investigations of the soil-concrete interface: physical mechanisms, cyclic mobilisation and behaviour at different temperatures. Can. Geotech. J. **14**, 1–44 (2015). https://doi.org/10.1139/cgj-2015-0294

Di Donna, A., Ferrari, A., Laloui, L.: Experimental investigations of the soil – concrete interface: physical mechanisms, cyclic mobilization, and behaviour at different temperatures. Can. Geotech. J. **53**, 1–14 (2016). https://doi.org/10.1139/cgj-2015-0294

Laloui, L., Moreni, M., Vulliet, L.: Comportement d'un pieu bi-fonction, fondation et échangeur de chaleur. Can. Geotech. J. **40**, 388–402 (2003). https://doi.org/10.1139/t02-117

Loveridge, F.A., Powrie, W., Wischy, M., Kiauk, J.: Long term monitoring of CFA energy pile schemes in the UK. In: Energy Geotechnics, pp. 585–592 (2016). https://doi.org/10.1201/b21938-92

McCartney, J.S., Murphy, K.D.: Strain distributions in full-scale energy foundations. DFI J. J. Deep Found. Inst. **6**, 26–38 (2012). https://doi.org/10.1179/dfi.2012.008

Minh Tang, A., Yavari, N., Tri Nguyen, V., Hassen, G., Pereira, J.-M., Vasilescu, R., Kotronis, P., Housse, P.-J., Fabien Szymkiewicz, F.: Etude expérimentale du comportement thermomécanique des pieux énergétiques dans l'argile Experimental studies on the thermo-mechanical behavior of energy piles in clay. In: Proceedings of the 19th International Conference on Soil Mechanics and Geotechnical Engineering. Seoul, pp. 3467–3470 (2017)

Pra-ai, S.: Behaviour of interfaces subjected to a large number of cycles. Application to Piles (2013)

Sémofi: Rapport d'étude géotechnique d'avant-projet (G11 + G12) Communauté de communes du pays Fertois, Reconstruction de la station d'épuration, Sept-Sorts 77 (2013)

Sutman, M., Olgun, C.G., Brettmann, T.: Full-scale field testing of energy piles. IFCEE (2015). https://doi.org/10.1061/9780784479087.148

Xiao, S., Asce, S.M., Suleiman, M.T., Asce, M.: Soil-concrete interface properties subjected to temperature change s and cycles using direct shear tests. Geotech. Front. (2017). https://doi.org/10.1061/9780784480472.018

Xiao, S., Suleiman, M.T., McCartney, J.: Shear behavior of silty soil and soil-structure interface under temperature effects. In: Geo-Congress 2014 Technical Papers. American Society of Civil Engineers, Reston, VA, pp. 4105–4114 (2014). https://doi.org/10.1061/9780784413272.399

Yavari, N., Tang, A.M., Pereira, J.M., Hassen, G.: Effect of temperature on the shear strength of soils and the soil: structure interface. Can. Geotech. J. **53**, 1186–1194 (2016). https://doi.org/10.1139/cgj-2015-0355

You, S., Cheng, X., Guo, H., Yao, Z.: Experimental study on structural response of CFG energy piles. Appl. Therm. Eng. **96**, 640–651 (2016). https://doi.org/10.1016/j.applthermaleng.2015.11.127

The Application of Retaining Walls and Slabs as Energy Structures in Underground Train Stations

Nikolas Makasis[1(✉)], Guillermo A. Narsilio[1], Asal Bidarmaghz[2], and Ian W. Johnston[1]

[1] The University of Melbourne, Parkville, Australia
nikolas.makasis@unimelb.edu.au
[2] University of Cambridge, Cambridge CB2 1PZ, UK

Abstract. Shallow geothermal technologies have proven to efficiently provide renewable energy for heating and cooling. Recently much attention has been given to utilising sub-surface structures, primarily designed for stability, to also transfer heat to and from the ground, converting them into energy geo-structures. This work investigates the potential of applying this technology to the geo-structures of underground train stations in the city of Melbourne (Australia) to fulfil some of their heating and cooling demands. The diaphragm retaining walls and slabs that form part of a case study station are designed to also incorporate geothermal pipe loops. A finite element numerical model comprising the station walls and slabs is presented and used to investigate the thermal performance of these systems, for the temperate climate and geological conditions of Melbourne, adopting an expected lifespan of at least 25 years. The technical applicability of this technology is discussed for different thermal load scenarios, showing the importance of thermal storage and the balanced distribution of the thermal load.

1 Introduction

With energy demand rising and the necessary movement towards cleaner sources of energy, significant attention has been given to shallow geothermal technologies, which can very efficiently provide thermal energy for heating and cooling buildings (Johnston *et al.* 2011). Traditionally, these technologies use boreholes or trenches, incorporating piping with a circulating carrier fluid, to form ground heat exchangers (GHEs) that use the ground as a heat sink/source (Florides and Kalogirou 2004). However, traditional GHEs come with high capital costs either due to drilling or the land space requirements. To overcome this drawback, a relatively recent alternative approach incorporates the piping loops in underground structures that are primarily designed for stability, such as tunnel linings, pile foundations or retaining walls (Brandl 2006, 2016). This makes energy provision a secondary function for these (energy) structures, but also introduces limitations to the geothermal designer, making the provision of the entire energy demands not guaranteed and instead encourages the use of a hybrid

A. Ferrari and L. Laloui (Eds.): SEG 2018, SSGG, pp. 43–50, 2019.
https://doi.org/10.1007/978-3-319-99670-7_6

system (Mikhaylova *et al.* 2016; Aditya *et al.* 2018), that incorporates energy structures with other auxiliary (conventional) heating and cooling systems.

The most well researched energy structure has been energy piles (Loveridge and Powrie 2013; Cecinato and Loveridge 2015), most likely due to the similarities with the traditional borehole. However, little research exists on the applicability and use of energy retaining walls (Bourne-Webb *et al.* 2016; Di Donna *et al.* 2016), which compared to energy piles, introduce an important difference, since walls are not all surrounded by soil, but instead one side of the wall faces the interior of the underground building (such as an underground train station's platform), as depicted in Fig. 1. There is currently limited information regarding how energy retaining walls can be best utilised, especially regarding long-term thermal performance. This study examines the suitability of energy diaphragm retaining walls for an underground train station based in the city of Melbourne, Australia, and presents a novel analysis focusing on thermal performance for two different geometrical configurations over an operating period of 25 years.

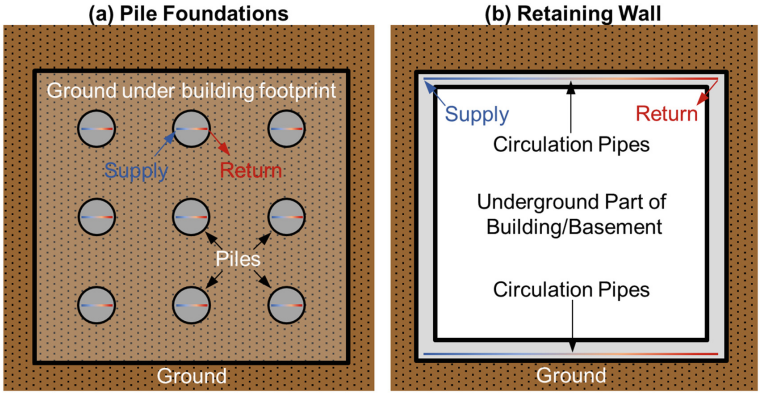

Fig. 1. Schematic top view of energy piles and energy retaining walls (not to scale)

2 Methodology

This study focuses on the *thermal* performance of energy diaphragm retaining walls. The main research questions relate to the importance of the thermal load distribution on the more thermally constrained energy retaining walls, as well as the benefits of adding piping in the bottom slab as well as the retaining walls. To perform this research 3D finite element modelling has been developed and used, adopting an experimentally validated methodology developed at the University of Melbourne (Bidarmaghz 2014). This approach is implemented using the software package COMSOL and couples the governing equations of heat transfer (energy balance) and fluid flow (momentum and continuity), modelling the heat transfer primarily by *conduction* (ground, concrete, pipe walls, partially in circ. fluid) and *convection* (circ. fluid). This methodology has been

experimentally validated with both traditional systems, as well as energy structures (Bidarmaghz *et al.* 2017; Bidarmaghz and Narsilio 2018).

The modelling, geometry and parameters used can be seen in Fig. 2 and Table 1. As can be noticed, the symmetry boundary condition has been used in both XZ and YZ planes to reduce the computational costs (the latter conservatively assuming an infinite wall length along the x axis). Moreover, a constant undisturbed temperature of 18.5 °C is used at the far boundary, assuming that the heat transfer will not influence the ground at this distance. The bottom surface is modelled as a no heat flux boundary (i.e., thermal insulation), assuming negligible bedrock heat flux. Finally, the surfaces of the wall and slabs inside the station have also been modelled as thermally insulated, to avoid thermal leaking in/out of the station, even though this technique may result in additional capital costs. A detailed investigation on the boundary conditions for these surfaces can be found in (Makasis *et al.* 2018). Regarding the geometry, it is worth noting that the pipes in the wall have 275 mm cover on the ground side while the ones in the slab have 156 mm cover on the bottom and 100 mm cover on each end along the y axis.

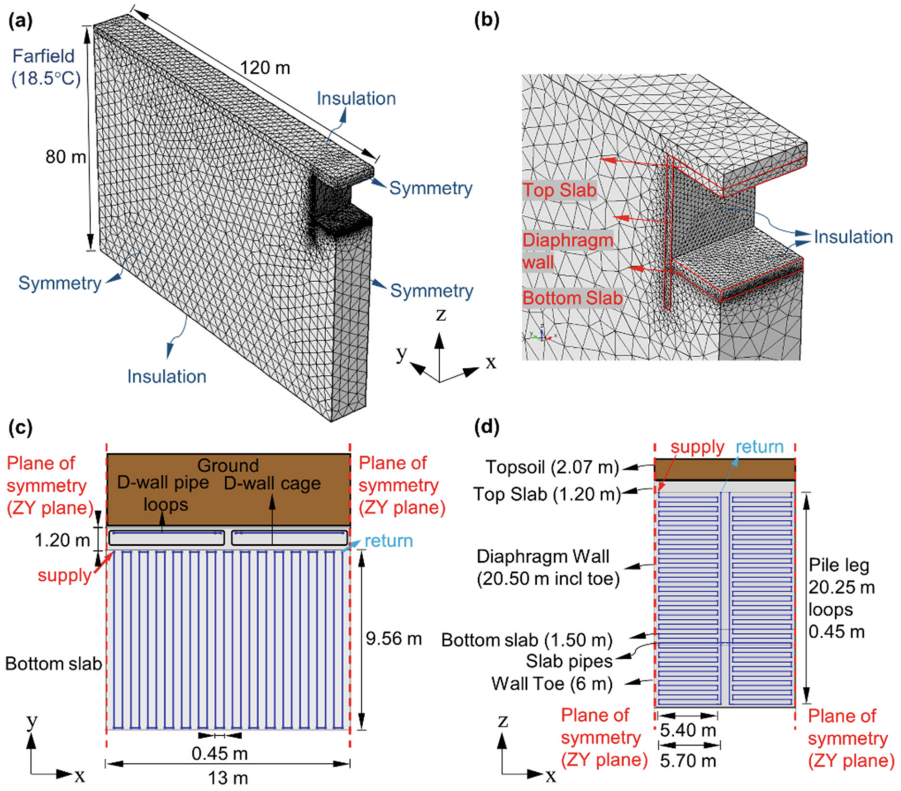

Fig. 2. Finite element modelling: overview (a), detail (b), model geometry in the XY (c) and ZX (d) planes

Table 1. Modelling parameters

Parameter	Value	Unit	Description
λ_{ground}	3.4	W/(mK)	Effective thermal conductivity of ground (from TRT)
ρ_{ground}	2400	kg/m^3	Density of ground
$C_{p\ ground}$	830	J/(kgK)	Specific heat capacity of ground
$T_{farfield}$	18.5	°C	Average annual ground temperature
$\lambda_{concrete}$	2.1	W/(mK)	Thermal conductivity of concrete
$\rho_{concrete}$	2250	kg/m^3	Density of concrete
$C_{p\ concrete}$	890	J/(kgK)	Specific heat capacity of concrete
λ_{fluid}	0.58	W/(mK)	Thermal conductivity of carrier fluid
ρ_{fluid}	1000	kg/m^3	Density of carrier fluid
$C_{p\ fluid}$	4180	J/(kgK)	Specific heat capacity of carrier fluid

A crucial parameter for the modelling is the thermal load distribution, representing the amount of thermal energy the system needs to provide. Figure 3 shows two thermal load distributions adopted for this work. The first one (*original)* represents typical requirements for an underground train station in Melbourne, Australia, those being heavily cooling dominant due to the large amounts of heat generated by the trains, plants and commuters. It should be noted that this distribution represents 100% of the heating demand for the entire station and 20% of the cooling demand, with the rest being supplemented using auxiliary means (such as chillers and cooling towers). The second one is a modified balanced version of the first (equal amounts of cooling and heating) where additional heating is supplied. Since the station has no need for more heating, this additional heating is assumed to be supplied to nearby buildings, such as schools, hospitals or apartment blocks amongst others. In all cases, the thermal load is equally distributed over 67 diaphragm wall pipe loops and (if applicable) 33 slab loops of the entire (about 200 m long) train station.

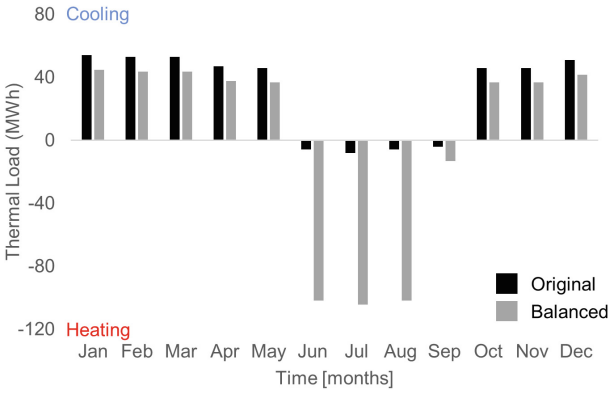

Fig. 3. Annual thermal load distributions

3 Results and Discussion

The results of the numerical simulations are presented Fig. 4, showing the average fluid temperature within the pipes (average of inlet and outlet of header pipe) over an operating period of 25 years. In the geothermal design of these systems, it is crucial that this temperature range is within the acceptable operating limits of the heat pump, as well as that they are not extreme such that can cause, for example, freezing in the ground. Therefore, in this work, the fluid temperatures are to be restrained between 0 °C and 40 °C, the latter of which is indicated on the figures for reference. Furthermore, the first figure shows the results when geothermal piping is implemented only in the diaphragm walls while the second when geothermal piping is implemented in both the diaphragm walls as well as the bottom slab. This shows the relative improvement on the system performance, by the addition of the slab, with an average lowering of about 1 °C in the maximum mean fluid temperature. Finally, each figure presents the results for both thermal load distributions presented in Fig. 3, as well as variations of the *original*, where the cooling load provided is reduced to make the design technically feasible (since providing 100% of the *original* thermal load results in temperatures over 40 °C).

Looking at Fig. 4(a), it can be seen that only about 80% of the *original* thermal demand can be satisfied, assuming that the system will stop running after 25 years to restore the thermal balance. This is because of the cooling dominant nature of the thermal load, with heat being continuously extracted from the station towards the ground, where it keeps accumulating, increasing the ground temperatures. This heat accumulation will make the operation of the geothermal system less efficient over the years as the temperatures become higher. Using the *balanced* load, on the other hand, results in a greatly improved system performance with the fluid temperatures kept stable, approximately between 7 °C and 25 °C. Since equal amounts of heat get injected to and extracted from the ground, thermal equilibrium is preserved each year and there are no thermal accumulation effects in the long term. Due to these reasons, a system adopting the *balanced* thermal load would also comfortably run for much longer periods of time.

Figure 4(b) shows similar results, with only about 85% of cooling being comfortably provided when the *original* thermal load is considered, while using the *balanced* thermal load results in a stable performance with the fluid temperatures fluctuating approximately between 10 °C and 24 °C. Therefore, the addition of the slab piping improves the performance of the system, by shifting the fluid temperatures away from the upper and lower limits (reducing the max and increases the min). In this particular case, it would allow the system to provide about 5% more cooling energy for the *original* load case. However, in the case where the extra heating could be supplied to balance the load, adding geothermal pipping in the slab would not result in significant improvements. Even though the fluid temperature extremes are reduced/increased by 1 to 3 °C, the temperature range without the slab piping is already acceptable and therefore the improvement would only be in terms of the coefficient of performance (COP), meaning that less electricity would be required to run the system, and therefore resulting in a small reduction in the operational costs. To properly quantify the benefits of adding the piping in the slab, a thorough analysis of the relevant cost is required,

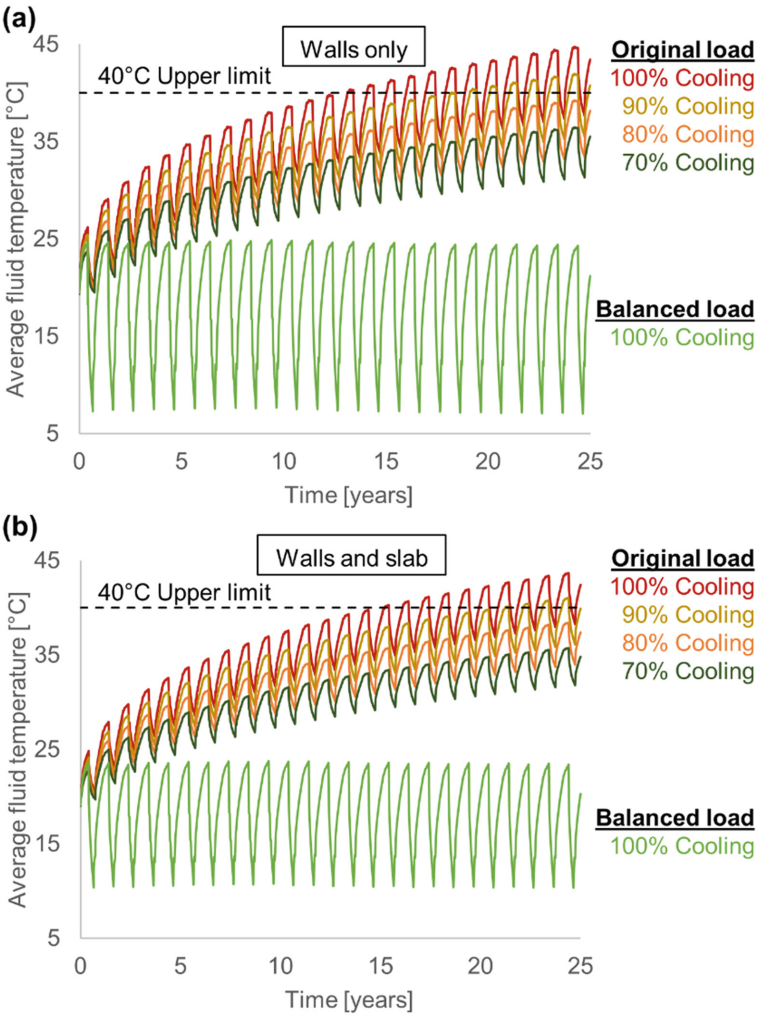

Fig. 4. Results for geothermal piping implemented in diaphragm walls only (a) and in diaphragm walls *and* bottom slab (b)

taking into account the relative novelty of this concept and therefore the associated risks, as well as the benefits, both monetary and environmental (such as providing more renewable energy).

The investigation shows that a large portion (80–85%) of its target cooling demand (or 16–17% of total station demand) can be provided by the energy walls (and slabs). However, the fluid temperatures keep rising, indicating that the system can only run for a finite amount of time, before requiring shutting down for some time, to restore the thermal state of the ground. On the other hand, balancing the thermal load not only results in a much better running system, but also would be less costly to operate and

would be able to run for much longer time. Moreover, the resulting fluid temperature ranges suggest that if even more heating demand existed for the surrounding structures, the system could be able to provide even more amounts of cooling, reducing the energy dependencies on auxiliary systems (for example 200% of the target cooling, or 40% of the total station cooling demand).

4 Conclusion

This work briefly presented an investigation on the use of diaphragm retaining walls as energy structures to provide geothermal energy for space heating and cooling purposes. An underground station in Melbourne, Australia, was adopted as a case study and the investigation focused on the importance of the thermal load distribution as well as two potential designs, one incorporating the technology only in the diaphragm walls and the second also adding it to the bottom slab of the station.

The thermal load investigation showed that this is a crucial parameter to energy retaining walls, likely more significant than for traditional boreholes or energy piles, due to the more limited available ground. An evaluation of the maximum feasible amount of thermal energy that can be provided for a typical underground station in Melbourne, showed that the system could only provide 80–85% of its initial target cooling demand (16–17% of the total cooling of the station) eventually overheating the ground, due to the cooling dominant load. On the other hand, *balancing* the thermal load by providing equal amounts of heating, transferred to nearby buildings, resulted in a much better running system that would be less costly to operate, be able to run for much longer time and could almost certainly exceed the initial target demands, given that sufficient heating demand is also present. Thermally activating the bottom slab marginally improves the system performance. However, these benefits may not outweigh the additional capital costs associated and a cost-benefit analysis should be undertaken for a definite position.

Overall, even though the thermal energy availability for energy retaining walls is lower than other structures, this investigation shows that there is potential in their application. The thermal load distribution will be a key factor on the viability of these structures and ideally the possibility of providing equal amounts of heating and cooling should be seriously considered, perhaps by providing heating to nearby buildings on the surface, since it very significantly affects the performance of the system, potentially solely determining its viability.

Acknowledgements. The Australian Research Council (ARC) FT140100227 and The University of Melbourne are acknowledged for their contributions to this work.

References

Aditya, G.R., et al.: Financial assessment of ground source heat pump systems against other selected heating and cooling systems for Australian conditions. In: IGSHPA Research Track Conference. Stockholm (2018) (Submitted)

Bidarmaghz, A.: 3D numerical modelling of vertical ground heat exchangers. The University of Melbourne (2014)

Bidarmaghz, A., et al.: Thermal interaction between tunnel ground heat exchangers and borehole heat exchangers. Geomech. Energy Environ. **10**, 29–41 (2017). https://doi.org/10.1016/j.gete.2017.05.001

Bidarmaghz, A., Narsilio, G.A.: Heat exchange mechanisms in energy tunnel systems. Geomech. Energy Environ (2018, in press). https://doi.org/10.1016/j.gete.2018.07.004

Bourne-Webb, P., et al.: Analysis and design methods for energy geostructures. Renew. Sustain. Energy Rev. **65**, 402–419 (2016). https://doi.org/10.1016/j.rser.2016.06.046

Brandl, H.: Energy foundations and other thermo-active ground structures. Géotechnique **56**(2), 81–122 (2006). https://doi.org/10.1680/geot.2006.56.2.81

Brandl, H.: Geothermal geotechnics for urban undergrounds. Procedia Eng. **165**, 747–764 (2016). https://doi.org/10.1016/j.proeng.2016.11.773

Cecinato, F., Loveridge, F.: Influences on the thermal efficiency of energy piles. Energy **82**, 1021–1033 (2015). https://doi.org/10.1016/j.energy.2015.02.001

Di Donna, A., et al.: Energy performance of diaphragm walls used as heat exchangers. Proc. Inst. Civil Eng. Geotech. Eng. **170**, 1–14 (2016). https://doi.org/10.1680/jgeen

Florides, G., Kalogirou, S.: Ground heat exchangers-a review. In: Proceedings of the 3rd International Conference on Heat Powered Cycles, HPC 2004-Cooling, Heating and Power Generation Systems. Cyprus University of Technology, Larnaca (2004)

Johnston, I.W., Narsilio, G.A., Colls, S.: Emerging geothermal energy technologies. KSCE J. Civ. Eng. **15**(4), 643–653 (2011). https://doi.org/10.1007/s12205-011-0005-7

Loveridge, F., Powrie, W.: Pile heat exchangers: thermal behaviour and interactions. Proc. ICE Geotech. Eng. **166**(2), 178–196 (2013). https://doi.org/10.1680/geng.11.00042

Makasis, N.: Further understanding ground source heat pump design using finite element methods and machine learning techniques. PhD Thesis, The University of Melbourne (2018)

Mikhaylova, O., et al.: Benefits and optimisation of district hybrid ground source heat pump systems. In: Wuttke, F., Bauer, S., Sanchez, M. (eds.) Energy Geotechnics—Proceedings of the 1st International Conference on Energy Geotechnics, ICEGT 2016, pp. 535–542. CRC Press, Kiel (2016)

Development of a CO_2 Heat Pipe for Hydronic Heated Bridge Decks

Manjarik Mrinal[1], Xiang Wang[1], Gang Lei[2], Xinbao Yu[2(✉)], Cheng Luo[1], and Anand Puppala[2]

[1] Department of Mechanical and Aerospace Engineering, The University of Texas at Arlington, Arlington, TX, USA
[2] Department of Civil Engineering, The University of Texas at Arlington, Arlington, TX, USA
xinbao@uta.edu

Abstract. Heated bridges using hydronic systems with PEX pipes embedded in the concrete deck are often used to remove snow and ice. In practice, State Department of Transportations (DOTs) are often resistant to use the hydronic heating due to its risk of pipe leaks. This paper concerns the design and tests of copper CO_2 heat pipes that can be used in the heated bridge to avoid the leak hazard and improve heating efficiency. A single heat pipe is developed using a sealed copper tube filled with pressurized CO_2 at constant room temperature. The single CO_2 heat pipe is designed and verified in the lab to work for the temperature range provided by working temperature of extracted fluids from an underground geothermal well and freezing temperature during snow events. The system is tested inside an environmental chamber and demonstrates its superior heating performance as compared with its counterpart. CO_2 heat pipes have a great potential to improve significantly heating efficiency and minimize the environmental impact of geothermal heated bridges.

1 Introduction

PEX (cross linked polyethylene) pipes are commonly used as the pipe materials for hydronic heating systems in bridges and pavements for deicing purpose. PEX pipes have the advantages of being noncorrosive, lightweight, flexible, and structurally sound (Lund 2000). However, the hydronic systems have a risk of potential catastrophic failure due to leaky pipes (Fliegel et al. 2010). An innovative alternative to the PEX pipe, a carbon dioxide heat pipe, was applied by Kruse (1998) as earth probes of coupled heat pumps. Performance comparisons of two 100 m deep earth probes with brine or CO_2 as heat carrier was shown by Kruse and Rüssmann (2010). Zorn et al. (2008) designed and built a ground coupled heat pipe with the working medium CO_2. Pumanertkul et al. (2017) presented a new design of heat pipe with carbon dioxide as working fluid to extract thermal energy from the geothermal reservoir. They showed the feasibility of the heat pipe for low-temperature geothermal reservoir. However, there is no information about the application of the carbon dioxide heat pipe in bridge deck deicing. This paper presents the laboratory design and evaluation of a single CO_2 heat pipe that can be used for heated bridge decks.

A. Ferrari and L. Laloui (Eds.): SEG 2018, SSGG, pp. 51–57, 2019.
https://doi.org/10.1007/978-3-319-99670-7_7

2 Design of a Single Heat Pipe

The heat pipe includes a K-type hard drawn copper tube with a diameter of 0.5 in. It can resist pressure as high as 1000–1500 psi. The working fluid is CO_2. As shown in Fig. 1, the tube has a tee joint at the top end, whose two sides are attached with a pressure gauge and a pressure control valve. The CO_2 inside the heat pipe is acquired from dry ice, the solid form of CO_2. The dry ice is fed into the heat pipe through the bottom end of the tube, which is capped after the filling is completed.

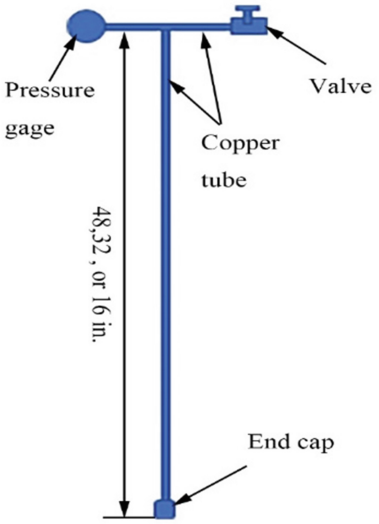

Fig. 1. Schematic of our heat pipe

Two requirements should be satisfied to assure that the developed heat pipe can be used to efficiently heat bridge deck. One end of the heat pipe will be submerged into heat carrying fluids circulated inside pipes from underground geothermal boreholes. The rest of the pipe will be attached to the bridge deck bottom to heat the bridge. CO_2 at the heating end will change from liquid to gas to absorb heat. The CO_2 gas will move to the cool bridge side and change to liquid due to condensation. The concrete deck quickly absorbs the heat due to the condensation process.

3 Relationship of Internal Pressure with the Volume Ratio of Filled Dry Ice

Dry ice has a temperature of −78.5 °C or below. After it is added to a heat pipe which originally had the ambient temperature, the temperature of the tube immediately decreases. After the dry ice phase change was completed, the pipe's temperature gradually increases towards ambient temperature, and the pipe pressure also rises.

As shown in Fig. 2, at 1 atm (about 1 bar, or say 14.7 psi), dry ice turns into gas when the temperature is −78.5 °C or above. The heat pipe in this research was placed in an environment with temperature variations from −10.0 to 25.0 °C. To obtain the desired liquid phase in this temperature range, it was vital to ensure that the pressure inside the heat pipe was above 5.19 bars (about 5.12 atm, or say 74.9 psi). Therefore, the tube was filled with various amounts of dry ice to examine whether such a high pressure could be obtained by this means.

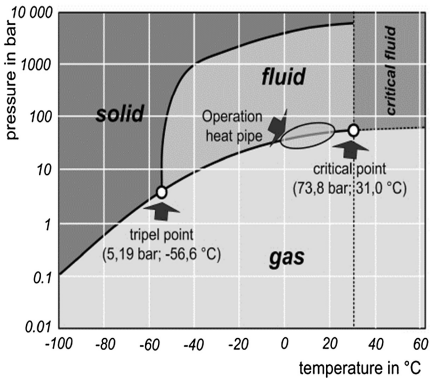

Fig. 2. Phase diagram of CO_2 (Zorn et al. 2008)

Heat pipes with three different lengths, 48, 32, and 16 in., and diameters of 0.5 in. were fabricated and tested. Each heat pipe was a closed system. After installation, the system was tested for leakage by submerging it in a water bath.

The mass density of dry ice is about 1.5 g/cm^3. The volume ratio between the dry ice and the tube was varied for each of the three pipes to determine the corresponding relationship of the internal pressure with the volume ratio. Figure 3 shows an example results of the 48 in. long pipe. In this test, the heat pipes were not heated; they were just exposed to an environment with a temperature of 22 °C. These results were compared with the ones predicted using the van der Waals equation (Reid et al. 1987):

$$\left(P + \frac{an^2}{V^2}\right)(V - nb) = nRT.$$

(See Table 1 for the meaning and value of each mathematical symbol.)

Three major points were observed from the experimental results (Fig. 3). First, the relationship between the internal pressure and the volume ratio varied very little for the three heat pipes. This indicates that the internal pressure mainly depends on the volume ratio, not the length of the pipe. Accordingly, in subsequent applications, the 48 in. heat pipe was adopted, since it can heat a larger area than the other two sizes of pipes. Second, when the volume ratio was 10% or higher, the internal pressure was above 650 psi, which is much higher than the required value of 74.9 psi, implying that a liquid phase of CO_2 may have existed in each pipe. Third, the internal pressure

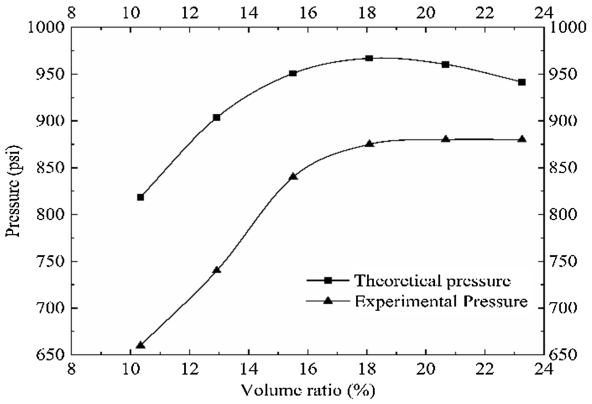

Fig. 3. Relationship of experimental and theoretical pressures with volume ratio (48 in.)

Table 1. List of properties and their values used in the calculation of theoretical pressure

Terms	Property	Value	Unit
P	Pressure	–	psi
n = m/M	Number of moles	–	mol
m	Mass of dry ice	Vary	g
a	van der Waal's coefficient	3.61	$L^2 * bar * mol^{-2}$
b	van der Waal's coefficient	0.0429	$L * mol^{-1}$
R	Gas constant	83.145	$J * K^{-1} * mol^{-1}$
T	Ambient temperature	295.15	K
M	Molar mass	44.01	g/mol
V	Internal volume of pipe	258	cm^3

dramatically increased when the volume ratio increased from 10 to 18%, but it remained at a constant of about 900 psi as the volume ratio increased to above 18%.

The theoretically-predicted pressures were about 34 to 159 psi higher than those determined experimentally. Since the difference between the corresponding values did not exceed 15%, the van der Waals equation was applied to roughly estimate the internal pressure inside a heat pipe. When this equation was used to calculate the internal pressure, it was assumed that all of the dry ice had become gas. However, in practice, the amount of gas is probably less than the assumed one, since the heat pipe may also have the liquid form of CO_2 inside its tube, which lowers the internal pressure.

4 Optimization of Performance by Changing Volume Ratio of Dry Ice

The 48 in. heat pipe was tested at an ambient temperature of 5–8 °C to examine the effect of the volume ratio on the temperature distribution at the cold end of a heat pipe. The tube was submerged 8 in. from the bottom of a water tank that had a constant temperature of 21 °C; the remaining body of the tube was exposed to ambient temperature. The volume ratio of dry ice in the pipe was varied to obtain optimal performance of the pipe. The results are depicted in Table 2. The pipe was first filled with 13% of dry ice. After 30 min, the temperature difference between the two ends was about 3.5 °C. The maximum temperature attained was 16.5 °C, near the spot where it was submerged. In contrast, when the pipe was filled with 18% of dry ice, there was only 1 °C of difference between the two ends of the pipe; if the volume ratio was 23%, there was no temperature difference. Thus, in our subsequent tests, the volume ratio selected was approximately 23%.

Table 2. Performance test of the 48 in. heat pipe with different dry ice volume ratios

Test sequence	Volume percentage of dry ice (%)	Water tank Temp. (°C)	Ambient Temp. (°C)	Maximum Temp. (°C)	Pressure in heat pipe (psi)	Time span (min.)
1	13	21. 0	7. 5	16.5	750	30
2	18	21. 0	7. 5	20.0	900	30
3	23	21. 0	7. 5	21.0	940	30

5 Comparison of a CO_2 Heat Pipe with a Hollow Copper Pipe

In an effort to understand the difference in heat transfers when the heat pipes were filled with and without CO_2, the variations of temperature with time in the 48 in. heat pipe were tested by using an open-ended pipe that was filled only with air (Fig. 4). For simplicity, the heat pipes filled with CO_2 and air are referred to as "CO_2 pipe" and "air pipe," respectively.

5.1 Testing Results Using Thermocouples

At an ambient temperature of 5–8 °C, the air and CO_2 pipes were both submerged 8 in. inside a water tank with a temperature of 33–34 °C. The volume ratio of dry ice in the CO_2 pipe was about 25%. Eight thermocouples were attached to the two pipes at four locations. The thermocouples were placed to divide the pipes into four equal parts, as can be seen in Fig. 4. The temperature values were recorded every 10 s. At t = 6 min., the CO_2 heat pipe reached its steady state of temperature distribution (Fig. 5). In this state, the temperature distribution on the CO_2 pipe was almost uniform. It had an average temperature of 28 °C, and there was only a 2 °C difference between the temperatures of the two ends of the pipe. In contrast, the air pipe had a high-temperature

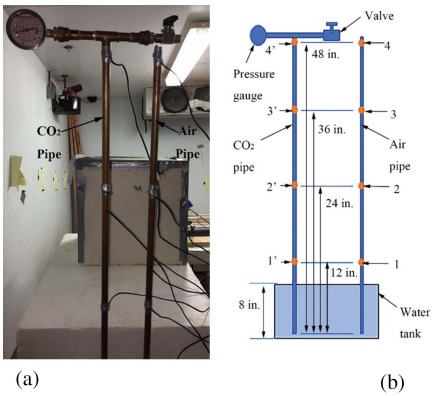

Fig. 4. (a) Image of the CO_2 and air pipes. (b) Schematic of the setup. Numbers 1' through 4' denote four locations on the CO_2 pipe, while 1 to 4 are their counterparts on the air pipe. Thermocouples were placed at eight locations to measure the corresponding temperatures.

gradient. At t = 15 min., it reached its steady state of temperature distribution. Position 1 had a maximum temperature of 23 °C, while the temperature of the other locations ranged from 9 to 11 °C.

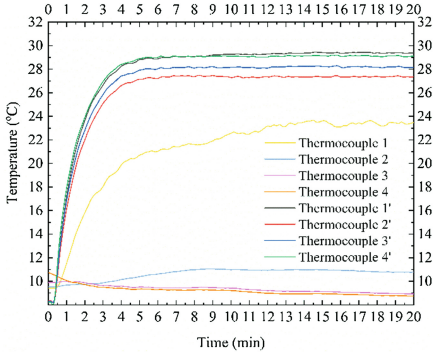

Fig. 5. Temperature changes of thermocouples attached to the CO_2 and air pipes at four locations

6 Summary and Recommendations for Future Work

In this paper, CO_2 heat pipes were designed and tested. According to the testing results, when the volume ratio of added dry ice was 23 to 25%, heat could be moved efficiently by using a CO_2 heat pipe. Within 6 min, the cold end of the heat pipe could reach the same temperature as that of the hot end, and the temperature distribution was almost uniform. It was also found that the van der Waals equation can be applied to roughly evaluate the internal pressure inside the heat pipe. Future work will include an in-situ

observation of phase changes inside a heat pipe to gain a better understanding of the heat transfer mechanism inside the pipe, and the application of the multi-pipe system to a bridge sample.

Acknowledgment. This study is funded by the Texas Department of Transportation.

References

Reid, R.C., Prausnitz, J.M., Poling, B.E.: The Properties of Gases and Liquids, 4th edn. McGraw-Hill, New York (1987)

Fliegel, J., Flyer, J., Katz, M., Le, A., Ngo, T., Roberts, K., Santoro, A., Sun, C., Weyforth, T.: Design and evaluation of a retrofittable electric snow melting system for pavements. Gemstone Program Final Report, University of Maryland, College Park, MD, p. 118 (2010)

Kruse, H.: Patent Application No. DE19860328A1 by the German Patent Office (1998). Accessed 20 Mar 2017

Kruse, H., Rüssmann, H.: The status of development and research on CO_2 earth heat pipes for geothermal heat pumps. In: International High Performance Buildings Conference at Purdue 2010, vol. 3493, pp. 1–8 (2010)

Lund, J.W.: Pavement snow melting. Geo Heat Center Q. Bull. **21**(2), 12–19 (2000)

Pumanertkul, C., Yamasaki, H., Ymaguchi, H., et al.: Supercritical CO_2 Rankine cycle system with low-temperature geothermal heat pipe. Energy Procedia **105**, 1029–1036 (2017). https://doi.org/10.1016/j.egypro.2017.03.448

Zorn, R., Steger, H., Kölbel, T., Kruse, H.: Deep borehole heat exchanger with a CO_2 gravitational heat pipe. In: GeoCongress 2008: Geosustainability and Geohazard Mitigation, pp. 899–906 (2008). https://doi.org/10.1061/40971(310)112

Static Load Testing of Short Pile and FEA Simulations for Utility-Scale Solar Energy Project

Jing Li[1], Dongyuan Wang[1,2(✉)], and Hongbin Huo[2,3]

[1] Department of Geotechnical Engineering, Southwest Jiaotong University, Chengdu City, China
Dongyuan.wang@gmail.com
[2] RRC Power and Energy, LLC, Round Rock, TX, USA
[3] College of Engineering, China University of Geosciences, Wuhan, China

Abstract. The total installation capacity of solar energy in the U.S. reached 2,000 MW in 2011 and exceeded 14,000 MW in 2016, respectively. Falling construction cost made the utility-scale solar energy affordable. This paper presents the details of pile load testing that is widely used in industry to help reduce the construction cost. Simulations using finite element analysis for the static pile load testing were carried out, and simulation results were compared with on-site testing data. Interpreted design parameters based on single tested pile and parameters obtained from codes were compared.

1 Introduction

Utility-scale solar power has much larger project size, typically defined as those 10 MW or larger, than distributed generation, and the electricity is sold to wholesale utility buyers. To support and maintain the solar units operate successfully, a ground-mounting system is necessary to be designed and built during the construction phase. Figure 1 shows such ground mounting system, foundations and posts supporting the trackers which hold the solar panels.

The total installation capacity of solar energy in the United States reached 2,000 MW in 2011 and exceeded 14,000 MW in 2016, respectively. The cost of construction decreases made the solar power more affordable. Corresponding to the increase of total installation of solar energy, statistical data (Fu et al. 2016) indicated that the cost of solar power decreases from $4.46/W in 4th quarter of 2009 to $1.42/W in first quarter of 2016. Based on our observations in engineering practice, cost-effective foundation greatly helped construction savings involved in utility-scale solar power. This paper aims to introduce how the pile load testing program is performed for utility-scale solar power project. Based two case studies of utility-scale solar power projects, simulations using Finite Element Analysis (FEA) were carried out and compared with the on-site testing data. Factors affecting the interpretation of pile design parameters based on site testing data were discussed, and then interpreted design parameters based on testing data and code were compared.

A. Ferrari and L. Laloui (Eds.): SEG 2018, SSGG, pp. 58–66, 2019.
https://doi.org/10.1007/978-3-319-99670-7_8

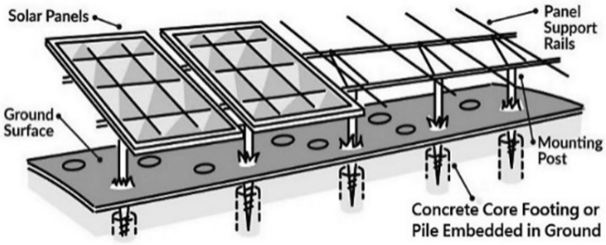

Fig. 1. Foundations typically used to mount solar panels

2 Static Pile Load Testing Program for Utility-Scale Solar Project

Foundation design procedure for solar projects is not different from conventional foundation design. However, it has its own characteristics. One of them is that PV power plant usually utilizes a very high number of relatively small and short piles (Donaldson and Brearley 2015). Moreover, the panel trackers have stringent allowable vertical and lateral movement for piles, which is usually refereed to 12.5 mm or less in practice. Since the amount of short piles are used to mount the solar system, the project cost is very sensitive to the pile design parameters, and thus static pile load testing is widely adopted in industry to obtain the quality data.

As shown in Fig. 1, concrete piers, H-Piles or W-Piles are frequently used in utility-scale solar projects to mount the solar system. Pile load testing is usually required and performed for H-pile foundations.

Procedure of pile load testing in solar project is referenced to pertinent ASTM standards for conventional deep foundations under static axial tensile load and under lateral load. However, both axial and lateral pile load testing for solar projects are modified to satisfy the objective of the specified testing program, including the numbers of testing piles, installation, reaction and applying pile load, load durations, etc.

A detailed testing plan shall be made first, which includes pile testing locations, types (tensile, compression or lateral), pile configurations, as well as the details for pile installation, load application and data record. Typically, the testing piles and installation methods shall be the same as production piles, and the maximum of the testing load shall be at least two times of the design loads. The increment of the testing load usually use 20% or 25% of the design load, and one minute duration is recommended for normal procedure but when the testing load reaches 100% of the design load, a longer duration is preferred. After that, unload completely and resume the procedure to the maximum testing load.

Static pushing method is usually adopted for H-pile or W-pile driving for solar projects. No specific requirement for testing pile installation machine but it is preferred to use the same driving machine and the same installation method as for production piles. Combination of backhoe or forklift with hydraulic jack or pull cylinder with pump is frequently employed to provide testing load or reaction.

Compression load cells, tension load indicators, vertical displacement and horizontal deflection indicators are installed to record the data, while shackles and flange clamps, reference beams, tripod, are also often used to transfer loads or help to record data. Setup for shackles and flange clamps are necessary, and pre-loading is usually needed to ensure the direction of the applied loads. Even the allowable movement and its influence on the load direction is very small, caution shall be given to keep the load in the same direction as initially applied. Figure 2 shows photos of pile load testing conducted on utility-scale solar project sites.

Fig. 2. Photos of pile load testing (left: uplift, upper right: compression, lower right: lateral. Courtesy of RRC power & energy, LLC)

3 Static Pile Load Testing and Numerical Simulations of Two Case Studies

Two case studies for solar power can be used *to illustrate* static pile load testing and numerical simulations. The two projects were geographically located in Texas and California, and the proposed solar power facilities comprise 180 MW(ac)/243.42 MW (dc) and 60 MW(ac), respectively. Wide flange piles with specification W6x8.5 were used for both projects to mount the solar panel trackers; group effects of piles were avoided by deliberate design in comply with Table 7-23 (FHWA 2016). Subsurface materials encountered predominantly are clay and silty clayey sands for the two projects, respectively. The Standard Penetration Testing (SPT) blow count value N for clay subsurface stratum varies from 16 to 62 with depths ranging from 0.6 m to 3.5 m, while N for silty clayey sand subsurface varies from 2 to 28 with depths ranging from 0.6 m to 5.0 m (RRC 2017), no shallow groundwater encountered for both sites.

3.1 Pile Load Testing, Data and Interpretation

Static pile load tests were performed for the above projects. Table 1 summarizes the details for the pile load testing program. Testing data including loads, duration, displacements in one or two measuring gauges for each testing cycle were recorded during the testing process. Graphs corresponding to the recorded data were generated to make analysis convenient.

Interpretation for the testing data based on compression and uplift load testing data for axial skin friction and end bearing capacity is almost the same as those for conventional pile foundations except much higher number of testing piles. Typically, envelopes covering most of the testing data are used for interpretation of skin friction. Lpile®, a p-y curve-based computer program, which is widely used to analyze the pile deflection in design, is utilized to calibrate the recorded data of lateral pile testing with Trial-Error approach.

3.2 Numerical Simulations

In-situ pile testing is costly and time-consuming. To validate the real pile testing results and explore on the influences of testing factors, simulations to the pile testing were conducted by using 3-D Finite Element Analysis (FEA) method with Midas NX. The simulations mimic static load testing with short W 6X8.5 piles embedded in clay and clayey sand, respectively.

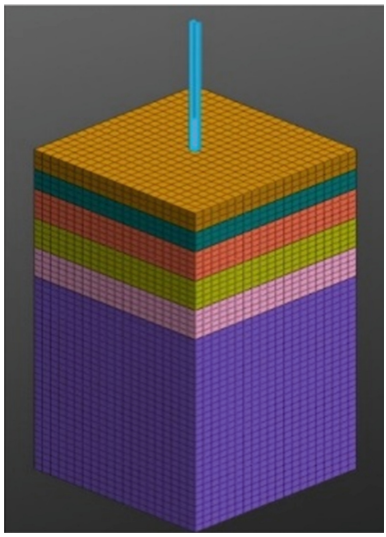

Fig. 3. 3-D finite element model for pile testing

Figure 3 shows the 3-D Finite Element Analysis model for simulations of static pile load testing. The pile was modeled as 1-D embedded trusses element. Ground boundary was set to the soil body while no boundary was set to the pile. Testing loads, i.e., compression, uplift and lateral force, were applied at the same place as real pile testing. The following construction stages were used in simulation: (1) Installing pile by activating all meshes of pile and soil body, activate boundary conditions; clear displacement; (2) Each load increment was simulated by each construction stage. When simulating pile testing, activate all these stages.

Unfortunately, the duration of pile testing load applied on the pile was not able to be simulated.

Table 2 summarizes the parameters used for 3-D FEA simulations of the pile testing. Based on the SPT N values in different soil types, friction angle for sand was interpreted with Eq. (1) (Das 2000):

$$\varphi = 27.1 + 0.3\mathrm{N} - 0.00054\mathrm{N}^2 (\text{in degree}) \tag{1}$$

Undrained shear strength of clay was interpreted with Terzaghi and Peck (1967) by using

$$\mathrm{Su} = 6.25\mathrm{N}\ (\text{in kPa}) \tag{2}$$

Table 1. Summary of the two case studies of pile load testing for solar power

Item	Project in Texas		
	Compression	Uplift	Lateral
Embedment (m)	1.5	1.5, 2.1	1.5, 2.1
Number of testing piles	21	39	40
Pile design capacity (kN)	12	8	6.7, 8.5
Max. loads applied for testing (kN)	48	32	13, 17
Testing load increment	25%	25%	25%
Testing load duration (Sec.)	60	60, 120 at 100% Load Increment	60, 120 at 100% Load Increment
Item	Project in California		
	Compression	Uplift	Lateral
Embedment (m)	1.5	1.5, 2.1	1.5, 2.1
Number of testing piles	21	39	40
Pile design capacity (kN)	12	8	6.7, 8.5
Max. loads applied for testing (kN)	48	32	13, 17
Testing load increment	25%	25%	25%
Testing load duration (Sec.)	60	60, 120 at 100% load increment	60, 120 at 100% load increment

Table 2. Parameters used in 3-D FEA simulations for pile testing

Soil type drainage conditions	Soil layers	Layer bottom (bgs, m)	SPT N	Unit weight γ (kN/m^3)	Poisson's ratio	Cohesion c (kN/m^2)	Friction angle ϕ (deg)	Elastic modulus (kPa)
Clay, undrained	(1)	0.6	16	18	0.33	99.6	5	29877
	(2)	1.5	16	18	0.33	99.6	5	29877
	(3)	2.5	40	18	0.32	249.0	5	74693
	(4)	3.5	42	18	0.32	385.9	5	115774
	(5)	10.0	42	18	0.32	385.9	5	115774
Clayey sand	(1)	0.6	2	18	0.35	0.0	28	5219
	(2)	1.5	13	18	0.33	0.0	31	8571
	(3)	2.5	28	18	0.30	0.0	35	13167
	(4)	3.5	28	18	0.30	0.0	35	123167
	(5)	4.5	26	18	0.30	0.0	35	12544
	(6)	10.0	26	18	0.30	0.0	35	12544

Modulus of Elasticity for different soils were interpreted with the following empirical equations (Bowles 1996):

$$Es = 500C \text{ (in kPa, for clay with PI} < 30) \tag{3}$$

$$Es = 320\ (N + 15) \text{ (in kPa, for clayey sands)} \tag{4}$$

3.3 Comparisons and Analysis of the Results

The FEA simulations were carried out using 3-D model and using the parameters summarized in Table 2, which are based on a selected boring of each project. Similarly, static pile load testing data near the same borings were selected. Figures 4, 5 and 6 summarize the comparisons of pile load testing data with FEA simulations for axial compression testing, lateral testing and uplift testing in terms of load-deformation relation, respectively.

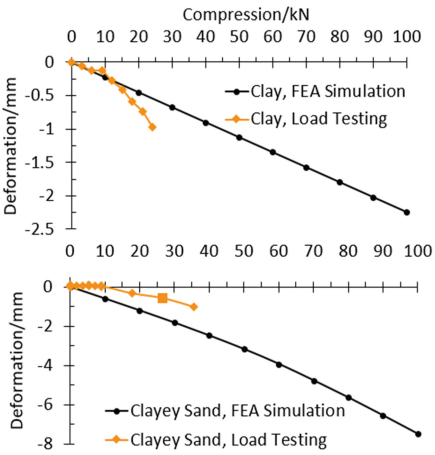

Fig. 4. Comparisons of axial compression testing with FEA simulations

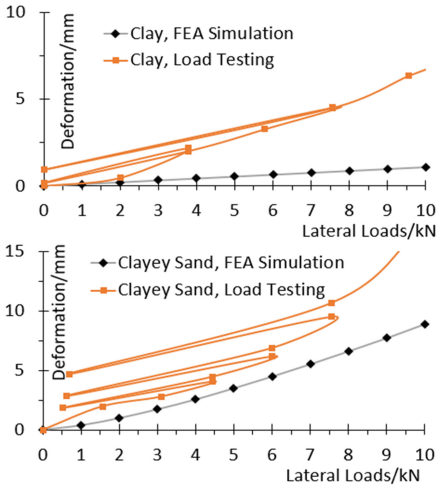

Fig. 5. Comparisons of lateral testing with FEA simulations

The FEA simulation results and the real data of pile load testing generally showed well-matched trend of the load-displacement relation. Discrepancies in magnitude were observed, they may be induced by the variation in model parameters and construction conditions. Figure 5 showed that when the compression load is less than 10 kN, the FEA simulations generated larger deformation than the real data of pile load testing, which implies that in this case, FEA simulation will be conservative than pile load testing to interpret the compression skin friction and end bearing capacity. Moreover, it is interesting to find that the FEA simulation always has larger deformations for clayey sand but shows the opposite for clay when compression loads are greater than 10 kN.

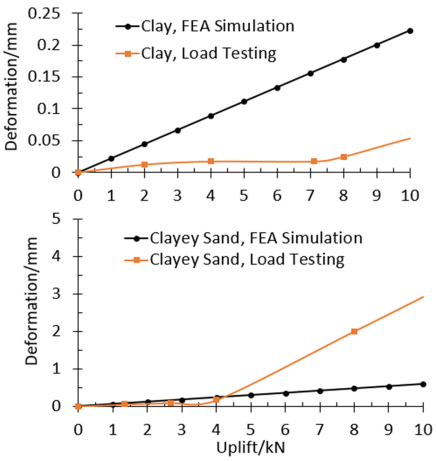

Fig. 6. Comparisons of uplift testing with FEA simulations

10 kN is a load that is much higher than the required compression bearing capacity by most solar-power facilities, thus, FEA simulations can be used to interpret the design parameters for pile subject to compression loads.

Figure 6 shows the comparisons of FEA simulation and lateral pile load testing which piles subject to horizontal loads. It is found that the testing piles have larger higher deformations than FEA simulations. Moreover, it is worth noting that larger gaps between the curves of FEA simulation and the pile load testing in clayey sand subsurface than in clay. It is reasonable to conclude that construction disturbs sandy soils more than clay, and the lateral displacement of piles is sensitive to the stiffness and intact of the upper layer due to the short length.

4 Comparisons of Skin Friction Interpreted by Code and Load Testing

Table 3 summarizes the pile design parameters interpreted with data of pile load testing and code-based. Movement criterion 6.25 mm is used for clay site (Texas project) and 12.5 mm for clayey sand site (California project), which were both provided by the manufacture of the tracker. These movement criteria are more stringent than typical practice. The criteria limit the load mobilization fully and thus have a potential to reduce the design parameters. Based on the data in Table 3, we can see that the skin friction interpreted with pile load testing data is about 1.5 to 2.5 times higher than those of the code-based. Although parameters based on this single pile testing data cannot be applied to the whole site, significant cost saving from pile load testing can be expected.

Table 3. Comparisons of interpreted pile design parameters (unfactored)

Bottom of soil layer (m)	Texas project (predominant subsurface material: lean clay)			
	Load testing		FHWA NHI-16-009	
	Uplift skin friction (kPa)	End bearing capacity (kPa)	Compression skin friction (kPa)	End bearing capacity (kPa)
0.6	84	3846	35	611
2.0	84	3846	32	2295
3.5	84	3846	32	2580
10.0	84	3846	32	2580
Bottom of soil layer (m)	California project (predominant subsurface material: clayey sand)			
	Load Testing		FHWA NHI-16-009	
	Uplift skin friction (kPa)	End bearing capacity (kPa)	Compression skin friction (kPa)	End bearing capacity (kPa)
0.6	28	3238	1	43
2.0	28	3238	12	1300
3.5	28	3238	22	2245
10.0	28	3238	33	3221

5 Conclusions

Typical pile load testing for utility-scale solar projects procedure and methodology have been presented in this paper with two case study projects in Texas and California, the United States. Filed measurements are compared with FEA simulation results, interpretation of pile design parameters based on testing data and code are also compared. Significant cost saving can be reached by carrying out pile load testing program for utility-scale solar power projects.

Comparison between pile load testing and FEA indicates a general agreement in terms of axial compression, uplift and lateral load applications. However, simulation results and on-site pile load testing showed more specific observations.

(1) For compression test, FEA simulations always generate more deformation than pile load testing for short H-piles or W-Piles. When the load is greater than certain threshold, compression deformation in clay may be less than on-site tested, but the threshold load is much smaller than typical need of solar power projects. Thus, if no pile load testing program available, FEA simulation can be applied.
(2) FEA simulation is somewhat cumbersome to address construction conditions, especially for sandy subsurface materials, which are easier to be disturbed by pile construction.
(3) Regarding uplift test, FEA simulations have a trend that generating larger deformations for clay but matching well with on-site testing data in sandy soil.
(4) Many factors may affect the final interpretation of pile load testing data. Based on the single pile testing data, the interpreted design parameters are 1.5 to 2.5 times larger than those code-based. The whole project shall look at the testing data of all tested piles.

References

Bowles, J.E.: Foundation Analysis and Design, 5th edn. McGraw-Hill Companies Inc, New York (1996)

Das, B.M.: Fundamentals of Geotechnical Engineering. Brooks/Cole, Pacific Grove, CA (2005)

Donaldson, B., Brearley, D.: Geotechnical analysis and PV foundation design. SolarPro Mag. **8**, 3 (2015)

Federal Highway Administration: Design and construction of driven pile foundations. FHWAHI NHI-16-009, September 2016

Fu, R., Chuang, D., Lowder, T., et al.: U.S. solar photovoltaic system cost benchmark: Q12016. Technical Report NREL/TP-6A20-66532, National Renewable Energy Laboratory (NREL), September 2016

RRC Power & Energy, LLC: Geotechnical Reports for Two Solar Projects in Texas and California (2017)

Terzaghi, K., Peck, R.B.: Soil Mechanics in Engineering Practice, p. 729. Wiley, New York (1967)

Behavior of Free and Fixed Headed Piles Subjected to Lateral Soil Movement

Saad Farhan Ibrahim AlAbdullah[1(✉)]
and Mohammed Khachi Hatem[2]

[1] Faculty of Engineering, Isra University, Amman, Jordan
drsaadfarhan@yahoo.com
[2] Civil Engineering Department, Al-Mustansiriyah University, Baghdad, Iraq

Abstract. Given extensive study conducted to investigate the response of free headed passive piles in sand subjected to lateral soil movement. The effect of pile head fixity condition was not often considered and systematically studied. For this reason, six tests were carried out on an aluminum pipes with a diameter of 30 mm and wall thickness of 1.4 mm embedded in sand soil. A specially designed apparatus for the laboratory model tests was manufactured to simulate piles subjected to triangular profile shape of lateral soil movements. Two typical pile head conditions (i.e., free and fixed headed conditions) and three different movable to stable depth (Lm/Ls) ratios were considered in these tests. Ten pairs of strain gauges attached at different locations along the pile shaft to measure the bending moments and deformations developed along the pile length. The results showed that the restrained of pile head (for fixed headed condition) leads to reduce the maximum positive bending moment by (18–24%), as compared with that of the free headed pile. Also the pile deflection and rotation along the shaft of fixed headed pile were very different as compared with free headed case.

Keywords: Soil movement · Piles · Active · Passive · Bearing capacity

1 Introduction

The majority of pile foundations, in general are designed to provide resistance against active load (vertical and horizontal) that applied directly to the pile head by a structure. However, with the increased construction activity in the form of road embankments, tunneling, deep excavations etc., piles are also subjected to passive load induced from the soil movements. Besides, there are situations where pile foundations are used to stabilize the moving slopes and liquefiable soils.

In all these conditions, the externally imposed ground movements will impart additional forces, cause increase in bending moments and lateral deflections in piles which may finally cause problems and even damage to the structure of piles (Pan et al. 2002 and Al-Abboodi et al. 2015). Lateral soil movement is more critical as pile foundations are not designed to sustain important lateral loads (Bauer et al. 2014). One of the most well-known damage caused by lateral soil movement was the collapse of a thirteen-storey building in China in 2009 under nearby excavation works and surcharge loading (Liang et al. 2013).

A. Ferrari and L. Laloui (Eds.): SEG 2018, SSGG, pp. 67–74, 2019.
https://doi.org/10.1007/978-3-319-99670-7_9

Extensive model tests have been conducted on free headed single piles and pile groups in cohesionless soil to investigate the response of pile under lateral soil movement. Some test results have been published previously with respect to (1) axially loaded piles subjected to rectangular (uniform) profile shape of lateral soil movement (Guo and Ghee 2004, 2005); and (2) vertically loaded piles undergoing arc and triangular profiles of lateral soil movement (Chen 1994; Guo and Qin 2010; Guo et al. 2005). Lingfeng (2005) studied the effect of pile head fixity condition on the behavior of piles in clay soil subjected to rectangular profile shape of lateral soil movement.

2 Test Set-Up

A special experimental apparatus was designed for the current study to investigate the effect of lateral soil movement on pile foundation. It consists of five main parts, i.e., a steel box, a loading system, a sand raining system, model piles, and a measurements system. Figure 1 shows the overall arrangement of the testing apparatus and all the component details are presented below.

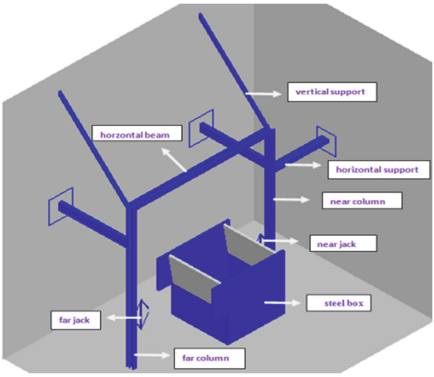

Fig. 1. Test setup

Fig. 2. Steel box

2.1 Steel Box

The designed steel box made of thick steel plate having a thickness of (6.5 mm) with internal dimensions of (80 cm × 80 cm) and (80 cm) height was used to apply triangular profile shape of lateral soil movements as shown in Fig. 2. Across the width of the box, it was divided into two parts, upper part and lower part. The two parts were connected by two hinges at the mid-height of the box. The upper portion is able to rotate while the lower portion is fixed which makes the soil in the box is divided into two layers (movable and stable). Four wheels were welded at the bed of the box in order to allow the box to travel from underneath sand raining to under the pile jacking system.

2.2 Loading System

Three mechanical jacks with capacity of 3 tons (for each one) were used to apply vertical and horizontal loadings on the instrumented pile and the box respectively. The vertical jack was used to drive the pile into the model ground. A load cell with a capacity of 5 tons was connected with the vertical jack to measure the load required to install the model pile into the sand. The base of the first horizontal (near) jack was welded perpendicular to the near column of the frame in order to apply horizontal force on the near upper part of the box. A load cell with a capacity of 5 tons was connected with this near jack to measure the horizontal force acting on the near upper part of the box.

By turning the near jack, the near upper moveable part of the model steel box was forced to rotate around its joints, and consequently causes the upper part of the soil in the box to move. The moving soil thus is subjected to a triangular profile of horizontal movement, with the maximum displacement at the soil surface and zero displacement at the level of joints of the upper and lower parts. The base of the second horizontal mechanical jack (rear jack) was welded perpendicular to the rear column of the frame to control on the movement of the rear upper part of the box.

2.3 Pile's Model

A hollow aluminum pipe of 30 mm outer diameter, 27.2 mm inner diameter and 1000 mm long with a bottom plugged was used as a model pile in this study. The model pile in each test was instrumented with ten pairs of strain gauges attached along it is shaft to measure the bending moments (at each pair location of the strain gauges) induced by lateral soil movement as shown in Fig. 3.

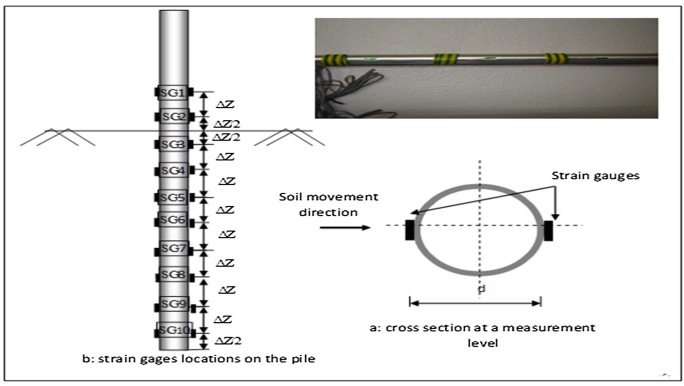

Fig. 3. Model pile instrumentation

2.4 Instrumentations and Measurements

Data logger, strain gauges and load cell were used in this study to measure the strains along the pile shaft and load required to cause movement in the upper movable part of the model box. A compact and handheld digital data logger (TC-32K) was used to

record and store data from strain gauge measurement for each pile test. TML strain gauges type (FLA-5-23-3L) having a gauge resistance of 120 ± 0.3 Ohm was used to instrument the model piles.

The strain gauges were fixed along the model piles using cyanoacrylate adhesive (type CN). The strain gauges were then coated by 1 mm epoxy resin in order to protect from damage during the pile driving and testing under lateral soil movement.

2.5 Sand Raining Device

A sand raining device was fabricated from timber pieces, having internal dimensions of 790 mm by 790, and 150 mm in height. The base of the sand raining consists of two timber plates; the bottom is fixed while the top is moveable. The thickness of the timber plates was 18 and 6 mm for fixed and moved respectively. The fixed plate was perforated with 6 mm diameter holes on a 40 mm by 40 mm grid pattern. The moveable plate can slide along the slots on one side of the sand raining.

The results showed that, the variation in sand density was less than (0.15 kN/m^3) within the box for each sand falling height. The falling height of sand was selected as 400 mm, which gave a relative density of sand about 59%, and a unit weight of 15.6 kN/m^3. Angle of internal friction.

2.6 Calibration of Strain Gauge

The strain gauges were calibrated by testing the instrumented pile as a simply supported beam under known applied bending moments. At the center of the beam (instrumented pile), dead loads and a pair of strain gauges were attached to apply bending moment and measure the strain respectively. The main aim of this calibration was to ensure an appropriate relationship between the strain gauge reading and the bending moment. A linear relationship was obtained between the actual calculated bending moment and the strain gauge readings for all piles used in this study.

3 Testing Program

Six model tests were conducted on single piles subjected to triangular profile shape of the lateral soil movement in sand. These tests were carried out to investigate the effect of pile head fixity condition on the lateral response of the model pile. Two pile head fixity conditions (free and fixed headed) and three different ratios (300/350, 350/350 and 400/350) of embedded length in the upper sand (Lm) layer to the lower sand layer (Ls) were used.

3.1 Test Results

A computer program written in MATLAB language was used to process and analyze the data recorded from the data logger. The profiles of the rotation and deflection along the pile were deduced by first and second order numerical integration of the bending moment profiles respectively.

3.1.1 Free Headed Test Results

Figure 4 presents the profiles of the bending moment along the pile shaft for free headed pile subjected to different values of lateral soil.

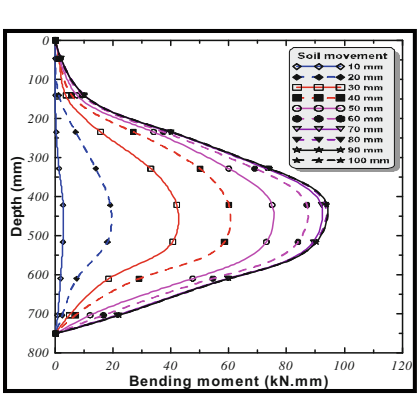

(a): Lm/Ls= 400/350

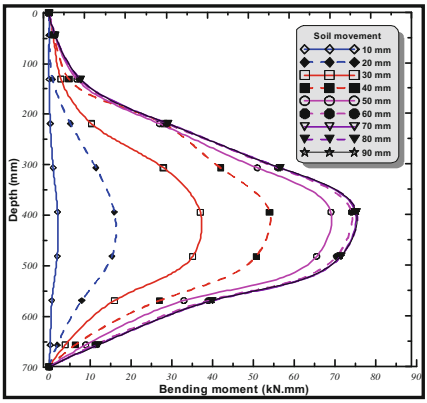

(b): Lm/Ls= 350/350

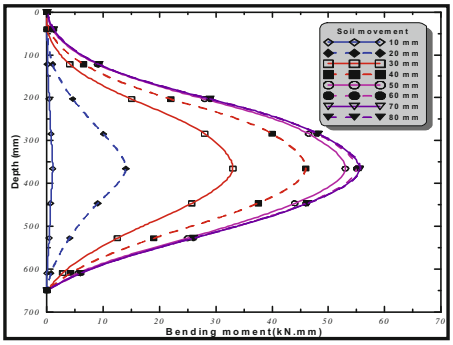

(c): Lm/Ls= 300/350

Fig. 4. Bending moment profiles for free headed pile with different movable to stable depth (Lm/Ls) ratios

3.2 Fixed Headed Condition

In order to investigate the effect of pile head condition on the response of pile subjected to lateral soil movement, three tests were conducted on the same pile of free headed pile except that the pile head was fixed against deflection and rotation. Figure 5a presents the profile of the bending moment along the pile shaft for fixed headed pile subjected to different values of lateral soil movements, Lm and Ls in this test were 400 mm and 350 mm respectively. The profile of the bending moment for the second test is shown in Fig. 5b, Lm and Ls in this test were 350 mm and 350 mm respectively. Figure 5c shows the profile of bending moment of the third test, Lm and Ls in this test were 300 mm and 350 mm. It can be noticed that, the bending moment profile for this test is

different from that of a free-headed pile. Because of the restrained of pile head, a quite large negative bending moments are developed at the pile head and relatively small negative bending moments are developed near the pile tip. Figure 5d shows the profiles of the bending moment of free-headed piles and fixed-headed piles subjected to lateral soil movement 60 mm for different Lm and Ls values. It can be seen that the negative bending moment leads to reduce the maximum positive bending moment by (18–24%), as compared with that of the free headed pile. The depth of the maximum positive bending moment is shifted upward to be above the interface between the moving and stable parts of the pile.

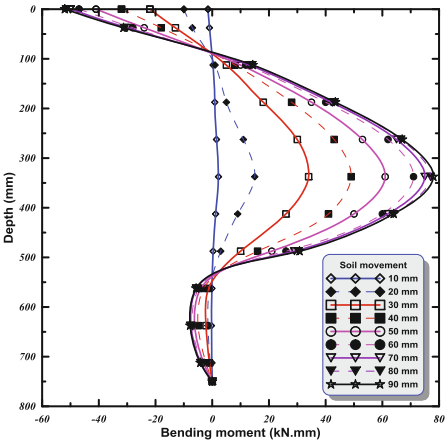

(a) Bending moment profile (Lm=400, Ls=350)

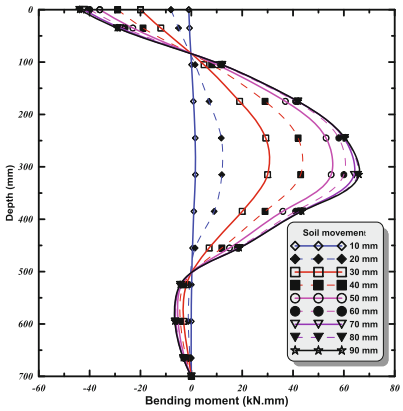

(b) Bending moment (Lm=350, Ls=350)

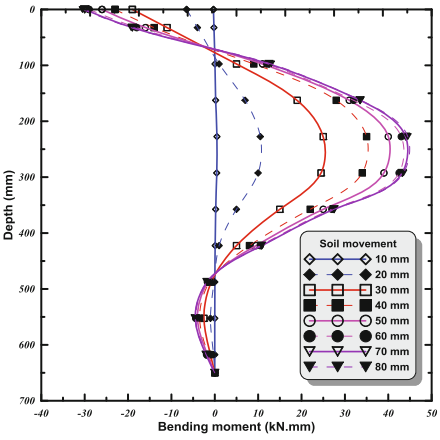

(c) Bending moment profile (Lm=300, Ls=350)

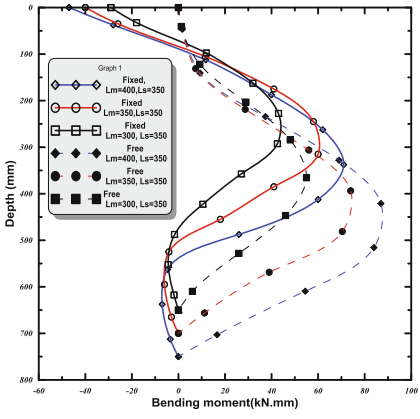

(d) Bending moment for free and fixedheaded

Fig. 5. Effect of pile head fixity on bending moment

The maximum shear force in the movable soil layer is seen to have increased substantially and its location was also shifted upward (Fig. 6a). The distribution of soil reaction along the pile shaft was also changed, with the value being increased substantially in the upper moving soil layer as shown in Fig. 6b. The pile deflection and rotation along the pile shaft are also very different for the two pile head cases as shown in Fig. 6c and d. Due to head fixity, the lower part of pile is seen to move substantially in opposite direction to that of soil movement.

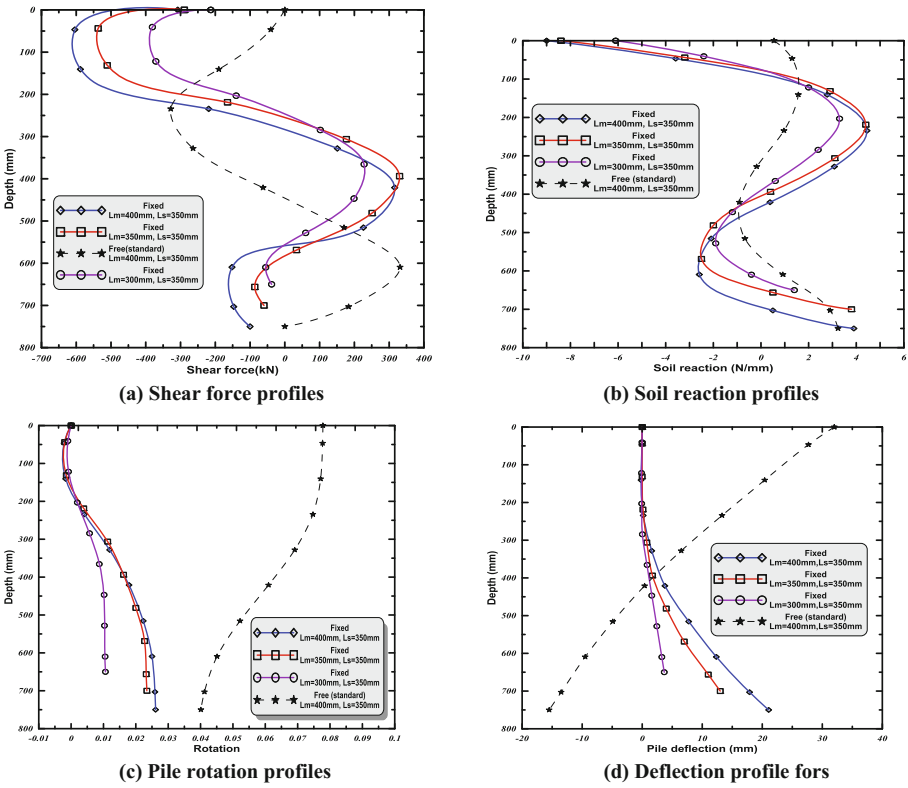

(a) Shear force profiles

(b) Soil reaction profiles

(c) Pile rotation profiles

(d) Deflection profile fors

Fig. 6. Pile responses for fixed (different Lm/Ls ratios) and free headed (Lm/Ls = 400/350)

4 Conclusions

Laboratory model tests have been conducted on single piles subjected to lateral soil movement in sand to investigate the effects of the pile end fixity on lateral response of piles. The results of the tests indicate that the restrained of pile head (for fixed headed condition) leads to reduce the maximum positive bending moment by (18–24%), as compared with that of the free headed pile. Also the shapes of shear force, soil reaction, deflection and rotation profiles along the shaft of fixed headed pile are very different as compared with free headed case.

References

Al-Abboodi, I., Sabbagh, T.T., Al-Jazaairry, A.: Modeling the response of single passive piles subjected to lateral soil movement using PLAXIS. Int. J. Eng. Res. Technol. **4**(3), 176–180 (2015)

Bauer J., Kempfert H.G., Reul O.: Lateral pressure on piles due to horizontal soil movement-1g model tests on single piles and pile rows. In: Proceedings of the 8th International Conference on Physical Modeling in Geotechnics, (ICPMG2014), Perth, Australia (2014)

Chen, L.F.: The effect of lateral soil movements on pile foundation. PhD Thesis, University of Sydney (1994)

Guo, W.D., Ghee, E.H.: Model tests on single piles in sand subjected to lateral soil movement. In: Proceedings of 18th Australasian Conference on the Mechanics of Structures and Materials, Perth, vol. 2, pp. 997–1004 (2004)

Guo, W.D., Qin, H.Y.: Thrust and bending moment for rigid piles subjected to moving soil. Can. Geotech. J. **47**, 180–196 (2010)

Guo W.D., Ghee E.H.: A preliminary investigation into the effect of axial load on piles subjected to lateral soil movement. In: Frontiers in Offshore Geotechnics (ISFOG), Perth, pp. 865–871 (2005)

Liang, F., Yu, F., Han, J.: A simplified analytical method for response of an axially loaded pile group subjected to lateral soil movement. KSCE J. Civ. Eng. **17**(2), 368–376 (2013)

Lingfeng, M.: Effects of lateral soil movements on piles. PhD Thesis, Nanyang Technological University (2005)

Pan, J., Goh, A., Wong, K., Selby, A.: Three-dimensional analysis of single pile response to lateral soil movements. Int. J. Numer. Anal. **26**(8), 747–758 (2002)

Laboratory Tests on Thermal Improvement of Soft Clay Under Elevated Temperatures

Atsushi Takai[1(✉)], Takuro Akama[1], Toru Inui[1], Takeshi Katsumi[1], and Atsushi Ogawa[2]

[1] Kyoto University, Kyoto, Japan
takai.atsushi.2s@kyoto-u.ac.jp
[2] Okumura Corporation, Kyoto, Japan

Abstract. This paper focuses on thermal improvement of soft clay under moderately elevated temperatures. Since soft clay can contract when heated, as is well known as thermal consolidation, heating of the ground can help consolidation of soft clay deposits. Although the temperature effects on consolidation of soft clay have been previously studied by element-scale tests, spatial heat transfer and its effect on consolidation are not fully understood. In this study, we conducted element-scale consolidation test under different temperatures up to 65 °C, to evaluate the temperature effect on the consolidation characteristics of clays. Large-scale soil tank test with a cartridge heater installed at the center was also conducted to assess uneven settlement of soft clay associated with radial heating. Experimental results confirmed that thermally induced volume change varies with the type of clay and a consolidation rate can be enhanced by temperature elevation.

1 Introduction

Thermally active geosystems using renewable energy sources, such as biomass energy, industrial waste heat and solar thermal energy, have been widely researched especially in Western countries and in China in the last several decades (e.g. Navarro et al. 2017; Rotta Loria and Laloui 2017; Ma et al. 2017). For a better understanding of thermal soil behavior, the processes and soil properties governing coupled heat transfer and water flow in soils as well as thermally induced changes in soil volume and pore water pressure have been observed to play increasingly important roles (e.g. Towhata et al. 1993; Abuel-Naga et al. 2007).

Thermal ground improvement is also an important research topic related to the energy geotechnics. The reclamation of soft soil sites is still a topic of interest due to the economic benefits related to the expansion of coastal cities in small countries such as Japan, because of limited land availability. For example, during construction of the Kansai International Airport, which was opened in 1994 on a man-made island in Osaka Bay, Japan, more than 2.2 million vertical sand drains fully penetrating the 17.3- to 24.1-m-thick soft Holocene clay layers and 430 million m^3 of fill material were used to drain pore water from the soft clay for prompt consolidation of the soft layers. Because consolidation of such soft clay layers takes a lot of time and effort, time-saving and cost-effective measures need to be further developed. Since permanent contraction

A. Ferrari and L. Laloui (Eds.): SEG 2018, SSGG, pp. 75–82, 2019.
https://doi.org/10.1007/978-3-319-99670-7_10

of soft clay can be expected, heating of the soft clay layers should accelerate consolidation when used with vertical drains (Abuel-Naga et al. 2006). Although thermal consolidation of clays have been well studied, mechanisms and factors governing thermal response of soils are not fully understood (Ghaaowd et al. 2017). In this study, two laboratory tests were conducted for a better understanding of the consolidation characteristics of clays having different Atterberg limits. The temperature effects on consolidation parameters were discussed based on one-dimensional consolidation test performed under different temperatures up to 65 °C. A large-scale consolidation test system which can follow uneven settlement was newly developed and applied for evaluating the consolidation of a soft clay layer radially heated by a heater.

2 Methodologies

2.1 Materials

In this study, we used commercially available two clay soils for the experiment. One is kaolinite clay from BASF Corporation, and the other is Kasaoka clay from Tachibana Material Co., Ltd. The geotechnical properties of the clays are summarized in Table 1. Although both clays are classified as CH according to the Unified Soil Classification System, they have different Atterberg limits and contents finer than 2 μm.

Table 1. Basic properties of clays used

	Kaolinite clay	Kasaoka clay
Particle density (g/cm^3)	2.58	2.68
Plastic limit (%)	30.2	24.6
Liquid limit (%)	77.0	58.5
Plastic index	46.8	33.9
Content finer than 2 μm (%)	92	43
Activity	0.50	0.78
Loss of ignition (%)	13.8	5.5
Major minerals	SiO_2 45.2%	SiO_2 56.0%
	Al_2O_3 38.8%	Al_2O_3 3.8%

2.2 One-Dimensional Consolidation Test

One-dimensional consolidation test was conducted under constant temperatures and incremental loading, according to the Japanese standard method (JIS A 1217:2009). First, water contents were adjusted to 1.1 times the liquid limit of each clay material in reference to water contents of actual dredged sediments. Second, the kaolinite clay and the Kasaoka clay were filled in a consolidation cell having a diameter of 10 cm and a height of 5 cm to achieve wet densities of 1.43 and 1.54 g/cm^3, respectively. The cell with clay was hit by a hammer to avoid the presence of air bubbles. A degree of saturation higher than 95% was confirmed before the test. Third, consolidation pressures were applied to the specimen via a bellofram cylinder.

Figure 1 shows the whole apparatus of the consolidation test. Specimen temperature was controlled by adjusting water temperature by circulation of hot water in a tank where the cell with a specimen were immersed. Consolidation pressures from 4.9 kPa to 628 kPa were applied with a load increment ratio of 2 under temperatures of 23 °C, 35 °C, 50 °C, and 65 °C. These temperatures were determined by considering possible elevation in ground temperature by circulation of hot water.

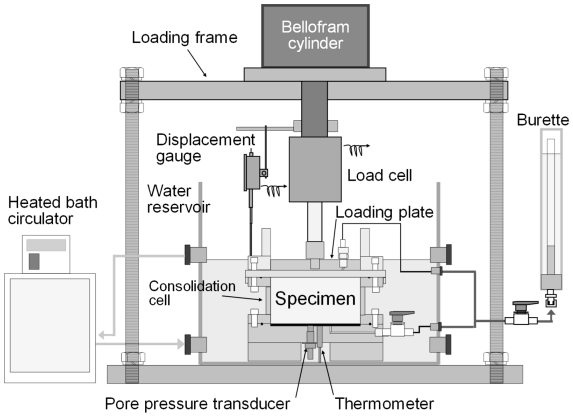

Fig. 1. Apparatus for the one-dimensional consolidation test

2.3 Large-Scale Soil Tank Test

We developed a new testing system shown in Fig. 2, for assessment of differential settlement by radial heating of soil. The soil tank has 0.8 m in inner diameter and 0.75 m in height. A sheath heater installed at the center of the tank can heat surrounding soil in the horizontal direction. Since a circular hole of 5.0 cm diameter is equipped on the loading plate, the heat is not loaded and affected even during the progression of consolidation with the help of this core-sheath structure. In addition to conventional vertical loading using a screw jack and a loading plate, loading by air pressure is also possible by this experimental system, as air can be supplied from an air pump to a gap between the loading plate and the rubber membrane placed beneath the plate. With the help of this loading system, overburden pressure on the surface can be kept constant even if the magnitude of settlement varies according to a distance from the heater surface. At a height of 10 cm from the bottom of a clay layer, three button-type wireless temperature data loggers (DS1920-F5 +) and pore pressure transducers (BPR-A-100KPS) were placed at 10 cm intervals. Settlement of the ground surface was measured by three laser displacement sensors (CD33-120NV) and two wired displacement transducers (DP-500E). Temperature of the rod heater was monitored and controlled by a thermocouple attached on the heater surface. Note that the apparatus was not covered by a heat insulation material during the test.

In the soil tank, a clay layer with a thickness of 20 cm was prepared with 10-cm sand layers on the top and bottom for drainage. The same kaolinite clay as the element-

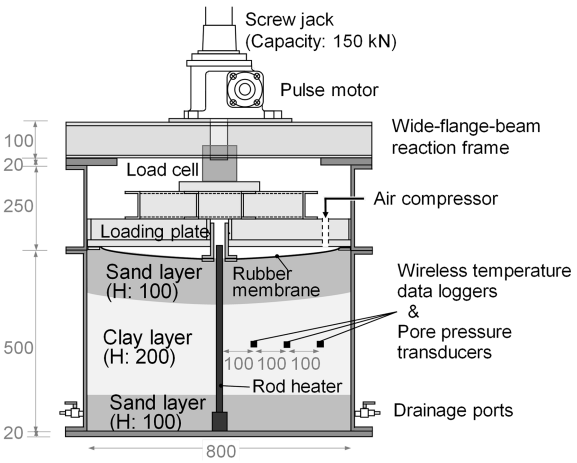

Fig. 2. Apparatus for the soil tank test (unit: mm)

scale test and silica sand 6 were used in the soil tank test. The kaolinite clay was mixed with water to attain a water content of approximately 90% and was deaired in a vacuum mixer. First, the rod heater was installed to a holder at the bottom of the tank. Second, the bottom sand layer was prepared by hydraulic compaction and was fully saturated. Third, the fully saturated clay layer was prepared with a thickness of 20 cm with carefully removing air bubbles inside a specimen. Last, after the top sand layer was prepared also by hydraulic compaction and fully saturated, the loading system, including the wide-flange-beam reaction frame and the loading plate, was assembled and placed on the specimen. At the boundaries between each layer, a thin non-woven geotextile was placed for prevention of a decrease in drainage performance. This test was conducted with two heater temperatures of 20 °C and 50 °C. In the case of 50° C, the specimen was heated at 50 °C for 24 h before applying consolidation pressure. In both cases, after the placement of the loading plate whose weight corresponds to 2.2 kPa of consolidation pressure, consolidation pressures of 20 kPa, 40 kPa, and 80 kPa were incrementally applied on the specimen. Each step of consolidation was lasted for 48 h by considering t_{100} obtained in the element-scale test. In the last step of the 50 °C case, the consolidation pressure of 80 kPa was applied by the air pressure, while the screw jack was used in other steps.

3 Results of the Element-Scale Test

Figure 3 shows e-log p curves obtained from the one-dimensional consolidation test, normalized by the initial void ratio of each specimen. In the cases of the kaolinite clay, the smaller e/e_0 values were obtained with the higher temperatures. The e/e_0 value significantly decreased with the consolidation pressure higher than 78.5 kPa, as observed in previous research (Eriksson 1989). The biggest Δe of 1.27 was observed at the consolidation pressure of 628 kPa. However, e/e_0 of the Kasaoka clay showed the

similar values regardless of consolidation pressure and temperature. As Ghaaowd et al. (2017) demonstrated that the thermally induced excess pore water pressure generated in saturated soils during undrained heating has a nonlinear decreasing trend with the plastic index of soil, the temperature effects were not significant in the Kasaoka clay having a relatively low plastic index.

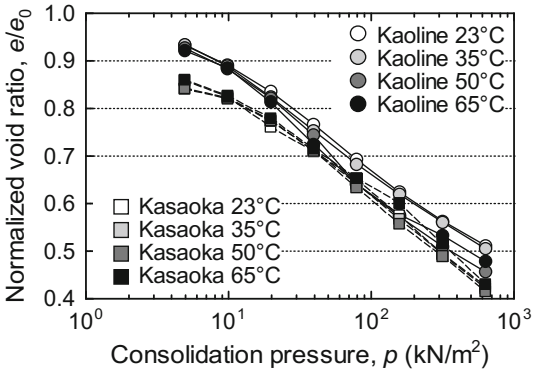

Fig. 3. e-log p curves obtained from the element-scale test

Figure 4 illustrates the relationship between an increase in specimen temperature and coefficient of consolidation (c_v) normalized by c_v at 23 °C. The average c_v value of all consolidation steps is plotted in this figure. It is obvious that the c_v value increased with an increase in temperature in both materials. The c_v values at 65 °C was almost double that at 23 °C. An increasing rate of log c_v was calculated according to the following equation on the assumption that c_v logarithmically increases with temperature.

$$\log c_v = a \cdot T + b \tag{1}$$

where, a = increasing rate of log c_v; T = temperature; and b = intercept.

Figure 5 shows the relationship between an increasing rate of log c_v and liquid limit of clay, including data from previous works. Values in the legend denote a diameter (D) and a height (H) of a specimen used in each research. An increasing rate of log c_v has a good linear correlation with liquid limit of clays for specimens with D/H smaller than 1.0. It is known that thickness of diffuse double layers of clay becomes larger with higher temperature (Mitchell and Soga 2005). Because of this, the temperature effect on c_v became more significant on clay with lower water retentivity and smaller liquid limit. However, further study is required to clarify the temperature effect on consolidation rate including the size effect.

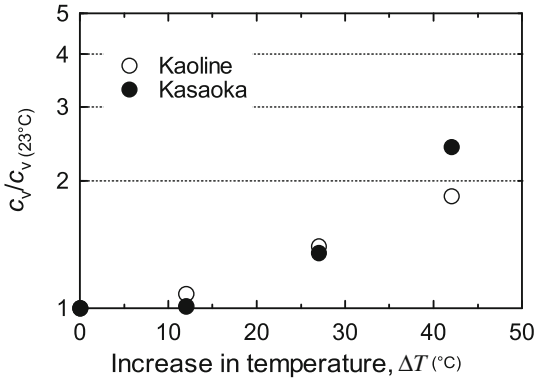

Fig. 4. Relationship between coefficient of consolidation and temperature

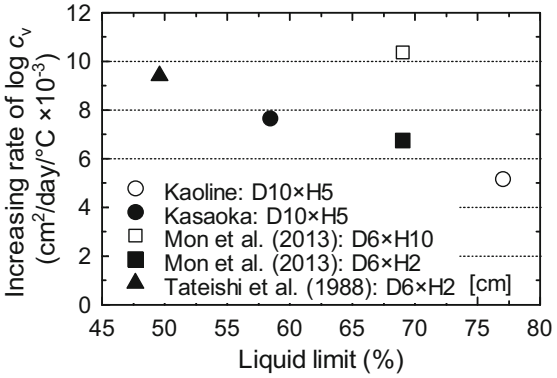

Fig. 5. Relationship between increasing rate of log c_v and liquid limit (including data adapted from Mon et al. (2013) and Tateishi et al. (1984))

4 Results of the Large-Scale Soil Tank Test

Figure 6 illustrates results of the soil tank test at the last loading step with consolidation pressure of 80 kPa. In this figure, a distance from the heater surface is put on the X-axis. The temperature was elevated overall by heating at 50 °C, compared with the case of 20 °C, and the highest temperature was observed at the nearest point from the heater surface. Thereby, the settlement near the heater was relatively large compared to that near the soil tank wall. This fact confirms that the clay layer was consolidated conically, which is consistent with the results of the element-scale test. A void ratio of the clay layer at a distance of 10 cm (approximately 30 °C) after the consolidation with 80 kPa was 1.62, while that was 1.35 in the element-scale test at 35 °C. This difference should be observed because the settlement of the clay layer was overestimated in the soil tank test due to no consideration of compressibility of the sand layers.

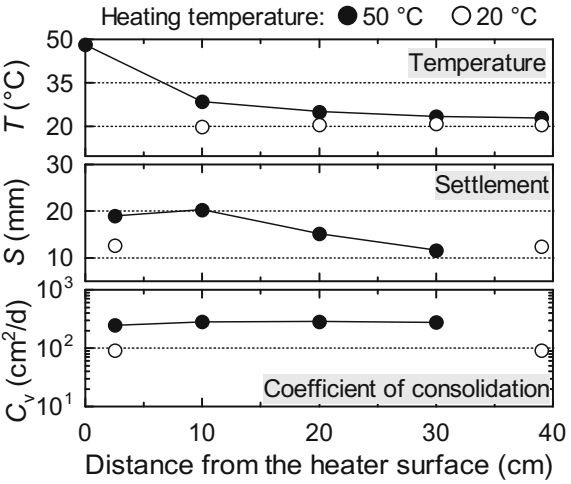

Fig. 6. Results of large-scale soil tank test (p = 80 kPa)

The c_v values were approximately 280 cm^2/day and almost the same at any points regardless of distance and temperature, different from the element-scale test, probably because specimen temperature did not significantly increased in the soil tank test. The c_v values observed at a heating temperature of 50 °C were almost double those at 20 °C. The fact that an increasing rate of c_v obtained in the soil tank test is much bigger than those values in Figs. 3 and 4 also implies the scale effect on thermally induced change in c_v.

5 Conclusions

In this study, we conducted one-dimensional consolidation test and large-scale soil tank test under different temperatures up to 65 °C, to evaluate the temperature effects on the consolidation characteristics of clays. The main achievements obtained in this study can be summarized as follows:

(1) The temperature effect on consolidation of clay becomes more significant under relatively high consolidation pressures.
(2) The magnitude of thermally induced volume change varies with the type of clay probably attributed to different water retentivity.
(3) Coefficient of consolidation increases with an increase in specimen temperature in the element-scale test.
(4) Although the specimen temperature and the settlement decreased with an increase in distance from the heater surface, a clear trend between specimen temperature and c_v was not observed in the large-scale soil tank test.

References

Abuel-Naga, H.M., Bergado, D.T., Suttisak, S.: Innovative thermal technique for enhancing the performance of prefabricated vertical drain system. Geotext. Geomembr. **24**(6), 359–370 (2006)

Abuel-Naga, H.M., Bergado, D.T., Bouazza, A., Ramana, G.V.: Volume change behavior of saturated clays under drained heating conditions: experimental results and constitutive modeling. Can. Geotech. J. **44**(8), 942–956 (2007)

Eriksson, L.G.: Temperature effects on consolidation properties of sulphide clays. In: Proceedings of the 12th International Conference on Soil Mechanics and Foundation Engineering, pp. 2087–2090 (1989)

Ghaaowd, I., Takai, A., Katsumi, T., McCartney, J.S.: Pore water pressure prediction for undrained heating of soils. Environ. Geotech. **4**(EG2), 70–78 (2017)

Ma, Q.J., Ng, C.W.W., Mašín, D., Zhou, C.: An approach for modelling volume change of fine-grained soil subjected to thermal cycles. Can. Geotech. J. **54**(6), 896–901 (2017)

Mitchell, J.K., Soga, K.: Fundamentals of Soil Behavior, 3rd edn. Wiley, New York (2005)

Mon, E.E., Hamamoto, S., Kawamoto, K., Komatsu, T., Moldrup, P.: Temperature effects on geotechnical properties of kaolin clay: simultaneous measurements of consolidation characteristics, shear stiffness, and permeability using a modified oedometer. GSTF Int. J. Geol. Sci. **1** (1), 1–10 (2013)

Navarro, L., de Gracia, A., Colclough, S., Browne, M., McCormack, S.J., Griffiths, P., Cabeza, L.F.: Thermal energy storage in building integrated thermal systems: a review. Part 1. Active storage systems. Renew. Energy **88**, 526–547 (2017)

Rotta Loria, A.F., Laloui, L.: The equivalent pier method for energy pile groups. Geotechnique **67**(8), 691–702 (2017)

Tateishi, Y., Yamanouchi, T., Ochiai, H., Hayashi, S.: Effects of temperature on consolidation characteristics of clays. Tech. Rep. Kyushu Univ. **57**(4), 415–422 (1984). (in Japanese)

Towhata, I., Kuntiwattanaku, P., Seko, I., Ohishi, K.: Volume change of clays induced by heating as observed in consolidation tests. Soils Found. **33**(4), 170–183 (1993)

Study on the Pavement Structure with Solar Panel

Yoonyoung Choi[1(✉)], Jaesoon Choi[1], Bonghyun Kim[2], Sungki Park[3], and Choonghee Hwang[1]

[1] Seokyeong University, Seoul, Republic of Korea
kurt8200@nate.com
[2] Geo.T.S., Seoul, Republic of Korea
[3] Contech ENG, Seoul, Republic of Korea

Abstract. This study is a development of road system applying solar panels to road pavement block. Concrete pavement block to mount solar panel is designed to verify effective of power generation. Pavement blocks with solar panels is photovoltaic block that enables to produce renewable energy. It is a combination of solar panel and pavement block. For road pavement structures, it is possible to make various shapes in accordance with general road design standards. Before prototyping, the road design standards and the concrete block design standards of South Korea have been reviewed and the prototype specifications were determined based on the findings of the review. The prototype is expected to have higher adaptability on roads in Korea because the concrete block design standards have been employed for determining the concrete strength and size of the prototype block. Power generation panels for photovoltaic power generation are designed to be manufactured by connecting commercially available solar panels in parallel, and to be mounted on mount hole within the blocks. Strength and slip resistance tests are included in follow up research plans to examine road function of the concrete blocks, and measurement of photovoltaic power generation efficiencies after the trial construction.

1 Introduction

Currently, solar panels already have been installed in various structures such as residential houses, parking lots, and bicycle paths In addition, 100 Thousand Green Home Policy is enforced by the Government of South Korea. About 268 MW of photovoltaic systems were installed in 2008 and approximately 170 MW were installed in 2009. Moreover, Sejong City provides bike road that consist of solar panel and roofs to provide efficient land usage and convenience in terms of both power generation and bikers. It was able to examine the energy efficiency matters and secure the structural safety by selecting high efficiency modules and determining the optimal installation angles.

In recent years, many studies have been conducted to improve efficiencies of photovoltaic power generation, development of continuous/automatic cooling and cleaning systems of solar panel, light and modular panel technologies and other similar technologies such as panel status monitoring technologies to improve the power generation and maintenance efficiencies.

A. Ferrari and L. Laloui (Eds.): SEG 2018, SSGG, pp. 83–89, 2019.
https://doi.org/10.1007/978-3-319-99670-7_11

Although there are similar researches, such as piezoelectric roads and current collecting roads, there is no research on integrated structure of road + solar panels in Korea. It is also difficult to find relevant studies overseas.

2 Related Researches in Korea

Solar panels installed in Korea are mostly focused on privately house, public building, canopies of bicycle paths, and etc., and this implies that the PV penetration rate in Korea is very low considering the nation's total land area. However, it would be possible to increase the usage of solar energy if more attention is made to solar panels that are integrated into roads. On the other hand, may studies on development of road systems with integrated electrical systems, such as piezoelectric road and current collecting roads, have been conducted, but there is no ongoing development of road integrated PV system, which is the main objective of this study. Based on the above, we have determined that it is necessary to develop a road system that is suitable for application in Korea, based on establishment of theoretical research and technical concept of photovoltaic system and to study the applicability of the system through applicable performance evaluation.

3 Overseas Research Cases

The Solar Roadway developed in the United States is a sidewalk and road that can be modularly combined with specially designed solar panels. It is possible to install the LED's inside the panels, so it is possible to display the lanes without being required apply painting, and to prevent snow accumulation and icing on the roads by inserting heated wires. Currently, pilot operations are planned for roads and parking lots, and plans to apply on highways in the future are scheduled. The energy generated by solar power generation from parking lots are expected to be helpful for electrical vehicles traffic on the road once charging infrastructure is installed on highways in the future.

In 2014, SolaRoad of Netherlands completed a pilot construction of the world's first photovoltaic bicycle path, which spans about 70 m length, in Amsterdam. It was able to confirm the potential of PV power generating roads by generating more than 2,000 kW per hour through the pilot project.

The Ministry of Environment of France reported an opening of a 1 km extension of the photovoltaic roads in a small village near Normandy at the end of 2016. It is estimated that 2,000 drivers will pass through the road every day during pilot project.

The total construction cost was 6.3 billion won and the energy generated from the pilot road is planned to be used for powering street lights in the nearby villages. In addition, plans to pave 1,000 km of roads with integrated PV power generation system during the next 5 years are in place.

3.1 Summary of Reference Literatures Used in This Study

3.1.1 Korean Road Design Standards

Roads are classified into highways and general roads, and the highways are further classified as urban expressways which are built in urban areas. The types of roads in accordance with Article 8 of the 「Road Law」, which describes the functional classifications of general roads, are major arterial roads and minor arterial roads.

The design speed is speeds of the vehicles that become the basis of the road design, and it is decided in accordance with functional classification of the road, the area and the topography.

Design section refers to a section in which the same design standards according to the condition of the terrain and the planned traffic volume of the area where the roads are located.

It is desirable to apply as the same design section in certain sections of the roads that have approximately similar nature, functionalities, importance, traffic volume, terrain, and area (Table 1).

Table 1. Design speeds by functions of roads

Functional classification of roads		Design speed (km/h)			
		Rural area			Urban area
		Flat lands	Hilly areas	Mountain areas	
Highways		120	110	100	100
General roads	Main arterial roads	80	70	60	80
	Minor arterial roads	70	60	50	60
	Collector roads	60	50	40	50
	Local roads	50	40	40	40

Road pavement is classified into asphalt pavement and concrete pavement, and the minimum thicknesses of pavement layers specified in the Road Design Standards are over 50 mm for the surface layer and over 100 mm for the base and sub-base layers. Guidelines for the design of cement concrete pavement mixing have been examined in order to support the vehicle loads and the following standards have been identified as the results (Table 2).

Table 2. Mixing standards for pavement concrete

Items	Test method	Unit	Standard
Design standard bending stiffness	KS F 2408	MPa	Above 4.5
Water/binder ratio		%	Below 45
Maximum amount of coarse aggregate		mm	Below 40
Slump value	KS F 2402	mm	10–60
Amount of air range	KS F 2409	%	5.5 ± 1.5

3.1.2 Concrete Block Pavement Standards

Standards for existing block have been examined in order to develop photovoltaic blocks. The KS regulations for the blocks currently in uses are KS F 4119 Concrete Interlocking Blocks for Sidewalks and Roads and KS F 4001 Concrete Plate for Pavement. In this study, the standards of blocks currently being installed were investigated by examining the KS F 4 4119 Concrete Interlocking Blocks for Sidewalks and Roads.

The performance of blocks presented in the KS regulations are classified into two types for vehicle uses and pedestrian uses respectively. And also standards for bending stiffness, water absorption rate, permeability coefficient, and etc. are presented (Table 3).

Table 3. Block performances presented in Korean standards

Classification	Bending stiffness (MPa)		Water absorption rate (%)		Permeability coefficient (mm/s)	
	For pedestrian use	For vehicle use	Individual	Average	Rating	Standard
Regular blocks	5.0	Below 10	Below 7	-		
Permeable blocks	Above 4.0	Above 5.0	-	-	Above 0.1	

The thicknesses of the blocks for sidewalks and vehicle roads are 60 mm and 80 mm, respectively. KS F 4001 the Standards for Concrete Plate for Pavement are classified in accordance with the dimensions and functions (Table 4).

Table 4. Plate types

Types	Nominal dimension	Dimension			Function
		Length	Height	Thickness	
Regular plate	300	300	300	30, 60, 80	-
	400	400	400		
	450	450	450	60, 80	
	500	500	500		
Permeable plate	300	300	300	60, 80	Permeability
	400	400	400		
	450	450	450		
	500	500	500		

The performance should be suitable in criteria of bending stiffness load, bending stiffness, water absorption coefficient, permeability coefficient, and etc.

3.1.3 Suggestion of Photovoltaic Power Generation Block System

In this study, photovoltaic power generation pavement method is proposed. PV power generation panels and concrete blocks are integrated into a single system in order to improve solar panel pavements systems which is large and heavy.

The following two types of pavement blocks have been devised in this study; (1) a PV pavement block in which PV panels and conventional pavement blocks are integrated, and (2) a hybrid PV pavement block in which conventional pavement blocks, PV panels, and piezoelectric systems are integrated (Fig. 1).

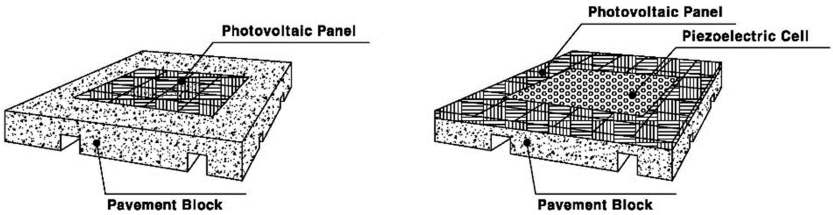

Fig. 1. PV block and hybrid (PV+Piezoelectric) pavement block

For block packing system of this study, 200 mm of the sub-base layer thickness given in the road design standard has been applied, and the surface layer thickness of 200 mm, which exceeds the standard of 80 mm or above, has been applied (Table 5).

Table 5. Standards applied in this study

Items	Unit	Standard		Application in this study
		Road design standards	KS F 4419	
Crushed rubble sub-base layer	mm	200	-	200
Surface layer thickness	mm	100	80	200
Block dimensions	mm	-	300–500	300
Design standard bending stiffness (f28) (material age: 28 days)	MPa	Above 4.5	Above 5.0	Above 5.0
Water/binder ratio	%	Below 45	Below 25	Below 25

4 Pilot Manufacturing

Concrete pavement and Korean road design standards are reviewed to devise prototypes of photovoltaic concrete blocks that satisfy the standards. Hybrid type block is capable of simultaneously generating photovoltaic power and piezoelectric power.

4.1 PV Integrated Road Pavement Blocks

Conventional photovoltaic panels are prone to panel damages because its entire surface is composed of glass. Therefore, there is possibility of increased maintenance costs.

The PV integrated concrete block reduces the risk of damages with solar panels and increases the easiness of maintenance with its modular construction design. In addition, it has the same size as currently used pavement blocks, Therefore, it seems to reduce the maintenance costs and improve the constructability (Fig. 2).

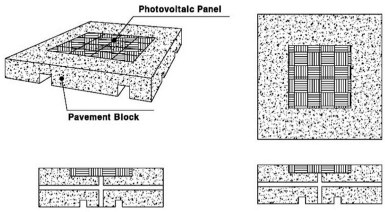

Fig. 2. PV block scheme

4.2 Hybrid Pavement Blocks with Integrated PV Panel and Piezoelectric Elements

The hybrid pavement block is a prototype product in which the piezoelectric block is placed along the longitudinal direction of the road and the block is characterized by a forward facing upwardly inclined surface on one side and a rearward facing downwardly inclined surface on the other side of the main body shown above (Fig. 3).

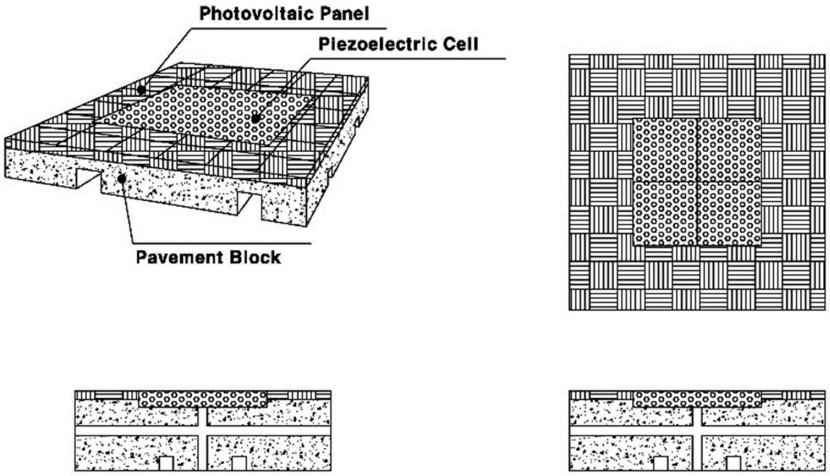

Fig. 3. Hybrid pavement block scheme

5 Follow Up Study Plan

As follow up study, various tests such as strength, slip resistance are planned to measure functionalities. The concrete block must satisfy the compressive strength suggested in this study and required slip resistance in terms of drivability of the road.

In addition, the power generation efficiency of the PV panel mounted on the block will be measured through trial constructions. The concrete block proposed in this study is expected to have decreased efficiency since damages to the surface of protective glasses. Those glasses are inevitable to certain extent due to its design in which vehicles are designed to pass above the PV panels. Therefore, it is our plan to conduct a comparative study of power generation efficiencies in two cases, one with undamaged protective glass surface and the other with damaged protective glass surface.

References

Ministry of Trade, Industry and Energy: 4th Basic Plan for New and Renewable Energy (2014)
Ministry of Land, Transport and Maritime Affairs: Korean Road Design Standards (2016)
National Technology Standards Agency: Concrete interlocking blocks for roads KS F 4419 (2016)

Numerical Study on the Long-Term Thermal Performance and Ground Temperature Variation of Energy Pile in Multi-layered Soil

Yimu Guo, Guozhu Zhang(✉), Songyu Liu, Yanjun Du, and Zhibin Liu

Institute of Geotechnical Engineering,
Southeast University, Nanjing 210096, China
zhanggz@seu.edu.cn

Abstract. Energy pile has been increasingly applied into buildings as both bearing structure and heat exchanger. In China, precast-high strength concrete (PHC) pipe pile is widely used in soft soil improvement, high-rise building construction and bridge foundation for its high bearing capacity, reliable quality, convenient installation and cost benefits. However, application of PHC pipe pile as geo-thermal structure is rare. Based on a field thermal response test on PHC pipe pile embedded in a particular multi-layered ground, the thermal response of pile is analyzed by numerical study. Thermo-physical properties of ground are tested from undisturbed soil samples from the site, then applied into multi-layered heat transfer model. Moreover, the influences of inhomogeneous thermal properties and thermal boundary conditions are analyzed in details, especially on long-term thermal performance and temperature field evolution in surrounded soil. The results indicate ground temperature varies apparently at the interface of soil layers, while temperatures within the layer are relatively uniform. Appropriate geological structure benefits the long-term performance of energy pile. This study provides a better understanding of energy pile performance in a more realistic ground condition and suggestions for design of PHC energy pile are proposed.

1 Introduction

Energy geo-structures can provide sustainable energy for many types of buildings. Successful applications have been reported on piles, tunnel linings, diaphragm walls and slabs (Brandl 2006; Laloui et al. 2006). The energy pile, serving as both bearing and heat exchanging element for buildings, has been investigated across the world via different methods (Bourne-Webb et al. 2009; Ng et al. 2014; You et al. 2014). Most of them simplified the surrounding soil as a homogenous medium for heat transfer (Philippe et al. 2009; Cui et al. 2011; Loveridge et al. 2014). However, flood plain sediments are widely distributed in southeast part of China and piles are usually driven into multi-layered soil. The physical properties of soil layers vary along the depth, which may influence the thermal response of the energy pile differently. The mechanical properties of soil and the soil-pile interaction may be sensitive to the temperature change (Campanella and Mitchell 1968; Cekerevac and Laloui 2004;

A. Ferrari and L. Laloui (Eds.): SEG 2018, SSGG, pp. 90–96, 2019.
https://doi.org/10.1007/978-3-319-99670-7_12

Abuel-Naga et al. 2006). Thus, temperature response of energy pile system should be investigated considering the layered feature of the ground.

In this paper, the pile and ground thermal responses were simulated based on the real operating and geological condition from a prototype thermal response test on a PHC energy pile. The PHC pipe pile was vastly used in soft soil for its rapid construction and cost efficiency. Transient and long-term temperature responses of PHC pile and surrounding soils were revealed. Finally, suggestions were made for the design of PHC energy piles in layered ground.

2 Geological Conditions and Pile Configuration

2.1 Site Characterization

The parameters of simulation were derived from the full-scale thermal response test located in the campus of Southeast University, Jiangsu, China. Borings test results showed the Qinhuai River floodplain unit sediments were encountered in this site and the soil were clearly divided into several layers. The water table was relatively stable at 1 m depth with no apparent ground water flow. The basic physical properties of undisturbed soil samples from each layers were tested according to ASTM standards. Thermal properties of the soils were tested by a plane heat source method listed in ISO S 22007-2. Soil samples were cut into 3 cm thick cylinders and the hot disk probe was clamped between them. The ground profile of the upper 24 m was listed in Table 1.

Table 1. Soil stratification and the thermal properties of materials used in simulation.

Material	Depth (m)	Thermal conductivity ($W\ m^{-1}\ K^{-1}$)	Specific heat capacity ($J\ kg^{-1}\ K^{-1}$)	Density ($kg\ m^{-3}$)
Soil 2-1	2.9–4.3	1.37	885	1890
Soil 2-2	4.3–11.5	1.15	877	1740
Soil 2-3	11.5–13.5	1.54	918	1970
Soil 2-3	13.5–16	1.71	934	1970
Soil 2-4	16–17.4	1.51	843	1950
Soil 2-5	17.4–24	1.30	775	1990
PHC		1.78	800	2490
HEPE pipe[a]		0.42	2300	957
Circulating water		0.591	4200	1000

[a]Given by manufacturer.

2.2 PHC Energy Pile Configuration

The PHC pipe pile in this study was 24 m in length with a single U-shape high-density polyethylene (HDPE) pipe inserted to the bottom of pile hole. The outer diameter and wall thickness of pile were 500 mm and 110 mm, respectively. The thermal properties

of concrete samples from pile were also tested by aforementioned method and the results are listed in Table 1. The pipe has a 25 mm outer diameter and 20 mm inner diameter. To maintain the leg distance of U-pipe, 220 mm long steel bars were installed between the pipes in every 3 m depth. Then, the pile hole was filled with water to enhance the heat transfer between pipe and pile wall. Four boreholes at 0.5 m, 0.65 m, 0.8 m and 1.15 m from pile center were drilled for ground temperature monitoring by placing temperature sensors in typical depths. The configuration of energy pile was shown in Fig. 1.

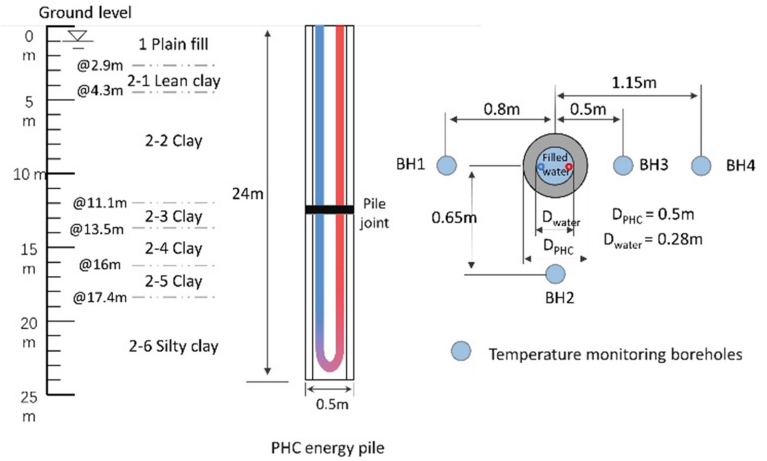

Fig. 1. Energy pile configuration.

3 Numerical Model

The heat transfer process of PHC energy pile has been investigated by a commercial finite element software COMSOL Multiphysics. A 3D numerical model was developed to simulate the thermal response test (TRT) and the long-term temperature field in multi-layered soils. Heat transfer in solid and non-isothermal pipe flow models were coupled in this model considering the convective heat transfer in pipes and heat conduction in pile and soil.

Figure 2 shows the model mesh of energy pile containing 446224 free tetrahedral elements with maximum and minimum element size of 2.72 m and 0.1 m. The dimensions in x, y, and z are 10 m, 10 m, and 34 m. The model is divided into 6 layers along z direction of which the thermal properties are chosen from Table 1. The soils at 0–2.9 m and 24–34 m are assumed to be same with soil 2-1 and soil 2-5. Dimensions of pile and pipe are built according to Sect. 2. Monitoring boreholes are created at 0.5 m, 0.65 m, 0.8 m, 1.15 m, 2 m and 4 m from pile center. The temperature at the top of soil surface is kept constant at 15 °C. The boundary conditions at outer lateral and bottom surfaces are set to be zero heat flux as the dimension of model is beyond thermal influenced district. Initial ground temperature is set to 18 °C. The governing

equation in conductive domains is Fourier's law. The energy equation for pipe flow can be expressed as Eq. 1.

$$\rho_f A C_p \frac{\partial T_f}{\partial t} + \rho_f A C_p u \cdot \nabla T_f = \nabla \cdot \left(\lambda_f A \nabla T_f\right) + \frac{1}{2} f_D \frac{\rho_f A}{2 d_h} |u| u^2 + Q + Q_{wall} \quad (1)$$

Where ρ_f is the water density (kg/m^3), A is the cross area of pipe (m^2), C_p is the heat capacity at constant pressure J/(kg·K), T_f is the fluid temperature (K), u is a tangential velocity of fluid (m/s), λ_f is the thermal conductivity of water (W/(m·K)), Q is a general heat source (W/m), Q_{wall} represents external heat exchange through the pipe wall (W/m). The second term on the right expresses the friction heat dissipated due to viscous shear based on Churchill's friction model.

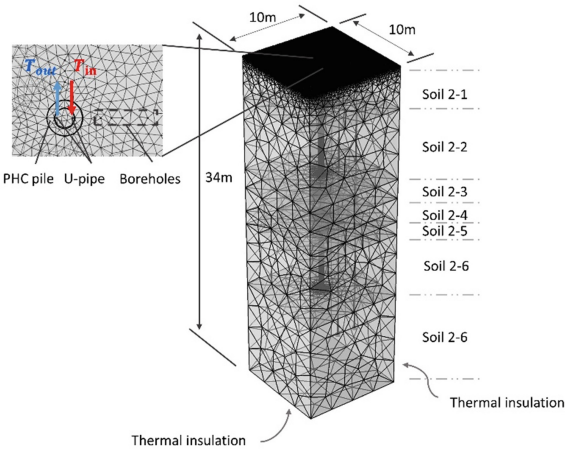

Fig. 2. 3D mesh of the PHC pile simulation.

This model is developed to simulate the TRT of PHC piles. To apply a constant heat flux to energy pile, the nodal temperature boundary at the pipe inlet is set ΔT °C higher than the temperature at pipe outlet. Thus, the constant heat injection rate can be calculated as:

$$Q_{in} = \Delta T \cdot \rho_f C_p u = (T_{\text{in}} - T_{\text{out}}) \cdot \rho_f C_p u \quad (2)$$

u in the model is 0.42 m/s which is usually used in a real TRT.

4 Results

4.1 Synthetic TRT Results

In TRT simulation, the difference between inlet and outlet temperature was set to 3.5 °C and test lasted for 5 days. The heat injection rate calculated by Eq. 2 was 3030 W.

Average fluid temperature was analyzed by traditional line source theory. It is to be noted that the early data should be discard because simplified line source model formula results large deviation at the beginning. Figure 3(a) shows that calculated comprehensive thermal conductivity value varied with the starting time of the fitting. The last data point fixed at the end of test (120 h). The estimated value decreased to the average thermal conductivity (1.34 W/(m·K)) at nearly 12 h, then it became stable. Thus, at least 12 h early data should be dismissed. Moreover, TRT analysis may be feasible on PHC pipe pile and can reflect the average thermal properties of multi-layered ground. Figure 3(b) shows the average fluid temperature evolution and the fitting line using line heat source theory.

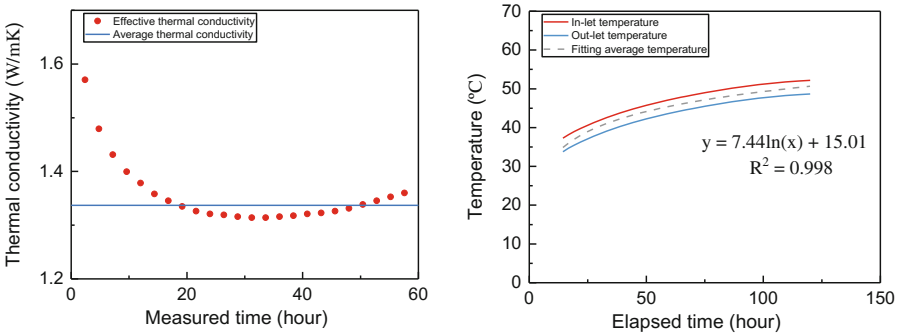

Fig. 3. Estimation of thermal response test.

4.2 Long-Term Ground Temperature Evolution

The long-term ground temperature response was investigated under the heat injection rate of 1730 W by inducing inlet temperature 2 °C higher than the outlet temperature.

Figure 4 shows the relatively short-term ground temperature distribution along depth at 0.5 m, 0.65 m, 0.8 m, 1.15 m, 2 m and 4 m from the pile center. After 4 days heating (Fig. 4(a)), the ground was mostly heated uniformly. The nearest borehole at 0.5 m reflected the influence of inhomogeneous soil thermal properties. The maximum temperature of 22.8 °C was found at 8.8 m depth while the minimum temperature of 22.1 °C was at 15.0 m depth. Soil beyond 2 m was still not heated. At 8th day (Fig. 4(b)), the inhomogeneity influence become more apparent with the heating process. Stratification of temperature emerged at distant soil. The maximum temperature difference caused by this effect was 1.4 °C in 0.5 m borehole. During the short-term heating, ground temperature distribution was mainly formed by the layered feature of soil.

Figure 5 shows the long-term ground temperature field. At 45th day (Fig. 5(a)), the upper boundary and lower unheated soil influenced the temperature distribution more evidently. At mid-depth of 0.5 m borehole, the maximum temperature of 33.2 °C was found at 8.8 m depth while the minimum temperature of 30.8 °C was at 14.6 m depth.

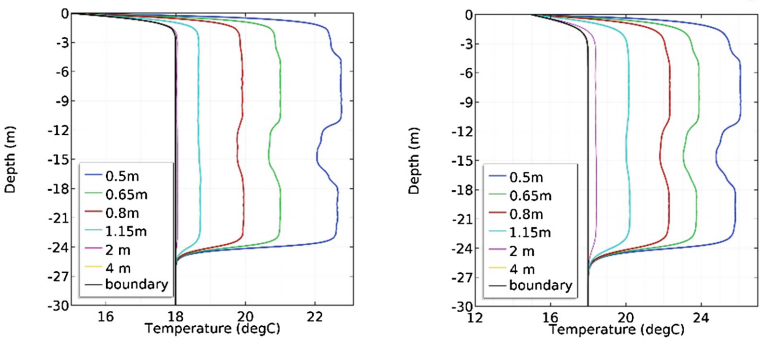

(a) 4 days (b) 8 days

Fig. 4. Short-term ground temperature distribution

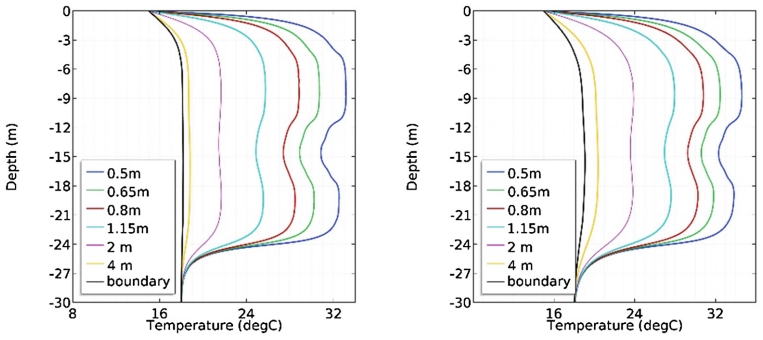

(a) 45 days (b) 90 days

Fig. 5. Long-term ground temperature distribution

Thus, the temperature difference between layers increased comparing to short-term temperature field. However, this uneven temperature increase diminished with distance from pile increase. Figure 5(b) shows the last status of ground temperature field. After another 45 days heating, the maximum and minimum temperature at 0.5 m borehole was 34.7 °C and 32.3 °C. The difference of them was same as that of 45th day, which indicates the temperature stratification was stable after long-term heating. Since the average ground temperature kept increasing, this layered influence was weaken by the time increase. It is to be noted that the soil temperature of upper and lower part were closer to their boundary temperature. Compared to the short-term situation, vertical heat transfer predominantly influenced the long-term soil temperature field rather than the inhomogeneity of layered subsurface.

5 Conclusion

The numerical study suggests the traditional TRT is feasible to be applied on PHC pile and the estimated thermal conductivity can reflect the average thermal properties of multi-layered soil. The distribution of thermal properties formed a stratified temperature field in soil. However, this factor only apparently influences the temperature distribution near the pile. The temperature difference between layers increased with time and approached to a constant value. At long-term heating stage, the thermal boundary effected the soil temperature more significantly than the inhomogeneity of soil. Therefore, the short-term near pile ground temperature calculation should consider the layered feature of soil, whereas the long-term distant temperature can ignore this influence but should consider the boundary effects.

Acknowledgments. The financial support from the National Natural Science Foundation of China (No. 51578146) is much appreciated.

References

Abuel-Naga, H.M., et al.: Experimental evaluation of engineering behavior of soft bangkok clay under elevated temperature. J. Geotech. Geoenviron. Eng. **132**(7), 902–910 (2006)

Bourne-Webb, P.J., et al.: Energy pile test at Lambeth College, London: geotechnical and thermodynamic aspects of pile response to heat cycles. Géotechnique **59**(3), 237–248 (2009)

Brandl, H.: Energy foundations and other thermo-active ground structures. Géotechnique **56**(2), 81–122 (2006)

Campanella, R.G., Mitchell, J.K.: Influence of temperature variations on soil behavior. J. Soil Mech. Found. Div. **94**, 709–734 (1968)

Cekerevac, C., Laloui, L.: Experimental study of thermal effects on the mechanical behaviour of a clay. Int. J. Numer. Anal. Methods Geomech. **28**(3), 209–228 (2004)

Cui, P., et al.: Heat transfer analysis of pile geothermal heat exchangers with spiral coils. Appl. Energy **88**(11), 4113–4119 (2011)

Laloui, L., et al.: Experimental and numerical investigations of the behaviour of a heat exchanger pile. Int. J. Numer. Anal. Methods Geomech. **30**(8), 763–781 (2006)

Loveridge, F., et al.: Comparison of two different models for pile thermal response test interpretation. Acta Geotech. **9**(3), 367–384 (2014)

Ng, C., et al.: Centrifuge modelling of heating effects on energy pile performance in saturated sand. Can. Geotech. J. **52**(8), 1045–1057 (2014)

Philippe, M., et al.: Validity ranges of three analytical solutions to heat transfer in the vicinity of single boreholes. Geothermics **38**(4), 407–413 (2009)

You, S., et al.: In-situ experimental study of heat exchange capacity of CFG pile geothermal exchangers. Energy Build. **79**, 23–31 (2014)

Numerical Modelling of Thermo-Active Shafts

Eleonora Sailer(✉), David M. G. Taborda, Lidija Zdravkovic, and David M. Potts

Imperial College London, London, UK
eleonora.sailerl3@imperial.ac.uk

Abstract. Geotechnical structures, such as foundation piles, retaining walls and tunnel linings, are increasingly employed to produce geothermal energy for space heating and cooling. However, the exchange of heat between the structure and the ground induces additional structural forces and contributes to further structural and ground movements, which may affect the serviceability and stability of such structures. While numerous field and numerical studies exist regarding the response of geothermal piles, no investigations have been carried out to characterise the response of thermo-active shafts. This paper presents a numerical study of the short and long term behaviour of hypothetical thermo-active shafts through fully coupled thermo-hydro-mechanical (THM) finite element (FE) analyses using the Imperial College Finite Element Program (ICFEP), where the effect of changing the structure's geometric characteristics is investigated.

1 Introduction

Shallow geothermal energy can be exploited by means of different types of systems either installed directly within the ground (closed and open loop systems) or embedded within geotechnical structures (such as foundation piles, tunnel linings, basement slabs and retaining walls). The latter systems may often be more economical as limited additional works are required since these geotechnical structures are needed to provide stability. Furthermore, they generally have a large contact area with the ground, which improves the thermal performance.

However, it has been demonstrated by numerous experimental studies (e.g. those performed by Campanella and Mitchell 1968) that temperature changes associated with heat flux affect the thermo-hydro-mechanical (THM) behaviour of soils, inducing volumetric expansion/contraction and, for low permeability soils, leading to the development of thermally-induced excess pore water pressures, hence affecting their strength and stiffness. Thus, various field and numerical studies have been undertaken to assess the effects of thermal loads on the stability and serviceability of thermo-active geotechnical structures. The majority of the work was carried out on thermo-active piles (e.g. Bourne-Webb et al. 2009; Gawecka et al. 2017), whereas very little literature is available regarding the performance of thermo-active retaining structures and, to the authors' knowledge, no studies have been published to date on the behavior of circular shafts employed as heat exchangers.

This paper presents a numerical study on the THM behaviour of a hypothetical thermo-active shaft embedded in London Clay, with the aim of analysing the effect of

A. Ferrari and L. Laloui (Eds.): SEG 2018, SSGG, pp. 97–104, 2019.
https://doi.org/10.1007/978-3-319-99670-7_13

heat exchange on the transient behaviour of the structure in terms of forces and displacements. Furthermore, the influence of varying the shaft's diameter on the structure's response is assessed. The analyses are carried out using the Imperial College Finite Element Program (ICFEP, Potts and Zdravkovic 1999), which is capable of performing fully coupled THM simulations. The THM finite element (FE) formulation, its implementation and validation are described in Cui et al. (2018).

2 Problem Description and Numerical Analysis

A circular shaft embedded within London Clay (γ_s = 20 kN/m^3) is considered in this study, with a 40.0 m deep and 1.0 m thick wall. The depth of excavation (H) is 36.0 m and a 2.0 m thick base slab is constructed above that level. Analyses with different diameters (D) have been carried out, with adopted values of 9.0 m, 18.0 m and 36.0 m. Half width of the excavation was modelled in axisymmetric conditions and the finite element mesh, shown in Fig. 1, extends 100 m beyond the extrados of the structure and 60 m below the bottom of the wall. Both the soil and concrete structures where modelled with eight-noded quadrilateral elements, with displacement and temperature degrees of freedom in every node and pore pressure degrees of freedom at the corner nodes (soil elements only).

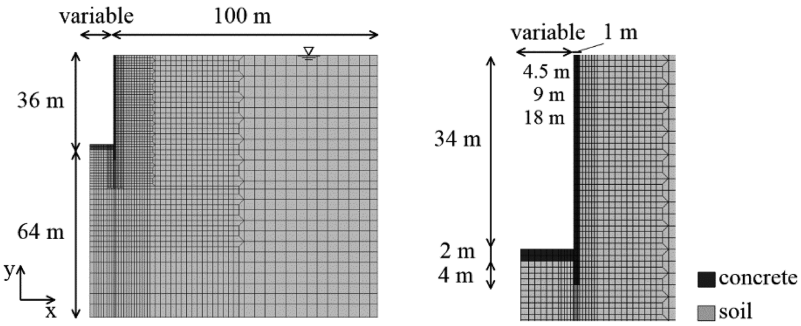

Fig. 1. Adopted finite element mesh

The initial conditions of the problem are characterised by a hydrostatic pore water pressure profile, with the water table located at ground level, a constant value of K_0 of 1.0 and a uniform temperature of 15 °C. The wall was wished in place and full friction was assumed along the soil-structure interface.

Axisymmetric FE analyses were performed using ICFEP. Since fully coupled THM analyses were carried out, thermal volumetric changes and thermally-induced excess pore water pressures were simulated. The latter result from a combination of two different contributions: pore water pressures due to the relative expansion/contraction of pore fluid with respect to that of soil and those due to mechanical volumetric changes of the soil skeleton induced by changes in temperature (Cui et al. 2018).

The concrete structures were modelled as isotropic and linear elastic, whereas the soil was modelled as non-linear elasto-plastic with a Mohr-Coulomb failure criterion coupled with the IC.G3S non-linear elastic stiffness model (Taborda et al. 2016) to better predict the pre-yield soil response. Unless otherwise stated, all the mechanical parameters were adopted from those listed for London Clay by Gawecka et al. (2017), whereas all other material properties are listed in Table 1.

Table 1. Material properties

Linear coefficient of thermal expansion of soil, α_s (m/m/K)	1.7×10^{-5}	Concrete Young's Modulus, E (GPa)	37.0
Linear coefficient of thermal expansion of pore water, α_w (m/m/K)	6.9×10^{-5}	Linear coefficient of thermal expansion of concrete, α_c (m/m/K)	8.5×10^{-6}
Permeability k (m/s)	1.0×10^{-10}	Concrete Poisson's ratio, μ (-)	0.3
Volumetric heat capacity of soil mixture, ρc_p (kJ/m^{3}K)	3000	Thermal conductivity of soil mixture, λ (W/mK)	2.0

The domain was restrained from moving in the vertical direction along the bottom boundary and in the horizontal direction along the lateral and bottom boundaries. Pore water pressures along the far-field lateral boundary and bottom boundary were assumed to remain constant throughout the analyses. The ground surface was kept at constant temperature, whereas, across all other boundaries, no heat flux was allowed. Furthermore, the temperature of the base slab was assumed to stay at its initial value (15 °C) during all performed analyses.

The heat exchange was simulated by applying a prescribed temperature change of 15 °C over 10 days to all elements of the wall and the final temperature was kept constant for 10 years. While this may not be a realistic scenario in terms of the operation of a ground source energy system, such a simplified approach provided valuable insights into the long-term behaviour of the analysed structures. Before the start of the thermal analysis, the excess pore water pressures due to excavation and construction were fully dissipated in order to facilitate the interpretation of the results, while the stiffness of the soil was reset to its maximum value (see Gawecka et al. (2017) for details on this procedure). Suitable values for the time-step were chosen according to the recommendations by Cui et al. (2016). Moreover, in order to obtain a realistic estimate of the stress state within the ground prior to heating the wall, the complete construction sequence of the shaft was simulated assuming a pin connection between the base slab and the wall. However, during the heating stage, for simplicity, this structural connection was removed, meaning that the two structural components work independently. Cleary, the nature of such connection is likely to have a considerable impact on the long-term behaviour of a retaining structure and will be, therefore, the object of a dedicated study.

3 Results

The results are presented in terms of excess pore water pressures, wall axial forces, wall displacements and ground surface movements. First, the behaviour of the shaft with D = 18 m is analysed in order to provide details on the transient behaviour of this type of structures. Subsequently, the effects of varying the diameter of the shaft is investigated. The adopted sign convention is such that positive values refer to compressive pore water pressures, compressive axial forces, upwards vertical movements and horizontal movements towards the retained side. All the quantities shown are calculated from the start of heating, in order to isolate the effect of temperature changes.

3.1 Transient Behaviour

The changes in pore water pressures after 10 days and 1 year from start of heating are displayed in Fig. 2(a) and (b), respectively. Compressive pore water pressures are generated around the structure as a consequence of both the changes in temperature as well as mechanical volumetric changes due to the thermal expansion of the shaft lining. Conversely, on the excavation side, the outward radial movement of the wall leads to tensile excess pore water pressures beneath the base slab. With time, the pore water pressures close to the structure on the retained side dissipate from about 100 kPa to 60 kPa. Concurrently, they increase in regions further away from the heat source, where larger changes in temperature are now taking place. It can be noted that, after 1 year, larger changes in pore water pressures develop beneath the base slab, with the suctions observed in the short-term being replaced by compressive pore water pressures. This is due to higher changes in temperature occurring in this area as a consequence of the proximity of the heat source to insulated boundaries, as shown in Fig. 2(d). It is also interesting to note that after 1 year, the area where changes in pore pressure have been registered (Fig. 2(b)) is considerably larger than the size of the heated region (Fig. 2(d)), highlighting the importance of THM interactions in this type of problems.

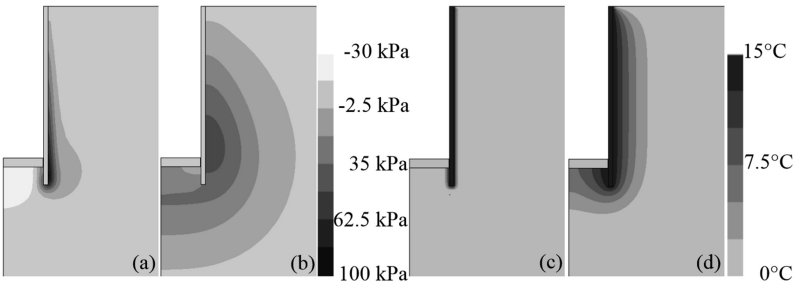

Fig. 2. Changes in pore water pressures for D = 18 m (a) after 10 days and (b) after 1 year and changes in temperature (c) after 10 days and (d) after 1 year

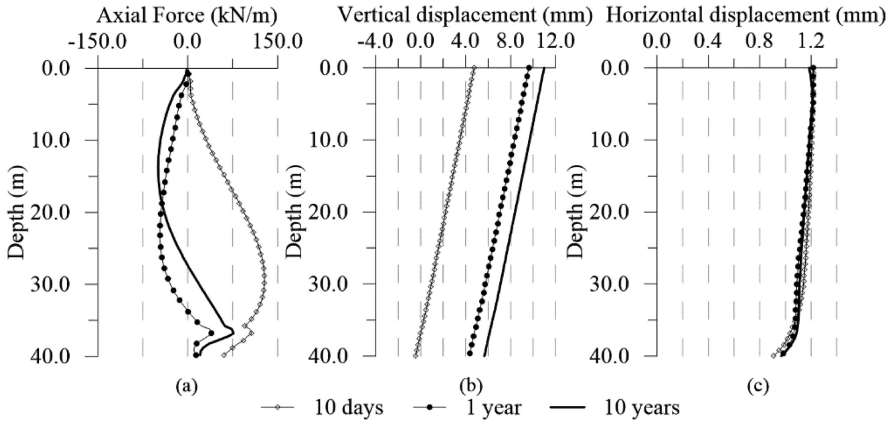

Fig. 3. Response of structure for $D = 18$ m at different time instants (a) axial forces, (b) vertical displacements and (c) horizontal displacements

Figure 3(a) shows the change in axial force with depth at different time instants (10 days, 1 year and 10 years from start of heating). In the short term, the axial forces are compressive along the whole depth of the wall (maximum 130 kN/m). This is due to soil restraining the thermal expansion of the wall in the axial direction through shearing at the soil-structure interface. As expected, the behaviour in the long term is affected by volumetric changes of the soil due to temperature and excess pore water pressure dissipation. In fact, after 1 year, the compressive axial forces reduce due to thermal volumetric expansion of the soil, releasing part of the restriction it was applying. The largest changes take place within the lower section, where the structure is subjected to larger tensile actions (maximum tensile axial force of − 45 kN/m). This is confirmed by observing the vertical displaced shapes in Fig. 3(b), where the elongation ΔL of the wall increases between 10 days and 1 year from 5.1 mm to 5.2 mm. Subsequently, the structure is subjected to compression due to soil settling as the compressive pore water pressures close to the structure (see Fig. 2(a) and (b)) dissipate, reducing the tension in the wall (by a maximum of 50 kN/m). Differently from the displacements in the vertical direction (Fig. 3(b)), where can be noted that the structure moves upwards with time as a consequence of soil thermal expansion, little changes in the structure's horizontal movements occur with time. This is because the circular structure is stiff in the circumferential direction, which is a major difference with respect to conventional retaining walls. Naturally, as no change in horizontal movements take place, no substantial changes in bending moments are expected throughout the analysis.

3.2 Effect of Shaft Diameter

The previous analysis has provided insight into the behaviour of a circular thermo-active shaft, demonstrating that the development of thermally-induced excess pore water pressures with time affects highly the response of the structure. Further THM analyses are carried out by varying the diameter of the shaft to $D = 9$ and $D = 36$ m.

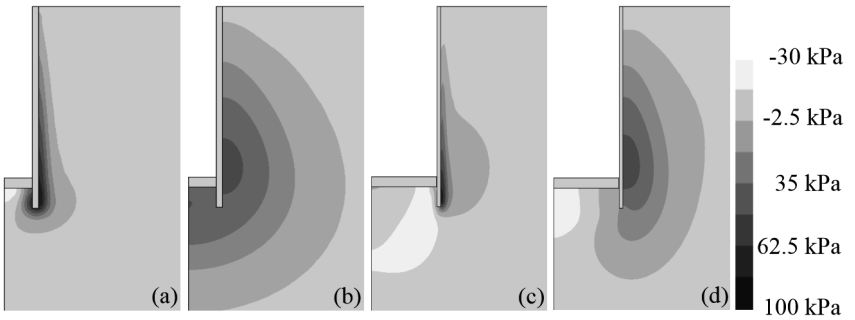

Fig. 4. Changes in pore water pressures a for D = 9 m (a) after 10 days, (b) after 1 year and for D = 36 m (c), after 10 days and (d) after 1 year

Figure 4 shows that the diameter has a considerable effect on the distribution of pore water pressures, although the applied temperature change is equal in all cases. On the retained side, while similar pore water pressures develop around the structure for all cases, such similarity reduces considerably with the distance from the wall. On the excavation side, pore water pressures are highly influenced by the build-up of temperatures beneath the base slab and by the lateral expansion of the shaft. Regarding the former, the distance between the heat source (i.e. the structure) and the axis of symmetry (i.e. insulated boundary) is larger with a larger diameter, which implies that the temperatures beneath the base slab will be lower in the case where D = 36 m, resulting in smaller thermally-induced excess pore water pressures. Conversely, the larger expansion in the radial direction obtained for larger diameters leads to larger suctions beneath the base slab.

Figure 5 depicts the development of axial forces at three different time instants for the three analysed cases. Both diameters – D = 9 m and D = 36 m – display a similar

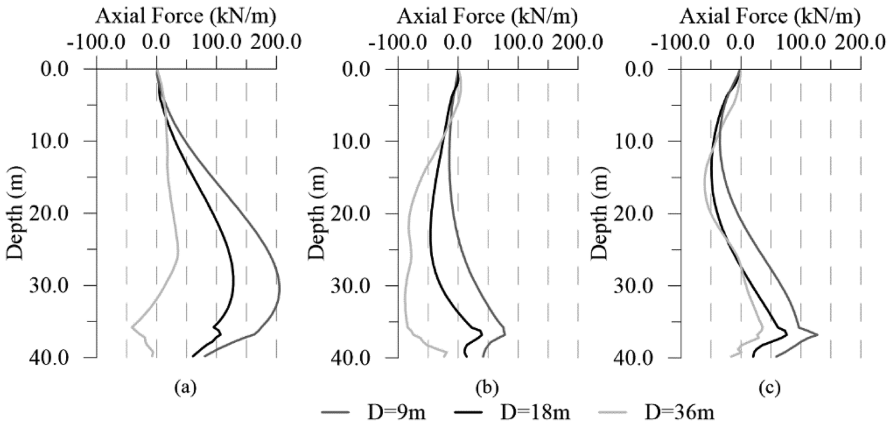

Fig. 5. Thermally induced axial forces for different diameters (a) after 10 days, (b) after 1 year and (c) after 10 years

behaviour as the one previously described. However, since the large diameter shaft has a larger contact area with the soil, this will be more affected by soil thermal expansion when compared to the other analyses, hence the lower axial force after 10 days of heating. Conversely, for the small diameter shaft, the restriction applied by the soil is larger, leading to a larger initial axial force. Similar to the behaviour observed for the shaft with D = 18 m, the transient response is first dominated by soil thermal expansion and then by compression induced by soil settling due to the dissipation of the thermally induced pore water pressures.

For all the diameters, the vertical displaced shapes of the wall and the vertical ground surface movements after 10 years of heating are illustrated in Fig. 6(a) and (b), respectively. In the short term, all diameters displayed a similar vertical movement profile (see Fig. 3(b)), with the largest diameter shaft suffering a slightly larger elongation (after 10 days, ΔL is equal to 5.3 mm for D = 36 m, compared to 5.0 mm calculated for D = 9 m), in agreement with the lower axial forces registered in this case. Furthermore, the vertical movement with time, which is governed by the gradual thermal expansion of the soil, is also larger for D = 36 m. As previously observed, a larger soil mass is affected by the temperature changes for the larger diameter shaft, hence the soil expands more with time when compared to the other two analyses. This behaviour is directly reflected in the ground movements at the surface, which are consequently largest for the larger diameter. It should be noted that these reach significant values at a large distance behind the wall (at a distance of 50 m, these are larger than 2.0 mm for all the analyses).

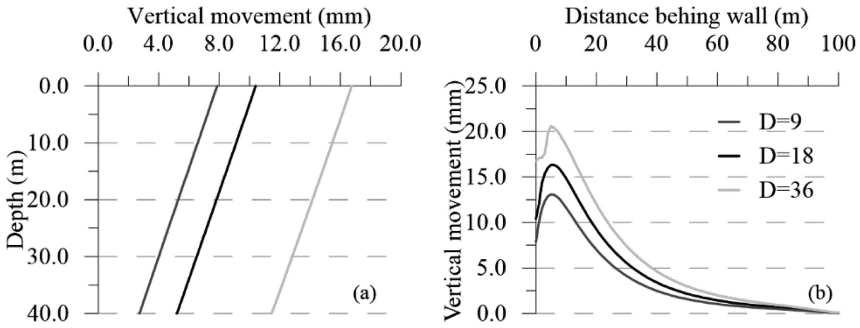

Fig. 6. Thermally induced vertical movements for different diameters after 10 years from heating (a) structure's displaced shape and (b) ground surface movements

4 Conclusions

Earth retaining structures are increasingly being employed as heat exchangers, however their behaviour under non-isothermal conditions is still uncertain. In this study, the effect of temperature change on the performance of circular shafts was investigated by performing fully coupled axisymmetric thermo-hydro-mechanical finite element analyses using the Imperial College Finite Element Program. Specifically, the transient

behaviour of shafts of different diameters was assessed. It was shown that, in general, the response of the structure is controlled by the volumetric expansion of soil upon changes in temperature, which occurs both due to thermal expansion as well as due to changes in pore water pressures, with the latter affecting substantially the transient behaviour. Varying the diameter of the structure led to the observation that these structures are influenced by the contact area between structure and soil, which impacts the transient effects. For larger diameters of the shaft, larger structural movements and thus lower forces were observed. It was also shown that there are interactions with the thermal boundary conditions, where temperatures beneath the base slab increase faster the closer the heat source is from insulated boundaries (e.g. axis of symmetry). Furthermore, large vertical wall and ground surface movements were calculated, indicating that possible influences on nearby structures should be investigated. In this study, the connection with the base slab was not modelled. However, it is envisaged that it may affect forces and displacements, and is hence the object of further study.

References

Bourne-Webb, P.J., Amatya, B., Soga, K., Amis, T., Davidson, C., Payne, P.: Energy pile test at Lambeth College, London: geotechnical and thermodynamic aspects of pile response to heat cycles. Geotechnique **59**, 237–248 (2009)

Campanella, R.G., Mitchell, J.K.: Influence of temperature variations on soil behaviour. ASCE J. Soil Mech. Found. Eng. Div. **4**(3), 709–734 (1968)

Cui, W., Gawecka, K.A., Taborda, D.M.G., Potts, D.M., Zdravković, L.: Time-step constraints in transient coupled finite element analysis. Int. J. Numer. Methods Eng. **106**(12), 953–971 (2016)

Cui, W., Potts, D.M., Zdravković, L., Gawecka, K.A., Taborda, D.M.G.: An alternative coupled thermo-hydro-mechanical finite element formulation for fully saturated soils. Comput. Geotech. **94**, 22–30 (2018)

Gawecka, K.A., Taborda, D.M.G., Potts, D.M., Cui, W., Zdravkovic, L., Haji Kasri, M.: Numerical modelling of thermo-active piles in London Clay. Proc. Inst. Civ. Eng. Geotech. Eng. **170**(3), 1–19 (2017)

Potts, D.M., Zdravković, L.: Finite Element Analysis in Geotechnical Engineering Theory. Thomas Telford, London (1999)

Taborda, D.M.G, Potts, D.M., Zdravkovic, L.: On the assessment of energy dissipated through hysteresis in finite element analysis. Comput. Geotech. **71**, 180–194 (2016)

Advanced Finite Difference Method for Study Energy Piles Behavior in Temperature Dependent Soils

Mohammad Oliaei(✉), Mohammad Amir Kiani, and Mahboubeh Torkaman

Tarbiat Modares University, Tehran, Islamic Republic of Iran
m.olyaei@modares.ac.ir

Abstract. Recently, the use of energy piles with the dual purpose of supplying energy and the bearing of superstructures is becoming widespread. Providing a proper and efficient numerical analysis can help to accelerate this process. For this purpose, this study tried to develop some features of finite difference method which is used in Thermo-Pile. The proposed numerical model can consider the effects of soil temperature dependence on energy piles behavior. Another capability of the proposed method to model temperature distribution in surrounding soil could result in applying temperature effect on soil behavior. This study has shown that there are good agreements between numerical results and experimental observations. Relating side shear resistance of soil to temperature gives a better prediction of pile response for the higher temperature. The pile behavior for various input parameters was studied. Based on obtained results, the pile response to thermomechanical loads depends on the various properties of pile and soil such as diameter, length, side shear and toe resistance.

1 Introduction

Regard to increasing energy consumptions around the world and limited fossil fuel resources, the challenge of supplying sustainable energy resources become a crucial problem for future. As geothermal energy for heating and cooling of the modern building is available in the most region of the world, this method gained more popularity. Adequate efficiency and economic benefit of using energy pile for heat exchanging results to more application of this type of piles in constructions. But the complex behavior of energy piles under thermomechanical loading needs to be studied carefully to overcome their obscurities. Results of field and centrifuge tests show that applying thermal loads on pile lead to a different distribution of axial strains and stresses along the pile (Bourne-Webb et al. 2009; Laloui et al. 2006) and consequently effect on its settlement and bearing capacity (Khodaparast et al. 2016). The magnitude of these changes depends on many parameters, which can be divided into two general categories, soil and pile properties. Most important parameters of the pile are thermal expansion coefficient and elasticity modulus. Proportionally for soils are elasticity modulus, thermal expansion coefficient, permeability, void ratio, saturation condition and etc. As soils are natural materials they show more complicated behavior than pile behavior.

A. Ferrari and L. Laloui (Eds.): SEG 2018, SSGG, pp. 105–112, 2019.
https://doi.org/10.1007/978-3-319-99670-7_14

Moreover, imposed restriction on head and toe of the pile have a great effect on its response to various imposed loads.

Bourne-Webb et al. (2009) propose a mechanism to describe energy pile's behavior in some special conditions. This mechanism was later extended by Amatya et al. (2012) to consider more situations. They define a Null Point (NP) as a location where induced thermal displacement is zero which the behavior of energy piles strongly depends on it. With respect to the mechanism of Bourne-Webb et al. (2009), Knellwolf et al. (2011) proposed a numerical method for studying pile behavior under thermomechanical loading. Their method was similar to Coyle and Reese (1966) for analyzing the pile behavior under mechanical loading and also developed to account the effect of thermal loads. The response of soil to thermal and mechanical loads was modeled with a bilinear function of Frank and Zhao (1982) to estimate the mobilization process of side shear and toe resistance With displacement. Using a bilinear function for soil resistance and displacement cause the persistence of calculation process (Chen and McCartney 2016). Similar to this method, Plaseied (2012) used a hyperbolic function to conjugate the pile displacement with the mobilization of soil resistance. Furthermore, the effect of the radial expansion of pile on increasing side resistance was considered. Therefore, a simpler and efficient calculation was obtained. But the location of NP must have specified by the user. So Chen and McCartney (2016) modify the procedure to account NP location based on an iterative procedure on induced thermal displacement until reaching equilibration. Their proposed method has this ability to calculate shear and toe resistance based on empirical relations proposed for usual conditions in geotechnical applications such as drained or undrained loading and semi-floating or end bearing pile.

In contrast to Knellwolf et al. (2011) method, the proposed analysis by Chen and McCartney (2016) can't consider various soil layer. Another limitation of the proposed method by Knellwolf et al. (2011) and Chen and McCartney (2016) is they don't consider transferred heat to surrounding soils on their response. This could arise from the absence of valid data for piles in temperature-sensitive soils. So in this paper, a heat transfer analysis was accompanied by a thermomechanical analysis of pile behavior. The results from heat transfer analysis were imported to pile's analysis to obtain more accurate analysis on the pile.

In later sections, the more details about heat transfer analysis and pile behavior under thermomechanical loading will be presented. After that, the calibration of implemented methods will be evaluated. The parametric study shows that the distribution of axial thermal strain and stress depends on various property of pile and soil such as diameter, length, side shear and toe resistance.

2 Finite Difference Model

In this study, the behavior of an energy pile with 1 m diameter and 26 m length in the corner of a four-story building at the Swiss Federal Institute of Technology (SFIT) in Lausanne was analyzed. The experimental results and material properties were adopted from Knellwolf et al. (2011) and Laloui et al. (2006). This case study due to accurate results and comprehensive instrumentation was selected for many numerical models validations. Since there isn't available data that show the distribution of temperature

adjacent to the energy pile for the selected case study, the results of heat transfer analysis implemented in this study, validated by numerical analysis performed by Khodaparast et al. (2016) which is done by using ABAQUS. The proposed models were attained by using MATLAB.

2.1 Heat Transfer Analysis

Considering a heat transfer around an energy pile analysis is a useful tool for considering temperature effect on soil response. Also, it can be used for assessing the efficiency of energy pile in terms of energy extraction. Heat transfer analysis is done by solving its governing equation by finite difference method as Eq. 1.

$$T_{i,j} = \alpha_{i,j}^{-1}\left(\frac{dx^2dy^2}{2(dx^2+dy^2)}\right)\left(\frac{\alpha_{i+1,j}T_{i+1,j}+\alpha_{i-1,j}T_{i+1,j}}{dx^2}+\frac{\alpha_{i,j+1}T_{i,j+1}+\alpha_{i,j-1}T_{i,j-1}}{dy^2}\right) \quad (1)$$

Where $T_{i,j}$ is the temperature in point i and j in x and y-direction respectively. $\alpha = \frac{C}{S \times d}$ is defined based on conductivity (C), density (d) and specific heat (S).

Table 1. The soil thermal and resistance properties for calibration model

Layer	Depth (m)	Conductivity (W/m.°C)	Density (kg/m^3)	Specific heat (J/kg.°C)	$q_{s,max}$* (kPa)	a_s ($\times 10^{-3}$)	b_s	ω
A1	0–5.5	1.8	2000	1200	102	4	0.8	0.5
A2	5.5–12	1.8	1950	1230	70	4	0.85	0.5
B	12–21.5	1.8	2000	1200	74	3.5	0.8	0.7
C	21.5–25.5	1.8	2200	1090	160	1	0.75	0.8
D	25.5–26	1.1	2550	785	160	1	0.75	0.8
D (Tip)	$q_{b,max}$* = 11000 kPa		a_b = 0.008		b_b = 0.8			-

*q_s: ultimate side shear resistance, q_b: ultimate toe resistance

The model geometry consists of a 5 m length and 52 m depth which in axisymmetric condition a pile with 1 m diameter and 26 lengths is placed in it. The material properties and depth of each soils stratum for heat transfer analysis are presented in Table 1. The thermal boundary conditions consist of allowing heat to be dissipated from the right side as well as top and bottom of the model. The Fig. 1 illustrates that implemented modeling can show heat transfer in multi-layered soils with good accuracy.

2.2 Thermomechanical Pile Analysis

By using finite difference scheme the considered pile in the previous section was discretized to n element. The solving procedure for pile response under mechanical loading start from *N-th* element and for thermal loads, it starts relative to NP towards upper and bottom sections. Due to limitations, further explanation is n't provided. More

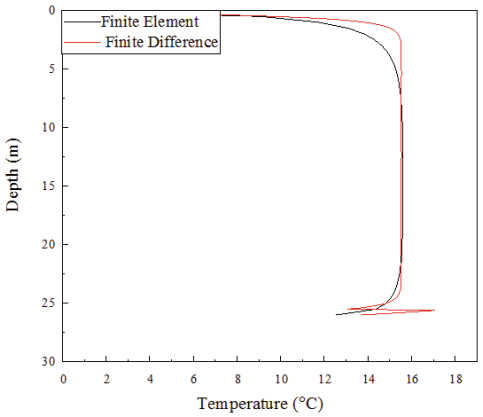

Fig. 1. Validation temperature distributions in soil-1 m distance from Pile

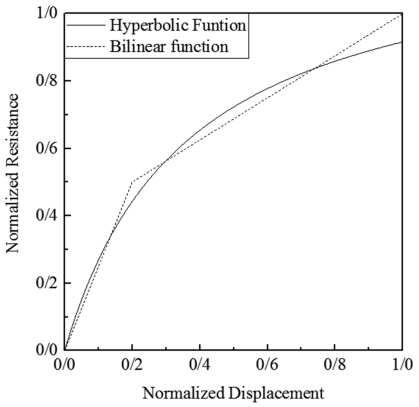

Fig. 2. Schematic of bilinear function approximation by hyperbolic equation

Table 2. The pile thermal and resistance properties for calibration model

Length (m)	Diameter (m)	Conductivity (W/m.°C)	Density (kg/m^3)	Specific heat (J/kg.°C)	Elasticity modulus (GPa)	Head stiffness (MPa)	Thermal expansion (°C^{-1})
26	1	2.1	2500	800	40	0	8.5×10^{-6}

detailed information on how to obtain the thermomechanical behavior of pile under thermomechanical loads can be found at Chen and McCartney (2016) and Knellwolf et al. (2011). The main difference between the proposed model in this paper with Chen and McCartney (2016) is that it can consider various layer. This development is important to make it possible to be used in real geotechnical conditions. The material properties are illustrated in Tables 1 and 2. Fitting parameter a_s, b_s, a_b, and b_b for hyperbolic function in Eqs. 4 and 5 are derived by best approximation for proposed load-settlement curves by Knellwolf et al. (2011) (Fig. 2).

Then, the hyperbolic functions (f_{T-z}) and (f_{Q-z}) are used for relating the side shear $\left(Q^i_{s,Max}\right)$ and toe ($Q_{b,max}$) resistances to shear displacement for each segment ρ^i_s and toe $\left(\rho^n_b\right)$, respectively.

$$Q^i_b = Q_{b,Max}.f_{Q-z}(\rho^n_b) \tag{2}$$

$$Q^i_s = Q^i_{s,Max}.f_{T-z}(\rho^i_s) \tag{3}$$

$$f_{Q-z}(\rho^n_b) = \frac{\rho^n_b}{a_b + b_b\rho^n_b} \tag{4}$$

$$f_{T-z}(\rho_s^i) = \begin{cases} \frac{\rho_s^i}{a_s + b_s \rho_s^i} & for\ loading \\ \frac{\rho_s^i}{a_s} + \frac{Q_s^i}{Q_{s,Max}^i} - \left(\frac{1}{\frac{Q_{s,Max}^i}{Q_s^i} - b_s} \right) & for\ unloading \end{cases} \quad (5)$$

3 Results and Discussion

As can be seen in Fig. 3 the modified method can show behavior of energy pile in multi-layered ground with adequate accuracy. Since in real cases, there are Fewer probabilities that there only be a single layer in the ground, it is important that all proposed numerical methods could consider multi soil layers. Since in the case of energy piles, surrounding soils control the intensity of produced axial stress and strain, considering the various layers and their response to thermal loads become more important.

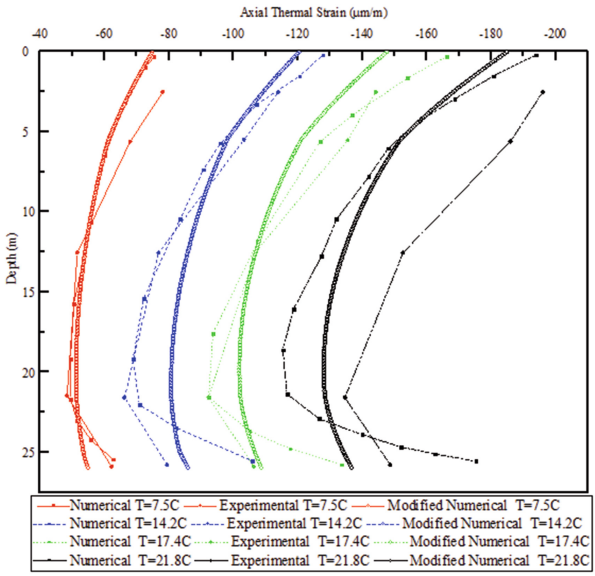

Fig. 3. Comparison between Numerical – Experimental axial thermal strains from Knellwolf et al. (2011) and modified method

3.1 The Effect of Soil Temperature Dependence on Piles Response

As can be seen in Fig. 3 none of the proposed model by current study and Knellwolf could demonstrate the accurate response of pile in higher temperature than 17.4 °C. Underestimation of this results could lead to uncertainty in the subsequent safety

analysis. For this reason, reduction factors (ω) for side shear resistance based on Eq. 6 was defined to reduce the side shear resistance of surrounding soils for a higher temperature than critical temperature (T_c).

$$Q^i_{s,Max} = \omega_i Q^i_{s,Max} \qquad if \;\; T_i > T_{cr} \tag{6}$$

Where $Q^i_{s,Max}$ is ultimate side shear resistance for each segment (i). T_i is the temperature of the soils in various depth at 30 cm toward radial distance from the pile. Figure 4 illustrate that with this consideration more accurate results can be obtained.

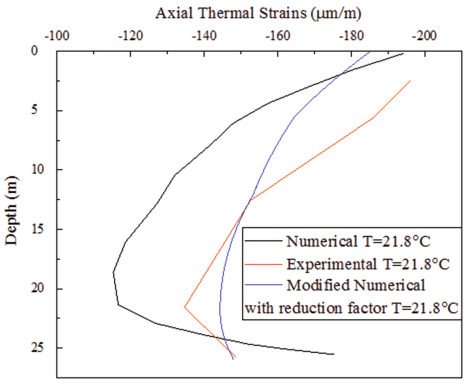

Fig. 4. Effect of considering reduction factor on better prediction

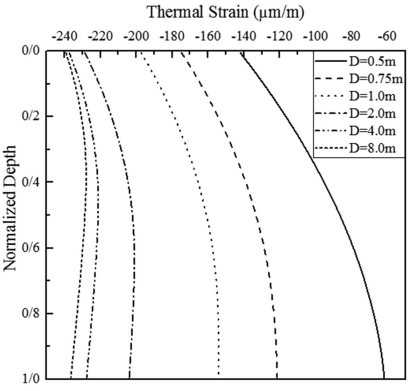

Fig. 5. Thermal strains along pile for various pile diameter

4 Parametric Study

A comprehensive parametric study was performed on various indicator parameters such as pile length and diameter, head-spring, ultimate side shear and toe resistance. The values of the parameters for each case are given in related figures and main model was constructed based on given characterize in Table 3. As shown in Figs. 5, 6, 7, 8 and 9 it can be deduced that increasing pile length, head-spring, side shear and toe resistance result to reducing thermal axial strains and vice versa by increasing diameter of pile, the thermal strain increases. The effect of increasing toe resistance is more complex. The effect of the tip resistance is summarized only in the tip region, and with its increase, the small effect is created at the upper sections of the pile. Except for diameter increasing other parameters results to increasing axial thermal compressive stress. This shows that in the case of thermal loads unlike mechanical loads, stiff soils or long piles could lead to more axial stress than what was expected for mechanical loads.

Based on observed response of energy piles, between the thermal axial strains and stress have indirect relationship. That mean more induced strain results to less stress. So wrong estimation of each case results to inaccuracy in settlement and structural design, respectively. Except for diameter, increasing other parameters mean there is more

Table 3. Main properties for parametric studies

Thermal properties		Resistance properties		Pile geometry and properties	
Conductivity (W/m.°C)	Soil = 1	a_s	0.0003	Length (m)	15
	Pile = 2	b_s	0.9	Diameter (m)	0.5
Density (kg/m^3)	Soil = 1800	q_s (kPa)	50	Elasticity modulus (GPa)	30
	Pile = 2500	a_b	0.002	Thermal expansion (°C^{-1})	12×10^{-6}
Specific heat (J/kg.°C)	Soil = 800	b_b	0.9	Head stiffness (MPa)	500
	Pile = 1000	q_b (kPa)	12000	Temperature (°C)	20

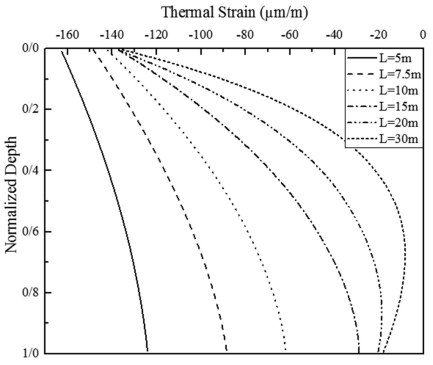

Fig. 6. Effect of pile length on axial thermal strains

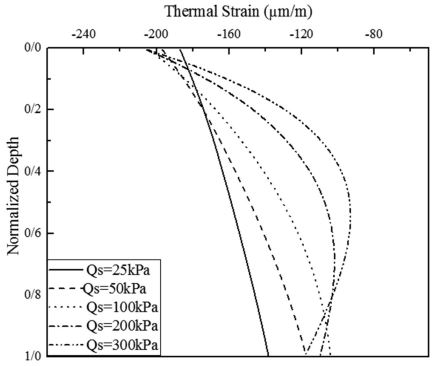

Fig. 7. Effect of ultimate side shear resistance on reducing thermal strain

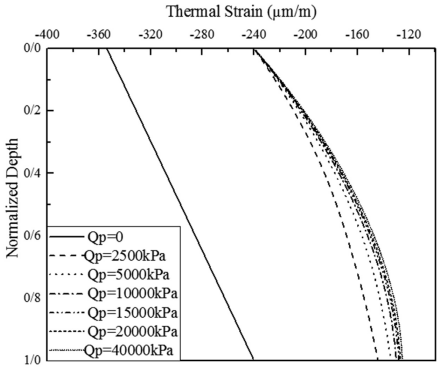

Fig. 8. Effect of toe resistance on pile response

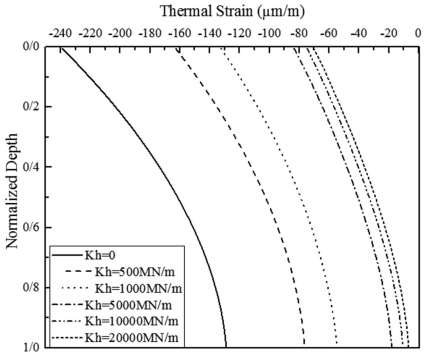

Fig. 9. Pile response for various head spring

resistance against free expansion of pile. So more compressive stress and less strain will be induced in the pile. The resistance against free thermal expansion of pile outcome from pile or soil properties. Another important factor is the intensity of imposed temperature and induced in soil. By increasing temperature in soil, initial elastic strain will be occurred. So the soil condition will get closer to plastic condition. It could result to decreasing in soil resistance against further loads. Consequently, using reduction factor for higher temperature than critical one, results to more accurate results.

5 Conclusion

In this paper, previous work by Knellwolf et al. (2011) and Chen and McCartney (2016) has been developed to achieve an efficient and suitable method that can be used in actual applications of energy piles. Based on obtained results, considering the effect of temperature on soil resistance in the analysis of energy piles can lead to better results. Energy pile behavior for different values of diameter and length of pile, soil resistance and head stiffness from superstructure was investigated. According to the observations, increasing these parameters except for the diameter of the pile, reduces the axial thermal strain of the pile and increases its stress.

References

Amatya, B.L., Soga, K., Bourne-Webb, P.J., Amis, T., Laloui, L.: Thermo-mechanical behaviour of energy piles. Geotechnique **62**(6), 503–519 (2012). https://doi.org/10.1680/geot.10.P.116

Bourne-Webb, P., Amatya, B., Soga, K., Amis, T., Davidson, C., Payne, P.: Energy pile test at Lambeth College, London: geotechnical and thermodynamic aspects of pile response to heat cycles. Géotechnique **59**, 237–248 (2009)

Chen, D., McCartney, J.S.: Parameters for load transfer analysis of energy piles in uniform nonplastic soils. Int. J. Geomech. **17**, 04016159 (2016)

Coyle, H.M., Reese, L.C.: Load transfer for axially loaded piles in clay. J. Soil Mech. Found. Div. **92**, 1–26 (1966)

Frank, R., Zhao, S.: Estimating the settlement of axially loaded bored piles in fine sand by PMT data. Bull. Liaison LPC 119 (1982)

Khodaparast, M., Kiani, M., Bayesteh, H.: Numerical study of bearing capacity and consolidation settlement of energy piles in fine-grained soils. In: Energy Geotechnics: Proceedings of the 1st International Conference on Energy Geotechnics, ICEGT 2016, Kiel, Germany, 29–31 August 2016, p. 57. CRC Press (2016)

Knellwolf, C., Peron, H., Laloui, L.: Geotechnical analysis of heat exchanger piles. J. Geotech. Geoenviron. Eng. **137**, 890–902 (2011)

Laloui, L., Nuth, M., Vulliet, L.: Experimental and numerical investigations of the behaviour of a heat exchanger pile. Int. J. Numer. Anal. Methods Geomech. **30**, 763–781 (2006)

Plaseied, N.: Load-Transfer Analysis of Energy Foundations. University of Colorado at Boulder, Boulder (2012)

Inlet and Outlet Pipe Heat Interaction in a Contiguous Flight Auger (CFA) Pile

Abubakar Kawuwa Sani[1(✉)], Rao Martand Singh[1], Ignazio Cavarretta[1], Cristina de Hollanda Cavalcanti Tsuha[2], and Subhamoy Bhattacharya[1]

[1] Department of Civil and Environmental Engineering, Faculty of Engineering and Physical Sciences, University of Surrey, Guildford GU2 7XH, UK
a.sani@surrey.ac.uk
[2] Department of Geotechnical Engineering, University of São Paulo at São Carlos, Av. Trabalhador Sãocarlense, 400, São Carlos 13566-590, Brazil

Abstract. The use of energy loop(s), fitted into the structural foundation elements dualizes the role of the pile in meeting the structural performance and the thermal comfort demand of the overlying structure. Heat carrier fluid (HCF) is circulated through the loops, to extract or reject heat energy into the ground, during the space heating or cooling operation. However, this results in thermal interaction between the inlet and outlet leg of the loop especially in contiguous flight auger (CFA) piles where the loops are bunched together to a central steel bar. This paper presents a numerical study to investigate the heat flow characteristics between the inlet and outlet loops installed in a CFA pile. It was found that the central steel bar, used in a CFA pile, contributes towards higher thermal interaction. Similarly, it was found that the use of plastic bar of adequate strength, to substitute the use of steel bar, has both economic advantage and positive significance on the performance of the CFA pile.

1 Introduction

The process of coupling the heat pump unit to foundation elements, such as structural piles, provide an effective and environmentally friendly approach of achieving sustainable space heating and cooling in residential and commercial buildings. Often referred to as energy pile system or ground source heat pump (GSHP) system, it is coupled by connecting the secondary heating elements (located in the underfloor slabs or ceilings within the buildings), the heat pump unit and the primary unit or ground heat exchanger (high density poly-ethylene, HDPE, incorporated into the concrete piles).

During operation, the system extracts and transfers low grade heat energy from the ground, via the circulation of heat carrier fluid (HCF) in the HDPE pipes, to the heat pump. At the heat pump, the low grade heat energy is amplified to a high temperature heat energy which is transferred to the secondary underfloor heating elements to achieve space heating. However, in cooling operation, the process is reversed. The heat is extracted from the building and injected into the ground for storage, to be used in the subsequent heating season. This cyclic heating/cooling operation imposes additional

A. Ferrari and L. Laloui (Eds.): SEG 2018, SSGG, pp. 113–122, 2019.
https://doi.org/10.1007/978-3-319-99670-7_15

thermal stresses and strains on the foundation pile. However, the effect was found to be thermoelastic in nature (Laloui et al. 2006; Sani et al. 2018a; Singh et al. 2015).

In addition, the location of the HDPE loop within the concrete pile has an influence on the thermal performance of the system. In rotary bored piles fitting the loops to the reinforcement cage ensures the inlet and outlet leg of the loops to be situated further apart. However, in contiguous flight auger (CFA) piles, the loops are bunched together around a central steel reinforcement and plunged into the fresh concrete prior to concrete setting (Loveridge and Powrie 2014; Sani et al. 2018b). Thus, result in likelihood of thermal interaction between the loops.

This paper presents the results of a numerical study carried out to investigate the heat flow characteristics within a CFA pile using finite element method (FEM).

2 Finite Element Modelling

A pseudo 2D finite element modelling and analyses were carried out using a numerical code known as COMPASS (Code for Modelling Partially Saturated Soils) in this study. The code is capable of numerically solving Thermo-Hydraulic-Mechanical and Chemical (THM-C) processes in partially saturated porous media. Its theoretical formulation is based on mechanistic approach and can be found in various publications (Thomas and He 1997; Thomas and Sansom 1995).

The current study only utilised the thermal (T) capability of the code. Hence, expressed the governing equations terms of primary variables i.e. heat flow due to liquid (pore water pressure, u_l) and that through solids (soil skeleton), owing to temperature gradient (∇T).

2.1 Heat Transfer

Predominantly, heat transfer through soil occurs via conduction, convection, and radiation. However, London clay was used in this study, thus, the radiation effect was neglected, because its effect in very fine soils is insignificant (Farouki 1981).

Thus, the law of conservation of energy governing heat flow dictates that the temporal derivative of the heat content (H_c) is equal to spatial derivative of heat flux (Q), mathematically expressed as:

$$\frac{\partial(H_c \partial V)}{\partial t} = -\nabla \mathrm{Q}(\partial V) \tag{1}$$

$$Q = -\lambda_T \nabla T + \left(C_{pl} v_l \rho_l\right)(T - T_r) \tag{2}$$

Where λ_T is the unsaturated soil thermal conductivity, C_{pl} is the specific heat capacity of liquid, v_l is the liquid velocity, ∇T is the temperature gradient, T_r is the reference temperature and ρ_l is the density of liquid.

3 Numerical Model Development

This section presents the detailed description of the numerical model. Also, it should be noted that only the radial heat transfer was investigated, because studies by (Singh et al. 2015) showed that radial heat transfer is the predominant mode of heat flow in an energy pile. In consequence, the axial heat flow was neglected here.

3.1 Model Description

A two-dimensional geometry of a single CFA pile (shown in Fig. 1a and b) was set up in COMPASS, with a dimeter of 600 mm and pipes incorporated to represent the inlet and outlet legs of a single and double U-loop. The pipes have an outer and an inner diameter of 32 and 28 mm, respectively. They are installed at the centre of the CFA pile, and having a distance of about 245 mm (concrete cover, cc) from the HDPE pipe surface to the CFA pile outer surface. The inlet and outlet legs are separated by a shank spacing (S) equal to the diameter of the central steel i.e. 40 mm. The properties of the steel bar are given in Table 1. In addition, the two models are installed in a soil domain which spans out to a radial distance of 5 m from the centre of the pile. The chosen domain size was ensured to be large enough to allow thermal processes to be fully implemented.

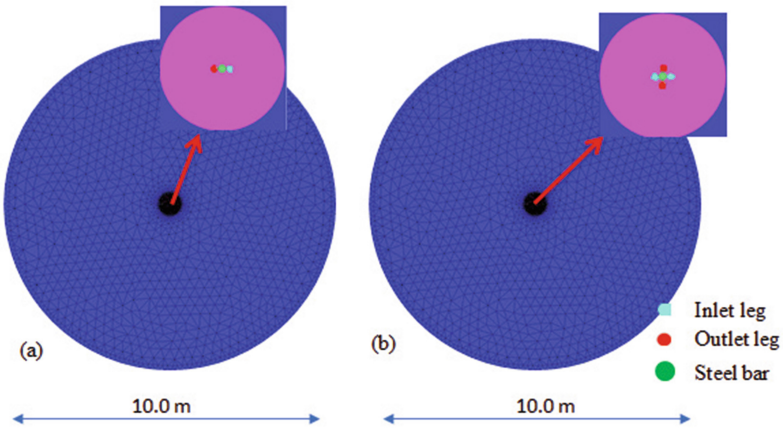

Fig. 1. Geometry of a CFA pile, with (a) 1-loop and (b) 2-loops attached to a central steel.

Equally, it should be noted that the HCF in the HDPE pipes was not modelled in all the numerical analyses. This is because the current study is mainly aimed at investigating the heat flow behaviour between the inlet and outlet loop leg within the pile.

The pile concrete surface was discretised using a uniform 4 noded triangular mesh elements with an equal size of 10 mm. On the other hand, the HDPE pipes were also discretised using 4 node triangular elements however, with smaller elements size of 1 mm. At the regions close to the pipes, 1 mm mesh sizes were applied at the pile-pipe

Table 1. Material parameters

Parameter	London clay	Concrete	HDPE pipe	Steel	Plastic bar
Hydraulic parameters					
Saturated hydraulic conductivity, k_{sat} (m/s)	5.8×10^{-1}[a]	–	–	–	–
Degree of saturation (%)	100[b]	–	–	–	–
Thermal parameters					
Thermal conductivity, λ (W/m K)	1.5[c]	1.5[c]	0.385[c]	43[e]	0.36[f]
Specific heat capacity, C_p (J/kg K)	1820[c]	1050[c]	1465[d]	47[e]	1500[f]
Other parameters					
Density, ρ_d (kg/m^3)	1968[g]	2210[c]	1100[d]	7801[e]	1150[f]
Porosity, n	0.37[h]	0.1	–	–	
Latent heat of vaporisation, L (J/kg)			2400000		
Henry's volumetric coefficient of solubility, H_s			0.02		
Specific gas constant			287.1		

[a]Hepburn (2013); [b]Loveridge et al. (2013); [c]Cecinato and Loveridge (2015); [d]Gao et al. (2008); [e]Metals (2005); [f]Midttømme (1998); [g]Low et al. (2015); [h]Midttømme (1998)

interface, and expand to 10 mm at other locations within the pile surface. Additionally, a 4 noded triangular mesh of 20 mm size was applied at the pile surface and the elements size increases to 500 mm at the far field boundary i.e. the farthest boundary of the soil domain.

3.2 Initial Conditions

The initial temperature of the concrete PHE, the HDPE pipes and the surrounding London clay were assumed to be around 13.4 °C. This agrees with the all-year-round constant ground temperature value measured at East London and reported by (Loveridge et al. 2013) during a thermal response test on a vertical borehole. Furthermore, the initial degree of saturation of the London clay was assumed to be 100% being a representative of the fact that the soil is fully saturated (Loveridge et al. 2013). Additionally, the effect of the interaction between the atmospheric air and the pile was neglected. This is because piles and their surrounding soil are covered by buildings thus are not exposed to the atmosphere.

3.3 Boundary Conditions

The boundary conditions applied to the inlet and outlet pipes were selected based on the data sheet of GSHP system specification obtained from Kensa heat pumps, UK and Water Furnace international heat pump manufacturers (Heat 2016; waterfurnace 2016).

A constant temperature of 308.15 K (35 °C) and 303.15 K (30 °C) were applied to the internal surface of the inlet and outlet leg of the HDPE pipes, respectively. This GSHP system mode of operation represents the process of heat injection into the soil or summer mode to provide space cooling. In addition, a fixed temperature of 286.55 K (13.4 °C) was applied at the outer surface of the soil domain (i.e. 5 m radial distance from the centre of PHE).

3.4 Material Parameters

The materials used in this study are adopted from the values that were measured and reported in literature. London clay was chosen as the soil type surrounding the PHE. Table 1 presents the set of material properties for the HDPE pipe, concrete PHE and the London clay. In addition to the material properties provided in Table 1, other parameters that were needed for the analyses include the specific heat capacity of water C_{pw} = 4200 (J/kg K) and the density of liquid water ρ_w = 1000 (kg/m^3).

3.5 Numerical Simulations

Transient thermal analyses were carried out by applying a continuous temperature of 308.15 K and 303.15 K at the HDPE pipe surfaces for 6 months (180 days) for the single and double U-loop geometry shown in Fig. 1. The duration of the analyses was chosen to represent a scenario where the system was used equal cyclic heating/cooling operation. However, only the heating aspect is considered here. This is to decouple the thermal loading process and gain better understanding of the heat flow behaviour in CFA pile under heat injection.

In addition, the central steel bar at the centre of the pile shown in Fig. 1 is expected to aid in higher thermal interaction between the inlet and outlet loop leg. Thus, the steel bar is substituted with a plastic bar of adequate strength and having a low thermal conductance properties in comparison to the steel. The plastic bar was made from Polyamide 66 which had an outer diameter of 40 mm. Its other thermal properties are given in Table 1. The results of the numerical simulations were obtained at points A, B, C and D (shown in Fig. 2a and b), in the form of temperature achieved at the end of the numerical simulations.

4 Results and Discussion

The COMPASS code has been extensively validated and reported in various publications, including (Thomas and He 1997; Thomas and Sansom 1995). Furthermore, the model in this are validated via the use of an analytical equation proposed by Loveridge and Powrie (2014). The equation computes for the resistance of an energy pile (R_{pile}) using Eqs. 3 and 4.

$$R_{pile} = \frac{1}{S_c \lambda_c} \tag{3}$$

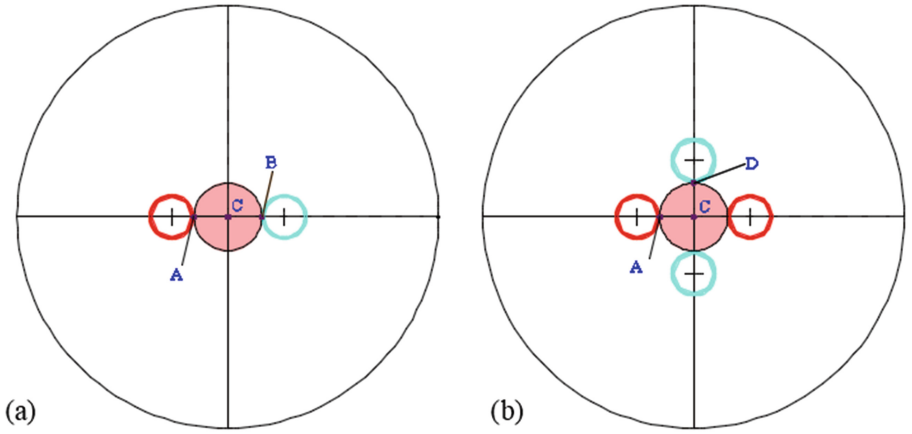

Fig. 2. CFA pile cross-section showing points A, B, C and D.

λ_c is the concrete thermal conductivity, S_c is the shape factor expression shown in Eq. 4 was obtained through sensitivity analyses of non-dimensional parameters (r_b/r_o) and (r_b/cc).

$$S_c = \frac{A}{Bln(r_b/r_o) + Cln(r_b/cc) + (r_b/r_o)^D + (r_b/cc)^E + F} \tag{4}$$

cc is concrete cover and A, B, C, D, E and F are constants fitting parameters given in Table 2, r_b and r_o are the pile and pipe radius.

Table 2. Curve fitting values for a single loop in a PHE (after Loveridge and Powrie (2014))

	A	B	C	D	E	F
$\lambda_c = \lambda_S$	4.919	0.3549	− 0.07127	− 11.41	− 2.88	0.06819

In addition, the pile resistance can be computed from the results obtained from the numerical analyses carried out by COMPASS using Eq. 5.

$$R_{phe} = (T_p - T_s)/q_p \tag{5}$$

T_p and T_s are the final temperature at the HDPE pipe surface and the outer soil domain respectively. q_p is the heat flux.

The results of the pile resistance computed using Eq. 3 and 5 were compared and the meshing refined untill the results do not vary by more than 0.3%.

Figures 3a and b present the results of the temperature distribution within a CFA pile after 6 months of continuous heating operation, for a single and double U-loops

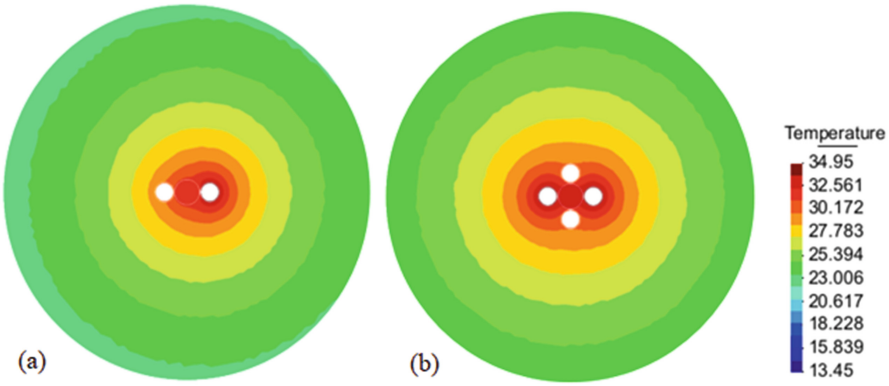

Fig. 3. Temperature distribution (in °C), for 1-loop and 2-loops installed in a CFA pile.

respectively. The constant temperature of 35 °C and 30 °C applied at the inlet and outlet loop leg decreases and propagates uniformly away from the loops location.

At the end of the heating operation, an average uniform temperature of about 22.5 °C and 24.5 °C were observed at the pile circumferential surfaces for the case with single and double U-loop, respectively. This reflects an increase of about 2 °C as a result of the increase in number of installed loop from 1 to 2.

In addition, the Figs. 3a and b also shows the increase in temperature of the central steel to a value close to that at the inlet and outlet pipe surfaces. The temperature at the centre of the steel bar (which corresponds to the centre of the pile), i.e. point C, increases from 13.4 °C at the start of the simulation to about 31.5 °C and 32.8 °C, at the end of the heat injection process, for the 1-loop and 2-loops, respectively. The reason for higher heat flow between the inlet and outlet loop leg is attributed to the good heat conductive properties of the central steel, thus could potentially result into thermal short-circuiting of the system.

Figures 4a and b present the results investigating the influence of central steel bar on the heat transfer between the inlet and outlet loops. The results are obtained at points A, B, C and D, as shown in Figs. 2a and b. It was found that the presence of the steel bar at the centre of the pile decreases the difference in temperature between the inlet and outlet loops.

For the case with a single U-loop, a temperature of about 31.05, 31.26 and 31.85 °C were observed at points A, C and B (shown in Figs. 2a and b) respectively when the central steel bar was installed. However, after substituting the steel bar with a plastic bar, lower temperature values of 29.95, 31.00 and 34.15 °C were observed at the same points i.e. A C and B (Fig. 4a).

In addition, Fig. 4b shows the results of final temperature for the case with 2-loops installed. Temperature values of 31.95, 32.35 and 32.65 °C were observed at points A, C and D for the case having the central steel installed. But, when substituted with a plastic bar, the temperature at those points became 30.55, 32.35 and 34.25 °C, respectively.

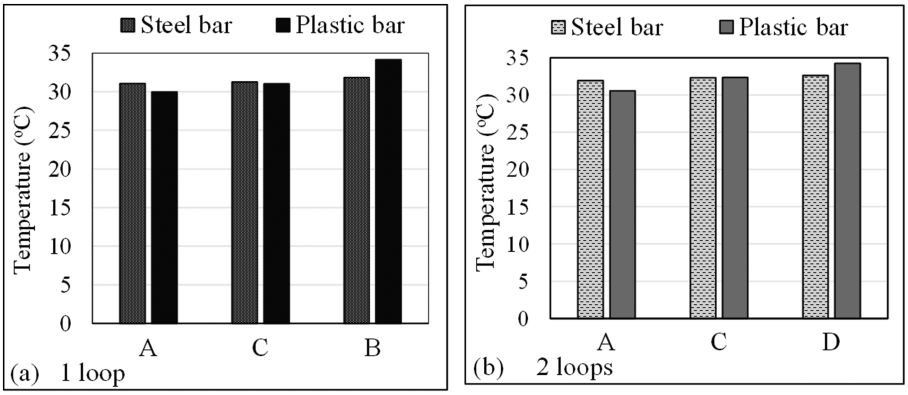

Fig. 4. Effect of Central steel in CFA piles for (a) 1-loop and (b) 2-loops

Therefore, it can be pointed out that the temperature gradient between the inlet and outlet loop leg is influenced by the central steel bar. For the case with 1-loop, the temperature gradient increases from 0.8 °C (when steel bar was installed) to 4.2 °C (when plastic bar was installed). Similarly, for the case with 2-loops, the temperature gradient increases from 0.7 °C (with steel bar installed) to 3.7 °C (with plastic bar installed). Thus, it is highly recommended that plastics of adequate strength should be used to install HDPE loops in a CFA pile. Additionally, the price of 40 mm steel bar is around £118 per meter length, in comparison to the price of a 40 mm plastic bar (£32 per meter length) (DirectPlastics 2008; The-Metal-Store 2018).

Thus, using plastic bar for installing energy loops provide a much more economical alternative compared to using steel bar.

Figure 5 shows the results of temperature distribution in the surrounding clay for the 1-loop and 2-loops, respectively. It was observed that the increase in number of installed loops from 1-loop to 2-loops does not significantly result in higher magnitude of temperature change in the surrounding soil. Similarly, the region that was influenced by the radial temperature distribution extends outward to a distance of about 4.1 m from the surface of the CFA pile, for the 1 and 2-loops, respectively.

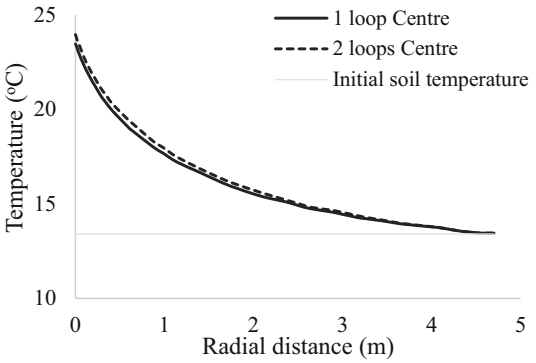

Fig. 5. Temperature distribution in soil for 1-loop and 2-loops

5 Conclusion

This study investigates the pipe-pipe heat flow between the inlet and outlet loops installed in a CFA pile. It was found that:

- Installing a central steel bar in a CFA pile results in higher thermal interaction between the inlet and outlet loops owing to higher conductive properties of steel. Therefore, it is recommended that plastic bar of adequate strength and poor thermal properties should be used when plunging loops into a CFA pile.
- Installing the loops at the centre results in uniform temperature distribution around the circumference of the CFA pile.
- Utilising plastic bar provide much more economical approach of installing energy loops in a CFA pile in comparison to using steel bar.
- In addition, increasing the number of loops from 1 to 2 does not significantly results in higher magnitude of temperature developed at the CFA circumference. Similarly, the thermally active region was found to extend to a radial distance of 4.1 m from the CFA pile surface. However, this is dependent upon soil type and other factors such as initial water content, grain size and initial temperature.

References

Cecinato, F., Loveridge, F.: Influences on the thermal efficiency of energy piles. Energy **82**, 1021–1033 (2015)

DirectPlastics: Polyamide material datasheet [WWW document] (2008). https://www.directplastics.co.uk/pdf/datasheets/Nylon66BlackDataSheet.pdf. Accessed 12 Jan 2017

Farouki, O.T.: Thermal properties of soils, 136 (1981)

Gao, J., Zhang, X., Liu, J., Li, K., Yang, J.: Numerical and experimental assessment of thermal performance of vertical energy piles: an application. Appl. Energy **85**, 901–910 (2008). https://doi.org/10.1016/j.apenergy.2008.02.010

Heat, K.: Single compressor compact heat pump installation and commissioning manual (2016)

Hepburn, B.D.P.: An investigation of the behaviour of the ground in response to energy extraction (2013)

Laloui, L., Nuth, M., Vulliet, L.: Experimental and numerical investigations of the behaviour of a heat exchanger pile. Int. J. Numer. Anal. Methods Geomech. **30**, 763–781 (2006)

Loveridge, F., Holmes, G., Roberts, T., Powrie, W.: Thermal response testing through the Chalk aquifer in London, UK. Proc. ICE Geotech. Eng. **166**, 197–210 (2013)

Loveridge, F., Powrie, W.: 2D thermal resistance of pile heat exchangers. Geothermics **50**, 122–135 (2014)

Low, J.E., Loveridge, F., Powrie, W., Nicholson, D.: A comparison of laboratory and in situ methods to determine soil thermal conductivity for energy foundations and other ground heat exchanger applications. Acta Geotech. **10**, 209–218 (2015)

Metals, A.S.: The Atlas Specialty Metals Technical Handbook of Bar Products. Atlas Specialty Metals, Mowbray (2005)

Midttømme, K.: Thermal conductivity of selected claystones and mudstones from England. Clay Miner. **33**, 131–145 (1998)

Sani, A.K., Singh, R.M., Amis, T., Cavarretta, I.: A review on the performance of geothermal energy pile foundation, its design process and applications. Renew. Sustain. Energy Rev. (2018a)

Sani, A.K., Secondary, C.A., Author, C., Sani, A.K., Singh, M.R., De Hollanda, C., Tsuha, C., Cavarretta, I., Sani, A.K.: Pipe-pipe thermal interaction in a pile heat exchanger. Acta Geotech. (2018b)

Singh, R.M., Bouazza, A., Wang, B., Haberfield, C.H., Baycan, S., Carden, Y.: Thermal and thermo-mechanical response of a geothermal energy pile. In: World Geothermal Congress 2015, vol. 7 (2015)

The-Metal-Store: Stainless steel round bar [WWW document]. https://www.themetalstore.co.uk/products/stainless-steel-304-round-bar-2m (2018). Accessed 2 Nov 18

Thomas, H.R., He, Y.: A coupled heat-moisture transfer theory for deformable unsaturated soil and its algorithmic implementation. Int. J. Numer. Methods Eng. **40**, 3421–3441 (1997)

Thomas, H.R., Sansom, M.R.: Fully coupled analysis of heat moisture and air transfer in unsaturated soil. J. Eng. Mech. **121**, 392–405 (1995)

waterfurnace: ENVISION2 NKW 50 Hz reversible chiller specification catalog (2016)

Thermal Characterization of Energy Pile Dynamics

Paolo Conti(✉), Eva Schito, and Daniele Testi

Department of Energy, Systems, Territory and Constructions Engineering (DESTEC), University of Pisa, 56122 Pisa, Italy
paolo.conti@unipi.it

Abstract. The heat transfer process in energy piles is strongly affected by the heat capacity of such foundation elements. This phenomenon is more pronounced for energy piles compared to borehole heat exchangers, because of the lower slenderness of the former compared to the latter, and involves axial thermal gradients. In literature, capacity effects of energy piles and their transient thermal performance have not been analysed in depth. Looking at such challenge, this paper investigates the dynamic thermal performance of energy piles at short-to-medium time scales. The work analyses the results of almost thirty 3D finite element simulations of an energy pile equipped with 3-U ducts by varying: (i) the velocity of the fluid circulating in the ducts, (ii) the slenderness ratio of the pile, (iii) the radial position of the ducts, and (iv) the boundary condition characterizing the uppermost surface of the model. Simulation results are analysed to identify for which times, geometries, and operative conditions the energy pile can be modelled with a 2D geometry, instead of a full 3D geometry. Our analysis highlights a limited relevance of the axial effects during the transient period in any tested configuration. These results are functional to the application of simplified analytical models and design criteria for energy piles.

1 Introduction

Energy piles (EPs) represent a promising solution to reduce the installation costs of GSHP systems, mainly because the heat exchanging pipes are embedded in the building foundations without significant additional costs with respect to the already-needed expenditure for geo-mechanical requirements (Fadejev et al. 2017; Batini et al. 2015). However, the EP design and performance assessment are ongoing multi-disciplinary and mechanical-thermal issues (Rotta Loria and Laloui 2016).

The thermal modelling of an EP is difficult for several reasons, e.g., EPs cannot be assumed as slender bodies, the heat transfer process is affected by the large heat capacity of the foundation or by possible interaction with outdoor climate and/or overhead buildings (Conti et al. 2016; Li and Lai 2015). However, an accurate EP model is fundamental for a proper analysis of the system, as ground-coupled heat exchangers are one of the main drivers of the overall GSHP performance (Casarosa et al. 2014).

A. Ferrari and L. Laloui (Eds.): SEG 2018, SSGG, pp. 123–131, 2019.
https://doi.org/10.1007/978-3-319-99670-7_16

At present, EPs are modelled through numerical methods and software as, to the best of our knowledge, there are no established dynamic analytical models (Fadejev et al. 2017; Zarrella et al. 2013). With respect to numerical methods, analytical approaches are attractive alternatives, representing an appropriate trade off among implementation efforts, computational time, and solution accuracy (Conti 2016, 2017; Conti et al. 2016). On the other hand, the development of new analytical methods always requires some simplification assumptions, to be verified through numerical or experimental analyses. For instance, the composite-medium line-source model (Li and Lai 2012) refers to the 2D thermal field evolution due to a linear thermal source located in composite cylindrical media, and it is potentially applicable to simulate EP thermal dynamics, provided that the 2D assumption is verified.

In this paper, we analyse the transient period of an EP to figure out the duration and the characteristics of the thermal field evolution at short-to-medium time scales. Specifically, we run 36 simulations varying geometrical parameters and operative conditions. We focus on two main points: the duration of transient period, the relevance of the thermal gradients over the axial direction with respect to the radial dimension. The findings will be functional to the application of the composite-medium line-source model in the EP context.

2 Description of the Numerical Model

The numerical analysis was performed through the widespread commercial software COMSOL Multiphysics® (COMSOL 2015). We performed 36 full transient 3D FEM simulation of a reference 3-U energy pile, varying the position of the U-loops, the flow rate within the ducts, the aspect ratio of the pile, and the upper boundary condition of the numerical domain from adiabatic to isothermal (see Table 1 and Fig. 1). All the media were assumed to be as constant-property, homogeneous, isotropic, and purely conductive. The ducts are assumed as purely thermal resistances, with a negligible thermal capacity. The thermal conductivity, λ, of the ground, EP concrete, and ducts are 1.5, 2.1, and 0.4 W/(m K), respectively. Thermal diffusivity α of the ground and EP concrete are 0.6 and 1.0 mm^2/s, respectively.

The heat transfer over the EP concrete and the ground are modelled through the classical heat equation based on the Fourier's law. The circulating fluid is assumed as water and it is modelled through a 1-D energy equation along the geometry edges representing the ducts (see Fig. 2):

$$\rho_f c_f \frac{\partial \theta_f}{\partial t} + \rho_f c_f u_f \frac{\partial \theta_f}{\partial s} = \lambda_f \nabla^2 \theta_f + \dot{q}_p / \left(\pi r_{p,i}^2 \right) \tag{1}$$

where s is curvilinear coordinate and $\dot{q}_p = 2\pi r_{p,i} U_p \left(\theta_{p,ext} - \theta_f \right)$. $\theta_{p,ext}$ is the local temperature of the duct-pile interface. The overall heat transfer coefficient, U_p includes the convective fluid-duct thermal resistance and the conductive duct thermal resistance. Further details can be found in Batini et al. (2015).

The actual number of mesh elements depends on the specific simulation. As general rule, we used a swept method over the EP axial direction and an unstructured triangular

Table 1. Parameters of tested configurations (r = 0.45 m)

Conf. #	U-loops arrangement	Pipes radial position [m]	Pile depth, H [m]	Fluid velocity, u_f [m/s]	Aspect ratio, $H/(2r_b)$ [–]	Boundary condition (B.C.)	$\tau_{\bar{\theta}_f}$ [s]	τ_p [s]	$\alpha_b \tau_b / r_b^2$
1	Type A	0.13	9	0.2	10	Isothermal	45	404	2.21
2	Type A	0.13	9	0.5	10	Isothermal	18	263	2.21
3	Type A	0.13	9	1	10	Isothermal	9	198	2.21
4	Type A	0.13	36	0.2	40	Isothermal	178	999	2.48
5	Type A	0.13	36	0.5	40	Isothermal	72	526	2.48
6	Type A	0.13	36	1	40	Isothermal	36	378	2.48
7	Type A	0.40	9	0.2	10	Isothermal	45	404	1.97
8	Type A	0.40	9	0.5	10	Isothermal	18	267	1.97
9	Type A	0.40	9	1	10	Isothermal	9	199	1.97
10	Type A	0.40	36	0.2	40	Isothermal	178	989	2.21
11	Type A	0.40	36	0.5	40	Isothermal	72	521	1.97
12	Type A	0.40	36	1	40	Isothermal	36	378	1.97
13	Type B	0.13	9	0.2	10	Isothermal	45	452	2.48
14	Type B	0.13	9	0.5	10	Isothermal	18	277	2.48
15	Type B	0.13	9	1	10	Isothermal	9	199	2.48
16	Type B	0.13	36	0.2	40	Isothermal	178	1293	2.78
17	Type B	0.13	36	0.5	40	Isothermal	72	640	2.46
18	Type B	0.13	36	1	40	Isothermal	36	429	2.48
19	Type B	0.40	9	0.2	10	Isothermal	45	410	2.21
20	Type B	0.40	9	0.5	10	Isothermal	18	269	2.21
21	Type B	0.40	9	1	10	Isothermal	9	201	2.21
22	Type B	0.40	36	0.2	40	Isothermal	178	994	2.48
23	Type B	0.40	36	0.5	40	Isothermal	72	524	2.48

(*continued*)

Table 1. (*continued*)

Conf. #	U-loops arrangement	Pipes radial position [m]	Pile depth, H [m]	Fluid velocity, u_f [m/s]	Aspect ratio, $H/(2r_b)$ [–]	Boundary condition (B.C.)	$\tau_{\bar{\theta}_f}$ [s]	τ_p [s]	$\alpha_b \tau_b / r_b^2$
24	Type B	0.40	36	1	40	Isothermal	36	384	2.48
25	Type A	0.30	28	0.2	31.1	Isothermal	138	797	1.97
26	Type A	0.30	28	0.2	31.1	Adiabatic	138	797	1.97
27	Type A	0.30	9	0.2	10	Isothermal	45	383	1.75
28	Type A	0.30	9	0.2	10	Adiabatic	45	370	1.97
29	Type A	0.30	36	0.2	40	Isothermal	178	966	1.97
30	Type A	0.30	36	0.2	40	Adiabatic	178	966	1.97
31	Type A	0.30	28	0.5	31.1	Isothermal	56	443	1.75
32	Type A	0.30	28	0.5	31.1	Adiabatic	56	443	1.97
33	Type A	0.30	9	0.5	10	Isothermal	18	262	1.75
34	Type A	0.30	9	0.5	10	Adiabatic	18	262	1.75
35	Type A	0.30	36	0.5	40	Isothermal	72	526	1.97
36	Type A	0.30	36	0.5	40	Adiabatic	72	526	1.97

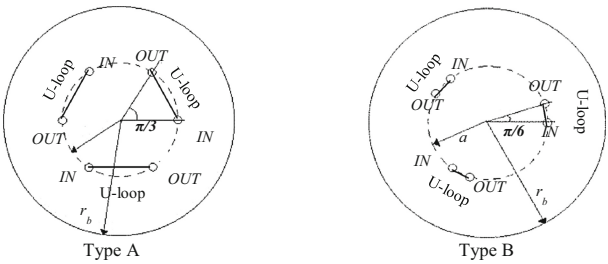

Fig. 1. Tested arrangements for U-loops. Type B refers to a closer position of the U legs.

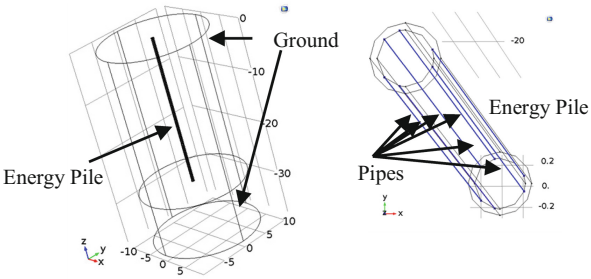

Fig. 2. Numerical domain (images from COMSOL Multiphysics GUI). The six blue lines represent the ducts embedded in the energy pile.

mesh on the upper surface (see Fig. 3). The maximum size of the triangular elements is 0.02 m within the pile and 3.3 m in the soil. The maximum height of the prisms is 3.1 m. The simulated period consists of 20 days divided in a logarithmically-spaced vector of pace $\log_{10}(\tau^n/\tau^{n-1}) = 0.05$. We used an intermediate backward differentiation formula as time-integration method (COMSOL 2015).

3 Results: Characteristic Periods and Axial Thermal Gradients

According to Li and Lai (2015), the heat transfer process in vertical ground-coupled heat exchangers (EPs included) can be split into three separate characteristic periods. The first period, $\tau < \tau_p$ refers to the fluid and ducts thermal dynamics. We define τ_p, as the time after which the heat exchange through the pipes is practically equivalent to the enthalpy variation of the fluid between the inlet and the outlet sections. The term "practically equivalent" refers to a relative deviation lower than 5%. To better quantify τ_p, we wrote a simplified energy equation of the fluid with a lumped-parameters approach, namely:

$$\tau_{\bar{\theta}_f} = \rho_f c_f V_f \big/ \left(2\dot{m}_{f,p} c_f + US\right) \tag{2}$$

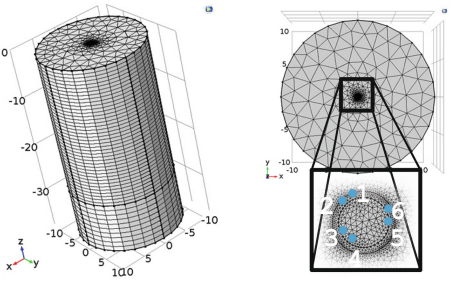

Fig. 3. Finite element mesh used in the simulations (images from COMSOL Multiphysics GUI). The position and the numbering of the ducts are highlighted in white.

where the mean operator refers to the arithmetic mean of the considered variable between the inlet and the outlet sections of a single U-loop. we expect that $\overline{\theta_f}$ reaches the steady-state value at a time proportional to the time constant of Eq. 2, $\tau_{\bar{\theta}_f} = \rho_f c_f V_f / \left(2\dot{m}_{f,p} c_f + US\right)$. The results shown in Fig. 4 confirms that $\tau_{\bar{\theta}_f}$ and τ_p are linearly dependent each other, according to a proportional factor of about 4. In Fig. 4 we see less than 36 markers as the others are overlapped to those with the same $\tau_{\bar{\theta}_f}$. In other words, the radial position of the pipes and the aspect ratio of the pile do not affect the dynamics of the circulating fluid at those short time scales $\tau < \tau_p$. We did not investigate shorter $\tau_{\bar{\theta}_f}$ as this would correspond to unrealistic high EP flow rate values.

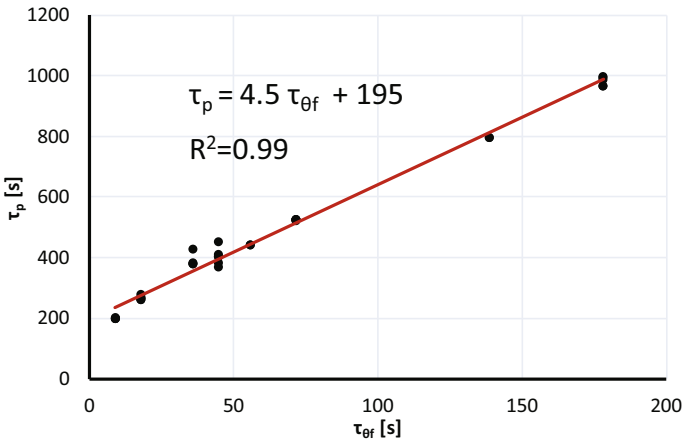

Fig. 4. Linear regression of τ_p as a function of the time constant $\tau_{\bar{\theta}_f}$.

The second period, $\tau_p < \tau < \tau_b$, refers to the thermal dynamics of the pile and it is driven by the heat capacity of the foundation. We can define τ_b as the time after which the thermal power exchanged through the ducts is practically equivalent to the thermal power exchanged through the pile-soil interface. Again, the term "practically equivalent" refers to a relative deviation lower than 5%. Table 1 shows the τ_b values for the

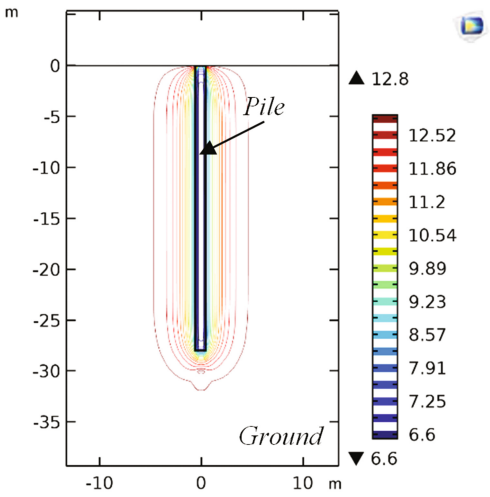

Fig. 5. Example of isothermal lines during the EP dynamics.

36 tested configurations, pointing also out that this value is approximately 2÷2.5 times the characteristic time of the pile, r_b^2/α_b. At $\tau > \tau_b$, namely the third period, the pile becomes a purely-resistance body and it can be modelled through the classical *borehole thermal resistance*, R_b (Conti et al. 2016).

The thermal dynamics of an EP occurs in the above-described second period. Figure 5 shows an example of the typical isothermal lines during that dynamics.

Those lines are practically parallel to the pile axis, hinting that no heat transfer occurs in axial direction. However, to better quantify the relevance of the heat conduction over the axial direction, we analysed the numerical results in term of thermal power over cross-axial surfaces at different depth z, namely:

$$\left|\dot{Q}_z\right|(z) = \int_0^{r_b}\int_0^{2\pi} |\dot{q}_z| r dr d\varphi = \int_0^{r_b}\int_0^{2\pi} \left|-\lambda_b \frac{\partial\theta}{\partial z}\right| r dr d\varphi \tag{3}$$

$\left|\dot{Q}_z\right|$ is not an actual quantification of the thermal performances of the pile, but it provides a reasonable indication on the entity of thermal flux over the axial direction. If it would result sufficiently small with respect to the enthalpy drop of the fluid, $\dot{Q}_p$, we can conclude that the heat conduction mainly occurs over the axial direction. Figure 6 show the evolution of $\left|\dot{Q}_z\right|/\left|\dot{Q}_p\right|$ values for all the tested configurations over the simulated 20 days. We note that $\left|\dot{Q}_z\right|/\left|\dot{Q}_p\right|$ is always practically null in the middle of the pile, with some "edge effects" on the top and bottom of the pile only for the shallow geometry (aspect ratio $H/2r_b < 10$). In any case, there are no significant effects of uppermost boundary conditions, flow rate and radial position of the ducts. We conclude that the transient periods for typical EP geometries can be analysed and modelled with a 2D approach.

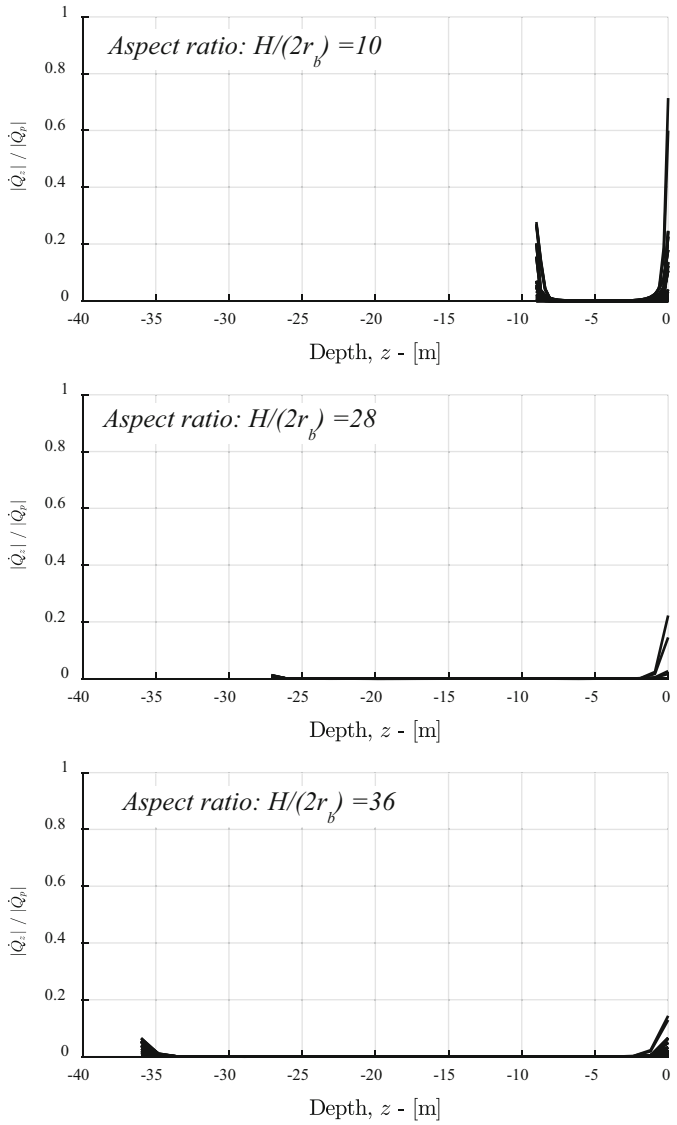

Fig. 6. 20-day evolution of the $|\dot{Q}_z|/|\dot{Q}_p|$ ratio for all tested configurations.

4 Conclusions

The paper analysed 36 full transient 3D FEM simulations, varying geometrical and operative conditions of a reference EP. We found the following limits for the three characteristic periods of the heat transfer in a single EP. The first one ends at four times the time constant of the fluid energy equation (see Eq. 2 and Fig. 4). The second

period, the most relevant for the dynamic performance, ends at 2÷3 times the dimensionless time, r_b^2/α_b, with a minor influence of the radial ducts position, aspect ratio of the pile, flow rate and uppermost boundary condition. Additionally, for the most of simulations the heat transfer was found mainly to occur in the radial direction, thus making possible a 2D modelling for typical EP geometries (i.e. $H/(2r_b) > 10$) during that second period. Future analyses concern the influence of the fluid flow rate and R_b on the axial thermal gradient.

Those results are functional to the application of simplified analytical methods, such as the composite-medium line-source model, which can be successfully employed in dynamic simulations and optimization codes to seek the best sizing, operation strategy, and RES integration for UTES and GSHP (Grassi et al. 2015).

References

Batini, N., Rotta Loria, A.F., Conti, P., Testi, D., Grassi, W., Laloui, L.: Energy and geotechnical behaviour of energy piles for different design solutions. Appl. Therm. Eng. **86**, 199–213 (2015). https://doi.org/10.1016/j.applthermaleng.2015.04.050

Casarosa, C., Conti, P., Franco, A., Grassi, W., Testi, D.: Analysis of thermodynamic losses in ground source heat pumps and their influence on overall system performance. J. Phys: Conf. Ser. **547**, 012006 (2014). https://doi.org/10.1088/1742-6596/547/1/012006

COMSOL Multiphysics® v. 5.2. www.comsol.com. COMSOL AB, Stockholm, Sweden (2015)

Conti, P.: Dimensionless maps for the validity of analytical ground heat transfer models for GSHP applications. Energies **9**, 890 (2016). https://doi.org/10.3390/en9110890

Conti, P., Testi, D., Grassi, W.: Revised heat transfer modeling of double-U vertical ground-coupled heat exchangers. Appl. Therm. Eng. **106**, 1257–1267 (2016). https://doi.org/10.1016/j.applthermaleng.2016.06.097

Conti, P., Testi, D., Grassi, W.: A brief compendium of correlations and analytical formulae for the thermal field generated by a heat source embedded in porous and purely-conductive media. J. Phys: Conf. Ser. **923**, 012056 (2017). https://doi.org/10.1088/1742-6596/923/1/012056

Fadejev, J., Simson, R., Kurnitski, J., Haghighat, F.: A review on energy piles design, sizing and modelling. Energy **122**, 390–407 (2017). https://doi.org/10.1016/j.energy.2017.01.097

Grassi, W., Conti, P., Schito, E., Testi, D.: On sustainable and efficient design of ground-source heat pump systems. J. Phys: Conf. Ser. **655**, 12003 (2015). https://doi.org/10.1088/1742-6596/655/1/012003

Li, M., Lai, A.C.K.: New temperature response functions (G functions) for pile and borehole ground heat exchangers based on composite-medium line-source theory. Energy **38**, 255–263 (2012). https://doi.org/10.1016/j.energy.2011.12.004

Li, M., Lai, A.C.K.: Review of analytical models for heat transfer by vertical ground heat exchangers (GHEs): a perspective of time and space scales. Appl. Energy **151**, 178–191 (2015). https://doi.org/10.1016/j.apenergy.2015.04.070

Rotta Loria, A.F., Laloui, L.: The interaction factor method for energy pile groups. Comput. Geotech. **80**, 121–137 (2016). https://doi.org/10.1016/j.compgeo.2016.07.002

Zarrella, A., De Carli, M., Galgaro, A.: Thermal performance of two types of energy foundation pile: helical pipe and triple U-tube. Appl. Therm. Eng. **61**, 301–310 (2013). https://doi.org/10.1016/j.applthermaleng.2013.08.011

Monitoring in a District Heating Pipeline System

Felipe Villalobos[1(✉)], Stefan Hay[2], and Ingo Weidlich[3]

[1] Catholic University of Concepción, Concepción, Chile
avillalobos@ucsc.cl
[2] AGFW, Frankfurt am Main, Germany
[3] HafenCity University, Hamburg, Germany

Abstract. District heating has been for many decades a well-established industry for supplying heat in several countries. Surplus heat from power plants and industrial processes are used as well as recently renewable heat sources such as solar thermal, geothermal and heat from biomass combustion. The success of heating distribution to the final users depends significantly on the pipeline network. The need for understanding the response of buried heating pipeline systems has led to the development of a monitoring programme. This programme includes the design, construction and operation of the connection of an instrumented pipeline section to an operating local district heating network. Particular conditions were tested such as thickness of cushion materials, medium temperature ranges and bedding soil type. This unique instrumented pipeline allowed the analysis of initial results of temperature and pipe axial displacements, which are relevant for the district heating industry. It was found that when temperature increased from ambient conditions up to 90 °C, pipes were moving all along their length. Moreover, after a temperature drop from 90 to 20 °C during 20 days and subsequent increase to 90 °C again, axial displacements did not return to the same values as before.

1 Introduction

The district heating distribution network is in general constituted by a net of buried pipelines, which represent an important part of the costs of a district heating system. Pipelines are normally made of steel, covered with insulation, a casing and joined using special welding technologies. Since the insulated pipelines carry a hot fluid under high levels of pressures, there is a risk for leakage and breakage. Moreover, large temperature changes in the steel pipelines can cause significant pipe deformations. For buried pipes, these deformations give place to a complex interaction between the moving pipe and the surrounding soil. The soil-pipe interaction phenomenon has been studied to determine the pipe forces and displacements due to temperature changes and earth pressures applied by and to the soil (e.g. Achmus and Rizkallah 1997; Weidlich and Wijewickreme 2012; Achmus and Weidlich 2016).

Research has been carried out to study pipe-soil interaction experimentally at small scales in the laboratory (e.g. Weidlich 2008; Weidlich and Achmus 2008) and using numerical analysis (e.g. Achmus 1995; Gerlach and Achmus 2017). Despite the great

A. Ferrari and L. Laloui (Eds.): SEG 2018, SSGG, pp. 132–139, 2019.
https://doi.org/10.1007/978-3-319-99670-7_17

contributions of these studies, they lack comparisons of the laboratory and numerical results with data obtained in the field in operating district heating pipelines. There have been only a few attempts for measuring in the field (Salveter 2000) and in a project using a special fluidised soil type (AGFW 2017). Therefore, there is a need for measuring in the field relevant data for the analysis and further design of district heating pipelines.

The present work is within a monitoring programme with several objectives for the improvement of the district heating design and maintenance and future challenging developments such as the use of renewable energy. Initially, there is a description of the connection to the local district heating network and materials used. Then, the monitored pipeline is explained and initial results are shown and finally last comments and conclusions are drawn.

2 Connection to the Local District Heating Network

A control system was designed to be able to regulate the temperature and pressure of the fluid which is supplied to the monitored pipes. The control is achieved by a combination of differential pressure regulator, pump, valves, temperature sensors and pressure gauges. In this way, for instance, a steady constant temperature can be targeted or variations such as temperature cycles can be applied. Figure 1 shows the control unit inside the container, where it can be seen the pressure regulator, vertical pump, pressure gauges and industrial thermometers. In the figure arrows indicate the flow direction coming from the district heating and passing through the control unit and then to the monitored pipeline and also the return fluid coming from the monitored pipeline. An internet web interface makes possible to receive the data from the experimental site and carried out the control from the office away from the site.

3 Materials Used

The pipes used were DN 150/250, which includes the central medium steel pipe, the covering insulation and the external plastic mantle. The dimensions are: steel pipe outside diameter d_a = 168.3 mm, steel pipe wall thickness t = 4 mm, plastic polyethylene jacketed pipe outside diameter D_a = 250 mm, mantle thickness t_m = 3.9 mm and foam insulation thickness t_f = 37 mm. The plastic jacketed pipes were wrapped in the bows with 80 mm thick Trocellen C30N cushions of 30 to 35 g/l density, i.e. of medium stiffness according to prEN 13941 (2016). The use of cushions attempts to reduce the soil pipe bedding reaction in the bows and therefore allowing larger displacements to occur.

For the joints, plastic shrink-on sleeves with welded plugs and sleeve pipe rings were considered, although in section 1, joints were performed with extruded sleeves. The design contemplated 12 insulated DN150/250 pipes of 12 m long from GermanPipe in the arrangement as shown in Fig. 2. In this testing design, two concrete blocks were located in each extreme and two in the middle of the monitored pipelines as shown in Fig. 2. The dimensions of the reinforced concrete blocks in the middle and

Fig. 1. Control unit showing devices and instruments, arrows indicate flow direction

in the bows were 1.2 × 0.8 m in the base and by 1.0 m height and 0.8 × 0.8 × 1.0 m, respectively. The connections of the monitored pipes to the container are made with insulated pipes DN 32/110.

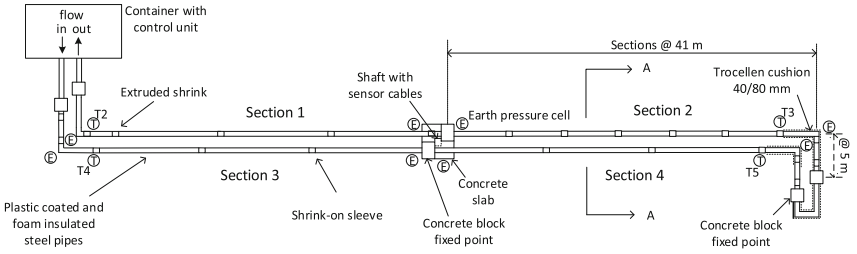

Fig. 2. Sketch of the monitored pipeline sections, showing fixed points, joints and cushions

4 Description of the Monitored Pipeline

The design and construction of the instrumented sections considers one pipeline of 194 m long turning in a way that creates two parallel pipes of 96 and 98 m long respectively as shown in Fig. 2. These two parallel pipes are separated 2 m from pipe centres. For monitoring and analysis reasons these two pipes are divided in half, resulting in four sections. The idea of having different sections is to test various combinations of materials such as type and amount of sleeves in the joints, soil beddings as well as with or without pad cushions in different steps of the testing programme. Figure 2 shows schematically the instrumented pipeline with 41 m each

section plus 5 m of pipe to the fixed point, where T and E inside circles represent temperature and earth pressure sensors.

Figure 3 shows a picture on site during construction showing reinforced concrete blocks and cushions on the corner. Figure 4 shows a trench cross section indicating the position of the pipes (buried depth), instrument cables and soils around the pipes.

Fig. 3. Construction of the buried pre-insulated steel pipeline of sections 2 and 4

Section 1 is composed of 3 steel tubes of 12 m plus two tubes of 1 m on each extreme and one of 3 m long in the corner. This corresponds to 6 pieces with 4 joints built with extruded sleeves and welded plugs. The thickness of the cushions on the corner is 80 mm. Since the joints were made of extruded sleeves by a special machine, the finishing of the joints has almost the same diameter of the insulated pipes. Therefore, this section offers the opportunity to assess the effect on displacements of these smooth pipelines. It is worth mentioning that this type of joint insulation procedure is not often carried out. In this section the bedding soil is fine sand.

Section 2 has also the same 5 plastic jacketed foam insulated steel tubes but with 8 joints with plastic shrink-on sleeves, welded plugs and shrink sleeves. This creates a thicker and hence more uneven surface of the pipeline which in practice is usually carried out. Then this section makes possible the comparison of results with the smooth section 1 and in this way it can be possible to observe the influence on the displacement of the standard shrink-on sleeve compared with extruded smooth joints in section 1. The bedding soil and cushion thickness are the same as in section 1.

Section 3 is similar to section 2, but with 5 joints with plastic shrink-on sleeve without the extra ones in the middle of the 12 m long pipes. Then the aim is also to compare the influence on the displacements of these standard 5 joints with plastic shrink-on sleeves with the smooth pipes of section 1 and with the 8 joints with plastic shrink-on sleeves, welded plugs and shrink sleeves of section 2. The bedding soil and cushion thickness are the same as in section 1.

Section 4 is similar to section 3 in relation to building and assessment conditions, but with a different bedding soil material, which is a coarser sand.

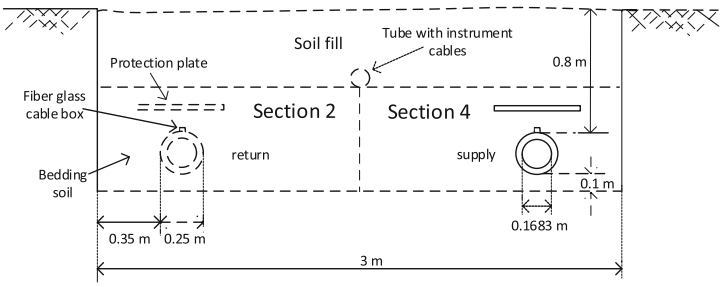

Fig. 4. Trench cross section A – A with pipes of sections 2 and 4

5 Temperature Measurements

Temperature sensors used were Ni1000 TK5000 with sealed cables IP68 which can measure in the range of −50 and 180 °C. Figure 5 illustrates the position of the temperature sensors in the bows with cushions in section 1, which is similar to section 3, although not shown.

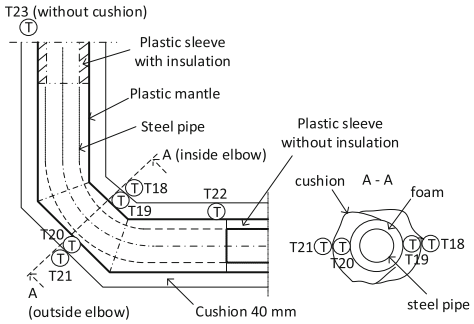

Fig. 5. View in plant and cross section showing the positions of the temperature sensors in the corner of section 1

Figure 6 shows the temperature variation with time during one month in the bow of section 1. The higher and constant value of 88 °C corresponds to the indirect measurement of the fluid temperature in the sensor T2 on the steel pipe in a joint. Moreover, there are 6 curves below with lower temperatures, but increasing temperature trends starting from a common value of 8 °C. The higher curve with temperature increasing up to 42 °C (with an initial bump) corresponds to the sensor T19, which is next to the side of the pipe on the mantle and covered by the cushion as shown in Fig. 5. Then the curve below for the sensor T20 is right in the elbow, on the mantle and covered by cushion too (Fig. 5) having a maximum temperature of 36 °C and following the same trend as T19. The curve further below with temperatures up to 32 °C is for the sensor T22, also in the cross section in the middle of the elbow and on the mantle covered by cushion, and follows the same trend as the other curves. Another

curve below belongs to T23, which is on the pipe mantle but without cushion, it shows the temperature steadily increasing up to 38 °C however not following exactly the same temperature increase trend as the T19, T20 and T22 curves. Finally, the last two curves show the temperature variation with time of the sensors T18 and T21 which are on the cushions (see Fig. 5). T18 and T21 temperatures reflect and follow in average the fluctuating outside ambient temperature. This is an indication of the cushion insulation effect.

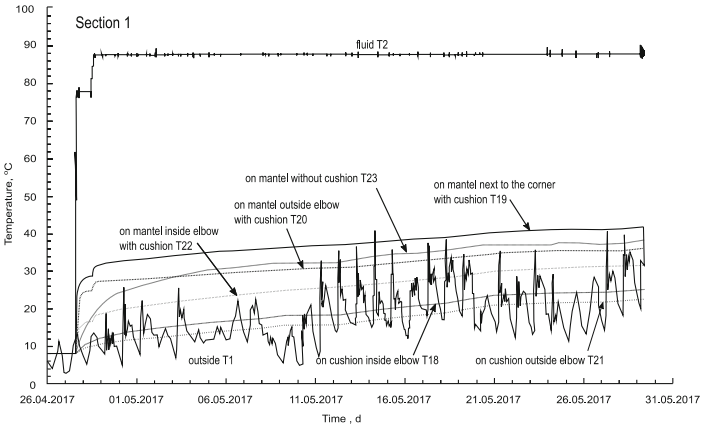

Fig. 6. Variation with time of temperature in and on the pipe in the corner of section 1, fluid and outside

Similar trends were recorded in section 3 for almost the same constant fluid and fluctuating ambient temperature. These are preliminary results and therefore, more time of measurement is needed to evaluate whether this temperature increase with time will stabilise or not and when. Moreover, temperature measurements in the soil are been recorded and they will be processed and analysed in subsequent studies.

6 Pipe Axial Displacements

The arrangement of the 6 extensometers in each section was at 1.5, 13.5, 25.5, 37.5, 39.4 and 40 m away from the centre. Figure 7 shows results of pipe axial displacements in section 3, where the heat enters the pipeline. It can be observed that once the fluid temperature increased to 79 °C from 13:45 to 16:50, the pipe moved axially towards the bow with displacements on the bow reaching values of 17 and 19 mm in one day. At 25.5 and 13.5 m displacement values of 9.2 and 3.6 mm were recorded, respectively, while at 1.5 m practically no movement is recorded. After 3 days under 89 °C, steady higher values of displacements were reached, namely 0.1, 5.3, 12.6, 22.3, 23.3 and 25.0 mm, respectively. After a month under 89 °C, steady values reached a plateau of maximum displacements of 0.2, 5.8, 13.2, 22.9, 24.2 and 25.8 mm, respectively.

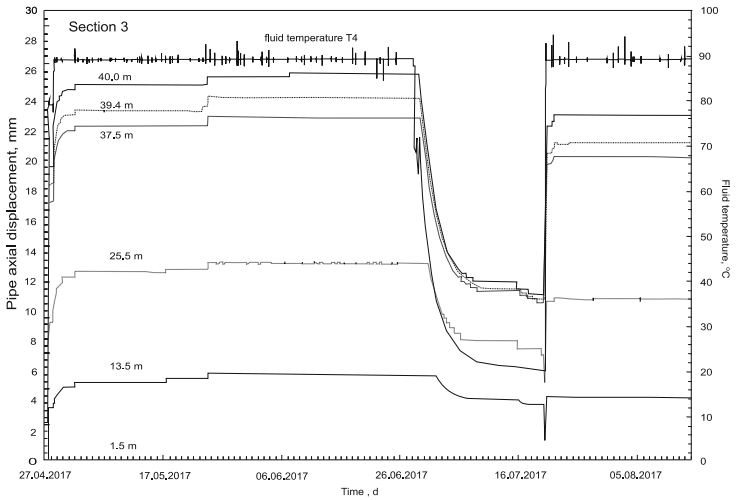

Fig. 7. Recording of the variation with time of pipe axial displacements measured on the mantle in section 3 for 6 and fluid temperature

These maximum values stayed almost constant for another 2 months until the temperature descended exponentially to 20 °C in 22 days as it can be seen in Fig. 7. Accordingly, displacements decreased to 0.05, 3.8, 7.6, 10.7, 10.9 and 11.1 mm, respectively. Once the temperature resumed again to the previous 89 °C, the displacements increased but to lower steady values than before (0.08, 4.3, 10.8, 20.3, 21.2, 23.0 mm). Probably this irrecoverable deformation is due to plastification of the soil and steel pipe which does not allow the pipe to come back exactly to the previous displacement values. This feature needs further research. The trend of temperature variation for the other sections was similar with slight differences in displacement magnitude.

7 Final Comments and Conclusions

Results of temperature variations with time showed that cushions acted as insulators, since temperatures registered on the cushions were almost similar to the ambient average temperature, between 10 and 20 °C. More time of measurement is needed to evaluate whether this temperature increase with time will stabilise or not and when.

The measurement of the axial displacements along the pipeline with time showed that as long as the temperature increases from the ambient condition up to 80 or 90 °C, pipes were moving all along their length.

It was found that after a temperature drop from 90 to 20 °C during 20 days and subsequent increase to 90 °C again, displacement did not return to the same values as before, but around 3 mm smaller. This opens the question of how unloading-reloading temperature cycles may affect the pipe deformation behaviour.

Finally, these initial results and analyses are the starting point for further studies on and comparison with analytical estimations and computer program calculations. The experimental data base is extremely valuable information that will help improving the understanding of pipe behaviour and therefore improve design, operation and maintenance of district heating networks.

Acknowledgements. This work is part of ongoing research programmes on district heating by AGFW for the development and improvement of pipeline networks. The authors are especially grateful to the BMWi German Federal Ministry of Economics and Energy for this funding support (funding code: 03ET13335). The first author would like to greatly acknowledge the funding support granted by ZEIT Stiftung by means of an academic Fellowship at HafenCity University Hamburg.

References

Achmus, M.: Zur Berechnung der Beanspruchungen und Verschiebungen erdverlegter Fernwärmeleitungen. Ph.D. Thesis, Universität Hannover (1995)

Achmus, M., Weidlich, I.: Interaction of district heating pipelines and the surrounding soil. Bautechnik **93**(9), 663–671 (2016). (in German)

Achmus, M., Rizkallah, V.: The interaction between underground district heating pipelines and the surrounding soil. In: ISSMGE Conference, Hamburg, vol. 2, pp. 943–946 (1997)

AGFW: EnEff: Wärme Einsatz fliessfähiger Verfüllstoffe zur KMR-Verlegung. Forschung und Entwicklung, Helft 43. AGFW (2017)

EN 13941: Auslegung und Installation von werkmäßig gedämmten Verbundmantelrohren für die Fernwärme. CEN, Brussels (2010)

prEN 13941: District heating pipes – Design and installation of thermal insulated bonded single and twin pipe systems for directly buried hot water networks: Part 1: Design. Part 2: Installation. CEN, Brussels (2016)

Gerlach, T., Achmus, M.: On the influence of thermally induced radial pipe extension on the axial friction resistance. Energy Procedia **116**, 351–364 (2017)

Salveter, G.: Validierung numerischer Verfahren zur Berechnung des Interaktionsverhaltens "Fernwärmeleitung-Baugrund". Ph.D. thesis, Univeristät Hannover (2000)

Weidlich, I., Wijewickreme, D.: Factors influencing soil friction forces on buried pipes used for district heating. In: 13th International Symposium on District Heating and Cooling, Copenhagen (2012)

Weidlich, I.: Untersuchung zur Reibung an zyklisch axial verschobenen erdverlegten Rohren. Ph. D. thesis, Leibniz Universität Hannover (2008)

Weidlich, I., Achmus, M.: Measurement of normal pressures and friction forces acting on buried pipes subjected to cyclic axial displacements in laboratory experiments. Geotech. Test. J. **31**(4), 334–343 (2008)

Waste Heat Recovery – Considerations for the Management of Thermally Polluted Urban Groundwater Resources

Jannis Epting[1(✉)], Matthias H. Müller[1], Alejandro García-Gil[2], and Peter Huggenberger[1]

[1] Department of Environmental Sciences, Applied and Environmental Geology, University of Basel, Basel, Switzerland
jannis.epting@unibas.ch
[2] Geological Survey of Spain (IGME), C/Manuel Lasala no 44, 9° B, 50006 Zaragoza, Spain

Abstract. Heating and cooling using groundwater is often performed without considering potential effects on subsurface resources and the multiple interactions of different subsurface utilizations. As a result, significantly increased subsurface temperatures have been observed in many urban areas. The current uncoordinated use of subsurface resources can lead to conflicts among different users and, specifically thermal pollution may lead to large-scale thermal impacts and impairments of groundwater quality.

Alternatively, current and future heat-demand in urban areas could be supplemented by recovering "waste heat" from the subsurface. Technologies for using this renewable energy resource would be particularly suitable in new buildings and infrastructures and in centers of economic growth.

We show that quantitative modeling approaches can serve as the scientific basis for thermal management strategies to better understand how thermal states of urban groundwater resources develop. On the one hand, we illustrate how to derive the potential for recovering waste heat from urban groundwater resources. On the other hand we demonstrate the applicability of the "integrated relaxation factor" (IRF) concept which facilitates optimizing and locating auspicious urban settings for developing thermal management strategies.

To our opinion, such strategies and advancements of practical solutions are indispensable in the debate on climate change and energy transition, as well as for reaching formulated development goals in different public initiatives such as the 2000-Watt-Society or the Europe 2020 Strategy.

1 Introduction

In many urban areas, significantly increased subsurface temperatures have been observed (Epting and Huggenberger 2013; Ferguson and Woodbury 2007; Menberg et al. 2013; Zhu et al. 2011). So far, only a few studies exist that approach resource management and the exploitation of ground source energy at the scale of urban aquifers (e.g. Epting and Huggenberger (2013); Mueller et al. (2018)).

A. Ferrari and L. Laloui (Eds.): SEG 2018, SSGG, pp. 140–146, 2019.
https://doi.org/10.1007/978-3-319-99670-7_18

A sustainable use of subsurface resources requires compulsory regulations as to which requirements are to be met for the approval of geothermal energy systems (Epting 2017). In general, such requirements target authorization procedures for individual installations. However, in most urban areas, the usage pressure on subsurface resources is high and today individual installations are already competing. New usage requests can therefore not be assessed without taking the overall context and the "current state" of the situation and existing subsurface uses into account (Huggenberger and Epting 2011).

This contribution outlines how to derive the heat potential for urban groundwater resources based on flow and heat-transport modeling. The evaluations are related to the results of the study "thermal management systems for the shallow subsurface of the Basel region" which was realized together with the Swiss Federal Office of Energy (SFOE). The evaluation of the heat potential also allows distinguishing those aquifer regions which are already over-heated nowadays, as a result of uncoordinated use and the present policy which more or less follows the rule "first come, first served". As a measure for a more controlled thermal management of urban subsurface resources, we illustrate the applicability of the "integrated relaxation factor" (IRF) concept as a scientific based criteria for a more equitable and sustainable geothermal use of shallow energy resources (Garcia-Gil et al. 2015).

2 Settings, Approach and Methods

The city of Basel is located in the north-western part of Switzerland (Fig. 1); the investigated unconfined gravel aquifer covers an area of approximately 32 km^2 of up to 38 m in thickness. The aquifer is underlain by an aquiclude consisting of mud to clay rich sediments of the Upper Rhine Graben (Huggenberger and Epting 2011). Due to the relatively high hydraulic conductivities of the unconsolidated gravel deposits, ranging from 10^{-4} to 10^{-2} ms^{-1}, heat-transport in the groundwater saturated zone is strongly driven by advection, which could be confirmed by calculated Péclet numbers (Epting et al. 2017).

Under natural conditions, the temperature of groundwater corresponds to the mean annual air temperature. Therefore, for the urban area of Basel, groundwater temperatures of around 10 °C would be expected. However, evaluations in highly industrialized and commercialized areas of Basel show that the groundwater is heated by up to 16–18 °C (Epting et al. 2017).

In total, about 50 groundwater users are currently operating in Basel. The total extracted amount of groundwater was about 25.2×10^6 m^3 in the year 2015. 62% was used for drinking water production and 38% for industrial applications such as heat exchange applications or as process water. Relatively "warm" water, which has been used for "cooling" and is reinjected into the aquifer, has strongly increased from about 5.0×10^5 m^3 in the year 1994 to about 1.0 to 1.6×10^6 m^3 in the recent years 2014 to 2016 (Mueller et al. 2018).

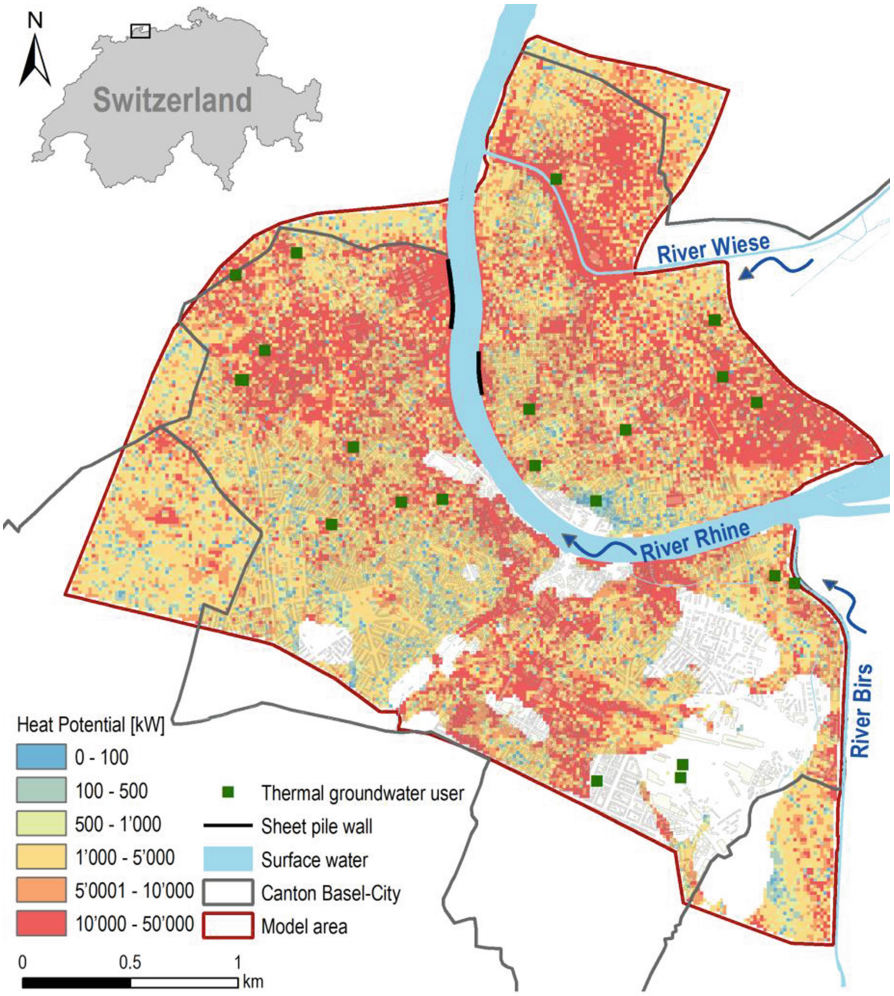

Fig. 1. Heat potential of the groundwater resources of Basel based on the mean simulated groundwater flow and temperatures for the years 2010–2015. Areas with no data depict locations with no or no perennial groundwater.

2.1 Deriving the Heat Potential of Groundwater Resources

High-resolution groundwater flow and heat-transport were simulated with FEFLOW© (Diersch 2002) for several groundwater body units (GWB) covering the urbanized areas of Basel. The implementation of boundary conditions are described in Epting et al. (2017); Mueller et al. (2018).

Based on the modeled hydraulic gradient (i) and the calibrated hydraulic conductivity field (k_f), Darcy velocities (v_D) and Darcy flow (Q_D) could be calculated. Furthermore, with the calibrated models, the average groundwater temperatures ($T_{Avg(2010–2015)}$) for the simulation period of 2010 to 2015 could also be calculated (Mueller et al. 2018).

Assuming a natural background temperature (T_{Nat}) allows to derive a temperature change (T_Δ). With these values, the thermal groundwater energy potential (E_G in kW) can be calculated using the equation:

$$E_G = c_W \times \rho_W \times Q_D \times T_\Delta \quad (1)$$

where c_w is the specific heat of water (4.20×10^6 kJ kg^{-1} K^{-1}), ρ_w is the density of water at 10 °C (999.7 kg m^{-3}), Q_D is the flow of water (m^3 s^{-1}); and T_Δ is the temperature change (K). We chose 10 °C for T_{Nat} which approximately corresponds to the average atmospheric temperatures in the region of Basel.

2.2 The Concept of the Relaxation Factor

Today, urban groundwater resources and, especially the thermal use of aquifers for cooling and heating is often uncoordinated and follows the law "first come, first served". For Basel, we observed that groundwater and thermal usage "claims" are requested which are, under consideration of natural groundwater availability and certainly concerning a sustainable qualitative development of subsurface resources, unrealistic. Based on the flow and heat-transport modeling results we can distinguish those aquifer regions which, as a result of uncoordinated use, are already over-heated today. Garcia-Gil et al. (2015) introduced the IRF-concept for a more equitable and sustainable geothermal use of shallow energy resources which was originally tested for Zaragoza, Spain. In Epting et al. (2017) the IRF-concept was applied to Basel for a simple interpolation of observed mean groundwater temperatures for the years 2010 to 2015. For this study, we present a reapplication of the IRF-concept for Basel using simulation results of the groundwater flow and heat-transport model. IRF was calculated as defined by Garcia-Gil et al. (2015):

$$IRF = \frac{T_\Delta - T_B}{T_{Max} - T_B} \quad (2)$$

with T_Δ as the temperature change induced by a thermal groundwater user (K), T_B as the background temperature of the aquifer and T_{Max} the maximum permitted temperature. For T_B we chose 12 °C (Mueller et al. 2018), which corresponds to the mean urban background groundwater temperature of Basel and 20 °C for T_{Max} according to the allowed limits in the Canton Basel-City. IRF values close to 0 indicate a relatively undisturbed thermal state, whereas IRF > 1 indicate a strong thermal impact on groundwater resources.

3 Results

Figure 1 shows the spatial distribution of the heat potential based on the mean simulated groundwater flow and temperatures for the simulation period of the years 2010 to 2015 (Mueller et al. 2018). Relatively high heat potentials (>10'000 kW) can be associated to urbanized areas, e.g. in the city center, and near rivers where seasonally

high temperature gradients from the surface waters to the groundwater, or vice versa, can be observed. Relatively low heat potentials (<1'000 kW) can be associated to less urbanized areas and open (green) spaces.

In Epting et al. (2017) the IRF, was calculated for the entire Canton Basel-City based on an interpolation of observed mean groundwater temperatures for the years 2010 to 2015 (Fig. 2). However, it has to be recognized that interpolations cannot capture the spatiotemporal heterogeneity of groundwater temperatures, which result from transient thermal boundary conditions such as thermal groundwater use or heat input by deep buildings or river-groundwater interaction processes. Therefore, the IRF in the presented study was calculated using the simulated mean groundwater temperatures for the years 2010 to 2015 (Fig. 2). Generally, the distributions of higher and lower IRF for both approaches are similar and the more densely urbanized areas are associated with elevated IRF-values.

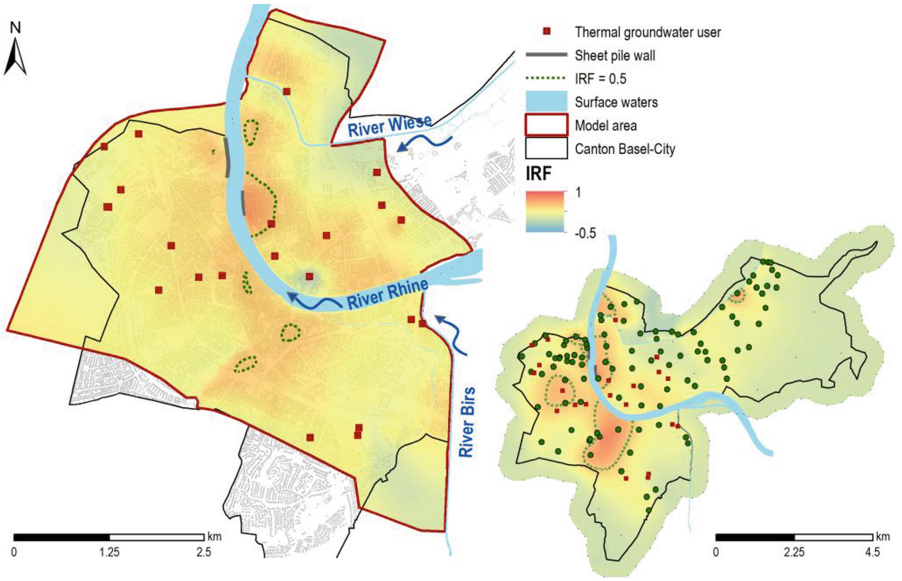

Fig. 2. Calculated IRF based on mean simulated groundwater temperatures for the years 2010 to 2015. Lower right: Originally calculated IRF based on interpolated mean groundwater temperatures for the years 2010 to 2015. Both calculations consider a background temperature of 12 °C and a maximum temperature for geothermal operations of 20 °C. The figure also shows green contour lines where IRF amounts to 0.5 and where geothermal exploitation already reaches 50% of the potentially usable cooling use capacity.

Evidently, the distribution of IRF, which is based on the simulated groundwater temperatures, is much more segregated with a mean of 0.28 and a range between −0.24 and 0.69. The IRF, which is based on interpolated groundwater temperatures, resulted in a mean of 0.15 and a range between −0.17 and 0.83. Whereas negative values depict

those areas where the potential of using groundwater for cooling is still possible, positive values indicate to what degree the cooling potential is already exhausted.

The larger mean IRF for the calculation, which is based on the simulated groundwater temperatures, may be attributed to the influence of the modeled heated building structures and groundwater users which lead to extensive areas of thermal influence down-gradient. On the contrary, the larger range of IRF for the calculation, which is based on the interpolated groundwater temperatures, may be explained by single measurement outliers that are not necessarily representative for local groundwater temperatures.

Originally, up to six urban areas (total area of 340 ha) could be delineated where IRF > 0.5 (one area is outside of the modeled area of the current investigations). For the current investigations, only one large and four small urban areas could be delineated where IRF > 0.5 (total area of 50 ha).

The influence of a reinjection of "cold" water can be seen at a site near the river Rhine, where the groundwater temperature is relatively low and the calculated IRF is close to 0. Hence, the reinjection of "cold" water reduces the effect of groundwater overheating by anthropogenic heat inputs.

4 Discussion and Conclusions

In general, it is accepted that in urban areas subsurface development should not lead to further thermal pollution of groundwater resources. It is obvious, however, that the current unregulated approach for managing energy resources, especially in urban areas, will not be able to sustain future cooling demands (Herbert et al. 2013).

Quantitative modeling approaches in combination with GIS can serve as the scientific basis for thermal management strategies to better understand how thermal states of urban GWBs develop. Thereby, evaluations of heat potentials can be the basis for management concepts and an overall economic and ecological planning of thermal subsurface resources. The IRF can be used to indicate thermal overexploitation of groundwater resources.

Alternatively, increased groundwater temperatures can also be considered as a heat potential which currently is wasted into the subsurface. This waste heat might be recovered, and thus represents potentially usable geothermal energy. In principle, urban aquifers could be directly "mined" to exploit and store waste heat, whereas technologies would be particularly suitable in new buildings and infrastructures in centers of economic growth. Likewise, active heat extraction from groundwater and reinjection of "cold" water (in the case of open loop systems) should be taken into consideration. Similarly, passive solutions which include the application of energy geostructures (piles, diaphragm walls, concrete slabs) could be appropriate. On the one hand, such solution could support in reducing groundwater temperatures and, on the other hand, substantial contribution to the heating demand of cities could be supplied.

Deriving the spatiotemporal distribution of heat potentials facilitates a more target-oriented thermal recovery of groundwater resources on the urban scale and incorporating this knowledge into urban district planning (Mueller et al. 2018). The IRF-concept, as a scientific based criteria for a more equitable and sustainable use of urban

subsurface resources, indicates the exploitation status of subsurface resources and distinguishes urban areas where thermal overexploitation is evident. Combining the information of the spatial distribution of heat potentials and the exploitation status of subsurface resources facilitates optimizing and locating auspicious urban settings for developing thermal management strategies. Our concepts and applied methods could be the basis for decisions regarding (1) preferred type of use (active or passive, open or closed system); (2) dimensioning of installations; (3) the location and number (density) of the intended installations; and (4) the reinjection of the groundwater used. In a next step, reasonable agreement has to be obtained between theoretical results and real city-scale examples.

Acknowledgements. We kindly acknowledge the financial support by the Swiss Federal Office of Energy (SFOE-Project: "Thermal Management Systems for the Shallow Subsurface of the Basel Region", SI/501044-01). We also want to thank the Cantonal Agency of Environment and Energy Basel-City (AUE BS) for their cooperation in scope of diverse projects related to the thermal management of urban groundwater resources in the Basel area.

References

Diersch, H.J.G.: FEFLOW Reference Manual. Institute for Water Resources Planning and Systems Research Ltd., Berlin, Germany (2002)

Epting, J.: Thermal management of urban subsurface resources − delineation of boundary conditions. Procedia Eng. **29**, 83–91 (2017)

Epting, J., García-Gil, A., Huggenberger, P., Vázquez-Suñe, E., Mueller, M.H.: Development of concepts for the management of thermal resources in urban areas − assessment of transferability from the Basel (Switzerland) and Zaragoza (Spain) case studies. J. Hydrol. **548**, 697–715 (2017)

Epting, J., Huggenberger, P.: Unraveling the heat island effect observed in urban groundwater bodies − definition of a potential natural state. J. Hydrol. **501**, 193–204 (2013)

Ferguson, G., Woodbury, A.D.: Urban heat island in the subsurface. Geophys. Res. Lett. **34**, L23713 (2007)

Garcia-Gil, A., Vazquez-Sune, E., Schneider, E.G., Sanchez-Navarro, J.A., Mateo-Lazaro, J.: Relaxation factor for geothermal use development − criteria for a more fair and sustainable geothermal use of shallow energy resources. Geothermics **56**, 128–137 (2015)

Herbert, A., Arthur, S., Chillingworth, G.: Thermal modelling of large scale exploitation of ground source energy in urban aquifers as a resource management tool. Appl. Energy **109**, 94–103 (2013)

Huggenberger, P., Epting, J.: Urban Geology − Process-Oriented Concept for Adaptive and Integrated Resource Management. Springer, Basel (2011)

Menberg, K., Bayer, P., Zosseder, K., Rumohr, S., Blum, P.: Subsurface urban heat islands in German cities. Sci. Total Environ. **442**, 123–133 (2013)

Mueller, M.H., Huggenberger, P., Epting, J.: Combining monitoring and modelling tools as a basis for city-scale concepts for a sustainable thermal management of urban groundwater resources. Sci. Total Environ. **627**, 1121–1136 (2018)

Zhu, K., Blum, P., Ferguson, G., Balke, K.D., Bayer, P.: The geothermal potential of urban heat islands (vol 5, 044002, 2010). Environ. Res. Lett. **6** (2011)

Numerical Analysis of the Thermo-Mechanical Behavior of an Energy Pile in Mexico

Norma Patricia López-Acosta[1(✉)], David Francisco Barba-Galdámez[1], and Marcelo Sánchez[2]

[1] Instituto de Ingeniería, Universidad Nacional Autónoma de México, Ciudad de México, Mexico
nlopeza@iingen.unam.mx
[2] Zachry Department of Civil Engineering, Texas A&M University, College Station, USA

Abstract. Energy geostructures, particularly energy piles, are foreseen as an alternative to reduce the environmental impact of the growing energy demand for space conditioning. This environmental friendly technology is a type of closed-loop Ground Source Heat Pump (GSHP) in which foundation elements are used to extract or inject thermal energy from/to the soil. Despite their multiple benefits, energy piles have not yet been employed in Mexico, where there is a general lack of knowledge about these systems. In the present paper the feasibility, limitations and challenges of using energy piles in the Mexican context are discussed. In order to understand the geotechnical implications of their functioning, a numerical simulation of the behavior of an energy pile subjected to different combinations of thermo-mechanical loads considering Coatzacoalcos (Veracruz) subsoil conditions is presented. The fully coupled thermo-hydro-mechanical analysis are made using the finite element program PLAXIS 2D Thermal. Vertical displacement and axial load distributions are obtained. The results of the parametric studies show that the magnitude of the thermal-induced stresses is significant, but their effects on the behavior of the foundation depends on the magnitude of the applied mechanical load.

1 Introduction

Electricity consumption in Mexico has grown at an annual average rate of 3% in the last decade. The building sector (that includes residential, commercial and public activity) accounts for about 18% of the total energy consumption of the country. Despite the limited data about its final use, the Secretariat of Energy (SENER) estimated that half of the energy employed by the residential sub-sector is designated to water heating and space conditioning. Since the Mexican energy system still depends heavily on fossil fuels (90.7% of the Primary Energy Supply) this growing demand has a significant impact on the environment and it is a serious obstacle for the accomplishment of the Mexican government commitment to reduce its greenhouse gas emissions 22% by 2030, and 50% by 2050 (SENER 2016).

Ground Source Heat Pump (GSHP) systems are one of the most promising techniques in the renewable energy field to meet space conditioning requirements. They are

A. Ferrari and L. Laloui (Eds.): SEG 2018, SSGG, pp. 147–154, 2019.
https://doi.org/10.1007/978-3-319-99670-7_19

thermal machines that exploit the temperature difference between the ground and the air for heating and cooling buildings. In spite of their growing popularity in different countries, to the authors' knowledge GSHP systems have not yet been used in Mexico. According to García and Martínez (2012), the high installation cost is the main obstacle to their implementation. In this context, energy piles are an appealing alternative. These structures consist of foundation elements equipped with closed loop pipes to exchange heat with the ground.

The following paper discusses the feasibility of employing energy piles in Mexico, their major limitations, and challenges. To understand the heating effects on the mechanical behavior of energy piles, a numerical analysis is performed considering Coatzacoalcos (Veracruz) subsoil conditions. The study is carried out with the finite element software Plaxis 2D Thermal and evaluates the response of a single energy pile subjected to different combinations of thermal and mechanical loads.

2 Energy Piles Feasibility in Mexico. Benefits, Limitations, and Challenges

Due to its particular geological conditions, Mexico has abundant geothermal reservoirs. However, nearly all the geothermal energy of the country is utilized to produce electricity. Direct uses of this resource have been restricted to recreational activities (e.g., bathing and swimming), while other types of applications are still under development (Lund et al. 2011).

Although mild temperatures prevail in most of the country, climate change and the development of northern and southeastern states (where it predominates extreme and hot humid climate respectively) have produced an increase in energy consumption for space conditioning. This growing demand is mostly fulfilled with low energy efficiency systems. In recent years, various attempts have been made to implement new environmental friendly techniques such as GSHPs. The Mexican Center of Innovation in Geothermal Energy (CeMIE-Geo) estimates that these systems can be employed in at least nine states (Baja California, Chihuahua, Nuevo León, Jalisco, Aguascalientes, Veracruz, Estado de México, Guerrero, and Quintana Roo), but their high initial investment reduces their competitiveness (García and Torres 2016). In this regards, adapting foundation elements with heat exchangers is an economically viable option to promote them. In particular, energy piles are an attractive alternative, considering that traditional piles are a common foundation element for commercial, industrial, and residential buildings on the largest cities in the country.

Despite all their benefits, many customers, policymakers, and practitioners still unknown what energy piles are. Furthermore, there is also a general lack of knowledge of soil thermal properties and its behavior in non-isothermal conditions. This is an important issue because large areas of the country lie on fine-grained soils. Several studies (Cekerevac and Laloui 2004; Abuel-Naga et al. 2006) have shown that temperature modifies the mechanical behavior of these materials and its impact on the performance of thermoactive geotechnical systems is also well documented (Di Donna et al. 2015; Yavari et al. 2016). Possible thermo-enhanced creep effects on energy piles in fine-grained soils has also been reported (Akrouch et al. 2014).

Finally, an additional inconvenient with the implementation of energy piles is the possible increase of soil temperature because of non-balance heat extraction-injection cycles. Researchers in countries with comparable climate conditions have expressed similar concerns (De Moel et al. 2010). Fan et al. (2008) have proposed some improvements to deal with this issue. However, their feasibility should be evaluated for the Mexican context.

3 Numerical Modelling of an Energy Pile

Temperature variations cause expansions and contractions on the pile and the surrounding soil. These thermal strains significantly affect the mechanical behavior of the foundation. To better understand the complex soil-structure interaction, a single energy pile is numerically simulated with the finite element program PLAXIS 2D Thermal. The example considers a 15-m long pile with a diameter of 0.6 m located in Coatzacoalcos (Veracruz). The effects of different combinations of thermo-mechanical loads on the pile performance are evaluated. The pile is initially subjected to a constant mechanical load, following by a monotonic thermal load. The constant mechanical loads applied correspond to factors of safety (FoS) of 5 (model A) and 2.5 (model B). These loads represent 20% and 40% of the ultimate axial load capacity, respectively. Five temperature variations, between +5 to +40 °C, are evaluated. These values represent the most likely thermal load of which an energy pile in Coatzacoalcos would be subjected. The sign convention adopted assumes compression stress and downward displacement (i.e. settlements) as positives.

Coatzacoalcos is a major port city located on the Atlantic coast of south-eastern Mexico and hosts one of the most important industrial areas of the country. It has a tropical monsoon climate with hot and humid summers. Coatzacoalcos has a daily mean temperature of 26.7 °C and an average annual rainfall of 2758.5 mm. Its maximums temperature is above 35 °C.

The subsoil conditions were obtained from geotechnical investigations based on standard penetration tests (SPT). The soil profile consists of five layers of eolian medium to dense poorly graded sand with silts (SP-SM) and silty sand (SM) (Fig. 1). The groundwater level is 3 m depth.

The different soil layers were modeled as isotropic thermo-elastoplastic materials with a Mohr-Coulomb failure criterion, whereas the concrete pile behavior was considered as thermo-elastic. Due to lack of experimental data, the mechanical soil properties were estimated based on SPT blow counts (N_{spt}). The soil solids thermal conductivity (λ) and specific heat capacity (c_s) correspond to typical values for silty sand according to Ochsner et al. (2001). The coefficient of thermal expansion (CTE) was established with the criteria proposed by Bourne-Webb et al. (2016). Tables 1 and 2 summarize all the properties assumed in the analyses.

Figure 2 shows the geometry and the boundary conditions of the axisymmetric model. The mesh consists of 4573-triangular elements, with a more refined distribution around the pile. The simulated domain is chosen to avoid any boundary effect. A perfectly rough contact between the pile and soil layers is assumed, so no interface elements are introduced.

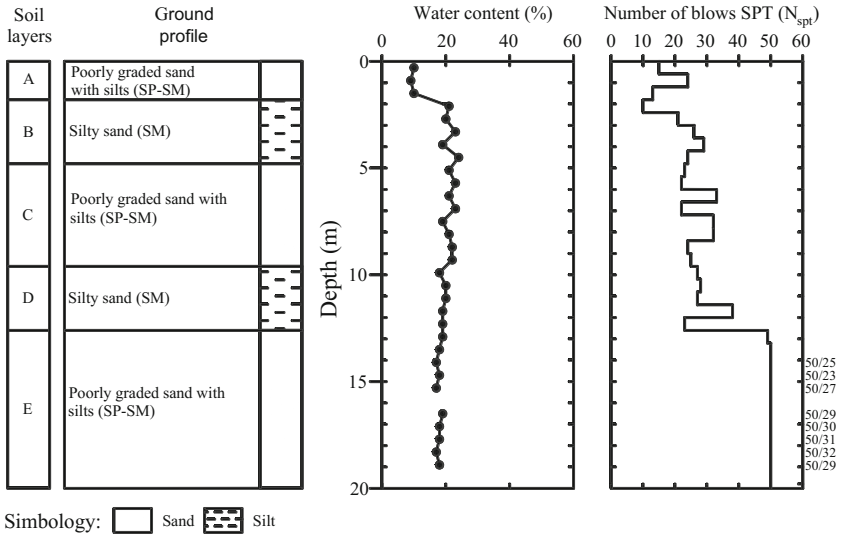

Fig. 1. Simplified soil profile at Coatzacoalcos (Veracruz, Mexico)

Table 1. Mechanical parameters assumed for soil layers and pile

Material/layer	A	B	C	D	E	Pile
USCS	SP-SM	SM	SP-SM	SM	SP-SM	–
Young modulus, E′ (MPa)	49.4	62.4	75.4	83.2	130	30000
Poisson modulus, ν′ (–)	0.3	0.3	0.3	0.3	0.3	0.2
Cohesion, c′ (kPa)	0	0	0	0	0	–
Friction angle, ϕ′ (°)	32.0	33.4	34.8	35.3	40.8	–
Dilatancy angle, ψ (°)	2.0	3.4	4.8	5.3	10.8	

Table 2. Thermal properties of the materials

Material/layer	A	B	C	D	E	Pile
Density, ρ (kN/m^3)	2600	2590	2610	2580	2590	2440
Thermal conductivity, λ (W/m/°C)	3.72	3.72	3.72	3.72	3.72	1.60
Specific heat capacity, c_s (J/kg/°C)	800	800	800	800	800	890
Linear CTE, α (με/°C)	12	12	12	12	12	10

Horizontal displacements are restricted along the right boundary, while the mesh bottom is completely fixed. Initial stress state is considered geostatic and is calculated assuming a hydrostatic pore water pressure profile and a coefficient of earth pressure at rest according to Jaky's formula. The axis of symmetry and the pile are assumed as impervious, while water flow is allowed through the right-hand and bottom boundaries. Thermal boundary consist in no heat flux across the axis of symmetry (adiabatic

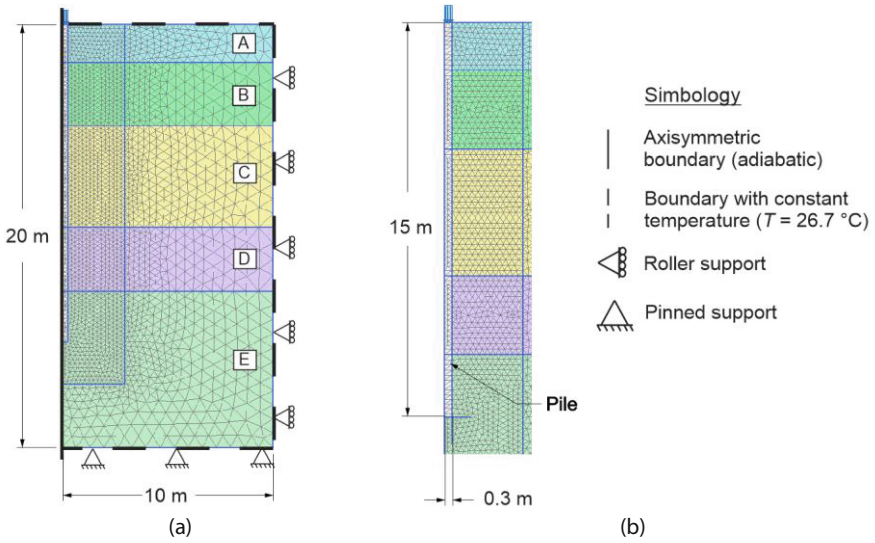

Fig. 2. (a) Finite element mesh and boundary conditions, (b) zoom in mesh detailing the pile

condition) and a constant temperature of 26.7 °C on the bottom, up and right boundary. To simulate the thermal loads, the temperature along the pile length is varied at a rate of 0.5 °C/day until reaching the targeted temperature change.

4 Numerical Results

Figure 3 shows the vertical displacement distribution for each case analyzed. Upon increasing temperature, the pile expands. The upper section of the element moves upwards, while the lower part goes in the opposite direction. In general, this behavior is consistent with measurements recorded in other load tests (Amatya et al. 2012). The thermal displacement magnitudes are similar for both cases. The value measured at the pile head is 5.80 and 5.41 mm for models A and B, respectively. This slight reduction is a consequence of the stronger restrictions imposed at the pile head.

Figure 4 presents the axial load measured along the pile for the different test performed. The results show that the thermal strains caused a redistribution of the pile forces, mainly on the mobilized shaft friction. For small temperature changes, thermal displacements produce a reduction in the forces transferred to the upper soil layers. As ΔT increases, the relative soil-pile displacement direction changes, mobilizing downward shear forces. The thermal load required to induce negative skin friction depends on the mechanical load applied (+15 °C for model A, and +25 °C for model B).

The thermal loads represent between 6%–48% of the mechanical load applied to model A and 2%–27% of model B. However, their impact on the total mechanical behavior of the pile is small (they induce a maximum increase of 12% and 2% of the

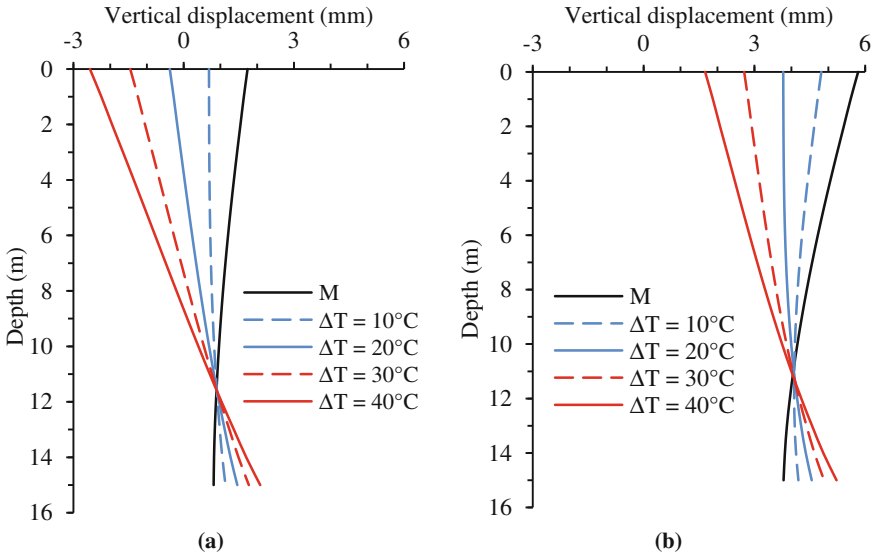

Fig. 3. Vertical displacement along the pile: (a) Model A, FoS = 5, (b) Model B, FoS = 2.5

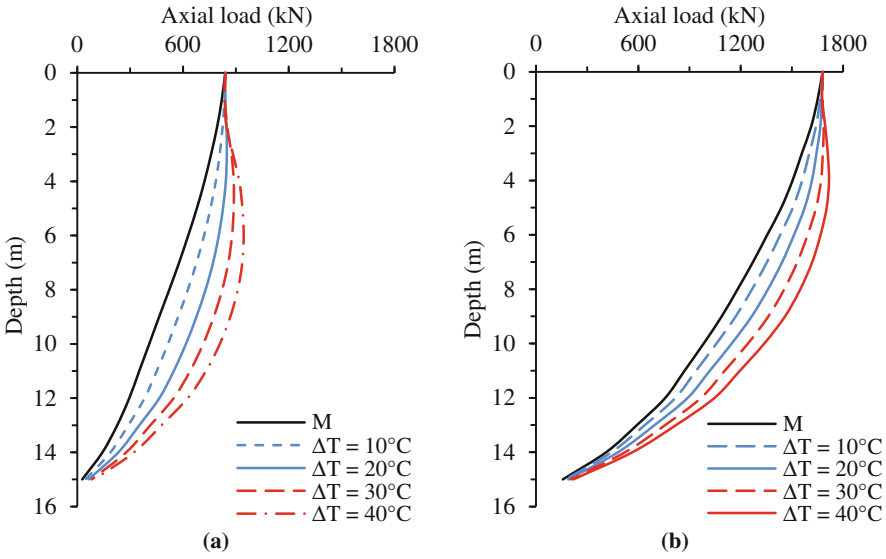

Fig. 4. Axial load distribution along the pile: (a) Model A, SoF = 5, (b) Model B, SoF = 2.5

total load for a ΔT = +40 °C). This is because the position of the maximum mechanical and thermal load does not match. The former is on the pile head, while the latter is located at the null point (about 9 m depth for model A and 8 m depth for model B). Rotta Loria et al. (2015) report similar results.

Figure 5 examines the maximum thermal stress variation respect to the temperature change. The data show a linear relationship between both variables, with an approximate slope of 40 kPa/°C (11% of fully restrained condition) regardless of the mechanical load applied. This value is small compared with the data presented by Amatya et al. (2012) and indicates that the pile is relatively free to expand during heating.

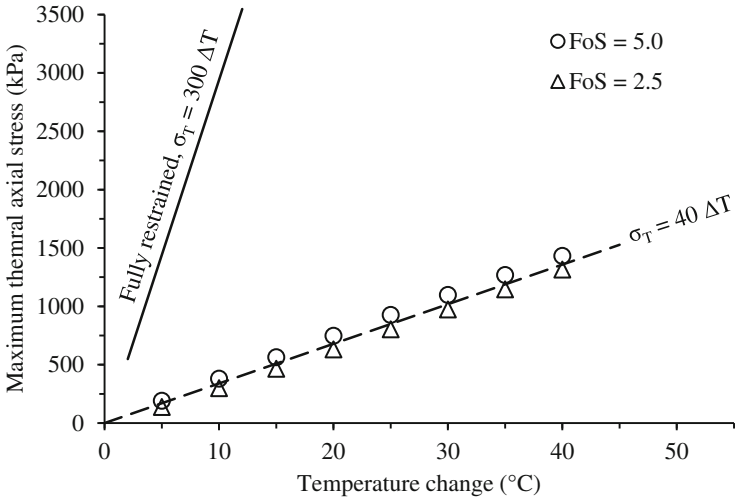

Fig. 5. Variation of the maximum thermal stress

5 Conclusions

Energy geostructures are one of the most innovative techniques in the field of renewable energy to respond to the growing energy demand for space conditioning. This article discusses the possible benefits, challenges and main obstacles to their implementation in Mexico. The analysis shows that the application of this technology, particularly of energy piles, is economically feasible in at least nine states of the country. However, laboratory and field investigations are required to characterize the behavior of national soils under thermal loading. From the above, it is concluded that a long-term research program on energy geostructures is indispensable, as well as more widespread dissemination and promotion of this technology.

References

Abuel-Naga, H.M., Bergado, D.T., Ramana, G.V., Grino, L., Rujivipat, P., Thet, Y.: Experimental evaluation of engineering behavior of soft Bangkok clay under elevated temperature. J. Geotech. Geoenviron. Eng. **132**, 902–910 (2006)

Akrouch, G., Sánchez, M., Briaud, J.-L.: Thermo-mechanical behavior of energy piles in high plasticity clays. Acta Geotech. **9**, 399–412 (2014)

Amatya, B.L., Soga, K., Bourne-Webb, P.J., Amis, L., Laloui, L.: Thermo-mechanical behaviour of energy piles. Géotechnique **62**, 503–519 (2012)

Bourne-Webb, P.J., Bodas-Freitas, T.M., Freitas-Assunção, R.M.: Soil–pile thermal interactions in energy foundations. Géotechnique **66**, 167–171 (2016)

Cekerevac, C., Laloui, L.: Experimental study of thermal effects on the mechanical behaviour of a clay. J. Numer. Anal. Method Geomech. **28**, 209–228 (2004)

De Moel, M., Bach, P.M., Bouazza, A., Sing, R.M., Sun, J.O.: Technological advances and applications of geothermal energy pile foundations and their feasibility in Australia. Renew. Sustain. Energy Rev. **14**, 2683–2696 (2010)

Di Donna, A., Ferrari, A., Laloui, L.: Experimental investigations of the soil-concrete interface: physical mechanisms, cyclic mobilisation and behaviour at different temperatures. Can. Geotech. J. **14**, 1–44 (2015)

Fan, R., Jiang, Y., Yao, Y., Ma, Z.: Theoretical study on the performance of an integrated ground-source heat pump system in a whole year. Energy **33**, 1671–1679 (2008)

García, A., Martínez, I.: Estado actual de desarrollo de las Bombas de Calor Geotérmico. Geotermia **25**, 58–68 (2012). (in Spanish)

García, A., Torres, V.: Estudio de Mercado para la aplicación de Bombas de Calor Geotérmicas en México (2016). (Internal Report, in Spanish)

Lund, J.W., Freeston, D.H., Boyd, T.L.: Direct utilization of geothermal energy 2010 worldwide review. Geothermics **40**, 159–180 (2011)

Ochsner, T.E., Horton, R., Ren, T.: A new perspective on soil thermal properties. Soil Sci. Soc. Am. J. **65**, 1641 (2001)

Rotta Loria, A.F., Gunawan, A., Shi, C., Laloui, L., Ng, C.W.: Numerical modelling of energy piles in saturated sand subjected to thermo-mechanical loads. Geomech. Energy Environ. **1**, 1–15 (2015)

Secretariat of Energy – SENER: Electricity Sector Outlook 2016-2030. México (2016)

Yavari, N., Tang, A.M., Pereira, J.-M., Hassen, G.: Effect of temperature on the shear strength of soils and the soil–structure interface. Can. Geotech. J. **53**, 1186–1194 (2016)

Assessment and Comparison of Soil Thermal Characteristics by Laboratory Measurements

Rute Ramos[1], Lazaros Aresti[2(✉)], Paul Christodoulides[3], Ana Vieira[1], and Georgios Florides[3]

[1] National Laboratory for Civil Engineering, Lisbon, Portugal
[2] Department of Electrical Engineering, Computer Engineering and Informatics, Cyprus University of Technology, Limassol, Cyprus
lg.aresti@edu.cut.ac.cy
[3] Faculty of Engineering and Technology, Cyprus University of Technology, Limassol, Cyprus

Abstract. Soil thermal characterization is an important aspect affecting the performance of Ground Heat Exchangers (GHE) in a Shallow Geothermal Energy (SGE) system application. Thermal conductivity and specific heat capacity are the sole requirements in designing such systems and can be obtained using empirical prediction models, laboratory tests and *in situ* tests. Laboratory thermal tests can be performed under steady-state or transient conditions. Transient tests have the advantage of being fast and of requiring a small volume of soil. This has led to recent developments and types of heat probes commercially available, but for which there is limited comparative assessment of results. This paper focuses on the evaluation of thermal properties, namely the ground thermal conductivity, specific heat capacity and thermal diffusivity by means of two different probes; a needle probe and a surface probe, and on comparing and testing their accuracy. Comparison of the different samples was also performed using two different transient needle probes, from two commercially available equipment, Isomet-2104 and Hukseflux-TPSY02. The laboratory measurements are supported by numerical modelling using the COMSOL Multiphysics software which applies a finite-element analysis method on the convection-diffusion equation for heat transfer.

1 Introduction

Ground thermal properties, in particular thermal conductivity and specific heat capacity are essential for a well-designed Shallow Geothermal Energy (SGE) system with regard to its energy efficiency, sustainability and structural performance (Vieira et al. 2017). Therefore, soil/rock thermal characterization is a crucial aspect that needs to be taken into account in the design of SGE systems. Based on soil multiphase nature, the use of empirical relations involving the thermal behaviour of the solid, liquid and gaseous phases to assess soil thermal properties goes back to decades (e.g., De Vries 1966; Farouki 1981). Such relations allow for the consideration of several factors such as soil particle size, mineralogy and saturation ratio, among others, and can be used as a first approach.

A. Ferrari and L. Laloui (Eds.): SEG 2018, SSGG, pp. 155–162, 2019.
https://doi.org/10.1007/978-3-319-99670-7_20

However, they imply simplistic assumptions related with soil elements' arrangement that can lead to significant errors in heat transfer calculations (Rees et al. 2000).

The soil/rock thermal properties can be also assessed using more sophisticated methods such as in situ tests, laboratory tests and empirical prediction models. Laboratory tests have the advantage of being cheaper and usually quicker than in situ tests. Nonetheless, they do not account for site specific conditions such as the presence of high groundwater flow, spatial heterogeneity and scale effects that directly impact the effective thermal properties (Vieira et al. 2017).

There are a large number of different types of laboratory tests available for the assessment of soil/rock thermal properties, based on different assumptions and procedures. Some of the set ups of such tests have been used for decades and are governed by classic standards (e.g. ASTM D5334 2014). Thermal conductivity is a measure of the property of a material that serves as a medium for heat transmission or a measure of the heat conducting capability of the material. In general, for the thermal characterization of bulk material, so-called steady-state and non-steady state (transient) methods are both used. Steady-state methods measure thermal properties by establishing a temperature difference across the sample that does not change with time, while transient methods measure time-dependent heat dissipation within a sample. The latter have the advantage of being fast, requiring simpler equipment and procedures, demanding smaller samples and reducing moisture migration.

The increase of SGE systems application has led to the development of different commercially available heat probes, for which there is limited comparative and reliability assessment of the results. The comparison between different methods and their influence on the final results are important issues that need to be studied.

This paper focuses on the evaluation of the thermal properties of different Cyprus geological materials, in particular its thermal conductivity, by means of two different transient methods (needle probe and surface probe), and the comparison of the results and accuracy. In order to reproduce some of the results, numerical modelling was also performed.

2 Location and Characteristics of the Samples

The thermal properties of seven samples (five soil samples and two rock samples), collected in the surrounding area of the Old Monastery of Archangel Michael located about 12 km northwest of Larnaca, were analysed (Fig. 1).

The soil samples, characterized by a diameter of 8 cm and length between 13.5 cm (sample 4) and 15.1 cm (sample 2), generally comprise greyish or brownish marly soils with limestone pebbles with variable size. The rock samples correspond to fragments of yellowish-whitish marly limestones with surface areas of about 100 to 125 cm^2 and variable thickness (ranging from 5 to 11.5 cm). The general aspect of the samples is shown in Fig. 2.

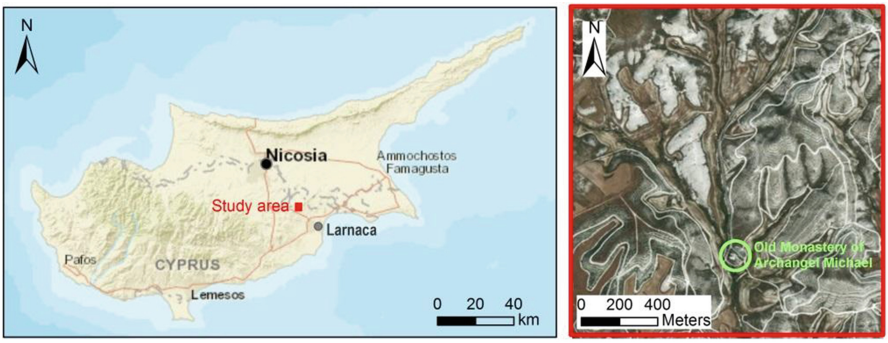

Fig. 1. Location of the samples.

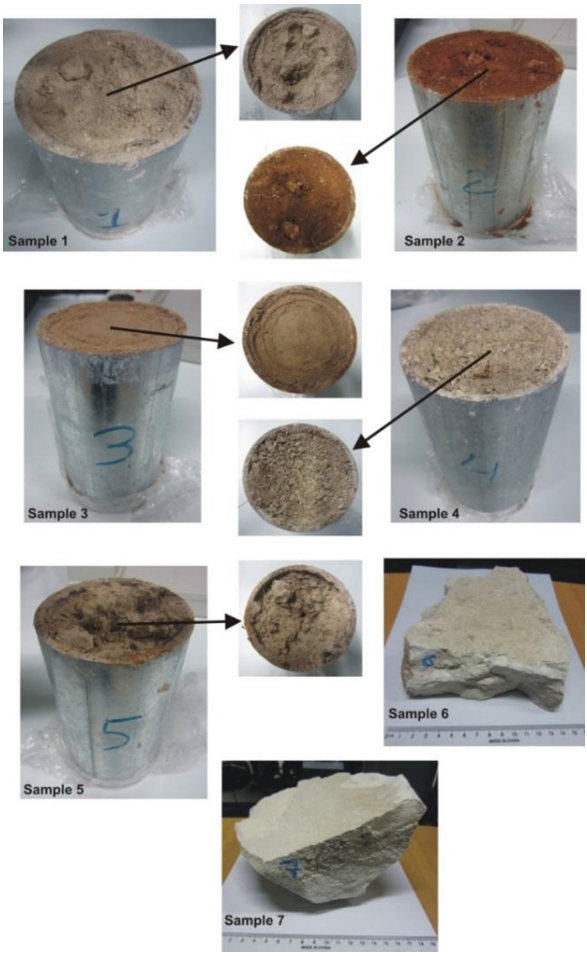

Fig. 2. General aspect of the samples analysed.

3 Methodology. Laboratory and Numerical Experiments

The thermal properties of the samples, namely thermal conductivity, volumetric heat capacity and thermal diffusivity, were obtained using a heat transfer analyser ISOMET 2104 from Applied Precision. In course of this procedure, a needle probe and a surface probe were applied in soil samples, whereas for the analysis of rock samples only a surface probe was used (Fig. 3a). Therefore, a narrow and long hole, smaller in diameter than that of the needle probe, was pre-drilled in each soil sample for an easy placement of the needle probe.

(a)

(b)

Fig. 3. Equipment used for the thermal characterization of the samples. (a) ISOMET 2104, (b) Hukseflux-TPSY02.

In order to compare and evaluate the precision of the methods, several measurements were carried out during three days, in particular on the samples where a greater discrepancy between results obtained with the two probes was observed. The time taken for performing each test ranged between 8 and 12 min.

In addition, after conducting the tests with the previously referred equipment, new measurements were performed in four soil samples using the Hukseflux-TPSY02 equipment (Fig. 3b). This equipment allowed for the thermal conductivity determination by means of a needle probe and provided the recording of all time-steps. The length and the diameter of the needle are different from the previous equipment and, as a consequence, an additional hole was drilled as close as possible to the previous one.

Following the completion of the laboratory tests, a numerical model was generated using the COMSOL Multiphysics software, which applies a finite-element analysis method on the convection-diffusion equation for heat transfer. The test samples were reproduced using 3D geometry and the probes were represented as 1D line source boundary conditions.

The Hukseflux-TPSY02 heat conductivity equipment with needle probe was simulated, as the specific device can monitor and log the temperatures at intervals of 0.5 s. This characterization of the equipment makes feasible the computational study comparison.

In order to validate the model a material with known thermal conductivity, density and specific heat capacity at constant pressure was chosen, namely glycerol. Liquid glycerol was placed in a tube with 15 cm height and 8 cm diameter.

Ambient temperature was set as a boundary condition and a 1D heat source was used to replicate the needle probe with constant power set at 2707 W/m as was the case for the laboratory experiments. The power is applied after the 100 s, where the system was confirmed (experimentally) to be in steady state, with a temperature difference (ΔT) of 0.1 °C. The obtained results are shown in Sect. 4.

4 Results and Interpretation

The results obtained with heat transfer analyser ISOMET 2104 from Applied Precision are shown in Table 1. It can be seen that the marly soils are characterized by thermal conductivity ranging between 0.42 and 1.02 W/m K, thermal diffusivity varying from 2.62×10^{-7} to 6.94×10^{-7} m^2/s and volumetric heat capacity between 1.35×10^6 and 1.98×10^6 J/m^3 K. Regarding the rock samples, only the thermal conductivity was possible to be assessed with the surface probe. In both samples, a value of about 1 W/m K was determined for this parameter. This value ranges between the thermal conductivity determined in Cyprus limestone and marls in dry conditions according to Stylianou et al. (2016).

The comparison of data acquired on soil samples using the needle probe and the surface probe reveals a good match (differences of less than 4%) only for samples 1 and 5. For the remaining samples the difference is greater (up to 22%). Depending on the samples' features, thermal conductivity measured by means of a surface probe can be higher or lower than the one obtained with the needle probe.

For the more homogeneous and compact samples (samples 2 and 3) mainly composed by fine particles (see Fig. 2), the thermal conductivity registered using the surface probe are higher than those obtained with the needle probe. A lower void index at the top surface of the sample and a higher proportion of consolidated fragments in contact with the probe are identified as the main causes of this discrepancy.

The opposite situation (i.e., lower thermal conductivity obtained with the surface probe) occurs in the more heterogeneous and less compact sample (sample 4), comprising mostly coarse particles (see Fig. 2) due to a higher void index and a poor contact between the probe and the sample.

The measurements conducted also suggest that the precision of the method is lower when using the surface probe. The reproducibility of the results obtained with the surface probe was a difficult task to accomplish. This means that this type of method is more sensitive to changes in sample properties, such as moisture content, void index and surface heterogeneities. Very consistent results were obtained in tests carried out with the needle probe on different days in samples 2, 3 and 4.

When comparing the thermal conductivity obtained using needle probes from different equipment (Tables 1 and 2), it verifies that the correlation is not so straightforward since the measurements were not conducted in the same hole and on the same day (1–2 days after). Nevertheless, significant differences in thermal conductivity were obtained in three samples (samples 1, 2 and 3) and are probably mainly due to water evaporation from the samples.

Table 1. Results obtained with ISOMET 2104 using a needle probe and a surface probe.

Type	Samples reference	Probe	Parameters		
			Thermal conductivity λ (W/m.K)	Volumetric heat capacity ρc (J/m^{3}K)	Thermal diffusivity a (m^2/s)
Soil samples	Sample 1	Needle	0.55	1.62×10^6	3.41×10^{-7}
		Surface	0.53	1.35×10^6	3.92×10^{-7}
	Sample 2	Needle	0.47	1.59×10^6	2.95×10^{-7}
			0.42	1.60×0^6	2.62×10^{-7}
		Surface	0.57	1.36×10^6	4.20×10^{-7}
			0.51	–	–
	Sample 3	Needle	0.68	1.73×10^6	3.93×10^{-7}
			0.69	1.73×10^6	3.98×10^{-7}
		Surface	0.80	1.46×10^6	5.52×10^{-7}
			0.76	1.41×10^6	5.37×10^{-7}
	Sample 4	Needle	0.88	1.82×10^6	4.85×10^{-7}
			0.87	1.83×10^6	4.75×10^{-7}
		Surface	0.72	1.41×10^6	5.13×10^{-7}
			0.68	1.37×10^6	4.97×10^{-7}
	Sample 5	Needle	1.02	1.98×10^6	5.17×10^{-7}
		Surface	0.99	1.42×10^6	6.94×10^{-7}
Rock samples	Sample 6	Surface	1.03	–	–
			0.99	–	–
	Sample 7	Surface	1.07	–	–

Table 2. Results obtained with Hukseflux-TPSY02 using a needle probe.

Type	Samples reference	Probe	Parameter
			Thermal conductivity λ (W/m.K)
Soil	Sample 1	Needle	0.61
	Sample 2	Needle	0.38
	Sample 3	Needle	0.61
	Sample 4	Needle	0.47

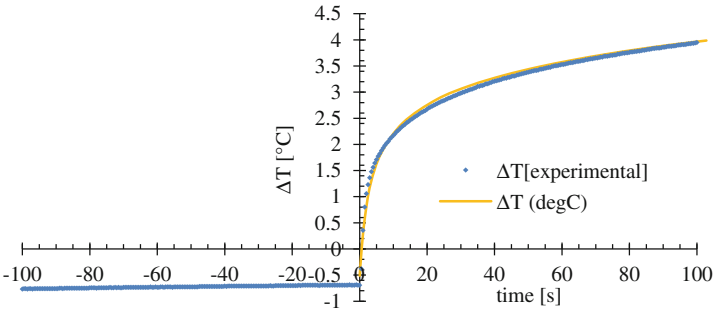

Fig. 4. Comparison between computational and experimental studies.

A comparison of the data obtained from Hukseflux-TPSY02 with the computational study, as explained in Sect. 3, is presented in Fig. 4, where the power is applied at time 0 s. The error is calculated to be 0.8% which is very acceptable.

5 Conclusions

The thermal properties of marly soils and marly limestone from the Cyprus Lefkara formation were characterized in transient conditions using a needle probe and a surface probe.

The experiments show that depending on soil physical properties (grain-size degree of compaction and moisture content), the results obtained with the surface probe can be considerably different from those acquired with the needle probe. In more homogenous fine-grained soils with very compact/consolidated zones at the top surface, higher thermal conductivity values were obtained using a surface probe. The opposite situation was observed for heterogeneous coarse-grained soils with a low compact top surface, suggesting that a good contact between the surface probe and the surface of the sample is crucial in order to obtain consistent results.

Regarding the precision of the methods, it was verified that the surface probe is more sensitive to changes in sample properties such as moisture content, void index and surface heterogeneities. Despite the measurements carried out using needle probes from different equipment were performed in different holes, satisfactory differences in thermal conductivity were obtained for some soil samples.

A computational study on COMSOL Multiphysics software gave comparable results with experimental data obtained by the Hukseflux-TPSY02 device.

It should be noted that for a full characterization of the ground formation a large number of samples need to be collected and analysed. More importantly, it can be easily concluded, through the discrepancies and the reasons behind them in results, for SGEs it is important to perform an in situ test using the TRT method.

Acknowledgments. The authors acknowledge Transport and Urban Development COST Action TU1405 – European Network for Shallow Geothermal Energy Applications in Buildings and Infrastructures (GABI; www.foundationgeotherm.org).

References

ASTM D5334: Standard test method for determination of thermal conductivity of soil and soft rock by thermal needle probe procedure (2014)

De Vries, D.A.: Thermal properties of soils. In: van Wijk, W.R. (ed.) Physics of Plant Environment, 2nd edn. North Holland Publishing Company, Amsterdam (1966)

Farouki, O.T.: Thermal properties of soils. Cold Regions Research and Engineering Lab Hanover NH, No. CRREL-MONO-81-1 (1981)

Rees, S., Adjali, M., Zhou, Z., Davies, M., Thomas, H.: Ground heat transfer effects on the thermal performance of earth-contact structures. Renew. Sustain. Energy Rev. **4**, 213–265 (2000)

Stylianou, I.I., Tassou, S., Christodoulides, P., Panayides, I., Florides, G.: Measurement and analysis of thermal properties of rocks for the compilation of geothermal maps of Cyprus. Renew. Energy **88**, 418–429 (2016)

Vieira, A., et al.: Characterisation of ground thermal and thermo-mechanical behaviour for shallow geothermal energy applications. Energies **10**(12), 2044 (2017)

Numerical Analysis of Geothermal System for Delhi Silt Soil in India

Debasree Roy(✉), Tanusree Chakraborty, and Bishwajit Bhattacharjee

Indian Institute of Technology Delhi, New Delhi 110 016, India
roydebasreel6@gmail.com

Abstract. The present study is focused on the numerical analysis of geothermal system to explore the feasibility of geothermal pile in Delhi silt soil under the summer dominant Indian climatic condition. The heat flow mechanism through geothermal system is simulated by developing finite difference models of a simple rod with the equivalent material property of heat carrying pipe and fluid, inserted in soil. The results of finite difference analyses show that the temperature of analysis domain is reached in a steady state within a reasonable time. Moreover, the feasibility of geothermal pile in Indian climatic condition for Delhi silt soil is established by showing that the heat exchange operation during the period of extreme summer or winter yields negligible change on surrounding soil temperature. The study also attempts to find the appropriate rod length condition (finite or infinite) in the analysis for the most realistic design solution.

1 Introduction

Geothermal pile is a sustainable option for using renewable energy. It acts as a heat exchanger apart from providing structural support. Ground soil at a certain depth surrounding the pile, where the temperature is constant throughout the year, acts as a heat sink in summer and heat source in winter. It is possible to utilize this ground energy through a system consists of the pile with an embedded pipe containing heat carrier fluid and surrounding soil. A heat flow mechanism between soil and pile is thus formed named as a shallow geothermal system. The surrounding atmosphere and solar heat help in recharging the system. This system is popular in different parts of the world especially in Western Europe, North America, Japan and Australia. However tropical countries like India face a unique challenge to use this technology as the cooling requirement is much higher in these places. Moreover, India has a variety of soil with different thermal properties. Thermal behavior of soil plays an important role in the heat flow mechanism. Therefore to explore the feasibility of geothermal system in India, a complete understanding of the response of energy system in each soil type is required.

A number of studies were conducted to understand the thermo-mechanical behavior of geothermal systems. Consequently, some empirical and experience-based design guidelines were provided in the literature (Brandl 2006; Amis et al. 2008; Laloui et al. 2006; Bouazza et al. 2011; Amatya et al. 2012; Bourne-Webb et al. 2009). However, those methods used a high value of factor of safety and caused an uneconomic design. Over the years a number of analytical solutions were proposed by several researchers

A. Ferrari and L. Laloui (Eds.): SEG 2018, SSGG, pp. 163–170, 2019.
https://doi.org/10.1007/978-3-319-99670-7_21

idealizing infinite or semi-infinite medium and infinite or finite line heat source which gives a knowledge of ground temperature response against heat conduction (Carslaw and Jaeger 1947; Lamarche and Beauchamp 2007; Lamarche 2013). Further several numerical studies of the geothermal system were recorded in the literature (Gao et al. 2008; Laloui et al. 2006; Ghasemi-Fare and Basu 2016). However literatures on the feasibility of a geothermal system in tropical country like India is limited.

The objectives of the present study are (a) exploring the feasibility of geothermal piles in Indian climatic condition (b) finding the appropriate rod length condition (finite or infinite) for analysis purpose to obtain the best design solution. Finite difference models are developed to simulate the behavior of heat exchange mechanism through a geothermal system. Analyses are performed considering two cases (a) a tropical summer condition where rod temperature is considered as ambient temperature (45 °C) whereas ground temperature is 25 °C (b) a winter condition where ambient temperature and consequently rod temperature is 4 °C whereas ground temperature is 22 °C. Based on the results of finite different analyses (FDAs), the feasibility of geothermal pile is explored. Moreover, a comparative study of FDA results is performed to obtain the best solution for an effective design of geothermal pile.

2 Problem Geometry, Initial & Boundary Conditions

The geometry of the problem (Fig. 1(*a*)) is considered as a rod, consist with an equivalent property of PVC pipe and heat carrying fluid. The rod is embedded in the ground soil for (a) a finite and (b) an infinite length. The surrounding soil is assumed as a cylindrical domain. Table 1 summarizes the value of parameters related to the overall geometry of the present models.

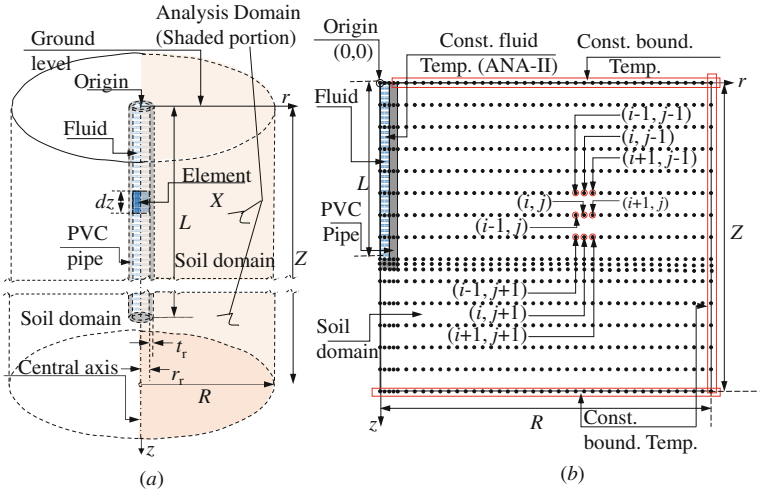

Fig. 1. (*a*) Proposed problem geometry, (*b*) finite difference grids and boundary conditions for finite length heat source/sink model (for infinite length heat source/sink model $Z = L$)

Table 1. Input parameters used for problem geometry

Trial	Geometry of embedded rod				Soil domain	
	Inner radius[a] (m)	Thickness[a] (m)	Length[a] (m)	Condition	Radius[a] (m)	Depth[a] (m)
1	0.04	0.006	15	Finite	12	50
2	0.04	0.006	30	Infinite	12	30

[a]Rod inner radius, r_r; rod thickness, t_r; rod length, L; soil domain radius, R; soil depth, Z.

To achieve the analogous situation for a geothermal pile, where the heat carrying fluid is being circulated through circulation tubes inside the pile, two types of analyses are performed. In the first type (ANA-I), the initial temperature of the entire heat-carrying fluid is constant. However, the temperature of the fluid is changed with time as heat exchange operation starts. The second type (ANA-II) is performed within a specific time range where the temperature of heat-carrying fluid throughout the entire time is constant. In both types, heat carrying fluid acts as a heat source in summer and heat sink in winter. Consequently, entire soil domain acts as a heat sink in summer and heat source in winter. From the result of ANA-I it can be showed that within a reasonable time, the entire domain can reach in steady state temperature. The thermal response and influence zone of soil domain within a specific time can be established from the result of ANA-II. Therefore combining both the results, the feasibility of geothermal pile for Delhi silt soil in Indian climatic condition is verified. Table 2 represents the initial temperature conditions for the entire analysis domain for both analyses. Further Table 3 gives a comprehensive view of boundary conditions for both analyses, which are used in the present study.

Table 2. Initial conditions for FDAs

Serial no.	Analysis domain	Cases	Initial temperature (°C)
1	Entire heat-carrying fluid and pipe inner wall i.e. $-r_r \leq r \leq r_r$ and $0 \leq z \leq L$	Summer[a]	45
		Winter[a]	4

[a]Ambient temperature 45 °C in summer and 4 °C in winter

To obtain the realistic situation of heat exchange mechanism a heat flux continuity at material boundaries is considered. Heat conduction through the analysis domain is assumed to be axisymmetric. Therefore one-half of the entire analysis domain (Fig. 1(*b*)) is modeled in the present study.

Table 3. Boundary conditions for FDA

Serial	Boundaries	Boundary conditions
1	Far end vertical boundary of cylindrical soil domain[a] (i.e. $r = \pm R$, $z \geq 0$ for both finite and infinite length condition)	Constant temperature (Summer 25 °C/winter 22 °C)
2	Bottom boundary of cylindrical soil domain ($-R \leq r \leq R$, $z = Z$, for finite length $-R \leq r \leq -r_r$, $z = Z$ & $r_r \leq r \leq R$, $z = Z$ for infinite length)[a]	Constant temperature (Summer 25 °C/winter 22 °C)
3	Top boundary of cylindrical soil domain ($-R \leq r \leq -r_r$, $z = 0$ & $r_r \leq r \leq R$, $z = 0$ for both finite and infinite length)[a]	Constant temperature (Summer 25 °C/winter 22 °C)
4	Entire heat-carrying fluid and pipe inner wall[b] ($-r_r \leq r \leq r_r$ & $0 \leq z \leq L$)	Constant temperature (Summer 45 °C/winter 4 °C)

[a]Applicable for both analyses (ANA-I & II)
[b]Applicable for second analysis only (ANA- II)

3 Finite Difference Analysis for Finite Length Rod

The time-dependent transient equation of heat conduction for an axisymmetric media is considered as the basic equation for heat flow through solid media. To incorporate the heat flow continuity from fluid to solid, heat balance equation at the boundary (fluid to pipe) is coupled with the transient heat conduction equation. The heat balance equation is developed for heat transfer between element X (Fig. 1(a)) and surrounding pipe. Solutions of aforesaid equations produce the time-dependent temperature profile within the analysis domain. In order to get the simultaneous solutions, present study adopts finite difference numerical techniques. Using explicit finite difference scheme, both equations (transient heat conduction and heat balance equation) are converted into the corresponding finite difference forms as expressed below. Here α = thermal diffusivity of solid media

$$\frac{T_{i,j}^{t+1} - T_{i,j}^{t}}{\alpha \Delta t} = \frac{T_{i-1,j}^{t} - 2T_{i,j}^{t} + T_{i+1,j}^{t}}{\Delta r_{i,j} \Delta r_{i+1,j}} + \frac{T_{i,j-1}^{t} - 2T_{i,j}^{t} + T_{i,j+1}^{t}}{\Delta z_{i,j} \Delta z_{i,j+1}} + \frac{T_{i+1,j}^{t} - T_{i,j}^{t}}{r_{i,j} \Delta r_{i+1,j}} \tag{1}$$

$$\frac{T_{i,j}^{t+1} - T_{i,j}^{t}}{\Delta t} = \frac{2k_r}{\rho_f C_{pf} r_r} \left(\frac{\partial T}{\partial r}\right)\Big|_{\text{fluid-pipe boundary}}, \frac{\partial T}{\partial r} = \frac{T_{i+1,j}^{t} - T_{i,j}^{t}}{\Delta r_{i+1}}. \tag{2}$$

Consequently solution of Eqs. (1) and (2) yield the temperature variation of the entire analysis domain in respect of time. However temperature variation of the pipe-soil boundary is obtained from additional equation as mentioned below.

$$\frac{T_{i,j}^{t+1}-T_{i,j}^{t}}{\Delta t}\left[\frac{\frac{k_r}{\alpha_r}\left(r_{i,j}^2-r_{i-1,j}^2\right)+\frac{k_s}{\alpha_s}\left(r_{i+1,j}^2-r_{i,j}^2\right)}{\left(r_{i+1,j}^2-r_{i-1,j}^2\right)}\right]=\frac{k_s r_{i+1,j}\left(\frac{T_{i+2,j}^{t}-T_{i+1,j}^{t}}{r_{i+2,j}-r_{i+1,j}}\right)}{\left(r_{i+1,j}-r_{i-1,j}\right)}$$
$$-\frac{k_r r_{i-1,j}\frac{T_{i,j}^{t}-T_{i-1,j}^{t}}{r_{i,j}-r_{i-1,j}}}{r_{i+1,j}-r_{i-1,j}}+\frac{k_r\left(r_{i,j}^2-r_{i-1,j}^2\right)+k_s\left(r_{i+1,j}^2-r_{i,j}^2\right)}{\left(r_{i+1,j}^2-r_{i-1,j}^2\right)}\frac{\left(T_{i,j-1}^{t}-2T_{i,j}^{t}+T_{i,j+1}^{t}\right)}{\Delta z_{i,j}\Delta z_{i+1,j}}. \quad (3)$$

4 Finite Difference Formulations for Infinite Length Rod

In case of infinite length rod, transient heat conduction happens along the radial direction. Due to the absence of temperature gradient in the vertical direction, no heat flow occurs along the depth (z). Therefore previous equations (Eqs. 1 and 3) are modified by neglecting the terms associated with z direction.

5 Analysis Result

In the present study heat transfer analyses are performed by developing MATLAB codes. Using the results of thermal response, the feasibility of the geothermal system for Delhi silt soil in India is evaluated. Further, a comparative study has been executed for finite and infinite length of the rod and accordingly best solution for appropriate rod condition is proposed. Table 4 represents the input properties of Delhi silt soil, heat carrier fluid, and PVC pipe.

Table 4. Input values for materials properties

Parameter	Notations	Values
Density of heat-carrying fluid (water)	ρ_f	1000 kg/m^3
Specific heat of heat-carrying fluid (water)	C_{pf}	4190 J/kg/K
Thermal conductivity of PVC rod[a]	k_r	0.41 W/m/K
Thermal conductivity of Delhi silt soil[b]	k_s	2.08 W/m/K
Thermal diffusivity of PVC rod[a]	α_r	0.284×10^{-6} m^2/s
Thermal diffusivity of Delhi silt soil[b]	α_s	1.04×10^{-6} m^2/s

[a]Values from Ghasemi-Fare and Basu (2016)
[b]Values from Paramanik and Aggarwal (2013)

Figure 2 shows the temperature variation of heat-carrying fluid, for summer and winter condition with time, which is obtained from ANA-I (finite length rod). The result indicates desire change of fluid temperature occurred within reasonable time.

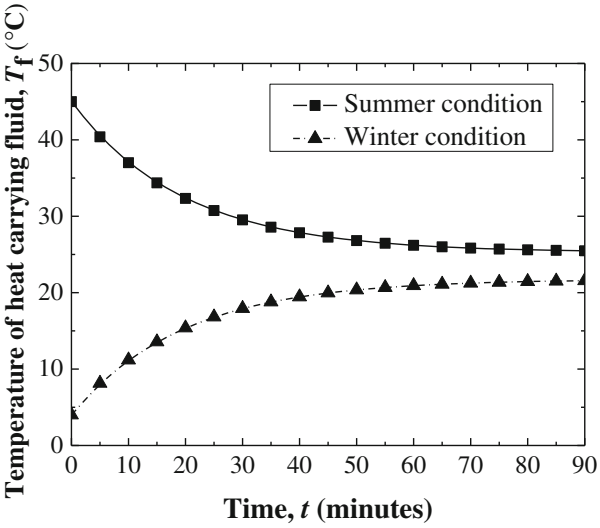

Fig. 2. Temperature variations of heat-carrying fluid (for finite length rod) with time

It establishes a positive confirmation for the workability of geothermal pile in Indian climatic. Figure 3 shows the temperature contour of analysis domain, after 7 days of heat flow, in winter (obtained from ANA-II for finite length rod). Results indicate, though the heat influence zone within the soil continuously grow with time but even after the 7 days of heat transfer, the growth is very small (<1.5 m radial distance). Further, temperature change of soil beyond thermal influence zone, is negligible.

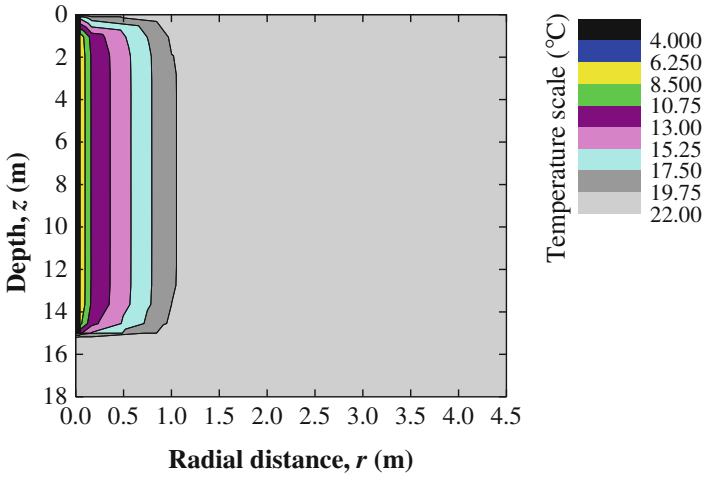

Fig. 3. Temperature contour of analysis domain after 7 days of heat flow during winter.

It is noted that the duration of extreme summer (maximum temperature 45 °C) or winter (minimum temperature 4 °C) in India is 45–60 days. To predict the thermal response of soil, during a long period, thermal influence zone variation with time is plotted (Fig. 4). The result shows that the increment rate of thermal influence zone is gradually decreased with time. Figure 5 shows a comparative study using data obtained from ANA-II for finite and infinite length rod (in summer condition).

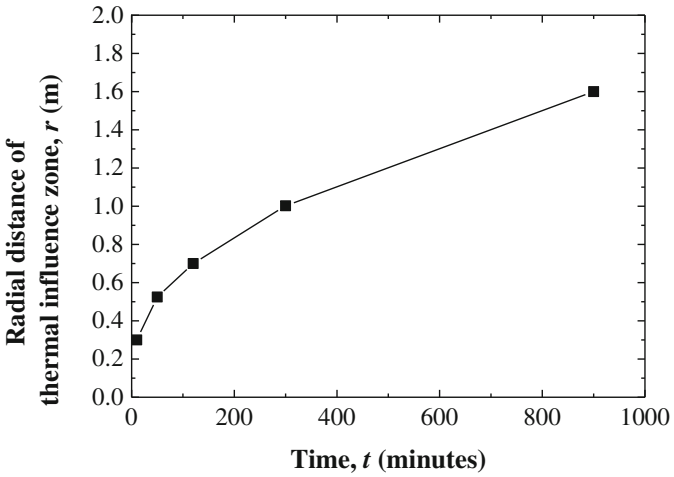

Fig. 4. Variation of thermal influence zone (considering finite-length rod) with time.

The result of the study reveals that radial extent of thermal influence zone for both the cases is more or less similar.

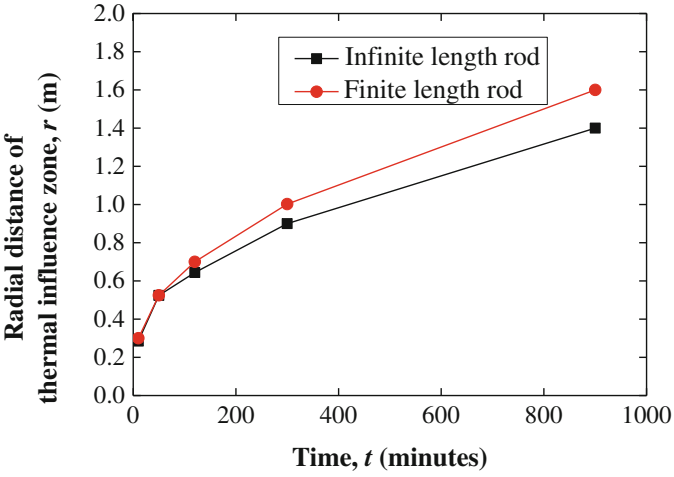

Fig. 5. Comparative study of thermal response using finite and infinite length rod.

6 Conclusions

Feasibility of the geothermal system for Delhi silt soil in Indian climatic condition is studied. The simple model of a rod comprises with the equivalent material property of PVC pipe and fluid, embedded in the soil, is proposed. FDA based MATLAB codes are developed to analyze the models in summer and winter condition. It can be concluded that (a) Even, after a long period of time (45–60 days) of the heat flow initiation, extent of the thermal influenced zone is within a reasonable limit. (b) The temperature change of soil beyond the thermal influence zone, during extreme summer or winter, is negligible. (c) A geothermal system is a feasible option for Delhi silt soil in India. (d) Appropriate design length of the geothermal system primarily depends on the temperature profile of the ground soil. Although both the finite and infinite length rod produce the similar thermal response, yet finite length model is preferable as it captures the heat transfer mechanism more realistically by allowing vertical heat flow.

References

Amis, T., Bourne-Webb, P.J., Davidson, C., Amatya, B., Soga, K.: The effects of heating and cooling energy piles under working load at Lambeth college. In: Proceedings of 33rd Annual and 11th International Conference of the Deep Foundations Institute, New York, UK (2008)

Amatya, B., Soga, K., Bourne-Webb, P.J., Amis, T., Laloui, L.: Thermo-mechanical behavior of energy piles. Géotechnique **62**(6), 503–519 (2012)

Bouazza, A., Singh, R.M., Wang, B., Barry-Macaulay, D.: Harnessing on site renewable energy through pile foundations. Aust. Geomech. **46**(4), 79–90 (2011)

Bourne-Webb, P.J., Amatya, B., Soga, K., Amis, T., Davidson, D., Payne, P.: Energy pile test at Lambeth College, London: geotechnical and thermodynamic aspects of pile response to heat cycles. Géotechnique **59**(3), 237–248 (2009)

Brandl, H.: Energy foundations and other thermo-active ground structures. Géotechnique **56**(2), 81–122 (2006)

Carslaw, H.S., Jaeger, J.C.: Heat Conduction in Solid. Claremore Press, Oxford (1947)

Gao, J., Zhang, X., Liu, J., Li, K., Yang, J.: Thermal performance and ground temperature of vertical pile-foundation heat exchangers: a case study. Appl. Therm. Eng. **28**, 2295–2304 (2008)

Ghasemi-Fare, O., Basu, P.: Predictive assessment of heat exchange performance of geothermal piles. Renew. Energy **86**, 1178–1196 (2016)

Laloui, L., Nuth, M., Vulliet, L.: Experimental and numerical investigations of the behavior of a heat exchanger pile. Int. J. Numer. Anal. Methods Geomech. **30**(8), 763–781 (2006)

Lamarche, L., Beauchamp, B.: A new contribution to the finite line-source model for geothermal boreholes. Energy Build. **39**(2), 188–198 (2007)

Lamarche, L.: Short-term behavior of classical analytic solutions for the design of ground-source heat pumps. Renew. Energy **57**, 171–180 (2013)

Paramanik, P., Aggarwal, P.: Comparison of thermal properties of three texturally different soils under two compaction levels. Afr. J. Agric. Res. **8**(28), 3679–3687 (2013)

Feasibility Study and Experimental Investigation of Heat and Mass Transfer in Dry and Moisturised Sand for Energy Savings

Andrea V. Galindo, Tariq S. Khan(✉), and Ebrahim Al Hajri

The Petroleum Institute, Khalifa University of Science and Technology, PO Box 2533, Abu Dhabi, UAE
tariq.saeedk@gmail.com

Abstract. Air-conditioning load and ventilation in buildings contribute more than 60% of the total energy consumption in United Arab Emirates (UAE), where the unavoidable extreme temperatures hit the region, especially during summer months. Literature survey indicates that at a depth of approximately 10 m, the soil reaches stability and it is no longer fluctuating drastically under the influence of external ambient temperatures. This relatively shallow location allows the use of soil's practical location as a possible source for sustainable energy recovery. The aim of this investigation is to explore the feasibility of using soil as a heat sink and experimentally analyse the soil heat transfer with variations in moisture saturations and heat flux rates in a testing rig. For this purpose, an axial to radial experimental analysis on Abu Dhabi soil is carried out on a lab scale test rig. This paper provides an insight into modular design of the experimental setup using spiral and U–shape heat exchangers. Experimental validation results are presented which deliver a heat profile in the sand, measured in time and depth for various heat flux rates. Moreover, thermal conductivity of the sand is estimated from experimentation and compared with literature. The results indicate presence of considerable potential for energy savings in the region.

1 Introduction

In the last 30 years, Abu Dhabi region has seen a drastic increase in its population, and the demand of energy is vital due to the harsh weather conditions. According to Middle East and North Africa (MENA) economic commentary, the MENA region has had recurring incidents involving power overload, particularly during summer air conditioning peak. As a result MENA power capacity has increased at rates of about 9% in recent years [1]. Abu Dhabi's air-conditioning load in buildings contributes more than 60% of the total energy consumption [2]. Thus, the study of effective and environmental conscious energy systems has become a target point for the region.

Current designs of air conditioning systems utilize the ambient temperature through the air intake. These structures are usually set-up on the roof-top of buildings, with a design that pushes AC systems to step down an enormous temperature difference, from inlet to outlet temperatures. An alternative to the current design is to utilize underground spaces/soil as a source of cooling load. According to Carmody and Sterling [3],

A. Ferrari and L. Laloui (Eds.): SEG 2018, SSGG, pp. 171–178, 2019.
https://doi.org/10.1007/978-3-319-99670-7_22

energy benefits can be obtained when considering the slow response of soil thermal mass. In regions of high temperature and humidity, the slow response of soil in underground spaces allows for an increase on the earth cooling contact, reducing the heating peak and cooling loads.

The soil temperature fluctuates according to the seasons' cycle and solar radiation. However, at depths of approximately 10 m the soil reaches temperature stability with small variations [4].

In a study on the prediction of subsurface temperature profile, Al-Temeemi et al. [5] predicted a subsurface temperature profile for Kuwait. When ambient air temperature was 41 °C the subsurface average temperature at a depth of 10 m was 27 °C.

Feasibility of utilizing underground cooling towards cooling buildings is presented in this study using Abu Dhabi sand. The particular interest in this study was to experimentally analyse the 3-D subsurface heat transfer for different moisture saturation levels and heat flux rates in the soil medium and to validate use of soil as a heat sink or cooling source.

2 Experimental Investigation

Experiments were carried out in a lab scale experimental setup. The setup included a heated fluid unit, a pipeline system, a robust stainless steel tank, a copper U-tube heat exchanger and sand as the heat transfer medium. A schematic of the experimental setup is presented in Fig. 1.

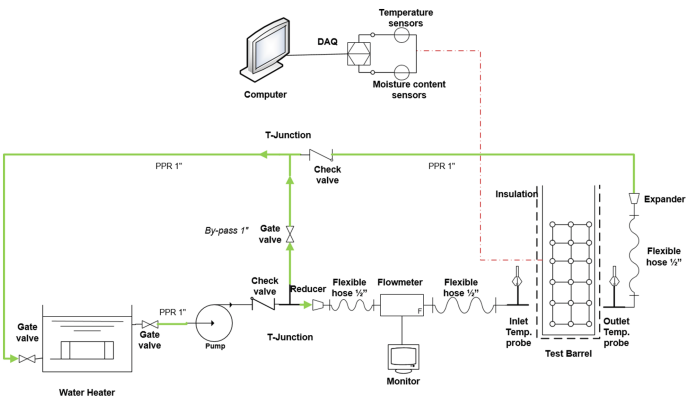

Fig. 1. Experiment process flow diagram

Copper tubing was the material of choice for heat exchangers due to its effectiveness as a thermal conductive medium. Experiments were conducted in a vertical sand filled test barrel while U shape and spiral tube heat exchangers were used for heat input. There were three different thermocouple meshes each containing 13 thermocouples that are placed every 0.2 m apart from each other and four Volumetric Water Content (VWC) sensors are placed 0.1 m above the thermocouple mesh as shown in

Figs. 2 and 3. A layer of 4 thermocouples at a height of 0.8 m from the bottom was also installed. The thermocouples placed at the centre of the test barrel at levels I and III are located 3.5 cm away from the copper tube. All the sensors are monitored using a DAQ system for real time data measurement.

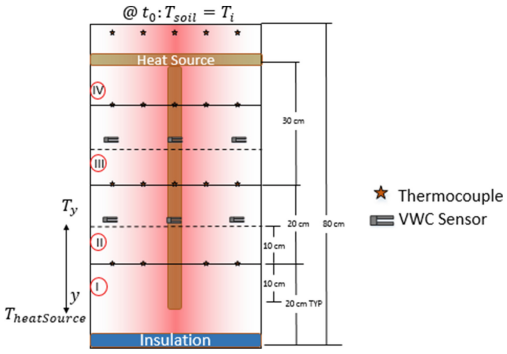

Fig. 2. U Tube Experimental diagram of test barrel and sensor location

Change in thermal energy characteristics for the porous media, mass migration from water saturation content and the change in temperature profile of the sand with respect to the heating source were evaluated using calibrated digital the instrumentation.

2.1 Experiment Implementation

In order to understand the heat transfer in soil-coupling techniques, it is necessary to have knowledge of the temperature profile of such soil. In a previous study, Jacovides et al. [6] utilized Fourier techniques to predict the surface and ground temperature of different depths assuming that the soil is homogeneous with constant physical properties. Their procedure was followed in current study as well. A logarithmic best-fit curve was applied for estimation of volumetric water content, θ, in order to reduce design stage uncertainties and measurement margins of error in this study.

$$\theta = 0.0019 * \text{mV} - 0.401. \tag{1}$$

The average time for each experiment was 60 h and the test barrel was tightly insulated around. The experiments were conducted for the parametric ranges listed in Table 1 for Abu Dhabi sands to investigate the effect of sand as a heat sink.

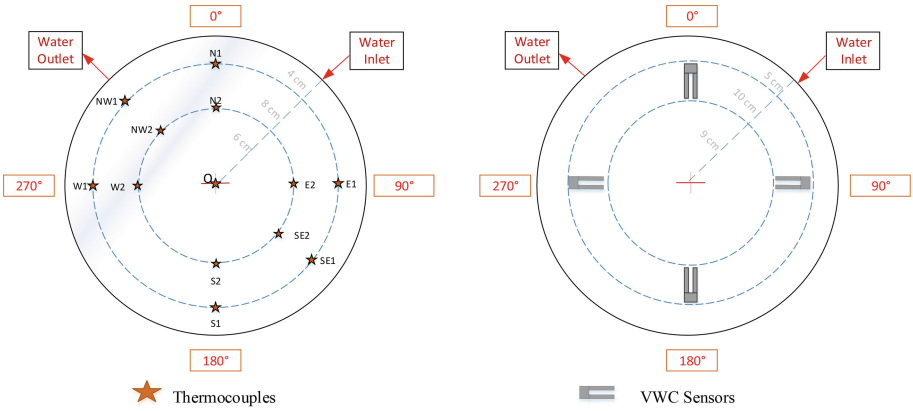

Fig. 3. Sensor distribution and naming

Table 1. List of mode performed.

Mode	Heat source temp. (°C)	Volume of water % (added to sand) (m^3/m^3)	Initial soil temp. (°C)	Flowrate (LPM)	Description
U tube heat exchanger					
I	50	0, dry	21	0.5	Radial temp. profile
J	70	0, dry	21	0.5	
Spiral coil heat exchanger					
D	50	0, dry	22	0.5	Axial temp. profile
F	50	39, saturated	27	0.5	

3 Results and Discussion

3.1 Radial Distribution of Heat Using a U-Tube Heat Exchanger (UTHE)

The transient heat and moisture dissipation in the radial direction on the sand was studied using the UTHE. The parametric study for the U-tube setup was done for heat source temperatures of 50 °C and 70 °C on dry sand.

Figure 4 shows the temperature distribution at three locations; centre of the test barrel, at a radius of 60 and 140 mm from the centre. The curves indicate that, even though the centre (r = 0 mm) sensors are located in close proximity to the copper tubes, the maximum temperature the sand reaches is 44 °C (which occurs at level C), when it reaches steady state after 40 h. This being approximately 10% less than the UTHE set temperature.

The temperature curve in level C is higher than level B, because of the influence of the maximum inlet working fluid temperature, which is located perpendicularly and 0.1 m away from the measured plane, see Fig. 5.

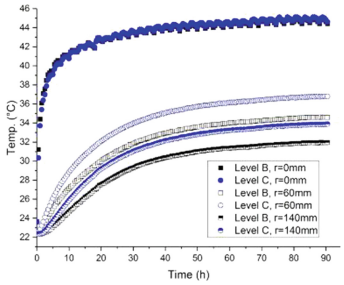

Fig. 4. UTHE temperature profile at levels II and III

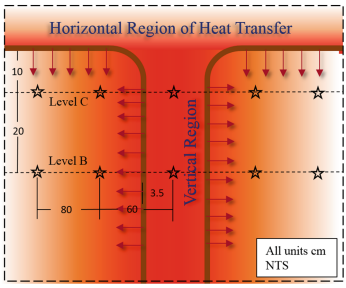

Fig. 5. Influence of horizontal and vertical regions of the UTHE

At the moment when the local temperature of the sand surrounding the UTHE approaches the tube temperature, the heat travels radially. This theory is exhibited in Fig. 6, where the temperature profile in the sand is shown over a span of 50 h for a UTHE buried at a depth of 0.6 m and an average heat source inlet temperature of 50 °C. The 3-D representation shows consistency with the sand temperature trend around the UTHE, saying that, the closer to the copper tube, the more evident the changes in temperature are on the sand as shown in the schematic for the horizontal and vertical heat transfer regions for the UTHE in Fig. 5. It is obvious in Fig. 6 that there is a higher temperature difference close to the tube compared to the area closest to the barrel walls. This is good news, as long as there exists a temperature difference in the soil there subsists heat transfer potential.

3.2 Radial Effect of VWC Using a U-Tube Heat Exchanger (UTHE)

Figure 7 shows that for a UTHE with dry sand, there is a VWC peak rise of 0.01 m^3/m^3 after 20 h at all locations. The results indicate an agreement with Chen et al. [7] which can be assumed as a representation of one of the layers (levels A, B or C) but in a smaller scale of the UTHE. The figure on the left indicates that peak VWC occurs at the position near the heat source and moves towards the cold end. The figure on the right indicates that the VWC sensor error is within the measurement ranges.

3.3 Axial Effect of Heat Flux and Volumetric Water Content (VWC) in Sand

A spiral tube heat exchanger was used in this case where the heat exchanger was placed at the bottom of test barrel while temperature and moisture measurements were taken in an arrangement shown in Fig. 3. Two cases are studied: the first case considered the sand with no water added, where the second case considered a fully saturated soil.

The temperature change in the saturated sand was found to occur much faster compared to dry sand and the temperature distribution for the saturated case showed an even distribution through the cross sectional area. Where saturated sand permitted a 17% greater heat transfer than dry sand. Overall, the heat transfer results in current

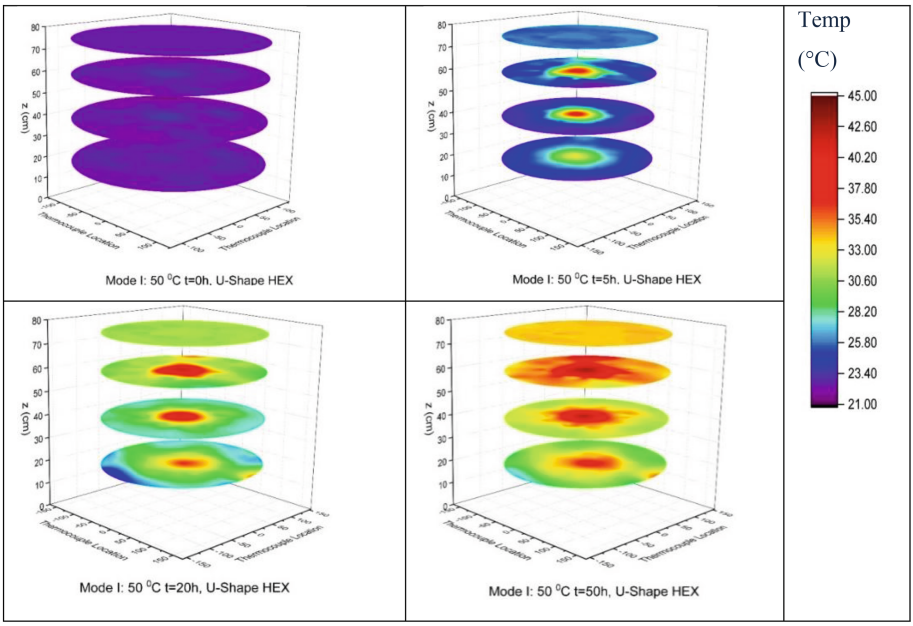

Fig. 6. Radial heat transfer in the sand for a UTHE set 50 °C

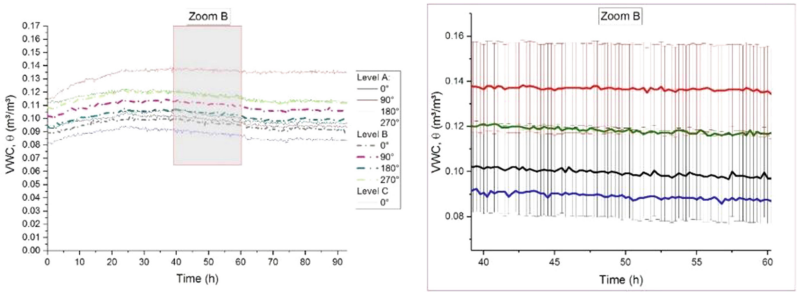

Fig. 7. VWC distribution for dry sand in UTHE

study show good potential of using underground soil as heat sink in the Middle East region where outdoor temperature and humidity severe in summer.

3.4 Thermal Conductivity of Sand

Several conduction heat transfer shape factors are provided by Rohsenow [8] and Hahne and Grigull [9]. Thermal conductivity of the sand was estimated by using shape factor of the nearest geometry stated by:

$$Q_{total} = kS\Delta T_{overall} \tag{2}$$

And the shape factor was estimated by:

$$S = \frac{4\pi r}{\left(\frac{\pi}{2}\right) - \tan^{-1}\frac{r}{2D}} \tag{3}$$

Table 2 below shows a sample calculated shape factor and soil thermal conductivity for one case. These values fall within known k values of sand from literature.

Table 2. Sand thermal conductivity

Length	Shape factor	Thermal conductivity sand
D (m)	S (m)	*k* (W/m °C)
0.1	4.656	3.251
0.3	2.671	3.272

4 Conclusion

This paper explores the feasibility of using sand as a heat sink and experimentally analyse the sand heat transfer with variations in moisture saturations and heat flux rates using lab scale testing rig. The range of experimental mode temperatures was selected based on literature review to simulate extreme real life conditions that could be encountered in roof-top equipment on a summer day. The experiments were conducted for the parametric ranges listed for dry and saturated moisture using a U- tube and spiral coil heat exchanger as a heat source. Data analysis delivered an axial to radial graphical description of the behaviour of heat and mass transfer in a 3-D sand test rig. The temperatures were found to be more uniformly distributed for the fully saturated soil conditions. Larger temperature difference across radial direction was observed for the U tube heat exchanger case that indicates good potential of using underground soil as heat sink. The experimental results are sensitive to the axial distance from the heat source, where level I achieved approximately 80% of the heat source temperature during transient thermal process and reduced to less than 30% from the slow transient conditions in the vertical direction, as it moves farther away from the spiral coil heat source. Higher heat transfer rate was achieved for fully saturated sand compared to the dry sand. The temperature gradient in the sand has a direct influence on the transfer of moisture. The estimated sand thermal conductivity falls closer to the known thermal conductivity of sand from literature. The experimental results indicate presence of considerable potential for energy savings in the Abu Dhabi region by using the soil as a heat sink.

References

1. Aissaui, A.: MENA power investment: set to keep fast growth despite a lull in other energy sectors. In: Economic Commentary, vol. 10. A. Research Ed. (2015)
2. Abu Dhabi Economic Vision 2030. Government of Abu Dhabi
3. Carmody, J., Sterling, R.L., Sterling, R.: Underground Space Design: Part 1: Overview of Subsurface Space Utilization Part 2: Design for People in Underground Facilities. University of Texas Press, Austin (1993)
4. Golany, G.: Ethics and Urban Design: Culture, Form, and Environment. Wiley, New York (1995)
5. Al-Temeemi, A.A., Harris, D.J.: The generation of subsurface temperature profiles for Kuwait. Energy Build. **33**, 837–841 (2001)
6. Jacovides, C., Mihalakakou, G., Santamouris, M., Lewis, J.: On the ground temperature profile for passive cooling applications in buildings. Sol. Energy **57**, 167–175 (1996)
7. Chen, H., Ding, H., Liu, S., Chen, X., Wu, W., Wang, Q.: Experimental study on heat and moisture transfer in soil during soil heat charging for solar-soil source heat pump compound system. Appl. Therm. Eng. **70**, 1018–1024 (2014)
8. Rohsenow, W., Harnett, J., Cho, Y.: Handbook of Heat Transfer, 3rd edn. McGraw-Hill, New York (1998)
9. Hahne, E., Grigull, U.: Heat Transfer in Boiling. United States (1977)

Geomechanical Analysis of Salt Caverns Used for Underground Storage of Hydrogen Utilised in Meeting Peak Energy Demands

Evan Passaris(✉) and Georgios Yfantis

Atkins Limited, Edinburgh HE3 8EG, UK
evan.passaris@atkinsglobal.com

Abstract. The geomechanical design of a H_2 storage salt cavern subjected to diurnal and seasonal storage operating cycles has been investigated. The investigations provided a better understanding of the geomechanical response of H_2 storage caverns by employing coupled thermo-mechanical numerical analyses. A salt cavern, located at a depth of 1.8 km, has been investigated by employing non-linear elasto-visco-plastic thermo-mechanical analyses by considering: the characteristics of the geological formations around the cavern, the changes in temperature and stress concentrations related to the H_2 storage operations and the *in situ* geostatic stresses that characterise the cavern's location. This work has proven the importance of using a coupled thermo-mechanical analysis to assess the geomechanical integrity of H_2 storage caverns.

1 Introduction

Underground H_2 storage in salt caverns is a promising way to deal with the issue of the intermittent nature of renewable energy sources. The production of low-cost bulk H_2, stored in salt caverns, may be used for power generation or directly as an energy source.

The UK possesses important bedded salt deposits which are currently used for the development of storage caverns (Evans and Holloway 2012). From the three salt bearing locations in the UK that have shown good potential for developing caverns for H_2 storage (Foster Wheeler Energy Ltd. 2013b), the East Riding of Yorkshire was selected for the investigations presented in this paper.

The source of the H_2 is taken to be a 89 mol% H_2 fuel gas stream, produced by gasification of biomass or coal H_2 plant capable of providing a continuous supply of H_2 (Foster Wheeler Energy Ltd. 2013a).

The investigations were carried out by modelling scenarios comprising daily storage cycles superimposed on seasonal storage cycles, to identify how a salt cavern behaves when subjected to challenging loading conditions. These demand data were employed in setting up the input data used in the thermodynamic software package that was utilised to calculate the cavern temperature and pressure when subjected to H_2 storage operations.

A. Ferrari and L. Laloui (Eds.): SEG 2018, SSGG, pp. 179–184, 2019.
https://doi.org/10.1007/978-3-319-99670-7_23

2 Thermodynamic Analysis

A thermodynamic analysis of an existing gas storage salt cavern, developed at a depth of approximately 1,800 m in the main salt formation of the Fordon Evaporites in East Riding of Yorkshire, was carried out by employing a software that simulating the thermodynamics and heat transfer processes related to storage operations in underground salt caverns.

The thermodynamic simulation was preceded by the modelling of the solution mining and the de-brining of the cavern, while the prescribed history of the H_2 flow rates (over a period of approximately six years) was used as part of the required input data. The thermal convection in the stored H_2 was assumed to be infinite, implying that the temperature in the cavern was homogeneous.

The results of the thermodynamic analysis are presented in Fig. 1 as the cavern pressure history and the respective cavern temperature history.

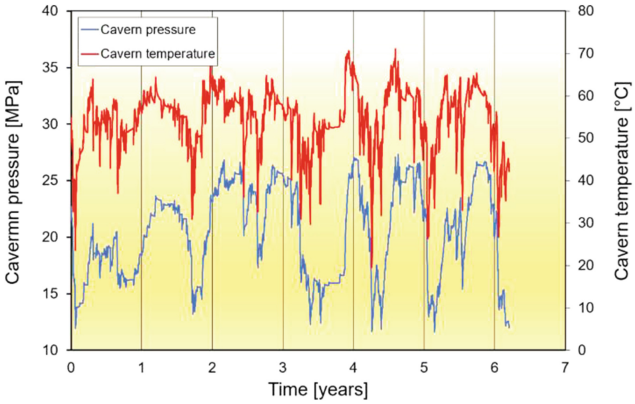

Fig. 1. Histories of cavern pressure and cavern temperature

Examination of Fig. 1 indicates that during injection operations, the H_2 in the cavern is compressed and the cavern pressure increases, leading to a rise in the cavern temperature because of the Joule-Thomson effect. When the H_2 in the cavern is withdrawn and the pressure in the cavern decreases, the resulting adiabatic expansion leads to a cavern temperature reduction. The salt that surrounds the cavern acts as a constant temperature heat source or heat sink, depending on whether the stored H_2 temperature is higher or lower than the geothermal temperature. The cavern pressure varies seasonally between 11.5 MPa and 27 MPa, resulting in a cavern temperature that varies between 20 °C and 71 °C. However, individual weekly cycles correspond to differential pressures of approximately 1 MPa occasionally causing differential temperatures of nearly 5 °C.

3 Coupled Thermo-Geomechanical Analysis

The thermo-mechanical coupled calculations were implemented by modelling the cavern using a three-dimensional axisymmetric configuration, employing the finite difference method which is well suited for modelling large distortions, typically encountered in underground openings that are developed in salt formations.

Taking into consideration the depth of the cavern and the creep characteristics of the salt that surrounds it, the ratio of the horizontal to the vertical geostatic stress will be close to unity; whereby the *in situ* stress state of the salt is assumed to be isotropic. The vertical geostatic stress was estimated using the densities of the superincumbent strata. During the thermo-mechanical analysis, the modelled ground was pre-stressed in accordance with the estimated *in situ* geostatic stress field.

The salt formation was modelled as a WIPP-creep visco-plastic material (Herrmann et al. 1980) whose plastic constitutive response conforms to the Drucker–Prager elasto-plastic model.

The upper boundary of the finite difference model was placed at the top of a marl layer at a depth of 1,540 m. The sequence of layers above the marl was not explicitly modelled; instead the overburden loading that corresponds to the gravitational loading of these beds was applied to the top end of the model as a uniform vertical pressure equal to 34 MPa.

The bottom boundary of the finite difference model was characterised by a vertical fixity that was placed approximately 180 m below the bottom of the cavern sump. In addition, no horizontal displacement along the vertical sides of the model were specified while the upper horizontal surface of the model was free to move both in the horizontal and vertical directions.

The stress concentrations at the walls and the roof of the cavern were analysed to determine whether the investigated temperature and pressure histories could initiate rock failure in the geological formations that surround the cavern. The primary goal of the thermo-mechanical analysis was to investigate, *inter alia*, the potential of tensile failure and/or shear failure that may be introduced at the roof and walls of the cavern. The geomechanical stability of the modelled cavern was assessed by generating contour diagrams for the ground temperature, the minimum σ_3 and maximum σ_1 principal stresses; and the von Mises stress component σ_{vm}. The von Mises or Equivalent stress component is defined by the following expression:

$$\sigma_{vm} = \sqrt{3J_2}$$

where J_2 is the second invariant of the deviatoric stress tensor.

The distribution of the temperature around cavern at the end of six years of modelling cyclic H_2 storage operations is shown in Fig. 2.

The temperature in the salt mass is modified from the original geothermal distribution, but this temperature change penetration which corresponds to a reduction of the order of 10 °C is significant over only 13 m from cavern wall, as shown in Fig. 2. To investigate the variation of the temperature profile, as we progress outwards from the

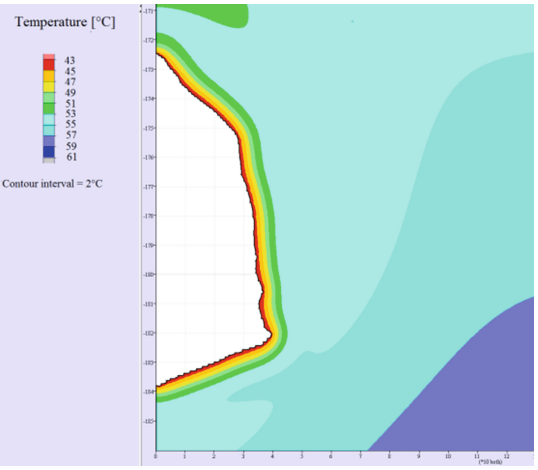

Fig. 2. Distribution of temperature around the investigated cavern at the end of six years of cyclic H_2 storage operations

cavern's surface, a set of graphs showing the temperature history at different depths (measured from the cavern's surface) has been produced in Fig. 3.

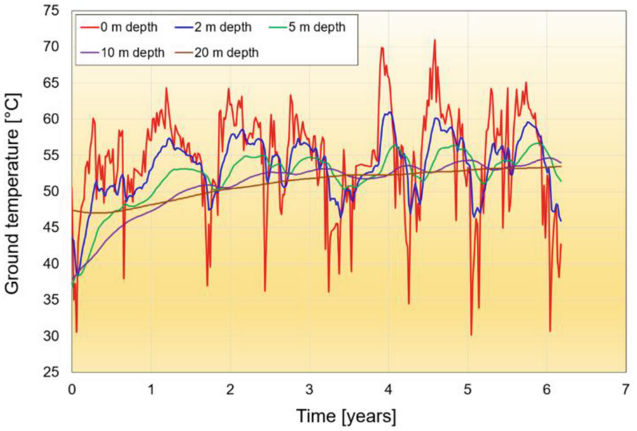

Fig. 3. History of temperature penetration at the walls of the investigated cavern

As shown in Fig. 3, in progressing outwards, from the surface of the cavern, the cyclic nature of the temperature history is preserved although the amplitude of the temperature cycles is reduced inversely proportionally to the distance from the cavern's wall, indicating a temperature dampening process.

The σ_3 contours, at the end of 6 years of modelling of cyclic H_2 storage operations, as shown in Fig. 4a, indicate that the walls of the cavern remain everywhere in

compression. The corresponding contour diagram for σ_{vm}, shown in Fig. 4b, indicates that most of the salt mass that forms the immediate surrounding of the cavern is subjected to moderate shear stresses, i.e. less than 20 MPa. Nevertheless, there are two locations (at the centre of the cavern's roof and at the side wall, where the sump begins) where σ_{vm} assumes values close to 26 MPa.

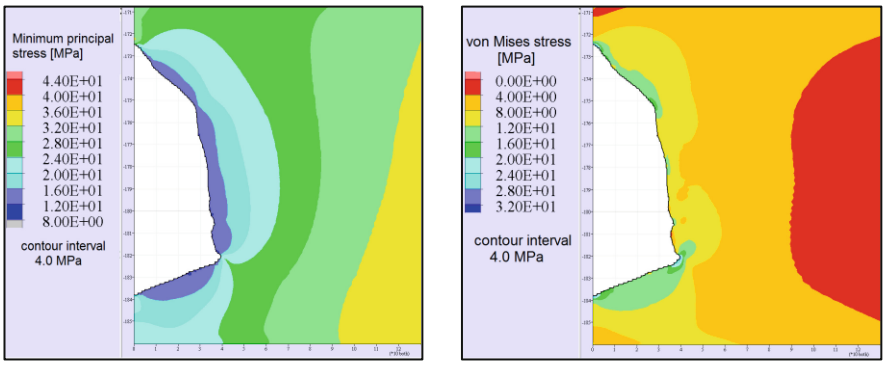

(a)Minimum principal stress **(b)von Mises stress**

Fig. 4. Stress distribution around the cavern at the end of 6 years of H_2 storage operations

Fortunately, these relatively high stress concentrations do not develop deeper than approximately 0.6 m inside the salt mass. Moreover, the stress concentrations in the sump area of the cavern have no particular significance on the structural stability of the cavern.

4 Conclusions

During injection operations, the H_2 in the cavern is compressed and the cavern pressure increases, leading to a rise in the cavern temperature. When the H_2 in the cavern is withdrawn and the pressure in the cavern decreases, the resulting adiabatic expansion leads to a reduction in the cavern temperature. The salt mass that surrounds the cavern acts as a constant temperature heat source or heat sink, depending on whether the cavern temperature is higher or lower than the geothermal temperature.

In progressing outwards from the surface of the cavern, although the cyclic nature of the temperature history is preserved, the amplitude of the temperature cycles is reduced inversely proportionally to the distance from the cavern's wall, indicating a temperature dampening process.

Assessment of the minimum principal stress distribution at the end of 6 years of modelling of cyclic storage operations, provides evidence that the walls of the investigated cavern remain everywhere in compression. The distribution of the von Mises stress around the cavern indicates that the majority of the salt mass that forms the immediate surrounding of the cavern is subjected to moderate shear stresses. Evidently,

the global geomechanical stability of the cavern is not affected by the investigated thermal effects, since they remain limited to only a few meters from cavern wall.

The results of the investigated H_2 storage operations, have shown that the long-term geomechanical stability of the salt caverns is not compromised. Consequently, the use of salt caverns for the underground storage of hydrogen, required to meet peak energy demands, satisfy the operator's requirements with respect to the flexibility of storage operations.

References

Evans, D.J., Holloway, S.: A review of onshore UK salt deposits and their potential for underground gas storage. In: Evans, D.J., Chadwick, R.A. (eds.) Underground Gas Storage: Worldwide Experiences and Future Development in the UK and Europe, Special Publications, vol. 313, pp. 39–80. The Geological Society, London (2012)

Foster Wheeler Energy Ltd: Hydrogen storage and flexible turbine systems. In: WP1 Report—Hydrogen Power Production, A Report Submitted to Energy Technologies Institute, 12 July 2013. http://www.eti.co.uk/ (2013a)

Foster Wheeler Energy Ltd: Hydrogen storage and flexible turbine systems. In: WP2 Report—Hydrogen Storage, A Report Submitted to Energy Technologies Institute, 29 July 2013. http://www.eti.co.uk/ (2013b)

Herrmann, W., Wawersik, W.R., Lauson, H.S.: Analysis of Steady State Creep of Southeastern New Mexico Bedded Salt. Sandia National Laboratories, report no. SAND80-0558 (1980)

Full-Scale Instrumented Residential Ground Source Heat Pump Systems in Melbourne, Australia

G. R. Aditya, G. A. Narsilio(✉), I. W. Johnston, and M. M. Disfani

The University of Melbourne, Parkville, VIC 3010, Australia
narsilio@unimelb.edu.au

Abstract. Ground-source heat pump (GSHP) systems typically show higher efficiencies than conventional systems for space heating and cooling of buildings. However, the availability of GSHP systems performance data is still limited, especially in Australia due to the small number of GSHP systems installed and monitored. This paper provides some initial results from a GSHP systems monitoring project conducted on ten residential properties in the greater Melbourne region of Australia. The data measured reveals an estimated Coefficient of Performance between 2 and 4.9. The reasons for these variations in measured system efficiency with respect to design expectations are discussed.

1 Introduction

Ground source heat pump (GSHP) or shallow geothermal systems can efficiently heat and cool buildings using sustainable geothermal energy accessed via ground heat exchangers (GHEs). In closed-loop systems, GHEs comprise pipes embedded in specifically drilled boreholes or trenches or even built into foundations. In Australia, most of the electricity is generated from fossil fuels. Given that GSHP systems generally operate at a coefficient of performance (CoP) of between 3 and 5, the substitution of commonly used electrical heating and cooling systems with GSHP systems could potentially significantly reduce energy consumption and greenhouse gas emissions.

Even though there have been experimental studies of GSHP systems published worldwide, the availability of high-quality datasets on performance and usage patterns are still rare, especially under real life thermal loads.

In Australia, the availability of these datasets are further limited due to the small number of GSHP systems installed, and fewer still that have their performance monitored in detail. To date, the only available performance data in Australia corresponds to a few commercial buildings, a school, a house and an aquatic centre (Geoscience Australia 2007; Huang 2015; Kivi 2014; Mikhaylova et al. 2015; Payne et al. 2015). To redress this, The University of Melbourne has been undertaking a full-scale pilot direct geothermal energy demonstration project, whereby the performance data from a number of properties in greater Melbourne have been collected for several years. This paper provides some initial experimental results from ten residential properties.

A. Ferrari and L. Laloui (Eds.): SEG 2018, SSGG, pp. 185–191, 2019.
https://doi.org/10.1007/978-3-319-99670-7_24

2 Full-Scale Experimental Studies

Melbourne has a temperate climate, and based on the typical meteorological year (TMY) gathered from Meteonorm (2017), typical design outside air temperatures vary between 1 and 37 °C. A residential GSHP system is typically designed for continuous operation based on the bin method (IGSHPA 2009), where no heating or cooling is needed when the outside air temperature is between 15.5 and 19.4 °C (60 and 67 °F). Outside this range, and accounting for 82% of the year, heating or cooling would be needed for Melbourne (see Fig. 1).

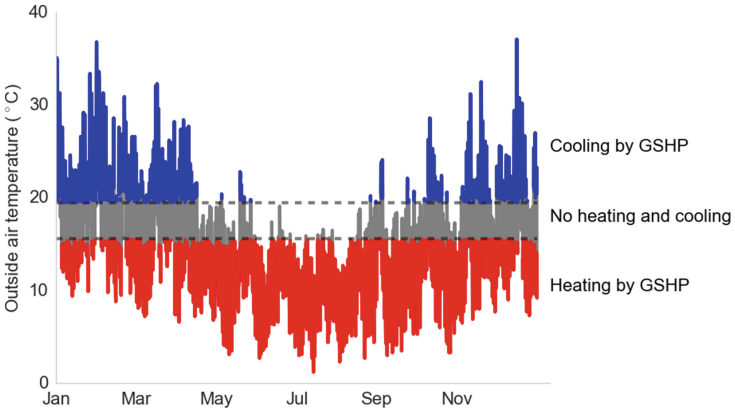

Fig. 1. Typical Melbourne design temperatures for GSHP systems

The locations of the residential properties monitored are shown in Fig. 2. This range of properties was expected to be able to give an indication of typical variations in performance of such properties for a range of house sizes, patterns of use, local weather conditions and variations in geology commonly encountered in Melbourne. The conditioned floor area, along with whether the building is retrofitted or newly built, the geology, the number, orientation and total length of GHEs, the capacity of the GSHPs and details of the distribution systems installed in these properties, are summarized in Table 1.

To measure GSHP system performance, sensors were installed in each of the systems installed at the properties. Figure 3 presents a typical instrumentation schematic for a property with vertical GHEs installed. The instrumentation consists of thermistors to measure the ground temperature along the ground loop, thermistors and flow meters to measure the temperatures and flow rate of the water flowing in and out of the GSHP on the ground side (and the building side when applicable in water to water systems), and a power meter to measure the electrical power consumption of the GSHPs, circulation pumps and fans required to run the system. All the monitoring data at each property is collected through a data logger, which can be accessed remotely for data transmission through the internet. Most of data collection in this project started in 2015.

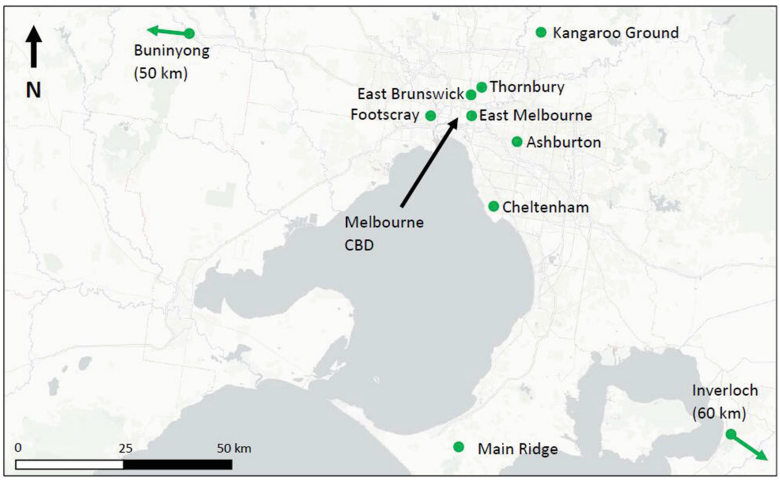

Fig. 2. Location of the ten monitored properties

3 Results and Discussion

A summary of the performance data for all monitored properties is shown in Table 2. It can be observed that all properties were heating dominant. This is confirmed by Fig. 4 which shows a typical energy demand pattern for a period of more than two years for one of the properties (Cheltenham).

Further, most of the properties have run fractions of only about 10–20%. This is in contrast to the expected usage of around 82% based on the bin method applied continuously. The temperate climate in Melbourne is mild enough to result in minimal heating and cooling demand throughout the year. In particular, during the shoulder periods around April and October, very little heating or cooling is required. This is in contrast to many other parts of the world where either heating or cooling is typically needed throughout the whole year.

It must be noted that, the bin method estimates a building's thermal demand based on the ambient air temperature and it does not account for user behavior which may be possible in a temperate climate. These conditions usually allow systems to be turned off during the day if occupants are out at work. In such a climate, it may also be possible to turn the systems off during the night. It follows that for such a climate, the actual usage observed can be significantly lower than the expected designed usage using the bin method.

The GSHP systems monitored have seasonal performance factors (SPF) between 1.6 and 4.5. These SPFs reflect the efficiency of the systems as a whole because they include the power consumption of the GSHPs, circulation pumps and fans to run the systems, as measured in this project. The CoPs of the GSHPs were estimated on the basis of the rated power consumption of the other mechanical equipment and are also presented in Table 2. These CoPs are between 2 and 4.9.

Table 1. Summary of site conditions and GSHP installations at the monitored properties

Property location (refer to Fig. 2)	Conditioned floor area (m^2)	Retrofitted (R) or newly built (NB)	Geology[a]	Number, orientation[b] and total GHE length (m)	GSHP[c,d,e] heating/cooling capacity (kW)	Distribution systems
Ashburton	300	NB	Siltstone & minor sandstone	4, V, 360	32/28[c]	Floor hydronic heating, FCU[f] for cooling, water & pool heating
Buninyong	150	R	Deep marine deposits & sandstone	4, H, 160	8/8[c,e]	FCU for heating and cooling
Cheltenham	100	R	Sands with minor clay	2, V, 110	6/9[d]	Ducted heating and cooling
East Brunswick	50	R	Basalt	2, V, 130	8/8[c,e]	FCU for heating and cooling
East Melbourne	60	NB	Basalt	2, V, 120	11/9[c]	Ducted heating and cooling, water & spa heating
Footscray	100	R	Basalt	2, V, 110	8/10[d]	Ducted heating and cooling
Inverloch	200	NB	Siltstone & sandstone	6, V, 300	18/17[c]	Floor hydronic heating and cooling & hot water
Kangaroo Ground	400	NB	Siltstone	9, S, 320	16/15[c]	Floor hydronic heating and FCU for cooling
Main Ridge	280	NB	Basalt	8, S, 320	22/17[c]	Floor hydronic heating and hot water
Thornbury	50	R	Siltstone & minor sandstone	2, V, 100	6/6[c,e]	FCU for heating and cooling

[a]Based on the Geological Map of Melbourne from Energy and Earth Resources (1959)
[b]V = vertical GHEs, H = horizontal GHEs (straight pipe), S = horizontal GHEs (slinky)
[c]Water to water GSHP
[d]Water to air GSHP
[e]Experimental GSHP manufactured locally
[f]Fan coil unit

The systems at East Brunswick and Thornbury have low CoPs because they were retrofitted with a locally manufactured experimental GSHP which turned out to perform less efficiently than expected. The system at Buninyong was driven by an updated but still experimental local GSHP which still produced a relative low CoP. Although not known at the design stage, the system at Footscray was significantly under designed and hence, returned a relatively low CoP.

If the results from these four locations were discounted, the CoPs recorded for the remaining six properties were between 3.3 and 4.9. This range seems to be similar to the range of CoPs for various GSHP systems reported in the literature including 3.4 in France (Trillat-Berdal et al. 2006), 3.3 at the ASHRAE headquarters in USA (Liu and Spitler 2014), 3.9 in Southern Germany (Luo et al. 2015), and 4.4–5.2 in Northern Greece (Michopoulos et al. 2007)

It may be worth noting that a close inspection of the monitored data showed that the GSHPs switched on and off more than would have been expected. This may have occurred because most of the GSHPs installed were single speed GSHPs without buffer

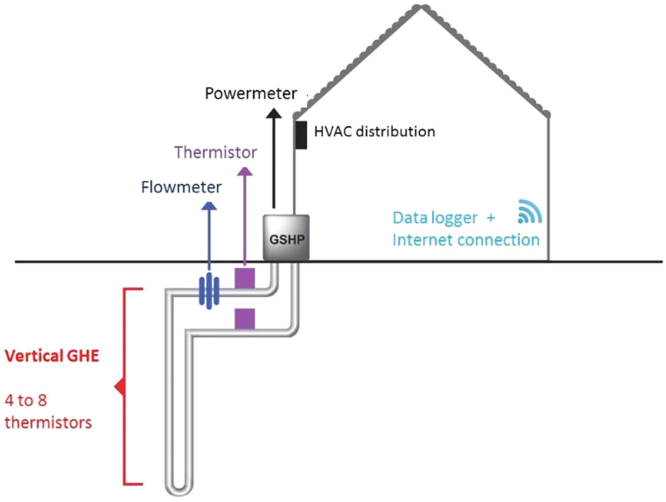

Fig. 3. Typical instrumentation for a property with a vertical GHE installed

Table 2. Summary of GSHP system performance at the monitored properties

Properties location (refer to Fig. 2)	Monitored period	Total usage (h)		Run time fraction (%)[h]	Total energy provided to the building (kWh)		Total electrical energy used (kWh)	SPF[i]	CoP[j]
		Heating	Cooling		Heating	Cooling			
Ashburton	Jun '15 – Jan '18[b]	4568	2967	36	80,508	16,495	26,339	3.7	4.6
Buninyong[a]	Nov '16 – Jan '18	757	288	10	4900	1495	2330	2.7	2.9
Cheltenham	Aug '15 – Jan '18	1186	145	6	6208	928	1978	3.6	4.1
East Brunswick[a]	Aug '15 – Jan '18[c]	177	–	–	538	–	294	1.8	2.3
East Melbourne	Jun '15 – Jan '18[d]	2232	1512	17	12,414	4593	6216	2.7	3.3
Footscray	Jun '15 – Jan '18[e]	2147	407	12	12,022	1861	5687	2.4	2.7
Inverloch	Jan '16 – Jan '18	2548	594	17	27,038	6328	9763	3.4	3.8
Kangaroo Ground	Sep'16 – Nov '17	720	302	10	5590	3033	1905	4.5	4.9
Main Ridge	Sep '15 – Jan '18[f]	1013	–	5	16,747	–	4736	3.5	4.0
Thornbury[a]	May '15 – Jan '18[g]	1245	858	9	2925	960	2412	1.6	2.0

[a]Properties with an experimental GSHP manufactured locally. GSHPs at East Brunswick and Thornbury were the first iteration, which may explain lower SPF than at Buninyong

[b]Excluding February 2017–July 2017 when the data logger malfunctioned

[c]GSHP often malfunctions, thus indicating minimal usage hours. For this reason, run time fraction was not calculated as it is not representative

[d]Excluding December 2017 when data logger was off

[e]Excluding January 2017–February 2017 when flow meter malfunctioned

[f]Excluding July 2017–September 2017 when data was not collected. This house is a holiday house and not the main place of residence, hence the low usage hours of the system. GSHP system was also designed for heating mode only

[g]Excluding June 2015 to August 2015 when data logger was off

[h]Run time fractions are adjusted to exclude periods when analysis could not be performed due to data collection problems (actual usage may be more than the stated run time fraction)

[i]Seasonal performance factor (SPF) = total energy provided to the building/total electrical energy used. The power consumption including GSHP, circulation pumps and fans

[j]Estimated CoP of the GSHP (without the circulation pumps and fans power consumption).

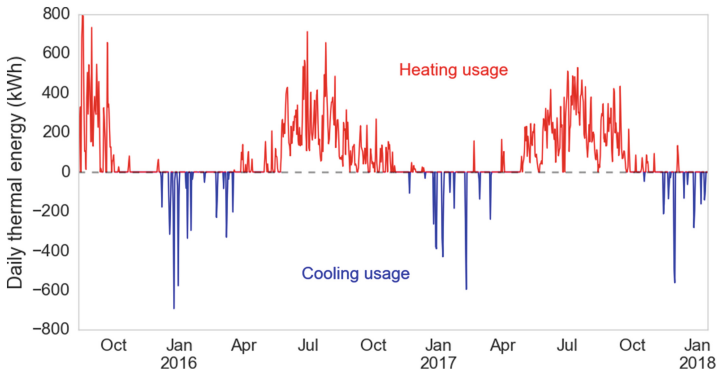

Fig. 4. Daily thermal energy demand for the Cheltenham property

tanks operating in relatively low demand systems. These conditions are likely to have had a negative impact on the observed CoPs, outweighing the potential ground thermal performance improvement resulting from a low run fraction.

The above discussion suggests that the bin method may not be the best design approach for residential GSHP systems in a temperate climate and another or modified design method may be required. Alternatively, hybrid GSHP systems may be a better option. This would require GSHP systems providing the base load thermal demand with conventional systems servicing the hotter and colder periods of the year.

4 Conclusions

This paper presents the preliminary results of the performance of GSHP systems installed in ten residential properties around Melbourne, Australia. The preliminary results indicate that these systems have CoPs that are comparable to other GSHP systems around the world.

However, what is clear is that the recorded run time fraction for all the properties was significantly lower than would have been expected through the use of the bin method. This is probably as a result of Melbourne having a temperate climate which allows heating and cooling systems to be turned off for significant parts of the day and the year. This suggests that a different design method may be more appropriate for GSHP systems in such a temperate climate so that smaller geothermal systems can be used to give lower capital costs. Alternatively, this pattern of usage may be better served through the use of hybrid GSHP systems.

Acknowledgements. The authors acknowledge the financial support for this project by the Victorian Government's Department of Environment, Land, Water and Planning. They are also grateful to all the property owners/tenants who allowed monitoring of their systems along with associated installers.

References

Energy and Earth Resources: Geological Maps of Melbourne. http://earthresources.efirst.com.au/categories.asp?cID=58 (1959). Accessed Sept 2017

Geoscience Australia: Geoscience Australia Building, Canberra, Geothermal Air Conditioning: 10 Year Review (2007)

Huang, S.: Energy Performance Evaluation and Optimisation of Ground Source Heat Pump Systems. University of Wollongong, Wollongong (2015)

IGSHPA: Ground Source Heat Pump Residential and Light Commercial Design and Installation Guide. Oklahoma State University, Stillwater (2009)

Kivi, A.V.: Development of design tools for direct geothermal systems. Ph.D. thesis, The University of Melbourne, Parkville (2014)

Liu, X., Spitler, J.: Performance of HVAC systems at ASHRAE HQ. ASHRAE J. **56**(12), 12 (2014)

Luo, J., Rohn, J., Bayer, M., Priess, A., Wilkmann, L., Xiang, W.: Heating and cooling performance analysis of a GSHP system in Southern Germany. Geothermics **53**, 57–66 (2015)

Meteonorm: Typical Meteorological Year. See http://www.meteonorm.com/ (2017). Accessed June 2017

Michopoulos, A., Bozis, D., Kikidis, P., Papakostas, K., Kyriakis, N.: Three-years operation experience of a ground source heat pump system in Northern Greece. Energy Build. **39**(3), 328–334 (2007)

Mikhaylova, O., Johnston, I.W., Narsilio, G.A., Kivi, A.V., Aditya, R., Noonan, G.: Performance of borehole ground heat exchangers under thermal loads from a school building: full-scale experiment in Melbourne, Australia. In: Proceedings World Geothermal Congress, pp. 19–25 (2015)

Payne, D., Lohrenz, E., Benvenuti, G., Kivi, A.V., Chisholm, T.: Aquatic centre retrofit of hybrid vertical and horizontal ground heat exchanger. In: World Geothermal Congress (2015)

Trillat-Berdal, V., Souyri, B., Fraisse, G.: Experimental study of a ground-coupled heat pump combined with thermal solar collectors. Energy Build. **38**(12), 1477–1484 (2006)

Base Displacement Response of Group of Geothermal Energy Piles

Rajni Saggu(✉)

Department of Civil Engineering,
Galgotias College of Engineering and Technology, Greater Noida, India
rajnirupal@gmail.com

Abstract. The behavior of geothermal energy piles in a group involves complex relation between change in temperature and deformations, strains and stresses in the pile and soil. The behavior of piles when acting as a group is further complex due to group interaction among the piles. Hence, it becomes important to quantify the displacements and stresses to understand the load transfer mechanism of these piles under thermal and mechanical loads. In the present study, rigorous numerical analyses are performed to investigate the thermo-mechanical behavior of the piles in sand using three dimensional non-linear finite element analysis procedure in Abaqus software. The stress-strain behavior of piles is considered as linear-elastic. The stress-strain response of sand is reproduced using constitutive model CASM. The raft on the piles is modeled to behave in a linear elastic manner. The state parameter based constitutive model CASM is implemented in finite element based software Abaqus through two user defined material subroutines, UMAT and UMATHT. The energy piles in a group are analyzed by considering different combinations of thermal and mechanical piles in a single layer of Ottawa sand. The results of numerical analyses have been presented for the pile base displacement. Parametric sensitivity analyses are carried out to investigate the influence of pile spacing and soil relative density on the base displacement of the piles. The results conclude that the thermal piles experience higher displacement as compared to the mechanical piles and soil relative density plays a key role in governing the pile response to thermal cycle. Differential settlement is noted for the pile groups containing the thermal and mechanical piles altogether.

1 Introduction

The use of geothermal energy is an emerging technology for sustainable design of buildings (Laloui et al. 2006; Bourne-Webb et al. 2009). In order to satisfy the space heating and cooling needs of a building, all the piles or selected piles in a group can be installed as geothermal energy piles (Brandl 2006; Salciarini et al. 2013). In current literature, most of the researchers have presented on the thermo-mechanical interaction between a single geothermal energy pile and the supporting soil (Laloui et al. 2006; Wang et al. 2011; GSHP 2012; Saggu and Chakraborty 2015a, 2015b, 2017). Laloui et al. (2006) have reported the temperature-induced axial stress in the pile through experimental investigation of a full scale energy pile. Wang et al. (2011) have presented the effect of coupled thermo-mechanical loading on the load carrying capacity of

A. Ferrari and L. Laloui (Eds.): SEG 2018, SSGG, pp. 192–202, 2019.
https://doi.org/10.1007/978-3-319-99670-7_25

a model geothermal energy pile and stated that temperature is an important parameter which influences the load carrying capacity of these piles. The design charts presented by GSHP (2012) for anticipating the generation of displacement and axial stress in the energy piles show that the increased pile temperature results in increased displacement and axial stress in the pile. Contrary to heating, the decrease in pile temperature causes decrease in pile axial stress. Saggu and Chakraborty (2015a) emphasized on the strong influence of pile end restraints and soil conditions on pile response. In another study, Saggu and Chakraborty (2015b) reported the cyclic thermomechanical pile-soil interaction in case of geothermal pile and noted an increase in thermally induced base displacement after each consecutive thermal cycle. Saggu and Chakraborty (2017) have reported that shaft capacity does not change significantly due temperature change in the pile. They have also reported increased magnitude of axial stress along the pile depth and pile base displacement due to increased thermal load on the pile. The geothermal energy piles possess group interaction and this group effect needs to be assessed prior to the design of a pile group. However, the research studies on group behavior of geothermal piles are rather limited. Dupray et al. (2014) carried two dimensional numerical analyses of thermo-hydro-mechanical interactions of piles in a group and observed that thermal cycle has a positive effect on the structural capacity of closely spaced piles in a group. Jeong et al. (2014) have reported a change in mobilized pile capacity due to thermal effects through numerical analysis of a group of geothermal piles. Saggu and Chakraborty (2016) have reported increased magnitude of axial stress for the thermal piles and decreased magnitude of axial stress for the non-thermal piles as a result of non-uniform distribution of load on the pile head through the raft during the heating induced expansion of the piles. Loria and Laloui (2017) have investigated the group effect for closely spaced energy piles and have emphasized on the thermally induced group effect on the geotechnical behavior of these piles. The specific objective of the present numerical work is to quantify the base displacement of individual piles placed as a group in sand considering different combinations of thermal and mechanical piles in the same group. To investigate the effect of soil state, parametric study is performed for different soil relative density, D_R = 40% and D_R = 50%. The response of corner and middle piles is presented in terms of pile base displacement. Analyses are performed for different center to center spacing between the piles. The base displacement of thermal piles and mechanical piles placed altogether in a single group are compared. The above stated objective have been accomplished with the highlight of nonlinear three dimensional (3D) finite element (FE) analyses of pile groups of six piles using the finite element based software Abaqus. The piles have been simulated to behave as linear elastic. To simulate the thermomechanical soil response, a constitutive model CASM (Yu 1998, 2006) which is based on the critical state concepts in soil mechanics and defines the current state of soil is incorporated in software Abaqus standard manual version 6.11 (2011). To define the CASM model in Abaqus, user-defined material subroutines; UMAT and UMATHT are used to state the stress-strain behavior of surrounding soil and to state the thermal characteristics of soil, respectively. A temperature change applied on pile is assumed to be uniform throughout the pile length (Laloui et al. 2006; Bourne-Webb et al. 2009).

2 Finite Element Model and Material Properties

For the 3D finite element analyses presented herein, separate parts are created for the pile, soil and raft geometries using Abaqus software. The concrete piles and the raft are assumed to be possessing ultimate compressive strength as 45 MPa with Young's modulus (E) as 33.7 GPa and Poisson's ratio (ν) as 0.2. The material properties of concrete are shown in Table 1. A tie constraint is defined between the raft and the pile head for the piles to tie all the degrees of freedom in horizontal as well as vertical directions. A single layered Ottawa sand is assumed as surrounding soil and stress-strain properties of soil are defined using the constitutive model CASM. The CASM formulation used in this study consists of seven parameters. The determination of CASM parameters can be achieved through triaxial testing of the soil. For the study conducted herein, a FORTRAN code is formulated for simulating triaxial compression test for the drained and undrained soil conditions to determine the required parameters of CASM model. The CASM model parameters are determined for Ottawa sand having minimum and maximum void ratio of 0.48 and 0.78, respectively (Murthy et al. 2006). The CASM code simulation results are compared with the experimental data for triaxial compression test under drained and undrained soil conditions for both loose and dense sand obtained from Sasitharan et al. (1994) and Carraro (2006). The values of the CASM parameters for Ottawa sand are presented in Table 1. A finite element mesh for the pile-raft-soil system is shown in Fig. 1. All piles are of same dimensions with 20 m length and 1 m diameter. The length and width of the raft are 15.5 m and 12.9 m, respectively. The thickness of raft is 1.2 m. The vertical boundaries in far-field soil are considered at 6.5 m from the raft edge along the smaller dimension of raft and 7.5 m along the larger dimension as presented in Fig. 1. The bottom soil boundary is placed at a distance equal to pile length from the pile base. The vertical displacement at far field soil boundaries is allowed by applying a roller support and at the bottom soil boundary, the displacements are restrained in all degrees of freedom. Thermal boundary conditions are applied for heat to flow through the side boundaries and the bottom of the soil. The initial ambient temperature of soil is applied as 15 °C (Laloui et al. 2006). The model domain is meshed using eight node thermally coupled brick, trilinear displacement and temperature (C3D8T) elements.

Near the pile-soil interface, the minimum mesh size is taken as 0.5 mm and the in the far-field soil regions, the maximum element size is considered as 1.5 mm. At the interface of pile and soil, a coefficient of friction μ ($=tan\delta$) as 0.55 is defined in the tangential direction to simulate a frictional contact between concrete and soil. A hard contact is considered in the direction normal to the pile and soil interface. Heat conduction is defined between pile and soil at the interface by assigning a thermal conductance value same as the soil thermal conductivity value.

Thermal displacement analysis in Abaqus involves the consideration of thermal properties of the materials which are thermal conductivity for concrete (k) and soil (k_s), specific heat for concrete (C) and soil (C_s) and the coefficient of thermal expansion of concrete (α) and soil (α_s). For the present analyses, constant values of thermal parameters k_s, C_s and α_s are considered for sand. The thermal model parameters of Ottawa sand are obtained from Tarnawski et al. (2009). A user-defined material

Table 1. Sand and pile material properties

Mechanical parameters	Value	References
CASM model and thermal parameters for Ottawa sand		
Slope of critical state line in e-ln(p') space, λ	0.02	Sasitharan et al. (1994), Carraro (2006), Loukidis (2006)
Slope of unloading-reloading line in e-ln(p') space, κ	0.005	Yu (2006)
Critical state line intercept at 1 kPa pressure, Γ	0.8	Model simulation
Reference state parameter, ξ_R	0.075	Yu (2006)
Model parameter, n	4.5	Model simulation
Slope of critical state line in q-p' space, M_{cc}	1.2	Yu (2006) and Loukidis (2006)
Poisson's ratio, υ_s	0.3	Yu (2006)
Shear modulus, G	32.6 MPa	Laloui et al. (2006)
Bulk modulus, K	15 MPa	
Thermal conductivity, k_s	0.274 W/m°C	Tarnawski et al. (2009)
Specific heat, C_s	722 J/°C	
Coefficient of thermal expansion, α_s	10^{-4}/°C	
Mechanical and thermal parameters for pile and raft		
Modulus of elasticity, E	33 GPa	Pile and raft material parameters assumed to be same as concrete
Poisson's ratio, υ	0.2	
Thermal conductivity, k	2.1 W/m°C	
Specific heat, C	800 J/°C	
Coefficient of thermal expansion, α	10^{-5}/°C	

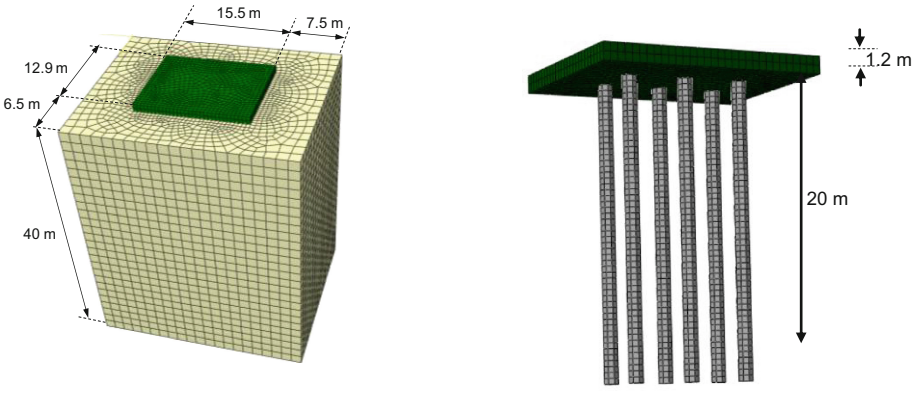

Fig. 1. Finite element mesh for geothermal pile-raft-soil system

subroutine UMATHT is used to implement the thermal constitutive model in Abaqus software. The thermal response of pile-raft-soil system is assumed to follow the energy balance equation (Green and Naghdi 1992) as given below

$$\int_V \rho \dot{U} dV = \int_V r dV + \int_S q_H dS \tag{1}$$

where V represents the volume of material, S is surface area, ρ defines the density of the material, $\dot{U}$ defines the time rate of the internal energy for the material, q_H represents the heat flux per unit area, and r defines the externally applied heat per unit volume of the body. The thermal constitutive relationship is presented in terms of thermal conductivity and specific heat as given below in Eqs. (2) and (3)

$$\frac{dU}{dT} = C_s \tag{2}$$

and

$$\frac{dq_H}{\partial T / \partial x} = -k_s \tag{3}$$

In Eq. (3), x defines the position coordinate of a point.

3 Validation Analysis of Finite Element Model of Geothermal Pile

The validity of thermo-mechanical FE simulation of geothermal energy piles using CASM constitutive model for sand is affirmed by comparing the current simulation results with the field load test and numerical analysis results presented by Laloui et al. (2006). For the purpose of validity of present analyses, the field test investigation of Laloui et al. (2006) has been modeled through coupled temperature-displacement analysis procedure in Abaqus using the material model CASM for soil layers. Figure 2(a) and (b) show the comparison of the vertical displacement of the pile head due to thermal loading and axial stress along the pile depth due to thermo-mechanical loading of the pile under an axial mechanical load of 1300 kN and thermal load ΔT of 21 °C.

The head displacement and axial stress along the pile depth are following the similar trend as presented by Laloui et al. (2006) and the magnitudes are comparable with reasonable accuracy for head displacement and axial stress along the pile.

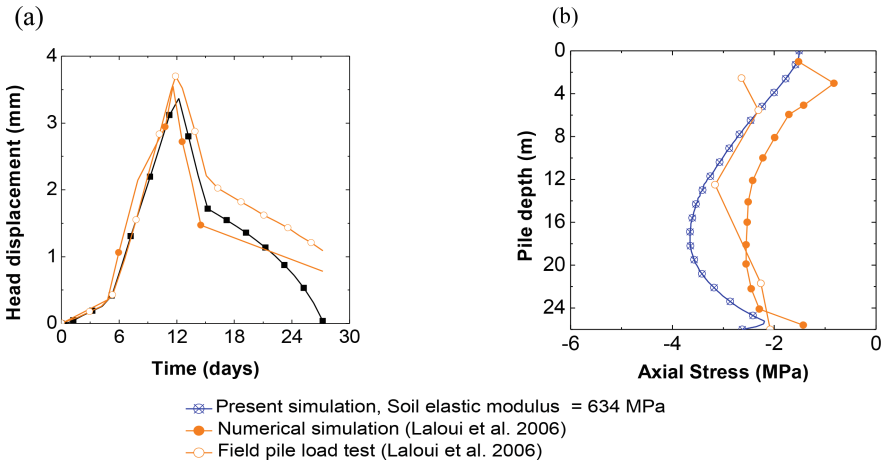

Fig. 2. Comparison of present simulation results for (a) head displacement under thermal cycle and (b) axial stress along pile depth at the end of heating of pile with results of Laloui et al. (2006)

4 Finite Element Simulation of Pile Group

A pile group consisting of six piles is analyzed numerically through three dimensional nonlinear finite element analysis procedure using Abaqus software for thermo-mechanical loading condition of the piles. The pile group is considered to be installed in Ottawa sand. The analyses are carried out for a geostatic step to establish the equilibrium with the geostatic stresses applied as initial conditions in the predefined fields and a coupled temperature-displacement step for applying the thermal as well as mechanical loads. Three sets of analyses are performed for different types of pile arrangements; (i) all six piles as geothermal piles (Type I), (ii) the corner piles as geothermal piles (Type II), and (iii) all piles as mechanical piles (Type III). The influence of center to center pile spacing on the mechanical response of the piles is investigated by varying the center to center pile spacing e.g. 4 m and 2.5 m. The analyses are performed for different soil relative density e.g. D_R = 40% and D_R = 50%. The thermal load of ΔT = 21 °C with thermal cycle consisting of heating period of 12 days and cooling period of 16 days is applied uniformly along the depth of the pile similarly as applied by Laloui et al. (2006). The ambient soil temperature is assumed to be 15 °C. The Ottawa sand is simulated using CASM model; a soil critical state constitutive model. The coefficient of lateral earth pressure at rest (K_0) is taken as 1 for the numerical analyses performed herein. An axial mechanical load of 6000 kN is applied over the raft surface in the form of pressure. For the pile group analyses, thermally induced expansive strain in the pile, tensile stress and strain induced in the pile, and upward shaft resistance are assumed as positive. Depth from the soil top surface and pile displacement in the upward direction are considered positive.

5 Results and Discussion

5.1 Load vs Displacement at Pile Base

Figures 3(a) and (b) show the load vs displacement plots at pile base. The results are compared for a corner pile and a center pile for the analyses; Type I (all piles as thermal) and Type II (corner piles as thermal piles). The analysis results are compared for piles at 4 m center to center spacing and for different soil relative density; D_R = 40% and D_R = 50%. It is clear from the figures that an increase in base displacement occurs under axial mechanical load for the thermal as well as mechanical piles. Upon heating, the expansion of the thermal piles in downward direction results in an increase in base displacement. The thermal piles experience excess load due to heating of these piles. On the contrary, the unloading of the mechanical piles occurs when the thermal piles are under heating load and pile base displacement of these piles decreases. The expansion of thermal piles in upward direction is also noted, thus, the piles tend to push the raft in the upward direction. Therefore, uneven distribution of axial load on the piles happens due to thermal cycle. The load on mechanical piles decreases whereas the load on thermal piles increases. It is noted that the pile base displacement is about 35–40% higher for the thermal piles in loose soil with D_R = 40% when compared with piles in soil with D_R = 50%. However, the cooling of piles results in higher decrease in base displacement of these piles. Table 2 summarizes the base displacement of thermal and mechanical piles at the end of heating of thermal piles for all analysis cases. The base displacement for all the piles in a group is compared for pile spacing; 4 m and 2.5 m and soil relative density; D_R = 40% and D_R = 50%. The thermal piles while under thermal loading experience higher magnitude of base displacement as compared to the

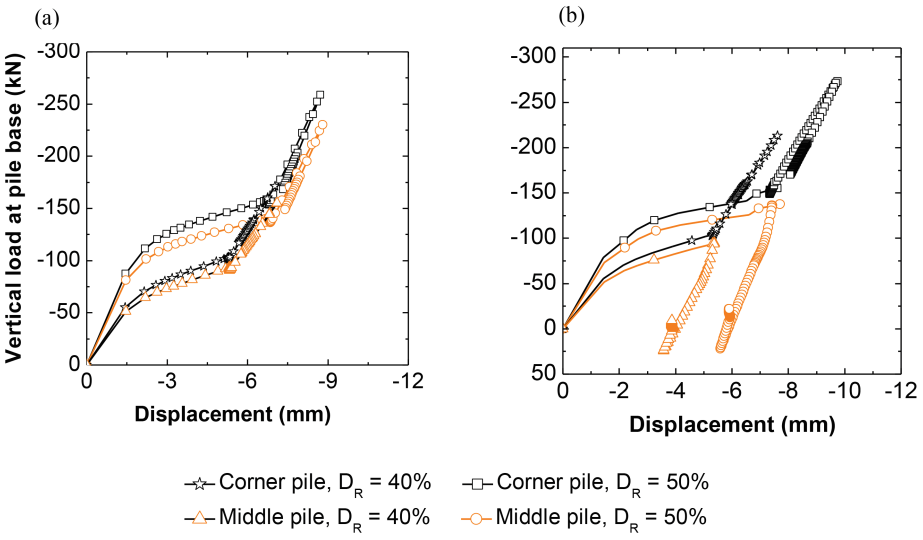

Fig. 3. Load-displacement response of piles spaced at 4 m center to center for (a) all piles as thermal piles and (b) only corner piles as thermal piles

Table 2. Pile base displacement of thermal and mechanical piles

Thermal loading cases	Pile no.	4 m spacing		2.5 m spacing	
		Vertical displacement (mm)		Vertical displacement (mm)	
		D_R = 40%	D_R = 50%	D_R = 40%	D_R = 50%
Type I All piles thermal	1	13.06	8.72	14.24	10.08
	2	13.21	8.81	14.40	10.19
	3	13.07	8.70	14.24	10.08
	4	13.07	8.73	14.24	10.08
	5	13.21	8.81	14.40	10.18
	6	13.06	8.70	14.24	10.08
Type II Corner piles thermal	1	13.68	9.74	14.69	11.02
	2	9.66 (11.48)	5.59 (7.71)	11.40 (12.22)	7.65 (8.67)
	3	13.69	9.77	14.69	11.02
	4	13.69	9.79	14.69	11.02
	5	9.66 (11.48)	5.61 (7.72)	11.40 (12.23)	7.64 (8.66)
	6	13.68	9.79	14.69	11.01
Type III Mechanical piles	1	8.16	7.43	8.68	7.86
	2	8.26	7.50	8.76	7.91
	3	8.16	7.43	8.68	7.86
	4	8.16	7.43	8.68	7.87
	5	8.26	7.50	8.76	7.91
	6	8.16	7.43	8.68	7.86

mechanical piles. In a pile group where all the piles are geothermal (Type I), for the piles at center to center spacing of 4 m, the maximum magnitude of pile base displacement is 8.81 mm for D_R = 50%, however, the maximum base displacement is 13.21 mm for D_R = 40%. The piles in loose sand with D_R = 40% experience 33% higher pile base displacement than for piles in sand with D_R = 50%.

In a pile group with all mechanical piles (Type III), the maximum magnitude of pile base displacement is 7.5 mm for D_R = 50% and 8.26 mm for D_R = 40%. These piles in loose sand with D_R = 40% experience 9.2% higher pile base displacement than for piles in soil with D_R = 50%. It is clear from Table 2 that the thermal load results in about 37% higher base displacement of geothermal piles as compared to mechanical piles. However, in a group where only corner piles are thermal piles (Type II), at 4 m center to center spacing, the maximum base displacement for the thermal piles is 13.69 mm for piles in sand with D_R = 40% and 9.79 mm for piles in sand with D_R = 50%.

For mechanical piles placed along with the thermal piles, the displacement reaches up to 7.72 mm and at the end of heating of thermal piles, the displacement decreases to 5.61 mm for D_R = 50% and the displacement reaches up to 11.48 mm and then decreases to 9.96 mm at the end of heating of thermal piles for D_R = 40%. In loose soil, the mechanical piles exhibit 42% higher base displacement in case of pile

arrangement of Type II. Hence, the differential settlement occurs for a pile group with thermal and mechanical piles altogether in a group. It is recommended to analyze the pile base displacement before the design of pile groups with thermal and mechanical piles in a same group. The differential settlement can be avoided by designing two pile groups, one with all thermal piles and another with all mechanical piles with different raft thickness (Poulos 2001). For the piles placed at 2.5 m center to center in a group, higher pile base displacement is noted for all the cases as compared to the piles placed at 4 m center to center in a group. The pile base displacement of thermal piles is also compared with analytical solution where pile base displacement w_{bi} is also calculated for all mechanical piles by using Eq. (4) given by

$$w_{bi} = \sum_{j=1}^{n_p} \alpha_{ij} \frac{Q_b}{K_b} \tag{4}$$

where Q_b is the load at the pile base and K_b is the soil stiffness near the pile base. Herein, Q_b has been taken from the simulation analysis results and the influence factor α_{ij} has been calculated by using equations and charts obtained from Salgado (2008). The base displacement of piles spaced at 4 m and 2.5 m in a pile group with all mechanical piles is 1.85 mm and 2.01 mm, respectively. However, base displacement of all mechanical piles obtained by elastoplastic analysis is four times higher than that calculated using analytical equation. The pile base displacement for all geothermal piles obtained from elastoplastic analysis is six times higher than base placement calculated from above equation. Therefore, the geothermal pile group should be designed on the basis of results of FE analysis of pile group by considering the elastoplastic behavior of soil.

6 Conclusions

Thermo-mechanical behavior of group of geothermal energy piles with raft and three combinations of thermal and mechanical piles considered to be installed in a single layer of Ottawa sand are analyzed numerically using three dimensional nonlinear finite element analysis procedure in Abaqus. The piles and raft are considered to exhibit linear elastic stress-strain relationship. The stress-strain relationship of sand is simulated through a state parameter based soil constitutive model CASM. The load-displacement response at pile base for the piles in a group when subjected to thermo-mechanical loading are investigated for different pile spacing and different soil stiffness. The analysis results conclude that pile base displacement under mechanical load increases and a further increase occurs for the thermal piles as a consequence of thermal loading. Contrary to base displacement of thermal piles, the base displacement of mechanical piles decreases when the thermal piles are undergoing through heating in the same group. For the thermal piles, about 47% increase in base displacement occurs as compared to the piles subjected to mechanical load for closely spaced piles at 2.5 m. Differential settlement of the piles occur in groups containing thermal and mechanical piles placed altogether. Hence, it is recommended to analyze the pile base displacement

for all the piles in group with thermal and mechanical piles placed in the same group. To prevent the differential settlement, two pile groups should be designed separately, one with all thermal piles and another with all mechanical piles with different raft thickness. Moreover, at least 4 m spacing between the thermal piles in field should be used for the piles considered herein. The base displacement of all mechanical piles calculated using equation is about six times lesser than the elastoplastic analysis results. Hence, numerical analysis can be considered as a viable tool to predict the geothermal energy pile group behavior. Upon heating, uneven distribution of axial load occurs. The load on the thermal piles increases and load on the mechanical piles decreases. However, the axial load on thermal piles decreases and the axial load on mechanical piles increases during the cooling of thermal piles. Soil relative density has a strong influence on pile base displacement of thermal piles.

References

Abaqus/Standard User's Manual, Version 6.11.: Dassault Systèmes Simulia Corporation, Providence (2011)

Bourne-Webb, P.J., Amatya, B., Soga, K., Amis, T., Davidson, C., Payne, P.: Energy pile test at Lambeth College, London: geotechnical and thermodynamic aspects of pile response to heat cycles. Géotechnique **59**(3), 237–248 (2009). https://doi.org/10.1680/geot.2009.59.3.237

Brandl, H.: Energy foundations and other thermo-active ground structures. Géotechnique **56**(2), 81–122 (2006)

Carraro, J.A.H.: Mechanical behavior of silty and clayey sands. Ph.D. Dissertation, Purdue University (2006)

Dupray, F., Laloui, L., Kazangba, A.: Numerical analysis of seasonal heat storage in an energy pile foundation. Comput. Geotech. **55**, 67–77 (2014)

Green, A.E., Naghdi, P.M.: On undamped heat waves in an elastic solid. J. Therm. Stress. **15**, 253–264 (1992)

GSHP Association: Thermal Pile Design, Installation and Materials Standards. Ground Source Heat Pump Association, National Energy Centre, Davy Avenue, Knowlhill, Milton Keynes, MK5 8NG (2012)

Jeong, S., Lim, H., Lee, K.J., Kim, J.: Thermally induced mechanical response of energy piles in axially loaded pile groups. Appl. Ther. Energy **71**, 608–615 (2014)

Laloui, L., Nuth, M., Vulliet, L.: Experimental and numerical investigations of the behavior of a heat exchanger pile. Int. J. Numer. Anal. Methods Geomech. **30**, 763–781 (2006)

Loria, A.F.R., Laloui, L.: Thermally induced group effects among energy piles. Géotechnique **67**(5), 374–393 (2017)

Murthy, T.G., Loukidis, D., Carraro, J.A.H., Prezzi, M., Salgado, R.: Undrained monotonic response of clean and silty sands. Géotechnique **57**(3), 273–288 (2006)

Loukidis, D.: Advanced constitutive modeling of sands and applications to foundation engineering. Ph.D. thesis, Purdue University (2006)

Poulos, H.G.: Piled raft foundations: design and applications. Géotechnique **51**(2), 95–113 (2001)

Saggu, R., Chakraborty, T.: Thermal analysis of energy piles in sand. Geomech. Geoeng. Int. J. **10**(1), 10–29 (2015a). https://doi.org/10.1080/17486025.2014.923586

Saggu, R., Chakraborty, T.: Cyclic thermo-mechanical analysis of energy piles in sand. Geotech. Geol. Eng. **33**(2), 321–342 (2015b). https://doi.org/10.1007/s10706-014-9798-8

Saggu, R., Chakraborty, T.: Thermo-mechanical response of geothermal energy pile group in sand. Int. J. Geomech. (2016). https://doi.org/10.1061/(ASCE)GM.1943-5622.0000567

Saggu, R., Chakraborty, T.: Thermo-mechanical response of geothermal energy piles in sand and parametric study. Int. J. Geomech. (2017). https://doi.org/10.1061/(ASCE)GM.1943-5622.0000962

Salciarini, D., Ronchi, F., Cattoni, E., Tamagnini, C.: Some remarks on the thermomechanical effects induced by energy piles operation in a small piled raft. Int. J. Geomech. (2013). https://doi.org/10.1061/(ASCE)GM.1943-5622.0000375

Salgado, R.: Engineering of Foundations. McGraw-Hill, New York (2008)

Sasitharan, S., Robertson, P.K., Sego, D.C., Morgenstern, N.R.: State-boundary surface for very loose sand and its practical implications. Can. Geotech. J. **31**(3), 321–334 (1994). https://doi.org/10.1139/t94-040

Tarnawski, V.R., Momose, T., Leong, W.H., Bovesecchi, G., Coppa, P.: Thermal conductivity of standard sands. Part I. Dry state conditions. Int. J. Thermophys. **30**(3), 949–968 (2009)

Wang, B., Bouazza, A., Haberfield, C.: Preliminary observations from laboratory scale model geothermal pile subjected to thermo-mechanical loading. In: Geo-Frontiers, ASCE 2011, pp. 430–439 (2011)

Yu, H.S.: CASM: A unified state parameter model for clay and sand. Int. J. Numer. Anal. Meth. Geomech. **22**, 621–653 (1998)

Yu, H.S.: Plasticity and Geotechnics. Springer, New York (2006)

Feasibility Study on the Implementation of Energy Recovery Tunnel Segmental Lining in the Lot 3 Tunnel on Railway Line 16 of the Grand Paris Express

Fabrice Rognon(✉), Phidias Marco, Bastien Chappuis, Eloïse Moradpour, and Nicole Calame

CSD INGENIEURS SA, Lausanne, Switzerland
f.rognon@csd.ch

Abstract. This study analyses the opportunity of using energy recovery tunnel lining segments to produce heating and/or cooling. A 1D finite-element modelling demonstrated that it is possible to extract a specific vault power between 15 W/m^2 during summer and 35 W/m^2 during winter from the ambient air and adjoining geological formations, which corresponds to the capacity between 120 to 280 kW over a 300 m section situated before the entrance to an underground station. The heat extraction is modelled so as to avoid durable deviation of the ground temperature. The thermal fluxes direction reverses depending on the ground or tunnel air temperature, which allows to use the ground as a seasonal heat storage. Given the expected temperatures, cooling production is not envisioned. Based on the modelling results, such a system should allow for a greater heat extraction than one based on thermo-active moulded walls. Indeed, the tunnel lining segments are able to extract heat from the geological formations as well as recover heat from the tunnel ambient air.

1 Introduction

The Grand Paris Express consists of an automatic metro comprising 200 km of lines which aims to reinforce and expand the present underground and fast regional railway network (RER).

The present study analyses the potential for heat and/or cooling production by a system of energy recovery tunnel segmental lining that could either replace or be complementary to the thermo-active moulded walls intended in the station of Chelles. The tunnel of lot 3 of line 16 will be built using a tunnel boring machine that will assemble the tunnel lining segments as it is drilled.

2 Foundations and Methods

2.1 Geological and Geotechnical Aspects

The 300 m long studied section is located at the south exit of the Chelles underground station towards the Noisy-Champs station (3'700 m interstation), between the kilometre

A. Ferrari and L. Laloui (Eds.): SEG 2018, SSGG, pp. 203–210, 2019.
https://doi.org/10.1007/978-3-319-99670-7_26

points (KP) 33 + 900 and 34 + 200. This section will be called “Chelles-Sud” in the further part of the study.

The ground surrounding the Chelles station consists, under the embankments, of thick alluvium, modern (AM) and especially old (AA) resting on the partly eroded Limestone of St-Ouen (SO), the Sands of Beauchamp (SB), the Marnes and Caillasses (MC), the Coarse Limestone (CG) and Ypresian terrain (AP and SC). In addition to these formations, embankments and alluvial deposits of the Marne cover the SO. Figure 1 illustrates the situation of the studied section as well as occurring geological layers. The different aquifer formations likely to interact with the project are: SO, SB, MC and CG. Since the flows are weak, convective heat flows from groundwater are not considered.

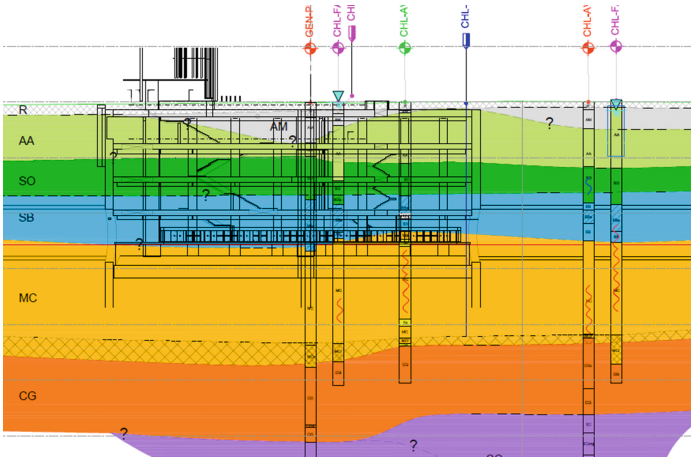

Fig. 1. Choice of a 300 m long southern section (« Chelles-Sud ») marked by the red arrow (Société du Grand Paris 2016)

The depth of the tunnel varies between 20 and 30 m below the natural terrain. The average temperature of flowing water is assumed to be 13 °C throughout the year (BRGM 1977). By analogy, it is considered that the groundwater keeps the formations MC, SB and SO at this temperature level all over the year.

The conductivities and thermal capacities of the terrain are considered isotropic above the tunnel vault. Their values are calculated as the average of the grounds around the vault (SO, SB and MC) following the Swiss Standard SIA 384/6.

2.2 Characteristics of Rolling Stock and Thermal Aspects in the Tunnel

The rolling M15 iron-on-wheel bearing type stock will be used. It is characterized by electrical power supply with braking energy recovery rate of 30%, efficiency of the traction chain of 80%, maximum speed 120 km/h, 3 cars, total length of the train 54 m, and estimated weight in comfort load of 115 tons (SGP 2013). The dissipated thermal powers are estimated at 430 kW during acceleration phase, 940 kW during braking

phase, 50 kW maintaining a constant speed on flat ground and 50 kW for air conditioning operation.

It is assumed that the trains accelerate linearly at 0.9 m/s^2 and brake at 0.7 m/s^2. The speed curves are used to determine the residence time in the studied section (SGP 2010).

The rolling stock hourly rate for line 16 is one train every 15 min per direction (14 h/day) and one train every 4 min per direction (5 h/day).

The considered internal heat sources are: thermal losses of the motors, energy dissipation during braking and heat discharges of the train cooling systems.

The average time spent by trains during acceleration and braking phase in the equipped section allows to estimate the maximum internal energy load. Expressed in W per m^2 of the intrados of the tunnel segmental lining, the average power released in the section is 16.5 W/m^2 during peak hours and 4.4 W/m^2 during off-peak hours, i.e. 6 W/m^2 on average.

It is assumed that the Chelles-Sud section is not directly influenced by the outside air temperature. The variation of the tunnel temperature at the Chelles station is considered similar to that of the Châtelet-les-Halles metro station, located at similar depth (Fig. 2). The hourly air renewal rate considered in the tunnel is 9.

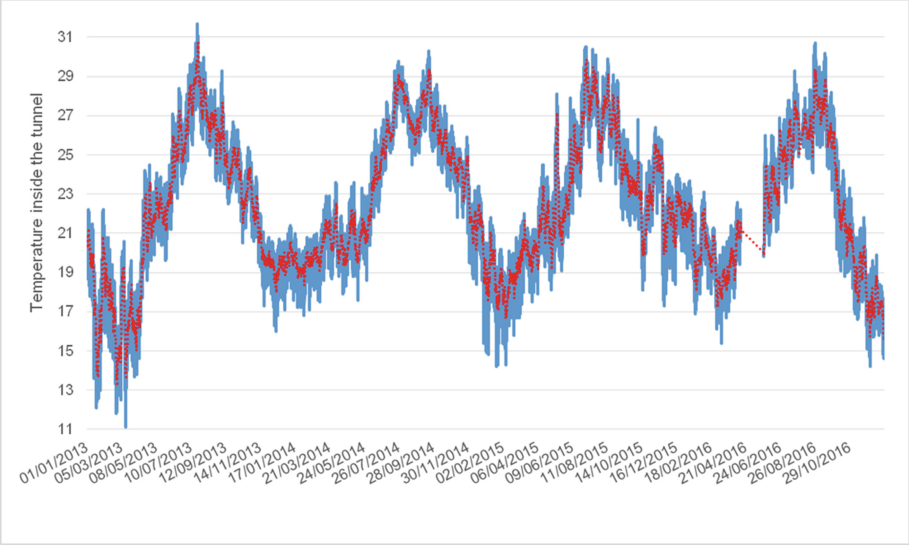

Fig. 2. Tunnel air temperature in Châtelet-les-Halles between 2013 and 2016 [RATP big data] (in blue: measured temperature, in red: moving average over 30 days)

2.3 Proposed Heat Recovery Concept and Thermal Flow Modelling

The proposed concept is based on local project conditions as well as experiments conducted in London (Nicholson et al. 2014), Jenbach (REHAU 2011) and Turin (Barla et al. 2016).

The energy system consists of three main parts: the energy recovery tunnel segmental lining, the distribution network and the heat pump. The heat produced in the tunnel is collected and extracted by a cooling circuit built into the tunnel lining segments. The heat is then raised to a useful temperature by a water-to-water heat pump. Figure 3 shows a simplified operating diagram with indicative temperatures.

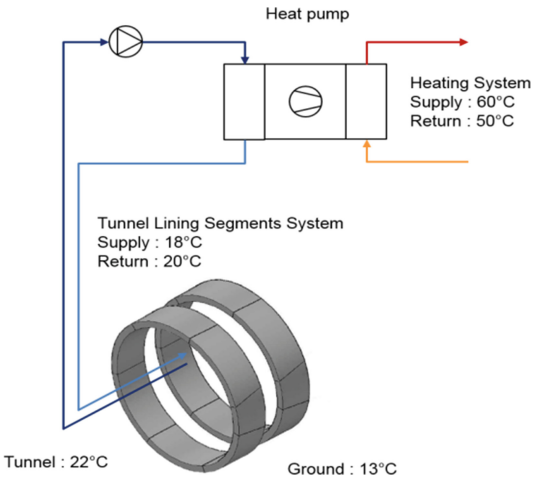

Fig. 3. Simplified schematic diagram of the proposed heat recovery concept

The tunnel lining segments forming the same ring are hydraulically connected in series. The rings are hydraulically connected in parallel to ensure homogeneous temperatures in the fitted section. The test section of 300 m consists of 30 groups of 5 rings. Each ring has about 130 m of cross-linked polyethylene (PEX) floor heating tubes. PEX has the advantage of being flexible with an extended lifetime, estimated over 100 years under normal temperature conditions.

This study includes a 1D model of the predictable thermal flows between the tunnel air and the segmental lining on the one hand and between the tunnel lining and the ground on the other hand. These heat flows are estimated based on the specific characteristics of the structure and its operation. A 10 m section was modelled using 1 m elements and simulated over a period of 5 years with a daily time step. Two variants of extraction have been studied.

The modelling only takes into account the heat source without interaction with the requirements of the heat customers on the surface.

3 Results

Given the expected temperatures, cooling production is not envisioned.

The potential heat production computed for two variants which are described hereafter reveal a significant difference. Figure 8 shows that the annual useful energy

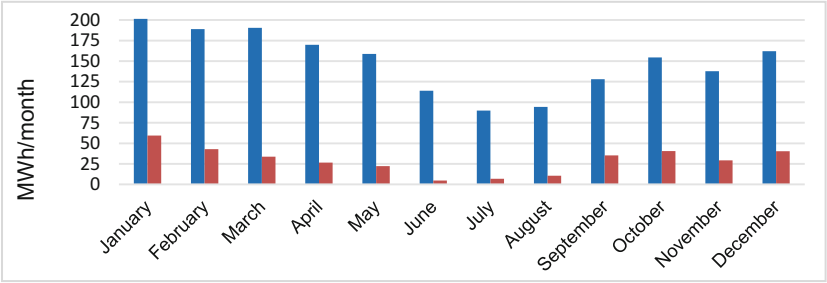

Fig. 4. Potential for heat recovery over a 300 m section (in red: heat extraction variant No.1; in blue: variant No. 2)

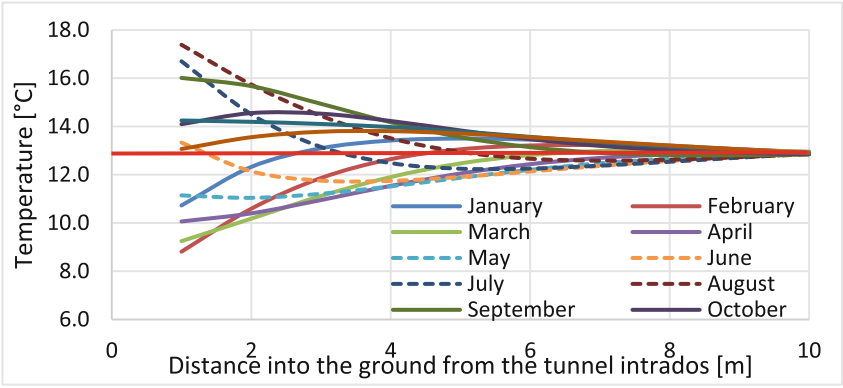

Fig. 5. Ground temperature during the year after 5 years of operation – extraction variant No. 2. The red line indicates the initial or undisturbed ground temperature.

that could be supplied by the system at the heat pump output varies by a factor of 5 between variant No. 1 (475 MWh/year) and variant No. 2 (2'390 MWh/year).

3.1 Heat Extraction

Variant No. 1 consists in extracting only the internal heat generated by the operation of the metro by maintaining the circuit temperature in the tunnel segmental lining at 1.7 K under the tunnel air temperature, corresponding to a thermal flux of 6 W/m^2. Results shows that the available power varies between 0.8 W/m^2 in summer and 9.8 W/m^2 in winter, or a power of 7 to 80 kW for the 300 m test section. The seasonal imbalance observed on the tunnel segmental lining - terrain flow indicates a continuous heat supply to the ground implying a gradual warming, as for a non-activated tunnel: +4 K after the 5 years exploitation at 10 m from the intrados). In this simulation, the tunnel air temperature has been lowered by up to 1 K (Fig. 6).

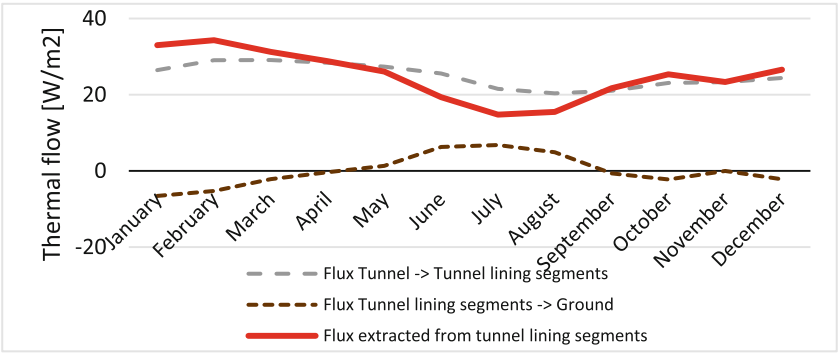

Fig. 6. Estimate of thermal flows during the year – extraction variant No. 2

Variant No. 2 consists in extracting the heat from the tunnel segmental lining so as to limit the thermal deviation of the ground. The surrounding land acts as a seasonal heat storage (Fig. 4). The heat withdrawn is modulated by the heat pump by varying the temperature of the circuit in the tunnel segmental lining. Thus, heat is extracted in winter and stored in the ground during summer.

The results illustrated in Fig. 5 show that the drawn vault power varies between 15 W/m^2 in summer and 35 W/m^2 in winter, which represent a power of 120 to 280 kW for the 300 m test section. In this simulation, the tunnel air temperature has been lowered by up to 4 K, which limits the need for forced ventilation.

4 Discussions

4.1 Heat Extraction Variants

A PEX tube with an internal diameter of 30 mm seems appropriate since it allows a turbulent flow along with acceptable pressure losses at the maximum withdrawn power.

Train fire cases were evaluated in the London model (Nicholson et al. 2013) which showed that a temperature of 60 °C is reached in the tubes buried 20 cm deep after 180 min of exposure. This tube burial depth is thus sufficient to avoid the effects of fires.

The impact of thermal effects on the structural conditions of the tunnel following changes in temperatures should be verified. Models carried out as part of the energy recovery tunnel segmental lining project in London (Nicholson et al. 2014) has shown that a heat extraction of 30 W/m2 causes compression and tractions forces which are below the maximum design limit of 5 MPa.

In variant No. 1, since the field's heat storage capacity is not actively used, the heat extraction is low in winter and almost non-existent in summer. The temperature of the ground deviating with the years, the thermal flows will evolve over time with the tunnel operation which does not represent a perennial situation.

Extraction variant No. 2 is very sensitive to the air renewal rate in the tunnel. In this simulation, the tunnel air temperature has been lowered by a maximum of 4 K (in

winter) on the basis of an hourly renewal rate of 9. It corresponds to an ideal situation with respect to the heat source, since a maximum of energy is extracted without inducing a deviation in the ground in the long term. This approach, where the heat extracted is dictated by the source conditions (ground, tunnel) requires a bivalent heat production to ensure a heat supply corresponding to the needs. The system must be calibrated so that the summer power from the tunnel segmental lining covers the summer needs of some heat consumers (production of domestic hot water for example). The regulation of the withdrawal rate, carried out *a posteriori* during the modelling, will be complex to achieve: in situ tests will be necessary.

4.2 Benefits of the System and Limitation of the Study

The system heat generation performance would be 30 to 50% higher than that of a conventional geothermal heat pump due to the source temperature.

Considering that the installation allows to reduce the mechanical ventilation of the studied section by 25% (tunnel air circulation speed from 1 m/s to 0.75 m/s in variant 2), the electricity saving is estimated to 60% on the ventilation station.

The carbon footprint of a heat supply from the tunnel segmental lining without fossil fuel complement is 85% lower than a conventional natural gas production.

According to (Geimer 2013) the energy recovery tunnel segmental lining system increases the cost of the segmental lining by only 2%. According to (Barla et al. 2016) the cost price of heat originating from an energy recovery tunnel segmental lining system is 41% more economical than a geothermal piles based solution.

Finally, according to (Nicholson et al. 2014), the tunnel lining segments made of fibre-reinforced concrete are not incompatible with an energy recovery tunnel segmental lining system.

Many assumptions or parameters will need to be refined as part of future execution studies in order to consolidate the obtained results.

In order to precisely characterize the mutual influence between the tunnel air, the energy recovery tunnel segmental lining system and the ground, dynamic modelling should be carried out, which should also take groundwater flows into account. In order to obtain a complete modelling, the future simulation will necessarily have to take the heat customers' needs profile into account. Ideally, a financial business plan should also be established to verify the profitability of the proposed system.

5 Conclusions

The energy recovery tunnel segmental lining system appears as an interesting concept to produce clean heat originating from the internal heat of a tunnel if the ground is used as a seasonal heat storage (extraction variant no 2);

This technology does not allow to cool a place when installed in a so-called "hot" tunnel, which is characterized by a summer internal temperature of more than 20 °C approximately (case of the Chelles tunnel);

The energy recovery tunnel segmental lining system is cheaper (Barla et al. 2016) and also more efficient than thermo-active moulded walls, since the segments are more

in contact with the ambient air of the tunnel. Moreover, according to (Geimer 2013), the energy recovery tunnel segmental lining system represents a small over-investment compared to the non-energy recovery one;

According to (Nicholson et al. 2014), fire resistance and mechanical stresses are acceptable;

The studied system impacts the construction schedule in that it is necessary to anticipate (i) the sections that will have to be equipped in order to start manufacturing and equip the segments and (ii) the special formworks that will have to be put in place in order to avoid concreting the pipe connection chambers.

The tunnel segmental lining system has the advantage of giving a second energy function to the infrastructure: the tunnel lining heat production can potentially offer an 85% lower carbon footprint than a conventional gas-fired production;

An implementation study is needed to confirm the results obtained in this study.

References

Barla, M., et al.: Application of energy tunnels to an urban environnement. Geothermics **61**, 104–113 (2016)

Geimer, C.: Metro Tunnels enable geothermal air-conditionning (2013)

Nicholson, D.P., et al.: Developments in thermal pile and thermal tunnel linings for city scale GSHP systems (2013)

Nicholson, D.P., et al.: The design of thermal tunnel energy segments for crossrail (2014)

REHAU: Geothermal Tunnel Lining—Turning infrastructure into green energy sources (2011)

Société du Grand Paris: Appréciation de l'impact de la vitesse maximale des trains du Métro Grand Paris (RATP) (2010)

Société du Grand Paris: Quel sera le matériel roulant de la future ligne 16, en quoi ses caracteristiques differeront t elles de celles de celui de la future ligne 15 sud? (2013). Accessed https://www.societedugrandparis.fr/question-reponse/quel-sera-le-materiel-roulant-de-la-future-ligne-16-en-quoi-ses-caracteristiques-differeront-t-elles-de-celles-de-celui-de-la-future-ligne-15-sud

Société du Grand Paris: Lot 3 - Mémoire de synthèse géologique, hydrogéologique et géotechnique (2016)

A Feasibility Study on Implementing the Energy Piles in Electric Power Industries

Amir Akbari Garakani[1(✉)], Ehsan Motevali Haghighi[2], Alireza Rahnavard[1], Majid Beigi[3], Matin Kabiri Tadi[3], and Tahereh Razmkhah[3]

[1] Niroo Research Institute, Tehran, Iran
aakbari@nri.ac.ir
[2] University of Tehran, Tehran, Iran
[3] Sharif University of Technology, Tehran, Iran

Abstract. The use of energy pile foundations for heat exchanging with the ground has caught significant attention in recent years. One of the potential fields for energy pile application is electric power industries. Implementing the energy piles in electric power industries can be majorly corresponded to two major subgroups, namely "direct applications" in power production facilities and power transmission-distribution networks and "indirect applications" in industrial target consumers. In both categories, some machineries or components need to be cooled or heated to assure proper operation. For heat exchange purposes, commonly a thermal fluid (e.g., water) circulation system is implemented which can be incorporated in energy pile foundations. Among the most important factors, which should be considered to select the energy pile system for heat exchange purposes in industrial machineries, are the magnitude of the flow rate and initial or final temperatures of the geothermal fluids and those corresponded to the operational capacity of the energy pile systems. In this paper, the possibility of direct or indirect usage of energy piles in electric power industries is studied. In this regard, technical aspects of the issue have been considered, analyzed and discussed. Results revealed that there are many principle or auxiliary devices in electric production and transmission-distribution networks or electric consuming industries, which an utilize the energy piles for heat exchange purposes. The economical and executional concerns of the issue are discussed, as well.

Keywords: Energy piles · Electric power industries
Direct and indirect usages · Operational characteristics
Economic and environmental studies

1 A Brief Review of the Geothermal Energy

Energy resources are categorized into renewable and nonrenewable energies. The repeatable and stable sources of energy are called the renewable energy, like Wind, Biomass, Tidal, Solar and Geo-thermal energies. On the other hand, Nuclear, Coal, Oil, Natural Gas fuels are the nonrenewable forms of energies.

A. Ferrari and L. Laloui (Eds.): SEG 2018, SSGG, pp. 211–217, 2019.
https://doi.org/10.1007/978-3-319-99670-7_27

The origin of geothermal resources results from the nuclear interactions which take place inside the earth. The various resources of geothermal energies are classified in the two groups of shallow and deep resources and the depth of the deep resources is more than 200 m. These resources consist of hydrothermal and developed resources which naturally contain fluid for heat exchanging, and lacks enough fluid to exchange the energy, respectively. One of the direct applications of the deep geothermal resources is extracting energy for generatin power. In addition, there are more utilization like heating or cooling systems, agriculture, animal husbandry, industrial applications and water treatment (Garakani 2017).

The shallow resources which are limited to the less than 200 m includes the open and the close systems. In the open systems, the water is extracted from the known place and after the exchanging of the energy it will be injected to the same place from which it was extracted. The shallow resources of geothermal energy are widely used for cooling and heating systems (Nooraliei 2015).

2 Geo-Thermal Structures and Energy Piles

The geo-structures which are used to exchange heat are divided into two separated systems, namely open and close systems. In open systems, the groundwater enters into the heat exchanger and returns back to the ground level where it was not extracted. In contrary, in closed systems, the extracted water is injected into the same place where it was extracted. In general, the heat exchanger geo-structures comprise of heat exchanger borehole, energy pile, energy tunnel, the shallow foundation of energy, sewage system of energy, energy wall, energy well, and energy column (Brandl 2006).

The borehole heat exchanger is a vertical borehole which is excavated near the energy consuming structure. In this case, set of pipes are placed inside the borehole and the exchange of energy is performed using an intermediate fluid. Another type of heat exchanging system is the energy tunnel, in which the contact area of the tunnel and the ground makes an efficient path to exchange the energy. The shallow foundation system is the other type of heat exchanger that is highly applicable due to the wide contact areas between the foundation and the upper ground surface, which exceeds the transformation of the energy. Energy wall is regarded as an option to exchange the energy, in which the sewage system is placed in ground depths and it is possible to implement considerable flow of water for energy exchanging. Energy column is established to exceed the consolidation process in soil (Adam and Markiewicz 2009; Rees 2016).

Energy piles play the same role as the structural piles (Fig. 1). Energy piles have both the structural and heat exchanging functions at the same time. The design of energy piles should satisfy the fact that heat exchanging procedure should not disturb the load transferring procedure. The best known application of energy pile is cooling and heating the domestic and commercial building. Energy piles provide the underfloor heating system with sufficient fluid to exchange the energy. This system can be applied to deice the runways. Furthermore, energy piles are implemented under the cereal silos to help the process of cereals drying. Switzerland, Austria, Germany, Great Britain are the pioneers through the using of energy piles. Australia, Japan, China, Netherland and

United State are the new comers in the utilization of energy piles (Hamada et al. 2007; De Moel et al. 2010).

In addition to residential or commercial structures, industrial implementation of energy piles is still a challenging field of interest for researchers and engineers (Lindal 1973). One of the best possible industries in which the shallow heat exchanging systems can be implemented is "electric power industry". Energy piles can be used for both "direct" and "indirect" purposes in electric power industries. In "direct" implementations, energy piles are used for heat exchanging (cooling or heating) in electric power facilities to increase using the renewable energy. In "indirect" implementations, energy pile can be used in electricity consuming industrial centers. Both types of implementation can help reduce using non-recoverable sources of energies.

Fig. 1. Implementation of Energy Piles in: Left) Keble College, UK. and, Right) a Walk Road in Japan

3 Direct Application of Energy Pile in the Power Industry

The direct application of energy pile in electric power industry can potentially results from cooling or heating demands in which large amount of energy consumes. To minimize the energy consumption, introducing energy pile into the power industry can be highly taken into attentions. The direct applications of energy piles in electric power industry is considered for cooling towers, electrical transformers, pre-heating the raw material and closed cooling water systems in gas plants.

3.1 Cooling Towers

Cooling towers are of the most important facilities in electric power plants (Fig. 2). This section exceeds the process of cooling water using evaporation. Through the process of evaporation large amounts of water evaporate to the air. The high volumes of water which is used in the cooling tower; plus, wasting water through evaporation

describe the needs for finding a more efficient solution. The water flux in cooling towers is on average of 50000 m^3/h. Hence, utilization of energy piles in cooling towers for cooling partial amounts of water can be regarded as a valuable idea (Garakani 2017).

Fig. 2. Cooling Towers in Electric Industries

3.2 Cooling Process of Electrical Transformer

Transformers are among the most fundamental components in electricity transmission lines. Transformer is a component which changes the level of electric voltage for different utilizations. Transformers generate a lot of heat during work and the need for the cooling process is inevitable. In addition, due to the high weight of transformers structure, strong foundation structures are needed to be placed beneath the main body of transformers to transfer the loads to the ground. The utilization of the energy pile in cooling system of transformers is a unique recommendation since the dual function of the energy piles (heat exchanging and structural load bearing) satisfies the needs for the cooling system and the bearing foundation. The fluid flow rate in cooling system of the transformer is on the average of 5 m^3/h which matches the working characteristics of the typical energy pile systems (Garakani 2017). The functional specifications of the cooling towers and cooling system of the transformers are presented in Table 1.

Table 1. Functional specification of the cooling tower and cooling system of transformer (Garakani 2017)

Power plant	Input temperature (°C)	Input temperature (°C)	Flux (m^3/hr)
Cooling tower	35	27	42000
Transformer cooling System	30	40.4	3.4

3.3 Pre-heating the Raw Material

In the electric power industry, sometimes it is needed to pre-heat the primary raw materials. For example, in thermal power plants it is necessary to warm up gasoline or

crude oil before entering the combustion chamber, or in boilers the inlet air must be preheated before entering the circulating procedure.

The flow rate of the consuming fuels is typically below 5 m^3/hr. Also, the volume of the air which enters to the boilers is about 120 kg/s. Hence, implementing the energy piles is possible for pre-heating the aforementioned materials (Garakani 2017).

4 Indirect Application of Energy Pile in Electric Power Industry

In this section, the utilizations of energy pile in electric consuming industries like oil industry, steel industry, and greenhouse ventilation systems is demonstrated.

4.1 Oil Industry

Heat exchangers are widely utilized in the oil industry. The fractionating column is the essential part of distillation procedure. To separate the mixture of crude oil in this column the heat exchangers are used. Furthermore, the gas and oil reservoirs are placed in a deep depth of ground; a suitable place to extract geo-thermal energy. The inlet temperature of distillation tower is about 15–30 °C which is regarded as the certified temperature for the utilization of energy piles.

4.2 Steel Industry

The steel industry is the basic economical foundation of the developed countries. The index of steel consumption is a criterion to evaluate the economical level of the country. Various heat exchangers are installed in the purifying process of ore. For instance, the outlet gases from the purifying process enter to the cooling system. Also, some facilities like compressors, drier and the hydraulic section need to the cooling systems. Using energy piles in the steel industry can be taken into consideration.

4.3 Greenhouse Ventilation System

Based on their application, the temperature of greenhouses should be selected with respect to the treated plants. Generally, the favorable temperature for plants is about 65°F. Thus, utilization of heating system in the greenhouses is inevitable. There are various methods to heat the greenhouses like using pipes on the surface of the soil, utilization of pipes on the surface of the lateral walls of the greenhouse, and using the unit heaters. Based on the functional properties of these systems, energy piles can satisfy the heating demands in greenhouse systems.

4.4 Food Production Industry

Utilizations of heat exchanger in the food and dairy industries are widely taken into consideration. For instance, milk and cream pasteurization, milk and cream cooling, thermal treatment of cream, cooling and heating oil and fat are regarded as the

applications of heat exchanger in the food, diary and drink industry. Based on the functional performance of the heat exchangers in the food industries, energy piles can be used for extracting the geo-thermal energies.

5 Economical and Environmental Evaluation of Energy Piles

In this research, a complete economic study has been performed to compare the cost of heating or cooling the electric power facilities for different types of energy sources. Accordingly, the average cost values for producing 1 MW.hr energy for cooling or heating purposes in electric power industries are presented in Table 2. As shown in Table 2, the very low cost of using the energy piles in compare to other sources of energy is very significant.

Table 2. Economic comparison between different types of energy resources used for cooling or heating demands in electric power industries

Energy type	Fossil fuels	Solar energy	Wind energy	Hydro-power plant	Biomass energy	Geo-thermal resources	Energy piles
Cost (US$/MW.hr)	133.3	77.8	73.3	50.0	93.3	115.6	40.0

Despite the fact that the renewable forms of energy have negligible effects on the environment, extracting energy poses destructive manipulations on the environment and the various cycles of producing power slightly change the environment. Figure 3 demonstrates the production of carbon dioxide per different methods of the energy generating. As it is depicted, the production of carbon dioxide for the fossil fuel is drastically high among other types of energy production. On the other hand, energy piles create the lowest environmental pollution among other sources of energy.

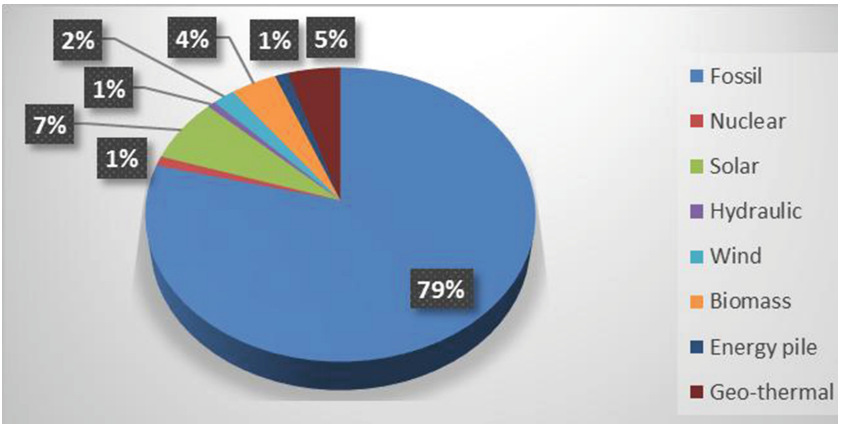

Fig. 3. The mount of greenhouse production (grams of CO2 per KW/h)

6 Conclusion

In this paper, a feasibility study on implementing the energy piles in electric power industries is investigated. The utilizations of energy pile in the power industry are divided into the two direct and indirect sections. Cooling towers, cooling system of electrical transformers, pre-heating the raw materials and closed cooling water systems are the examples for direct applications of energy piles and, oil, steel and food industries are the indirect utilizations of this clean source of energy. Based on the functional specifications and economic-environmental considerations, the utilizations of the energy piles in electric power facilities or electric consuming industries are worth to be taken into account.

References

Nooraliei, J.: Strategic Document and Road Map for Development of Geothermal Energy Related Technologies. Niroo Research Institute, Tehran (2015)

Garakani, A.A.: A Feasibility Study on Implementation of the Energy Piles in Electric Power Industry. Niroo Research Institute, Tehran (2017)

Adam, D., Markiewicz, R.: Energy from earth-coupled structures, foundations, tunnels and sewers. Géotechnique **59**(3), 229–236 (2009)

Brandl, H.: Energy foundations and other thermo-active ground structures. Geotechnique **56**(2), 81–122 (2006)

De Moel, M., Bach, P.M., Bouazza, A., Singh, R.M., Sun, J.O.: Technological advances and applications of geothermal energy pile foundations and their feasibility in Australia. Renew. Sustain. Energy Rev. **14**(9), 2683–2696 (2010)

Hamada, Y., Saitoh, H., Nakamura, M., Kubota, H., Ochifuji, K.: Field performance of an energy pile system for space heating. Energy Build. **39**(5), 517–524 (2007)

Lindal, B.: Industrial and other applications of geothermal energy: (except power production and district heating) (1973)

Rees, S.: Advances in Ground-Source Heat Pump Systems. Woodhead Publishing, Sawston (2016)

Thermo-mechanical Schemes for Energy Piles

Alessandro F. Rotta Loria(✉) and Lyesse Laloui

Laboratory of Soil Mechanics, Swiss Federal Institute of Technology
in Lausanne, EPFL, Station 18, 1015 Lausanne, Switzerland
alessandro.rottaloria@epfl.ch

Abstract. Currently, schemes based on seminal empirical knowledge about energy piles subjected to mechanical and thermal loads are available to describe the response of such foundations. However, schemes based on theoretical principles may more closely reflect the predictions made for the analysis and design of energy piles. Looking at such challenge, this paper presents thermo-mechanical schemes based on thermo-elasticity theory to address the response of single energy piles to mechanical and thermal loads. The proposed schemes highlight a number of key aspects associated with the modelling of energy pile response to loading and may be considered in analysis and design.

1 Introduction

Understanding the influence of the mechanical and thermal loads associated with the structural support and heat exchanger roles of energy piles on the related mechanical response is paramount for the analysis and design of such foundations. Currently, thermo-mechanical schemes based on the results of full scale in situ tests are available (Bourne-Webb et al., 2009; Bourne-Webb et al., 2011) and may be considered for the previous purpose. However, a number of conditions of validity of the quoted schemes have never been explicated and schemes based on theoretical principles may more closely reflect the predictions made for the analysis and design of energy piles. In this context, this paper presents novel thermo-mechanical schemes for describing the response of single energy piles subjected to mechanical and thermal loads based on linear thermo-elasticity theory, and provides a description of the conditions of validity characterising the currently available schemes.

2 Thermo-mechanical Schemes

The general equation that governs the axial equilibrium of energy piles is

$$P + \frac{\pi D^2}{4} K_h w(z=0) + W + Q_{s,mob} + Q_{b,mob} = 0 \tag{1}$$

where P is the applied mechanical load, D is the pile diameter, K_h is the head stiffness of the structural element connected to the pile head, $w(z=0)$ is the pile vertical head displacement (with z being the vertical coordinate), W is the pile weight, $Q_{s,mob}$ is the

A. Ferrari and L. Laloui (Eds.): SEG 2018, SSGG, pp. 218–225, 2019.
https://doi.org/10.1007/978-3-319-99670-7_28

mobilised portion of the pile shaft capacity Q_s, and $Q_{b,mob}$ is the mobilised portion of pile base capacity Q_b. The term $Q_{s,mob}$ is associated with the mobilised shaft resistance τ along the external surface of the pile shaft $A_s = 2\pi RL$ (with R and L being the pile radius and length, respectively), and the term $Q_{b,mob}$ is proportional to the appropriate vertical stress σ_{vb} mobilised at the level of the pile toe characterised by a cross-sectional area A_b.

To distinguish the different mechanical response of energy piles subjected to mechanical and thermal loads, $Q_{s,mob}$ and $Q_{b,mob}$ can be written in terms of a mechanical and a thermal contribution as

$$Q_{s,mob} = Q^m_{s,mob} + Q^{th}_{s,mob} \tag{2}$$

and

$$Q_{b,mob} = Q^m_{b,mob} + Q^{th}_{b,mob} \tag{3}$$

The reason for this is that, in contrast to the influence of conventionally applied mechanical loads that cause a pile displacement in a unique direction (e.g., downward), thermal loads applied to energy piles generally involve two pile portions that displace in opposite directions from the so-called null point of the vertical displacement (located at a depth, $z_{NP,w}$) (Laloui et al. 2003). Accordingly, shear stress is mobilised in opposite directions at the pile shaft to ensure equilibrium with the surrounding soil from the so-called null point of the shear stress (generally located at a different depth, $z_{NP,\tau}$, than that of the null point of the vertical displacement (Rotta Loria et al. 2018)). Based on the above, $Q^{th}_{s,mob}$ reads

$$Q^{th}_{s,mob} = Q_{s,mob,up} + Q_{s,mob,down} \tag{4}$$

where $Q_{s,mob,up}$ and $Q_{s,mob,down}$ are the portions of shaft capacity mobilised above and below the null point of the shear stress, respectively, with

$$Q_{s,mob,up} = \pi D \int_0^{z_{NP,\tau}} \tau dz \tag{5}$$

and

$$Q_{s,mob,down} = \pi D \int_{z_{NP,\tau}}^{L} \tau dz \tag{6}$$

Based on the previous framework, thermo-mechanical schemes for energy piles can be formulated. In the following, schemes resorting to linear thermo-elasticity theory are presented. The schemes proposed in this work associate the influence of thermal loads applied to energy piles with non-linear evolutions of the vertical stress (and strain) as well as with linear evolutions of the shear stress along their length. These features are in contrast with the linear evolutions of the vertical stress (and strain) and constant

step-wise evolutions of the shear stress presented by Bourne-Webb et al. (2009) and Bourne-Webb et al. (2011). However, they are in accordance with continuum mechanics theory. Non-linearity actually characterises all of the considered fields and increases for increasing non-uniformity and decreasing relative stiffness between the energy pile and the soil. The thermo-mechanical schemes proposed in this work may also be applied considering the following (which also applies to the original schemes): (i) greater magnitudes of applied loads cause linearly greater variations of the stress, strain and displacement along energy piles without any movement of the null points only as long as linear (thermo-)elasticity theory is employed (Rotta Loria et al. 2015); (ii) heating and cooling thermal loads cause a symmetrical response of energy piles for the same applied temperature change only as long as reversible conditions are ensured (Rotta Loria and Laloui 2016; Rotta Loria and Laloui 2017a); and (iii) the response of energy piles is a predominant function of the thermal expansion coefficient of the pile and the applied temperature change only in the usual situations where the soil-pile thermal expansion coefficient ratio reads $X \leq 1$ (Bourne-Webb et al. 2016; Rotta Loria and Laloui 2017b, c).

The mechanical response of an energy pile with no base and head restraints is depicted in Fig. 1. For the case of vertical mechanical loading only (cf., Fig. 1(a)), Eq. (1) can be written as

$$P + Q_{s,mob}^{m} = 0 \tag{7}$$

The application of an axial mechanical load to the pile head causes an approximately linearly decreasing distribution of compressive vertical stress σ_z along the pile and uniform and approximately constant distributions of positive shear stress τ at the pile-soil interface and downward pile displacement w with depth z. The higher the pile stiffness, the more uniform and linear the distribution of σ_z with z, and the more uniform and constant the distributions of τ and w with z. Soil layering causes a less uniform distribution of all the considered variables.

For the case of thermal loading only (cf., Fig. 1(b, c)), Eq. (1) reads

$$Q_{s,mob}^{th} = Q_{s,mob,up} + Q_{s,mob,down} = 0 \tag{8}$$

The application of a heating or cooling thermal load to the pile causes a non-linear distribution of σ_z with z, which is characterised by a maximum that coincides with the mid-length of the energy pile, where the null points of the vertical displacement and shear stress are also located. The application of a heating thermal load mobilises negative shear stress and causes heave for the energy pile portion above the null points, while it mobilises positive shear stress and causes settlement for the pile portion below the null points. The shear stress and vertical displacement caused by a heating thermal load develop in the opposite direction compared to those caused by a mechanical load above the null points, whereas these develop in the same direction below the null points. The opposite is true for a cooling thermal load. Shear stress and vertical displacement evolve approximately linearly with depth. The higher the pile stiffness, the more uniform the evolution of σ_z with z, and the lower the variation of σ_z for the same

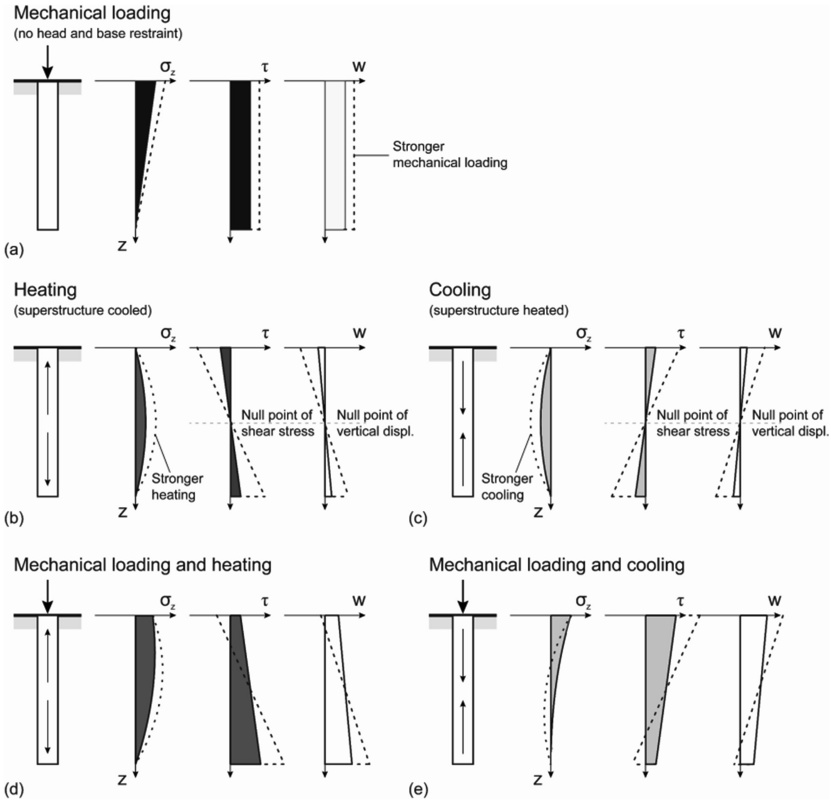

Fig. 1. Schemes for energy piles characterised by no base and head restraints.

applied thermal load. Similarly, the higher the pile stiffness, the more uniform the evolutions of τ and w but the higher their variation.

For the case of mechanical and thermal loading (cf., Fig. 1(d, e)), Eq. (1) can be rewritten as

$$P + Q_{s,mob} = P + Q^{m}_{s,mob} + Q^{th}_{s,mob} = 0 \tag{9}$$

The distributions of stress and displacement can be obtained via superposition of the previous ones. Tensile stress along the energy piles can arise for low magnitudes of applied mechanical loads and significant cooling.

The mechanical response of an energy pile with base or head restraints is depicted in Fig. 2. For the case of vertical mechanical loading only (cf., Fig. 2(a, b)), Eq. (1) can be rewritten as

$$P + Q^{m}_{s,mob} + Q^{m}_{b,mob} = 0 \tag{10}$$

where only the base restraint is present, whereas

$$P + \pi \frac{D^2}{4} K_h w(z=0) + Q^m_{s,mob} = 0 \tag{11}$$

where only the head restraint is present.

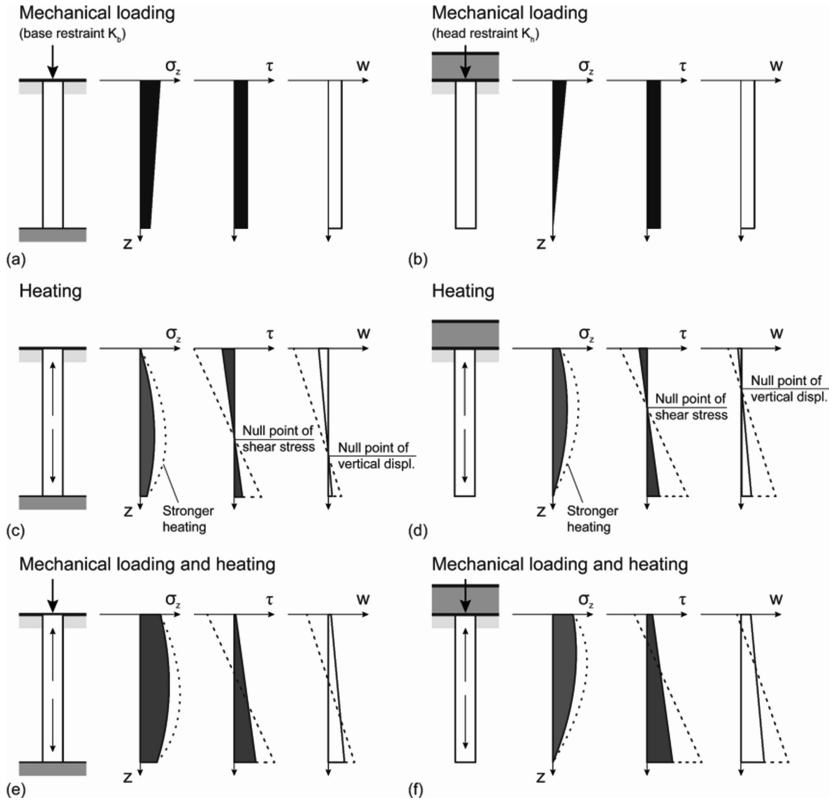

Fig. 2. Schemes for energy piles characterised by base or head restraints.

When a base restraint is present, a greater average vertical stress σ_z and lower shear stress τ and vertical displacement w develop along the pile compared to the case of no base and head restraints. This phenomenon arises because of the contribution provided by the base capacity to the vertical pile equilibrium.

When a head restraint is present, a smaller average vertical stress σ_z and lower shear stress and vertical displacement variations develop along the pile compared to the case of no base and head restraints. This phenomenon arises because the head restraint reduces the effect of the downward mechanical load. This effect vanishes when the interplay between the mechanical load and the head restraint is not considered because the latter term is neglected.

For the case of heating only (cf., Fig. 2(c, d)), Eq. (1) reads

$$Q_{s,mob}^{th} + Q_{b,mob}^{th} = 0 \tag{12}$$

where only the base restraint is present, whereas

$$\pi \frac{D^2}{4} K_h w(z=0) + Q_{s,mob}^{th} = 0 \tag{13}$$

where only the head restraint is present.

Different from the situation where no base or head restraints are present, when either a base or head restraint is present, vertical stress σ_z is generated at the restrained pile end by the applied thermal load. The vertical stress distribution is greater than that in the case with no base and head restraints. The null points of the vertical displacement and shear stress do not coincide but are shifted towards the region of the system characterised by the higher restraint. A cooling thermal load yields a symmetrical pile response. In reality, the reduction of the compressive stress experienced at the pile toe for the case where a base restraint is present can attain at most the sum of any vertical mechanical load applied to the pile and its weight. This occurs because soils generally cannot withstand tensile stress.

For the case of mechanical and heating thermal loading (cf., Fig. 2(e, f)), Eq. (1) can be rewritten as

$$P + Q_{s,mob} + Q_{b,mob} = 0 \tag{14}$$

where the base restraint is present, whereas

$$P + \pi \frac{D^2}{4} K_h w(z=0) + Q_{s,mob} = 0 \tag{15}$$

where the head restraint is present. The distributions of stress and displacement can be obtained via superposition of the previous ones.

The mechanical response of an energy pile with base and head restraints is depicted in Fig. 3. Two different cases involving a base restraint equal to the head restraint and a base restraint equal to one-half of the head restraint are shown. For the case of vertical mechanical loading only (cf., Fig. 3(a, b)), Eq. (1) reads

$$P + \pi \frac{D^2}{4} K_h w^m(z=0) + Q_{s,mob}^m + Q_{b,mob}^m = 0 \tag{16}$$

In the proposed schemes, the effect of the presence of the slab on the influence of the mechanical load on the pile response is considered. Hence, lower developments of vertical stress and shear stress as well as of vertical displacement are observed for a higher head restraint, compared to the case of a base restraint only. This behaviour may be expected in reality. However, many analyses and designs usually do not account for the interplay between the action of the mechanical load and the head restraint, neglecting the latter term.

For the case of heating only (cf., Fig. 3(c, d)), Eq. (1) reads

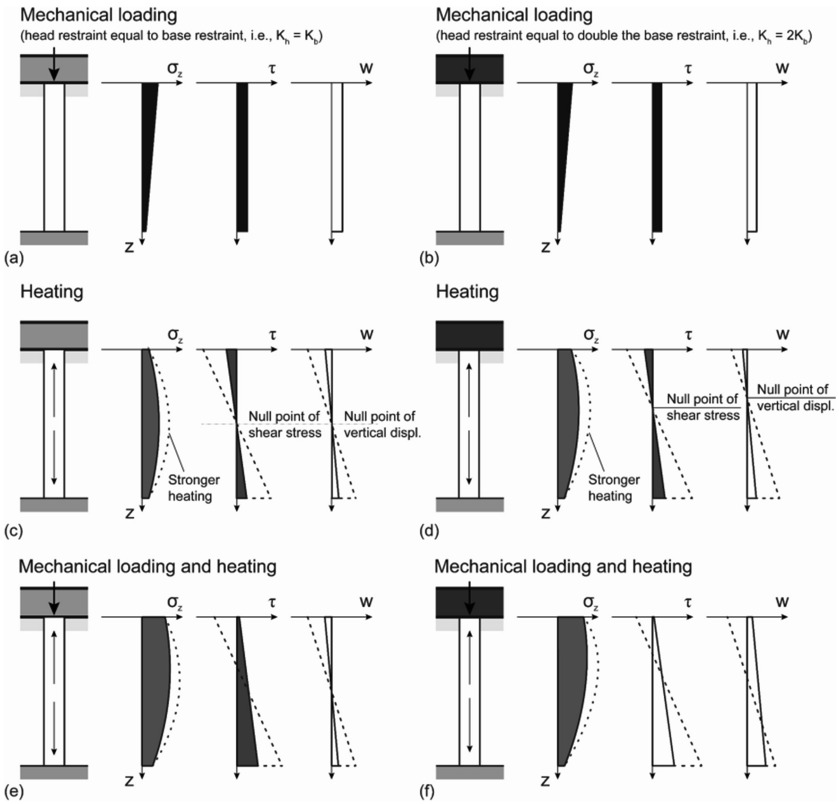

Fig. 3. Schemes for energy piles characterised by base and head restraints.

$$\pi \frac{D^2}{4} K_h w^{th}(z=0) + Q_{s,mob}^{th} + Q_{b,mob}^{th} = 0 \tag{17}$$

The vertical stress σ_z caused by the thermal load is characterised by a symmetrical distribution with depth z when the base and head restraints are of the same magnitude, whereas by an asymmetrical distribution when different magnitudes characterise the end restraints. Higher stress develops towards the region of the system characterised by higher restraint. The higher the restraint provided by the end conditions, the higher the vertical stress and the lower the mobilised shear stress and vertical displacement.

For the case of mechanical and heating thermal loading (cf., Fig. 3(e, f)), Eq. (1) governs the system, the response of which can be obtained via superposition of the analysed situations.

3 Concluding Remarks

This paper presented simplified yet representative schemes of relevant stress, strain and displacement evolutions caused along energy piles by mechanical and thermal loads. Being based on linear thermo-elasticity theory, the presented schemes can be superimposed in a wide range of design situations where the response of energy piles is reversible and may serve as a reference for developing preliminary considerations related to more involved situations characterised by irreversible conditions.

References

Bourne-Webb, P., Bodas Freitas, T., Freitas Assunção, R.: Soil–pile thermal interactions in energy foundations. Geotechnique **66**(2), 167–171 (2016)

Bourne-Webb, P.J., Amatya, B., Soga, K.: A framework for understanding energy pile behaviour. Proc. ICE Geotech. Eng. **166**(2), 170–177 (2011)

Bourne-Webb, P.J., Amatya, B.L., Soga, K., Amis, T., Davidson, C., Payne, P.: Energy pile test at Lambeth College, London: geotechnical and thermodynamic aspects of pile response to heat cycles. Geotechnique **59**(3), 237–248 (2009)

Laloui, L., Moreni, M., Vulliet, L.: Comportement d'un pieu bi-fonction, fondation et échangeur de chaleur. Can. Geotech. J. **40**(2), 388–402 (2003)

Rotta Loria, A.F., Gunawan, A., Shi, C., Laloui, L., Ng, C.W.W.: Numerical modelling of energy piles in saturated sand subjected to thermo-mechanical loads. Geomech. Energy Environ. **1** (1), 1–15 (2015)

Rotta Loria, A.F., Laloui, L.: The interaction factor method for energy pile groups. Comput. Geotech. **80**, 121–137 (2016)

Rotta Loria, A.F., Laloui, L.: Displacement interaction among energy piles bearing on stiff soil strata. Comput. Geotech. **90**, 144–154 (2017a)

Rotta Loria, A.F., Laloui, L.: Group action effects caused by various operating energy piles. Geotechnique (2017b). https://doi.org/10.1680/jgeot.17.p.213

Rotta Loria, A.F., Laloui, L.: Thermally induced group effects among energy piles. Geotechnique **67**(5), 374–393 (2017c)

Rotta Loria, A.F., Vadrot, A., Laloui, L.: Analysis of the vertical displacement of energy pile groups. Geomech. Energy Environ. (2018). https://doi.org/10.1016/j.gete.2018.04.001

Thermo-Hydro-Chemo-Mechanical Behaviour of Geomaterials

Experimental Study on Erosive Effects of Sodium Hydroxide Solution on Compacted Clay

Yu Song, Xuejun Chen, Hongbin Chen(✉), Lijie Chen, Xiang Huang, Xing Zhou, and Yue Yang

College of Civil Engineering and Architecture, Guilin University of Technology, Guilin, China
344036473@qq.com

Abstract. Direct shear tests were performed on red clay soaked in different concentrations of sodium hydroxide solution and different soaking time. The microstructure of red clay samples was observed by scanning electron microscopy (SEM). The results show that the shear strength of red clay soaked in sodium hydroxide solution decreases as the soaking time and the sodium hydroxide solution concentration increases. The sodium hydroxide solution eroded the cement in the red clay, resulting in the increase of pores between clay particles. The fractal dimension of the red clay particles increased with the increase of the corrosion. The average particle size and average particle area of the red clay particles decrease with the increase of the sodium hydroxide corrosion, and the shape of the soil particles becomes irregular.

1 Introduction

Urban domestic wastewater containing detergents, chemical wastewater from phosphate fertilizer plants or paper mills, ore-washing wastewater generated from ore dressing plants and landfill leachate are alkaline. The complex physical and chemical reactions of lye and soil particles will lead to the destruction of the original structure of the soil. When the soil is soaked in a high concentration of sodium hydroxide solution, its shear strength, cohesion and internal friction angle increase, and there is a maximum value. When the red clay is soaked in a low concentration of sodium hydroxide solution, its shear strength decreases (Chen 2017). When the silt clay is consolidated in alkaline environment, its compressibility and rebound modulus increase with the increase of alkalinity (Chunpeng 2008). The plasticity index of clay decreases in alkaline environment and the plastic limit increases (Qian and Cuihua 2001). After the foundation soil has been eroded by lye, it turns black and soft, and even changes from hard plastic to cast plastic (Gu 1988).

In summary, some scholars have studied the effect of alkaline solution on the mechanical properties of red clay, but no scholar has analyzed the microstructure of red clay soaked in alkali solution. In this experiment, a direct shear test was performed on red clay soaked in sodium hydroxide solution to study the mechanical properties of red clay in different concentrations of sodium hydroxide solution and different soaking

A. Ferrari and L. Laloui (Eds.): SEG 2018, SSGG, pp. 229–235, 2019.
https://doi.org/10.1007/978-3-319-99670-7_29

time. The microstructure of red clay soaked in sodium hydroxide solution was observed by scanning electron microscopy to study the change of the microstructure of the clay in the lye.

2 Experimental Materials, Devices and Methods

2.1 Experimental Materials

The red clay used in this experiment was taken from Yanshan, Guilin. The mineral composition of the red clay was measured by X-ray diffractometer as listed in Table 1. The natural dry density of red clay is 1.65 g/cm^3, and its physical and mechanical parameters are listed in Table 2.

Table 1. Mineral composition of red clay

SiO_2	Fe_2O_3	CaO	K_2O	Na_2O
68.7%	0.86%	0.69%	23.32%	6.43%

The alkaline solution used in the experiment was a sodium hydroxide solution with concentrations of 0%, 3%, 6%, and 12%. The sodium hydroxide used to formulate the solution is a solid particle, neglecting the effect of the volume of sodium hydroxide solid particles on the volume of the solution because of its small volume ratio to the formulation solution.

2.2 Preparation of the Soil Specimens

The air-dried red clay passing through the sieve with a diameter of 2 mm was taken and used to prepare soil specimens with a moisture content of 24.5% (optimal moisture content). The wet red clay was made into specimens with a height of 20 mm and a diameter of 61.8 mm. The specimens were placed in an calorstat (20 °C) for 10 days and then soaked in a sodium hydroxide solution (keeping the temperature at 25 °C and a humidity of 95%).

2.3 Experimental Device

The experiment used a ZJ strain-controlled direct shear apparatus with a shear rate of 0.8 mm/min. Hitachi's S-3400N scanning electron microscope was used to observe the microstructure of the specimens.

Table 2. Physical and mechanical properties of red clay

Physical quantity	Value
Maximum dry density (g/cm^3)	1.87
Optimum moisture content (%)	24.5
Liquid limit water content (%)	58.5
Plastic limit moisture content (%)	36
Plasticity index (%)	22.5
Particle size distribution (> 0.05 mm) (%)	22
Particle size distribution (0.05 ~ 0.005 mm) (%)	38
Particle size distribution (0.005 ~ 0.002 mm) (%)	33
Particle size distribution (< 0.002 mm) (%)	7

3 Results Analysis and Discussion

3.1 Shear Strength of Soil Specimens

The direct shear tests were carried out with four pressures (100 kPa, 200 kPa, 300 kPa and 400 kPa).

From Figs. 1 and 2 can be drawn as follows:

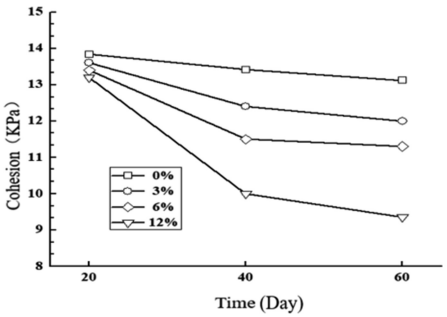

Fig. 1. Cohesion of red clay as a function of time and sodium hydroxide concentration

With the prolongation of soaking time, the cohesion and internal friction angle of red clay soaked in pure water decrease, but their changes are not significant. The cohesion decreases from 13.84 kPa to 13.14 kPa, and the internal friction angle decreases from 10.18° to 10.01°.

At the same soaking time, the cohesion of red clay decreases with the concentration of sodium hydroxide solution. The cohesion of red clay rapidly decreases when it is soaked in sodium hydroxide solution for 20 days to 40 days, and the cohesion decreases slowly when it is soaked for more than 40 days.Take a specimen soaked in 12% sodium hydroxide solution for example. When the red clay specimens were soaked in sodium hydroxide solution for 20 days to 40 days, the cohesion decreases from 13.2 kPa to 11.3 kPa. When the red clay specimens are soaked for 40 days to 60 days, the cohesion decreases from 11.3 kPa to 10.2 kPa, and the changes are not significant.

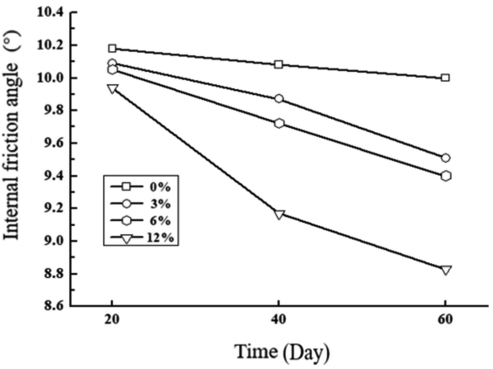

Fig. 2. Internal friction angle of red clay as a function of time and sodium hydroxide concentration

The internal friction angle of red clay decreases with the increase of the concentration of sodium hydroxide solution and the soaking time, but the changes are not significant. When soaked in 12% sodium hydroxide solution for 60 days, the internal friction angle of red clay decreases from 9.9 to 8.9.

3.2 Analysis of Moisture Content of Soil Specimens

From Fig. 3, it can be seen that:

The red clay specimen soaked in a concentration of 0% sodium hydroxide solution showed a slow increase in water content, which is maintained between 35.0% and 35.6% with a growth rate of only 1.71%.

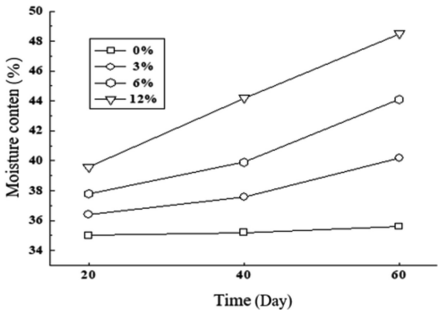

Fig. 3. Graph of water content of red clay as a function of time and solution concentration

In red clay soaked in the same concentration of sodium hydroxide solution, the moisture content increases with the soaking time. Taking a specimen soaked in a 6% sodium hydroxide solution as an example, the water content of the soil specimen after soaking for 20 days is 36.4%, and the water content after soaking for 60 days is 40.2%.

The growth rate of water content of red clay soaked in 6% sodium hydroxide solution is 10.44%, which is far more great than that of red clay soaked in 0% sodium hydroxide solution. This shows that the moisture content of red clay soaked in sodium hydroxide solution is higher than that of red clay soaked in pure water.

The moisture content of red clay at the same soaking time increases with the concentration of sodium hydroxide solution. Taking red clay soaked for 40 days as an example, the moisture content of red clay is 44.2% when soaked in 12% sodium hydroxide solution, which is significantly greater than the 39.9% moisture content of red clay soaked in 3% sodium hydroxide.

3.3 Microstructure Characteristics of Red Clay Specimens

It can be seen from Fig. 4 that the clay surface was not eroded by the sodium hydroxide solution has few pores and is arranged in a laminated manner. With the increase of corrosion, the pores on the surface of red clay increase, forming a structural system composed of granular and massive particles, and the soil structure becomes loose. As the concentration of the sodium hydroxide solution increases, the cement in the red clay is corroded, resulting in a decrease in the volume of the cement and an increase in the pore volume between the clay particles.

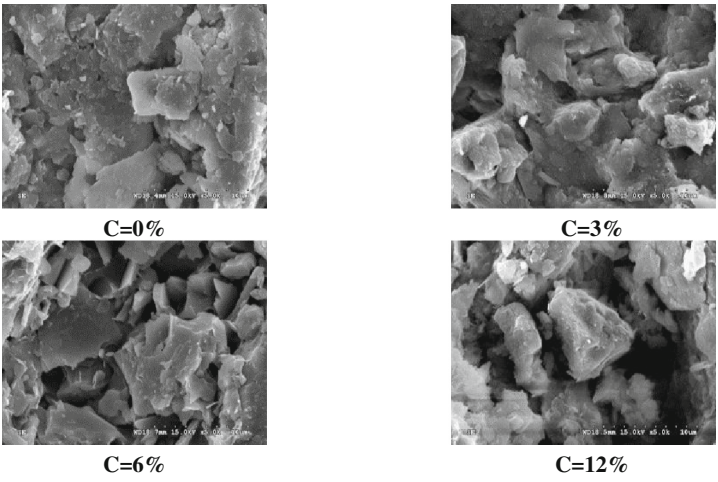

Fig. 4. Microstructure of soil specimens soaked for 60 days in different concentrations of sodium hydroxide

In order to analyz the influence of concentration of sodium hydroxide solution on the microstructure parameters of clay, the average particle size and particle area were calculated by the image analysis program. The statistical results are showned in Fig. 5. The average particle size of red clay decreases with increasing concentration of sodium hydroxide solution, and at a concentration of 0% to 3%, the red clay particle size changes little. When the concentration of sodium hydroxide increases from 6% to 12%,

the average particle size of red clay decreases rapidly. The decrease of the average particle size reflects the erosion of red clay by the sodium hydroxide solution, resulting in an uneven particle size distribution of the red clay. As the red clay erosion increases, the clay particle area decreases rapidly from 1000000 um^2 in 0% concentration to 25000 um^2 in 12% concentration.

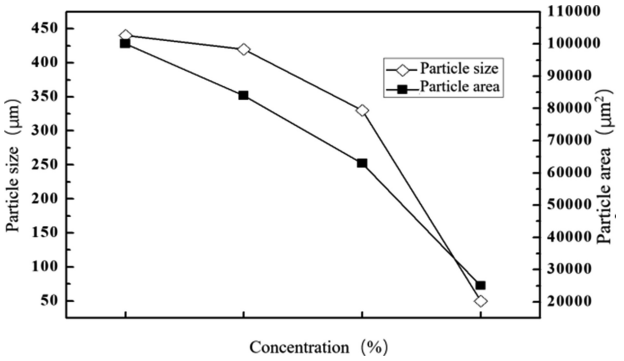

Fig. 5. Variation of mean diameter and area of particle soaked by sodium hydroxide solution

The fractal dimension reflects the complexity of the particle profile curve. The function diagram in Fig. 6 shows that the concentration of sodium hydroxide has a significant effect on the fractal dimension of the red clay particles, from the initial 1.04 to the final 7.6, the growth rate is 630%, which reflects the corrosion of red clay by sodium hydroxide solution.

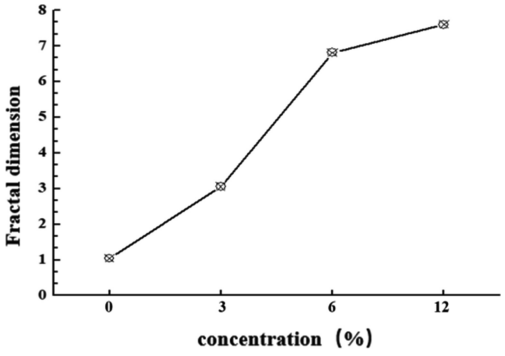

Fig. 6. Fractal dimension change of clay particles

Figure 7 shows the microstructure of red clay soaked in a 12% sodium hydroxide solution for different soaked times. It can be seen that the red clay has a compact structure in the early stage of soaking, and the clay particle size is uniform, indicating that the sodium hydroxide solution is not a severe red earth erosion.

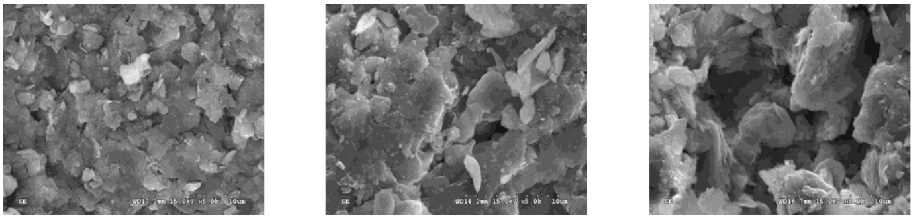

(a) T=20d (b) T=40d (c) T=60

Fig. 7. The microstructure of the soaked clay with 12% sodium hydroxide solution changes with time

As the soaking time increases, the surface of the red clay becomes rough, the soil particles begin to gather, the arrangement is loose and disorderly, and the honeycomb structure appears, and the pore size between the soil particles expands. When soaked for 60 days, the pores of red clay become significantly larger, and the agglomerated soil particles show a flocculent structure.

4 Conclusion

With the increase of sodium hydroxide concentration and soaking time, the cohesion and internal friction angle of clay show a decreasing tendency. At the initial stage of soaking, the cohesive force decreases sharply and tends to be stable in the later period.

From the microstructure of red clay, it can be seen that when the erosion concentration increases, the voids of the red clay increase, the average particle size and area of the particles decrease, and the particle fractal dimension increases, indicating that the sodium hydroxide solution has a significant effect on the red clay erosion.

The main reason for the decrease of the shear strength of red clay is that the sodium hydroxide solution chemically reacts with the cement in red clay, the cement is eroded, the connection between soil particles weakens, and the pores become larger.

References

Chen, J.: Experimental study on shear strength of alkali-contaminated red clay. J. Yangtze River Sci. Res. Inst. **34**, 94–100 (2017). https://doi.org/10.11988/ckyyb.20160816

Zhu, C.: Experimental study on the compressive properties of acid-base contaminated soils. Chin. J. Geotech. Eng. **30**, 1477–1483 (2008). https://doi.org/10.3321/j.issn:1000-4548,2008.10.010

Qian, S., Cuihua, L.: Experimental study on the effect of acid and alkali on the physical properties of clay. J. Wuhan Univ. Hydraul. Electr. Eng. **34**, 84–87 (2001). https://doi.org/10.3969/j.issn.1671-8844.2001.05.019

Gu, J.: Effects of acid-base waste on erosion of foundation soil. Chin. J. Geotech. Eng. **4**, 72–78 (1988). https://doi.org/10.3321/j.issn:1000-4548.1988.04.008

Experimental Study on Strength Characteristics of Red Clay Under Different Particle Size of Calcium Carbonate

Xuejun Chen, Lijie Chen, Yu Song(✉), Hongbin Chen, and He Wang

College of Civil Engineering and Architecture,
Guilin University of Technology, Guilin, China
songyull9@l26.com

Abstract. The calcium carbonates of different particle sizes were incorporated into red clay, and the consolidated undrained triaxial test on red clay was performed by the TKA-TTS-1 triaxial apparatus to analyze the effects of different particle sizes of calcium carbonate and the different incorporation rates of calcium carbonate on the mechanical properties of red clay. The results show that the incorporation of calcium carbonate reacts with the cement formed by free ferric oxide in red clay, resulting in a decrease in cohesion and changing the strength of red clay. With the increase of nano-calcium carbonate incorporation rate, the shear strength of red clay decreased, and it showed a trend of decreasing first and then increasing. Because the specific surface area of nano-calcium carbonate is larger than that of ordinary calcium carbonate, it has a significant effect on the mechanical properties of red clay.

1 Introduction

After decades of research, the fields involved in nanomaterials have become more and more extensive. When the particle size of the material becomes extremely small, they will have great changes in optical properties, electrical properties, magnetic properties, mechanical properties, thermodynamic properties, surface properties and interface properties.

Nano-calcium carbonate is a kind of mineral micro-powder material with low activity. Incorporating nano-calcium carbonate into bitumen significantly improves the high temperature performance of the bitumen (Liu et al. 2005). Nano-calcium carbonate improves the particle size distribution of the concrete. It fills the gaps between the materials, enhances the micro-aggregate effect, and helps to increase the strength of the concrete in the same water-binder ratio (Meng et al. 2008). The incorporation of nano-calcium carbonate effectively improves the compressive strength and splitting strength of the concrete, and the nano-calcium carbonate fills the voids of the material, reduces the spacing of the bubbles, significantly increases the number of freeze-thaw cycles of the concrete, and delays the attenuation of the relative dynamic elastic modulus of the concrete (Zhou 2016). However, the effect of calcium carbonate incorporation on the mechanical properties of red clay has not been studied so far. In this paper, calcium carbonate with different particle sizes was incorporated into red clay to study the effect of calcium carbonate particle size on the mechanical properties of red clay.

A. Ferrari and L. Laloui (Eds.): SEG 2018, SSGG, pp. 236–242, 2019.
https://doi.org/10.1007/978-3-319-99670-7_30

2 Experimental Research Overview

2.1 Experimental Materials

The red clay used in the experiment was taken from the 3–4 m underground in Yanshan district, Guilin. The dried red clay was crushed and sieved through a 2 mm-diameter soil sieve and then placed in a storage tank for later use. The chemical composition of the red clay used in the experiment are listed in Table 1, and the basic physical indexes are listed in Table 2.

Table 1. The main chemical composition of red clay

Mineral elements	SiO_2	Fe_2O_3	CaO	K_2O	Na_2O
Content	69.60%	1.16%	0.79%	22.42%	6.03%

Table 2. Basic physical indexes of red clay

Physical quantity	Index
Maximum dry density (g/cm^3)	1.67
The best moisture content (%)	30
Liquid limit moisture content (%)	59.5
Plastic limit moisture content (%)	37.0
Plasticity index (%)	22.5
Particle size distribution (>0.05 mm) (%)	21.5
Particle size distribution (0.05 ~ 0.005 mm) (%)	37.0
Particle size distribution (0.005 ~ 0.002 mm) (%)	33.0
Particle size distribution (<0.002 mm) (%)	8.5

Three types of calcium carbonate were used in the experiment. The particle sizes of calcium carbonate are listed in Table 3. The scanning electron microscope (SEM) of calcium carbonate particles are shown in Fig. 1(a), (b) and (c). Calcium carbonate III has a particle size of 0.1 nm to 100 nm and belongs to nano-calcium carbonate.

Table 3. The particle size of calcium carbonate

Number	Average particle size (μm)	PH value (10% suspension)
I	38	9.0–10.0
II	10	9.0–10.0
III	0.8	8.0–10.0

2.2 Preparation of Soil Specimens

The incorporation rate in this paper refers to the ratio of the mass of calcium carbonate to the total mass of red clay and calcium carbonate. The moisture content of the red clay in this experiment was set at 30% (the optimum moisture content of red clay was 30%). In order to mix the calcium carbonate with the red clay evenly, the calcium

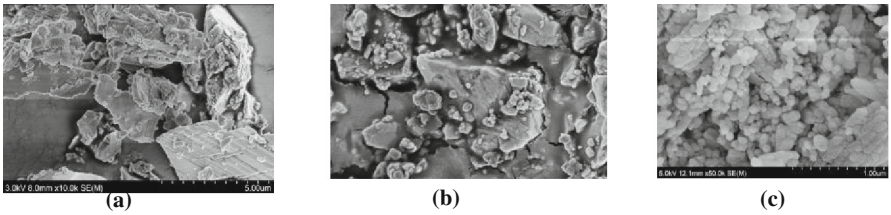

Fig. 1. (SEM) image of calcium carbonate. (a) (SEM) image of calcium carbonate I. (b) (SEM) image of calcium carbonate II. (c) (SEM) image of calcium carbonate III.

carbonate was added to the air-dried red clay and then stirred by a whisk for fifteen minutes. Spray a predetermined amount of pure water into the red clay and seal the wet red clay for 24 h. When the red clay's moisture content is within (30 ± 1)%, it is made into a cylindrical specimen with a height of 80 mm and a diameter of 39.1 mm. The air in the specimens was evacuated and the specimens were soaked in pure water for 24 h. After the sample was saturated, a consolidated undrained triaxial test was performed.

2.3 Experimental Apparatus and Experimental Scheme

TKA-TTS-1 triaxial apparatus produced by Nanjing TKA Technology Co., Ltd. was used in the Experiment. The shear rate of the consolidated undrained triaxial test was 0.8 mm/min, and the experimental variables are listed in Table 4.

Table 4. Test control indicators

The number of calcium carbonate incorporated	Incorporation rate				Soil specimen dry density (g/cm^3)	Soil specimen moisture content	Confining pressure (KPa)			
I	0%	1%	2%	4%	1.4	30%	100	200	300	400
II	0%	1%	2%	4%	1.4	30%	100	200	300	400
III	0%	1%	2%	4%	1.4	30%	100	200	300	400

3 Experimental Results and Analysis

3.1 Effect of Calcium Carbonate with Different Partical Size on Cohesion and Internal Friction Angle of Red Clay

The effect of calcium carbonate with different particle sizes on the cohesion of red clay is shown in Fig. 2(a). The effect of calcium carbonates II and III on the cohesion of red clay is similar. With the increase in the incorporation of calcium carbonate II and calcium carbonate III, the cohesion of the red clay first decreased and then increased, and finally it tended to be stable. With the increase in the incorporation rate of calcium carbonate I, the cohesion of red clay decreases, and it tends to stabilize when the incorporation rate exceeds 2%.

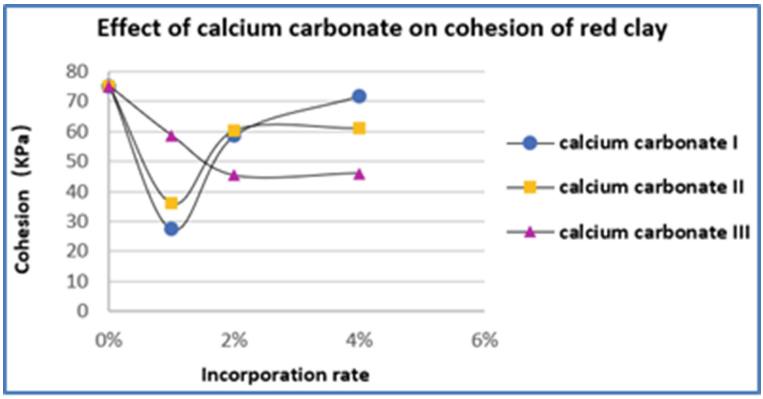

(a)

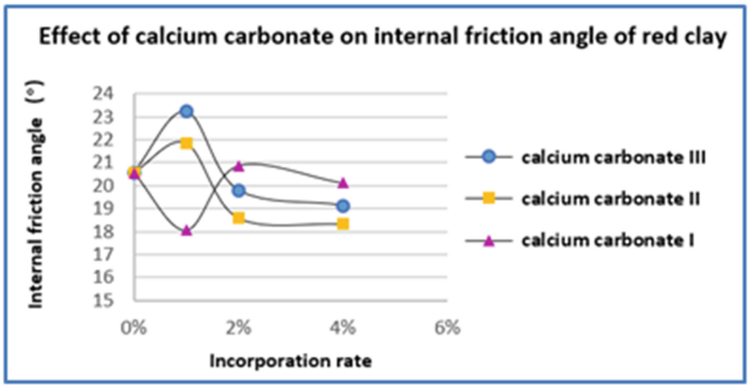

(b)

Fig. 2. Effect of calcium carbonate on red clay

The effect of calcium carbonate with different particle sizes on the internal friction angle of red clay is shown in Fig. 2(b). The effect of calcium carbonate II and III on the internal friction angle of red clay is similar. With the increase of the incorporation ratio of calcium carbonate II and III, the friction angle of red clay first increased and then decreased, and finally it became stable. With the increase of the incorporation rate of calcium carbonate I, the friction angle of red clay first decreased and then increased, and finally it became stable.

When the incorporation rate of three kinds of calcium carbonate is the same, calcium carbonate III has the greatest effect on red clay.

3.2 Effect of Different Calcium Carbonate Sizes on Shear Strength of Red Clay

From Fig. 3(a), the shear strength of red clay mixed with calcium carbonate I is reduced, but the increase of incorporation rate has little effect on the shear strength of red clay.

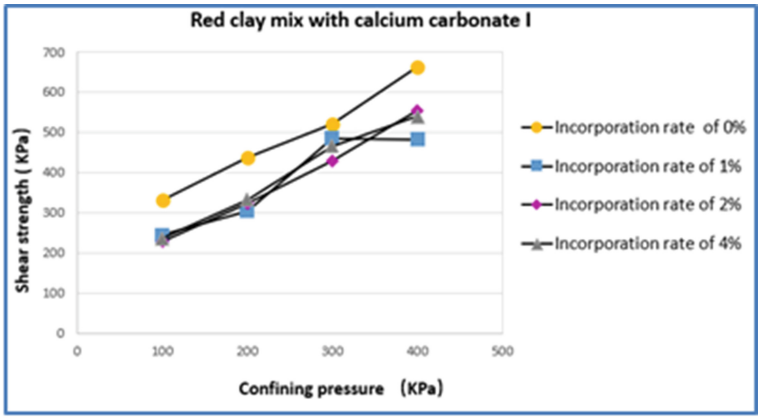

(a)

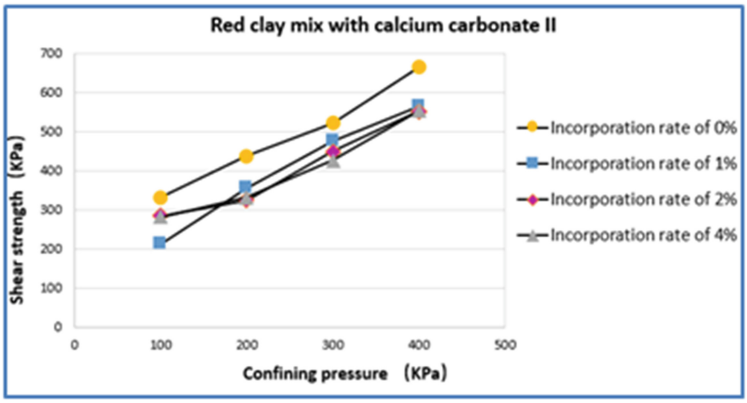

(b)

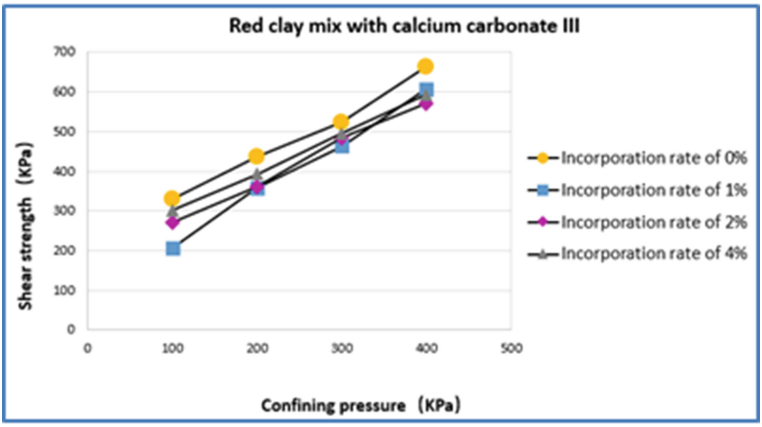

(c)

Fig. 3. Shear strength-confining pressure curve of calcium carbonate red clay

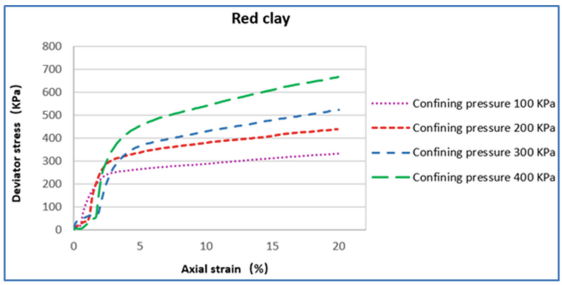

(a)

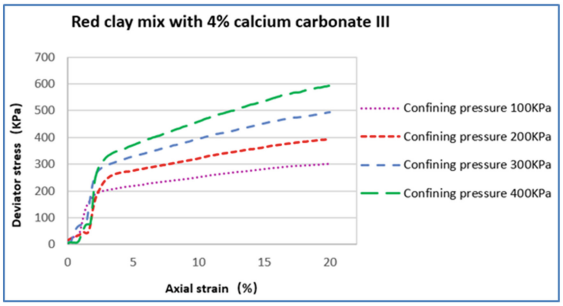

(b)

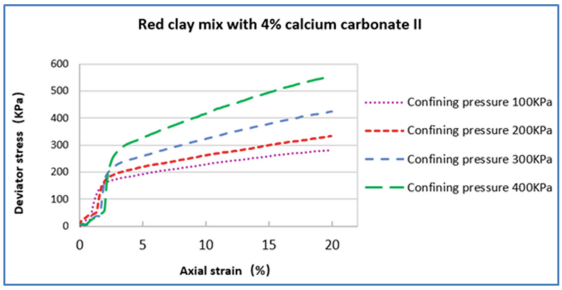

(c)

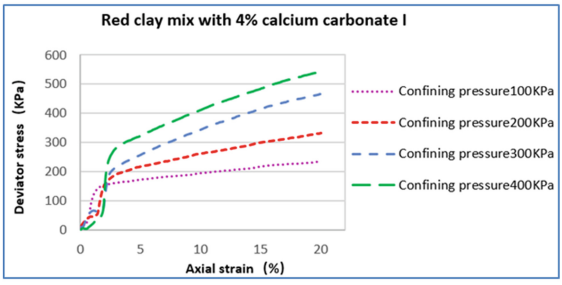

(d)

Fig. 4. (a), (b), (c): Calcium carbonate red clay stress-strain curve. (d) Calcium carbonate red clay stress-strain curve

From Fig. 3(b), the shear strength of red clay gradually decreases as the incorporation rate of calcium carbonate II increases. From Fig. 3(c), the shear strength of red clay decreases first and then increases as the incorporation rate of calcium carbonate III increases. When the incorporation rate reaches 4%, the shear strength increases to the maximum.

3.3 Triaxial Compression Stress - Strain Strength Characteristics

Consolidated undrained triaxial test obtained saturated calcium carbonate red clay stress strain diagram were showned in Fig. 4. The particle size of calcium. carbonate has little effect on the characteristics of stress-strain curve. The stress-strain curve of red clay is obviously affected by confining pressure.

4 Conclusion

The nano-calcium carbonate has a large specific surface area, and when the calcium carbonate is in the same incorporation rate, the nano-calcium carbonate has a significant influence on the mechanical properties of the red clay. With the increase of nano-calcium carbonate content, the shear strength of red clay decreased first and then increased.

Calcium carbonate with different particle sizes and different dosages has little effect on the stress-strain curve of red clay.

The incorporation of calcium carbonate reacts with the cementitious material formed by free ferric oxide in red clay, resulting in weaker cohesion and changing the strength characteristics of red clay.

The addition of calcium carbonate changes the optimum moisture content of laterite and reduces the shear strength of red clay.

References

Liu, D., Luo, L., Yue, A., Chen, L.: Study on nanometer calcium carbonate modified. Highway **06**, 145–148 (2005). https://doi.org/10.3969/j.issn.0451-0712.2005.06.032

Meng, T., Qian, Y., Qian, X., Shulin, Z.: Effect of nano-CaCO3 particles on cement hydration and interface properties. Rare Met. Mater. Eng. **S2**, 667–669 (2008). https://doi.org/10.3321/j.issn:1002-185X.2008.z2.175

Zhou, Y.: Effect of different nano-calcium carbonate content on mechanical properties and frost resistance of fly ash concrete. Sci. Technol. Eng. **28**, 277–281 (2016). https://doi.org/10.3969/j.issn.1671-1815.2016.28.051

Impact of Drained Heating and Cooling on Undrained Shear Strength of Normally Consolidated Clay

Radhavi Samarakoon, Ismaail Ghaaowd, and John S. McCartney(✉)

University of California San Diego, La Jolla, CA, USA
mccartney@ucsd.edu

Abstract. This study focuses on the effects of a heating-cooling cycle on the undrained shear strength of normally consolidated clay specimens. A clear increase in undrained shear strength was observed for specimens sheared after drained heating to an elevated temperature, while a further increase in undrained shear strength was observed for specimens sheared after a drained heating-cooling cycle. This is attributed to the permanent decrease in volume during drained heating followed by the elastic decrease in volume during drained cooling. The initial mean effective stress was also observed to play an important role in the magnitude of the increase in undrained shear strength, with greater increases observed for normally consolidated specimens with lower mean effective stresses.

1 Introduction

The impact of temperature on the shear strength of clays has been widely studied since the 1960's and several constitutive relationships have been developed to consider the impacts of stress history and drainage conditions (Laloui et al. 2014). General observations from the literature include: (1) temperature changes are not expected to affect the friction angle of clays (defined at peak or critical state conditions), (2) the undrained shear strength is dependent on the pore water pressure during shearing, the initial effective stress, and the void ratio; and (3) the drainage conditions during heating will lead to different trends in the shear strength. Shearing after undrained heating typically leads to a decrease in undrained shear strength associated with the increase in excess pore water pressures (and decrease in mean effective stress) during undrained heating, while shearing after drained heating leads to an increase in undrained shear strength for normally consolidated clays due to a reduction in void ratio during drained heating. One situation that has not been fully studied is shearing of normally consolidated clays after a drained heating-cooling cycle, such as that experienced by the soil surrounding a thermal drain system (Abuel-Naga et al. 2006). It is expected that plastic contraction will occur during drained heating, followed by elastic contraction during drained cooling. This implies that after cooling, specimens will have a slightly lower void ratio and should have a greater undrained shear strength than that observed during shearing after drained heating. However, it is not clear if the change in temperature will lead to a transition in the magnitude of excess pore water pressure during undrained shearing.

A. Ferrari and L. Laloui (Eds.): SEG 2018, SSGG, pp. 243–249, 2019.
https://doi.org/10.1007/978-3-319-99670-7_31

This study focuses on results from triaxial compression tests on saturated normally consolidated clay following different temperature paths and drainage conditions.

2 Methods

2.1 Materials

Kaolinite clay obtained from M&M Clays Inc. of McIntyre, GA was used in this study. As the clay has a liquid limit of 47% and a plasticity index of 19, the clay is classified as CL according to the Unified Soil Classification Scheme. The clay has a specific gravity of 2.6, and the slopes of the normal compression line (λ) and recompression line (κ) are 0.100 and 0.016, respectively. The excess pore water pressure during undrained heating of this clay was characterized by Ghaaowd et al. (2015), while the volume change during drained heating was characterized by Takai et al. (2016).

2.2 Experimental Setup

The nonisothermal triaxial compression tests were performed using the thermal triaxial system developed by Alsherif and McCartney (2015) that was further adapted for testing saturated clays by Takai et al. (2016). A schematic of the system is shown in Fig. 1. The cell is comprised of a Pyrex pressure vessel exhibiting low thermal creep while remaining transparent after repeated heating and cooling cycles. The temperature within the cell is controlled by circulating heated water from a temperature-controlled circulating bath through a stainless-steel pipe bent into a "U" shape over the specimen. A pump able to accommodate high fluid temperatures and pressures is used to circulate the cell water to ensure that it is uniformly mixed. The cell fluid temperature was monitored using a thermocouple and temperature recorder having a precision of 0.5 °C. The cell pressure and specimen backpressure were controlled using a pressure panel, and a temperature-corrected pore water pressure transducer was used to measure changes in pore water pressure during undrained heating and shearing. In addition to monitoring the drainage from the specimen during consolidation and drained heating and cooling, images of the specimens were taken using a high-resolution camera (model D610 from Nikon) during the tests to measure changes in volume using the approach of Uchaipichat et al. (2011).

2.3 Procedures

The clay specimens were prepared from sedimentation using an approach described by Ghaaowd et al. (2015), and trimmed specimens were backpressure-saturated in the thermal triaxial cell, which involved applying the cell pressure and backpressure in stages until reaching a value of Skempton's pore water pressure parameter B of at least 0.95. The specimens were then consolidated isotropically to a desired mean effective stress. Some specimens were sheared in undrained conditions at room temperature conditions to provide a baseline case for comparison. For the specimens tested at different temperatures, the drainage valves at the top and bottom of the specimen were

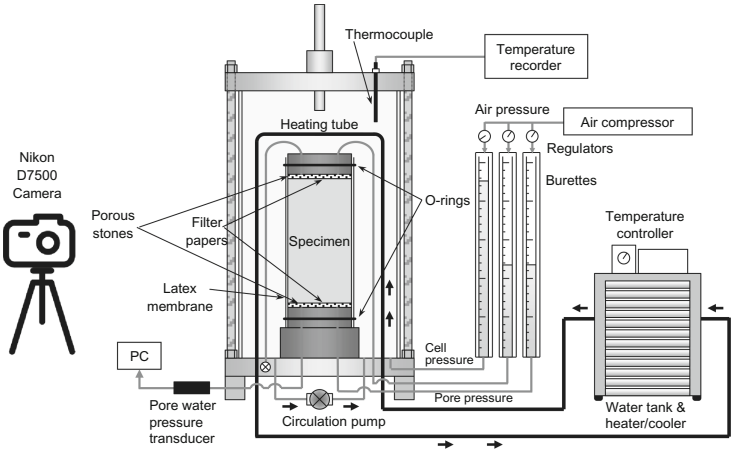

Fig. 1. Thermal triaxial setup

kept open during heating and cooling. Another set of specimens were heated from 23 to 66 °C at a relatively fast rate (0.2 °C/min) after which the elevated temperature was maintained until the volume change stabilized, after which the specimens were sheared in undrained conditions. The last set of specimens were heated from 23 to 66 °C in drained conditions, then cooled back to 23 °C before shearing in undrained conditions.

3 Results and Discussion

The principal stress difference versus axial strain results from three consolidated undrained triaxial compression tests conducted at a mean effective stress of 310 kPa following three different temperature paths are shown in Fig. 2. The OCR of 1.0 refers to the initial state of the specimen where it was normally consolidated prior to the application of any mechanical or thermal loading. An increase in the maximum principal stress difference can be observed for the specimen sheared after drained heating to 66 °C, and a further increase in undrained shear strength is observed for the specimens sheared after drained heating to 66 °C followed by drained cooling back to 23 °C. The shapes of the stress-strain curves for the three tests were relatively similar despite different peak values. The corresponding reductions in the excess pore water pressure for each of the three tests are shown in Fig. 2(b). Although the magnitude of excess pore water pressure was similar in all three tests, all three specimens showed positive strains during shearing as expected for normally consolidated specimens. The effective stress paths for the three tests are shown in Fig. 3. An interesting observation is that the maximum principal stress values fall onto the same peak failure envelope.

The results from tests performed at other initial mean effective stresses are shown in Fig. 4. Like the observation drawn from the effective stress paths in Fig. 3, the results in Fig. 4 indicate that the specimens following different temperature paths tested at different initial mean effective stresses all fall onto the same peak failure envelope. The slope shown in Fig. 4 of 1.29 is not equal to the slope of the critical state line but

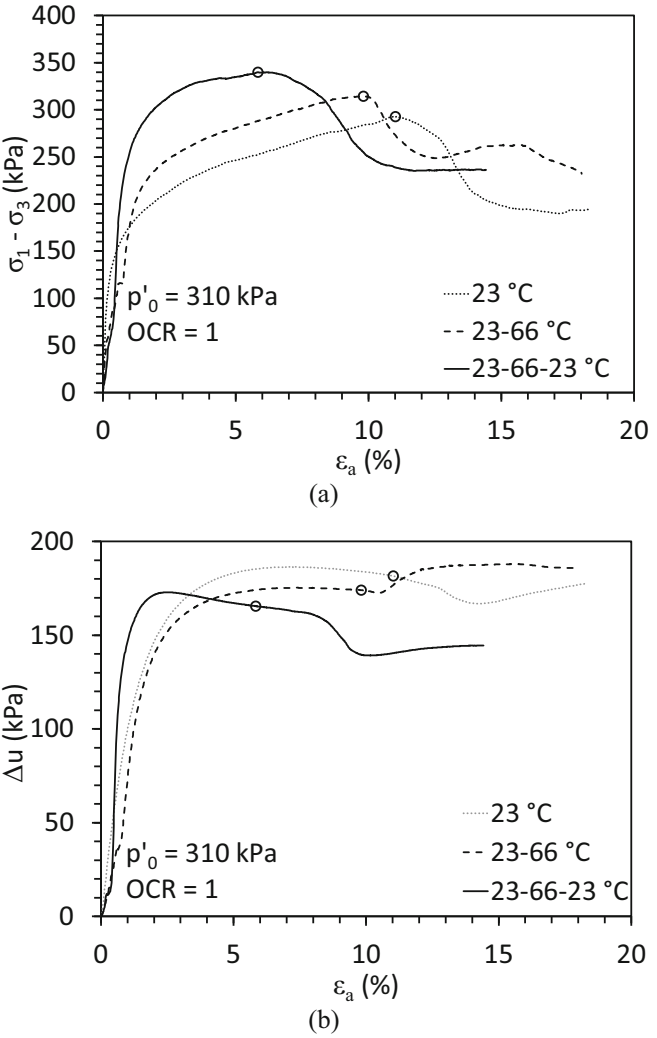

Fig. 2. Examples of consolidated undrained triaxial compression test results for the saturated clay following different temperature paths (points denote the maximum principal stress): (a) maximum principal stress difference vs. axial strain (b) excess pore water pressure vs. axial strain

corresponds to the slope of the peak failure envelope. Assuming that the maximum principal stress differences from each of the tests corresponds to the undrained shear strength of the soil, the trends in the undrained shear strength for specimens sheared under room temperature conditions, after heating, and after a heating-cooling cycle are shown in Fig. 5(a). A clear increase in undrained shear strength after a heating-cooling cycle is observed. The percent increase in undrained shear strength following a heating-cooling cycle is appreciable, and ranges from 16 to 54%. The percent increase in

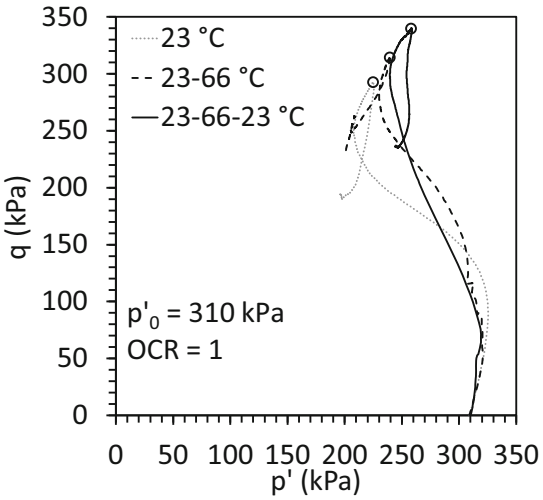

Fig. 3. Examples of effective stress paths for the saturated clay following different temperature paths

undrained shear strength was observed to decrease as the initial mean effective stress increased, which is counterintuitive to the trends in the thermally induced excess pore water pressures during undrained heating observed by Ghaaowd et al. (2015). Specifically, it was observed that greater changes in excess pore water pressure are observed for specimens with higher initial mean effective stress. The final void ratio values of specimens sheared at room temperature, after heating and after a

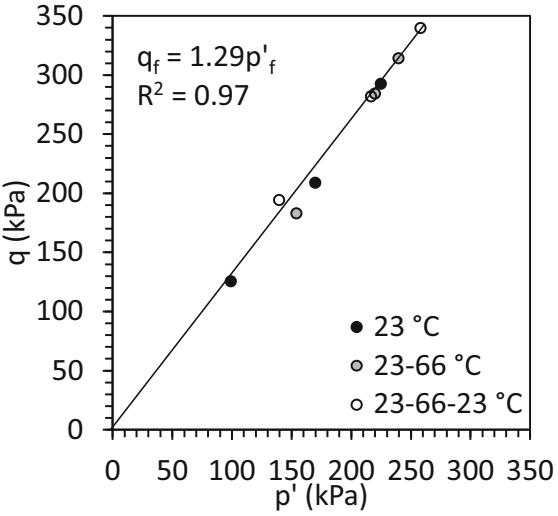

Fig. 4. Maximum principal stress differences for specimens sheared at room temperature, after heating, and after a heating cooling cycle versus the mean effective stress at failure

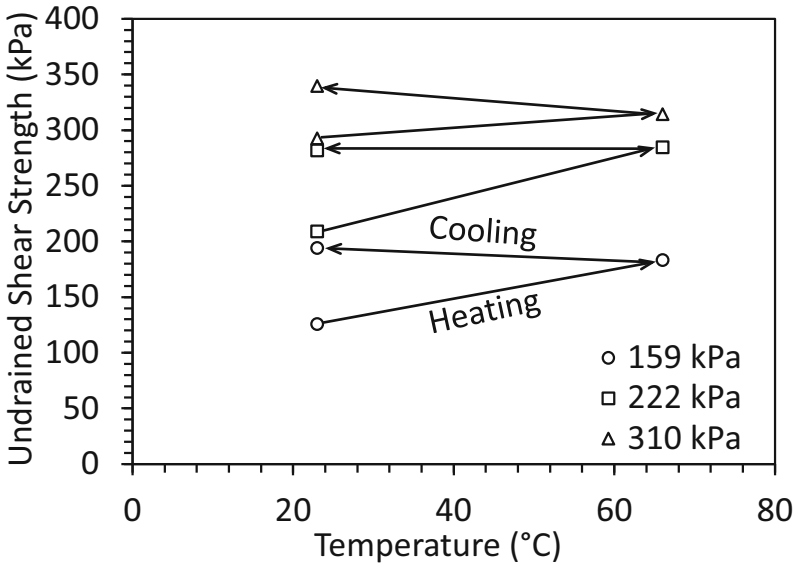

(a)

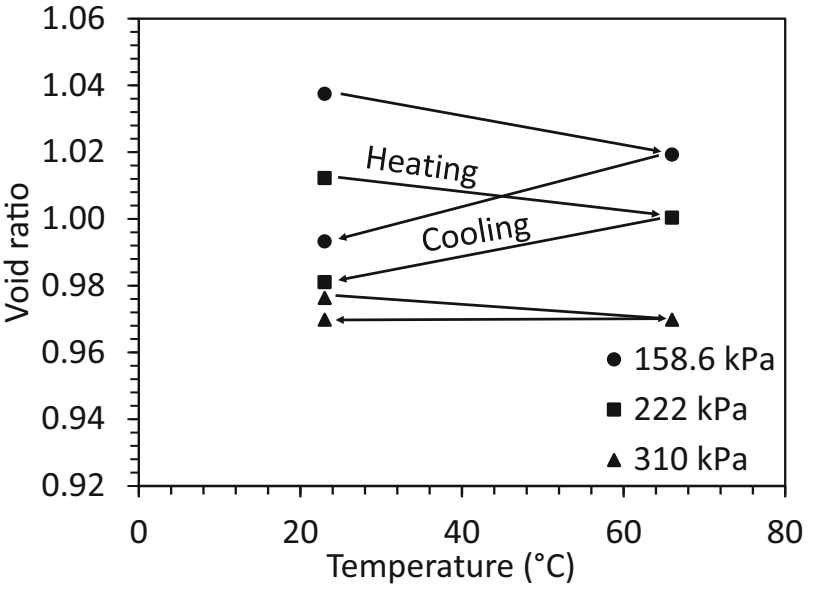

(b)

Fig. 5. (a) Undrained shear strength at different mean effective stresses for specimens sheared at room temperature, after heating, and after a heating cooling cycle; (b) Final void ratio at different mean effective stresses for specimens sheared at room temperature, after heating and after a heating cooling cycle

heating-cooling cycle are shown in Fig. 5(b). It can be observed that the void ratio decreases when the specimen is subjected to drained heating and even further after a drained heating-cooling cycle, conforming to the corresponding increase in undrained shear strength.

4 Conclusions

The results presented in this study indicate that the impact of a heating-cooling cycle such as that used in a thermal improvement application (i.e., thermal drains) will have a positive effect on the undrained shear strength of normally consolidated clays. This trend in undrained shear strength is attributed to the plastic decrease in volume during drained heating combined with the elastic decrease in volume during drained cooling. It was observed that this positive effect was greater for specimens tested at lower initial mean effective stresses. Despite the clear effects of temperature on the undrained shear strength, the changes in temperature were not observed to affect the slope of the peak failure envelope, which is consistent with previous studies on the effects of temperature on the shear strength of clays.

Acknowledgements. Funding provided by the University of California San Diego is gratefully acknowledged.

References

Abuel-Naga, H.M., Bergado, D.T., Suttisak, S.: Innovative thermal technique for enhancing the performance of prefabricated vertical drain system. Geotext. Geomembr. **24**, 359–370 (2006)

Alsherif, N.A., McCartney, J.S.: Nonisothermal behavior of compacted silt at low degrees of saturation. Géotechnique **65**(9), 703–716 (2015). https://doi.org/10.1680/geot./14-P-049

Ghaaowd, I., Takai, A., Katsumi, T., McCartney, J.S.: Pore water pressure prediction for undrained heating of soils. Environ. Geotech. **4**(2), 70–78 (2017)

Laloui, L., Olgun, C.G., Sutman, M., McCartney, J.S., Coccia, C.J.R., Abuel-Naga, H.M., Bowers, G.A.: Issues involved with thermo-active geotechnical systems: characterization of thermo-mechanical soil behavior and soil-structure interface behavior. J. Deep Found. Inst. **8** (2), 107–119 (2014)

Takai, A., Ghaaowd, I., Katsumi, T., McCartney, J.S.: Impact of drainage conditions on the thermal volume change of soft clay. In: GeoChicago 2016: Sustainability, Energy and the Geoenvironment, Chicago. 14–18 August, pp. 32–41 (2016)

Uchaipichat, A., Khalili, N., Zargarbashi, S.: A temperature controlled triaxial apparatus for testing unsaturated soils. Geotech. Test. J. **34**(5), 1–9 (2011)

Gas Shale Water Imbibition Tests with Controlled Suction Technique

Alberto Minardi[1(✉)], Alessio Ferrari[1], Russell Ewy[2], and Lyesse Laloui[1]

[1] Laboratory for Soil Mechanics – Chair "Gaz Naturel" Petrosvibri, Swiss Federal Institute of Technology, EPFL, Station 18, Lausanne, Switzerland
alberto.minardi@epfl.ch
[2] Chevron Energy Technology Co., Richmond, CA, USA

Abstract. Water loss during flowback operations represents one of the main challenges related to the use of hydraulic stimulation to exploit shale gas resources. About 20% of the injected fracturing fluids are usually recovered after stimulation. Fluid imbibition is expected to be one of the main mechanisms responsible for the water uptake of shale gas reservoirs. Imbibition tests are typically performed to analyse this issue. This study presents a new experimental methodology based on the control of total suction to quantify the impact of the swelling response of gas shales on the water uptake during imbibition processes. The obtained results demonstrate that a precise quantification of the gas shale water uptake cannot be performed neglecting the volumetric behaviour and the presence of the mechanical stress during the imbibition process.

1 Introduction

Water loss during flowback operations represents one of the main environmental issues related to the use of hydraulic fracturing to exploit unconventional shale gas reservoirs (e.g. Makhanov et al. 2014). The water imbibition by the material reservoirs plays a major role among the main involved causes. The presence of clay minerals in the composition of gas shales makes these geomaterials capable to absorb a great amount of the injected fracturing fluids. Imbibition tests are usually performed at the laboratory scale to evaluate the water uptake in gas shales (Dehghanpour et al. 2013). These tests foresee the immersion of gas shale specimens in water (or other fluids) with the following assessment of the amount of imbibed water through the measurement of the weight variation of the specimens.

Despite the importance of imbibition tests for the upscaling of imbibition data at the reservoir scale, two fundamental aspects are usually neglected. Firstly, as typical of clay-rich materials (e.g. Airò Farulla et al. 2010; Ferrari et al. 2014; Minardi et al. 2016), also gas shales might exhibit a significant expansion during the imbibition process which may significantly affect the amount of imbibed water. Secondly, the swelling observed in the laboratory might not be representative of the response experienced by the material under reservoir conditions; indeed, the presence of the in-situ stress is expected to play a major role in controlling the expansion of the material.

A. Ferrari and L. Laloui (Eds.): SEG 2018, SSGG, pp. 250–257, 2019.
https://doi.org/10.1007/978-3-319-99670-7_32

Hence, running imbibition tests without accounting for these two aspects may lead to a misleading quantification of the amount of imbibed water by the shale gas reservoir.

This work aims at showing the impact of the swelling response of a gas shale when subjected to imbibition processes on the water uptake. A testing set-up and an experimental methodology based on the control of total suction have been used to assess the volumetric response of the tested gas shale during the imbibition process considering also the presence of a mechanical stress.

2 Materials and Methods

The material used to perform the experimental analysis was retrieved from a shale gas reservoir at a depth of 2700 m. The core sample exhibits a visible laminated structure and a balanced mineralogical composition analyses dominated by quartz (17%), carbonate (24%), and clay (28%) minerals; the remaining of the composition is dominated plagioclase, K-feldspar and pyrite. In particular, smectite minerals are the majority in the clay content (61%).

The tested specimens used for the experimental analysis were obtained from the core sample using a mechanical saw and a mechanical lathe without any liquid to avoid possible alteration of the material.

Imbibition and desiccation processes were applied to the tested materials through both vapour diffusion and direct flooding with water. The vapour equilibrium technique, which foresees the control of relative humidity in a closed desiccator by using different saline solutions, was used to impose imbibition processes in different steps through vapour diffusion mechanism. The relative humidity can be converted to total suction (Ψ) according the psychrometric law; total suction represents the potential of the material's pore fluid and it accounts for both matric and osmotic components; this methodology is currently considered as the best technique to control the partial water saturation state in gas shales (Ferrari et al. 2018). The following salts, with corresponding values of total suction, were used for the preparation of the saturated saline solutions: $MgCl_2$ (Ψ = 150 MPa), NaCl (Ψ = 39 MPa), KNO_3 (Ψ = 10 MPa). De-ionized (DI) water was also used to perform the direct flooding of the tested specimens.

Two different testing set-ups were used to investigate the gas shales response during imbibition and desiccation processes in both free stress and under stress conditions. A comprehensive description of testing layout can be found in Minardi et al. (2018a).

The analysis of the volumetric behavior in free stress conditions was carried out in a simple desiccator (Fig. 1) where two twin cylindrical specimens with a dimeter of 30 mm and height of 20 mm were placed inside it and subjected to imbibition and desiccation processes. The first specimen was used to assess its mass evolution during the test for the quantification of the water uptake, while the second specimen was equipped with two biaxial strain gauges with microstrain resolution (10^{-6}) for the measurement of the strains in the directions perpendicular ($\varepsilon^{\perp}$) and parallel ($\varepsilon^{//}$) to the bedding planes. The strain gauges were covered with a coating to protect them from the direct contact with DI water. This methodology allows having the continuous assessment of the volumetric response during the imbibition process, leading to a proper

interpretation of its coupling with the water uptake. To quantify the impact of the mechanical stress on the volumetric response of gas shales, a uniaxial stress testing apparatus developed from the experimental device presented by Ferrari et al. (2016) and Minardi et al. (2018b) was used. Tested specimens have diameter of 20 mm and height of 30 mm, and they were prepared with the bedding planes perpendicular to the applied axial load. To apply imbibition and desiccation processes through vapour diffusion, a glass container filled with given saline solution was connected to the testing apparatus and a peristaltic pump was used to force the circulation of vapour from the container to the tested specimen (Fig. 2); direct flooding with DI water was also possible. Also in this testing configuration, two biaxial strain gauges were glued on the tested specimens to assess its response in the directions perpendicular and parallel to the bedding planes. The tested specimens were not initially oven-dried to avoid any impact on the material (e.g. Favero et al. 2016a).

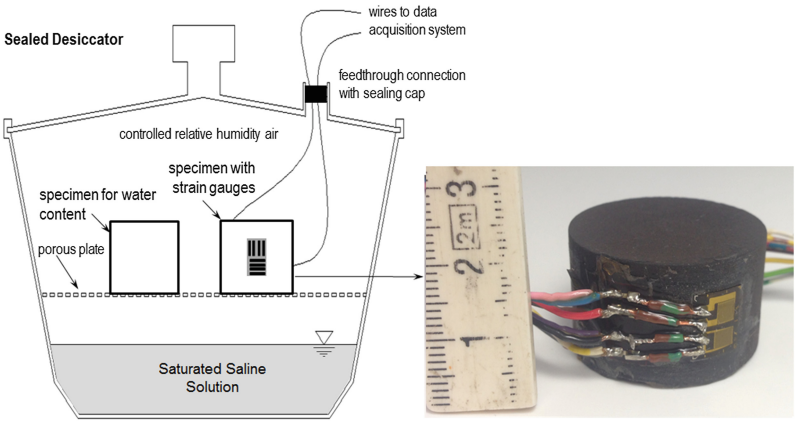

Fig. 1. Experimental set-up adopted to perform imbibition tests in free stress conditions with an example of tested specimen (Minardi et al. 2018a).

Three tests were performed on specimens obtained from the core sample. One test (Test A in the following) was performed in free stress condition, and two tests (Test B and Test C in the following) were carried out under stress conditions at 7 and 15 MPa of axial stress (σ_a). An initial equalization to a total suction of 150 MPa ($MgCl_2$ saline solution) was always performed to have the same reference conditions for all of the performed tests. After this initial equalization, imbibition and desiccation processes were applied in steps. In particular, the Test A foresaw an initial imbibition/desiccation cycle between 150 and 10 MPa of total suction, followed by a final imbibition to 0 MPa with direct flooding. An imbibition process performed in three steps from 150 to 0 MPa of total suction was adopted in the Test B. An imbibition/desiccation cycle was carried out in the Test C between 150 and 10 MPa of total suction.

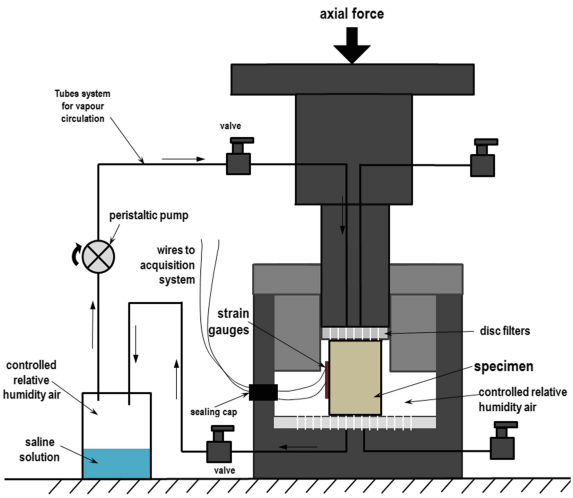

Fig. 2. Experimental set-up adopted to perform imbibition tests under stress conditions (Minardi et al. 2018).

3 Results

This section presents the obtained results from the three performed tests. A summary on the evolution of the volumetric response with total suction is reported in Fig. 3 for the three tested specimens. After preparation the specimens were in different conditions in terms of total suction, so the comparison of their volumetric behavior is presented starting after the equalization to 150 MPa of total suction.

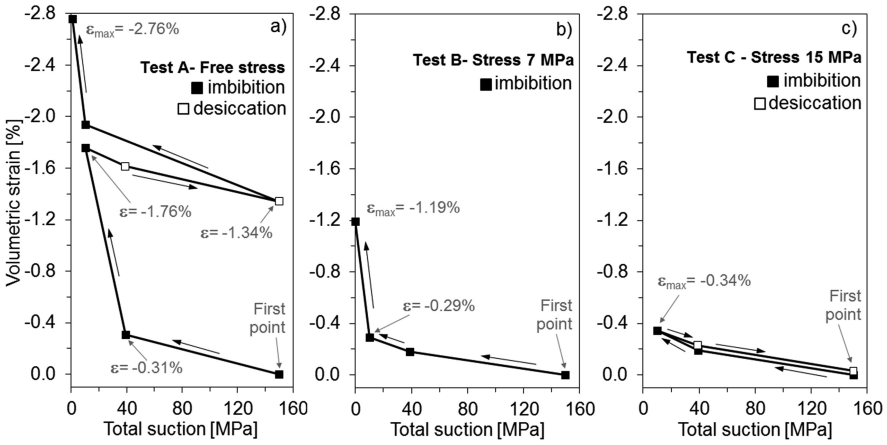

Fig. 3. Comparison of the volumetric response between the three performed tests: (a) Test A (0 MPa), (b) Test B (7 MPa), (c) Test C (15 MPa).

Figure 3a shows the response exhibited by specimen tested in free stress conditions (Test A). The material experienced significant swelling during the first two imbibition steps, from 150 to 39 and 10 MPa of total suction. The observed response of the material is highly nonlinear, showing a more significant swelling for lower total suction values (<39 MPa). A significant irreversible deformation is exhibited during the desiccation phase, from 10 MPa of total suction to 150 MPa (with an intermediate desiccation step to 39 MPa); this response highlights a linear behaviour during the desiccation process. During the following imbibition phase to 10 MPa, the specimen experienced almost a reversible response, with a slight increase of swelling. Finally, the last total suction step to 0 MPa highlights a further significant swelling of the material.

The volumetric response experienced by the specimens tested under stress is presented in the Fig. 3b and c. The impact of the mechanical stress is clearly highlighted and two main effects can be observed. A significant reduction of the volumetric swelling during the imbibition processes is observed for both specimens tested under stress (Test B and Test C) with respect to the specimen in the Test A. In particular, regarding the Test B (at σ_a = 7 MPa), the overall volumetric expansion exhibited at 0 MPa of total suction is more than 50% lower compared to the Test A (−1.19% against −2.76%); this result is mainly caused by the different response observed during the second imbibition step to 10 MPa of total suction. Hence, lower total suction values have to be imposed under stress conditions to observe a significant increase of volumetric strain. Similar feature is observed for the Test C where at end of the imbibition phase (at 10 MPa of total suction) the experienced volumetric expansion is almost 90% lower compared to free stress conditions (−0.34% against −1.76%). Moreover, the Test C highlights also another important feature. Indeed, while in the Test A a significant irreversible expansion is observed at the end of the cycle performed between 150 and 10 MPa of total suction, the response in the Test C is almost completely reversible with negligible accumulation of swelling at the end of the desiccation phase to 150 MPa of total suction.

As typical for shales, the presence of the bedding planes - which follows the depositional and post-depositional processes (Favero et al. 2016b) - influences significantly the behaviour of the tested gas shale. Figure 4 shows the response in terms of strain for the specimen tested in free stress conditions (Test A) in the directions perpendicular and parallel to the bedding. The anisotropic response is clearly highlighted by the graphs and the ratio between the strain perpendicular ($\varepsilon^{\perp}$) and parallel ($\varepsilon^{//}$) to the bedding. This feature is typical of claystones and shales, as presented in Valès et al. (2004) and Minardi et al. (2016). The obtained results clearly demonstrate that the irreversible volumetric expansion of the tested gas shale over the imbibition/desiccation process is mainly related to the response in the direction perpendicular to bedding. This aspect suggests that microfractures may be generated along the bedding planes during the imbibition process, which may represent preferential pathways for vapour and liquid water flow (Ghanbari and Dehghanpour 2015). Besides the natural anisotropic structure of gas shales, this feature provides a further addition contribution to a faster and higher water uptake in the direction parallel to the bedding planes during the imbibition process. Hence, the anisotropic volumetric expansion observed in the Test A plays an important role on the dependence of the imbibition rates and imbibed amount of water on the bedding planes orientation.

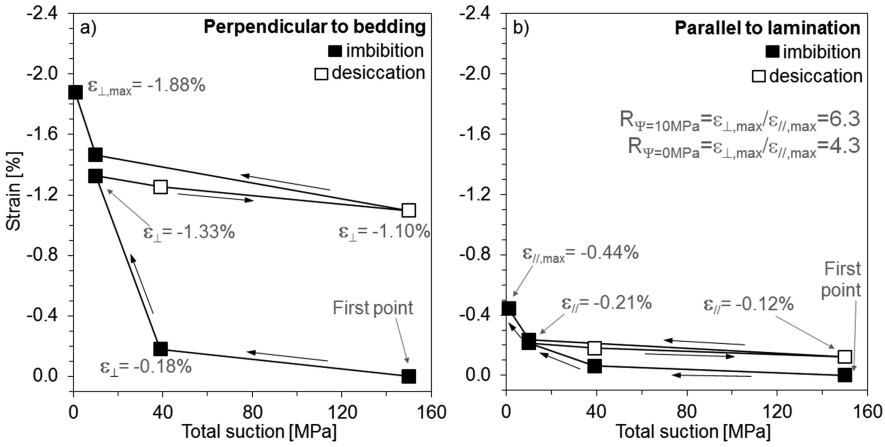

Fig. 4. Anisotropic response of the specimen in the Test A: (a) strain perpendicular to the bedding planes ($\varepsilon^{\perp}$), (b) strain parallel to the bedding planes ($\varepsilon^{//}$).

The presented outcomes allow having a reliable assessment of the impact of the volumetric behaviour on the water uptake of the material. Figure 5 summarizes the pore and water volumes of the specimen tested in free stress conditions (Test A) at the beginning of the test (after the initial equalization to 150 MPa of total suction) and at the end of the imbibition process (equalization to 0 MPa of total suction). The graph clearly shows the high water uptake of the specimen. The final water volume exceeds significantly the initial pore volume of the material; indeed, the excess of water volume has to be addressed to the expansion experienced by the specimen during the imbibition process. In particular, the swelling response is responsible for 45% of the final water volume. The graph in Fig. 5 shows also the final pore volume if the swelling deformation measured under stress in the Test B (−1.19%) is applied to the initial pore volume of the specimen in the Test A. A comparison with the increase of pore volume in free stress conditions suggests that under stress the water uptake during the imbibition process has to be lower.

The experimental technique based on the control of total suction coupled with a precise assessment of the volumetric deformations with strain gauges has been proved to be an efficient tool the quantify the impact of the volumetric behaviour on the water uptake during imbibition and desiccation processes.

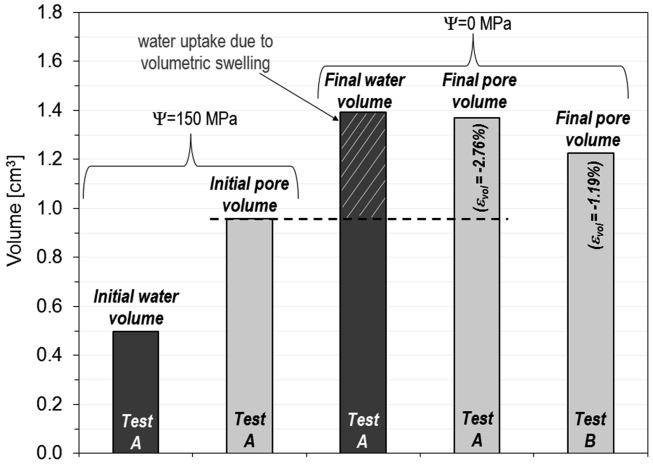

Fig. 5. Pore and water volumes comparison for the evaluation of the impact of the swelling response on the water uptake of the tested specimens.

4 Conclusions

The volumetric swelling behavior of gas shales during spontaneous imbibition tests is one of the main reasons for the measurement of excess water uptake. The presented work has shown an experimental methodology to properly assess the impact of the volumetric response of gas shales on their water uptake. The methodology is based on the control of total suction combined with the use of strain gauges to properly monitor the specimen's deformations perpendicular and parallel to the bedding. The presented results have demonstrated that, if the volumetric response of gas shales is not properly quantified during the imbibition process, a significant overestimation of the imbibed water volume can be obtained. Moreover, the mechanical stress has been found to significantly affect the swelling behaviour of the tested material, where the volumetric expansion is much lower compared to the response observed in the free stress test. These outcomes are expected to play a key role on the upscaling of imbibition data to evaluate the water loss at the field scale; indeed, a lower imbibed water volume must be considered when the material is subjected to an imbibition process under mechanical stress.

References

Airò Farulla, C., Battiato, A., Ferrari, A.: The void ratio dependency of the retention behaviour for a compacted clay. In: 5th International Conference on Unsaturated Soils, vol. 1, pp. 417–422 (2010)

Dehghanpour, H., Lan, Q., Saeed, Y., Fei, H., Qi, Z.: Spontaneous imbibition of brine and oil in gas shales: effect of water adsorption and resulting microfractures. Energy Fuels **27**(6), 3039–3049 (2013)

Favero, V., Ferrari, A., Laloui, L.: Thermo-mechanical volume change behaviour of Opalinus Clay. Int. J. Rock Mech. Min. Sci. **90**, 15–25 (2016a)

Favero, V., Ferrari, A., Laloui, L.: On the hydro-mechanical behaviour of remoulded and natural Opalinus Clay shale. Eng. Geol. **208**, 129–135 (2016b)

Ferrari, A., Laloui, L.: Advances in the testing of the hydro-mechanical behaviour of shales. In: Multiphysical Testing of Soils and Shales, pp. 57–68. Springer, Berlin (2013)

Ferrari, A., Favero, V., Marschall, P., Laloui, L.: Experimental analysis of the water retention behaviour of shales. Int. J. Rock Mech. Min. Sci. **72**, 61–70 (2014)

Ferrari, A., Favero, V., Laloui, L.: One-dimensional compression and consolidation of shales. Int. J. Rock Mech. Min. Sci. **88**, 286–300 (2016)

Ferrari, A., Minardi, A., Ewy, R., Laloui, L.: Gas shales testing in controlled partially saturated conditions. Int. J. Rock Mech. Min. Sci. **107**, 110–119 (2018)

Ghanbari, E., Dehghanpour, H.: Impact of rock fabric on water imbibition and salt diffusion in gas shales. Int. J. Coal Geol. **138**, 55–67 (2015)

Makhanov, K., Habibi, A., Dehghanpour, H., Kuru, E.: Liquid uptake of gas shales: a workflow to estimate water loss during shut-in periods after fracturing operations. J. Unconv. Oil Gas Resour. **7**, 22–32 (2014)

Minardi, A., Crisci, E., Ferrari, A., Laloui, L.: Anisotropic volumetric behaviour of Opalinus Clay shale upon suction variation. Géotech. Lett. **6**(2), 144–148 (2016)

Minardi, A., Ferrari, A., Ewy, R., Laloui, L.: The impact of the volumetric swelling behavior on the water uptake of gas shale. J. Nat. Gas Sci. Eng. **49**(1), 132–44 (2018a)

Minardi, A., Ferrari, A., Ewy, R., Laloui, L.: Nonlinear elastic response of partially saturated gas shales in uniaxial compression. Rock Mech. Rock Eng. 1–12 (2018b)

Valès, F., Minh, D.N., Gharbi, H., Rejeb, A.: Experimental study of the influence of the degree of saturation on physical and mechanical properties in Tournemire shale (France). Appl. Clay Sci. **26**(1), 197–207 (2004)

Thermal Cyclic Stability Analysis of Porous Heat Storage Materials

Henok Hailemariam(✉) and Frank Wuttke

Geomechanics and Geotechnics, Kiel University, Kiel, Germany
henok@gpi.uni-kiel.de

Abstract. Assessing the thermal cyclic stability of energy storage materials is of utmost importance in the design and overall serviceability of sensible heat storage systems. In particular, care should be taken to ensure that the plastic strains accumulated upon short and long term cyclic operations are within the design limits, thus preventing critical failure of the different components of the heat storage system. In this study, the thermal cyclic stability of a commercial cement-based porous heat storage material is analyzed in water-saturated conditions by performing heating/cooling cycles in the temperature range from 20 to 80 °C with a newly developed cyclic thermo-mechanical device. The thermo-mechanical device produces a homogenously linear temperature distribution across the specimen, thus recreating the actual heat flow and distribution within sensible heat storage materials upon heat loading/unloading operations. The cyclic thermal, peak induced and accumulated plastic strains due to charging/discharging operations of the sensible heat storage material are studied for several lower and upper temperature cycle limits (20–40 °C, 20–60 °C, 20–80 °C and 60–80 °C) and dwelling periods (0, 10, 40 and 120 min), and the results are analyzed in terms of the intrinsic porous medium structure and cementation behavior.

1 Introduction

Thermal energy storages (Braun et al. 1981; Hesaraki et al. 2015) in general and sensible heat storages (Dincer et al. 1997) in particular, are nowadays typically used to capture solar thermal power. Sensible heat storages are generally preferred to other forms of thermal energy storage, such as latent and thermo-chemical heat storages, due to their comparatively low cost and technical development. Of the various forms of sensible heat storage materials, solid sensible heat storage materials (Laing et al. 2006; Laing et al. 2012; Hailemariam and Wuttke 2018) such as rocks, concrete, geomaterials and cemented porous media have recently gained much interest in the renewable energy storage sector. The use of such media in domestic heat energy storage applications is preferable when compared to other forms of heat storage media, such as water, due to their low investment costs and high operability (Laing et al. 2006), as well as their ability to carry loads as part of the foundation of structures (Hailemariam and Wuttke 2018).

If the thermo-mechanical effects of cyclic thermal loads are not properly considered in the design of sensible heat storage systems, the unaccounted accumulation of plastic

A. Ferrari and L. Laloui (Eds.): SEG 2018, SSGG, pp. 258–265, 2019.
https://doi.org/10.1007/978-3-319-99670-7_33

strains can lead to the formation of excessive stresses and cracks in the heat storage material, particularly in areas near the interface between the heat storage material and the heat exchanger pipes. The formation of cracks lowers the effective thermal conductivity of the heat storage material, causing a significant reduction in the loading/unloading rates of the sensible heat storage system. In this research, the thermal cyclic stability of a commercial water-saturated cement-based porous heat storage material (called Füllbinder L, SCHWENK Zement KG[1]) is analyzed by performing heating/cooling cycles in the temperature range between 20 and 80 °C with a cyclic thermo-mechanical device.

2 Experimental Program

2.1 Tested Material

In Table 1, a list of the obtained physical properties of the Füllbinder L material is presented. The test specimens were prepared with a selected design water to solids ratio of 0.8, and then stored in water for 28 days. Storage in water ensures full saturation and prevents possible cracking of specimen due to cement hydration (Abdolhosseini Qomi et al. 2015).

Table 1. Physical properties of the Füllbinder L heat storage material

Property	Füllbinder L (saturated)
Bulk density (kg m^{-3})	1583
Porosity (–)	0.543
Specific gravity of solids (–)	2.28
Thermal conductivity (W m^{-1} K^{-1})[a]	0.960
Specific heat capacity (J kg^{-1} K^{-1})[a]	2083.4
Hydraulic conductivity ($\times 10^{-8}$ m s^{-1})	11.95
Coefficient of thermal expansion ($\times 10^{-6}$ K^{-1})	10.7
Modulus of elasticity (GPa)	1.9

[a] Data obtained using Decagon KD2 Pro TR-1 and SH-1 transient needle probes

2.2 Thermal Cyclic Test Apparatus

A cyclic thermo-mechanical device (Figs. 1 and 2), which works on the principle of thermo-mechanical expansion analysis is used to study the cyclic thermal stability of the heat storage material. Thermo-mechanical analysis measurements are typically performed to obtain coefficient of thermal expansion of materials, and commonly consist of a specimen holder, a furnace or heating plate for the homogeneous heating of the specimen, a transducer that measures the change in length of the specimen upon

[1] http://www.schwenk-zement.de/.

heating, a thermocouple or temperature sensing element and a means of data recording apparatus. The cyclic thermo-mechanical device used in this research produces a homogenously linear temperature distribution across the specimen to represent the actual heat flow process in sensible heat storage systems (Hailemariam et al. 2016). The apparatus consists of a top heating plate (representing the imposed thermal load on the heat storage material from the heat exchanger), a bottom cooling plate and a PPS Laticonther thermoplastic reference disc with known thermal conductivity (Fig. 2a).

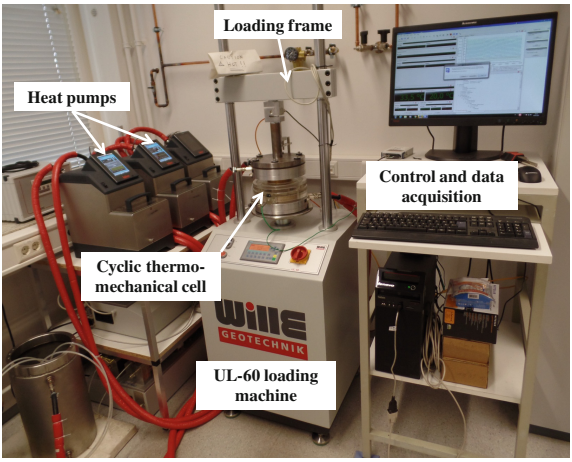

Fig. 1. Cyclic thermo-mechanical device.

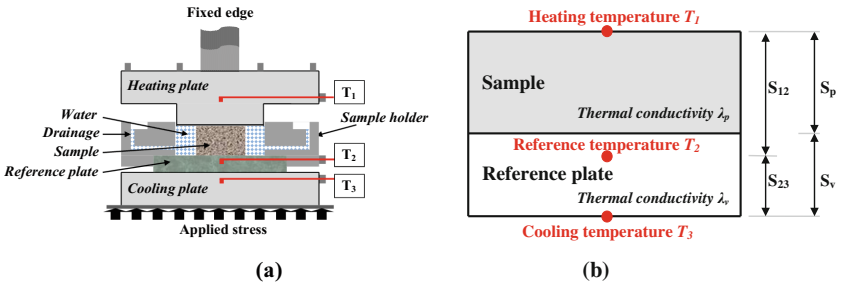

Fig. 2. (a) Schematic representation and (b) dimensional analysis, of the cyclic cell.

The temperature of the top heating T_1 and bottom cooling T_3 plates is controlled via a circulating fluid (distilled water + glycol), which is pumped using Huber Ministat 125 Pilot ONE heat pumps, and the resulting temperature of the reference plate T_2 is recorded. The water-saturated Füllbinder L specimen is sandwiched between the top heating and reference plates and is laterally insulated by a PMMA Plexiglas sample holder with a very low thermal conductivity. Generally sensible heat energy systems may be designed to be in-direct contact with the confining lateral soil (foundation of

structures) or an additional heat insulating material may be provided. In any case, the proposed experimental scheme can be modified to suit the required in situ criteria. The top and bottom heating/cooling plates consist of extremely thin PT 100 temperature sensors with an accuracy of 0.05 °C. The system measures sample thermal expansion or contraction with a TRS-0050 linear displacement transducer with an independent linearity of 0.15% and repeatability of 2 μm. Vertical stress (with a maximum force limit of 60 kN) can be applied to the specimen via a UL-60 loading machine integrated with the system (Fig. 1).

The thermal cyclic expansion tests were conducted by heating the top plate at a constant rate of 1 °C/min within the temperature range of 20–80 °C, as it is a water-based storage system. The specimens were prepared with a diameter of 50 mm and sufficient height of 40 mm to ensure creation of a linear temperature gradient across the samples upon heating. In addition, the higher specimen length produces a greater length change signal upon heating or cooling, providing a higher accuracy of the measurement of the specimen expansion/contraction. Care was taken to ensure that the top and bottom faces of the used specimens are perfectly flat so that the nominal stress of 5 kPa applied over the specimens to ensure proper contact with the heating/cooling plates is spread out uniformly over a wide enough surface area avoiding minor specimen deformations. The mathematical description of the one dimensional conductive heat transport (Cannon 1984) within the device has been described by Hailemariam and Wuttke (2018), and the average sample temperature (at the center of specimen) T_{av} (°C) can be obtained based on the temperatures T_1, T_2 and T_3 (°C), and the distances S_v and S_{23} (m) of Fig. 2(b) as:

$$T_{av} = \frac{1}{2}\left\{T_1 + T_3\left[1 + \frac{S_v(T_2 - T_3)}{T_3 S_{23}}\right]\right\} \tag{1}$$

3 Results and Discussion

3.1 Thermal Cyclic Loading at Different Dwelling Periods

Figure 3 shows the results of the cyclic thermal tests on the Füllbinder L material heated in the temperature range of 20–80 °C at waiting/dwelling periods of 0, 10, 40 and 120 min. The fluid pumped in to the top plate leads to either a contraction (when a cold fluid is pumped) or a dilation (when a hot fluid is pumped) of the heat storage material. These dimensional changes on a macroscopic level, which are mainly caused due to changes in the thermal vibrations that are always present in the crystals of the material, are mostly reversible. However, a prolonged heating/cooling cyclic loading causes small plastic/irrecoverable thermal strains, which in this study is confirmed by the permanent reduction in specimen height, i.e. −ve net strain ε, between any two consecutive heating + cooling cycles of all the specimens upon cyclic loading. In our study, the actual top heating plate temperature T_1 recorded with the top thermocouple (max. between 74.5 to 76.4 °C) is always lower than the target (set) temperature of the heat pumps (max. 80 °C) due to the heat loss in the carrier fluid, tubes and used connections (Figs. 3 and 4).

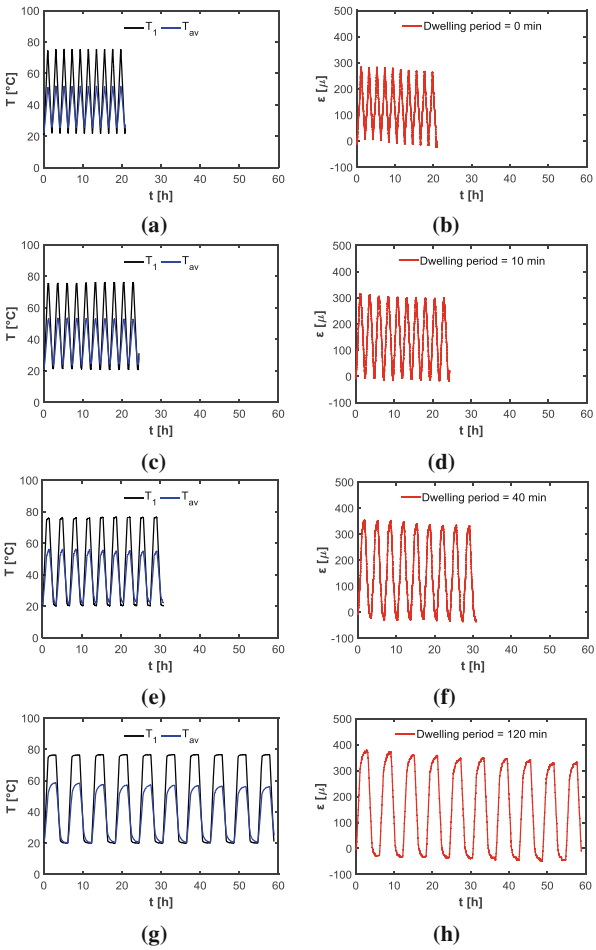

Fig. 3. Plots of time t, temperature T and strain ε of the cyclic thermal tests at dwelling periods of: (a, b) 0 min, (c, d) 10 min, (e, f) 40 min and (g, h) 120 min.

The heat conduction and thermal strain behavior of the Füllbinder L is mainly influenced by the presence of: (i) solid matrix (Hailemariam and Wuttke 2018), mainly: limestone/sedimentary minerals, calcium silicate hydrates (CSH) derived from the cementing bonds, and to a small extent quartz minerals (Hailemariam et al. 2017), and (ii) entrapped pore-water. Generally, in saturated porous multiphase materials, thermal expansion of in situ pore-water due to a rapid change in the ground surface temperature contributes to the volumetric change of the materials, thus influencing the stress fields of the media. However, since the tests in this study are conducted under fully drained conditions with a low rate of heating/cooling, volume changes caused by pore-water expansion/contraction due to heating/cooling operations are negligible and have not been considered.

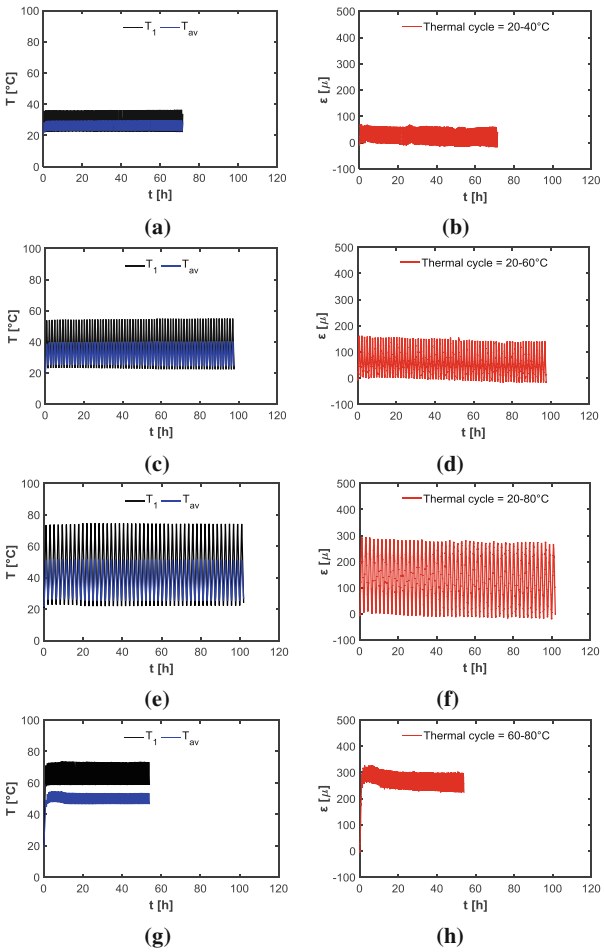

Fig. 4. Plots of time t, temperature T and thermal strain ε of the cyclic thermal loading tests at temperature ranges of: (a, b) 20–40 °C, (c, d) 20–60 °C, (e, f) 20–80 °C and (g, h) 60–80 °C.

Calcite along with a small quantity of dolomite is the dominant limestone mineral present. The main cementing minerals (Abdolhosseini Qomi et al. 2015) present are: alite (Ca_3SiO_5 or C_3S), portlandite [$Ca(OH)_2$ or CH], belite (Ca_2SiO_5 or C_2S) and calcium silicate hydrates [$(CaO)_x(SiO_2)_1(H_2O)_y$ or CSH]. Depending on the chemical composition of the phase, the molecular structures of the solid phases in the hardened cementing minerals typically vary from crystalline to amorphous. Minerals such as alite and belite (anhydrated clinker phases) and portlandite are crystalline. Alite is a chemically modified form of pure tricalcium silicate (C_3S), and exhibits a series of reversible phase transitions upon heating and cooling (Taylor 1997). Since the radiative heat transfer by photons, which follows the T^3-law, is absent at temperatures below 727 °C (Hofmeister 1999; McKenzie et al. 2005), the dominant form of heat transfer in the solid matrix of the Füllbinder L heat storage material is conduction via the

collective atomic vibrations or phonons. Phonons are harmonic at low temperatures, and become progressively anharmonic with increasing temperature (Abdolhosseini Qomi et al. 2015). Upon heating, the phonon density (also known as the vibrational density of state) of the calcite and calcium silicate hydrates in the solid matrix of the Füllbinder L increases, resulting in a subsequent reduction of the mean free path between the phonon collisions and the conduction of heat in the medium (Hailemariam and Wuttke 2018).

With an increase in the dwelling period, the peak thermal strains ε_{pk} induced upon heating of the material increases (from 282.2 to 375.2 μm, for dwelling periods of 0 and 120 min, respectively) (Fig. 3). This is mainly due to the extended exposure to the maximum temperature (i.e. at high dwelling periods compared to low), which in turn causes extra dilations in the case of heating due to an increase in the thermal crystalline vibrations of the solid matrix of the material. For all dwelling periods considered, the magnitudes of the peak thermal strains ε_{pk} decrease with an increase in the number of heating/cooling cycles, indicating an accumulation of plastic thermal strains ε_{pl} due to the softening or mechanical weakening of the cementitious bonds of the solid matrix of the Füllbinder L.

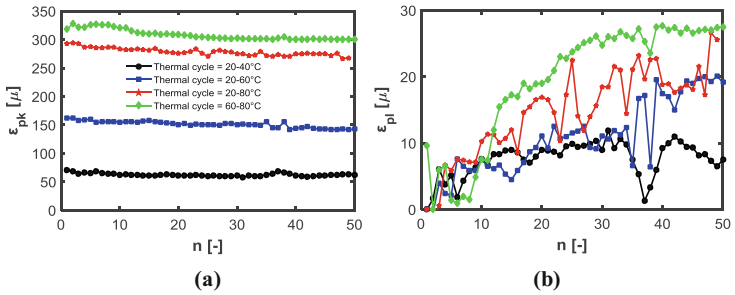

Fig. 5. Plots of the number of thermal cycles n vs: (a) peak thermal strain ε_{pk} and (b) accumulated plastic strain ε_{pl}, of the cyclic thermal loading tests.

Figures 4 and 5 show the results of thermal cyclic tests on Füllbinder L material heated in the temperature ranges of 20–40 °C, 20–60 °C, 20–80 °C and 60–80 °C with a dwelling time of 0 min. The quantity of the accumulated plastic thermal strain ε_{pl} due to an increase in the number of heating/cooling cycles is directly proportional to the applied average specimen temperature T_{av} (considered temperature range). The measured ε_{pl} after 50 thermal cycles are: 7.3, 19.2, 26.7 and 27.0 μ for temperature ranges 20–40 °C, 20–60 °C, 20–80 °C and 60–80 °C, respectively (Fig. 5b). For all the considered temperature ranges, the majority of the accumulation of the plastic strains occur within the first 25 cycles (Fig. 5b), as most of the thermally induced mechanical weakening of the cementitious bonds occurs within the few initial cycles upon the dilation/contraction mechanisms of the material. At high thermal cycle numbers, the induced plastic strains in the material decrease rapidly and the thermo-mechanical behavior of the material approaches a state of near fully-elastic mode of dilation/contraction process.

4 Conclusions

A newly developed cyclic thermo-mechanical device was used to study the thermal cyclic stability of a cement-based heat storage material. Unlike traditional thermo-mechanical cyclic stability analysis methods, which assume a uniform temperature distribution in a material upon heating/cooling, the new thermo-mechanical cell produces a uniformly linear temperature distribution across the specimen, representing the actual heat flow and distribution within porous medium sensible heat storage systems. The variations of the cyclic thermal, peak induced and accumulated plastic strains of the material were assessed for several dwelling times, temperature ranges and thermal cycles with good results.

Acknowledgements. The authors gratefully acknowledge the financial support provided by the German Federal Ministry for Economic Affairs and Energy (BMWi) under Grant numbers 0325547B (Project IGLU) and 03ET6122A (Project ANGUS II).

References

Abdolhosseini Qomi, M.J., Ulm, F.-J., Pellenq, R.J.-M.: Physical origins of thermal properties of cement paste. Phys. Rev. Appl. **3**(6), 064010 (2015)

Braun, J.E., Klein, S.A., Mitchell, J.W.: Seasonal storage of energy in solar heating. Sol. Energy **26**(5), 403–411 (1981)

Cannon, J.R.: The one-dimensional heat equation. In: Encyclopedia of Mathematics and Its Applications, 3rd edn., vol. 23, pp XXV+483. Addison-Wesley Publishing Company, California (1984)

Dincer, I., Dost, S., Li, X.: Performance analyses of sensible heat storage systems for thermal applications. Int. J. Energy Res. **21**(12), 1157–1171 (1997)

Hailemariam, H., Shrestha, D., Wuttke, F.: CTE analysis of saturated cement-based sensible heat storage materials. In: Wuttke, F., Bauer, S., Sánchez, M. (eds.) Proceedings of the 1st International Conference on Energy Geotechnics ICEGT 2016, pp. 299–304. Taylor & Francis Group, Kiel (2016)

Hailemariam, H., Shrestha, D., Wuttke, F., Wagner, N.: Thermal and dielectric behaviour of fine-grained soils. Environ. Geotech. **4**(2), 79–93 (2017)

Hailemariam, H., Wuttke, F.: Temperature dependency of the thermal conductivity of porous heat storage media. Heat Mass Transf. **54**(4), 1031–1051 (2018)

Hesaraki, A., Holmberg, S., Haghighat, F.: Seasonal thermal energy storage with heat pumps and low temperatures in building projects—a comparative review. Renew. Sustain. Energy Rev. **43**, 1199–1213 (2015)

Hofmeister, A.: Mantle values of thermal conductivity geotherm from phonon lifetimes. Science **283**, 1699–1709 (1999)

Laing, D., Steinmann, W.-D., Tamme, R., Richter, C.: Solid media thermal storage for parabolic trough power plants. Sol. Energy **80**(10), 1283–1289 (2006)

Laing, D., Bahl, C., Bauer, T., Fiss, M., Breidenbach, N., Hempel, M.: High-temperature solid-media thermal energy storage for solar thermal power plants. Proc. IEEE **100**(2), 516–524 (2012)

McKenzie, D., Jackson, J., Priestley, K.: Thermal structure of oceanic and continental lithosphere. Earth Planet. Sci. Lett. **233**, 337–349 (2005)

Taylor, H.F.W.: Cement Chemistry, 2nd edn. Thomas Telford, London (1997)

A New Lattice Element Method (LEM) with Integrated Interface Elements to Determine the Effective Thermal Conductivity of Rock Solids Under Thermo-Mechanical Processes

A. S. Sattari(✉), H. B. Motra, Z. H. Rizvi, and F. Wuttke

Geomechanics and Geotechnics, Institute of Geoscience,
Kiel University, Kiel, Germany
amir.shoarian-sattari@ifg.uni-kiel.de

Abstract. In order to determine the change of thermal conductivity of rock solids under coupled thermo-mechanical processes and developed microstructure fractures, an application of a new lattice element method (LEM) with additional interface elements representing the bond between the particles is investigated. The thermo-mechanical loadings in many engineering applications, such as deep geothermal systems, can result in a change of mechanical and thermal properties of rock solids. In the proposed model, the change of thermal conductivity under mechanical loading, thermal expansion and developed fractures due to coupled thermo-mechanical processes are considered. The main advantage of the new model is that it considers the thermal expansion while increasing the compression stresses in particles contact zone, which captures the true stress-strain behavior of the rock sample under coupled processes. The numerical results are eventually compared to the experimental results obtained from multi-anvil apparatus in Laboratory of CAU Kiel. It is shown that the new model is able to estimate the change of thermal conductivity under coupled thermo-mechanical loadings and developed microcracks.

Keywords: Lattice element method · Rock mechanics
Effective thermal conductivity · Coupled thermo-mechanical processes
Numerical modeling

1 Introduction

In many geotechnical engineering applications, such as mining and tunneling in rock or utilization of natural resources like enhanced geothermal systems, the fracture initiation and propagation due to coupled mechanical, thermal and hydraulic processes can result in major damage or decrease the efficiency of designed structure (Bažant 2003). The development of cracks in a microstructure of rock leads to degradation of the overall stiffness and material strength. Beside the existing experimental methods, which are tedious and expensive to conduct, numerical methods were developed in order to replace the experimental tests with more efficient and low-cost methods. During the

A. Ferrari and L. Laloui (Eds.): SEG 2018, SSGG, pp. 266–275, 2019.
https://doi.org/10.1007/978-3-319-99670-7_34

past decades, simulation of fracture growth using continuum based methods is studied. A progressive failure of rock using traditional finite element method (FEM) is modeled (Tang 1997). With the implementation of boundary element method (BEM), fractures and faults in the earth's crust are simulated (Thomas 1993). Zhang et al. (2011) developed a multi-scale FEM for simulation of thermal conduction in granular materials. Recently, Rattanadecho et al. (2014) analyzed the heat transport and water infiltration in a granular packed bed. However, FEM is not the optimal solution to such problems, since it struggles to deal with displacement discontinuities, different material interfaces and the consideration of micro- and meso-scope heterogeneities, as grain or mineral distributions. With the application of discrete element method (DEM), analytical expressions relating the elastic parameters of the continuous body, such as Young's modulus and Poisson's ratio, are presented (Tavarez and Plesha 2007). In a different approach, a bonded particle model is implemented to model the fracture in rocks (Potyondy and Cundall 2004). The application of DEM is also extended to cover the thermal loading between circular and spherical particles, known as thermal discrete element method (TDEM) (Feng et al. 2008). The thermal contact model can also consider the thermal resistance of rough surfaces in a DEM (Kumlutas and Tavman 2006). In this regard, a DEM study on the effective thermal conductivity of granular assemblies is performed (Karkri et al. 2011).

The lattice element method (LEM) represents a meso-scale medium with series of spring, truss or beam elements. The LEM is mainly used to simulate the fracture processes of the heterogeneous medium in microstructures. While using truss elements, the fracture process in concrete is modeled by Schlangen and van Mier (1992). In LEM, the heterogeneous medium is presented with 1D lattice elements and while removing the elements exceeding their strength threshold the fracture initiation and growth are simulated (Liu et al. 2007). With the extension of LEM into 3D model, Liu (2001) studied the mechanical behavior of short-fiber reinforced composites using a 3D springs. The implementation of LEM into thermal loading is recently carried out by Sattari et al. (2017). The study of effective thermo-mechanical parameters in solid mechanics is done by Wuttke et al. (2017). In this work, the change of effective thermal conductivity while increasing the mechanical loading is simulated. In another work done by Rizvi et al. (2017), the effective thermal conductivity of modified high thermal backfill material for energy transportation using 3D lattice is estimated. In the rigid body spring network (RBSN) model the contact between the particles is represented with three spring elements transmitting the axial, shear forces and moment between the particles (Bolander and Saito 1998). In this model and while using the Mohr-Coulomb tension cutoff failure surface, the fracture process is modeled. The 3D three-point-bending simulation with the pre-existing opening is simulated with RBSN by Yip et al. (2006). The simulation of the rate dependent fracture in concrete geocomposites is carried out by Kim and Lim (2011).

The main object of this research is to develop a model which is not only able to capture the fracture initiation and propagation under thermo-mechanical loads but also can result in true stress-strain behavior under coupled processes, which can result in accurate effective thermal conductivity prediction. The application of lattice elements with spring or beam elements cannot solely represent the expansion of the geomaterial as well as the increment of compression forces in particles contact surfaces under

thermal loads. The developed code in geomechanics group of CAU Kiel consists of following steps: initially, the medium is discretized and the mechanical model for LEM with interface elements is implemented. Then the thermal model according to Sattari et al. (2017) is considered and eventually the coupled scheme with integrated fracture model is applied. The MATLABs parallel computing toolbox is implemented for reducing the computation costs.

2 Implemented Mechanical Model

In order to begin with LEM, the medium should be discretized into small particles using vectorized random lattice (Moukarzel and Herrmann 1992) and Delaunay triangulation for generation of lattice elements transmitting the loads between the nodes. The discretized medium with the mesh size of 20 × 20 is shown below (Fig. 1).

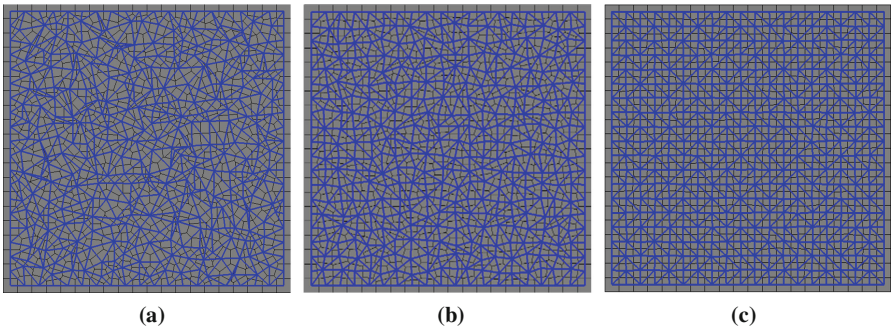

Fig. 1. Descrtized medium with lattice elements shown with blue lines (a) randomness factor 0.9, (b) randomness factor 0.5, and (c) randomness factor 0.1

Subsequently, while implementing the Euler-Bernoulli beam elements and minimizing the potential energy of the system, the displacement (U) and forces (F) in the elements based on assembled global stiffness (K) are calculated. The displacement method for strain control and softening factor (Bolander and Kobashi 1995) for modeling quasi-brittle materials are considered. The elements fracture mechanism is based on Mohr-Coulombs tension cutoff surface (Bolander and Saito 1998) as shown in Fig. 2. The tensile strength (S_{TS}), cohesion (C) and slope of the failure envelope (tan ϕ) are the input parameters of the fracture mechanism. When an element axial stress (σ_n) exceeds its tensile strength threshold (S_{TS}) or similarly the element shear stress (σ_s) exceeds the shear strength (τ) the element is removed from the domain.

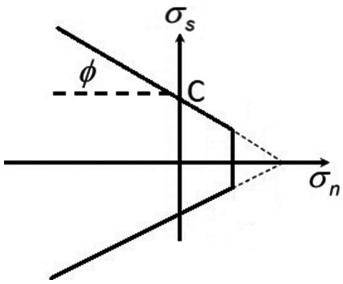

Fig. 2. The Mohr-Coulombs tension cutoff surface

$$F_{Global} = K_{Global} U_{Global}, \quad \sigma_n = \frac{f_n}{A}, \quad \sigma_s = \frac{f_s}{A}, \quad \tau = \sigma_n \tan\phi + C \quad \text{if } \sigma_n > S_{TS} \text{ or } \sigma_s > \tau, \text{element breaks} \tag{1}$$

where, A is the cross-section of elements, f_n is the axial force and f_s is a shear force. The simulation of fracture initiation and propagation in a three point-bending test is shown in Fig. 3. The mesh size of 240 × 60 with Young's Modulus of 30 GPa (E) and tensile strength of 1.8 MPa is considered.

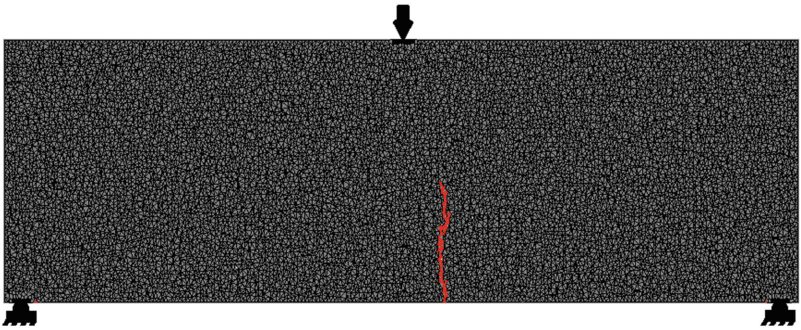

Fig. 3. The three-point bending test and propagated fracture shown with red path

As shown in Fig. 4, the lattice elements $L_{i,1}$ and $L_{j,2}$ transfer the axial loads from nodes to contact interface element ($L_{1,2}$). These interface elements represent the bond between the particles.

The same fracture mechanism as in RBSN model is considered and the lattice elements representing the particles are considered to be not breakable so that the fracture solely happens in the interface elements. The interface length ($L_{1,2}$) is assumed to be 50 μm.

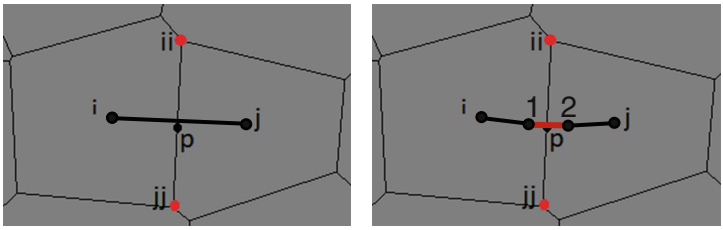

Fig. 4. The (a) lattice element without interface element, and (b) lattice element with integrated interface element (red element)

3 Implemented Thermal Model

The thermal model is based on Sattari et al. (2017), where the lattice elements are used to transform the thermal and mechanical loads. According to this model, the lattice model is able to predict the heat flow as well as the change of effective thermal conductivity under various mechanical loadings in cemented geomaterials such as rock. The fracture mechanism in this model is neglected and the change of contact area under mechanical load is the main reason for the change of the effective thermal conductivity. In the steady state condition, when the sum of heat flux (q) into particle *i* is equal to zero,

$$\nabla.(k\nabla T_i) = \sum_{i=1}^{N_c} q_i = 0, \quad q_{ij} = h_{ij}(T_i - T_j), \quad h_{ij} = k\left(L_{ii,jj}t \pm 2\left(\frac{3f_n L_{i,j}}{4E}\right)^{\frac{1}{3}}\right) \tag{2}$$

where, N_c is a number of the contacts of particle *i*, T is temperature, t is thickness, h_{ij} is a heat conductance and k is thermal conductivity of minerals. Similarly, in the transient condition,

$$\sum_{i=1}^{N_c} q_i = \rho_i c_i v_i \frac{dT_i}{dt} \tag{3}$$

where, ρ is density, c is specific heat capacity, v is volume and $\frac{dT_i}{dt}$ is temperature gradient. The effective thermal conductivity (k_e) is determined based on constitutive relation.

$$q = -k_e \nabla T \tag{4}$$

Figure 5 depicts the heat flow in a cemented rock material. While using the image processing toolbox the microscopic image is transferred into the lattice code. Two different materials (gray and green) with different thermal properties are considered and the thermal load is applied from the upper boundary (1 °C) and lower boundary (0 °C). Figure 6 shows the change of thermal conductivity of metamorphic rock under mechanical confinement pressure while comparing the LEM and experimental results. In the experimental results, a cubic sample with the dimension of 43 mm is undergone a hydrostatic mechanical and thermal loading.

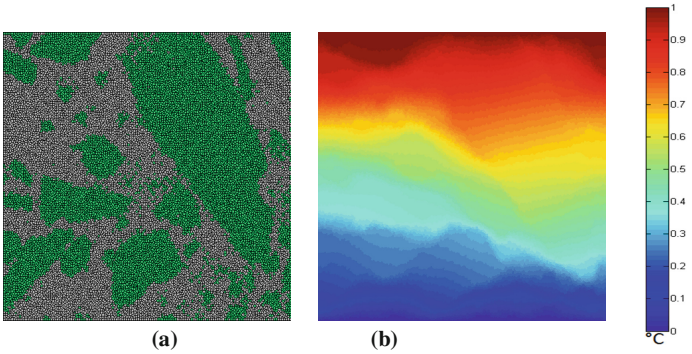

Fig. 5. The 2D meso-scale (a) image processing result in LEM (b) the 2D heat transfer in a heterogeneous material (Sattari et al. 2017)

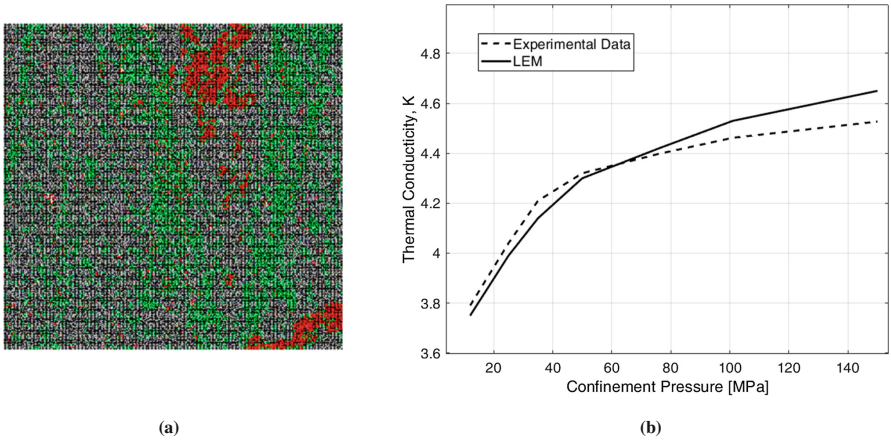

Fig. 6. (a) The result of image processing of metamorphic rock, (b) the comparison of ETC obtained from LEM and experimental data for metamorphic rock (Sattari et al. 2017)

The elongation of the elements $L_{i,1}$ and $L_{j,2}$ will introduce compression thermal forces (f_n^T) on the interface element $L_{1,2}$, however with the increment of length (L) and volume of cells (v), according to Eq. 3, the effective thermal conductivity even without fracture initiation will decrease. The linear thermal strain can be calculated using the thermal expansion coefficient (α'). Eventually, the total strain (ε) will be equal to mechanical strain (ε_m) plus thermal strain (ε_t).

$$\varepsilon = \varepsilon_m + \varepsilon_T, \quad \varepsilon_T = \alpha' \Delta T, \quad f_n^T = EA\varepsilon_T \tag{5}$$

The following steps for determining the effective thermal conductivity of rocks under coupled thermo-mechanical processes are considered:

(1) Applying the mechanical load on the boundary nodes
(2) Calculating the forces in the elements and determining the heat flow under thermal loading
(3) Measuring the thermal strain based on thermal expansion coefficient
(4) Applying the thermal expansion as well as mechanical loading and determining the total strain and stresses under coupled thermo-mechanical processes
(5) Applying the fracture mechanism and removing the failed elements
(6) Increasing the mechanical and thermal loads and repeating the above-mentioned steps

4 Comparison with Experimental Results

The experimental setup is based on measuring the P and S waves and using analytical equations to measure the change of mechanical and thermal properties in rock samples (Motra and Zertani 2018). The multi-anvil apparatus in laboratory of CAU Kiel is able to apply thermal loads from 20 °C to 600 °C and apply confined hydrostatic pressure till 600 MPa. A rock sample composed of quartz mineral (Table 1), where its quartz mass percentage is greater than 95%, is simulated. For an initial load, the k value in Eq. 2 is 6.2 [Wm^{-1} K^{-1}]. From the experimental data, the E = 77 GPa and Poisson's ratio is 0.071.

Table 1. Quartz rock mineral composition

Minerals composition	SiO2	Al2O3	Rest
Percentage (%)	95.11	2.02	<1

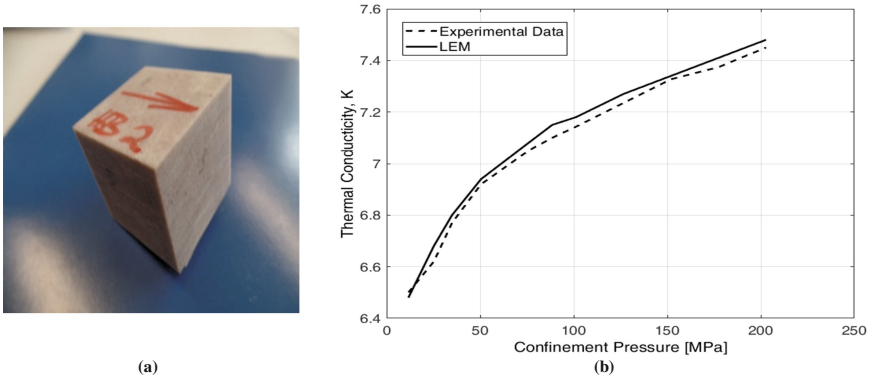

Fig. 7. (a) The quartz rock, and (b) comparison of experimental and numerical ETC under room temperature (20 °C) and confinement pressure increment

The effect of mechanical loading on heat flow and change of effective thermal conductivity (ETC) in Quartz rock is shown in Fig. 7. Similarly for a setup shown in Fig. 8a, the effect of thermal loading, while keeping the mechanical hydrostatic pressure constant at 200 MPa, on fracture initiation and propagation (Fig. 8b) as well as the change of effective thermal conductivity (Fig. 8c) is presented. The temperature is increased from 20 °C to 600 °C and the confinement mechanical pressure (σ_c) and thermal loads (T) are applied from all the boundaries of the domain (Fig. 8a). When an

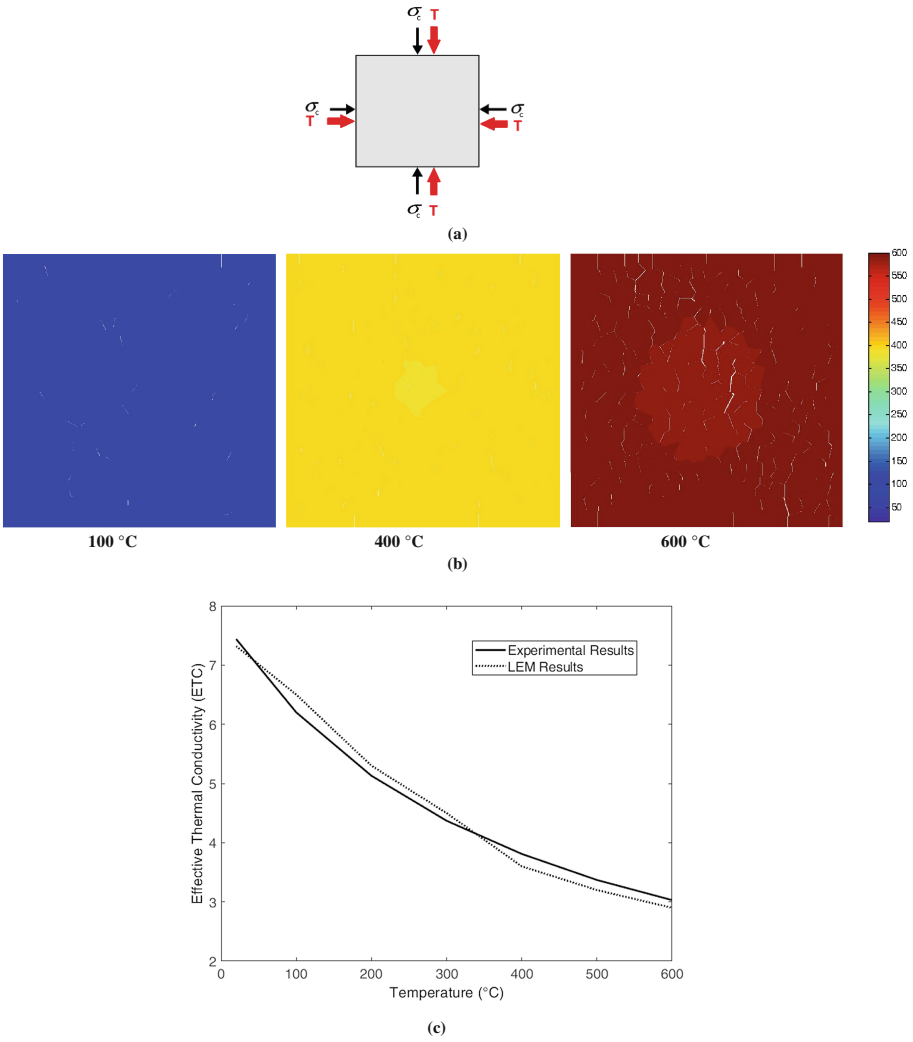

Fig. 8. (a), (b): For a quartz rock (a) the domain boundary condition for both confinement mechanical pressure (σ_c) and thermal loads (T), (b) the heat flow and developed fractures in three different temperatures (100°, 400°, 600 °C), (c) Comparing the ETC under the mechanical constant pressure of 200 MPa

interface element is removed, the thermal conductivity between two cells is broken, therefore the air thermal conductivity of 0.02 [Wm^{-1} K^{-1}] is considered in broken elements. According to the results, it can be said that while increasing the temperature the effective thermal conductivity decreases. This is mainly due to the expansion of the medium and re-opened or initiated micro-cracks in the domain. According to Fig. 8b, it is obvious that with increasing the temperature from 400 °C to 600 °C the generated cracks result in cooler region in center of the domain while comparing to outer boundaries. The diameter of this cooler region in 600 °C is way bigger than 400 °C. According to Fig. 8c, the main drop in ETC happened when the temperature is raised to 400 °C, which is in agreement with the increment of developed fractures in the domain.

5 Conclusion

The developed Lattice Element Method (LEM) with interface elements is able to predict the change of effective thermal conductivity due to coupled thermo-mechanical processes. The stress-strain behavior due to implemented coupled model is able to show the expansion of the medium while increasing the compression forces in the interfaces. The results show a satisfactory outcome while comparing to experimental results obtained from multi-anvil apparatus in laboratory of CAU Kiel. It is shown that with increasing the temperature and keeping the mechanical loading constant, the effective thermal conductivity is decreased. This is due to development of microcracks as well as volume expansion in the medium. On the contrary, the mechanical load increment while keeping the temperature constant causes in effective thermal conductivity increment. This is however due to the closure of microcracks and increment of contact area between the particles. With the extension of the model in 3D as well as the implementation of the hydro model in near future, the application of the proposed method into coupled thermo-hydro-mechanical processes will be investigated.

Acknowledgment. This research project is financially supported by Bundesministerium für Bildung und Forschung (BMBF) (Federal Ministry of Education and Research) under the research grant number of 03G0866B (GeomInt).

References

Bažant, Z.P.: Scaling of Structural Strength. Hermes-Penton, London (2003)

Bolander Jr., J.E., Kobashi, Y.: Size effect mechanisms in numerical concrete fracture. In: Wittmann, F.H. (ed.) Fracture Mechanics of Concrete Structures, pp. 535–542. AEDIFICATIO Publishers, Freiburg (1995)

Bolander, J.E., Saito, S.: Fracture analyses using spring networks with random geometry. Eng. Fract. Mech. **6**, 1569–1591 (1998)

Feng, Y.T., Han, K., Li, C.F., Owen, D.R.J.: Discrete thermal element modeling of heat conduction in particle systems: basic formulations. J. Comput. Phys. **227**, 5072–5089 (2008)

Karkri, M., Garnier, B., Boudenne, A.: Numerical and experimental study of the thermo physical properties of spheres composite materials. High Temp. High Press. **40**(1), 61–84 (2011)

Kim, K., Lim, Y.M.: Simulation of rate dependent fracture in concrete using an irregular lattice model. Cement Concr. Compos. **33**, 949–955 (2011)

Kumlutas, D., Tavman, I.: A numerical and experimental study on thermal conductivity of particle filled polymer composites. J. Thermoplast. Compos. **19**, 441–455 (2006)

Liu, X.Y.: 3-D network model and mechanical behaviour simulation of short-fiber reinforced composites. Ph.D. thesis, Institute of Mechanics, CAS, Beijing, China (2001)

Liu, J.X., Deng, S.C., Zhang, J., Liang, N.G.: Lattice type of fracture model for concrete. Theoret. Appl. Fract. Mech. **48**, 269–284 (2007)

Motra, H.B., Zertani, S.: Influence of loading and heating processes on elastic and geomechanical properties of eclogites and granulites. J. Rock Mech. Geotech. Eng. **10**, 127–137 (2018)

Moukarzel, C., Herrmann, H.J.: A vectorizable random lattice. J. Stat. Phys. **68**, 911–923 (1992)

Potyondy, D., Cundall, P.: A bonded-particle model for rock. Int. J. Rock Mech. Min. Sci. **41**(8), 1329–1364 (2004)

Rattanadecho, P., Suttisong, S., Somtawin, T.: The numerical and experimental analysis of heat transport and water infiltration in a granular packed bed due to supplied hot water. Numer. Heat Transf. Part A **65**, 1007–1022 (2014)

Rizvi, Z.H., Shrestha, D., Sattari, A.S., Wuttke, F.: Numerical modelling of effective thermal conductivity for modified geomaterial using lattice element method. Heat Mass Transf. (2017). https://doi.org/10.1007/s00231-017-2140-2

Sattari, A.S., Rizvi, Z.H., Motra, H.B., Wuttke, F.: Meso-scale modeling of heat transport in a heterogeneous cemented geomaterial by lattice element method. Granular Matter **19**, 66 (2017). https://doi.org/10.1007/s10035-017-0751-4

Schlangen, E., van Mier, J.G.M.: Experimental and numerical analysis of micromechanisms of fracture of cement-based composites. Cem. Concr. Compos. **14**, 105–118 (1992)

Tang, C.: Numerical simulation of progressive rock failure and associated seismicity. Int. J. Rock Mech. Min. Sci. **34**(2), 249–261 (1997)

Tavarez, F.A., Plesha, M.E.: Discrete element method for modelling solid and particulate materials. Int. J. Numer. Meth. Eng. **70**, 379–404 (2007)

Thomas, A.L.: POLY3D: A three-dimensional, ploygonal element, displacement discontinuity boundary element computer program with applications to fractures, faults, and cavities in the Earth's crust. Msc thesis, Stanford University (1993)

Wuttke, F., Sattari, A.S., Rizvi, Z.H., Motra, H.B.: Advanced meso-scale modelling to study the effective thermo-mechanical parameter in solid geomaterial. In: Advances in Laboratory Testing and Modelling of Soils and Shales (ATMSS). Springer Series in Geomechanics and Geoengineering (2017). https://doi.org/10.1007/978-3-319-52773-4_9

Yip, M., Li, Z., Liao, B.S., Bolander, J.E.: Irregular lattice models of fracture of multiphase particulate materials. Int. J. Fract. **140**, 113–124 (2006). https://doi.org/10.1007/s10704-006-7636-6

Zhang, H.W., Zhou, Q., Zheng, Y.G.: A multi-scale method for thermal conduction simulation in granular materials. Comput. Mater. Sci. **50**, 2750–2758 (2011)

Hydraulic Effects During Large-Scale Hydrogen Storage in Porous Formations

Wolf Tilmann Pfeiffer(✉) and Sebastian Bauer

Institute of Geosciences, Kiel University, Kiel, Germany
wolf.pfeiffer@ifg.uni-kiel.de

Abstract. Hydrogen storage in porous geological formations could be employed in future energy systems to mitigate shortages due the fluctuating power production from renewable sources. In this work, hydraulic effects of a hypothetical large-scale hydrogen storage site using 11 wells are investigated using numerical scenario simulations. It is found that, the storage site can sustain a power output of 700 to 1140 MW for one week depending on storage permeability. The storage operation is associated with a regional pressure increase of up to 3 bars in 5 km distance to the storage wells.

1 Introduction

Electricity produced from renewable sources is subject to fluctuations due to changes in local weather conditions. If the share of renewable power production is significant, continuous shortage periods of several days could occur (Klaus et al. 2010). The geologic subsurface, e.g. using porous formations, could provide ample capacity for energy storage to mitigate shortage periods in such energy systems. One option for this is the use of hydrogen (H_2) as an energy carrier in a power-to-gas concept, an idea that has already been introduced in the mid-1970s (Sørensen 1975). More recently, the idea of chemical energy storage using e.g. H_2 has regained traction (e.g. Sørensen et al. 2004; Klaus et al. 2010; Schiebahn et al. 2015). A key benefit of utilizing H_2 instead of e.g. CH_4 is the higher system efficiency, as no additional methanation process is required (e.g. Schiebahn et al. 2015).

With the increasing use of the subsurface, e.g. for groundwater abstraction, geothermal applications and large-scale energy storage as described previously, and the usable subsurface space being limited, induced effects and impacts of specific usages should be investigated prior to deployment (Bauer et al. 2013). For this numerical scenario, simulations can be used with examples being the investigation of compressed air energy storage (Wang and Bauer 2017) and hydrogen gas storage in porous formations (Pfeiffer et al. 2017). The focus of the latter study was on storage dimension and induced hydraulic effects in case of a hydrogen gas storage operation in a heterogeneous sandstone formation in Northern Germany.

A. Ferrari and L. Laloui (Eds.): SEG 2018, SSGG, pp. 276–283, 2019.
https://doi.org/10.1007/978-3-319-99670-7_35

2 Storage Scenario, Simulation Model and Storage Setup

An analysis of hydraulic effects of a storage operation requires the definition of the underlying storage demand since the magnitude of induced effects will depend on the required injection and withdrawal rates. The storage demand scenario used in this study is taken from Pfeiffer et al. (2016, 2017), assuming weeklong shortage periods where no power production from renewable sources is available. The required delivery rate the storage must provide is based on the average weekly power demand of the state of Schleswig-Holstein, Northern Germany, which has a population of around 2.8 million people. In 2011 the total electricity consumption of Schleswig-Holstein was 42.82 million GJ (MELUR 2013). A weeklong shortage period would thus result in a deficit of about 0.82 million GJ (228,113 MWh) with the average load at any time being 1358 MW.

The efficiency of the re-electrification process is assumed 60% (e.g. Klaus et al. 2010). With the energy density of H_2 being around 125 MJ/kg (Carden and Paterson 1979) and the H_2 density at surface conditions (prefix s; defined here as 1 bar and 15 °C) of 0.085207 kg/m^3, at least 129 million sm^3 of H_2 gas must be stored.

The structure used in this analysis (Fig. 1) is based on an existing structure in the North German Basin (NGB), adapted from Pfeiffer et al. (2016, 2017). The extent of the Rhaetian beyond the original model domain is determined based on depth information of the overlying caprocks given by the large-scale regional model from Hese et al. (2012) and residual thickness data of the Rhaetian (Baldschuhn et al. 2001). The size of the resulting structural model is about 41 by 48 km in lateral direction, with the lateral spatial discretization ranging from 50 m near the storage site to 1000 m near the model boundaries. The vertical discretization varies from 0.2 to more than 15 m depending on the local thickness of the individual horizons. In areas where the Rhaetian strikes out hydraulic closed boundaries are assumed. At the remaining boundary sections the extent of the Rhaetian beyond the boundary is included by applying a pore volume multiplier and a permeability reduction factor (equal to the reciprocal) to the boundary elements of the grid. The extent towards the north is assumed to increase from 3.5 km in the west to 16 km in the east. The extent beyond the eastern model boundary is assumed to be 10 km. Towards the south the extent is estimated at 8, 10, and 3.5 km from east to west in the three sections where the Rhaetian does not strike out (Fig. 1). The caprocks are assumed tight and are consequently excluded from the simulation.

The hypothetical storage site is placed at the shallower eastern flank of the structure, with the storage operation being carried out using 11 horizontal wells with screen lengths ranging from 300 to 425 m (Figs. 1b, 5). The maximum allowable overpressures are calculated using an estimate of the minimum horizontal stress gradient of 15 MPa/km (Röckel and Lempp 2003) in combination with a safety factor 0.9. The resulting upper BHP limits are in the range of 62.6 to 73.7 bars. The lower BHP limit is set to 30 bars.

The analysis presented here includes two simulation cases with different hydraulic permeabilities. The hydraulic properties are based on preliminary simulations investigating different generalization schemes of the heterogeneous simulation ensemble

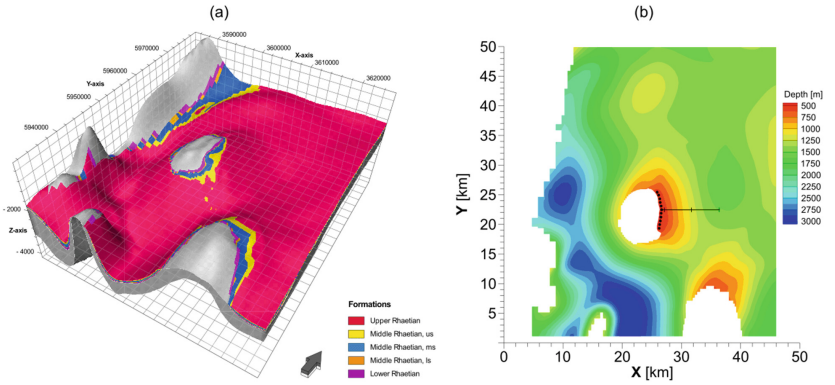

Fig. 1. (a) Structural model of the storage complex and (b) depth of the Middle Sandstone of the Middle Rhaetian. Well positions are depicted by black circles; the positions of the observations points are marked on the transect depicted by the black line.

described in Pfeiffer et al. (2017). It was found, that generalizing permeability using a simple arithmetic mean of the values of the heterogeneous ensemble provided simulations results in good agreement of the 75th percentile of the ensemble. Generalizing permeability by calculating the arithmetic average of the vertical harmonic means of the ensemble provided results close to the 25th percentile ensemble results. Thus, for this study these two generalization schemes, from herein referred to the high and low permeability case, are used (Table 1), which provide an estimate for the spread of possible results. All remaining reservoir properties such as porosity and the multi-phase properties are averaged using a simple arithmetic mean in both presented cases from the values given in Pfeiffer et al. (2017). Capillary pressure is determined using the formulation by Brooks and Corey (1946); relative phase permeability is calculated using a Corey-type equation (Burton et al. 2009).

Table 1. Hydraulic properties of the simulation runs based on the heterogeneous scenario simulations presented in Pfeiffer et al. (2017).

Formation	Permeability [mD]		Porosity [–]	Sr_w [–]	kr_{gmax} [–]	pd [bar]
	High	Low				
Upper Rhaetian	1.81	0.39	0.13	0.53	0.12	9.69
Upper Shale, Middle Rhaetian	120.43	70.85	0.28	0.42	0.37	1.68
Main Sandstone, Middle Rhaetian	598.36	474.81	0.33	0.35	0.68	0.22
Lower Shale, Middle Rhaetian	1.34	0.02	0.11	0.55	0.09	11.06
Lower Rhaetian	46.87	2.86	0.15	0.52	0.17	8.89

The simulated storage schedule consists of three phases: an initial injection of Nitrogen (N_2) at 15,000 sm^3/d/well for 548 days, an initial H_2 injection at 15,000 sm^3/d/well for 274 days, and the cyclic storage operation with increasing withdrawal rates (Fig. 2). Each storage cycle consists of a weeklong withdrawal period with the final target rate being 1.845 million sm^3/d/well, followed by a refilling phase at 225,961 sm^3/d/well for 60 days and a subsequent shut-in period of 30 days. Operating at maximum capacity the simulated storage should be capable to provide H_2 equivalent to 251,000 MWh in each storage cycle, with the power output being 1494 MW. The target N_2 volume is set to be 20% of the total cushion gas volume, which itself is set to 60% of the total gas in place (GIP) at maximum storage capacity of 710 million sm^3. The H_2 injections are schedule so that the H_2 fraction in the total GIP does not fall below 30% at any time. The multiphase-multicomponent reservoir simulator ECLIPSE E300 (© Schlumberger) is used for all cases.

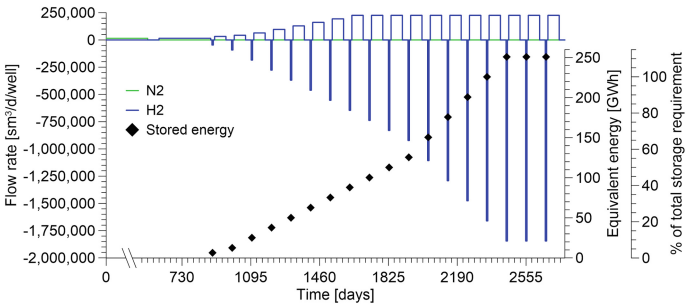

Fig. 2. Simulated storage schedule and target storage capacity in each storage cycle.

3 Simulation Results

All simulation results are reported as pressure change versus a base case without a gas storage operation. The injection of gas results in a pressure increase of no more than 16 bars at the storage wells, governed by the upper BHP limits. At 500 m distance the overall pressure increase is less than 10 bars for the low permeability case and around 8.5 bars in the high permeability case (Fig. 3a). At greater distances the pressure build-up is smaller with an overpressure of slightly more than 2 bars in 5 km (Fig. 3b) and less than 1 bar in about 10 km (not shown). The perturbations caused by the following storage operation increase in magnitude with the number of storage cycles as the applied well flow rates increase (compare Fig. 2). During the withdrawal periods significant pressure reductions of up to −15 bars occur near the storage wells (Fig. 3a). This results in a zonation with overpressures in the far field of the storage and pressures below hydrostatic levels near the wells (Figs. 3, 4). Overall the pressure levels decrease with time as local pressure differences are compensated for by fluid movements (Fig. 4).

The injected gas accumulates in the top of the structure due to its lower density (Fig. 5a). The volume of N_2 injected is about 83 to 90 million sm^3, depending on the

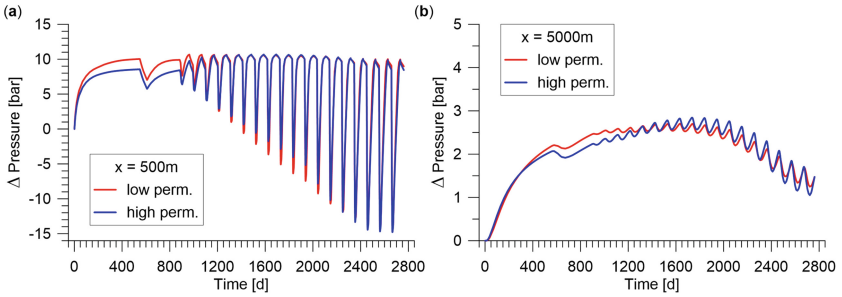

Fig. 3. Pressure change at (a) 500 m and (b) 5000 m along the transect through the well gallery for both simulation cases (for position of transect see Fig. 1b).

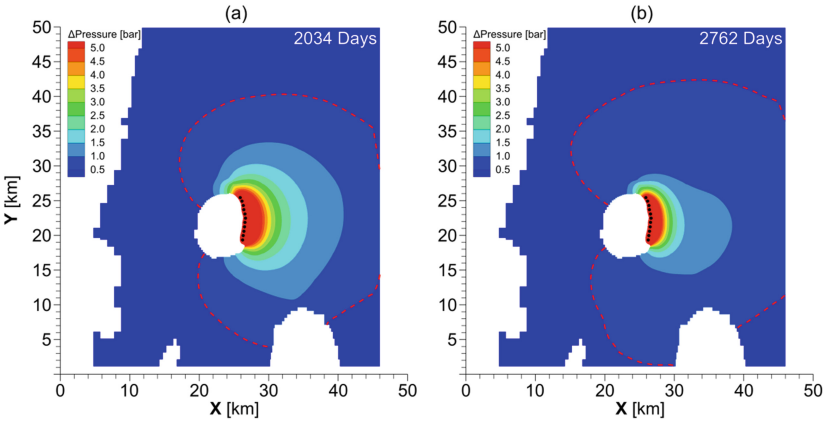

Fig. 4. Pressure change compared to the initial hydrostatic pressure after the (a) the 12th and (b) the last storage cycle for the high permeability case. The dashed red line depicts the 1 bar pressure isocline; the black circles indicate the well positions.

reservoir permeability. The initial volume of H_2 in place is 42 to 45 million sm^3. Due to the injection scheme and the homogeneous parameterization of the storage formation the H_2 fraction in the GIP is more than 90% in most of the gas phase (Fig. 5c). Near the well connections, the gas saturation varies only slightly, while the gas-water contact at the bottom of the storage formation moves several meters during each storage cycle (Fig. 5b). Thus, the GIP is not sufficient to support the storage operation completely through gas compression and expansion. The fraction of H_2 within the gas phase shows changes of up than 20% near the edges of the gas phase (Fig. 5d). Near the storage wells changes are minimal. The gas phase distribution as well as the distribution of the components within the gas phase do not show major differences between the two considered cases. The overall extent of the gas phase is about 7 km by 750 m in lateral directions (Fig. 5a).

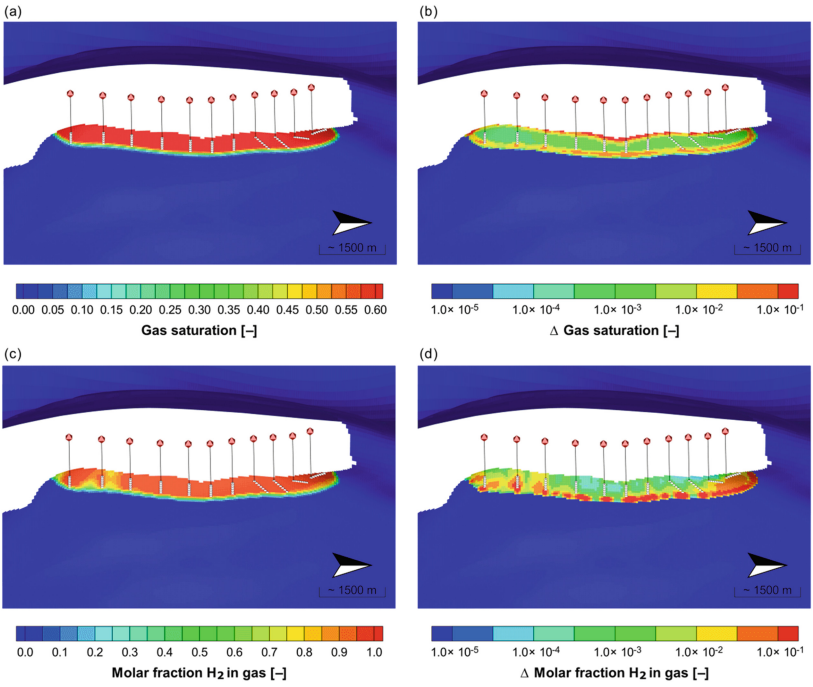

Fig. 5. (a) Gas saturation and (c) molar fraction of H_2 in gas in the storage formation prior to the 16th storage cycle for the high permeability simulation case and differences during one cycle in (b) gas saturation and (d) H_2 fraction at the end of the withdrawal phase.

In the first 9 storage cycles the target well flow rates are achieved for most withdrawal periods in both simulation cases. The GIP is therefore sufficient to support the desired flow rates. From the 10th storage cycle onwards the GIP is not sufficient to support the target withdrawal rates such that a decrease in storage flow rates towards the end of each withdrawal is observed, with the minimum storage flow rates never falling below 10 and 16 million sm^3/d for the low and high permeability simulation cases, respectively (Fig. 6a).

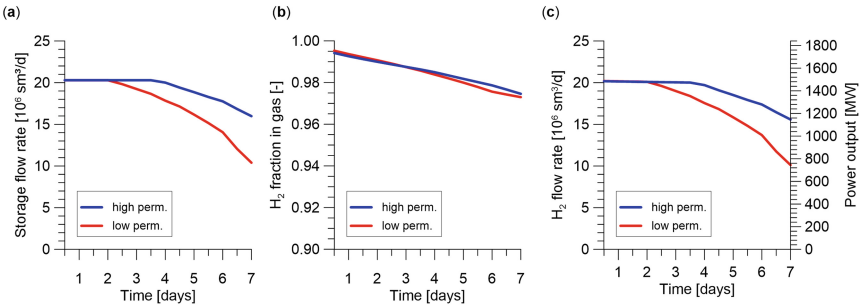

Fig. 6. (a) Storage flow rate, (b) H_2 fraction in the withdrawn gas, and (c) corresponding H_2 flow rate and power output for both simulation cases in the last storage cycle (18th).

The H_2 fraction in the withdrawn gas varies from initially 90% to 78% in the first storage cycles for the low permeability case. In the following storage cycles, and as the storage size in terms of gas and H_2 in place increases, higher and more consistent H_2 fractions are achieved during the withdrawal periods. From the 11th cycle onwards, H_2 fractions remain well above 90% throughout all withdrawal periods showing only small variations indifferent of the simulation case (Fig. 6b).

The power output from the storage is a given by the achieved H_2 flow rate which in turn depends on the storage flow rate and the H_2 fraction in the withdrawn gas. While peak H_2 flow rate can be much higher, the minimal H_2 flow rate achieved at the end of each storage cycle can be taken as the sustainable flow rate during that specific cycle. In the low permeability case the sustainable H_2 flow rate is around 10 million sm^3/d, corresponding to a power output of around 700 MW. In the high permeability case the corresponding values are 15.5 million sm^3/d and 1140 MW. In total the storage site can provide at least 116 and 132 million sm^3 of H_2 (204,950 and 232,860 MWh) in the low and high permeability simulation case respectively, which is sufficient to cover 90 to 100% of the defined storage demand.

4 Conclusions

For the simulated storage schedule the achieved H_2 flow rates and thus the storage performance does not vary much during the first cycles, with a storage capacity of 5100 MWh being available after the initial filling. Depending on the permeability of the storage formation, a maximum of around 205,000 to 233,000 MWh can be withdrawn within one week after 2450 days build-up time. With that, the storage site can supply 90 to 100% of the defined storage demand. The peak power output from the storage is 1480 MW independent of the reservoir permeability, while the sustainable power output is found to be around 700 to 1140 MW. Therefore, the storage site can provide for around 52 to 84% of the average load required in the storage demand scenario of 1358 MW. The offset between the coverage of power and energy demand is due to a decline in storage flow rate during the withdrawal cycles. This can be attributed to the gas volume in place being too low, also shown by the changing gas-water contact. However, as the spill points of the structure are not yet reached more gas could be injected.

The overall extent of the gas phase is about 7 km by 750 m. The storage operation induces overpressures in the formation, which can reach more than 10 bars within the first 500 m from the wells and thus in the region of the injected gas. Beyond the gas phase, the pressure build-up is significantly reduced with less than 3 bars overpressure in 5 km and less than 1 bar in 10 km, independent of reservoir permeability. Compared to the absolute pressure values in these regions, which are above 150 bars, the induced pressure perturbations are small.

References

Baldschuhn, R., Binot, F., Fleig, S., Kockel, F.: Geologisches Jahrbuch A153: Geotektonischer Atlas von Nordwest-Deutschland und dem deutschen Nordseesektor. Schweizerbart'sche Verlagsbuchhandlung, Hannover (2001)

Bauer, S., Beyer, C., Dethlefsen, F., Dietrich, P., Duttmann, R., Ebert, M., Feeser, V., Görke, U., Köber, R., Kolditz, O., Rabbel, W., Schanz, T., Schäfer, D., Würdemann, H., Dahmke, A.: Impacts of the use of the geological subsurface for energy storage: an investigation concept. Environ. Earth Sci. **70**, 3935–3943 (2013)

Brooks, R.H., Corey, A.T.: Hydraulic Properties of Porous Media. Hydrological Papers Colorado State University 3, 61p (1946)

Burton, M., Kumar, N., Bryant, S.L.: CO2 injectivity into brine aquifers: why relative permeability matters as much as absolute permeability. Energy Proc. **1**, 3091–3098 (2009)

Carden, P.O., Paterson, L.: Physical, chemical and energy aspects of underground hydrogen storage. Int. J. Hydrog. Energy **4**, 559–569 (1979)

Hese, F.: 3D Modellierungen und Visualisierung von Untergrundstrukturen für die Nutzung des unterirdischen Raumes in Schleswig-Holstein. Dissertation, Kiel University (2012)

Klaus, T., Vollmer, C., Werner, K., Lehmann, H., Müschen, K.: Energieziel 2050: 100 Prozent Strom aus erneuerbaren Quellen. Umweltbundesamt, Dessau-Roßlau (2010)

MELUR: Energiebilanz Schleswig-Holstein 2011. Ministerium für Energiewende, Landwirtschaft, Umwelt und ländliche Räume, Kiel (2013)

Pfeiffer, W.T., Al Hagrey, S.A., Köhn, D., Rabbel, W., Bauer, S.: Porous media hydrogen storage at a synthetic, heterogeneous field site: numerical simulation of storage operation and geophysical monitoring. Environ. Earth Sci. **75**, 1177 (2016)

Pfeiffer, W.T., Beyer, C., Bauer, S.: Hydrogen storage in a heterogeneous sandstone formation: dimensioning and induced hydraulic effects. Pet. Geosci. **23**, 315–326 (2017)

Röckel, T., Lempp, C.: Der Spannungszustand im Norddeutschen Becken. Erdöl Erdgas Kohle **119**, 73–80 (2003)

Schiebahn, S., Grube, T., Robinius, M., Tietze, V., Kumar, B., Stolten, D.: Power to gas: technological overview, systems analysis and economic assessment for a case study in Germany. Int. J. Hydrog. Energy **40**, 4285–4294 (2015)

Sørensen, B.: Energy and resources. Science **189**, 255–260 (1975)

Sørensen, B., Petersen, A.H., Juhl, C., Ravn, H., Søndergren, C., Simonsen, P., Jørgensen, K., Nielsen, L.H., Larsen, H.V., Morthorst, P.E., Schleisner, L., Sørensen, F., Pedersen, T.E.: Hydrogen as an energy carrier: scenarios for future use of hydrogen in the Danish energy system. Int. J. Hydrog. Energy **29**, 23–32 (2004)

Wang, B., Bauer, S.: Compressed air energy storage in porous formations: a feasibility and deliverability study. Pet. Geosci. **23**, 306–314 (2017)

Evaluation of Reconstruction and Segmentation Techniques on High Temporal Resolution μCT Scans for Geotechnical Applications

K. Liu[1(✉)], F. A. Loveridge[2], R. Boardman[1], and W. Powrie[1]

[1] University of Southampton, Southampton, UK
kl5gl4@soton.ac.uk
[2] University of Leeds, Leeds, UK

Abstract. Coupled hydro-thermal phenomena are often relevant to applications in energy geotechnics, such as nuclear waste disposal and ground heat storage or transfer. It is then necessary to obtain data for use in and validation of models. Micro-focus X-ray computed tomography (μCT) has the potential to investigate hydro-thermal phenomena, both qualitatively and quantitatively. However it is difficult to obtain representative CT scan data for dynamic processes as a compromise must be made between image quality and scan time. For example, in thermally-driven water flow, moisture migration in the pore space could occur rapidly and over the course of a single scan. Reducing the scan time to obtain representative temporal data leads to a different set of challenges in terms of image quality and data processing. This paper investigates the potential of algebraic reconstruction techniques (ART) to improve the quality of reconstructed images from fast undersampled scans or noisy projection data, with reference to a uniformly-graded dry sand specimen. Results using ART are compared with those obtained using data reconstructed by the conventional filtered back-projection technique (FBP). In both cases, phase proportions are determined by Gaussian decomposition (GD) rather than traditional thresholding methods. It is shown that there is no need to attempt to improve the image quality by altering the image reconstruction algorithm, because GD is tolerant of undersampling and noisy data.

1 Introduction

Coupled hydro-thermal flow phenomena are relevant to applications in energy geotechnics, such as nuclear waste disposal and in-ground heat thermal storage. However, it is challenging to obtain real data for model evaluation and validation. Micro-focus X-ray computed tomography (μCT) has the potential to investigate hydro-thermal flow phenomena both qualitatively and quantitatively, although it can be difficult to obtain representative data because a compromise may need to be made between image quality and scan time. For example, in thermally-driven water flow, moisture movement in the pore space can occur rapidly, over the course of a single

A. Ferrari and L. Laloui (Eds.): SEG 2018, SSGG, pp. 284–290, 2019.
https://doi.org/10.1007/978-3-319-99670-7_36

scan. Reducing the scan time to minimise movement artefacts in the reconstructed image brings challenges in data processing and image quality.

To improve the image quality from fast undersampled scans or noisy projection data, it is possible to employ alternative reconstruction algorithms [beyond the de facto standard of filtered back projection (FBP) (Ketcham and Carlson 2001)]. Previously, Myers et al. (2011b), based on prior information in Myers et al. (2011a), used algebraic reconstruction techniques (ART) (Gordon 1974) to study two-phase flow scenario. They show the potential of ART to offer sensible reconstructed image data from fast temporal scans, although quantitative data analyses and comparisons were not provided. This potentially useful reconstruction approach has not been extended to the X-ray CT applications in geotechnics; this is the subject of our study.

In this article, we investigate the use and present quantitative analyses of algebraic reconstruction techniques (ART) (Gordon et al. 1970) for fast scans on soils. Comparisons are made with analyses based on data from the conventional filtered back-projection reconstruction (FBP) (Dudgeon and Mersereau 1984), achieved by Gaussian decomposition analysis; these are also presented.

2 X-Ray CT Reconstruction Approaches

2.1 Filtered Back-Projection Reconstruction Technique (FBP)

Filtered back-projection reconstruction (FBP) is a conventional analytical reconstruction technique. As illustrated by Ketcham and Carlson (2001), in FBP each view is first filtered in the frequency domain; the filtered views are then sequentially superimposed over a rectangular grid back in the direction appropriate to its acquisition orientation, to produce the reconstructed image data. A view is a 1D attenuation profile based on the position at the corresponding orientation. Filtration of views will suppress the low frequencies, resulting in sharp image data; however, the filtered image data can be very noisy due to the amplified high frequencies [resulting in low contrast-to-noise ratio (CNR) (BSI 2011)]. FBP works well when a large number of projections are available. However, it cannot provide high quality data when the number of projections is small (Chetih and Messali 2015).

2.2 Algebraic Reconstruction Techniques (ART)

As an iterative algorithm for image reconstruction, ART (Gordon et al. 1970) reconstructs a tomographic slice image from projections by continual approximation. The projections corresponding to the current estimate are compared with the measured projections. The result is used to modify the current estimate to create a new approximation (Gordon 1974). This assumes that the cross sections contain arrays of unknowns, and the reconstruction process is analogous to solving a set of linear equations via a finite collection of basic functions (Chetih and Messali 2015), using an iterative method [SART (Andersen and Kak 1984)].

Image data from ART is less noisy (higher CNR), but may also be less clear [higher point spread function (PSF) (Ketcham and Hildebrandt 2014)], than that derived from

FBP under the same imaging conditions. This is because random error (i.e. noise in this case) during ART reconstruction tensions the resulting matrix, and hence tends to become minimised.

3 Experimental Design

In our work, ART is the primary reconstruction approach tested for its potential application to fast scans in geotechnics. A number of experiments was carried out on a dry sand specimen. Two scans were implemented for comparison; one scan was carried out at normal scanning settings as the control group (CG), and the other scan as the test group (TG) in undersampled fast scan conditions.

3.1 Specimen Characteristics

The CT scan experiments were carried out using a dry sand specimen prepared by air pluviation (Cresswell et al. 1999). This specimen was prepared from uniformly-graded Fraction E Leighton Buzzard sand (BSI 1998), with an inside diameter of 5 mm and a height of $\sim$10 mm. The solid proportion, determined by gravimetric measurement, was 60% $\pm$ 1% (porosity 40% $\pm$ 1%). Air pluviation is known to give suitably repeatable results.

3.2 Scan Settings

The scans were conducted using the Benchtop scanner at the University of Southampton μ-VIS Imaging Centre (University of Southampton 2017), which features a standard 160 kVp reflection tungsten target. The scan settings are given in Table 1. The only difference between the test group (TG) and the control group (CG) was the number of projections, with all other parameters being the same. Consequently, scanning for the TG was more than six times faster than that for the CG, with scan times of about 21 min (TG) and 135 min (CG).

Table 1. Scan settings of CT experiments

Scan	Energy	Intensity	Exposure time	Frames (per projection)	Projection count	Resolution
TG	80 kV	75 μA	1067 ms	4	300	9 μm
CG	80 kV	75 μA	1067 ms	4	1905	9 μm

3.3 Protocol of Reconstruction and Processing

The FBP reconstruction was implemented using vendor-specific implementations of the Feldkamp Davis Kress algorithm (Feldkamp et al. 1984) via Nikon X-TEK CT Pro 3D (Version XT 2.2 Service Pack 11). Possessing the same algorithm as ART, the simultaneous algebraic reconstruction technique (SART) (Andersen and Kak 1984), which is a superior implementation, was adopted for the algebraic reconstruction. It was implemented by the X-ray tomography 3D reconstruction software Digisens (2011).

As FBP is able to reconstruct image data perfectly provided a sufficient number of projections is acquired; thus the CG data were reconstructed only by FBP to offer a basis for the assessment of the TG results. The TG data were reconstructed by both FBP and ART methods.

Gaussian decomposition (GD) via the Levenberg–Marquardt algorithm (Levenberg 1944; Marquardt 1963) was used to process the reconstructed unsigned 16-bit image data; although segmentation of the solid and air phases in soil specimen would have to be performed, this will give good threshold values. GD was carried out using Gnuplot, a mathematical plotting package (Williams et al. 1986). GD is not normally used in soil image segmentation, but has recently been shown to be a promising approach when segmenting three phases in soils from undersampling scan or noisy data (e.g. Liu et al. 2017).

Compared with the implementation of FBP reconstruction for the entire image data, the ART reconstruction was implemented on a small central range (e.g. $1212 \times 1212 \times 5$ voxels for this case) to save computing resource, with a reconstruction period in the order of hours for the entire dataset. Primary comparisons and analyses were based on the same image slice located in the middle of the specimen; global results based on the entire image data from both TG and CG are also presented for comparison. Typically, the solid phase fraction is used as the key metric of performance.

4 Analysis and Discussions

4.1 Evaluation of Image Quality

4.1.1 PSF and CNR

Image quality was assessed initially on the basis of the results of PSF and CNR, along with visual observation of the reconstructed images; they also assist the judgement of whether the loss in clarity around the boundaries of the solid particles is likely to be less significant than the possible gain in terms of CNR. A number of small regions of solid and air phases was selected from the targeted image, and their average grey values (GVs) used for the calculation of the contrast to noise ratio between solid and air (CNR_{sa}). For the assessment of point spread function (PSF_{sa}), a straight line was drawn across the centre of the selected areas from these two phases, perpendicular to their interface.

The same TG data were evaluated; the CNR_{sa} outcomes from the tested ART settings are mostly around 8, compared with about 6 from FBP. The PSF_{sa} values from both reconstruction algorithms were close to each other, at approximately 6.

As the iteration number will influence the reconstruction time, the setting with the lower iteration number is usually selected, provided a similar image quality can be guaranteed. In this case, the iterative setting with 10 iterations and a convergence speed of 0.05 were chosen.

4.1.2 ART Versus FBP

Using the TG data, the same image slice reconstructed by ART (from the optimal settings) and the standard FBP are compared. As can be seen from the zoomed-in local images (Fig. 1), image (i) looks less noisy but more blurred than that from FBP (image (ii)). This is plausible, as ART is able to denoise and minimise image errors. Although image (i) is not visually as sharp as image (ii), this can be attributed to the repeated corrections involved in the iterative calculation algorithm in ART.

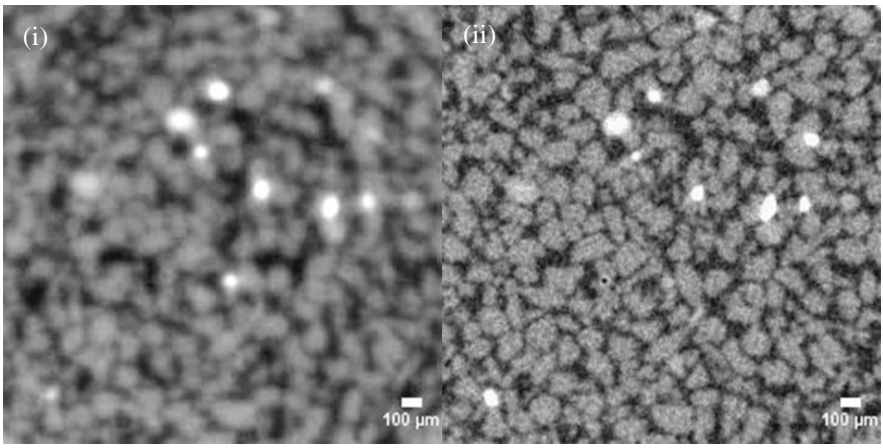

Fig. 1. Zoomed-in region from the same image; (i) ART and (ii) FBP

4.2 Quantification Analysis

To analyse quantitatively the feasibility of the approach, the solid fraction of the same image slice from the three different datasets is assessed by GD. The three datasets are the image reconstructed from the TG by ART, the image reconstructed from the TG by FBP, and the image reconstructed from the CG by FBP.

The global solid proportions were determined for the FBP reconstructed TG data (61.2%) and the CG data (60.9%) from the full dataset, excluding slices suffering from the cone effect. The results are quite consistent with the gravimetric measurement of 60% (±1%).

For the assessment of the local solid fraction, a same image slice reconstructed by ART and FBP from the TG data and that reconstructed by FBP from the CG scan data were compared. The FBP reconstructed TG data (61.4%) provides a close result to that from the CG data (61.3%). This indicates that the GD analysis is reasonably tolerant of the relatively poor image data. However, a noticeable overestimate from the ART reconstructed data (67.0%) was obtained. This may be due to a GV error probably arising from the imperfection of the convergence calculation from the ART reconstruction, to which the GD may be more susceptible.

5 Summary and Conclusions

For X-ray CT applications in geotechnology, the challenge of improving the quantitative interpretation of poor quality image data (e.g. undersampled fast scan data) has not been widely studied. In this article, an alternative type of image reconstruction technique (ART) was assessed, to explore the possibility of decreasing the scan time without compromising the image quality by using a different image reconstruction algorithm.

Based on a study of a dry sand specimen, it was found that the FBP reconstructed image data are able to provide a sensible result, based on Gaussian decomposition (GD) analysis. The same GD analysis on ART reconstructed image data gave an overestimate of the solid fraction, which may be resulting from a GV error due to imperfect convergence in ART reconstruction.

It can be concluded that GD analysis is able to provide sensible results for the phase fraction from FBP reconstructed undersampled image data, without the need to explore the ART reconstructed data.

Finally, it is proposed that for the phase proportion analysis, there is no need to rely on improving the image quality by altering the image reconstruction algorithm (e.g. ART). However, a different reconstruction approach (e.g. ART) may still be attempted and useful, for example when an analysis from the particle morphology perspective is needed from poor image data (e.g. undersampled fast scan data).

References

Andersen, A.H., Kak, A.C.: Simultaneous algebraic reconstruction technique (SART): a superior implementation of the ART algorithm. Ultrason. Imaging **6**(1), 81–94 (1984)

BSI: Testing Concrete. Methods for Testing Cement in a Reference Concrete. British Standards Institution, London (1998)

BSI: Non Destructive Testing - Radiation Methods - Computed Tomography Part 3: Operation and Interpretation. CEN, Brussels (2011)

Chetih, N., Messali, Z.: Tomographic image reconstruction using filtered back projection (FBP) and algebraic reconstruction technique (ART). In: 2015 3rd International Conference on Control, Engineering & Information Technology (CEIT), pp. 1–6. IEEE (2015)

Cresswell, A., Barton, M.E., Brown, R.: Determining the maximum density of sands by pluviation. ASTM Geotech. Test. J. **22**(4), 324–328 (1999)

Digisens: 3D X ray computed tomography software (2011). http://www.digisens3d.com/en/soft/3-Digi_XCT.html. Accessed 27 Mar

Dudgeon, D.E., Mersereau, R.M.: Multidimensional Digital Signal Processing. Prentice-Hall Signal Processing Series. Prentice-Hall, Englewood Cliffs (1984)

Feldkamp, L., Davis, L., Kress, J.: Practical cone-beam algorithm. JOSA A **1**(6), 612–619 (1984)

Gordon, R.: A tutorial on ART (algebraic reconstruction techniques). IEEE Trans. Nucl. Sci. **21**(3), 78–93 (1974)

Gordon, R., Bender, R., Herman, G.T.: Algebraic reconstruction techniques (ART) for three-dimensional electron microscopy and X-ray photography. J. Theor. Biol. **29**(3), 471–481 (1970)

Ketcham, R.A., Carlson, W.D.: Acquisition, optimization and interpretation of X-ray computed tomographic imagery: applications to the geosciences. Comput. Geosci. **27**(4), 381–400 (2001)

Ketcham, R.A., Hildebrandt, J.: Characterizing, measuring, and utilizing the resolution of CT imagery for improved quantification of fine-scale features. Nucl. Instrum. Methods Phys. Res. Sect. B Beam Interact. Mater. Atoms **324**, 80–87 (2014)

Levenberg, K.: A method for the solution of certain non-linear problems in least squares. Q. Appl. Math. **2**(2), 164–168 (1944)

Liu, K., Loveridge, F.A., Boardman, R., Powrie, W.: Study of short-term evaporation in sand specimens via micro-focus X-ray computed tomography. Paper presented at 2nd international symposium on coupled phenomena in environmental geotechnics (CPEG2), Leeds (2017)

Marquardt, D.W.: An algorithm for least-squares estimation of nonlinear parameters. J. Soc. Ind. Appl. Math. **11**(2), 431–441 (1963)

Myers, G.R., Kingston, A.M., Varslot, T.K., Turner, M.L., Sheppard, A.P.: Dynamic tomography with a priori information. Appl. Opt. **50**(20), 3685–3690 (2011a)

Myers, G.R., Kingston, A.M., Varslot, T.K., Turner, M.L., Sheppard, A.P.: Dynamic X-ray micro-tomography for real time imaging of drainage and imbibition processes at the pore scale. In: International Symposium of the Society of Core Analysts, Austin, 18–21 September, pp. 1–12 (2011b)

University of Southampton: μ-VIS: multidisciplinary, multiscale, microtomographic volume imaging (2017). http://www.southampton.ac.uk/muvis/about/index.page. Accessed 26 Mar

Williams, T., Kelley, C., Bröker, H.-B., Campbell, J., Cunningham, R., Denholm, D., Elber, G., Fearick, R., Grammes, C., Hart, L.: An interactive plotting program. Environment **4**(10Exit), 5 (1986)

Underground Storage of Latent Heat: Theory and Experiments

Silvia Bersan[1(✉)], Jacco K. Haasnoot[1], Benno van der Werff[2], Wijnand J. H. Heems[2], and David Smeulders[2]

[1] CRUX Engineering BV, Amsterdam, The Netherlands
bersan@cruxbv.nl
[2] Department of Mechanical Engineering,
TU Eindhoven, Eindhoven, The Netherlands

Abstract. Thermal heat storage in the subsurface can be in the form of latent heat. In this way heat can be stored in the form of ice, where heat is stored when ice melts, and heat is extracted by ice formation. We investigate the use of a borehole device for heat exchange with the subsurface. The main advantage in comparison with existing underground storage devices is the limited size of the required excavation. The device is equipped with extraction and recharge circuits arranged in two concentric helices connected at the bottom of the cylinder. The performance of the device is predicted with finite element COMSOL modelling and tested in the laboratory. Some key aspect are identified that will help optimizing the design and the usage of the system.

1 Introduction

Heat storage is becoming more and more important to facilitate the energy transition. In order to mitigate climate change, low temperature heat will be used in the built environment to replace the traditional gas-fired boilers. The heat can be provided by solar collectors, for example. However, this energy source is typically not able to produce "on demand". Contrary to gas-fired boilers, there can be a mismatch between heat demand and heat production, for example in winter, when there is not enough solar energy available for domestic heating. The option of harvesting surplus heat in summer and use it in winter is therefore of paramount importance for large-scale implementation of renewable energy systems in domestic applications. One possibility is to simply store hot water in huge ponds (200,000 m^3 or more), in insulated water tanks or gravel-water tanks (Schmidt et al. 2003). Hot water produced in summer can also be stored in the underground by pumping it through a closed loop pipe (closed loop geothermal system) or infiltrating it in the aquifer through a well (open loop geothermal system).

Also storage in the form of latent heat has been investigated (Carbonell et al. 2014; Winteler et al. 2014). In this case heat is stored when a solid melts and extracted by re-solidification. One of the advantages is that during the phase transition the temperature stays the same so that no insulation is needed. Subsurface ice storages so far installed (Viessman 2013; Punktwissen 2017; SolarEis 2017) have volumes from 10 to 700 m^3, depending on the function and number of the buildings served. They require therefore large excavations, which is difficult in densely built areas. In this paper, we investigate a

A. Ferrari and L. Laloui (Eds.): SEG 2018, SSGG, pp. 291–298, 2019.
https://doi.org/10.1007/978-3-319-99670-7_37

borehole application. The borehole has a diameter of 0.4 m and a length of 20 to 30 m, thus minimizing the space usage and the influence on the surrounding (sensitive) objects.

The volume of water/ice in the cylinder is ten to twenty times smaller than in the abovementioned ice storages. On the other hand the contribution of the ground is expected to be more important considering both the larger depth and the slenderness of the cylinder in comparison with previously designed ice tanks.

A finite element numerical model of the ice tank has been developed in COMSOL Multiphysics with the aim of optimizing the geometry of the tank and circuits as well as the operation strategy. Moreover, in order to get a better understanding of the physical processes occurring in the tank and calibrate the numerical model, a physical model has been built that reproduces on a scale 1:1 the basic unit of the ice tank.

2 Description of the System

The concept design of the heat storage system is shown in Fig. 1. It consists of two circuits, heat recharge and heat extraction circuit, which are inserted in a cylindrical tank installed below the ground surface. The tank is hydraulically connected to the aquifer and the phase change of the groundwater is exploited to extract heat during the cold period. Heat extraction and heat recharge circuit are arranged in two concentric helixes and are interdigitated so as to facilitate ice melting. Indeed one major issue with ice storages is that if the ice layer on the heat exchanger grows too thick, lower and lower source temperatures are required to satisfy the heat demand, leading to a quick depletion of the resource. The extraction circuit is connected to a heat pump. The recharge circuit is connected to absorber panels which exchange heat with the outside environment mostly by convection. Outer and inner circuit can be connected either in parallel or in series. The cylinder has a diameter of about 0.4 m and a length of 20 to 30 m. The diameter is based on practical considerations: the cylinder has to accommodate all the components but at the same time the effort for the installation must be kept limited. Moreover, since the operation strategy is keeping the amount of ice limited, a large volume of phase change material is not needed. The length of the cylinder has to be determined on the base of the heat demand of the building served and on the climate. The system is set up of modular components, which means that additional capacity can be made using extra length or extra cylinders.

Based on both performance simulation (Winteler et al. 2014) and real data (Punktwissen 2017) related to similar ice storage systems, direct extraction from the absorber panels is expected to be the main source of heat, while the ice storage will be mostly used for cold spells. Heat will be extracted directly from the panels until the outside temperature drops below the temperature in the tank. At that point heat will be extracted from the tank. When the outside temperature is higher than the temperature in the tank, the panels can also feed the recharge circuit to store heat in the ground. The circuits are triggered using data from sensors installed in the tank. The system can also be used in summer for active/passive cooling. In this case the extraction circuit releases heat in the ground and the recharge circuit injects cool fluid when the outside temperature drops below the temperature in the tank. Excluding cold spells, the recharge is expected to occur on a nearly daily basis during the warmest hours (in winter mode) or

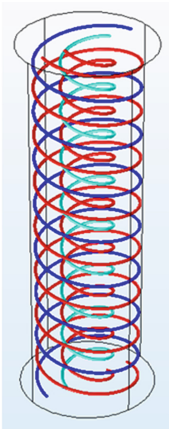

Fig. 1. Schematic view of the ice tank with extraction and recharge circuits.

coolest hours (in summer mode). The amount of phase change material is too small to provide passive cooling for the whole summer but with daily recharge the system can serve as a buffer between day and night.

3 Physical Model

The experimental facility consists of two 25 mm pipes inserted in a PVC cylindrical container (Fig. 2). The cylinder has a diameter of 31.5 cm and a length of 100 cm. Cold and warm fluid can be circulated through the pipes by means of a liquid cooler and a liquid heater. In the experiments the cylinder was horizontal and filled with water. A 50% glycol-water mixture at a constant temperature of −10 °C was circulated in the top pipe for 28 h. The bottom pipe was filled with the glycol mixture but was not activated. Temperature was measured continuously by means of six type-T thermocouples. Three were installed at fixed locations in the cylinder; one measured ambient temperature and two measured the input and output temperature of the refrigerated fluid. The sensors inside the cylinder were installed at the same height and increasing distance from the vertical axis (Fig. 2). A separate thermocouple probe was used to manually sample temperature in different points inside the cylinder during the experiment.

Figure 3 shows the results of the first experiment. The profiles of the temperatures measured at different locations lay are on top of each other, indicating that the temperature is independent of the distance from the cold pipe. After a period of 24 h the temperature inside the container reached a steady value of 9.8 °C. According to the measurements performed with the probe thermocouple, the temperature was the highest at the top of the container (16.1 °C) and the lowest at the bottom (9.5 °C). It was inferred that stratification took place inside the container due to buoyancy movements. No ice formation was observed at the outer surface of the cold pipe.

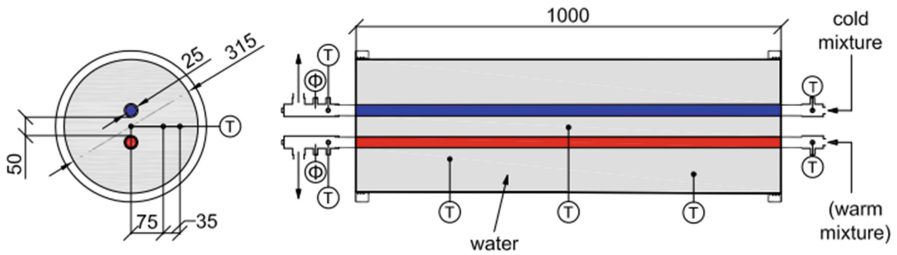

Fig. 2. Scheme of the experimental setup

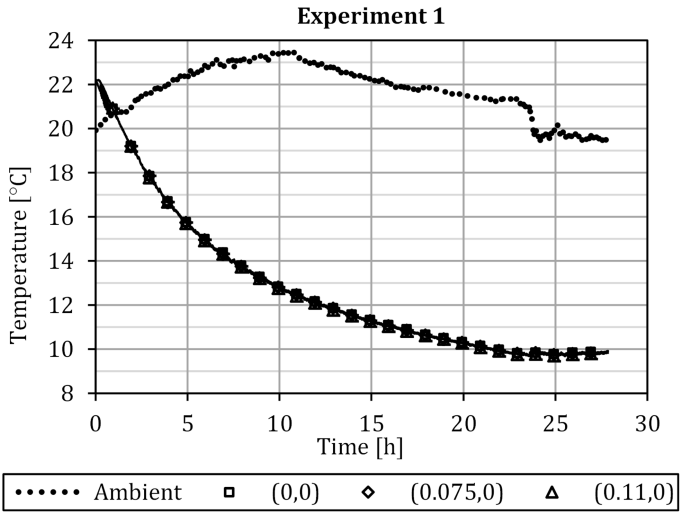

Fig. 3. Experimental results. Temperature measured at three locations inside the cylinder along the horizontal diameter: x = 0, x = 0.075 m and x = 0.11 m.

4 Numerical Model

A numerical simulation of the experiment was performed using a two-dimensional model representing a transversal cross-section. The model was developed with COMSOL Multiphysics. Two different cases were considered: one including free (density driven) convection and one where convection was not included. The results are shown in Fig. 4.

In order to counteract convection in the solidified material a volume force has been added following an approach already adopted by other authors (e.g. Chenzhen et al. 2018). We notice that when free convection is added in the model, all temperatures follow the same profile, which is in agreement with our experimental results. There is still a difference in the equilibration time, however. Steady state is indeed predicted by the numerical model but at a later stage than observed in the experiment. At steady state the temperature at the wall of the pipe is about 5 °C, therefore no ice develops.

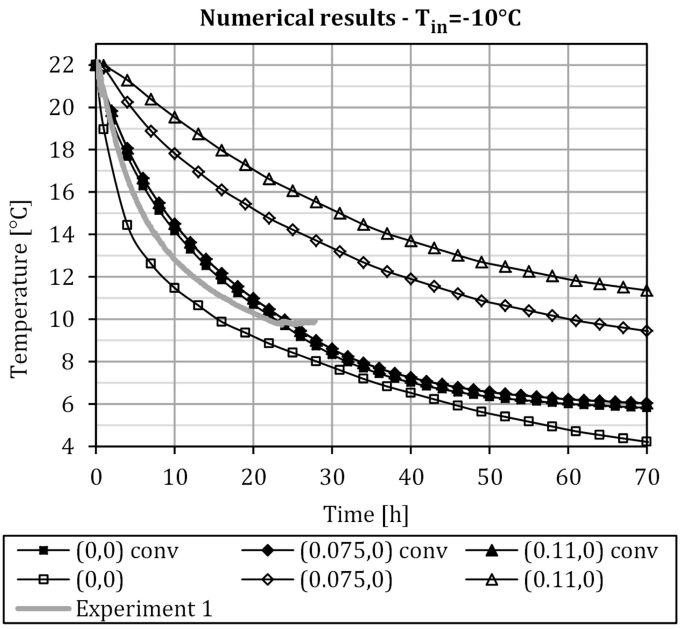

Fig. 4. Comparison between experimental results (grey line) and results from preliminary numerical model (void markers) and model including free convection (filled markers).

The velocity field is portrayed in Fig. 5 next to the temperature contours. The water that is cooled down around the cold pipe moves towards the bottom of the cylinder. In the lower part of the cylinder continuous mixing occurs, resulting in nearly uniform temperature; in the top part nearly no mixing takes place so that temperature stratification can occur. The calculated heat flux across the wall of the cold pipe is two times larger in the model including free convection than in the model without convection (800 W/m^2 vs 400 W/m^2 after 10 h). Since freezing could not be achieved with the initial setup, the experiment was repeated after surrounding the cylinder with a 5 cm layer of insulation material. The results of both the experiment and simulation are presented in Fig. 6.

The initial temperature is lower than the ambient temperature (22 to 24 °C) because the cylinder was filled with cool water lower in order to speed up the ice growth. Around 20 h the temperature in the centre (black line) shows a plateau and the temperature at the top of the cylinder (grey line) becomes lower than the temperature in the centre. This is the moment when thermal inversion occurs: below 4 °C the colder water is lighter and moves upwards. After 100 h a layer of about 5 cm had formed around the cold pipe.

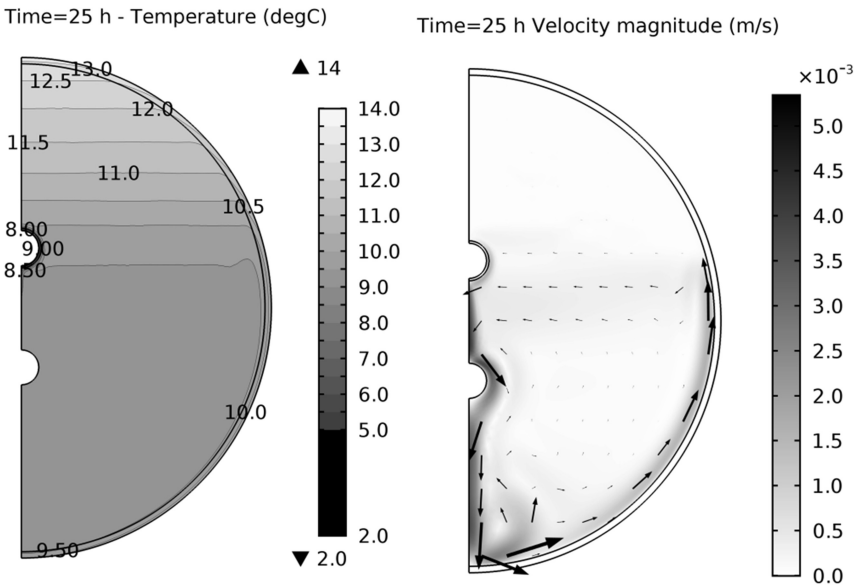

Fig. 5. Temperature and flow velocity field after 25 h obtained form numerical simulation

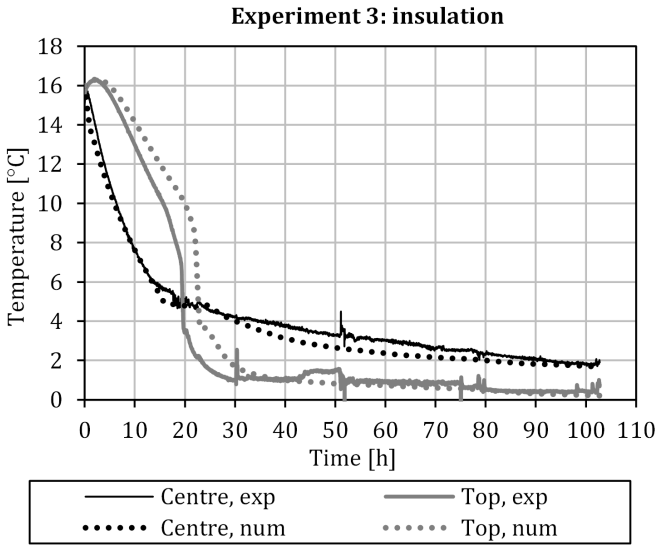

Fig. 6. Experimental and numerical results for the experiment with insulation.

5 Prototype

A full prototype will be installed in the summer 2018 in Eindhoven. It will be used for heating and cooling a two-storey office building with a total surface of about 200 m^2. The ice storage will be integrated with pipe absorber modules placed on the roof of the building. The building is currently provided with radiators which require a high temperature source. To exploit the low temperatures delivered by the heat pump a fan coil unit system will be installed.

Chains of temperature sensors (either PT100 or Fiber Bragg Grating) will be installed both in the ice storage and in the surrounding soil. The data will be used both to calibrate simulation parameters and to provide real-time indications for the dynamic operation of the heating/cooling system.

6 Conclusions

In order to investigate some aspects of a borehole heat exchanger that exploits the phase change of water a physical model has been developed and two experiments were run. The experiments have been reproduced using a finite element model developed in COMSOL. After free convection was included in the numerical model, the latter was capable to reproduce quite well the important features observed in the experiments. Combining experiments and numerical modelling, it has been demonstrated that density driven convection strongly enhances the exchange of heat allowing a higher power to be extracted and decelerating the ice growth. It follows that the contribution of free convection should not be neglected in the design of the complete system, although modelling free convection in complex geometries can be time consuming. Free convection is also expected to cause temperature stratification in the tank. A full prototype will be installed soon and closely monitored over the whole length to get further insights.

Acknowledgements. This research has been made possible by a grant from the Netherlands Enterprise Agency. The research is conducted in close cooperation with WolfDikken Consultants and Park-Id.

References

Carbonell, D., Haller, M.Y., Philippen, D., Frank, E.: Simulations of combined solar thermal and heat pump systems for domestic hot water and space heating. Energy Procedia **48**, 524–534 (2014). https://doi.org/10.1016/j.egypro.2014.02.062

Chenzhen, J., Zhen, Q., Zhenghua, L., Swapnil, D., Fook, H.C., Fei, D.: Non-uniform heat transfer suppression to enhance PCM melting by angled fins. Appl. Therm. Eng. **129**, 269–279 (2018). https://doi.org/10.1016/j.applthermaleng.2017.10.030

Frei, W.: Modeling a coil heat exchanger, COMSOL Blog (2014). https://www.comsol.com/blogs/modeling-coil-heat-exchanger/. Accessed 1 Mar 2018

Mikhaylova, O., Johnston, I.W., Narsilio, G.A.: Ground thermal response to borehole ground heat exchangers. In: Proceedings of the 1st International Conference on Energy Geotechnics, ICEGT 2016, Kiel, 29–31 August 2016

Punktwissen: Measurement data for pilot system heat pump system LEO_2 (2017). https://punktwissen.at/pdf/punktwissen-Measurement-Data-Pilot-System-LEO.pdf. Accessed 10 Apr 2018

Schmidt, T., Mangold, D., Muller-Steinhagen, H.: Seasonal thermal energy storage in Germany. In: ISES Solar World Congress, Goteborg, 14–19 June 2003

SolarEis: In de praktijk (2017). http://www.solareis.nl/projecten.html. Accessed 10 Apr 2018

Viessmann: TopTechniek. Verwarmen met ijs (2013). https://www.viessmann.nl/content/dam/vi-brands/NL/pdfs%20warmtepompen/Vitofriocal/IJsbuffer.pdf/_jcr_content/renditions/original./IJsbuffer.pdf. Accessed 10 Apr 2018

Winteler, C., Dott, R., Afjei, T., Hafner, B.: Seasonal performance of a combined solar, heat pump and latent heat storage system. Energy Procedia **48**, 689–700 (2014). https://doi.org/10.1016/j.egypro.2014.02.080

Simple Method of Rock Pore Structure Determination Presented with the Most Common Rock Types Quarried in Slovakia

Martin Ondrášik(✉), Jana Frankovská, Miloslav Kopecký, and Martin Brček

Slovak University of Technology, Bratislava, Slovakia
martin.ondrasik@stuba.sk

Abstract. Porosity is a very important rock property because it controls many other rock properties. However, not only the total or open porosity but also the rock pore structure (RPS) is important because of its relation to some rock properties. The RPS includes characteristics such as the rock pore size and shape, pore size distribution, total and open porosity, active interior pore wall surface, and interconnectivity of pores. Not all the RPS characteristics are easy to identify and express numerically. Porosity is commonly tested in all commercial laboratories of rock mechanics, but the other RPS characteristics are tested in advanced scientific laboratories only, because their determination depends on expensive laboratory devices and highly skilled staff. In the paper we present the practical use of a very simple alternative method of determining RPS. The method is based on an assumption: if water sorption (adsorption and absorption) into rock pores is controlled by RPS, then water sorption under various controlled conditions can determine RPS. The RPS determination is demonstrated on rock samples, from 80 localities, of eight the most common rock types widely used in civil engineering practice in Slovakia. All the results are given as the percentage weight of water in rock pores of four different categories, which are defined by their size and accessibility to water. The results also reveal the average values and ranges of RPS for each tested rock type.

1 Introduction

In engineering practice, the total porosity is routinely tested in laboratories (STN EU 1636 2007). However, to understand the relationship with various rock properties and processes related to the presence and behaviour of water in rock pores, knowing the total porosity is not sufficient. Also, if we want to predict rock resistivity against deterioration, it is important to understand the rock pore structure (RPS) (Prikryl 2013; Moh'd et al. 1996; Benavente et al. 2004; Ruedrich and Siegesmund 2007; Ordónez et al. 1997; Ondrášik and Kopecký 2014). The rock pore size and geometry, pore size distribution (PSD), and architecture of pore interconnection are characteristics which are not commonly studied in engineering and geological practice but are only investigated in specific research projects focused on the properties of porous material and the consequences resulting from them (Sun and Scherer 2010; Kaneuji et al. 1980). The reason for this is that the most common methods of pore structure determination

A. Ferrari and L. Laloui (Eds.): SEG 2018, SSGG, pp. 299–306, 2019.
https://doi.org/10.1007/978-3-319-99670-7_38

(Anovitz and Cole 2015) are tedious, expensive, and time consuming and require special laboratory equipment and skilled operator.

In our researches, focused on identification of the role of RPS in rock deterioration, we identify some of the most important characteristics or features of the RPS by a simple method similar to the one suggested by Kate and Gokhale (2006). Our method is based on water sorption under three different conditions and the assumption that if water sorption (adsorption and absorption) into rock pores is controlled by RPS then water sorption under various controlled conditions can determine (or indicate) RPS. Using this method, we present the indicative RPS of eight rock types quarried in Slovakia for use in civil engineering. The rock samples are from 80 localities.

2 Theoretical Background and Basis

As one of the most important features of the RPS, the PSD is determined by many methods. Anovitz and Cole (2015) summarized 19 methods. Mercury intrusion porosimetry and gas sorption are the most commonly used methods. However, like any of the other methods, they are also limited by assumptions accepted in their theories regarding the final pore size and PSD calculations and by architecture, and geometry of pores (Anovitz and Cole 2015; Thommes et al. 2015). These limits can be crucial for the accuracy of the results, because, as can be seen from the numerous microscopic images of rock pores published in scientific papers (Kate and Gokhale 2006; Labus and Bochen 2012; Benavente et al. 2004) and on the Internet, the pores in rocks have any shape but the ideal cylinder or slot-like shapes with a smooth wall surface.

To avoid the problem of not uniform size and shape of a pore, Brunauer et al. (1967) suggested using the hydraulic radius for calculating the pore size from water vapour adsorption isotherms. Based on this hydraulic radius, Kate and Gokhale (2006) suggested a simple modified water vapour adsorption method to estimate a complete PSD.

According to experiences from our researches concerning the influence of pore water on rock properties, the most important role of the RPS is its influence on the accessibility of pores to water and the quality and quantity of interactions between pore walls and water. The pore accessibility controls the presence of water in pores, that is, the speed of water saturation and degree of saturation. The pore-wall–water interaction controls the water properties, that is, water with interaction is adsorbed water and water without interaction is free water. These two types of water have different thermodynamic properties, which control some of the processes occurring in rock pores, which are especially strong when the temperature passes the freezing point of water (Powers 1955; Hudec 1991, 1993; Ondrášik and Kopecký 2014).

The pore size classification, which takes into account the presence of adsorbed water in pores (physisorption), is the one given by IUPAC (Sing et al. 1985). According to this classification, pores smaller than 2 nm are called micropores, pores with sizes between 2 and 50 nm are mesopores, and pores greater than 50 nm are called macropores. Pores entirely filled with adsorbed water are micropores (micropore filling) and mesopores (monolayer-multilayer adsorption and capillary condensation) (Sing et al. 1985). Free water (also called bulk water) is found in macropores.

The accessibility of pores to water depends on the shapes of the pores, interconnectivity, and pore architecture. Through pores with two ends (openings to external space) or a pore network with three or more ends (Rouquerol et al. 1994) can be filled with water instantly. We call them "easily accessible pores". One-ended pores (blind pores, ink-bottle pores) or pores with a narrow throat are pores that can only be filled with water under special conditions. We can call such pores "not easily accessible pores". The last type of rock pore is those which are not accessible to water at all. We call them "closed pores".

To satisfy our need to understand the basic features of RPS, we have developed a method for the determination of indicative RPS. It is based on the determination of (1) micropores and mesopores by water adsorption, (2) easily accessible macropores by water absorption, and (3) not easily accessible macropores by boiling or vacuum absorption. Also, the content of (4) closed pores can be determined by using the total porosity. The content of the four defined categories of pores is given not as the recalculated PSD in length units but as the percentage weight of water occupying these pores in relation to the dry rock weight.

3 Tested Rock Samples and Test Methods

A new and simple indicative RPS identification is presented here using data from 80 rock samples collected from 80 localities in Slovakia. The samples included rock types quarried for the building industry, either as rock aggregates or as construction or decorative stone: granite, andesite, basalt, rhyolite, tuff, sandstone, travertine, and limestone. All the rock samples were "leftovers" from a project, *The Engineering Geological Atlas of Rocks of Slovakia* (Holzer et al. 2009), in which rocks from 146 localities from Slovakia are described in detail, including 20 physical and mechanical rock properties (basic set of properties required by standards on natural stone). The tested rocks were dimensioned cubes of 50 × 50 × 50 mm or cylinders of 50 × 50 mm.

The indicative RPS determination presented herein is based on suction tests performed under three different conditions: 59-day water vapour adsorption at 98% RH (relative humidity), 48 h water absorption under atmospheric pressure, and 3 h water absorption by boiling.

The 59-day water vapour adsorption test at 98% RH was performed to identify the content of micropores and mesopores in the rock samples. Usually, a shorter test is sufficient (hours to three days), but a long time was required for the dimensioned 50 × 50 × 50 mm cubes and 50 × 50 mm cylinders to establish a balance between 98% RH and adsorption; that is, after 59 days there was no gain in the weight of the tested samples. All 80 samples were tested at one time in a climatic chamber with 98% RH controlled by a saturated solution of $CaSO_4$ and an electrical fan. The rock weight gain was measured.

The 48 h water absorption test, carried out according to STN EN 13755 (2003), was used to identify macropores that were easily accessible to water. The test results were taken from the project *Atlas* (Holzer et al. 2009).

The 3 h water absorption by boiling was performed to identify rock macropores which are not easily accessible to water. The test was performed according to STN EN 13755 (2003).

For identification of the content of closed pores, the rock total porosity determined as part of the *Atlas* project was used. This porosity, determined according to STN EN 1936 (2007) and given as a volume percentage, was converted into a weight percentage of the dry weight of the rock.

To calculate the content of (1) micropores and mesopores (N_{ADS}), (2) easily accessible macropores (N_{BULK}), (3) not easily accessible macropores (N_{VOID}), and (4) closed pores of any size (N_C) from the test results, the following equations were used:

$$N_{ADS} = N_{AD98} \quad [\text{wt.}\%] \tag{1}$$

$$N_{BULK} = N_{48} - N_{AD98} \quad [\text{wt.}\%] \tag{2}$$

$$N_{VOID} = N_V - N_{48} \quad [\text{wt.}\%] \tag{3}$$

$$N_{CLOSE} = n * \frac{\rho_w}{\rho_d} - N_V \quad [\text{wt.}\%] \tag{4}$$

where N_{AD98} is the content of adsorbed water, N_{48} is the content of absorbed water after 48 h saturation, N_V is the content of water saturated in pores by 3 h boiling, n is the total porosity as a volume percentage, ρ_w is the density of water, and ρ_d is the apparent density of dry rock.

The content of the four defined pore types of the indicative RPS is given as a weight percentage (weight of water occupying the space in the pores related to the weight of dry rock). This RPS determination has the advantage that no assumptions are made for the final calculation of the pore size or PSD.

4 Test Results

The indicative RPS of the eight rock types used in civil engineering in Slovakia is given in Table 1 and in the bar graphs in Figs. 1 and 2. Table 1 gives the indicative RPS data for each rock type in two lines. The first line shows the number of samples (n), content of micropores and mesopores (M_{ADS}), easy accessible macropores (N_{BULK}), not easily accessible macropores (N_{VOID}), closed pores of any size (N_{CLOSE}), and total porosity (n). All the data except the total porosity are expressed as weight percentages. The total porosity is given as the volume percentage. The second line shows the same data as the first line but in relation to the total porosity; that is, the contents of (1) micropores and mesopores, (2) easily accessible macropores, (3) not easily accessible macropores, and (4) closed pores of any size are expressed as percentage of the total porosity (recalculated to weight percentage). There are minimal, average, and maximal values. The average values in one line give sum 100%. The last part of the second line shows the maximal and minimal values of total porosity as volume percentages. The average value is in the line above.

Table 1. Indicative RPS of eight rock types from Slovakia (80 rock samples)

Rock type	n	M_{ADS}	N_{BULK}	N_{VOID}	N_{CLOSE}	n
		[wt.%]	[wt.%]	[wt.%]	[wt.%]	[vol.%]
Granite	4	0.16	0.18	0.04	0.04	0.89
↓(Ø)↑		28.8 (39.1) 46.3	21.5 (42.1) 59.7	4.6 (9.3) 15.7	0.2 (9.6) 35.5	0.17 () 1.41
Rhyolite	5	1.43	2.81	1.14	2.87	17.44
↓(Ø)↑		11.3 (17.0) 23.9	12.2 (34.5) 50.3	1.9 (12.4) 29.8	14.6 (36.1) 57.3	15.18 () 21.33
Basalt	3	0.67	0.02	0.05	0.26	2.75
↓(Ø)↑		56.5 (66.9) 74.9	0.0 (0.3) 9.4	2.1 (6.1) 11.9	13.6 (27.3) 38.8	2.07 () 3.40
Tuff	4	7.28	3.63	2.81	3.64	30.62
↓(Ø)↑		36.3 (42.7) 55.0	18.8 (21.3) 24.9	6.3 (15.6) 22.8	2.3 (20.4) 35.6	21.13 () 41.61
Andesite	17	1.71	0.0	0.18	0.82	6.31
↓(Ø)↑		20.2 (70.8) 116.1	0.0 (15.0) 32.2	0.0 (5.2) 14.4	0.0 (33.3) 80.0	0.61 () 16.98
Sandstone	12	0.84	0.46	0.16	0.15	3.61
↓(Ø)↑		3.5 (56.6) 93.0	8.8 (25.4) 105.9	0.0 (7.0) 40.6	0.0 (11.0) 73.2	1.16 () 8.69
Travertine	2	0.71	2.60	1.37	0.23	9.4
↓(Ø)↑		10.9 (14.8) 18.6	50.8 (53.2) 55.6	19.0 (27.2) 35.3	3.0 (4.9) 6.7	9.23 () 9.65
Limestone	33	0.13	0.29	0.19	0.46	1.93
↓(Ø)↑		2.4 (24.1) 87.6	0.0 (30.4) 86.7	6.9 (11.6) 43.8	0.0 (33.9) 94.3	0.11 () 19.24

↓(Ø)↑ = minimal (average) maximal values

The graphs present the indicative RPSs of granite (Fig. 1a), rhyolite (Fig. 1b), basalt (Fig. 1c), tuff (Fig. 1d), andesite (Fig. 1e), sandstone (Fig. 2a), travertine (Fig. 2b), and limestone (Fig. 2c). For each rock type, there is one graph with four bar groups. The first bar group represents the content of micropores and mesopores. The second bar group represents the macropores that are easily accessible to water, the third represents macropores that are not easy accessible to water, and the fourth represents closed pores. The content of the pores is expressed as a weight percentage. The bars in each group have the same order and represent the same rock sample. For example, the second rhyolite sample is represented by the second bar in the first group of bars (Fig. 1b), by the second bar in the second group of bars, by the second bar in the third group of bars, and by the second bar in the fourth group of bars. This means of visualization of the results of the indicative RPS was used for better presentation of the RPS of the rock types and not the RPS of the individual rock samples, which are not the priority of this paper.

For a better understanding of the indicative RPS data in relation to the routinely tested total porosity, an extra bar graph is given to each indicative RPS bar graph. The extra graph illustrates the total porosity for each rock sample given as a volume percentage.

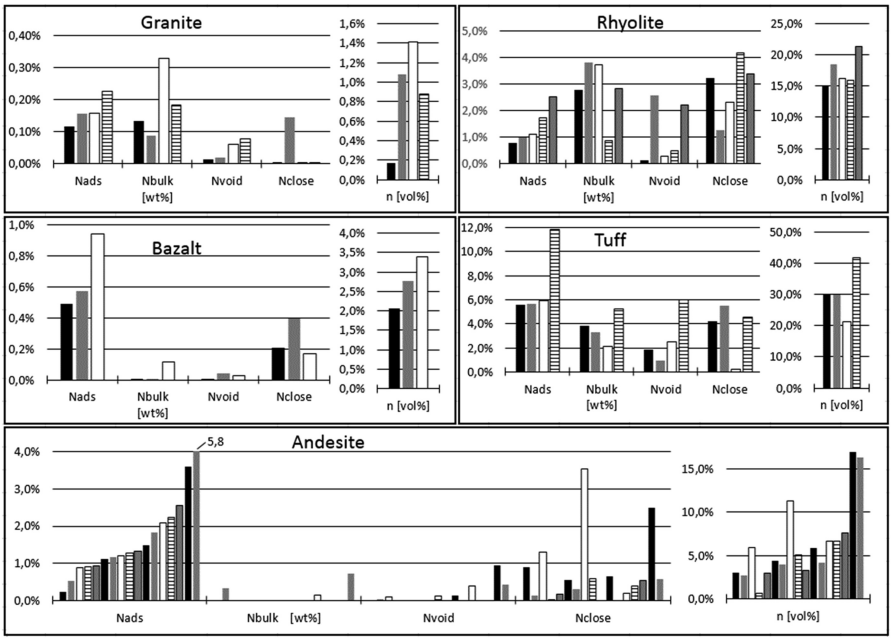

Fig. 1. Indicative RPS of some igneous rocks: (a) granites, (b) rhyolites, (c) basalts, (d) tuffs, and (e) andesites

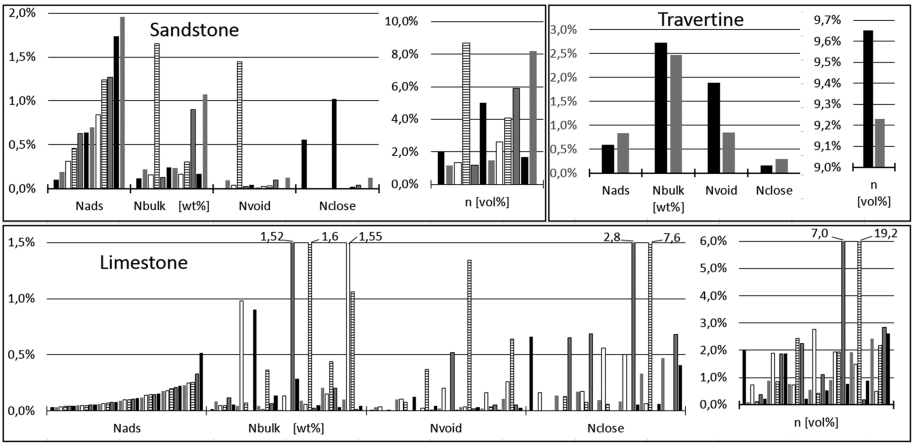

Fig. 2. Indicative RPS of some sedimentary rocks: (a) sandstone, (b) travertine, and c) limestone

5 Discussion and Conclusions

The results of total porosity (Table 1) for the particular rock types were expected (Matula and Pašek 1986). But the data indicating the RPSs of eight rock types (granite, rhyolite, basalt, tuff, andesite, sandstone, travertine, and limestone) obtained from 80 localities in Slovakia are published for the first time. The data include the average, minimal, and maximal values for each of the four defined pore types of the indicative RPSs of the eight rock types (Table 1) and data for each rock sample from 80 localities (Figs. 1 and 2).

Comparison of the data suggests that each graph shows a unique indicative RPS pattern: unique for each rock type and unique for each rock sample. It can be taken as the rock's "fingerprint", which is characteristic for each rock type and for each locality from which the rock sample was taken. We can also assume that rocks of the same petrological type with similar rock properties which are controlled by RPS also have similar indicative RPSs. This assumption can be used for identification or prediction of the rock properties.

The data from the indicative RPS can be analysed in relation to any other data (permeability, frost resistivity, uniaxial compression strength, tensile strength, and many others) and their possible mutual relationship can be identified.

The advantages of the suggested method are that it is simple (no special sample treatment or laboratory equipment is required), many rock samples can be tested at one time, and the results can be correlated directly with other rock properties.

Acknowledgement. This article was created with the support of the Ministry of Education, Science, Research and Sport of the Slovak Republic through grant VEGA No. 1/0842/18.

References

Anovitz, L.M., Cole, D.R.: Characterization and analysis of porosity and pore structures. Rev. Miner. Geochem. **80**, 61–164 (2015)

Moh'd, B.K., Howarth, R.J., Bland, C.H.: Rapid prediction of building research establishment limestone durability class from porosity and saturation. Q. J. Eng. Geol. Hydrogeol. **29**, 285–297 (1996)

Benavente, D., García del Cura, M.A., García-Guinea, J., Sánchez-Moral, S., Ordónez, S.: Role of pore structure in salt crystallization in unsaturated porous stone. J. Cryst. Growth **260**, 532–544 (2004)

Brunauer, S., Mikhail, R., Bodor, E.E.: Pore structure analysis without a pore shape model. J. Colloid Interface Sci. **24**, 451–463 (1967)

Holzer, R., Laho, M., Wagner, P., Bednarik, M.: Inzinierskogeologický atlas hornín slovenska (in Slovak, Engineering Geological Atlas of Rocks of Slovakia), ŠGÚDŠ Btarislava, 532 p. (2009). ISBN 978-80-89343-29-4

Hudec, P.P.: Freezing or osmosis as deterioration mechanism of concrete and aggregate? In: Proceedings of the Second Canadian/Japanese Workshop on Low Temperature Effects on Concrete, Ottawa, 1–2 August 1991

Hudec, P.P.: Aggregate and concrete durability as controlled by water and cation adsorption and osmosis. In: Proceedings Del Seminario International Sobre Technologia del Concreto, Concrete Durability, Monterrey, pp. 32–52 (1993)

Kaneuji, M., Winslow, D.N., Dolch, W.L.: The relationship between an aggregate pore size distribution and its freeze thaw durability in concrete. Cem. Concr. Res. **10**(3), 433–441 (1980)

Kate, J.M., Gokhale, C.S.: A simple method to estimate complete pore size distribution of rocks. Eng. Geol. **84**, 48–69 (2006)

Labus, M., Bochen, J.: Sandstone degradation: an experimental study of accelerated weathering. Environ. Earth Sci. **67**, 2027–2042 (2012)

Matula, M., Pašek, J.: Regionálna inžinierska geológia ČSSR (in Slovak, Regional Engineering Geology of Čekoslovakia), Alfa Bratislava, 295 p. (1986)

Ondrášik, M., Kopecký, M.: Rock pore structure as main reason of rock deterioration. Studia Geotechnica et Mechanica **36**(1), 79–88 (2014)

Ordónez, S., Fort, R., García del Cura, M.A.: Pore size distribution and the durability of a porous limestone. Q. J. Eng. Geol. **30**, 221–230 (1997)

Powers, T.C.: Basic considerations pertaining to freezing and thawing tests. Proc. Am. Soc. Test. Mater. **55**, 1132–1155 (1955)

Prikryl, R.: Durability assessment of natural stone. Q. J. Eng. Geol. Hydrogeol. **46**, 377–390 (2013)

Ruedrich, J., Siegesmund, S.: Salt and ice crystallisation in porous sandstones. Environ. Geol. **22**, 225–249 (2007)

Rouquerol, J., Avnir, D., Fairbridge, C.W., Everett, D.H., Haynes, J.H., Pernicone, N., Ramsay, J.D.F., Sing, K.S.W., Unger, K.K.: Recommendations for the characterization of porous solids (Technical report). Pure Appl. Chem. **66**(8), 1739–1758 (1994)

STN EN 13755: Natural Stone Test Methods. Determination of Water Absorption at Atmospheric Pressure (2003)

STN EN 1636: Natural Stone Test Methods. Determination of Real Density and Apparent Density, and of Total and Open Porosity (2007)

Sing, K.S.W., Everett, D.H., Haul, R.A.W., Moscou, L., Pierotti, A., Rouquerol, J., Siemieniewska, T.: Reporting physisorption data for gas/solid systems with special reference to the determination of surface area and porosity. Pure Appl. Chem. **57**(4), 603–619 (1985)

Thommes, M., Kaneko, K., Neimark, A.V., Olivier, J.P., Rodriguez-Reinoso, F., Rouquerol, J., Kenneth, S.W., Sing, K.S.W.: Physisorption of gases, with special reference to the evaluation of surface area and pore size distribution (IUPAC Technical report). Pure Appl. Chem. **87**(9–10), 1051–1069 (2015)

Sun, Z., Scherer, G.W.: Pore size and shape in mortar by thermoporometry. Cem. Concr. Res. **40**(5), 740–751 (2010)

Time-Dependent Deformation of Chalk Marl Under a Triaxial State of Stress

Nuri Al-Mohamadi(✉)

Applied Science University, Amman 11931, Jordan
nurimohamadi@gmail.com

Abstract. In recent years considerable effort has been directed to the study of stress-strain time effects on soil and soft rock, including; creep, stress relaxation, long term strength of soil and the effect of strain rate on shear strength. These aspects seem to be very important in design and construction of all underground structures. However, long term creep data from drained triaxial creep tests on undisturbed soil samples are very limited in literature. Most of published research work was concerned with the undrained behaviour. Five triaxial drained creep tests were carried out. In addition, three drained tests were used as control tests to determine the drained strength of the material. The applied constant creep stress level ranged from 30% to 80% of the failure stress. Four consolidated undrained triaxial creep tests were conducted at stress level of 30% to 90%. It has been found that the chalk marl is characterised with time-dependent deformations which cannot be accounted for by the anisotropic elastic model. Any constitutive relationship which realistically describes the deformation behaviour of the material must, therefore, include the time factor. Time-dependent deformations of chalk marl in drained and undrained triaxial states of stress will be discussed. For undrained triaxial creep tests, the response of pore pressure during a creep period is also presented. From this study, it can be mentioned that, for triaxial drained creep tests, the axial strain after 100 days of sustained stress ranged from 0.94% to 2.22% for stress levels ranging from 30% to 80%. For a creep period of 200 days, the axial strain ranged from 1.0% to 2.43% for stress levels of 30% and 80% respectively. The proportional increase of axial strain ranged from 24% to 41% at different stress levels. For undrained creep tests, the axial strain ranged from 0.45% to 2.16% for stress levels of 30% to 90%. It can be concluded from this study that time-dependent deformations (creep) of chalk marl constitute a large percentage of the total deformation. It must be taken into consideration in the design of important projects, such as hydro power plants tunnels, nuclear reactor foundations, and underground metro stations.

Keywords: Creep deformations · Drained creep · Undrained creep
Triaxial tests

A. Ferrari and L. Laloui (Eds.): SEG 2018, SSGG, pp. 307–314, 2019.
https://doi.org/10.1007/978-3-319-99670-7_39

1 Introduction

The main objective of this paper is to study the time dependent deformation of chalk marl under a triaxial state of stress. It should be realized that the chalk marl displays anisotropic elastic behavior. Therefore, at least five independent elastic parameters (E_v, E_h, μ_v, μ_h, and G_{vh}) are required to describe the deformation relationship of the chalk marl in terms of effective stresses, where; E_v, E_h are elastic moduli in vertical and horizontal directions respectively μ_v, μ_h = Poisson's ratio in vertical and horizontal directions, G_{vh} = shear modulus. In addition, chalk marl displays time–dependent rheology or viscous deformation. Any constitutive relationship which realistically describes the behavior of the material must, therefore, include the time factor. Creep behavior of chalk marl has been studied experimentally by Al-Mohamadi (2017), under zero lateral strain, and a uniaxial state of stress in specially built creep rigs. In the present paper, creep behavior in drained and undrained triaxial states of stress, in a specially modified triaxial creep apparatus will be presented. The experimental results are discussed. The following triaxial compression tests were carried out in this series: Five consolidated drained triaxial creep tests under different stress levels, four of which were on vertical samples and one test was on a horizontal sample. These tests lasted from 14 days to 330 days. Four consolidated undrained triaxial tests at different stress levels on vertical samples were carried out, Table 1.

Table 1. Triaxial testing program.

Test type & no.	Orient.	Depth m	σ_3 MN/m^2	U_b MN/m^2	Stress level %	Duration
Drained tests						
1	*V*	99.2	1.380	0.690	80	14 days
2	*V*	25.8	1.380	0.690	50	125 days
3	*H*	25.9	1.380	0.960	50	113 days
4	*V*	18.1	0.793	0.552	30	330* days
5	*V*	18.1	0.793	0.552	80	325* days
Undrained tests						
1	V	18.4	0.862	0.621	30	12,660 min
2	V	18.4	0.862	0.621	50	10,000 min
3	V	18.6	0.862	0.621	70	11,300 min
4	V	18.6	0.862	0.621	90	4670 min

σ_3 = Cell Pressure, U_b = back pressure, V = vertical sample, H = horizontal sample

2 Brief Review of Some Important Past Research

In recent years considerable effort has been directed to the study of stress–strain –time effects in soils, including creep, stress relaxation, long term strength of soils and the effect of strain rate on shear strength. However, long term creep data from drained triaxial creep tests on undistributed samples are very limited in literature. Most of the

published research work has been concerned with the undrained creep behavior. The reason may be the practical difficulties involved in carrying out long term drained triaxial creep tests and the long time required to perform such tests. Mitchell (1964) studied the undrained creep characteristics of San Francisco Bay mud and illite. The theory of rate process was applied to derive an expression relating different factors. It was shown that for constant structure, temperature and effective stress, the logarithm of axial strain rate is directly proportional to the deviatoric stress. Murayama and Shibata (1964) reported a linear relationship between axial strain and log time during undrained creep tests on Osaka clay tested at stresses below the upper yield point. The relationship is concave upward during the whole period of creep when the applied creep stresses were higher than the upper yield point. Bishop and Lovenbury (1969) presented a detailed study of the drained creep characteristics of the London clay and normally consolidated Pancone clay from the tower of Pisa under long term drained conditions. The axial strain rate with time is characterized by marked instabilities of strain rate with time which was attributed to the modification in soil structure during creep. They warned of the danger of using simple logarithmic or power laws relating strain and time to predict long term creep strain because of the limited period of applicability of these laws. Davies (1975) presented a comprehensive study of creep behavior of drained and undrained conditions of several clays. The axial strain rate was characterized with strain instabilities which are attributed to the internal structural breakdown of the soil. Al-Mohamadi (1976) studied the strength and deformation characteristics of chalk marl from the Channel tunnel project, including creep behavior. Lacasse and Berre (2005–2006), presented a detailed study on the undrained creep susceptibility of clays. They showed the results of triaxial and simple shear undrained creep tests on Norwegian clay and compared with them other clay results. They proposed a creep susceptibility diagram for several types of clays. Wang et al. (2014) studied creep characteristics of saturated clay in the triaxial test, under two stress paths of axial loading and lateral lightening. They found that volumetric strains were much smaller than axial strains. The creep coefficient was closely related to deviatoric stress levels and had no relation to confining pressure and loading path. It can be seen that these few examples of the past work carried out to investigate drained creep behavior of undistributed samples are very scarce in literature, most of the published creep research was on undrained tests.

3 Apparatus and Testing of Drained and Undrained Triaxial Tests

Samples used in this series were 38 mm diameter and 76 mm long. They were trimmed carefully from 113 mm diameter cores. Triaxial cells with rotating bushing (to reduce friction) were used. A dead weight lever system was constructed to apply a constant creep load. An internal perspex cylinder was used inside the triaxial cell around the specimen and filled with mercury to prevent any water transfer into the specimen. Axial strain and volumetric strain were also measured. The samples were consolidated under back pressure to the desired effective stress for at least one week before applying creep. The frame of the ring shear apparatus was modified to accommodate the triaxial

cell. Back press was applied to saturate the samples. Four tests were carried out under constant creep stress for 7 to 8 days. The sample subjected to 90% stress level failed after about 5 × 103 min after the last increment was applied. The other three samples were loaded to failure after the creep period was completed.

4 Time-Dependent Deformations of Drained Triaxial Tests

4.1 Variation of Axial Strain with Log Time

Axial strain, ε, was plotted versus log time in Fig. 1. The relationship is linear for only a limited period of time ranging from 1 to 10 days, when it becomes nonlinear or changes to another relationship having a different slope. The range of linearity is greater for tests with low stress levels. The characteristic shape of nonlinear relationship is concave upwards. Non-linearity is more pronounced for creep tests with higher stress levels (e.g. test no. 5 in Fig. 1). For tests with low stress levels the characteristic shape of the nonlinear relationship is concave upwards with a tendency to become concave downwards at periods longer than 150 days (e.g. test no. 4 in Fig. 1). Bishop and Lovenbury (1969) found that the relationship between ε and log *t* for London clay is linear for periods up to 100 days for all stress levels and for somewhat longer periods at low stress levels. For Pancone clay the range of linearity was much shorter, up to 10 days only.

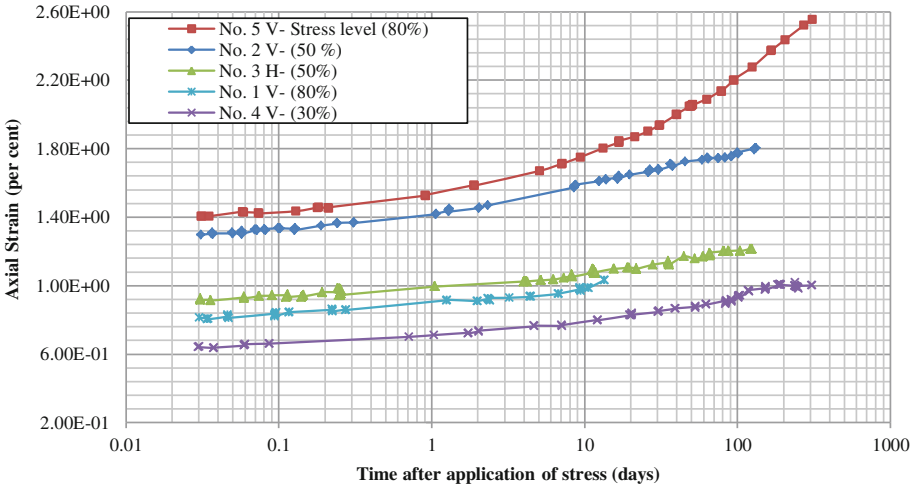

Fig. 1. Development of axial strain with time (drained triaxial creep tests)

Values of the initial one day strain ε_1 ranged from 0.7% to 1.5% depending on the applied stress level and the orientation of the sample. For the same stress level, ε_1 is 0.7 of the corresponding value of the vertical sample. This implies that the initial secant

modulus of the horizontal specimen E_s is 1.44 times that of the vertical specimen. Values of the proportional increase of axial strain $(\varepsilon_t - \varepsilon_1)$ are summarized in Table 2.

Table 2. Results of drained triaxial tests.

Test number	Orientation	Stress level %	Axial strain (Per Cent)					
			ε_1	ε_{10}	ε_{100}	ε_{1000}	ε_{10000}	$\frac{(\varepsilon_{1000}-\varepsilon_1)*100}{\varepsilon_1}$ percent
1	V	80	0.88	1.00	–	–	–	–
2	V	50	1.43	1.60	1.78	–	–	24
3	H	50	1.00	1.07	1.21	–	–	22
4	V	30	0.72	0.78	0.94	1.00	1.01	31
5	V	80	1.54	1.76	2.22	2.43	2.56	41

*Where ε_{100} denotes the axial strain at 100 days after application of stress and so forth.

At 10 days after application of creep stress, the proportional increase of axial strain, i.e. $(\varepsilon_{10} - \varepsilon_1)$ range from 0.06% to 0.22%. At t = 100 days $(\varepsilon_{100} - \varepsilon_1)$ = 0.22% to 0.68%. At t = 300 days $(\varepsilon_{300} - \varepsilon_1)$ = 0.29% for test no. 4 subjected to a stress level of 30% and 1.02% for test no. 5 at stress level of 80% see Table 2. It appears that both the proportional increase of axial strain ε with time t, $(\varepsilon_t - \varepsilon_1)$ and the proportional increase in creep ratio $R_\varepsilon = (\varepsilon_t - \varepsilon_1)/\varepsilon_1 \times 100\%$ are stress level dependent, the higher the applied stress level the greater the value of $(\varepsilon_t - \varepsilon_1)$ and R_ε. This finding is not with agreement with that of Bishop and Lovenbury (1969) for drained creep tests on London clay and Pancone clay, who found that $(\varepsilon_t - \varepsilon_1)$ was independent at stress level up to 100 days, but for longer periods there was tendency for the lower stress level to exhibit larger proportional increase of strain.

4.2 Volumetric Creep Behavior with Time

The relationship is characterized with a marked non linearity at high stress levels and a sharp volume decrease to level off. The horizontal specimen test no. 3, exhibited the lowest volumetric strain, which is attributed to the greater stiffness of the soil in horizontal direction: (figure is not shown because of space limitations). Modifications in soil structure appear to be associated with continuous volumetric strain up to certain limit, after which the modifications in soil structure continue without significant volumetric strain. The greater the intensity of the sustained creep stress the more effective it will be in producing structural change and for longer period of time.

5 Time-Dependent Deformations of Undrained Triaxial Tests

5.1 Axial Strain Development with Time

Four consolidated undrained triaxial creep tests were carried out at different stress levels. All tests were consolidated isotropically to an effective stress of 0.241 mN/m^2,

applying a back pressure of 0.621 mN/m^2. The specimens were subjected to creep stress levels of 30, 50, 70 and 90% of failure stress of the control specimen. Figure 2 shows the relationship between axial strain ε and log time. The effect of stress level on this relationship is very clear, the non-linearity being more pronounced as stress level increases. In test no. 4 subjected to a stress level of 90%, failure occurred after about 5000 min. The nonlinearity relationship of axial strain with log t has been observed by many investigators, Murayama and Shibata (1964). The proportional increase of axial strain was summarized in Table 3. At t = 10 min, the proportional increase of axial strain ranged from 0.03% to 0.07% depending on stress level. At t = 1000 min, the values ranged from 0.09% to 0.52%. The proportional strain ratio $R_\varepsilon = (\varepsilon_t - \varepsilon_1)/\varepsilon_1 \times 100\%$ is hardly affected by the applied stress level.

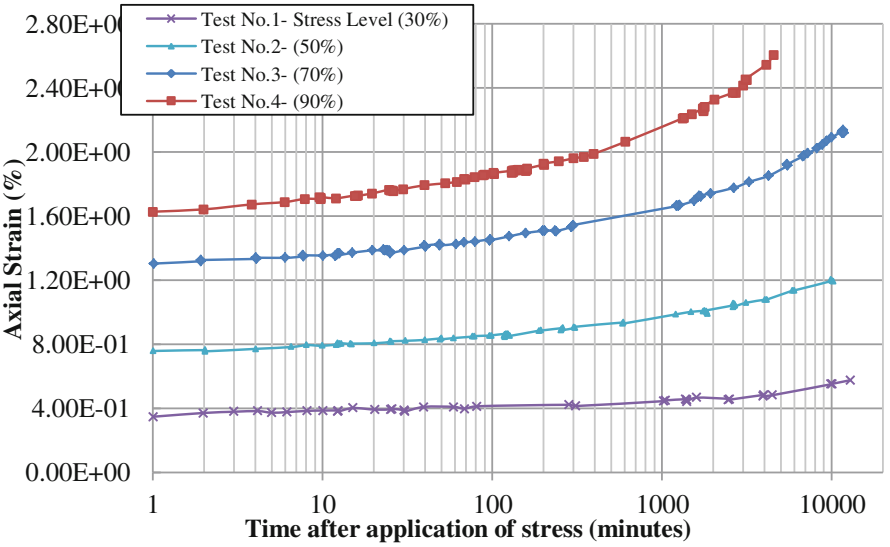

Fig. 2. Axial strain vs. log time (undrained triaxial tests)

5.2 Pore Pressure Behavior with Time

Information about pore pressure response under sustained stress in undrained triaxial conditions of over consolidated stiff soils is very scarce in soil mechanics literature. Most of the reported data of undrained creep behavior were on remolded or undistributed soft soils. For low stress levels pore pressure increases up to 2000 min. then starts to decrease. At higher stress levels pore pressure decreases shortly after the application of stress. It was noticed in some tests that after 600 to 1000 min, the pore pressure started to level off or increase slightly. The decrease of pore pressure may be attributed to the tendency of the over consolidated stiff material to dilate at low stress levels (below 30%), or probably due to the transfer of stress from pore pressure to the friction component of the soil.

Table 3. Results of undrained triaxial tests.

Test no.	Stress level %	Axial strain (Per Cent)					
		ε_1	ε_{10}	ε_{100}	ε_{1000}	ε_{10000}	$\frac{(\varepsilon_{1000}-\varepsilon_1)*100}{\varepsilon_1}$ percent
1	30	0.36	0.39	0.42	0.45	0.55	25
2	50	0.76	0.80	0.86	0.96	1.19	26
3	70	1.30	1.35	1.46	1.64	2.08	26
4	90	1.64	1.71	1.86	2.16	–	32

6 Conclusions

Based on the information presented in this paper, the following conclusions can be made:

6.1 Time-Dependent Deformations in Drained Triaxial Tests

a. The relationships between axial strain and time are linear for a limited period of time ranging from 1 to 10 days; the higher the stress level, the shorter the range of linearity, after which the relationships become concave upwards or linear with a different slope in some cases. The non linearity is more pronounced at higher stress levels. At all stress levels the curves may become concave downwards at periods longer than 150 days.
b. In a logarithmic plot of ε vs t, the curves are linear and approximately parallel to each other except during instabilities which are attributed to the breakdown and modifications of internal soil structure.
c. The relationship between volumetric strain and log time are characterised with marked non linearity at high stress levels and sharp volume decreases, before it starts to level off and remains essentially constant.
d. Creep strain at 100 days ranged from 0.94% to 2.22% for stress levels of 30% to 80% respectively.

6.2 Time-Dependent Deformation of Undrained Triaxial Tests

a. The relationship between ε and log t is linear up to 1000 min at a 30% stress level and up to 100 min at a 50% stress level, whereas it is non linear over the whole creep period at higher stress levels. All curves are concave upwards.
b. Pore pressure increases up to 2000 min at a 30% stress level, then decreases steadily with time. At higher stress levels, pore pressure starts to decrease shortly after application of creep stress. The rate of pore pressure decrease is higher for greater stress level. After about 5000 to 10,000 min pore pressure tends to become steady.
c. The rate of ε vs t showed similar behavior to that of drained tests. At t = 1000 min, ε ranged from 0.45% to 2.16% for stress levels 30% to 90%. The proportional strain ratio, $R_{\varepsilon,}$ is 25% for tests no. 1, 2 and 3.

Acknowledgment. The author would like to show his appreciation to the Applied Science University for their financial support of this work.

References

Al-Mohamadi, N.M.: Strength and deformation characteristics of Chalk Marl from the channel tunnel. Ph.D. thesis University of Surrey, UK (1976). (unpublished)

Al-Mohamadi, N.M.: Creep characteristics of Chalk Marl under uniaxial and confined compression state of stress. In: The Ninth International Structural Engineering and Construction Conference (ISEC-9) Valencia Spain (2017)

Bishop, A.W., Lovenbury, H.T.: Creep characteristics of two undisturbed clays. In: Proceedings of the 7th International Conference on Soil Mechanics and Foundation Engineering, Mexico City, vol. 1, pp. 29–37 (1969)

Davies, R.: Creep characteristics of three undisturbed clays. Ph.D. thesis, University of London (1975)

Lacasse, S., Berre, T.: Undrained creep susceptibility of clays. In: Proceedings of the 16th International Conference on Soil Mechanics and Geotechnical Engineering. Milli Press Science Publishers (2005–2006)

Mitchell, J.K.: Shearing resistance of soils as a rate process. J. SMFD ASCE **90**(SM1), 29 (1964)

Murayama, S., Shibata T.: Flow and stress relaxation of clays. In: Proceedings of IUTAM Symposium on Rheology and Soil Mechanics, Grenoble, pp. 99–129 (1964)

Wang, Y.F., Zhou, Z.G., Yin Cai, Z.: Studies about creep characteristics of silty clay in triaxial drained creep tests. Appl. Mech. Mater. **580**, 355–358 (2014)

Modelling EM Heating of Porous Media with Lattice Element Method

Henok Hailemariam(✉) and Frank Wuttke

Geomechanics and Geotechnics, Kiel University, Kiel, Germany
henok@gpi.uni-kiel.de

Abstract. Electromagnetic (EM) heating of porous media has recently gained much interest in the energy and construction sectors in general, and the recovery of highly viscous bituminous or heavy oils from oil sands and shales in particular. In this study, a new model for solving the coupled heat transfer and EM equations using the lattice element method (LEM), to analyze the spatial and temporal temperature distribution of porous media reservoirs is presented. The new model provides a good basis for simulating the meso-scale behavior of EM heated porous media in view of the phenomenon of selective heating, as the different constituent phases of the porous medium can be modeled as discrete nodal elements which dissipate applied EM energy according to their loss content (polarization), which is difficult to model with continuum based models such as the finite element method (FEM).

1 Introduction

Understanding the coupled heat transfer and electromagnetic (EM) porous media processes is vital in conducting analysis and modeling operations in various fields of geomechanics and geotechnics, engineering, geology, hydrology, agriculture, radioactive decay, food processing, EM radiation on biological tissues, industrial applications etc. In this regard, knowledge of EM processes and geophysical approaches have recently gained much interest in solving major problems facing the fields of energy geotechnics and geotechnical engineering in monitoring the spatial and temporal variations of temperature and moisture content (Hailemariam et al. 2017), as well as the recovery of bituminous or heavy oils from oil sands and shales by lowering the viscosity of the bituminous phase by EM heating (Robinson et al. 2009). The focus of this study is on the latter part, i.e., on the recovery of heavy oils from oil sands and shales by EM heating.

Conventional methods of processing oil sands, such as ex-situ hot water separation and in-situ thermal and non-thermal techniques, have limitations, such as restrictions of depth, formation type and medium permeability, high energy requirements, long processing times, difficulty processing clay fines, need for the addition of hot water, solvents and/or gases etc. EM heating of oil sands provides a greener, economic and environmentally friendlier alternative, which overcomes these limitations via its unique ability to heat phase-selectively and volumetrically (Robinson et al. 2009), leading to the possibility of significant energy savings with smaller process equipments. Considering the various applications of EM heating, it is vital to develop models for solving

A. Ferrari and L. Laloui (Eds.): SEG 2018, SSGG, pp. 315–322, 2019.
https://doi.org/10.1007/978-3-319-99670-7_40

the coupled heat transfer and EM equations necessary to predict the thermo-dynamic properties of oil sand reservoirs. Niziołek (2009) reviewed the existing numerical models for the simulation of EM heating, and specified the strength and weakness of each model. Majority of the available models fail to include information on the nature of the porous media fabric at the meso-scale (actual EM and heat transfer paths), do not include provisions for the natures of selective and progressive heating of the different phases of porous media and neglect pore-water evaporation effects. To overcome these shortcomings, a new model for solving the coupled thermo-dielectric porous media behavior based on the LEM approach is presented in this study.

2 Model Development

2.1 Model Structure

EM heating problems are solved on the basis that the power P absorbed (dissipated) by the porous medium due to an applied external electric field is the source term in the heat transfer equations to calculate transient temperature profiles in the porous medium (Ma et al. 1995). Hence, the Fourier's conductive heat flow rule can be written as:

$$\rho c \frac{\partial T}{\partial t} = \nabla \cdot (\lambda \nabla T) + P \tag{1}$$

Due to its effectiveness, lack of anisotropy and simplicity, the vectorizable random lattice (VRL) technique (Lilliu and van Mier 2003) is used for generating the nodal elements of the lattice model (Fig. 1a). The nodes are generated randomly according to the desired volumetric proportions of solids, bitumen and pore-water present in the oil sand. The corresponding dielectric (polarization and dissipation parameters), thermal and other constituent properties are then assigned to each node. The Delaunay lattice elements (connecting the nodes) and the associated Voronoi cells (containing and representing each node) are then generated via the Voronoi scaling approach using MATLAB, and the cross-sectional area of the Delaunay lattice elements is calculated. In the VRL technique of random lattice generation, disorder is introduced at the geometrical level by placing the nodes inside sub-cells of the original regular sized meshes (Fig. 1a) via a tunable parameter (known as the randomness factor R). Randomness R is defined as the ratio of the size of the sub-cell A to the main cell (generated mesh) s_m. Hence, the randomness factor R ($0 \leq R \leq 1$) produces lattice elements with a maximal randomness when $R = 1$ and a regular reference lattice when $R = 0$.

2.2 Electromagnetic Part of the Model

Maxwell's equations and the constitutive relations, which are needed to describe the coupled behavior of EM fields, are given by Eqs. 2 and 3, respectively. An adequate approach for solving the magnitude of electric field from Maxwell's equations is the plane wave approach (Ma et al. 1995). For a time-harmonic electromagnetic plane

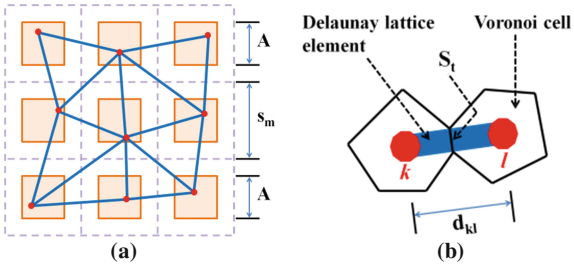

Fig. 1. (a) Node generation via the VRL technique, after Lilliu and van Mier (2003), and (b) thermo-dielectric interaction between two neighbouring Voronoi cells k and l.

wave traveling in **z**-direction of a k^{th} constituent phase (Fig. 1b) of a lossy porous medium, the electric field vector $\mathbf{E_k}$ is expressed by Eq. 4.

$$\nabla \times \mathbf{E} = -\frac{\partial \mathbf{B}}{\partial t}; \nabla \times \mathbf{H} = \mathbf{J} + \frac{\partial \mathbf{D}}{\partial t}; \nabla \cdot \mathbf{D} = \rho_v; \nabla \cdot \mathbf{B} = 0 \tag{2}$$

$$\mathbf{D} = \varepsilon^* \mathbf{E}(\omega);\ \mathbf{B} = \mu^* \mathbf{H}(\omega);\ \mathbf{J} = \sigma^* \mathbf{E}(\omega) \tag{3}$$

$$\mathbf{E_k}(\mathbf{z}, t) = \mathbf{E}_{0,\mathbf{k}} e^{j\left(\omega t - k_k^* \mathbf{z}\right)} \tag{4}$$

$$k_k^{'} = k_0 n_k^{'};\ k_k^{''} = k_0 n_k^{''};\ k_0 = \frac{2\pi f}{c};\ v_k = \frac{c}{n_k^{'}};\ c \approx 3 \times 10^8 \text{m s}^{-1} \tag{5}$$

$$n_k^{'} = \left[\frac{\sqrt{\left(\varepsilon_{r,k}^{'}\right)^2 + \left(\varepsilon_{r,k}^{''}\right)^2} + \varepsilon_{r,k}^{'}}{2}\right]^{1/2};\ n_k^{''} = \left[\frac{\sqrt{\left(\varepsilon_{r,k}^{'}\right)^2 + \left(\varepsilon_{r,k}^{''}\right)^2} - \varepsilon_{r,k}^{'}}{2}\right]^{1/2} \tag{6}$$

where, $\mathbf{E_{0,k}}$ and $k_k^* = k_k' - jk_k''$ are the amplitude factor and the complex wavenumber of the k^{th} constituent phase, respectively. The real part k' of the wavenumber acts as the phase constant and determines the wavelength and propagation velocity of the electromagnetic wave, whereas, the imaginary part k'' of the wavenumber attenuates the wave. The relations between the wavenumber k_k^*, relative complex permittivity $\varepsilon_{r,k}^*$, index of refraction n_k^* and propagation velocity v_k of the k^{th} constituent phase of a porous medium are given by Eqs. 5 and 6.

2.3 Thermodynamic Part of the Model

As electromagnetic energy is absorbed by the constituent phases of a porous medium according to their degree of polarization, the magnitudes of the heat generation term or the average dissipated power per unit volume P_k and the average temperature rise ΔT_k for a given time step Δt of each nodal constituent phase are obtained from the magnitude of its attenuated electric field intensity using Eqs. 7 and 8, respectively (Ma et al. 1995). The conductive heat transfer between two neighboring Voronoi cells (Fig. 1b)

$\Delta T_{cond,k}$ can be derived by combining the Fourier's law and the rate of thermal energy gain (Terreros et al. 2013) of the constituent phases or Voronoi cells using Eq. 9.

$$P_k = \sigma_k \left|\mathbf{E_{rms,k}}\right|^2 = 2\pi f \varepsilon_0 \varepsilon'_{r,k} \tan\delta_k \left|\mathbf{E_{rms,k}}\right|^2 \tag{7}$$

$$\Delta T_k = \frac{\sigma_k \left|\mathbf{E_{rms,k}}\right|^2}{\rho_k c_k} \Delta t = \frac{P_k}{\rho_k c_k} \Delta t \tag{8}$$

$$\Delta T_{cond,k} = \frac{S_t \lambda_{kl} (T_l - T_k)}{d_{kl} \rho_k c_k V_k} \Delta t \tag{9}$$

where, ε_0 = 8.854187817 F m^{-1} is the dielectric permittivity of free space, σ_k, tan δ_k, V_k and $\left|\mathbf{E_{rms,k}}\right| = 0.707 \left|\mathbf{E_{peak,k}}\right|$ are the electrical conductivity, loss tangent, volume and the root mean square of the magnitude of the peak electric field intensity of the k^{th} nodal constituent phase, respectively, S_t, λ_{kl} and d_{kl} are the heat transmission x-sectional area, thermal conductivity and length of the Delaunay lattice element $k - l$, respectively, T_k and T_l are the temperatures of Voronoi cells k and l, respectively. Once, the variations/interactions in temperature of Voronoi cell k with each of its neighbors/Voronoi cells is calculated separately and stored, its total variation of temperature due to conductive heat transfer is obtained by adding the individual contributions. The process is repeated for every node/Voronoi cell in the domain.

The following boundary and initial conditions are assumed in solving the equations of the coupled thermo-dielectric model:

- A uniform initial temperature of $T_k = T_{int}$ (which is the domain/reservoir temperature at the start of EM heating) is assigned to all Voronoi cells.
- The initial nodal electric field strength in the reservoir is zero, $\mathbf{E_k} = 0$.
- A thermal insulation specifying a zero flux is assigned to the outer boundary of the domain as: $\mathbf{n} \cdot (\lambda \nabla T) = 0$, where $\mathbf{n}$ is a vector normal to the boundary.
- A non-reflecting EM wave scattering boundary condition (SBC) is assigned to the outer boundary of the domain as: $\mathbf{n} \cdot (\nabla \mathbf{E}) + jk * \mathbf{E} = 0$.

2.4 Thermo-dielectric Parameters of the Model

The dielectric (especially of the entrapped pore-water) (Wagner and Scheuermann 2009), thermal (Smith-Magowan et al. 1982) and bitumen dynamic viscosity (Miadonye et al. 1994) properties of the constituent phases of oil sands are highly influenced by changes in temperature. The dielectric properties are additionally dependent on the frequency of irradiation of the EM wave (Hailemariam et al. 2017). In Table 1, a list of the models for obtaining the temperature and frequency dependence of the thermo-dielectric and bitumen viscosity parameters is given. The dielectric properties of water given in Table 1 are for pure-water with no salinity. For saline pore-water, the modified Debye model for pure water given in Table 1 should be customized with additional salinity modification factors.

Table 1. Temperature & frequency dependence of the thermo-dielectric model parameters

Constituent phase	Model/Quantity	Suggested by
Solids	$\lambda_s(T) = \lambda_{To} - q\left(\frac{1}{2}\right)^{(To/T)}\lambda_{dom}\left(\frac{T-To}{T}\right)$	Hailemariam and Wuttke (2018)
	$c_s(T) = [0.738 + 1.518 \times 10^{-3}T - 2.026 \times 10^{-6}T^2]10^3$	Smith-Magowan et al. (1982)
	$\varepsilon'_{r,s} = (1.01 + 0.44G_s)^2 - 0.062$; $\tan\delta_s = 0.16 \times 10^{-4}$	Dobson et al. (1985); Oloumi and Rambabu (2016)
Bitumen	$\lambda_b(T) = 0.1289 - 1.3 \times 10^{-4}T$	API (1997)
	$c_b(T) = [1.557 + 5.219 \times 10^{-3}T - 8.686 \times 10^{-6}T^2]10^3$	Smith-Magowan et al. (1982)
	$\varepsilon'_{r,b} = 2.5; \tan\delta_b = 5.2 \times 10^{-4}$	Oloumi and Rambabu (2016)
	$\log(\mu_v) = b_v/\left(1 + \frac{T-30}{303.15}\right)^{S_v} + C_v$	Miadonye et al. (1994) Bitumen dynamic viscosity
Pore-water	$\lambda_w(T) = \lambda_{w,298.15}[-1.48445 + 4.12292\left(\frac{T}{298.15}\right) - 1.63866\left(\frac{T}{298.15}\right)^2]$	Ramires et al. (1995)
	$c_w(T) = 95909 - 184.43T + 1.3833 \times 10^{-1}T^2 - 2.0119 \times 10^7T^{-1} + 1.6358 \times 10^9T^{-2}$	Hirono and Hamada (2010)
	$\varepsilon^*_{r,w}(\omega, T) = \varepsilon_\infty(T) + \frac{\Delta\varepsilon(T)}{1 + j\omega\tau_w(T)} - j\frac{\sigma_{DC}(T)}{\omega\varepsilon_0}$	Wagner and Scheuermann (2009)

3 Results and Discussion

A conceptual oil sand reservoir/domain (basic data given in Table 2) with a single well and an irradiation antenna located at the center of the pay zone is considered for the application of the 2D EM-LEM heating model. Due to geometrical symmetry, only half section of the domain is analyzed. The generated nodes, the Delaunay lattice elements and the associated Voronoi cells representing the nodes are shown in Fig. 2, and the electrical and thermo-dynamic modelling results of the domain after 1 and 25 h of EM irradiation are shown in Fig. 3.

When an electric field is applied to the oil sand domain, the pore-water and to a slight extent the bituminous nodes are heated up at a higher rate when compared to the solid phases, and hence exhibit a higher initial temperature (Fig. 3g) with an effect on the overall heat flow path (Fig. 3h) and the reduction of bitumen viscosity (Fig. 3i) in

Table 2. Conceptual reservoir data used for the application of the new EM-LEM model

Property	Value	Property	Value
Pay zone thickness (m)	0.4	Operating frequency (GHz)	2.45
Domain half length, symmetry (m)	0.5	Oil sand grade (–)	High
Domain initial temperature (°C)	20	Weight fraction of solids (–)	0.80
Well diameter (m)	0.25	Weight fraction of bitumen (–)	0.13
EM source/antenna height (m)	0.2	Weight fraction of pore-water (–)	0.07
Irradiation time (h)	25	Vol. quartz fraction of solids q_f (–)	0.35
Power input (kW)	0.4	Bitumen viscosity @ 30 °C $\mu_{v,30}$ (Pa s)	1.45

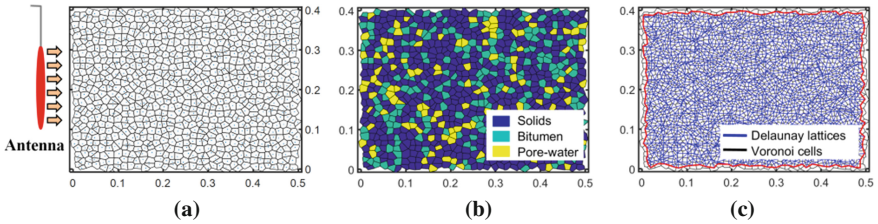

Fig. 2. (a) Domain with R = 0.8 & 891 elements, (b) oil sand phases, and (c) Voronoi scaling.

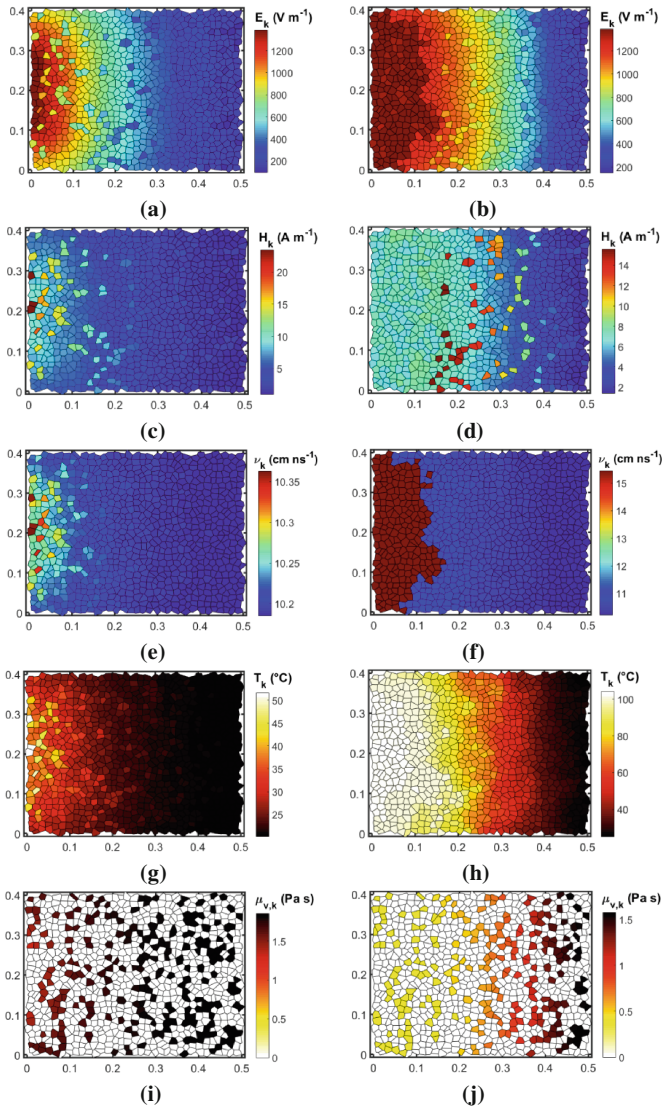

Fig. 3. Spatial distributions of the magnitudes of the different thermo-dielectric fields: (a, c, e, g, i) after 1 h of irradiation, and (b, d, f, h, j) after 25 h of irradiation.

the porous medium, the phenomenon which is usually referred to as selective heating (Robinson et al. 2009). This is primarily due to the higher loss content and dielectric polarization of pore-water and bitumen as compared to the solids, which results in their higher rate of heat dissipation. Gradually, heat is transferred via conduction from the pore-water to the bituminous and solid constituent phases (and to a lower extent from the bituminous to the solid phases), resulting in a quasi-uniform heating of the overall domain after 25 h (Fig. 3h). The subsequent heating of the reservoir produces a gradual reduction in the dynamic viscosity of the bitumen (usually below 0.1 Pa s at temperatures above 100 °C, where the heavy oil becomes flowable and can be readily collected (Cerutti et al. 2013)), initially near the irradiating element and gradually extending deep into the reservoir (Figs. 3i and j).

In terms of the EM properties, the pore-water nodes show a higher rate of attenuation/decay of the electric field intensity when compared to the solid and bituminous phases due to their comparatively higher complex dielectric permittivity and polarization (Figs. 3a and b). Overall, an increase in temperature of the reservoir (e.g. between heating periods of 1 and 25 h), results in a reduction of the complex dielectric permittivity of the medium at frequencies lower than 10 GHz, which in turn results in an increase of the nodal/effective wave velocities and electric as well as magnetic field densities (Fig. 3). When the temperature of the oil sand near the irradiating element reaches around 100 °C, the nodal pore-water phase starts to evaporate (Cerutti et al. 2013), leading to a subsequent reduction of the effective dielectric loss content and rate of heat dissipation of the oil sand around the EM source. This enables the EM waves to penetrate deeper (progressive heating) into the reservoir resulting in an energy efficient mechanism, providing the technique of EM heating a distinct advantage over conventional methods of recovery of oil sands. The clear interface between the dried and still wet parts of the irradiated oil sand as well as the changes in the distributions of the electric and magnetic fields, effective wave velocity and temperature due to the effect of progressive heating can be seen by comparing the plots after 1 and 25 h of irradiation (Fig. 3).

4 Conclusions

A new model for solving the spatial and temporal temperature distribution of electromagnetically heated porous media using the coupled thermo-dielectric equations with the LEM was presented. The new model provides a good basis for simulating the behavior of electromagnetically heated porous media reservoirs in view of the phenomenon of selective and progressive heating, meso-scale EM and heat flow paths and pore-water evaporation effects, which in terms of numerical modeling approaches, can be effectively and accurately simulated via discrete modeling approaches such as LEM as opposed to continuum based models.

Acknowledgements. The authors are grateful for the financial support provided by the German Federal Ministry for Economic Affairs and Energy under Grant number 03ET6122A.

References

American Petroleum Institute: Technical Data Book: Petroleum Refining, 6th edn. Refining Department, American Petroleum Institute, Washington, DC (1997)

Cerutti, A., Bandinelli, M., Bientinesi, M., Petarca, L., De Simoni, M., Manotti, M., et al.: A new technique for heavy oil recovery based on electromagnetic heating: system design and numerical modeling. Chem. Eng. Trans. **32**, 1255–1260 (2013)

Dobson, M.C., Ulaby, F.T., Hallikainen, M.T., El-Rayes, M.A.: Microwave dielectric behaviour of wet soil - part II: dielectric mixing models. IEEE Trans. Geosci. Remote Sens. GE **23**(1), 35–46 (1985)

Hailemariam, H., Shrestha, D., Wuttke, F., Wagner, N.: Thermal and dielectric behaviour of fine-grained soils. Environ. Geotech. **4**(2), 79–93 (2017)

Hailemariam, H., Wuttke, F.: Temperature dependency of the thermal conductivity of porous heat storage media. Heat Mass Transf. **54**(4), 1031–1051 (2018)

Hirono, T., Hamada, Y.: Specific heat capacity and thermal diffusivity and their temperature dependencies in a rock sample from adjacent to the Taiwan Chelungpu fault. J. Geophys. Res. **115**, B05313 (2010)

Lilliu, G., van Mier, J.G.M.: 3D lattice type fracture model for concrete. Eng. Fract. Mech. **70**, 927–941 (2003)

Ma, L., Paul, D.-L., Pothecary, N., Railton, C., Bows, J., Barratt, L., et al.: Experimental validation of a combined electromagnetic and thermal FDTD model of a microwave heating process. IEEE Trans. Microw. Theory Tech. **43**(11), 2565–2572 (1995)

Miadonye, A., Singh, B., Puttagunta, V.R.: Modelling the viscosity-temperature relationship of Alberta bitumen. Fuel Sci. Technol. Int. **12**(2), 447–450 (1994)

Niziołek, M.: Review of methods used for computational electromagnetics. In: 2nd International Students Conference on Electrodynamic and Mechatronics, Silesia, pp. 15–16 (2009)

Oloumi, D., Rambabu, K.: Microwave heating of heavy oil reservoirs: a critical analysis. Microwave Opt. Technol. Lett. **58**(4), 809–813 (2016)

Ramires, M.L.V., Nieto de Castro, C.A., Nagasaka, Y., Nagashima, A., Assael, M.J., Wakeham, W.A.: Standard reference data for the thermal conductivity of water. J. Phys. Chem. Ref. Data **24**, 1377–1381 (1995)

Robinson, J.P., Kingman, S.W., Snape, C.E., Barranco, R., Shang, H., Bradley, M.S.A., et al.: Remediation of oil-contaminated drill cuttings using continuous microwave heating. Chem. Eng. J. **152**, 458–463 (2009)

Smith-Magowan, D., Skauge, A., Hepler, L.G.: Specific heats of Athabasca oil sands and components. J. Can. Pet. Technol. **21**(3), 28–32 (1982)

Terreros, I., Iordanoff, I., Charles, J.L.: Simulation of continuum heat conduction using DEM domains. Comput. Mater. Sci. **69**, 46–52 (2013)

Wagner, N., Scheuermann, A.: On the relationship between matric potential and dielectric properties of organic free soils: a sensitivity study. Can. Geotech. J. **46**(10), 1202–1215 (2009)

The Permeable Concrete: A Low Energy Consumption Solution for Deep Draining Trenches

Maurizio Ziccarelli(✉), Alessio Ferrari, and Marco Rosone

Department of Civil Environmental, Aerospace, Materials Engineering (DICAM), Università degli Studi di Palermo, Palermo, Italy
maurizio.ziccarelli@unipa.it

Abstract. The reduction of pore water pressures is one of the very effective measures to improve the stability conditions of marginally stable water-bearing slopes or to stabilise landslides. For this purpose the trench drains have been used long since. Like filling material of deep trenches the permeable concrete can be effectively employed. It presents relatively high hydraulic conductivity, filtering capacity in order to prevent the internal erosion of the soil in which the trench drain is installed, enough residual hydraulic conductivity after possible clogging, sufficient shear strength after a short curing time to avoid the instabilisation of adjacent previously built panels or piles. Results of a laboratory experimental research on the mix-design, hydraulic conductivity and strength of pervious concrete are reported in the paper, proving that proper mix-design can be devised meeting the above requirements. Permeable concrete is a very poor material and a low energy consumption solution for slope stabilisation.

1 Introduction

Construction industry is responsible for about the 40% of total energy consumption (e.g. Horvath 2004; Dixit et al. 2010). The optimization of the material design can significantly contribute to reduce this impact. In this paper, the use of permeable concrete is presented as an efficient and low energy consumption solution for slope stability problems. As is well known, the improvement of the conditions of stability of the slopes in which high interstitial pressures exist can be achieved in a very effective way by inducing an increase of effective stresses in the ground by reducing the pore water pressures (Terzaghi 1950; Airò Farulla and Rosone 2014; Ferrari et al. 2011; Rosone et al. 2018). Many and different measures can be implemented to this end, such as subhorizontal drainholes, drainage galleries, and draining trenches (e.g. Hutchinson 1977; Kenney et al. 1977; Valore and Ziccarelli 2013, 2015). The draining trenches, or trench drains, are often the most convenient solution, at least for slopes that are not very steep. Deep trenches are usually built by using the equipment available for the construction of diaphragm walls and secant piles, whether shallow trenches (whose depth does not exceed about 5 m) are usually built by means of common excavation techniques and unbonded granular material. In any case, the trenches must be hydraulically

A. Ferrari and L. Laloui (Eds.): SEG 2018, SSGG, pp. 323–330, 2019.
https://doi.org/10.1007/978-3-319-99670-7_41

continuous. Therefore no open discontinuity and no fine-grained material should be interposed between adjacent panels or between secant piles. This problem can be easily solved by using permeable concrete since it has sufficient shear strength and stiffness to permit the excavation of an intermediate panel (or secant pile) in-between two previously built ones without instabilising the latter. The material used for draining trenches needs to be sufficiently permeable and to comply with filter requirements that are well known in the field of earth dams. Another requirement is that the granular particles of the drain should be only partially bonded so that it has true cohesion but, at the same time, interconnected pores. Pervious concrete has been used ever since in other fields of civil engineering such as for draining road pavements. Many researches have been carried out in that field, focused essentially on no-fines concrete containing very little or no sand which has high permeability but poor or no filtering properties (e.g. ACI 2011). Recent researches (Valore et al. 2018; Marzulli et al. 2018; Ziccarelli and Valore 2018) pointed out that it is possible to devise mix-designs that meet many requirements simultaneously. Some of such concretes were extensively investigated by means of laboratory tests. Results concerning the influence of the composition and curing time on the permeability, strength and other properties are reported in this paper.

2 Requirements of Permeable Concrete for Deep Trench Drains

Permeable concrete for deep draining trenches must meet the following requirements. (1) Have relatively high hydraulic conductivity to permit the needed reduction of the piezometric head inside the trench. This head is to be selected by taking the permeability of the soil mass to be drained, the geometry of the problem (spacing of the trenches and their thickness) and the boundary conditions into account. The thickness of the trench must be sufficient to discharge the maximum expected seepage flow rate. It must not undergo unacceptable reductions in hydraulic conductivity over time, as a result of clogging by particles coming from the surrounding soil. (2) Act as a filter to stop the erosion of the soil in which the trench is inserted. (3) Have sufficient strength after a short curing time to allow the excavation of an intermediate deep vertical panel between two previously built ones, without instabilising them. Requirement 1 can be easily satisfied by using no-fines concrete, but it does not comply with requirement 2. Requirement 3 can be satisfied by carefully increasing the cement content and decreasing the aggregate–cement ratio; however, these two decisions must be adequately weighed up to avoid compromising requirements 1 and 2. The strength of properly mix-designed pervious concrete is high enough that vertical panels can stand up tens of meters just after a short curing time. This allows an efficient and cost-effective organization of the worksite and makes the permeable concrete a very low energy consumption material for slope stabilisation.

3 Materials

The permeable concrete is a material formed by aggregates (gravel and sand), cement, water and, when necessary, additives. Four sands and three gravels were used; their index properties are summarised in Table 1, while their grading is shown in Fig. 1(a). Sands S_a–S_d and gravel G_a are composed of silica; gravels G_b and G_c are calcareous; they are almost monogranular with coefficients of uniformity CU ranging from 1.41 to 1.79 for sand and from 1.17 to 1.51 for gravels. The sand and gravel particles are from sub-rounded to angular. High early strength Portland cement Tecnocem II B-LL 32,5 R, (EN 197-1 – Cem II/B-LL 32,5) was used. Cement composition by mass: Clinker: 65%–79%; limestone: 21%–35%; TOC (total organic carbon) $\leq 0.20\%$; minor constituents (including sulphates such as SO_3, chlorides $\leq 0.10\%$). The municipal water of the city of Palermo was used for the concrete specimens, for the permeability tests and for curing the wet specimens. The composition and properties of the water are the following. $pH = 7.72$; electric conductivity: 770 µS/cm at temperature of 20 °C; alkalinity: 194/mg/l; Sodium: 161 mg/l; sulphates: 161 mg/l; Calcium: 99 mg/l; chlorides: 48.5 mg/l; Magnesium: 2 mg/l; nitrites: 5.9 mg/l; Potassium: 4.6 mg/l. Other components are present in quantities lower than 1 mg/l.

Table 1. Properties of sands and gravels used for permeable concrete. n_{min} and n_{max} were determined according to ASTM standards (ASTM 2004).

Material	G_s (-)	d_{max} (mm)	d_{60} (mm)	d_{50} (mm)	d_{10} (mm)	d_{min} (mm)	CU (d_{60}/d_{10})	n_{min} (%)	n_{max} (%)	γ_{dmin} (kN/m^3)	γ_{dmax} (kN/m^3)
Sand S_a	2.65	0.85	0.50	0.45	0.28	0.075	1.79	38.8	47.3	13.7	15.9
Sand S_b	″	1.41	0.65	0.61	0.46	″	1.41	38.1	45.2	14.2	16.1
Sand S_c	″	2	0.99	0.95	0.60	″	1.4	37.7	44.4	14.5	16.2
Sand S_d	″	2	1.38	1.27	0.96	″	1.4	38.2	47.7	13.6	16.1
Gravel G_a	2.7	5	2.55	2.50	2.05	0.3	1.4	38.9	45.5	14.2	15.9
Gravel G_b	″	20	8	7.7	5.2	2	1.51	39.2	49.4	13.4	16.1
Gravel G_c	″	38	23.3	22.5	19.9	2	1.17	40.8	50.9	13	15.7

Mix-design was selected by trial. It was soon realised that no-fines concrete is not eligible for trench drains since it does not meet filter requirements. The "common" permeable concrete (or no-fines concrete) is a composite material consisting of coarse aggregate made of gravel with no or a very small amount of sand, Portland cement and water.

The water–cement ratio W/C was varied between 0.3 and 0.5. Although a value of $W/C = 0.3$ is sufficient for the complete formation of the chemical bonds, for good workability a value of W/C equal to about 0.4 is necessary. Larger values of W/C can result in better fluidity of the concrete and thus a better workability but it can easily lead to the formation of lenses made of cement paste, that may decrease or even jeopardise the functionality of the draining trenches. It is commonly thought that pervious, and especially no-fines concrete, can be dropped from considerable height without causing segregation. However, this is not the case of permeable concrete containing both gravel

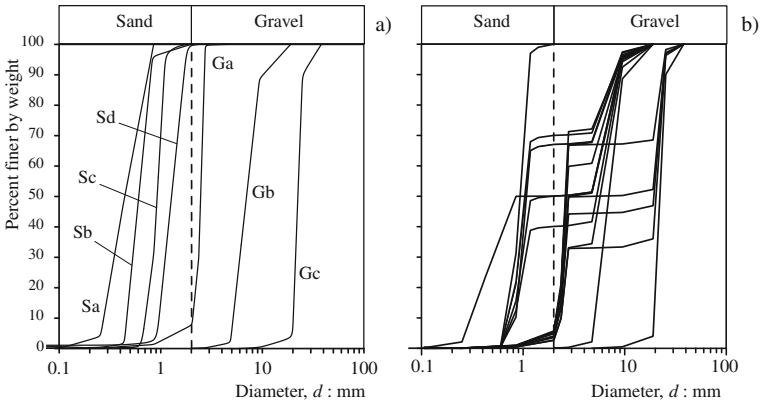

Fig. 1. Initial grading of aggregates (a), and (b) grading of the mixtures of aggregates used to make up permeable concrete.

and sand nor for no-fines concrete: in fact, the cement paste may separate from the aggregates and tend to form almost impervious lenses. It is therefore clear that in deep trenches permeable concrete must be poured by the tremie pipe method. The aggregates–cement ratio *A/C* was varied between 6 and 11, while the cement content *C* varies from 115 to 300 kg.

The specimens tested were made by placing the concrete from very small height and without vibrating or compacting it. Concrete was placed in cylindrical PVC containers respectively with inner diameter and height of 135 mm and 300 mm. Specimens were cured in air or submerged into fresh municipal water in the laboratory at temperatures varying from 20 to 22 °C. The grain size distribution of the aggregates used for making up the pervious concretes are shown in Fig. 1b. The inspection of the bases and lateral surface of the specimens as well as the fragments of specimens brought to failure under uniaxial compression reveal that (excluding sand or gravel only specimens) each gravel grain is surrounded, almost always, by sand particles only. The coordination number of individual gravel grains is high and its 2D value varies from about 10 to 35; it is greater than the one in very dense sands, locked sands and for sands subjected to very high stress levels (Oda 1977; Valore and Ziccarelli 2009; Celauro et al. 2014; Ziccarelli 2016; Valore et al. 2017; Ziccarelli et al. 2017). Gravel-to-gravel contacts are very rare. This implies that the space occupied by the gravel cannot be crossed by flowlines that have to circumvent the gravel particles, thus increasing the tortuosity and reducing the hydraulic conductivity of the concrete. The fact that the seepage takes place prevailingly in small pores of the sand fraction helps to promote laminar, rather than turbulent, flow conditions.

3.1 Strength and Stiffness of Permeable Concrete

The strength and stiffness of the tested concretes were determined by means of uniaxial compression tests. The diameter of the specimens range from 95 mm to 136 mm, their height from 93 mm to 170 mm. Compressive uniaxial tests have been carried out with

a servo-controlled testing machine at a constant loading rate of 0.005 MPa/s. Typical stress-strain curves are shown in Fig. 2. The compressive strength σ_f (of the mixture P36, Fig. 2a) varies from about 1.8 MPa to about 7.3 MPa for C = 230 kg/m^3 while for the specimen P37 (Fig. 2b) σ_f = 2 MPa for curing time of 28 days and for C = 140 kg/m^3. The compressive strength presents high variability (0.49 $\leq \sigma_f$ 7.44 MPa); it depends on many factors such as the water–cement ratio (*W/C*), aggregate–cement ratio (*A/C*), cement content (*C*), grading of aggregates and curing time. These factors are interdependent and determine the structure, texture, unit weight, porosity, pore size and pore distribution, that are the main features that determine the values of σ_f. The influence of the aggregate/cement ratio *A/C* and the dry unit weight γ_d on σ_f is considerable as shown in Fig. 3. In particular, higher σ_f values have been found for high γ_d and low *A/C* ratio (high cement content *C*). These results seem to be independent from the type of mixture. The mean secant value of Young's modulus *E* ranges from 250 to 1360 MPa. *E* increases with *C* and decreases with both *A/C* and *W/C* ratios, it increases, with the curing time, from 225 MPa to 900 MPa and 1200 MPa after 3, 14 and 31 days, respectively. The stiffness of the specimens cured in wet conditions is lower than that of specimens cured in dry conditions at the same curing time. The stiffness increases strongly in the first 7 days. Young's moduli of the investigated pervious concretes are about ten times lower than those of common structural concrete, yet it is much higher than that of soils into which most trench drains are installed. The above results are in good agreement with the data reported in the literature for no-fines concrete of similar void ratio (e.g. Ghafoori and Dutta 1995; Zhong and Wille 2016).

3.2 Hydraulic Conductivity

The hydraulic conductivity *k* was determined on saturated specimens by means of a falling head permeameter (e.g. Kevern 2008). The explored interval of the hydraulic gradient *i* ranges from 0.1 to 6. The values of *i* relevant for trench drains installed in fine-grained soils, fall in the interval between 0.1 and 1. The linearity of the relation between *v* and *i* implies that the seepage in the tested concretes follows the Darcy law; similar conclusions were drawn by Montes and Haselbach (2006). The hydraulic conductivity *k* ranges in a wide interval, from 0.019 to 3.08 cm/s for the specimens used in the experimentation. The values of *k* depend on the grading of the aggregates, the water–cement ratio *W/C* (it increases as the ratio *W/C* decreases) the aggregates–cement ratio *A/C* (*k* is higher for higher *A/C* ratios), the cement content *C* (*k* is lower for higher values of *C*). Figure 4 shows the influence of the curing time on the hydraulic conductivity *k* and velocity *v* for *i* = 0.1–5.8. These factors are interdependent and all influence the texture, the distribution and the size of pores, the porosity *n* of the concrete and hence the values of *k*. The residual hydraulic conductivity k_r, defined as the value of *k* after the number of clogging cycles *N* (which corresponds to a low incremental variation of *k*) is, for *N* = 30, about 40% of its initial value k_0. However, the value of k_r (about 0.12 $\times$ 10^{-2} m/s) is sufficient to satisfy the requirement of a relatively high hydraulic conductivity of the pervious concrete for the trench drain. Further tests are in progress on this topic.

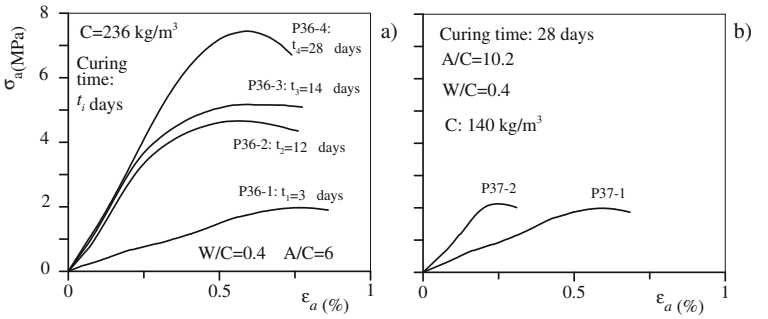

Fig. 2. Influence of curing time and cement content on the uniaxial compressive strength σ_f and on stress-strain relationship. Permeable concrete: (a) P36 (gravel G_b: 50% in weight, sand S_a: 50% in weight); (b) P37 (gravel G_b: 50% in weight, sand S_a: 50% in weight).

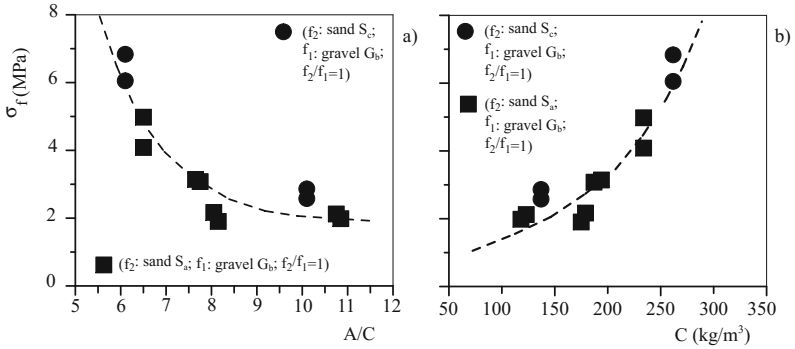

Fig. 3. Influence of aggregates–cement ratio *A/C* (a) and dry unit weight γ_d (b) on σ_f.

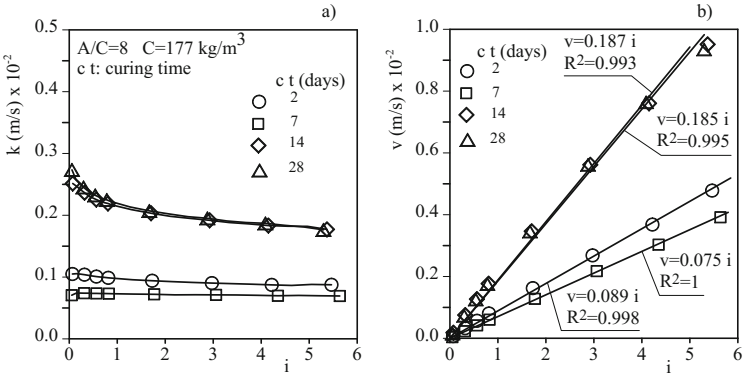

Fig. 4. Influence of curing time on permeability k and nominal velocity v for i = 0.1–5.8.

4 Conclusions

An experimental investigation into the strength, the draining and filter properties of permeable concrete for deep draining trenches was performed. The hydraulic conductivity of all the tested concretes is high and in any case adequate for deep trenches installed in sandy and fine-grained soils. It is possible to devise the mix-design for pervious concrete so that it meets filter and residual permeability requirements for the protection of silty and, hopefully, fine-grained soils, as well as strength and draining demand. These properties make properly designed permeable concrete convenient and effective for deep draining trenches. Results of ongoing researches demonstrate that the tested concrete mixtures are also satisfactory like their filtering capacity and resistance to clogging. The residual hydraulic conductivity k_r is about 40% of the initial one (k_0); however, it is sufficient to satisfy the requirement of a relatively high long-term hydraulic conductivity. The strength of the pervious concrete is sufficient to build very deep trenches safely and without long delays in the excavation of in-between panels or secant piles. Hence, considerable are the advantages in costs and in efficient planning of the construction site, and, hence, with very low consumption energy to stabilizing slopes marginally stable or landslides in which high interstitial pressures are present.

References

ACI American Concrete Institute: Pervious concrete. ACI Committee 522, 2011; Technical Committee Document 522R-10 (R2011) (2011)

Airò Farulla, C., Rosone, M.: Modeling Round Robin test: an uncoupled approach. In: 3rd IWL—Hydrol. Resp. of Slopes through Phys. Experiments, Field Monit. and Mathem. Modeling, 23–24 Oct. 2013, Naples (Italy). Procedia Earth and Planetary, Science, vol. 9, pp. 195–200 (2014)

ASTM: Standard test methods for maximum index density and unit weight of soils using a vibratory table (D4253-00 and D4254-00). In: 2004 Annual Book of ASTM Standards. American Society for Testing and Materials, Philadelphia (2004)

Celauro, C., Ziccarelli, M., Parla, G., Valore, C.: An automated procedure for computing the packing properties of dense and locked sands by image analysis of thin sections. Granul. Matter **16**(6), 867–880 (2014)

Dixit, M.K., Fernández-Solís, J.L., Lavy, S., Culp, C.H.: Identification of parameters for embodied energy measurement: a literature review. Energy Build. **42**(8), 1238–1247 (2010)

Ferrari, A., Ledesma, A., González, D., Corominas, J.: Effects of the foot evolution on the behaviour of slow-moving landslides. Eng. Geol. **117**, 217–228 (2011)

Ghafoori, N., Dutta, S.: Laboratory investigation of compacted no-fines concrete for paving materials. J. Mater. Civ. Eng. ASCE **7**(3), 183–191 (1995)

Horvath, A.: Construction materials and the environment. Annu. Rev. Energy Environ. **29**, 181–204 (2004)

Hutchinson, J.N.: Assessment of the effectiveness of corrective measures in relation to geological conditions and types of slope movement. Bull. Int. Assoc. Eng. Geol. **16**, 131–155 (1977)

Kenney, T.C., Pazin, M., Choi, W.S.: Design of horizontal drains. J. Geotech. Eng. Div. Proc. ASCE **103**(GT11), 1311–1323 (1977)

Kevern, J.T.: Advancements in pervious concrete technology. Ph.D. Dissertation, Iowa State University. Retrospective Theses and Dissertations. 93 (2008). http://lib.dr.iastate.edu/rtd/93

Marzulli, V., Cafaro, F., Ziccarelli, M.: Hydraulic characterization of a pervious concrete for deep draining trenches. J. Mater. Civ. Eng. ASCE **30**(6), 04018100-11 (2018). https://doi.org/10.1061/(asce)mt.1943-5533.0002274

Montes, F., Haselbach, L.M.: Measuring hydraulic conductivity in pervious concrete. Environ. Eng. Sci. **23**(6), 960–969 (2006)

Oda, M.: Co-ordination number and its relation to shear strength of granular material. Soils Found. **17**(2), 29–42 (1977)

Rosone, M., Ziccarelli, M., Ferrari, A., Airò Farulla, C.: On the reactivation of a large landslide induced by rainfall in highly fissured clays. Eng. Geol. **235**, 20–38 (2018)

Terzaghi, K.: Mechanism of landslides. In: Paige, S. (ed.) Application of Geology to Engineering Practice (Berkey Volume), pp. 83–123. Geol. Soc. Am, New York (1950)

Valore, C., Ziccarelli, M.: The evolution of grain-size distribution of sands under 1-D compression. In: Hamza, M., et al. (eds.) 17th International Conference on Soil Mechanics Geotechnical Engineering, Alexandria, Egypt, October 2009, vol. 1, pp. 84–88. IOS Press (2009)

Valore, C., Ziccarelli, M.: The preservation of the Agrigento Cathedral. In: Proceedings 18th International Conference on Soil Mechanics and Geotechnical Engineering—Challenges and Innovations in Geotechnics – Paris, France, 2–6 September 2013, vol. 4, pp. 3141–3144 (2013)

Valore, C., Ziccarelli, M.: The stabilization of a slope-viaduct system without closing traffic. In: 16th European Conference on Soil Mechanics Geotechnical Engineering, Edinburg, Scotland, 13–17 September 2015, pp. 367–372 (2015)

Valore, C., Ziccarelli, M., Muscolino, S.R.: An experimental investigation into the permeability and filter properties of pervious concrete for deep draining trenches. Ital. Geotech. J. (Rivista Italiana di Geotecnica), **3**, 14–37 (2018). https://doi.org/10.19199/2018.2.0557-1405.30

Valore, C., Ziccarelli, M., Muscolino, S.R.: The bearing capacity of footings on sand with a weak layer. Geotech. Res. **4**(1), 12–29 (2017)

Ziccarelli, M.: Evolution of grain-size distribution of pumice sands in 1-D compression. Procedia Eng. **158C**(6), 27–32 (2016)

Ziccarelli, M., Valore, C., Muscolino, S.R., Fioravante, V.: Centrifuge tests on strip footings on sand with a weak layer. Geotech. Res. **4**(1), 47–64 (2017)

Ziccarelli, M., Valore, C.: Hydraulic conductivity and strength of pervious concrete for deep trench drains. Submitted to Geomech. Energy Environ. (2018)

Zhong, R., Wille, K.: Compression response of normal and high strength pervious concrete. Constr. Build. Mat. **109**, 177–187 (2016)

Unconventional Resources, Hydraulic Stimulation and Induced Seismicity

Gravel Sizing Criteria for Hydrate Exploitation Wells and Its Application

Yanlong Li[1,2(✉)], Changling Liu[1,2], Gaowei Hu[1,2], Nengyou Wu[1,2], Qiang Chen[1,2], and Jing'an Lu[3]

[1] Key Laboratory of Gas Hydrate, Ministry of Land and Resources, Qingdao Institute of Marine Geology, Qingdao 266071, China
liyanlongupc@163.com
[2] Laboratory for Marine Mineral Resources, Qingdao National Laboratory for Marine Science and Technology, Qingdao 266071, China
[3] Guangzhou Marine Geological Survey, China Geological Survey, Guangzhou 510760, China

Abstract. In order to deal with sand production problems during the process of producing natural gas from hydrate-bearing sediments (HBS) with reservoir-fluid extraction method, a new gravel sizing method named "Hold coarse while eliminate fine particle (HC&EF method)" was developed for clayey hydrate-bearing formations. A hydrate-bearing site in Northern South China Sea was taken as an example to describe detailed gravel sizing procedures. Based on the analysis of basic particle size distribution (PSD) characteristics of HBS at SITE Y, the formation sand was divided into two components, which are coarse component and fine component. Secondly, gravel size for retention of coarse component and elimination of fine component were calculated, respectively. Finally, Intersection of those two gravel sizes was taken as the proper gravel size for marine hydrate exploitation well. The research results show that original formation at SITE Y is clayey sand with poor sorting and uniformity coefficient properties, and proper gravel size for upper segment was recommended as 143–215 μm, while that for lower segment was 240–360 μm. In considering the difficulty of layered sand control operation on offshore platform, proper gravel packing size for SITE Y was recommended as 215–360 μm.

Keywords: Hydrate production test · Sand management · Gravel sizing
HC&EF method · Northern South China Sea · Clayey hydrate-bearing formation

1 Introduction

Previous studies have proved the existence of huge amount of natural gas hydrate in Northern South China Sea (Wu et al. 2011; Zhang et al. 2015), China's first hydrate production test has been carried out by China Geological Survey (CGS) since May

Main idea of the paper has been published on the journal of petroleum exploration and development at 2017, 44(6):1016–1021. This paper is a substantial improvement of the 2017 version.

A. Ferrari and L. Laloui (Eds.): SEG 2018, SSGG, pp. 333–343, 2019.
https://doi.org/10.1007/978-3-319-99670-7_42

10th. During the first eight days of this production test, cumulative volume of natural gas extracted from hydrate-bearing sediment(HBS) was around 12×10^4 $STDm^3$, with methane fraction up to 99.5% and average daily production of 1.6×10^4 $STDm^3$ (Guo and Liu 2017). After that, the production was continued until July 9th, with cumulative gas volume of 30.9×10^4 $STDm^3$ and average daily production of more than 5000 $STDm^3$ (Chen and Zhu 2017). Reservoir-fluid extraction method was used and huge amount of production test data was obtained for further study. Both hydrate production tests and laboratory studies have proved that sand production is unavoidable for hydrate production formations (Li et al. 2016a; Jung et al. 2012), especially for marine clayey HBS, which is widely spread in Northern South China Sea (Yoshihiro et al. 2014; Li et al. 2016b). Sand management strategy plays an important role in extending hydrate production test duration.

HBS in Northern South China Sea was characterized with shallow bury depth, weak consolidation and high shale content (Liu et al. 2017), gravel packing (which include open hole gravel pack, internal gravel pack and pre-packed screen) is one of the best choice for this kind of reservoirs (Deng et al. 2011, 2012). Under gravel packing condition, the packing layer acts as both sand blocking mesh and flow channel of reservoir fluid. Large gravel size leads lower skin coefficient and benefits for improving well productivity, but it will lead vast sand production and formation deficit simultaneously. On the other hand, small gravel size is good for sand retention but it may lead blockage of near wellbore flow channel, which is fatal for well productivity. Therefore, gravel size design for clayey HBS should take into account both the requirement of sand retention and blockage avoidance in the near wellbore flow channel.

At present, gravel sizing for packing operation is always done based on the following two assumptions. The first way is to retain formation sand entirely, and petroleum standard recommends less than 0.3‰ of solid content for sand control wells. The second method was named as moderate sand-control, and field operation should meet the demand that solid content in wellhead production fluid is less than 0.5‰ (Wang et al. 2011). However, shale content of clayey HBS is more than 30%, which is the main content that may lead blockage in the near wellbore flow channel (Hu et al. 2004; Valdes and Santamarina 2006; Dong et al. 2016). For marine clayey HBS, if we keep large fraction of shale content stay in the near wellbore flow channel to meet the standard of the above sand-control methods, productivity of hydrate production wells might be cut enormously. To ensure productivity of hydrate production wells and prolong duration of hydrate exploitation test, sand management operation should guarantee elimination of all those shale content. This also means there is more than 0.5‰ solid content in wellhead production fluid. As a result, both entirely sand-control and moderate sand-control design method are not suitable for marine clayey HBS. We have to consider sand management operation in a brand new way for marine clayey HBS.

In this paper, a new gravel sizing method will be proposed, which is specialized for hydrate production test wells in marine clayey HBS using reservoir-fluid extraction method. A typical marine clayey HBS SITE Y in Pearl River mouth basin, Northern South China Sea will be taken as an example to describe detailed design procedures of the above gravel sizing method. Finally, suitable gravel size for SITE Y will be suggested.

2 Gravel Sizing Method

In considering the basic characteristics of marine clayey HBS, main purpose of gravel sizing for hydrate exploitation test well is: ensure elimination of both shale content and very fine sand particles, while prevent migration of relatively coarse particles from formation to wellbore. The new gravel sizing method based on the above criteria can be called "Hold coarse while eliminate fine particle (HC&EF method)". In another word, HC&EF method eliminates fine particles to avoid blockage and improves permeability of near wellbore formation. Retention of coarse particle is also essential for improvement of permeability and avoid vast formation deficit.

Detailed gravel sizing implementation steps based on HC&EF method are as follows. Firstly, analyze the uniformity and sorting characteristics of the HBS via original particle size distribution (PSD) curve, and set preliminary target and demand for gravel sizing. Secondly, some mathematical transformation can be used to divide the original formation solid into two components, which are coarse component and fine component. Cutoff point of these two components can be defined as critical particle diameter of formation size partition. Critical particle diameter of formation size partition can be used to calculate minimum gravel size which can ensure elimination of shale content and fine sand content. Thirdly, dislodge fine segment from original PSD curve, new PSD curve only for coarse component can be obtained through afresh cumulative calculation. Uniformity and sorting characteristics of coarse component can be obtained. After that, gravel sizing models based on entirely sand-control theory should be absorbed to calculate the gravel size that can retain coarse component entirely. Finally, we get two set of size rage, which are determined by fine component elimination and coarse component retention. Intersection of these two set can be defined as the proper gravel size for marine clayey HBS based on HC&EF method.

It is noteworthy that the above described HC&EF method should also take the other factors into consideration, such as shale fraction and layered sand-control demand. Therefore, gravel size used for real hydrate exploitation wells should be matched according to the result obtained from HC&EF method and industrial gravel size array.

3 Original PSD Characteristics

PSD characteristics are the base of proper gravel size design for packing operations. Main properties of marine clayey HBS in Northern South China Sea are shallow depth, low permeability, weak consolidation and very high shale content. Original semi-log PSD range of HBS for SITE Y is shown in Fig. 1. It is obvious that median grain diameter of original PSD locates between 6.0 μm and 15.9 μm. Previous studies also demonstrate that shale content of HBS for SITE Y is around 25%–36%, in which montmorillonite fraction is about 38% and illite fraction is around 32%. For this reason, HBS at SITE Y can be classified into clayey formation. What's more, as for particle size of HBS at SITE Y, the deeper the bury depth, the coarser the particle size.

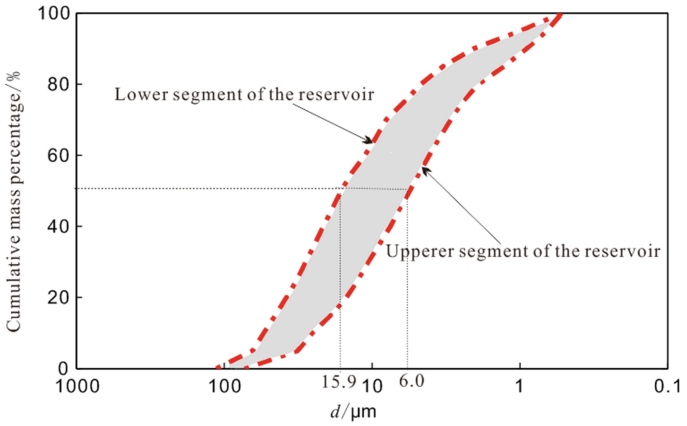

Fig. 1. Original PSD curves of HBS at SITE Y

Except median grain diameter, proper gravel sizing result should also consider the influence of sorting coefficient and uniformity coefficient. Sedimentologist's formula (Eq. (1)) and Berg's correlation (Eq. (2)) (Oyeneyin 2015) are always used for determination of sorting coefficient:

$$F = \frac{\phi_{84} - \phi_{16}}{4} + \frac{\phi_{95} - \phi_5}{6.6} \tag{1}$$

$$F = \frac{\phi_{90} - \phi_{10}}{2} \tag{2}$$

Where, $\phi_{84} = -\log_2 d_{84}, \phi_{16} = -\log_2 d_{16}$, $\phi_{95} = -\log_2 d_{95}, \phi_5 = -\log_2 d_5, \phi_{90} = -\log_2 d_{90}, \phi_{10} = -\log_2 d_{10}$.

According to Eqs. (1) and (2), original formation sand can be divided into four classifications, which are well sorted ($F \leqslant 0.5$), normal sorted ($0.5 < F \leqslant 1.0$), poor sorted ($1.0 < F \leqslant 2.0$) and extremely poor sorted ($F > 2.0$) (Oyeneyin 2015). Then, sorting coefficient for HBS at SITE Y can be calculated, which is 1.85–2.30 on the base of Sedimentologist's formula, while that is 2.35–2.95 on the base of Berg's correlation. It is obvious that sorting coefficient obtained from Berg's correlation is higher than that obtained from Sedimentologist's formula. But both of them indicate that sorting properties for HBS at SITE Y are extremely poor, which increase the difficulty of sand control operation. Because the poorer the sorting coefficient is, the larger the gravel size range is needed for sand management. And large gravel size range might lead poor sand retain efficiency and decrease the ability of anti-blockage for gravel layers.

Uniformity coefficient of formation particles can be calculated via Eq. (3) (Dong 2012):

$$C = d_{40}/d_{90} \tag{3}$$

Formation sand can be divided into three classifications according to Eq. (3), which are uniform sand (C \leqslant 5), heterogeneous sand ($5 < C \leqslant 8$) and extremely distributed sand ($C > 8$) (Dong 2012) . Uniformity coefficient for HBS at SITE Y is 8.4–12.3 and original HBS belongs to extremely distributed sand, which also increases the difficulty of sand-control operation.

Overall, HBS at SITE Y can be defined as extremely distributed clayey fine formation with high shale content and very poor sorting properties. All those properties gain great challenges for sand-control management.

4 Properties of Coarse Component and Fine Component

4.1 Particle Size Partition of Coarse Component and Fine Component

It has been proved by Markestad that formation sand sample can be divided into two components normally (Markestad et al. 1995). The first component is fine component which includes shale content and fine sand content. The second is coarse component. As for the clayey HBS in Northern South China Sea, when hydrate is decomposed, the formation becomes very loose. Main skeleton can be viewed to be formed by coarse component and fine component filled in the pore space formed by coarse component. Under driving of pressure draw-down, fine component may be carried by water/gas and flow into the packed layers and wellbore. In order to balance the demand for productivity and formation stability, the following two factors have to be taken into consideration. On the one hand, eliminate fine component to decrease skin factors and promote hydrate decomposition. On the other hand, keep basic formation skeleton by retention of coarse component. Detailed methods for formation sand partition has been described in Li et al. (2017).

It is easy to conclude from the method that demarcation point for upper segment and lower segment are 5.3 μm and 7.2 μm, respectively.

4.2 Characteristics of Coarse Component

After partition of particle size, in order to calculate gravel size for retention of coarse component, some critical characteristics like median grain diameter, sorting coefficient and uniformity coefficient should be analyzed independently for coarse component.

After all fine components can be removed from Fig. 1. New semi-log PSD curves can be obtained specialized for coarse component at SITE Y, as shown in Fig. 2.

Based on Fig. 3, median grain sizes for coarse component of HBS at SITE Y locate between 15.9 μm and 24.4 μm. Sorting coefficient based on Eqs. (1) and (2) are 0.9–1.2 and 1.1–1.5, respectively. And uniformity coefficient based on Eq. (3) is 1.98–2.98. It can be seen from the above parameters that both sorting coefficient and uniformity coefficient decrease if fine component is cut off from original formation. Thus it could decrease the difficulty of sand management and prolong expiration date of sand management operation.

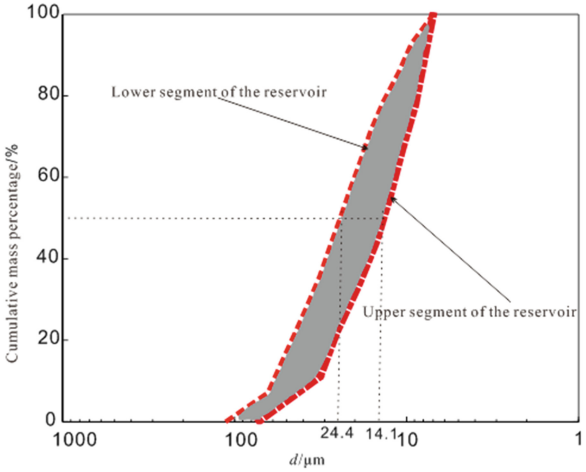

Fig. 2. PSD curves for coarse component of HBS at SITE Y

5 Gravel Sizing for Packed Layers

5.1 Design of Minimum Gravel Size for Elimination of Fine Component

After systematic drainage experiment on gravel-sand ratio (GSR) matching performance, Saucier (1974) concluded that, with irrespective of shale content, formation sand can be eliminated and pass through gravel layers smoothly if GSR⩾14. Therefore, minimum gravel size for packed layers in hydrate exploitation wells should be:

$$D'_{\text{fmin}} = 14d_{\text{fmax}} \tag{4}$$

Moreover, minimum gravel size for upper segment and lower segment of SITE Y can be calculated via Eqs. (5) and (6), respectively.

$$D'_{\text{fmin}} = 14 \times 5.3\,\mu\text{m} = 74.2\,\mu\text{m} \tag{5}$$

$$D'_{\text{fmin}} = 14 \times 7.2\,\mu\text{m} = 100.8\,\mu\text{m} \tag{6}$$

Except fine component, there exist large amount of shale content in clayey hydrate bearing formation, which is the main reason that causes blockage of packed layers (Dong et al. 2011). The more the shale content, the more seriously the blockage of packed layers. In another words, existence of shale content leads enlargement of needed gravel size in order to eliminate fine component. It has been proved by previous work that proper gravel size should be 1.54 times of normal designed size if shale content is 21.36% in formation sand (Ma et al. 2013).

Therefore, the concept of gravel size enlargement factor (represented as R_m) can be used to describe the influence of shale content. Proper gravel size with consideration of shale content for packed layer can be written as Eq. (7).

$$D_{\text{fmin}} = R_{\text{m}} D'_{\text{fmin}} \tag{7}$$

Finally, minimum gravel sizes for elimination of fine component (including shale content) are 118.7 μm and 161.3 μm, respectively, for upper segment and lower segment at sit *X*.

5.2 Design of Gravel Size for Retention of Coarse Component

Under condition of eliminate all possible fine component, gravel size for retention of coarse component can be calculated on the base of normal gravel sizing models.

Typical gravel sizing models for coarse component are Karpoff method, Tausch & Corley method, Saucier method and so on.

Particularly, d_{50} and d_{10} on PSD curve are used by Saucier method and Tausch & Corley method, respectively, to calculate proper gravel size for packed layers. Detailed calculation equations are shown in Eqs. (8) and (9).

$$\begin{cases} D_{\text{cmin}} = 5d_{50} \\ D_{\text{cmax}} = 6d_{50} \end{cases} \tag{8}$$

$$\begin{cases} D_{\text{cmin}} = 4d_{10} \\ D_{\text{cmax}} = 6d_{10} \end{cases} \tag{9}$$

On the other hand, both uniformity coefficient and d_{50} are used for Karpoff model.

$$\begin{cases} D_{\text{cmin}} = 5d_{50}, \ D_{\text{cmax}} = 10d_{50} & C < 3 \\ D_{\text{cmin}} = 4d_{50}, \ D_{\text{cmax}} = 8d_{50} & C \geq 3 \end{cases} \tag{10}$$

Based on Fig. 2 and Eqs. (8)–(10), proper gravel size for retention of coarse component can be predicted, which was shown in Table 1.

Table 1. Gravel size for retention of coarse component at SITE Y

Segment	Gravel size/μm		
	Tausch & Corley method	Saucier method	Karpoff method
Upper layer	143–215	69–82	69–137
Lower layer	240–360	122–146	122–244

5.3 Determination of Gravel Size for Sand Management at SITE Y

For clayey hydrate exploitation wells, proper gravel size should meet the demand of both eliminate fine component and retain coarse component. If the gravel size for retention of coarse component and elimination of fine component are viewed as two independent mathematical aggregations, intersection of the above two aggregations can be used as the proper gravel size for clayey hydrate exploitation well. As an example, proper gravel size for SITE Y is shown in Table 2. Empty set in Table 2 indicates unfeasibility of gravel sizing method for clayey hydrate exploitation wells.

Table 2. Gravel sizing result for SITE Y

Segment	Gravel size/μm		
	Tausch and Corley method	Saucier method	Karpoff method
Upper layer	[143, 215]	∅	[118.7, 137.0]
Lower layer	[240, 360]	∅	[161.3, 244.0]

It can be concluded from Table 2 that Saucier method is not suitable for SITE Y, which indicates its unfeasibility for clayey hydrate exploitation wells. Gravel sizing result based on Karpoff method looks conservative and that based on Tausch & Corley method is a little bit risky.

Decision of final packed gravel size should be based on balance of productivity demand and sand management validation. On one hand, if wellbore sand-carrying condition is restricting, productivity should be sacrificed a little bit to ensure safety of artificial lift. Then gravel sizing result based on Karpoff method should be used. On the other hand, if the artificial lift equipment can bear relatively high percentage of solid content, result based on Tausch & Corley method will be suggested. It is notable that all the above research results are based on the assumption that gravel packed layer can retain all coarse component. Therefore, if sand bridge can be formed and exist timelessly in the near wellbore, the results based on Tausch & Corley method is enough to retain coarse component theoretically. Therefore, the result based on Tausch & Corley method was recommended here for calyey hydrate exploitation wells. According to Table 2, suggested gravel packing size for upper segment at SITE Y should be 143–215 μm, while that for lower segment should be 240–360 μm. However, hydrate always located in the shallow formation and in a limited depth interval. Layered gravel packing may increase the difficulty of field operation. In order to decrease the difficulty and take into account of both upper segment and lower segment, gravel size range should be suggested as 215–360 μm.

With the decomposition and production of natural gas hydrate, formation depletion may be propelled gradually. Only inner-hole gravel pack operation or pre-packed screen operation can keep original packing compaction during the whole process of reservoir fluid extraction. It should be noted that the gravel sizing method provided in this paper should be only used for inner-hole gravel pack operation or pre-packed screen operation. For open hole gravel packing operation, gravel size should be reappraised. It is possible that smaller gravel size is more suitable for open hole gravel pack operation for clayey hydrate exploitation wells.

6 Conclusion

New gravel sizing method named "HC&EF method" for clayey hydrate exploitation wells was provided in this paper. Minimum gravel size was calculated to ensure elimination of fine component in the formation, and appropriate gravel size for retention of coarse component can be calculated via different models. Intersection of the above two aggregations can be viewed as proper gravel size for packed layers in hydrate exploitation wells.

SITE Y, which located in Pearl River mouth basin, Northern South China Sea was taken as an example to describe detailed gravel sizing schedule based on HC&EF method. The research result suggests that gravel size for SITE Y should be 215–360 μm.

As described above, elimination of fine component is the essence of HC&EF method. It means all fine components, including shale component, should flow into the wellbore. For this reason, fluid infusion into the wellbore and keeping sand carrying is very important for gravel packing wells based on HC&EF method. Coordination of sand management system is the only way to ensure effective and long-term hydrate exploitation operation.

Nomenclature:

C	Uniformity coefficient of formation sand, dimensionless
d	Particle size of formation sand, m
d_5, d_{10}, d_{16}, d_{40}, d_{84}, d_{90}, d_{95}	Particle diameter when cumulative mass/volume is 5%, 10%, 16%, 40%, 84%, 90% and 95% on PSD curve, μm
d_{50}	Median grain size, μm
d_{fmax}	Maximum particle size of fine component, μm
D_{cmax}, D_{cmin}	Maximum gravel size and minimum gravel size for retention of coarse component, respectively, μm
D_{fmin}	Minimum gravel size for elimination of fine component when take into account of shale content, μm
D'_{fmin}	Minimum gravel size for elimination of fine component except shale content, μm
F	Sorting coefficient, dimensionless
M	Total sand quality used for particle size analysis, kg
N	Total particle quantity used for particle size analysis
R_{m}	Gravel size enlargement factor caused by shale content, 160%
W	Mass fraction for given size in formation sand, %
ρ	Density of formation sand, kg/m^3

References

Chen, H., Zhu, X.: 20 years to catch up and 60 days to break: catching up recording of China's coastal combustible ice exploration test [EB/OL], 17 July 2017. http://www.cgs.gov.cn/ddztt/jqthd/trqshw/zxbdshw/201707/t20170717_435792.html. Accessed 26 July 2017

Deng, J., Li, P., Zhou, J., et al.: Sand control optimization applied to moderately sanding wells in offshore loose sandstone reservoirs. Acta Petrol. Sin. **33**(4), 676–680 (2012)

Deng, J., Li, P., Wang, L., et al.: The optimization of sand control method for moderate sand control technique application in Bohai Bay. Oil Drill. Prod. Technol. **33**(1), 98–101 (2011)

Dong, C., Jia, B., Liu, C., et al.: Blocking mechanism and blocking laws experiments of sand retention media in mechanical screens. J. China Univ. Pet. (Ed. Nat. Sci.) **35**(5), 82–88 (2011)

Dong, C.: Sand Control Theories and Technologies in Oil and Gas Wells, pp. 91–97. Press of China University of Petroleum, Dongying (2012)

Dong, C., Zhang, Q., Gao, K., et al.: Screen sand retaining precision optimization experiment and a new empirical design model. Pet. Explor. Dev. **43**(6), 991–996 (2016)

Guo, X., Liu, F.: China announced combustible ice test success in the Shenhu area, South China Sea [EB/OL], 18 May 2017. http://china.cnr.cn/xwwgf/20170518/t20170518_523762235.html. Accessed 01 June 2017

Hu, C., Pei, B., Li, X., et al.: Laboratory research on plugging mechanism in gravel packed well. J. Univ. Pet. China (Ed. Nat. Sci.) **28**(3), 40–42 (2004)

Jung, J.W., Jang, J., Santamarina, J.C., et al.: Gas production from hydrate-bearing sediments: the role of fine particles. Energy Fuels **26**(1), 480–487 (2012)

Li, Y., Liu, C., Liu, L.: Damage statistical constitutive model of hydrate-bearing sediments and the determination method of parameters. Acta Pet. Sin. **37**(10), 1273–1279 (2016a)

Li, Y., Liu, L., Liu, C., et al.: Sanding prediction and sand-control technology in hydrate exploitation: a review and discussion. Mar. Geol. Front. **32**(7), 36–43 (2016b)

Li, Y., Hu, G., Liu, C., et al.: Gravel sizing method for sand control packing in hydrate production test wells. Pet. Explor. Dev. **44**(6), 1016–1021 (2017)

Liu, C., Meng, Q., Hu, G., et al.: Characterization of hydrate-bearing sediments recovered from the Shenhu area of the South China Sea. Interpretation **5**(3), 13–23 (2017)

Ma, S., Xiong, Y., Yu, D., et al.: Research on precision design of sand control on high yield offshore gas field. Oil Drill. Prod. Technol. **35**(6), 48–51 (2013)

Markestad, P., Christie, O., Espedal, A., et al.: Selection of screen slot width to prevent plugging and sand production. SPE 31087 (1995)

Oyeneyin, B.: Developments in Petroleum Science, pp. 191–223. Elsevier, Amsterdam (2015)

Saucier, R.J.: Consideration in gravel pack design. J. Pet. Technol. **26**(2), 205–212 (1974)

Wang, L., Deng, J., Zhou, J., et al.: Experimental study on premium screen mesh opening design for reasonable sand control. China Offshore Oil Gas **23**(2), 107–110 (2011)

Wu, N., Zhang, H., Yang, S., et al.: Gas hydrate system of Shenhu area, Northern South China Sea: geochemical results. J. Geol. Res. **2011**, 1–10 (2011)

Valdes, J., Santamarina, J.: Particle clogging in radial flow: microscale mechanisms. SPE J. **11**(11), 193–198 (2006)

Yoshihiro, T., Duncan, M.W., Hay, W.J., et al.: Deepwater methane hydrate gravel packing completion results and challenges. OTC 25330-MS (2014)

Zhang, G., Liang, J., Lu, J., et al.: Geological features, controlling factors and potential prospects of the gas hydrate occurrence in the east part of the Pearl River Mouth Basin, South China Sea. Mar. Pet. Geol. **67**, 356–367 (2015)

Zhang, W., Liang, J., Lu, J., et al.: Accumulation features and mechanisms of high saturation natural gas hydrate in Shenhu Area, northern South China Sea. Pet. Explor. Dev. **44**(5), 670–680 (2017)

Gas Driven Fracture During Gas Production Using 3D Synchrotron Computed Tomography

Zaher A. Jarrar[1], Khalid A. Alshibli[1(✉)], Riyadh I. Al-Raoush[2], and Jongwon Jung[3]

[1] University of Tennessee, Knoxville, USA
alshibli@utk.edu
[2] Qatar University, Doha, Qatar
[3] Chungbuk National University, Cheongju, Chungbuk, Korea

Abstract. During methane gas production from hydrate bearing sandy sediments, fine particles can migrate or clog the pores of sediments. Fines clogging induces a change in pressure gradient which affects the gas flow pattern and might induce gas driven fracture. A fundamental understanding of these phenomena is needed to enhance gas production strategies. Effects of fines migration and clogging on gas flow path and gas driven fracture were studied for Carbon Dioxide (CO_2) using 3D Synchrotron Micro-computed Tomography (SMT). Multiphase flow experiments were conducted on brine saturated uniform F75 silica sand mixed with kaolinite at different percentages by weight (2%, 4%, and 6%). Sand-fines mixtures were deposited into a small acrylic cylinder that has two ports; one connected to a flow pump to withdraw the brine solution and the other one was used to inject CO_2 gas at a constant pressure (4 psi). The gas migrated through percolation with no major particle displacement of sand for low fines concentration (2% and 4%). Moreover, gas driven fracture was observed for higher fines content. Fines were observed to clog the pores near the CO_2-brine boundary interface. SMT is considered to be a powerful tool that can be used to monitor and visualize fines clogging and the flow of gas through sandy sediments.

1 Introduction

The availability of methane hydrates and the expected increase in energy demand encouraged researchers to consider methane production from methane hydrates as a potential energy source. It is estimated that more than 95% of methane hydrates occur in marine environments where the conditions of high pressure and low temperature are satisfied (Max et al. 2013). The production of methane from hydrate-bearing sediments requires hydrate dissociation for releasing mobile methane gas in sediments prior to gas production operation. Multiphase flow is defined as simultaneous flow of two or more fluids with different states (i.e. gas or liquid). Fines migration and clogging in single-phase and multi-phase flow have been investigated using two-dimensional (2D) microfluidic pore models, three-dimensional (3D) porous sediments models, and numerical simulations (Wan and Wilson 1994; Imdakm and Sahimi 1991; Holtzman and Juanes 2010; Jung et al. 2017; Agbangla et al. 2012; Jang and Santamarina 2014).

A. Ferrari and L. Laloui (Eds.): SEG 2018, SSGG, pp. 344–351, 2019.
https://doi.org/10.1007/978-3-319-99670-7_43

During methane production, fines may migrate and/or clog through the pore space of sandy sediments depending on fines concentration, flow rate and geometry and topology of the pore scale (i.e., pore size distribution, throat size distribution and the ratio of the size of the pore throat to the size of the fine particle).

It is known that the preferential path of gas invasion for clay-rich sediments usually takes place through conduit opening or fracturing (Choi et al. 2011; Wiseall et al. 2015). However, Jung et al. (2012) showed that during multiphase flow of CO_2 through saturated sandy sediments with small amount of fines fraction (i.e. $\sim$4%), fracture could also develop due to fines clogging. Therefore, to better explore the mechanisms of gas production from hydrate bearing sediments, a comprehensive understanding of the associated physical processes such as fines migration, clogging and gas-driven fracture is needed.

In this paper, direct visualizations of fines, fines clogging and gas driven fracture are presented by means of 3D SMT imaging. Multiphase flow experiments were conducted on brine saturated uniform F75 silica sand mixed with kaolinite at different percentages by weight. Effects of fines migration and clogging on gas flow paths and gas driven fracture were studied for CO_2 gas.

2 Experimental Setup and Procedure

Uniform F75 silica sand with grain size between US sieve #60 (0.250 mm) and sieve #70 (0.210 mm) was used in this study. The sand was obtained from the US Silica Company and has a specific gravity of solids (G_s) of 2.65 g/cm^3, a maximum void ratio (e_{max}) of 0.78 and a minimum void ratio (e_{min}) of 0.50. Dixie Clay Kaolin supplied by Vanderbilt Minerals Company was used to represent the fines. It has a mean particle size of 0.6 μm and a G_s of 2.62 g/cm^3. Dry sand was first mixed with kaolinite powder at different kaolinite fraction by weight. The specimens were prepared to be in loose packing state since gas hydrates in marine environment are deposited in loose sediments (Hyodo et al. 2014). Then, the sand-kaolinite mixture was deposited in a 9.52 mm (3/8 in.) diameter acrylic cylindrical cell that was partially filled with distilled water. The cell has two ports; an upper port that was connected to a DigiFlow pressure-volume actuator (flow pump); and a bottom port that was connected to a pressure regulator connected to a CO_2 gas source.

3 3D Synchrotron Micro-computed Tomography (SMT)

X-ray computed tomography is a powerful non-destructive imaging technique in which an x-ray beam impinges a rotating object and the passing attenuated x-ray is collected by a detector. The collected attenuation data are then processed to produce a reconstructed 3D volume of the object. An enhancement to the conventional X-ray computed tomography is the use of a synchrotron radiation source that produces higher resolution images with less noise (Alshibli et al. 2014).

In this study, the SMT scans were acquired at Beamline 13D, Advanced Photon Source (APS), Argonne National Laboratory (ANL), Illinois, USA. Potassium Iodide

(KI) was added to the water to serve as a doping agent when analyzing the images to enhance the contrast of the brine phase and hence facilitate its segmentation in the images. At each state of the experiments, two different scans at two energy levels were acquired. The first energy level was below the edge of iodine (33.069 keV) while the second one was above it (33.269 keV). The resolution of the acquired images was approximately 3.9 μm/pixel. Six specimens with different kaolinite content (2%, 4%, and 6%) were scanned at four states. The first scan was acquired at the initial state of the specimen. The second scan was acquired after pumping out 0.4 ml of brine solution out of the saturated specimen while injecting CO_2 at a constant pressure of 27.6 kPa (4 psi). Then, another 0.6 ml of water was drained out and the scan was acquired. Finally, CO_2 pressure was increased to 41.4 kPa (6 psi) and the scan was acquired without pumping out more water.

4 Image Analysis

4.1 Three-Phase Segmentation

Once raw 3D SMT images were obtained, images were processed, enhanced and segmented using AVIZO 9.4 software. First, anisotropic diffusion filter was applied on the greyscale images to reduce noise and enhance contrast of edges. Then, user-defined values of image intensity ranges were input in the interactive thresholding module that allowed binarizing the images into voxels of values zeros and ones. Images acquired at the energy level below Iodine edge were used to identify the sand and voids whereas gas was identified from the other phases using the images acquired at the higher energy level. Next, arithmetic operations were performed on the binarized images that resulted in one segmented image where sand particles have a voxel value of two, brine has a voxel value of one, and gas has a voxel value of zero. Figure 1 presents the steps of the image segmentation that was performed on the images acquired at the second stage of the test for the 2% kaolinite specimen.

4.2 Fines Segmentation

Separation of fines from other phases was a challenging task due to their small sizes and since they are mixed with the water phase. One way to infer regions with high concentration of fines is by considering regions in the water phase with a higher density (higher CT number). After selecting the voxels within this region, opening algorithm is applied to remove small particles. After that, the detected regions with high concentration of fines are highlighted in the filtered image and appear as bright white spots. Figure 2 shows the greyscale image of 3rd state scan for the 6% kaolinite specimen with regions of high fines concentration displayed as bright voxels. Both clogging and gas driven fracture are detected in Fig. 2. Clogging of fines is observed near the boundary of the CO_2 brine interface.

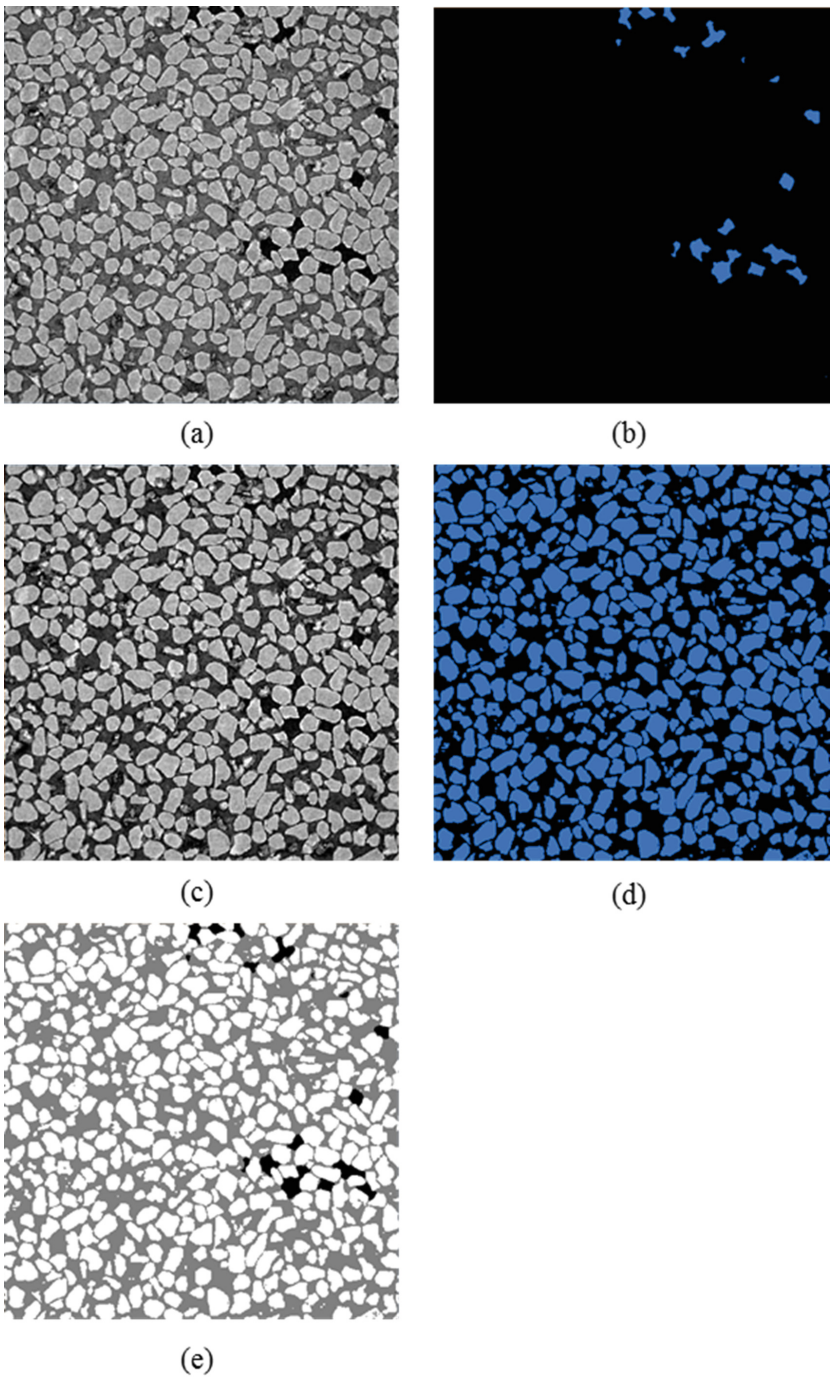

Fig. 1. Image post-processing steps: (a) filtered image acquired at energy level higher than Iodine edge; (b) gas phase binarized image; (c) filtered image acquired at lower energy level than Iodine edge; (d) solids phase binarized image; (e) three-phase segmented image for the 2% kaolinite specimen acquired at the second stage of the test, sand is white, brine is grey and gas is black

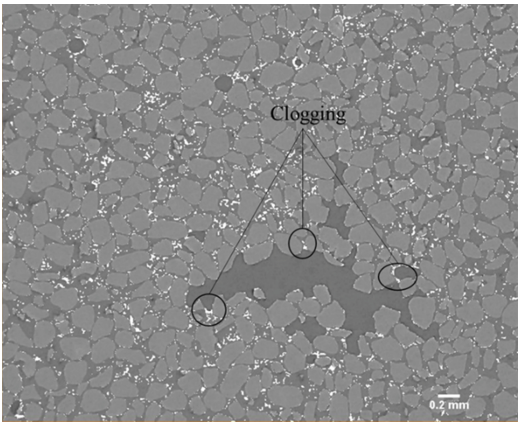

Fig. 2. Greyscale image of the 3rd state scan for 6% kaolinite specimen with regions of high fines concentration displayed as bright voxels

5 Results

Table 1 presents volume based measurements (porosity, brine saturation, and gas saturation) of the tested specimens based on the segmented images. The porosity of the 4% kaolinite specimen is slightly higher than those of the other two specimens. Gas invades the 2% and 4% kaolinite specimens by "percolation" (Fig. 3), while it invades the 6% specimen by "fracturing" or "conduit opening" (Fig. 2). Gas saturation in the final state of the 2% specimen is 11.9% while it reaches 16.3% for the 6% kaolinite specimen. The 4% specimen has gas saturation of 45.6%. For the 2% specimen, capillary pressure (the difference between gas pressure and water pressure) was slightly higher than the capillary entry pressure. Increasing fines content will cause an increase in the capillary pressure. The excessive clogging in the 6% specimen caused the capillary pressure to overcome the effective stress between sand particle, and fractures were initiated.

Image-based measurements of fines content during different stages of the tests are presented in Table 2. The measured fines content using image analyses did not differ significantly from calculated values based on measured weights during specimens' preparation. This observation helps to develop confidence in the selected intensity range used in segmentation of fines. Values provided in Table 2 were calculated based on volume measurements obtained from the segmented images and using the specific gravity of solids for sand and kaolinite. The amount of fines for 2% and 4% specimens decreased as CO_2 was injected through the Table 2. Fines migrated through the pores without observed clogging. On the other hand, the measured fines content for the 6% specimen was found to increase compared to the initial state by almost 7%. Clogging was excessive which lead to an increase in the measured fines.

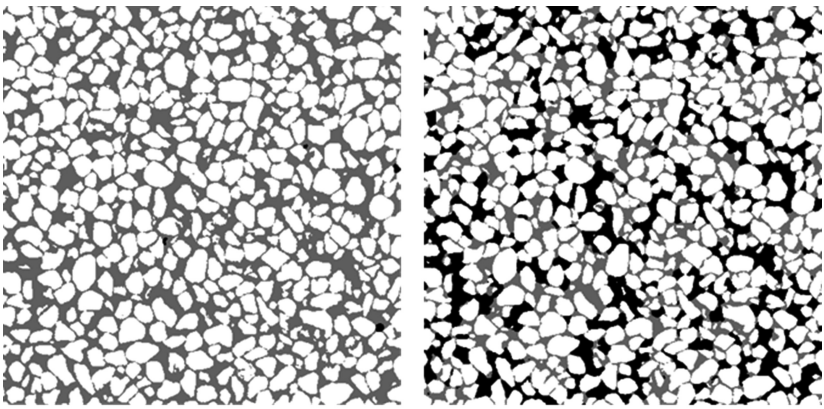

Fig. 3. Three-phase segmented image for 4% kaolinite specimen at (a) initial state; and (b) final state (sand is white, brine is grey and gas is black).

Table 1. Image-based measurements of porosity, brine saturation and gas saturation for the tested specimens

Fines type	Fines content (%)	Initial porosity (%)	Initial brine saturation (%)	Final brine saturation (%)	Final gas saturation (%)
Kaolinite	2	40.8	99.2	89.6	11.9
Kaolinite	4	35.6	99.5	53.6	45.6
Kaolinite	6	39.9	98.3	83.5	16.3

Table 2. Image-based measurements of fines content at different flow states

Specimen	Measured fines content	Change in fines content with reference to load the initial (1^{st}) state (%)*		
	1st state	2nd state	3rd state	4th state
2% kaolinite	–	–	–	−9.5
4% kaolinite	4.6	−9.4	−18.1	−17.2
6% kaolinite	6.5	7.8	5.3	7.0

*Assuming G_s = 2.65 for sand and 2.62 for kaolinite

6 Conclusions

Production of methane from hydrate-bearing sediments requires hydrate dissociation for releasing mobile methane gas in sediments prior to gas production operations. Fines may migrate through or clog the pore space of sandy sediments depending on pore network geometry. Multiphase flow experiments were conducted on brine saturated

uniform F75 silica sand mixed with kaolinite and at different percentages by weight with similar preparation procedure. Direct visualization of fines, fines clogging, and gas driven fracture were presented in this paper using 3D SMT images at different flow states.

Fines were segmented by selecting voxels with high CT numbers in the brine phase of the images. Fines content were calculated based on image analyses and found to be close to the values that were calculated based on weight measurements during specimens' preparation. For low fines concentration, fines tend to migrate through the pores of the sediments. Increasing fines content leads to clogging which increases the pressure gradient within the pores that can lead to a gas driven fracture if it overcomes the effective stress between sand particles. 3D SMT imaging offers a valuable quantitative and qualitative analyses of fines migration and clogging during multi-phase flow through sandy sediments.

Acknowledgement. This research was made possible by NPRP Grant # NPRP8-594-2-244 from Qatar National Research Fund (a member of Qatar Foundation). The findings achieved herein are solely the responsibility of the authors. The SMT images were collected using the X-ray Operations and Research Beamline Station 13-BMD at Argonne Photon Source (APS), Argonne National Laboratory. The authors thank Dr. Mark Rivers of APS for help in performing the SMT scans. They also acknowledge the support of GeoSoilEnviroCARS (Sector 13), which is supported by the National Science Foundation, Earth Sciences (EAR-1128799), and the US Department of Energy (DOE), Geosciences (DE-FG02-94ER14466). Use of the Advanced Photon Source, an Office of Science User Facility operated for the DOE Office of Science by Argonne National Laboratory, was supported by DOE under contract no. DE-AC02-06CH11357.

References

Agbangla, G.C., Climent, É., Bacchin, P.: Experimental investigation of pore clogging by microparticles: evidence for a critical flux density of particle yielding arches and deposits. Sep. Purif. Technol. **101**, 42–48 (2012)

Alshibli, K.A., Druckrey, A.M., Al-Raoush, R.I., Weiskittel, T., Lavrik, N.V.: Quantifying morphology of sands using 3D imaging. J. Mater. Civ. Eng. **27**(10), 04014275 (2014)

Choi, J.H., Seol, Y., Boswell, R., Juanes, R.: X-ray computed-tomography imaging of gas migration in water-saturated sediments: from capillary invasion to conduit opening. Geophys. Res. Lett. **38**(17), L17310 (2011)

Holtzman, R., Juanes, R.: Crossover from fingering to fracturing in deformable disordered media. Phys. Rev. E **82**(4), 046305 (2010)

Hyodo, M., Li, Y., Yoneda, J., Nakata, Y., Yoshimoto, N., Nishimura, A.: Effects of dissociation on the shear strength and deformation behavior of methane hydrate-bearing sediments. Mar. Pet. Geol. **51**, 52–62 (2014)

Imdakm, A., Sahimi, M.: Computer simulation of particle transport processes in flow through porous media. Chem. Eng. Sci. **46**(8), 1977–1993 (1991)

Jang, J., Santamarina, J.C.: Evolution of gas saturation and relative permeability during gas production from hydrate-bearing sediments: gas invasion vs. gas nucleation. J Geophys Res Solid Earth **119**(1), 116–126 (2014)

Jung, J., Cao, S.C., Shin, Y.-H., Al-Raoush, R.I., Alshibli, K., Choi, J.-W.: A microfluidic pore model to study the migration of fine particles in single-phase and multi-phase flows in porous media. Microsyst. Technol. **24**(2), 1071–1080 (2017)

Jung, J.W., Jang, J., Santamarina, J.C., Tsouris, C., Phelps, T.J., Rawn, C.J.: Gas production from hydrate-bearing sediments: the role of fine particles. Energy Fuels **26**(1), 480–487 (2012). https://doi.org/10.1021/ef101651b

Max, M.D., Johnson, A.H., Dillon, W.P.: Natural gas hydrate-arctic ocean deepwater resource potential, pp. 19–23. Springer, Cham (2013)

Wan, J., Wilson, J.L.: Colloid transport in unsaturated porous media. Water Resour. Res. **30**(4), 857–864 (1994)

Wiseall, A., Cuss, R., Graham, C., Harrington, J.: The visualization of flow paths in experimental studies of clay-rich materials. Mineral. Mag. **79**(6), 1335–1342 (2015)

Influence of Temperature on the Fracture Toughness of Several Rocks

J. Justo[1(✉)], J. Castro[1], S. Cicero[2], and M. A. Sánchez-Carro[3]

[1] Group of Geotechnical Engineering, Universidad de Cantabria, E.T.S. de Ingenieros de Caminos, Canales y Puertos, Av/Los Castros 44, 39005 Santander, Spain
justoj@unican.es

[2] LADICIM (Laboratory of Materials Science and Engineering), Universidad de Cantabria, E.T.S. de Ingenieros de Caminos, Canales y Puertos, Av/Los Castros 44, 39005 Santander, Spain

[3] Group of Engineering Geology, Universidad de Cantabria, E.T.S. de Ingenieros de Caminos, Canales y Puertos, Av/Los Castros 44, 39005 Santander, Spain

Abstract. This paper aims to analyse the variability of the fracture toughness of rocks with temperature, which implies a critical parameter for rock fracture prediction and assessment methodologies. Four types of rocks with different characteristics and lithologies have been chosen with this purpose: the Floresta Sandstone, the Moleano Limestone, the Macael Marble and the Carrara Marble. The research is based on the results obtained in an exhaustive, systematic and rigorous experimental programme comprising 48 notched specimens tested in four-point bending conditions both at room temperature and at 250 °C, being this latter temperature quite common in high enthalpy geothermal applications. All the test specimens consist of parallelepiped pieces with a U-shaped notch located in the middle. These notches have a radius of 0.15 mm, which make it possible to assume that they behave as cracks rather than as notches. Based on this assertion, the performed tests allow calculating the fracture toughness with reasonable accuracy. Rock attributes like low- and high-porosity, grain size and microstructure, together with the temperature, show a direct influence on the mechanical behaviour of geological materials. For this reason, changes in their behaviour are studied in this work through the deviations in the already mentioned key parameter: the fracture toughness.

Keywords: Temperature · Rock · Fracture toughness · Notch
Crack

1 Introduction

This study aims to investigate the influence of temperature on the mode I fracture toughness using Single Edge Notched Beam (SENB) specimens of four different types of rocks: the Floresta Sandstone, de Moleano Limestone, the Macael Marble and the Carrara Marble. The fracture toughness reflects the rock's resistance to crack propagation, and therefore represents an important mechanical property that can be used to

A. Ferrari and L. Laloui (Eds.): SEG 2018, SSGG, pp. 352–359, 2019.
https://doi.org/10.1007/978-3-319-99670-7_44

characterize the residual strength of rocks with crack structures. Understanding, controlling and being able to predict rock fracturing is crucial in many underground engineering fields, where the effect of temperature cannot be considered negligible (e.g. geothermal extractions, oil-gas exploitations, etc.).

The authors of this paper have successfully applied in previous works different methodologies for fracture prediction of several rocks at room temperature: the Theory of the Critical Distances (Cicero et al. 2014; Justo et al. 2017) or the Strain Energy Density criterion (Justo et al. 2018 – under revision). In all of them, the fracture toughness turns out to be a key parameter for the fracture assessment, so its correct characterization is of the utmost importance. Thus, this work aims to analyze the variation of the fracture toughness comparing the results obtained at room temperature with those corresponding to 250 °C, which is a common temperature in high enthalpy geothermal applications.

Different studies can be found in the literature about the influence of temperature on the fracture toughness of rocks. Meredith and Atkinson (1985), for example, studied the fracture toughness of a granite and a gabbro and showed that it decreased at temperatures above 100 °C. The reduction of the fracture toughness of both rocks was caused by the development of micro-cracks induced by differential thermal expansion between adjacent mineral particles. By contrast, Al-Shayea (2002) reported a case of a limestone where the fracture toughness increased at 116 °C by approximately 25%, probably due to the closure of micro-cracks or pores caused by the thermal expansion. Similarly, Zuo et al. (2014) focused on the fracture behavior of a siltstone after thermal treatment and observed that when temperature was below 200 °C, fracture toughness increased, mainly because of the pore pressure changes induced by temperature. Thus, it seems evident that the variations in the fracture toughness of the rocks are dominated by micro-mechanisms derived from changes in temperature. This study aims to provide further information on different rocks.

2 Experimental Program: Materials

This section provides an individual and detailed microstructural description of each of the chosen rocks, which were previously studied by the authors of this paper at Justo et al. (2017). Table 1 gathers some of the most relevant technical properties of the analyzed rocks:

Table 1. Some technical properties of each material.

	(F)	(C)	(M)	(I)
Bulk density (kg/m^3)	2320	2500	2715	2709
Open porosity (%)	16.3	6.4	-	-
Water absorption (%)	4.8	2.7	0.075	0.15

2.1 Floresta Sandstone (F)

The Floresta Sandstone can be classified as a sedarenite, consisting of medium-fine grain (62–500 μm) quartz (monocrystalline, polycrystalline and chert grains) and abundant medium size carbonated grains (250–500 μm). Carbonates [C] are mainly subrounded and consist of intraclastic grains (mudstone texture), sparitic crystals and dolomite. On the other hand, quartzes [Q] are mainly subrounded and subangular shaped, or angular occasionally. The presence of large packing and dissolution voids [V] is common, cement [Sp] is very scarce and depositional structures are not recognizable (see Fig. 1a).

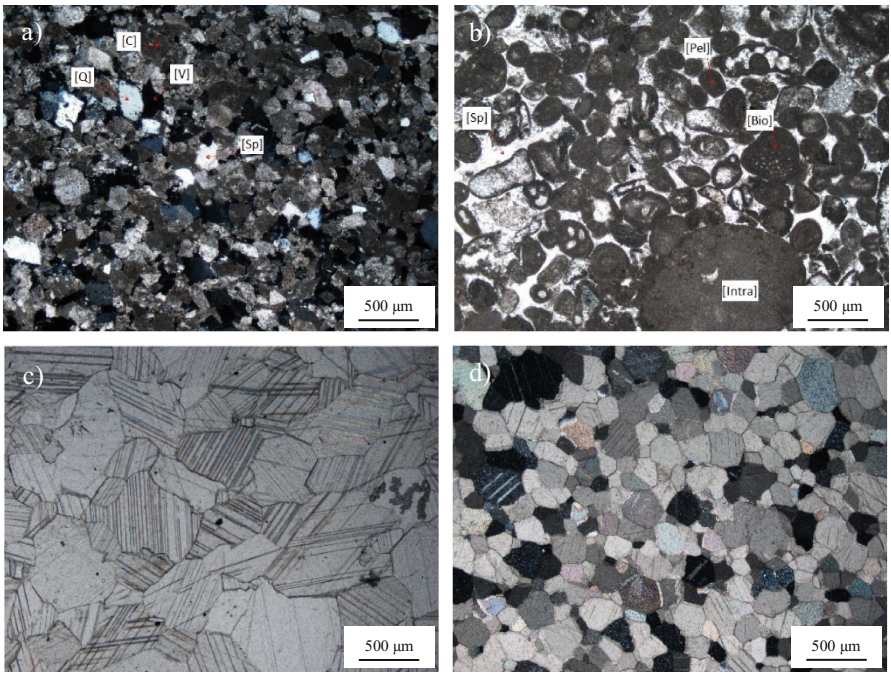

Fig. 1. Microstructure of the analysed rocks: (a) Floresta Sandstone (4x, crossed Nicols), (b) Moleano Limestone (4x, crossed Nicols), (c) Macael Marble (4x, parallel Nicols), (d) Carrara Marble (4x, crossed Nicols).

2.2 Moleano Limestone (C)

The Moleano Limestone can be classified as an intrasparitic-pelsparitic limestone (Folk 1959) or grainstone (Dunham 1962) that consists of intraclasts, bioclasts, pellets and sparite crystals as shown in Fig. 1b. Intraclasts [Intra] correspond to the largest subrounded-rounded shaped grains with sizes varying in the range of coarse sand and microconglomerate (500–2000 μm), showing a micritic texture. By contrast, bioclasts [bio] are mainly fragments of bivalves and corals which occasionally show internal sparitic recrystallization, and pellets [Pel] are the dominant allochemical component.

The size of the latter varies in the range of fine and medium sand (125–500 μm) and always shows a micritic internal texture. Sparite crystals [Sp] cement to a great amount the allochemical components, so porosity is much lower than in the case of the Floresta Sandstone.

2.3 Macael Marble (M)

Macael Marble shows a very well developed granoblastic texture with equidimensional idiomorphs leucocratic crystals and null porosity (see Fig. 1c). The grain sizes vary in a wide range of values that oscillate between 200 and 1180 μm.

2.4 Carrara/Italian Marble (I)

The microstructural composition of the Carrara Marble is very similar to the one described for the Macael Marble. The most important difference is the crystal sizes (see Fig. 1d), which are smaller and more homogeneous in the Carrara Marble (112–500 μm).

3 Experimental Program: Fracture Toughness Tests

A wide variety of testing methods can be found in the literature for fracture toughness assessment of rocks, all of them considering different specimen geometries (e.g., Ouchterlony 1988; ASTM-PS70 1997; CEN/TS 14425-1:2003; Kuruppu et al. 2014). None of the existing tests stands out among the rest from a methodological point of view, and even those 'suggested methods for determining fracture toughness of rock' (Ouchterlony 1988) specified by the International Society for Rock Mechanics (ISRM) have been frequently questioned or modified.

For this reason, among all the methods collected by Amaral et al. (2008) for rock fracture toughness evaluation, the CEN/TS 14425-1:2003 standard has been selected here with some minor geometrical modifications based on the Spanish standard UNE-EN 13161:2008 dealing with natural stone test methods. It was originally proposed by Srawley and Gross (1976) for ceramic materials and uses SENB specimens subjected to four-point bending conditions.

With all this, Fig. 2 shows a scheme of the used fracture specimens in the present experimental campaign, which consist of 180 × 30 × 30 mm size parallelepiped beams with a straight U-shaped notch in the middle with a radius (ρ) equal to 0.15 mm. The notch is performed using a diamond wire, so the possible slight variations in the notch length are attributable to the precision of the cutting process. In any case, the relative notch length (α_0), which is defined as the ratio between the initial notch length (a_0) and the total height (h) of the specimen, will always guarantee high confinement conditions ($0.45 \leq a_0/h \leq 0.55$).

All in all, 48 four-point bending tests have been performed for this study, six for each material and temperature (room temperature and 250 °C). They were all carried out in displacement control with a constant rate of 0.05 mm/min till failure. In all the tests, both the applied load and the vertical displacement were recorded.

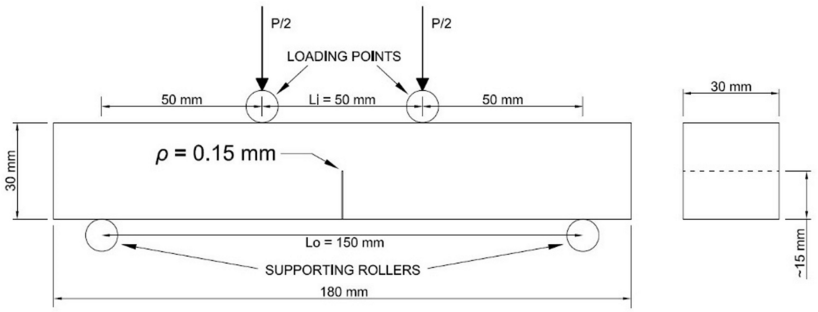

Fig. 2. Scheme of the geometry of the fracture specimens.

The experimental setup is shown in Fig. 3. The rollers of the testing device have been designed to allow rotation and lateral tilting. This will minimize friction between them and the specimens and will reduce possible torsion effects that may arise when opposite faces are not perfectly parallel. Besides, the upper head has a spherical joint that allows a greater degree of adjustment and ensures a centered load application axis. Likewise, the apparatus is placed inside an oven that has been previously coupled to the press, which permits performing the tests under constant temperature conditions. Those specimens tested at 250 °C were preheated during at least 48 h to ensure an inner constant temperature of the pieces before testing.

Fig. 3. Experimental setup for fracture toughness tests at different temperatures.

Mode I fracture toughness values (K_{IC}) for the SENB specimens analyzed in this article can be calculated with the following expression initially developed by Srawley and Gross (1976) and defined at CEN/TS 14425-1:2003:

$$K_{IC} = \frac{F \cdot Y}{b \cdot h^{1/2}} \tag{1}$$

where F is the failure load obtained in the tests, b is the specimen thickness, h is the specimen height and Y is the compliance factor given by:

$$Y = \frac{3 \cdot (L_o - L_i) \cdot \alpha_0^{1/2} \cdot X}{2h \cdot (1 - \alpha_0)^{3/2}} \tag{2}$$

with

$$X = 1.9887 - \left[\frac{\left(3.49 - 0.68\alpha_0 - 1.35\alpha_0^2\right) \cdot \alpha_0 \cdot (1 - \alpha_0)}{(1 + \alpha_0)^2} \right] - 1.32\alpha_0 \tag{3}$$

L_o and L_i being the spans between the supporting rollers and the inner loading points, respectively (see Fig. 2), and α_0 the relative notch length ($\alpha_0 = a_0/h$). It is important to note that fracture toughness testing methodologies are supposed to consider a crack-type defect ($\rho \approx 0$ mm). However, introducing a proper crack with controlled geometry in rocks is not feasible, so limited finite radii are accepted at the defect tip as long as the notch effect is negligible. The authors of this paper demonstrated in a previous work (Justo et al. 2017) that the notches with a radius ρ = 0.15 mm behave as crack-type defects, developing the notch effect with larger notch radii (of the order of few millimeters) in the case of the analyzed rocks.

4 Results and Conclusions

Figure 4 shows the results of each of the performed fracture toughness tests, both at room temperature (23 °C) and at 250 °C. Dots correspond to the individual results, while the crosses represent the mean values of the fracture toughness. Two clear trends can be directly observed: in the case of the Moleano Limestone (Fig. 4a) and the Floresta Sandstone (Fig. 4b), those rocks with relatively high porosity, the fracture toughness increases at 250 °C by approximately a 47% and a 21%, respectively. The experimented increment may probably be caused by the closure of the existing pores and micro-cracks due to the temperature rise, making the rocks stiffer and more compact.

By contrast, the fracture toughness of the two analyzed non-porous marbles (Fig. 4c and d) decreases considerably at 250 °C, around a 40% in both cases. This clear reduction in the fracture toughness is produced by the development of micro-cracks as a response to uneven thermal dilation between adjacent confined crystals with no space for expansion.

The obtained results are consistent with those found in the bibliography (e.g., Al-Shayea 2002; Gan et al. 2017), where similar fracture behaviors and trends were recorded for other rocks with comparable properties. In the future, other intermediate temperatures will be tested to deeper analyze changes in the microstructure.

In conclusion, it is essential to understand the micro-mechanisms produced in the rocks exposed to heating processes. The changes induced by temperature both in the internal composition and in the structure of the rocks define their fracture behavior.

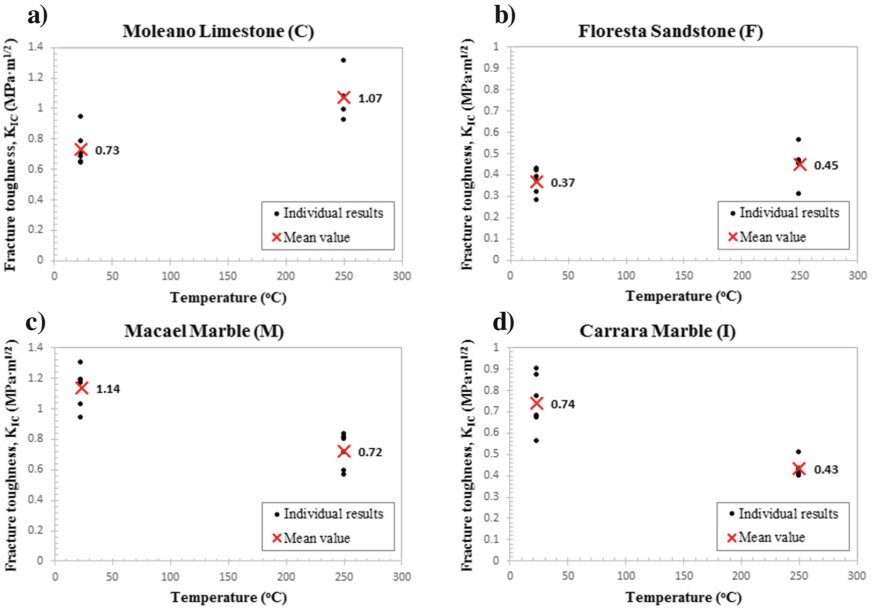

Fig. 4. Fracture toughness at different temperatures: (a) Moleano Limestone, (b) Floresta Sandstone, (c) Macael Marble, (d) Carrara Marble.

Consequently, the fracture toughness can be considered a key parameter, as it allows to characterize the residual strength of the rock under those conditions.

Acknowledgement. The authors of this work would like to express their gratitude to the Spanish Ministry of Economy and Competitiveness and to the European Regional Development Fund (ERDF) for financing the National Plan Project (Ref.: BIA2015-67479-R) under the name of 'The Critical Distance in Rock Fracture'.

References

Al-Shayea, N.: Comparing reservoir and outcrop specimens for mixed mode I-II fracture toughness of a limestone rock formation at various conditions. Rock Mech. Rock Eng. **34**(4), 271–297 (2002)

Amaral, P.M., Guerra, R.L., Cruz, F.J.: Assessment of fracture toughness in ornamental stones. Int. J. Rock Mech. Min. Sci. **45**, 554–563 (2008)

ASTM-PS70:1997, Provisional Test Methods for Determination of Fracture Toughness of Advanced Ceramics at Ambient Temperatures, American Society for testing and materials, Philadelphia

CEN/TS 14425-1:2003, Advanced Technical Ceramics – Test Methods for Determination of Fracture Toughness of Monolithic Ceramics – Part 1: Guide to Test Method Selection, Committee for Standarization, European

Cicero, S., García, T., Castro, J., Madrazo, V., Andrés, D.: Analysis of notch effect on the fracture behavior of granite and limestone: an approach from the theory of critical distances. Eng. Geol. **177**, 1–9 (2014)

Dunham, R.J.: Classification of carbonate rocks according to depositional textures. Am. Assoc. Petrol. Geol. Mem. **1**, 108–121 (1962)

Folk, R.L.: Practical petrographic classification of limestones. Bull. Am. Assoc. Pet. Geol. **43**(1), 1–38 (1959)

Gan, F., Yong, K., Tao, M., Yao-qing, H., Xiao-hong, L.: The influence of temperature on mode I fracture toughness and fracture characteristics of sanstone. Rock Mech. Rock Eng. **50**, 2007–2019 (2017)

Justo, J., Castro, J., Cicero, S., Sánchez-Carro, M.A., Husillos, R.: Notch effect on the fracture of several rocks: application of the theory of the critical distances. Theor. Appl. Fract. Mech. **90**, 251–258 (2017)

Justo, J., Castro, J., Cicero, S.: Energetic approach for fracture assessment on several rocks containing U-shaped notches: application of SED criterion. Manuscript under revision (2018)

Kuruppu, M.D., Obara, Y., Ayatollahi, M.R., Chong, K.P., Funatsu, T.: ISRM suggested methods for determining the mode I fracture toughness using semi-circular bend specimens. Rock Mech. Rock Eng. **47**(1), 267–274 (2014)

Meredith, P.G., Atkinson, B.K.: Fracture toughness and subcritical crack growth during high-temperature tensile deformation of Westerly granite and Black gabbro. Phys. Earth Planet. Inter. **39**(1), 33–51 (1985)

Ouchterlony, F.: ISRM suggested methods for determining the fracture toughness of rock. Int. J. Rock Mech. Min. Sci. Geomech. **25**, 71–96 (1988)

Srawley, J., Gross, B.: Cracks and fracture. ASTM Spec. Tech. Publ. **601**, 559–579 (1976)

UNE-EN 13161:2008. Natural Stone Test Methods – Determination of Flexural Strength under Constant Moment, AENOR. (in Spanish)

Zuo, J.-P., Xie, H.-P., Dai, F., Ju, Y.: Three-point bending test investigation of the fracture behavior of siltstone after thermal treatment. Int. J. Rock Mech. Min. Sci. **70**(9), 133–143 (2014)

Naturally Fractured Basement Reservoir Potential Quantification from Fracture Model and Petrophysical Analysis by Leveraging Geostatistics and Seismic Interpretation: A Case Study in Jabung Block, South Sumatra Basin

Putra Herianto[1], Muhammad Fadhil[2], Suci Handayani Qolbi[3], Mohammad Risyad[4(✉)], and Beiruny Syam[4]

[1] Kasetsart University, Kamphaeng Saen, Thailand
[2] Bandung Institute of Technology, Bandung, Indonesia
[3] Department of Geophysics, Universitas Gadjah Mada, Yogyakarta, Indonesia
[4] PetroChina International Jabung Ltd., Jakarta, Indonesia
Mohammad.Risyad@petrochina.co.id

Abstract. Northeast Betara (NEB) field is the biggest producing gas field of Tertiary sediment reservoir in Jabung Block, South Sumatra Basin. Mesozoic basement exploration has been anticipated by regional explorationists for more than a decade. Two deviated-basement-well have drilled the same granite lithology in 2013 to 2015, but surprisingly they showed different results. NEB Base-1 have gas and condensate discoveries, NEB Base-2, on the other hand, where is located 5.7 km away from NEB Base-1, do not have any hydrocarbon in the basement section. Absence of conventional core data challenges this study to maximize the utilization of well and 3D seismic data. This paper applies the fracture model and petrophysical method including integrating the subsurface datasets to estimate fractured basement reservoir reserves. Fracture model was created by using Gaussian Random Function Simulation which incorporates multi-attributes aided by Artificial Neural Network and interpreted well data to show potential fractured zones. Combination of petrophysical method, well-test and image log analysis was also performed to calculate reservoir porosity and permeability. The result shows that edge-detection and ant-tracking attributes are able to give the distribution of high-intensity fractured zone. It also shows that the deeper the well, the less conductive fractures exist. The fractures dip-azimuth have the mean magnitude of >50° which major orientation towards Southeast direction. The fracture porosity and permeability consecutively ranges from 0.24% to 18.82% and 1.7×10^{-7} to 2.44 mD. The optimum porosity and permeability values can be then used to calculate reserves in order to give reliable results.

A. Ferrari and L. Laloui (Eds.): SEG 2018, SSGG, pp. 360–368, 2019.
https://doi.org/10.1007/978-3-319-99670-7_45

1 Introduction

Fractured reservoirs are more difficult and expensive to evaluate than conventional reservoirs (Nelson 2001). Therefore, a fully understanding about the fracture distribution and orientation, and its role to basement reservoirs may be the evidence for the enhanced exploration and production concepts for this hidden source. Owing to exploit this kind of reservoir, comprehensive study must be done. These are determination of the distribution, orientation, and morphology of the fractures and possible migration and trap of the area. How to identify the distribution and the orientation of the fractures is a difficult problem. Simply, both fault and fractures can be identified using seismic profiles. This study attempts to quantify the potential reservoir area using seismic attributes methods and well data (core and image logs). Furthermore, petrophysical analysis is applied to calculate the reserves area.

1.1 Regional Geology

The research location is located in Jambi Sub-Basin which is included in Betara High bounded by some other highs such as Tigapuluh Mountain to the West, Kelapagajah Hill and Marlang Hill to the South and also Sempilang High on to the Southeast. Stratigraphy succession of Jambi Sub-Basin from oldest to youngest consecutively (Saifuddin et al. 2001; Ginger and Fielding 2005) are Basement, Lahat Formation, Talang Akar Formation, Baturaja Formation, Gumai Formation, Air Benakat Formation, Muara Enim Formation, and Kasai Formation. Granite basement of the area, portion of the Northern to Eastern region of South Sumatra Basin, is considered part of the Malacca Microplate formed during late Cretaceous. Tectonic stress and extension, resulting from northward movement of both the Australian and the India tectonic plate, and rotation of Borneo (Kalimantan), formed rifts or half-graben complexes along much of the Southern margin of the Sunda Shelf plate (now Sumatra and Northwest Java) in the Eocene to Oligocene. Fracture development in Jabung Block is controlled by structural history and stress character of the area (Risyad et al. 2017). Structural lineaments found in the research area has trends on NE–SW and NW–SE trends depicted in Fig. 1. Those two trends are affecting the hydrocarbon accumulation and migration.

1.2 Methodology and Data

The main data of this study are Post-Stack 3D seismic and image Logs (NEB Base-1 and 2). Among 6 wells, 2 wells are deviated well (NEB Base-1 and 2). Mud logs and wireline logs, however, were needed for petrophysical analysis and calculation.

As the beginning, the existence of fractures and fault are interpreted from image logs, and seismic. This step is including picking faults and fractures that could possibly be detected, fracture characterization and petrophysical calculation. Secondly, selected seismic attributes were generated to enhance the lateral distribution of minor faults. Later on, both attributes and fracture intensity are simulated using co-kriging and combined using Artificial Neural Network (ANN) to give heterogeneity. Finally, a model is obtained to show the potential zones of interest.

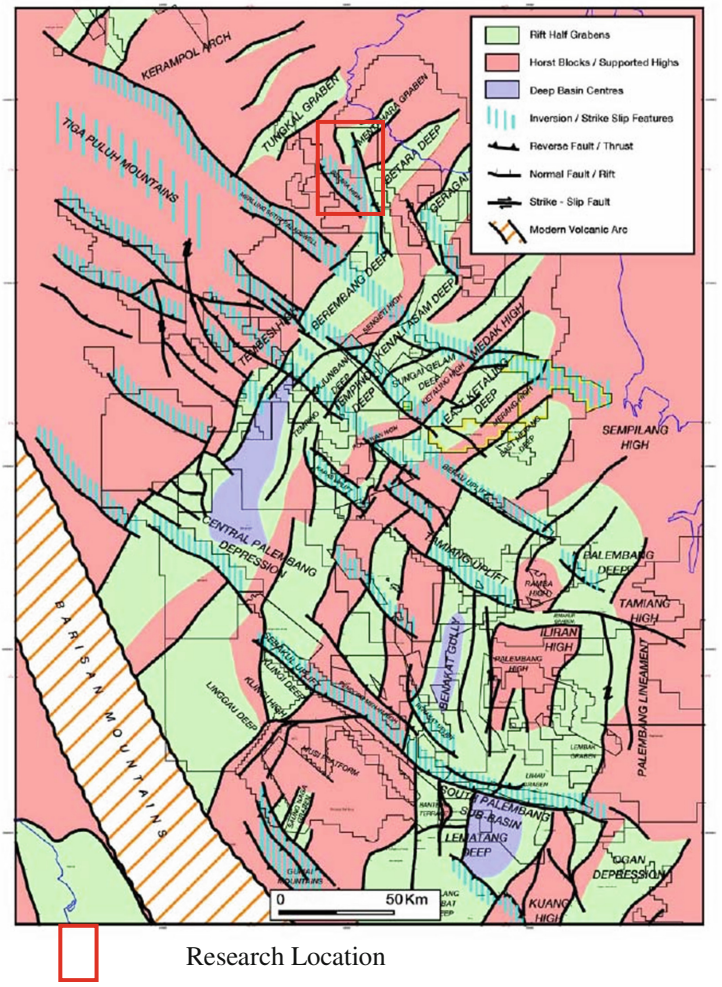

Fig. 1. Structural Geology of South Sumatera Basin (Ginger and Fielding 2005). Note that the red box is the location of study

a. Fracture Characterization
Two fracture zones were created based on image log on Fig. 2. The first zone is conductive zone, which is found mostly on the shallower depth with lower resistivity, density, gamma ray value, and mostly shows the black sinusoidal on image log. Whereas the second zone is the resistive one found on the deeper depth, and have higher resistivity, density, gamma ray value, and shows bright sinusoidal on image log. Then, aperture of each zones were calculated using Eq. 1 by Luthi and Souhaite (1990).

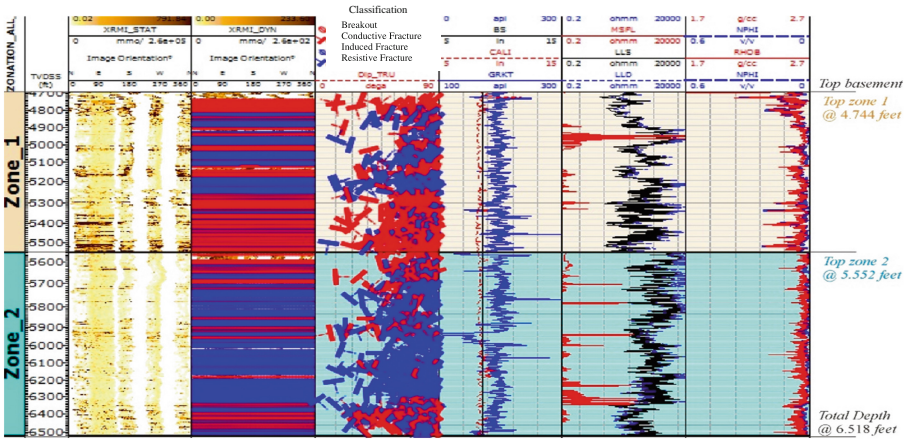

Fig. 2. Two main zones on image logs, the red colour shows conductive fracture, where the blue colour shows the resistive fracture.

$$W = cAR_m^b R_{xo}^{1-b} \tag{1}$$

Where, W is the fracture aperture, c is constant coefficient, A is the current value of resistivity, R_m is the mud resistivity, R_{xo} is the flushed zone resistivity, and b is the exponent of device. The aperture mainly ranges from 0.17 mm to 63.93 mm, whereas average dip is 65°, and strike N 15 °E in zone 1 and N 5 °E in zone 2.

b. Petrophysical Analysis

To emphasize the vertical distribution of fractures, based on log characterization and fracture domination, 2 main zones and 16 detailed zones were separated. Furthermore, porosity and permeability calculated using Eq. 2 by Poupon et al. (1970) and 3 by Tiab and Donaldson (2012).

$$\varphi_f = \left(\frac{\varphi_N^2 - \varphi_D^2}{2}\right)^{\frac{1}{2}} \tag{2}$$

Where φ_f is the fracture porosity, φ_N is porosity from neutron log (%), φ_D is porosity from density log (%). Equation for permeability is given by

$$k_f = 8.33 \times 10^{-4} w_f^2 \varphi_f \tag{3}$$

Where k_f is fracture permeability (Darcy), w_f is the fracture aperture (mm), and φ_f is fracture porosity (%).

c. Generating Seismic Attributes

Several structural attributes were chosen to enhance lateral resolution of faults. This study only takes account on structural attributes since the other attributes cannot show the pattern of fracture distribution and orientation. Visual inspection is conducted by employing variance, curvature, and ant-tracking seismic attributes.

Variance can work on detecting small differences or anomalies of one trace to the adjacent traces (Juanda 2010). On the other hand, curvature can detect small changes on horizon, and consider it as fault (Roberts 2001). Therefore, they are very suitable for basement condition that tends to be below seismic resolution. Ant-tracking is a well-known attribute for fault mapping and fracture system characterization. All of the anomaly values from attribute input (variance) will be re-calculated using ant-algorithm, and stated as fault. Hence, azimuth, dip angle, and lateral density of fracture system are obtained. Ant-track cube shows good fault imaging and density around two basement crests (Fig. 3), located around two basement wells.

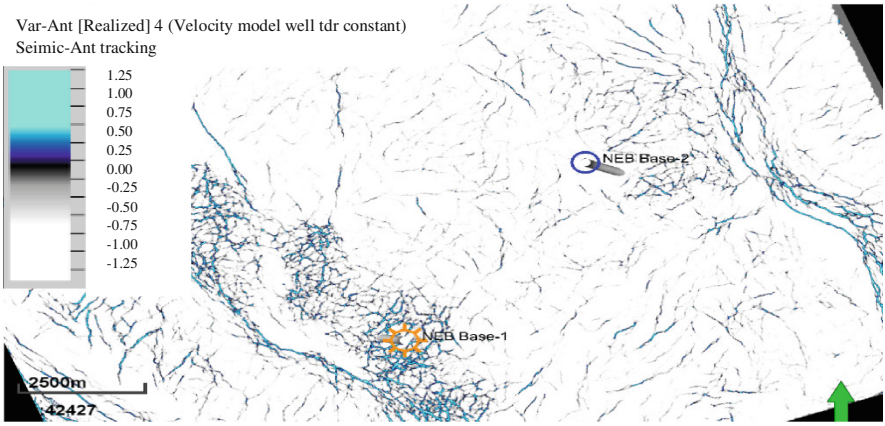

Fig. 3. Ant-Tracking at 5,000 ft TVD

d. Obtaining Fracture Model
The three different attributes (variance, curvature, and ant-track) were chosen to be the best attribute to be combined with ANN. The process is supervised by well data and creating the fracture intensity and lateral porosity model. By using Gaussian Random Function Simulation (GRFS), intensity fracture model is generated. Furthermore, porosity model is also produced later on.

2 Results and Discussions

From 16 zones on Fig. 4, the most porous and permeable zones are located in 4,700 ft–5,500 ft SSTVD. The most porous zone is located on the very top of the basement, the A zone, and the lowest one is the G zone. Generally, A-L zone have a greater conductivity then M-P zone. It also can be stated that high aperture considered as having high porosity and permeability, as shown in Table 1. Remarkably, most of the fracture intensity has a high value in conductive zone than the resistive zone, showing that it is a good potential area. This is because basement reservoir really depends on the secondary porosity and permeability (Nelson 2001), and the uplifted basement will always

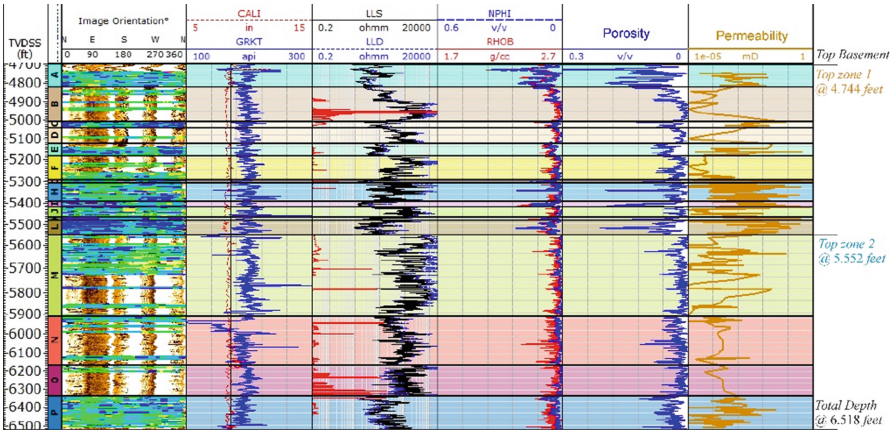

Fig. 4. 16 fracture zones based on porosity, resistivity, and density log. Zone A-L are in Zone 1 on the previous interpretation, whereas Zone M-P are in Zone 2. Porosity and Permeability log were obtained by calculation.

have fracture intensity decreased along with depth. In other words, in this case, possible reservoirs are located on the shallow zones.

It also shows from the analysis that relatively the deeper the well, the less conductive fractures exist. Dip-azimuth of the fractures have the mean magnitude of >50° and major orientation towards Southeast direction. The fracture porosity and permeability consecutively ranges from 0.24% to 18.82% and 1.7×10^{-7} to 2.44 mD.

Several methods have been implemented including Discrete Fracture Network (DFN), and ANN. However, Halo preserving distance-to-fault attribute of the model is excluded because it chiefly depends on how much fault that can be interpreted, and assumes that the porosity remains unchanged along fault planes.

Modeling result merely driven by image logs seems to be too optimistic. Thus, DFN is embedded to create connectivity between fracture and fault system based on image logs and interpreted faults. However, DFN has the same drawback since it cannot afford heterogeneity.

In order to promote the role of seismic attributes in porosity model building process, ANN has been applied. This method is able to combine 3D seismic and well data to produce a porosity model which reflects the vertical and horizontal porosity variation trends. Based on GRFS modeling, on conductive depth, intensity zones are accumulated highly along NNW-SSE major fault and NEB Base-1. On the contrary, NEB Base-2 shows a very low value. The porosity model also presents the same condition as intensity model.

Based on porosity model, depth structure, and intensity model, the possible reservoir areas are overlaid on each other and concluded on one spot as shown on Fig. 5. For porosity and intensity model, the yellow to orange spot were picked. For depth model, potential area is located on crest zone along near NEB Base-1.

Table 1. Zones of fracture

Zone	(SSTVD, ft)	Fracture Numbers	Thickness (ft)	Fracture Intensity	Conductivity	Average Aperture of Conductive Fracture (mm)	Strike (N…E)	Dip (degree)	Azi muth (N…E)
A	4,695.2–4,821.6	30	126.4	0.24	Conductive	5.71	8	62	98
B	4,821.6–5,006.4	37	184.8	0.2	Resistive	1.28	0	67	90
C	5,006.4–5,041.4	11	35	0.31	Conductive	11.42	42	65	132
D	5,041.4–5,122.4	33	81	0.41	Resistive	0.61	15	68	105
E	5,122.4–5,183.3	20	60.9	0.33	Conductive	9.07	355	63	85
F	5,183.3–5,290.7	73	107.4	0.68	Resistive	1.87	79	66	349
G	5,290.7–5,305.3	13	14.6	0.89	Conductive	26.03	342	71	252
H	5,305.3–5,390.2	61	84.9	0.72	Conductive	9.64	20	72	110
I	5,390.2–5,414.8	12	24.6	0.49	Conductive	11.58	29	64	119
J	5,414.8–5,463.0	35	48.2	0.73	Conductive	9.78	22	69	112
K	5,463.0–5,478.5	14	15.5	0.9	Conductive	17.32	0	69	90
L	5,478.5–5,549.1	54	70.6	0.76	Conductive	13.05	43	61	133
M	5,549.1–5,907.8	132	358.7	0.37	Conductive	4.31	348	64	258
N	5,907.8–6,163.5	114	255.7	0.45	Resistive	3.36	12	61	102
O	6,163.5–6,343.4	68	179.9	0.38	Resistive	1.73	16	65	106
P	6,343.4–6,518.2	132	174.8	0.76	Conductive	4.46	3	64	93

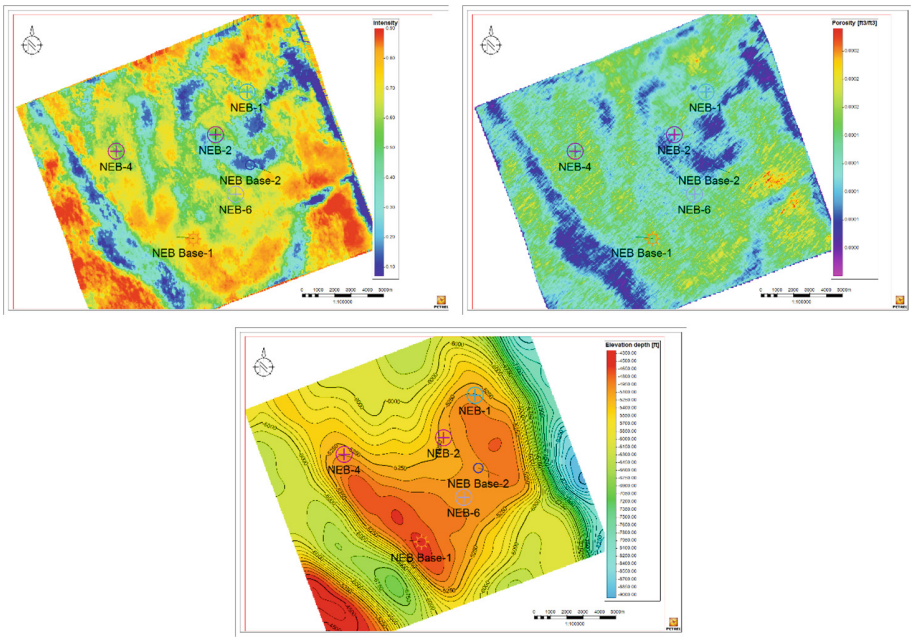

Fig. 5. Intensity model (top left), porosity model (top right), and depth structure map (bottom). Note that the potential zone is on top of depth structure map (white zone).

Deviation for proposed well is also analyzed, it should be optimized that it comes close to perpendicular to the dominant fractures at the area in order to obtain greater permeability.

3 Conclusions

Fracture in Jabung Block grew strongly in the top of the basement, and the amount plunge to the deeper depth. In other words, the deeper the well, the less fracture growth exists.

From the image logs, it shows that the deeper the well, the less conductive fractures exist.

The fractures dip-azimuth have the mean magnitude of > 50° with the orientation of Southeast.

The fracture porosity ranges from 0.24% to 18.82% and the permeability ranges from 1.7×10^{-7} to 2.44 mD.

ANN is able to represent the condition of dry well using representation of fracture very well. Thus, the potential are is located near NEB Base-1 and along the NNW-SSE major fault.

References

Ginger, D., Fielding, K.: The petroleum systems and future potential of the South Sumatra Basin. In: Proceedings of the 30th Annual Convention on Indonesian Petroleum Association (IPA), Jakarta (2005)

Juanda, A.: Integrated Seismic Attributes Analysis for Fractured Basement Reservoir Identification in The South Sumatra Basin, Indonesia. M.Sc. Thesis, Institut Teknologi Bandung (2010)

Luthi, S.M., Souhaite, P.: Fracture apertures from electrical borehole scans. Geophys. J. **55**(7), 821–833 (1990)

Nelson, R.A.: Geologic Analysis of Naturally Fractured Reservoirs, 2nd edn. Gulf Professional Publishing, Woburn (2001)

Poupon, A., Clavier, C., Dumanoir, J., Gaymard, R., Misk, A.: Log analysis of sand-shale sequences: a systematic approach. J. Pet. Technol. **22**(07), 867–881 (1970)

Roberts, A.: Curvature attributes and their application to 3D interpreted horizons. First Break **19**(2), 85–100 (2001)

Risyad, M., Suta, I.N., Haris, A.: Fault assessment for basement reservoir compartmentalization: case study at Northeast Betara gas field, South Sumatra Basin. In: AIP Conference Proceedings, vol. 1862, no. 1, p. 030186. AIP Publishing (2017)

Saifuddin, F., Soeryowibowo, M., Suta, I.N., Chandra, B.: Acoustic impedance as a tool to identify reservoir targets: a case study of the Betara-11 horizontal well, Jabung Block, South Sumatra. In: Proceedings of the 28th Annual Convention on Indonesian Petroleum Association (IPA), Jakarta (2001)

Tiab, D., Donaldson, E.C.: Petrophysics: Theory and Practice of Measuring Reservoir Rock and Fluid Transport Properties, 3rd edn. Gulf Professional Publishing, Woburn (2012)

Autonomous Decision-Making Against Induced Seismicity in Deep Fluid Injections

Arnaud Mignan[1,2,3(✉)], Marco Broccardo[2], Stefan Wiemer[3], and Domenico Giardini[1]

[1] Swiss Federal Institute of Technology, Zurich, Switzerland
arnaud.mignan@sed.ethz.ch
[2] Swiss Competence Center for Energy Research – Supply of Electricity, Zurich, Switzerland
[3] Swiss Seismological Service, Zurich, Switzerland

Abstract. The rise in the frequency of anthropogenic earthquakes due to deep fluid injections is posing serious economic, societal, and legal challenges to geo-energy and waste-disposal projects. We propose an actuarial approach to mitigate this risk, first by defining an autonomous decision-making process based on an adaptive traffic light system (ATLS) to stop risky injections, and second by quantifying a "cost of public safety" based on the probability of an injection-well being abandoned. The ATLS underlying statistical model is first confirmed to be representative of injection-induced seismicity, with examples taken from past reservoir stimulation experiments (mostly from Enhanced Geothermal Systems, EGS). Then the decision strategy is formalized: Being integrable, the model yields a closed-form ATLS solution that maps a risk-based safety standard or norm to an earthquake magnitude not to exceed during stimulation. Finally, the EGS levelized cost of electricity (LCOE) is reformulated in terms of null expectation, with the cost of abandoned injection-well implemented. We find that the price increase to mitigate the increased seismic risk in populated areas can counterbalance the heat credit. However this "public safety cost" disappears if buildings are based on earthquake-resistant designs or if a more relaxed risk safety standard or norm is chosen.

1 Introduction

Increasing energy needs mean increased interactions with the underground, such as fracking activities, gas extraction, waste disposal (wastewater from fracking, CO_2 storage), and Enhanced Geothermal Systems (EGS), all potentially inducing earthquakes (e.g., Giardini 2009; Ellsworth 2013; van Thienen-Visser and Breunese 2015; Mignan et al. 2015; White and Foxall 2016). Phasing out of nuclear energy and/or decreasing the dependence on fossil fuels also infer the increased use of alternative technologies such as EGS, or for instance CO_2 sequestration to cancel fossil fuel emissions. However, with increasing anthropogenic activity, larger earthquakes, damaging ones, have now become a real concern (Ellsworth 2013; van Thienen-Visser and Breunese 2015).

A. Ferrari and L. Laloui (Eds.): SEG 2018, SSGG, pp. 369–376, 2019.
https://doi.org/10.1007/978-3-319-99670-7_46

Solutions exist to limit induced seismicity, so-called traffic light systems (TLS; e.g., Bommer et al. 2006). TLSs are based on a decision variable (earthquake magnitude, peak ground velocity, *etc.*) and a threshold above which actions must be taken (e.g., stopping the injection or reducing injection rates). The definition of this threshold is so far based on expert judgment and regulations (Bosman et al. 2016). Instead, Mignan et al. (2017) proposed an actuarial approach to induced seismicity mitigation where the ATLS (for Adaptive TLS) is defined for a specific risk-based safety standard or norm. We will describe this new approach below, testing its underlying statistical model on additional EGS data. The decision-making procedure being autonomous and based on normative rules (i.e., safety standards), we can foresee a next application, which is the updating of the EGS levelized cost of electricity (LCOE) taking into account the "public safety cost", i.e., the potential cost of injection-wells being abandoned because of the ATLS. All of these steps provide the vision of an autonomous induced seismicity risk governance scheme for the geo-energy sector (Fig. 1).

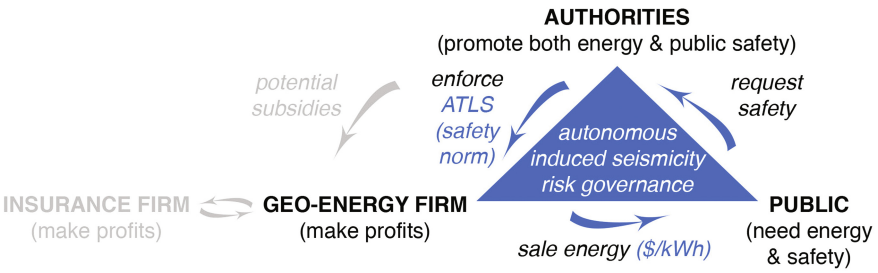

Fig. 1. Induced seismicity risk governance scheme for the geo-energy sector, comprising three actors: Public, authorities, and geo-energy firm. The full process runs autonomously via an ATLS and energy price updating, in blue (not considered here, in grey: potential government subsidies and insurances).

2 Adaptive Traffic Light System (ATLS)

2.1 Induced Seismicity Statistical Model

Mignan et al. (2017) presented an ATLS that evaluates the earthquake magnitude threshold m_{th} not to exceed to conform with a specific risk-based safety standard or norm. This threshold can be updated in real time (Broccardo et al. 2017), based on the temporal forecasting of the induced seismicity rate $\lambda(t)$, function of the known injection flow profile $\dot{V}(t)$:

$$\lambda(t, \geq m) = \begin{cases} 10^{a_{fb}-b_{fb}m}\dot{V}(t); & t \leq t_{shut-in} \\ 10^{a_{fb}-b_{fb}m}\dot{V}(t_{shut-in})\exp\left(-\frac{t-t_{shut-in}}{\tau}\right); & t > t_{shut-in} \end{cases} \quad (1)$$

The injection phase is described by a linear relationship between seismicity rate and flow rate in line with previous publications (Dinske and Shapiro 2013; Mignan 2016a; van der Elst et al. 2016) while the post-injection phase, after time $t_{shut-in}$, is described

by a normal diffusion process (Mignan 2015, 2016b; Mignan et al. 2017; Broccardo et al. 2017). Equation (1) has been validated for a number of fluid injections by Mignan et al. (2017): 1994 KTB, Germany (KTB94); 1994 Paradox Valley, USA (PV94); 2006 Basel, Switzerland (B06); 2011 Garvin, USA (G11); 2012 and 2014 Newberry, USA (Nb12, Nb14). In the present study, we further test Eq. (1) on 2003 Cooper Basin, Australia (CB03; Baisch et al. 2006). Results are shown in Fig. 2 (for further statistical tests, see Broccardo et al. 2017).

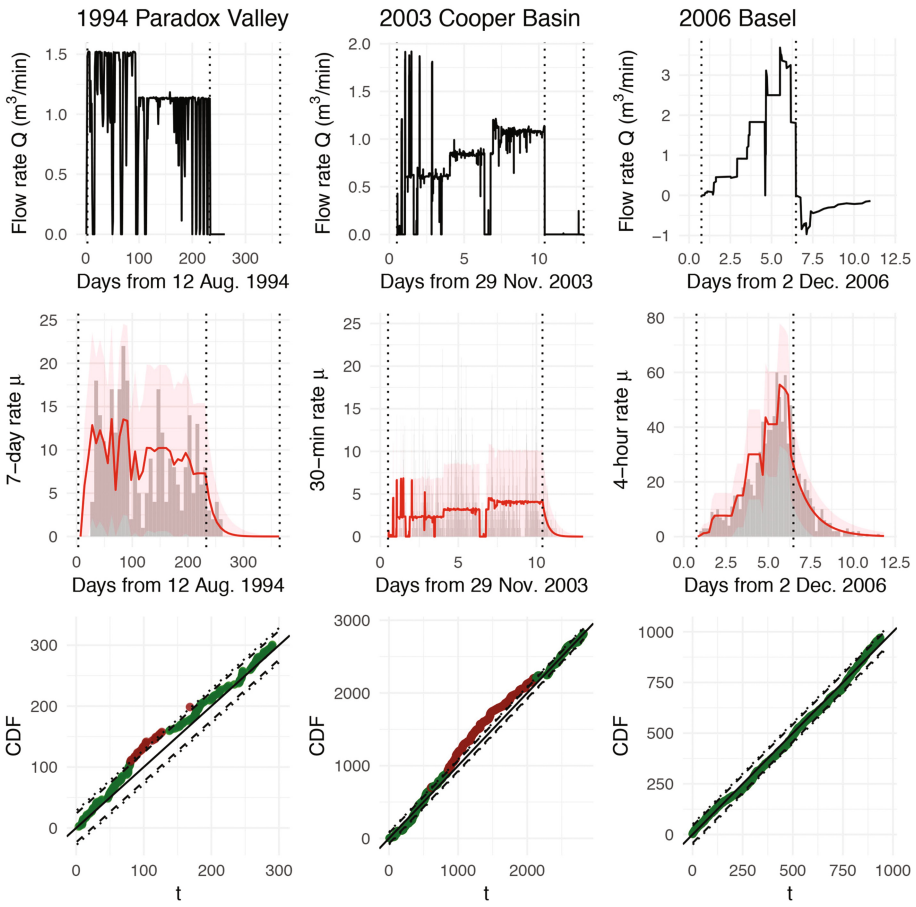

Fig. 2. ATLS statistical model (red curve in central row). Paradox Valley and Basel results reproduced from Mignan et al. (2017); new results for 2003 Cooper Basin dataset shown with maximum likelihood estimates $a_{fb} = -0.6$, $b_{fb} = 0.97$ and $\tau = 0.32$ days. Some local variability in the data cannot be explained by Eq. (1) for constant parameter values (red dots outside the Kolmogorov-Smirnov confidence bounds on third row; see Mignan et al. (2017) for details).

It should be mentioned here that the activation feedback parameter a_{fb} is analogue to the seismogenic index Σ of Dinske and Shapiro (2013). Using a_{fb} is preferrable to remain agnostic as to whether induced seismicity is due to poro-elasticity (Σ; Dinske and Shapiro 2013), static overpressure (Mignan 2016a), or any other physical process. Although a_{fb} provides the average activation feedback per stimulation, a Kolmogorov-Smirnov test shows that Eq. (1) may fail locally (Fig. 2). This can be due to missing on-site information, pressure changes not linearly correlated to the injection flow rate or other second-order processes not yet considered in the model. More complex models could be implemented in the ATLS presented below, if necessary. Broccardo et al. (2017) also showed that the parameters of Eq. (1) can be updated on-line using a hierarchical Bayesian framework during stimulation (note that the framework applies also to the production phase, although the highest seismicity risk occurs during stimulation).

2.2 Mapping Between Risk-Based Safety Norm and Magnitude Threshold

Integrating Eq. (1) yields

$$\Lambda\left(\geq m_{saf}\right) = 10^{a_{fb}-b_{fb}m_{saf}}\left[V(t_{shut-in}) + \tau\dot{V}(t_{shut-in})\right] \approx Y\left(\geq m_{saf}\right) \tag{2}$$

with Y the safety standard or norm in the magnitude space, i.e. the probability of exceeding a given (relatively large) magnitude m_{saf}. To avoid exceeding Y, one must stop the injection when the following magnitude threshold is reached:

$$m_{th} = \frac{1}{b_{fb}}\log_{10}\left[Y - 10^{a_{fb}-b_{fb}m_{saf}}\tau\dot{V}(t_{shut-in})\right] + m_{saf} \tag{3}$$

based on the condition $10^{a_{fb}-b_{fb}m_{th}}V(t_{shut-in}) = 1$, true if the injection is stopped as soon as m_{th} is observed (Mignan et al. 2017).

Safety standards and norms defined for diverse hazardous environments (Jonkman et al. 2003) are often defined in terms of individual risk IR (i.e., the probability that a statistically representative individual dies). Such standards or norms could also be applied to geo-energy sites. For any given IR threshold fixed by the authorities, this value can be mapped to the magnitude space in terms of probability Y of exceeding m_{saf}. Those parameters then depend on the risk parameters in the region of interest (mainly the seismic spatial attenuation and building type). Figure 3 reproduces the ATLS example of Mignan et al. (2017) where $Y\left(m_{saf} \geq 5.8\right) = 10^{-5}$ for $IR \leq 10^{-6}$ (Basel injection profile simulated with EMS-98 class A building at distance d = 0 km above z = 4 km borehole, and with seismic intensity attenuation relationship derived from USGS "*Did You Feel It?*" (Atkinson and Wald 2007) corrected at the time for induced seismicity; see macroseismic risk method application to induced seismicity in Mignan et al. 2015). If the injection is stopped at m_{th}, the safety standard or norm is

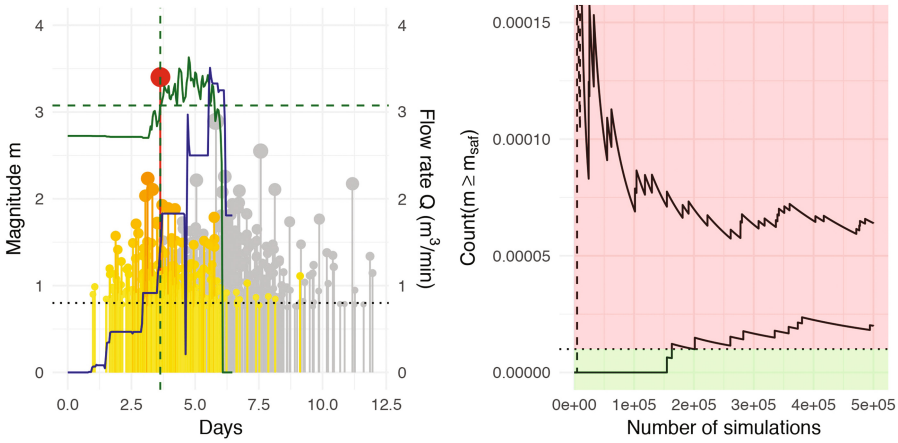

Fig. 3. ATLS in action. Left: Time series without ATLS (in grey) compared to a time series where the stimulation is stopped by the ATLS (m_{th} in green); Right: Verification that the safety standard or norm is respected in average when the ATLS is used (bottom curve), in contrast to no ATLS (top curve) - Recomputed from Mignan et al. (2017).

respected in average over many simulations. m_{th} evolves over time since it depends on other time-varying parameters such as the b_{fb} value, the ratio between small and large earthquakes, which may dramatically change during fluid injections (as was the case for the 2006 Basel experiment).

The proposed ATLS is autonomous in the sense that once a safety standard or norm is selected by the authorities, the decision-making (based on Eq. 3) is done without any human intervention. All parameters and risk estimates can be estimated on-the-fly in a hierarchical Bayesian framework (Broccardo et al. 2017) and the decision (m_{th}) recomputed accordingly. The approach is statistically robust and transparent, which is an advantage over the standard clinical approach (e.g., Dawes et al. 1989).

3 LCOE Updating in ATLS Context

3.1 New LCOE Formulation for Different Risk Behaviours

If the ATLS were to be used systematically for a safety standard or norm selected by the authorities, one could in principle estimate the added cost of increased public safety. This is of importance in energy governance, as a trade-off must be found between public seismic safety and energy safety (produced by deep geo-energy). This can be quantified by including the "cost of public safety" in the LCOE, which corresponds to the added cost of wells abandoned due to ATLS injection termination (as represented in Fig. 3). We will assume that once a stimulation is stopped, the well will

not be used again for the foreseeing future, hence requiring the use of another well. We formulate the LCOE, or price - $P = C/E$ [CHF/kWh] - as the null expectation of the following Bernoulli trial:

$$(1-\pi)(PE-C)-\pi C_{ATLS}=0=\mathbb{E}[X]=(1-\pi)x_1+\pi x_2 \tag{4}$$

where C are the standard costs [CHF] (installation, operation, and maintenance), E the energy or amount of electricity produced [kWh], and π the probability that a well will be abandoned due to the ATLS with associated costs C_{ATLS} [CHF] (note that $\pi = 0$ leads back to $P = C/E$). $X = \{x_1, x_2\}$ represents the set of possible outcomes with x_1 representing stimulation success and x_2 stimulation failure due to too high seismic risk. Equation (4) is formulated such that the outcome x can be replaced by its utility $u(x)$, hence taking into account the possible risk aversion of the geo-energy firm to having a well abandoned with high *a priori* uncertainty (e.g., based on Cumulative Prospect Theory (CPT); Tversky and Kahneman 1992). For any non-zero π, the LCOE (price P) increases.

3.2 Illustrative Example

Let us now estimate the probability π of a well being abandoned and calculate the change in price P from Eq. (4). We consider the following scenario: volume $V = 40{,}000$ m^3 injected during planned stimulation, a maximum possible magnitude $M_{max} = 7$, and two possible safety standards or norms $IR \leq 10^{-6}$ and $IR \leq 10^{-5}$ applied for a building located at a distance d from the borehole (at depth $z = 6$ km). Hazard uncertainty is defined from the underground feedback uncertainty (Table 2 of Mignan et al. (2017), plus our results for Cooper Basin - $\tau = 0$ to simplify Eq. 2) and seismic attenuation uncertainty (from Atkinson and Wald (2007) for the U.S.). Risk is then computed using the macroseismic risk approach (Lagomarsino and Giovinazzi 2006), as applied to the induced seismicity context by Mignan et al. (2015) (incl. fatalities in Mignan et al. 2017), for two types of buildings (EMS-98 class C – reinforced concrete without earthquake-resistant design, and class D – with earthquake-resistant design). Some fatality curves are shown in Fig. 4 (left) with π the ratio of curves failing to pass a safety standard or norm (cases for which the ATLS would stop the injection before V is reached). As the seismic risk decreases with distance d, so does the price increase, as illustrated in Fig. 4 (right) (with $P_{base} = 0.35$ CHF/kWh and $E = 1.38\ 10^9$ kWh from an annual net generation of 46 GWh and a project duration of 30 years, yielding $C = 483$ million CHF, and $C_{ATLS} = C_{well} + C_{fracturing} = 20.9 + 1 = 21.9$ million CHF; taken from CH-base case of Hirschberg et al. 2015).

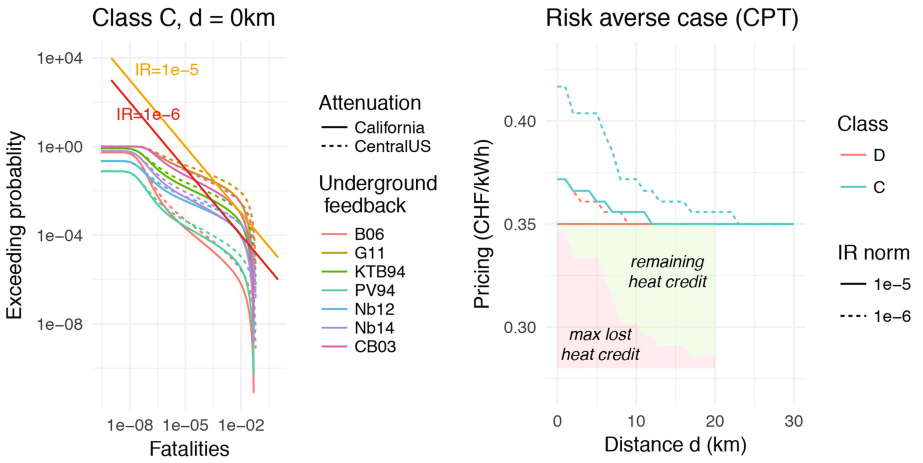

Fig. 4. Change in price P (i.e. LCOE) due to an injection-well being abandoned with probability π (right) computed from the ratio of fatality curves failing to pass a safety threshold (left). The price increase might counterbalance the heat credit (here 0.07 CHF/kWh; Hirschberg et al. 2015). The LCOE is further increased by risk aversion, not knowing in advance the underground feedback conditions to which the ATLS would apply. Values are illustrative only.

4 Conclusions

The proposed method provides the basis for an autonomous induced seismicity risk governance framework in the geo-energy sector (Fig. 1). The public requires safety from seismicity, which the authorities quantify as a risk threshold not to exceed (safety standard or norm). This can be enforced by making the geo-energy firm use the ATLS, which quantifies when a stimulation must be stopped (Eq. 3). For increased public safety comes more financial risk. This can be quantified by updating the EGS LCOE for injection-well loss (Eq. 4). The proposed actuarial/algorithmic approach could be considered in smart electricity markets (e.g., Peters et al. 2013) and in insurance smart contracts (e.g., Buterin 2013) for induced seismicity risk.

References

Atkinson, G.M., Wald, D.J.: "Did you feel it?" Intensity data: a surprisingly good measure of earthquake ground motion. Seismol. Res. Lett. **78**, 362–368 (2007)

Baisch, S., Weidler, R., Vörös, R., Wyborn, D., de Graaf, L.: Induced seismicity during the stimulation of a geothermal HFR reservoir in the Cooper Basin, Australia. Bull. Seismol. Soc. Am. **96**, 2242–2256 (2006). https://doi.org/10.1785/0120050255

Bommer, J.J., et al.: Control of hazard due to seismicity induced by a hot fractured rock geothermal project. Eng. Geol. **83**, 287–306 (2006)

Bosman, K., Baig, A., Viegas, G., Urbancic, T.: Towards an improved understanding of induced seismicity associated with hydraulic fracturing. First Break **34**, 61–66 (2016)

Broccardo, M., Mignan, A., Wiemer, S., Stojadinovic, B., Giardini, D.: Hierarchical Bayesian modelling of fluid-induced seismicity. Geophys. Res. Lett. **44**, 11357–11367 (2017). https://doi.org/10.1002/2017gl075251

Buterin, V.: Ethereum White Paper, a next generation smart contract & decentralized application platform (2013). https://github.com/ethereum/wiki/wiki/White-Paper

Dawes, R.M., Faust, D., Meehl, P.E.: Clinical versus actuarial judgment. Science **243**, 1668–1674 (1989)

Dinske, C., Shapiro, S.A.: Seismotectonic state of reservoirs inferred from magnitude distributions of fluid-induced seismicity. J. Seismol. **17**, 13–25 (2013). https://doi.org/10.1007/s10950-012-9292-9

Ellsworth, W.L.: Injection-induced earthquakes. Science (2013). https://doi.org/10.1126/science.1225942

Giardini, D.: Geothermal quake risks must be faced. Nature **462**, 848–849 (2009)

Hirschberg, S., Wiemer, S., Burgherr, P.: Energy from the earth, deep geothermal as a resource for the future? TA Swiss (2015). https://doi.org/10.3218/3655-8

Jonkman, S.N., van Gelder, P.H.A.J.M., Vrijling, J.K.: An overview of quantitative risk measures for loss of life and economic damage. J. Hazardous Mater. **A99**, 1–30 (2003)

Lagomarsino, S., Giovinazzi, S.: Macroseismic and mechanical models for the vulnerability and damage assessment of current buildings. Bull. Earthq. Eng. **4**, 415–443 (2006)

Mignan, A.: Modeling aftershocks as a stretched exponential relaxation. Geophys. Res. Lett. **42**, 9726–9732 (2015). https://doi.org/10.1002/2015GL066232

Mignan, A., Landtwing, D., Kästli, P., Mena, B., Wiemer, S.: Induced seismicity risk analysis of the 2006 Basel, Switzerland, Enhanced Geothermal System project: influence of uncertainties on risk mitigation. Geothermics **53**, 133–146 (2015). https://doi.org/10.1016/j.geothermics.2014.05.007

Mignan, A.: Static behaviour of induced seismicity. Nonlinear Process. Geophys. **23**, 107–113 (2016a). https://doi.org/10.5194/npg-23-107-2016

Mignan, A.: Revisiting the 1894 Omori aftershock dataset with the stretched exponential function. Seismol. Res. Lett. (2016b). https://doi.org/10.1785/0220150230

Mignan, A., Broccardo, M., Wiemer, S., Giardini, D.: Induced seismicity closed-form traffic light system for actuarial decision-making during deep fluid injections. Sci. Rep. **7**, 13607 (2017). https://doi.org/10.1038/s41598-017-13585-9

Peters, M., Ketter, W., Saar-Tsechansky, M., Collins, J.: A reinforced learning approach to autonomous decision-making in smart electricity markets. Mach. Learn. **92**, 5–39 (2013)

Tversky, A., Kahneman, D.: Advances in prospect theory: cumulative representation of uncertainty. J. Risk Uncertain. **5**, 297–323 (1992)

van der Elst, N.J., Page, M.T., Weiser, D.A., Goebel, T.H.W., Hosseini, S.M.: Induced earthquake magnitudes are as large as (statistically) expected. J. Geophys. Res. Solid Earth **121**, 4575–4590 (2016)

van Thienen-Visser, K., Breunese, J.N.: Induced seismicity of the Groningen gas field: history and recent developments. Lead. Edge **34**, 664–671 (2015)

White, J.A., Foxall, W.: Assessing induced seismicity risk at CO_2 storage projects: recent progress and remaining challenges. Int. J. Greenh. Gas Control **49**, 413–424 (2016)

Simulation on Reservoir-Induced Seismicity Considering Thermo-Hydro-Mechanical Couplings

Yujie Zhu, Xiaoli Liu(✉), Enzhi Wang, and Jianwen Zhong

State Key Laboratory of Hydro-Science and Engineering, Tsinghua University, Beijing, China
Xiaoli.liu@tsinghua.edu.cn

Abstract. Reservoir-induced seismicity (RIS) might happen when impounding over a critical level, changing the water load and seepage field. Statics show that the depth of seismic source increases gradually after thousands of seismicity inside or near the reservoir, implying that water might be a factor to break the initial balance and propagate fractures. The process is a coupling of multiple fields, such as stress field, permeability field and thermodynamic field. This paper presents a 2D Finite Element Model (FEM) to simulate the effect of Thermo-Hydro-Mechanical (THM) coupling on a 2-m pre-existing crack placed at a different inclination. Elastic and damage model are introduced to simulate generation and propagation of crack under the conditions of different temperature at the corresponding depth. A discover is summarised that inclination of fracture could determine length of crack propagation and thermal field definitely has influence in reservoir-induced seismicity, while the deformation of crack depends on thermal expansion and softening of rock. When the inclination of fault is above 45°, either wall will have obvious movement. Therefore, fault will be triggered to active if the angle is above 45°, relative displacement will rise with the increasing temperature.

1 Introduction

Fractures in rock mass is a significant character controlling mechanical behavior. Especially in a reservoir, rock mass beneath is saturated in liquid. Permeability in fractures controls the seepage field in rock mass. At the moment of impoundment of the reservoir, a sudden change in pore pressure will alter the distribution of stress and strain, subsequently causing hydraulic fracturing and break the initial equilibrium of forces and seepage. Generation and propagation of cracks would release the energy inside the geological body. At the mean while, this would activate the existing fault and inducing seismicity. However, fractures will propagate deeper and deeper after impounding. When reaching thousands of meters, mechanic field, seepage field and thermal field would enroll in a sophisticating process.

A synthetical damage composed by hydraulic and thermal effects threats the initial balance and deteriorates rock mass. Rock instability is likely to result from the superposition of hydraulic and thermal effects because the injection of cold water would induce thermal stresses due to rock contraction. Simulation shows that when the

A. Ferrari and L. Laloui (Eds.): SEG 2018, SSGG, pp. 377–383, 2019.
https://doi.org/10.1007/978-3-319-99670-7_47

largest confining stress acts perpendicular to the fractures, thermoelastic effects dominate and could trigger induced seismicity (De Simone et al. 2013). The coupled THM processes in porous geological media has been numerically modeled and validated with laboratory and field experiments (Chen et al. 2009). A simulation in three dimension thermo-hydro-mechanical coupled model of fractured media shows variation in the field of temperature, stress, seepage and fracture aperture during heat variation (Zhao et al. 2015). An accurate review is provided in hydro-mechanical coupling within fractured rock as well as the relevance in the geothermal field (Rutqvist and Stephansson 2003). Overpressure is the main cause of failure during hydraulic stimulation (Parotidis et al. 2004). Especially in geothermal energy production field, seismicity occurred on a subvertical, approximately two-dimensional structure which might reflect a pre-existing fissure of the Rhine-Graven complex (Baisch et al. 2010). Pure shear slips on pre-existing faults are determined as the source mechanism of induced seismicity (Šílený et al. 2014).

The relation of solid deformation, seepage and thermal field is complicated, affecting each other and modifying characteristics until new balance is established. The reservoir-induced seismicity is determined by the reaction between overpressure of fluid and seepage in fractures. However, thermal gradient compromise a huge temperature difference from the depth of 0 m to 2000 m. The damage behavior of hydraulic fracturing might be influenced due to temperature. Many researchers focused on the energy exchange with the movement of fluid in rock mass instead of considering the thermal field. This paper would introduce a simulation of reservoir-induced seismicity considering thermo-hydraulic-mechanic coupling.

2 Method

Coupled T-H-M numerical simulation is performed to investigate the effect of thermo field effect on hydraulic fracturing. A 2-m pre-existing fracture is embedded in one idealized geometry. The inclination of fracture will be changed to figure out the relation between angle of pre-existing fracture and geostress under different temperature. Hypothesis are listed in the following. (1) The host rock around the fracture is homogeneous and linear elastic. (2) Deformations and distribution of stress will be simulated due to cold water injection, ignoring heat conduction between fluid and rock. (3) Fluid in the model is incompressive and the phase does not change since the temperature would not excess 100 °C (372.15 K). Assuming the range of temperature is 20 °C–80 °C (292.15 K–352.15 K), correspondingly the depth is 0 m–2000 m if the ground temperature is 20 °C (292.15 K). (4) Permeability either in porous media or in fracture obeys Darcy's law. (5) Fluid density is constant.

2.1 Damage of Brittle Materials

We adopt elastic-damage model, characterized by a homogeneous matrix embedding nested microstructures of different length scales (Pandolfi et al. 2006; De Bellis et al. 2017). Since during the elastic stage, Hook is a common constitutive law that fits in most conditions. Here we discuss the damage stage for the aperture and propagation of cracks (Fig. 1).

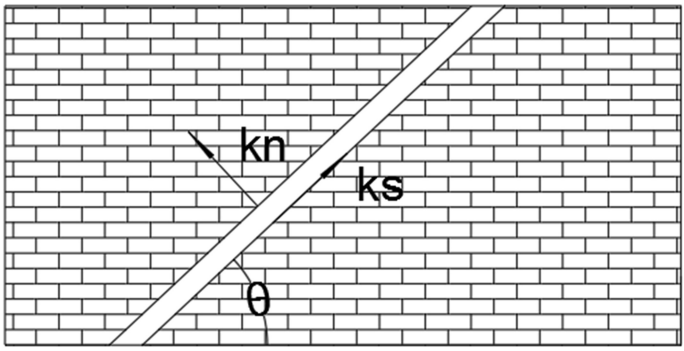

Fig. 1. Schematic of the assumed kinematics of deformation decomposed in normal component and tangential component. kn and ks are the normal stiffness and shear stiffness of the fracture.

Assuming the opening of fault is resisted by cohesive forces during the early stage of damage, immediately following the inception of the fault (Pandolfi et al. 2006). An effective opening displacement of the form is introduced in the following (Ortiz and Pandolfi 1999)

$$\Delta = \sqrt{\left(1-\beta^2\right)(\Delta \cdot N) + \beta^2 |\Delta|^2} \tag{1}$$

Where $|\Delta|$ is the magnitude or norm of Δ and β is a material constant which assigns different weights to the normal and tangential components of the opening displacement (Pandolfi et al. 2006).

2.2 T-H-M Coupling

Stresses are a function of strain, fluid pressure and temperature according to linear theory of poro-thermalelasticity (McTigue 1986).

$$\Delta\sigma = K\varepsilon_v \mathbf{I} + 2G\left(\varepsilon - \frac{\varepsilon_v}{3}\mathbf{I} + \frac{1}{2G}\Delta p_f \mathbf{I} - \frac{3K}{2G}\alpha_T \Delta T \mathbf{I}\right) \tag{2}$$

Where σ is the total stress tensor. K is bulk modulus. G is shear modulus. v is Poisson ratio. ε_v is volumetric strain and $\mathbf{I}$ is identity matrix. p_f is fluid pressure. α_T is the linear thermal expansion coefficient and T is temperature.

Combining the Eq. (2), kinematic equation, mechanical equilibrium equation, continuity equation and constitutive laws, an additional equation governing energy balance can be accounted for thermo-hydro-mechanical coupling (De Simone et al. 2013).

$$\frac{\partial\left(c_s\rho_s(1-\phi)T + c_f\rho\phi T\right)}{\partial t} + \nabla\cdot\left(-\lambda\nabla T + c_f\rho T\mathbf{q} + c_f\rho\phi T\frac{d\mathbf{u}}{dt} + c_s\rho_s(1-\phi)T\frac{d\mathbf{u}}{dt}\right) = f_Q \tag{3}$$

c_s and c_f are the specific heat capacity of the solid and the fluid. ρ_s is solid density. λ is the equivalent thermal conductivity and f_Q is external or internal supply of energy. This equation shows a strong coupling of T-H-M problem (Zimmerman 2000).

3 Simulation

3.1 Establish a Model

To demonstrate the influence of THM coupling on reservoir-induced seismicity, a two-dimensional model is established with a pre-existing crack. The plane of size 50 m × 50 m is taken to eliminate size effect caused by Saint Venant's Principle. Both horizontal direction 'x' and vertical direction 'y' are constrained (Fig. 2). The water head is 100 m, which means the loading is 1 MPa in this model. Pore pressure will be added according to the water pressure. Different inclination of faults is pre-defined to figure out the relation between inclination and induced seismicity. The parameters are listed in Table 1 (Zhao et al. 2015).

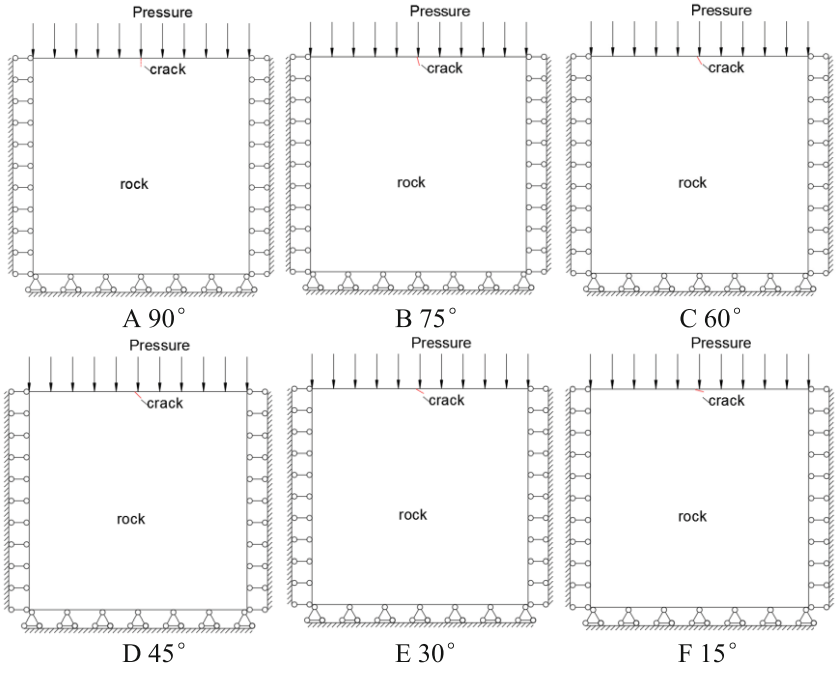

Fig. 2. 2D model to demonstrate the simulation, with pre-existing crack at different and confined plane, mimicking constraints around the test area

Table 1. Properties of the fracture and intact matrix

Parameters	Fracture	Matrix	Units
Young's modulus	2.84×10^{10}	4.84×10^{10}	Pa
Poisson's ratio	0.25	0.15	
Void ratio		0.1	
Permeability		1.0×10^{-7}	ms^{-1}
Viscosity		0.0001	
Thermal expansion coefficient		1.0×10^{-5}	K^{-1}
Thermal conductivity	2.5	1.5	$Wm^{-1}\ K^{-1}$
Specific heat capacity	800	800	$J\ kg^{-1}\ K^{-1}$

To simplify the model, geo-stress is neglected to demonstrate how thermal field act on the stress and strain distribution. That is, with the depth increasing, geostress will not change with it.

Effective stress will reduce on the contrary of rising pore pressure when impounding according to Terzhagi's Principle. Therefore, the existing fault could be triggered at the moment when stress balance is destroyed. The integral homogeneous rock would be damaged and new crack would be produced and propagate.

3.2 Results and Discussions

According to the models and parameters above, simulations have been completed and the results are shown in the following (Fig. 3).

Based on the data above, it can be deduced that inclination of existing fracture determines the length of crack propagation while the opening of crack depend on temperature. When the fracture is perpendicular to ground, the length of crack is not the longest, for the hanging wall is rising up, consuming energy of hydraulic injection. When the inclination of fault is decreasing to 75°, hanging wall will descend below the origin ground, which would release more energy and make the water pressure become higher to destroy the rock. This phenomenon is not all the same until a critical value. Total water head of reservoir is the same when impounding reservoir to a specific height, but energy will be divided into two parts: one part is to connect the original crack to the ground; another part is for hydraulic fracturing. Thus the propagation of crack becomes more difficult as the inclination decreasing. When the pre-existing crack tends to be parallel to the ground, compression on fissures becomes a dominate behaviour. Thus the crack length is defined as minus because the fracture is closed instead of opening. Since the thermal field of this simulation is from 292.15 K to 352.15 K, fluid phase would not change into gas. The rules concluded above will fit in this range of temperature. Besides, relative displacement of hanging wall and foot wall will increase linearly, indicating that induced seismicity would be more likely to produce when the water percolates into the crack.

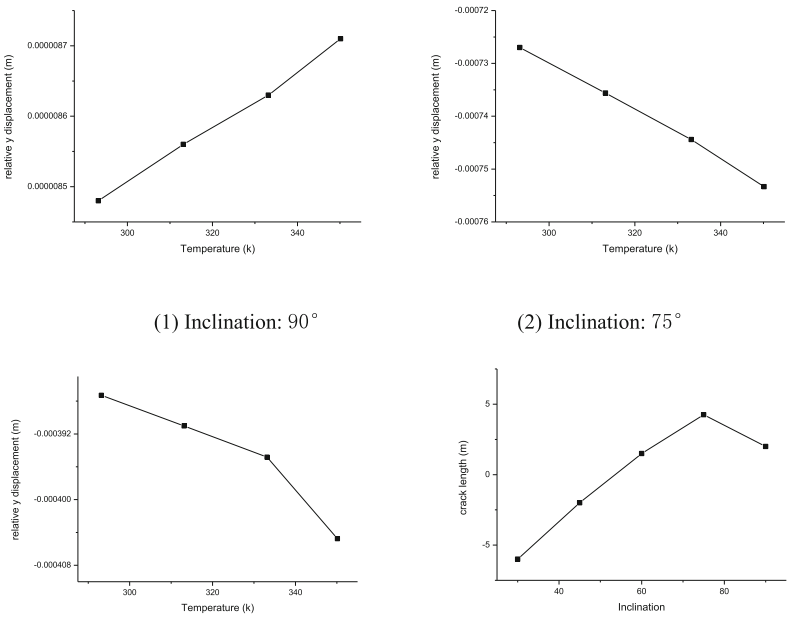

(1) Inclination: 90°

(2) Inclination: 75°

(3) Inclination: 60°

(4) Crack length

Fig. 3. Figures of simulation results

4 Conclusion

Based on T-H-M coupling method and simulations above, we investigate the relation of stress field, temperature field and inclination of single fracture. Firstly, inclination of fracture could determine length of crack propagation. Secondly, thermal field definitely has influence in reservoir-induced seismicity, while the deformation of crack depends on thermal expansion and softening of rock. Though the permeability of matrix is decreasing according to researchers, relative displacements would rise with the temperature increasing. When the inclination of fault is above 45°, neither wall will have obvious movement. Therefore, fault will be triggered to active if the angle is above 45°. It is also observed that relative displacement will rise with an increase in temperature.

References

Rawal, C., Ghassemi, A.: A reactive thermos-poroelastic analysis of water injection into an enhanced geothermal reservoir. Geothermics **50**, 10–23 (2014). https://doi.org/10.1016/j.geothermics.2013.05.007

Chen, Y., Zhou, C., Jing, L.: Modeling coupled THM processes of geological porous media with multiphase flow: theory and validation against laboratory and field scale experiments. Comput. Geotech. **36**, 1308–1329 (2009). https://doi.org/10.1016/j.compgeo.2009.06.001

De Bellis, M.L., Della Vecchia, G., Ortiz, M., Pandolfi, A.: A multiple model of distributed fracture and permeability in solids in all-round compression. J. Mech. Phys. Solids **104**, 12–31 (2017). https://doi.org/10.1016/j.jmps.2017.03.017

Šílený, J., Jechumtálová, Z., Dorbath, C.: Small scale earthquake mechanisms induced by fluid injection at the enhanced geothermal system reservoir Soultz (Alsace) in 2003 using alternative source models. Pure. Appl. Geophys. **171**, 2783–2804 (2014). https://doi.org/10.1007/s00024-013-0750-2

McTigue, D.F.: Thermolelastic response of fluid-saturated porous rock. J. Geophys. Res. **91**, 9533–9542 (1986)

Ortiz, M., Pandolfi, A.: A class of cohesive elements for the simulation of three-dimensional crack propagation. Int. J. Numer. Methods Eng. **44**, 1267–1282 (1999)

Pandolfi, A., Conti, S., Ortiz, M.: A recursive-faulting model of distributed damage in confined brittle materials. J. Mech. Phys. Solids **54**, 1792–2003 (2006). https://doi.org/10.1016/j.jmps.2006.02.003

Parotidis, S., Shapiro, A., Rothert, E.: Back front of seismicity induced after termination of borehole fluid injection. Geophys. Res. Lett. **31**, 1–5 (2004). https://doi.org/10.1029/2003glo18987

Rutqvist, J., Stephansson, O.: The role of hydromechanical coupling in fractured rock engineering. Hydrogeol. J. **11**, 7–40 (2003)

De Simone, S., Vilarrasa, V., Carrera, J., Alcolea, A., Meier, P.: Thermal coupling may control mechanical stability of geothermal reservoirs during cold water injection. Phys. Chem. Earth Parts A/B/C **64**, 117–126 (2013). https://doi.org/10.1016/j.pce.2013.01.001

Baisch, S., Roert Vörö, R., Rothert, E., Stang, H., Jung, R., Schellschmidt, R.: A numerical model for fluid injection induced seismicity at Soultz-sous-Forêts. Int. J. Rock Mech. Min. Sci. **47**, 405–413 (2010). https://doi.org/10.1016/j.ijrmms.2009.10.001

Bao, X., Eaton, D.W.: Fault activation by hydraulic fracturing in western Canada. Science **354**, 1406–1409 (2016). https://doi.org/10.1126/science.aag2583

Zhao, Y., Feng, Z., Feng, Z., Yang, D., Liang, W.: THM (Thermo-hydro-mechanical) coupled mathematical model of fractured media and numerical simulation of a 3D enhanced geothermal system at 573 K and buried depth 6000–7000 M. Energy **82**, 193–205 (2015). https://doi.org/10.1016/j.energy.2015.01.030

Zimmerman, R.W.: Coupling in poroelasticity and thermoelasticity. Int. J. Rock Mech. Min. Sci. **37**(1–2), 79–87 (2000). https://doi.org/10.1016/s1365-1609(99)00094-5

CO_2 Geological Storage and Nuclear Waste Disposal

Advanced Mineral Carbonation: An Approach to Accelerate CO_2 Sequestration Using Steel Production Wastes and Integrated Fluidized Bed Reactor

Abdel-Mohsen Onsy Mohamed, Maisa El-Gamal(✉), and Suhaib Hameedi

Zayed University, Abu Dhabi, United Arab Emirates
Maisa.Elgamal@zu.ac.ae

Abstract. Industrial pollution is the major source of global warming through emissions of greenhouse gases (GHG's) like CO_2, CH_4, and NO_2, causing noticeable increasing in the world's temperature. Mineral carbonation is a method of carbon capture and storage (CCS) through which CO_2 is sequestered with advantage of permanent sequestration and no need for post-storage surveillance and monitoring through stabilizing the reactive mineral wastes released from metal industries. This paper applied a simple and an inexpensive hydration process as a pre-treatment step for the carbonation of Ladle Furnace (LF) slag, one of the steel production by-products in UAE, followed by direct gas-solid carbonation in a new designed integrated fluidized bed reactor (FBR). About (10–15)% by weight of produced steel, alkaline solid residues were generated, based on the characteristics of the manufacturing process. The integrated FBR was designed to control the flow rate up to 50 l/min with step accuracy of 0.1 l/min, and temperature up to 200 °C through a double jacket electrical heater. Operating pressure can be adjusted up to 6 bars. All parameters are monitored by SCADA system. A mixture gas of 10% CO_2, balanced with air, was used to perform the carbonation process and evaluation the carbonation efficiency as well. A gas analyzer installed at the outlet of FBR was used to measure unreacted CO_2 gas after leaving the reactor, and calculate the amount of CO_2 captured accordingly. Results of analytical techniques like TGA and XRD emphasized the sequestration of CO_2 and show a high efficient carbonation process.

1 Introduction

Green house gas (GHG) emissions, the major source of global warming, remain increasing significantly due to accelerated increasing of human activities such power generation and industries. There are different ways to mitigate GHG emissions into atmosphere through reducing the dependence of carbon-source energy. Carbon capture and storage is one noticeable way to minimize emissions of CO_2 gas, the major contributing source of GHG (Benson and Orr 2008; Huijgen and Comans 2005).

A. Ferrari and L. Laloui (Eds.): SEG 2018, SSGG, pp. 387–393, 2019.
https://doi.org/10.1007/978-3-319-99670-7_48

Mineral carbonation has been showing reasonable method of carbon capture and storage through geochemical stability and safe storage of mineral carbonates; avoiding the need to costly gas separation (Lackner et al. 1995; Olajire 2013) This method needs further work to optimize its conditions and then generalized to be applied in industries.

Alkaline waste materials like steel slag can be used for carbonation due to the presence of alkaline oxides, hydroxides or silicates in their composition (Huijgen et al. 2005) The mineral carbonation of steel slag involves the reaction of calcium and magnesium oxides with CO_2 to form stable mineral carbonates. Steel industry is considered as both capital and energy intensive and has high production and long process chains through many different technologies applied. The aim of this paper is to investigate the integration of a carbon capture system, based on the pre-treated LF slag, which is generated as by-product of steel production with usual range of 130–170 kg per ton molten steel, (EmiratesSteel 2018) as raw materials for mineral carbonation. The optimum CO_2 capture by LF slag will be significantly improved based on the design of carbonation reactor and the optimised operating conditions.

2 Experiments

2.1 Raw Materials

LF slag was collected from Emirates Steel in Abu Dhabi, UAE. Samples were taken from open storage piles in a weathering area. The slag was characterized in terms of the alkalinity, elemental composition, and mineralogy. The mineral phases of the slag were detected by XRD. It was found that the diffraction peaks of LF slag are composed of wollastonite ($\beta CaO{\cdot}SiO_2$), anorthite $CaO{\cdot}Al_2O_3{\cdot}2SiO_2$, CaS and αAl_2O_3. The metal composition was determined using ICP-AES, Table 1. The cumulative grain size distributions are ranging from 850–38 μm, Fig. 1. Particles with size range from 300 to 38 μm were used in carbonation.

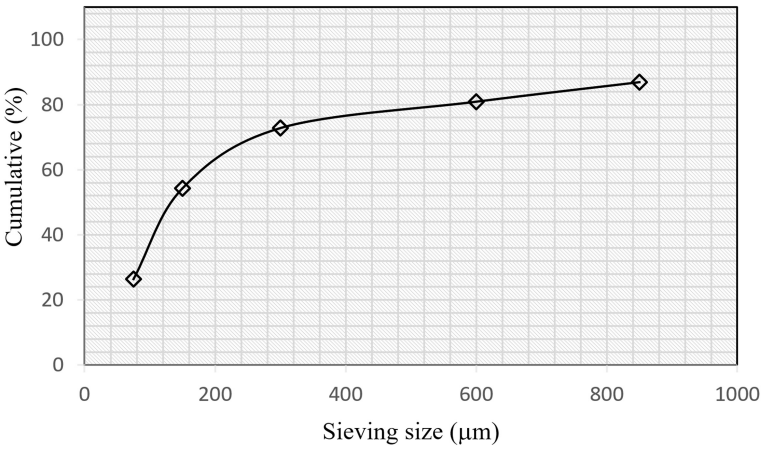

Fig. 1. The cumulative grain size distributions of LF slag

Table 1. Chemical analysis of the LF slag using ICP

Metal oxide	SiO_2	Al_2O_3	FeO	CaO	MgO	MnO
(wt.%)	30.41	10.12	2.34	51.32	4.33	4.36

3 Methods

Two pretreatment steps were performed: hydration by steam (El-Naas et al. 2015), followed by free drying and sieving, before running carbonation of LF slag into the integrated FBR through direct gas-solid carbonation reaction with pressurized CO_2 gas mixture existed in a cylinder with 10% (v/v) CO_2, balanced with air. This Stainless-steel FBR reactor has dimensions of 100 cm height and 8 cm ID was fabricated to achieve direct gas-solid carbonation with pressure up to 6 bar and temperature up to 200 °C by automatic double jacket electrical heater, Fig. 2. Professional controlling program, SCADA, was installed to control and measure the flow rate up to 50 l/min and 0.1 l/min precision. Temperature at three positions along the reactor can be spontaneously measured. Pressure is also measured by the system but controllable manually by valves. The FBR has excellent feature to measure 10 parameters at a time, and so it enables good study of many affecting parameters like flow rate, temperature, pressure and time with wide range levels.

Fig. 2. The new designed fluidized bed reactor (FBR)

The concentration of the outlet CO_2 gas from FBR was measured using a gas analyzer, CAI-NDIR-600 series. Readings are taken manually or automated via professional data acquisition program operated by LabVIEW 14 and designed by Dr. Tom Engl, where time can be set precisely up to a millisecond period scale.

3.1 Optimization of Carbonation in the FBR

The mass uploaded is optimized at 0.5 kg, the particle sizes is ranging between 38 and 300 μm. The flow rate was also fixed at value of 4 l/min, slightly above the minimum fluidization velocity, U_{mf}, which was determined experimentally through plotting pressure drop across the bed versus flow rate.

Three levels of carbonation temperature were tried: 25, 50 and 75 °C, beside three levels of pressure: 1.0, 1.5, and 2.0 bar too.

4 Results and Discussion

4.1 Carbonation Process

Several industrial wastes from metal industries in the UAE have been identified to be recycled as low-cost materials for carbon capture and sequestration. In this study, the LF slag was used as a good source of calcium and magnesium oxides. The measured pH of LF slag solution was 11.15, total dissolved solid (TDS) was 632 ppm and specific gravity was 3300 kg/m^3. The reactions of these oxides with water are spontaneous and exothermic. Free lime and magnesia readily react with water, event at ambient conditions, to form calcium hydroxide (Portlandite) and magnesium hydroxide (Brucite) respectively.

Carbonation of LF slag was performed by the circulation of CO_2 through the solid particles in the new designed FBR. Fluidization occurs when small solid particles are suspended in an upward flowing stream of fluid. The fluid velocity (U_{mf}) is sufficient to suspend the particles, but it is not large enough to carry them out of the vessel. The solid particles swirl around the bed rapidly, creating excellent mixing among them (Fogler 1981). When the superficial gas velocity increases beyond which the bed is fluidized, all particles are suspended by upward flowing gas. The frictional force between particle and fluid counterbalances the weight of the particle (Fogler 1981). Calculation of U_{mf} was measured experimentally by plotting the pressure difference across the bed versus flow rate, which represents the velocity.

4.2 CO_2 Captured by LF Slag

Mineral carbonation is based on the spontaneous and exothermic reaction of CO_2 with metal hydroxides and metal silicates. The reactions are represented in the following equations:

$$Ca(OH)_{2(s)} + CO_{2(g)} \rightarrow CaCO_{3(s)} + H_2O(l)$$

$$4CaO \cdot 3SiO_2 \cdot 1.5H_2O(s) + 4CO_{2(g)} \rightarrow 4CaCO_{3(s)} + 3SiO_{2(s)} + 1.5H_2O(l)$$

The captured CO_2 by LF slag was calculated using gas analyser which is connected to the FBR, by plotting the instantaneous CO_2 concentration difference between inlet constant CO_2 concentration and the outlet ones versus time, as represented in Fig. 3. Area under the curve of the plot represents numerically the amount of CO_2 consumed (captured) during carbonation reaction.

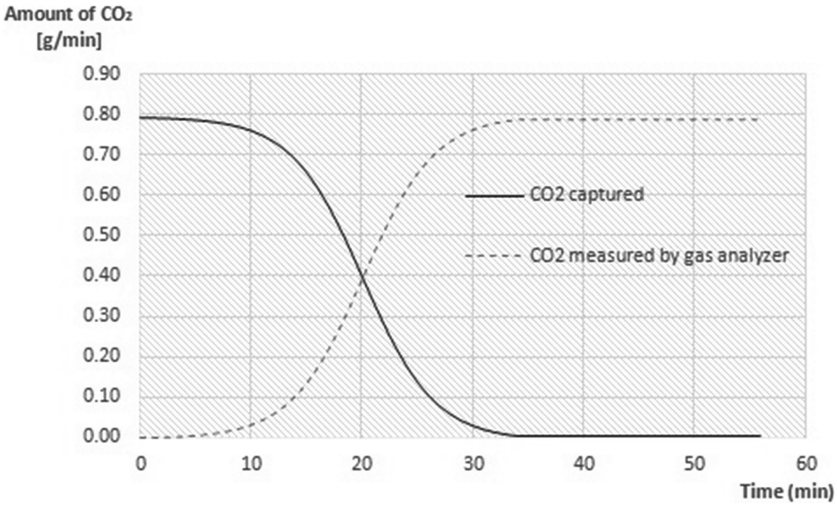

Fig. 3. Trend of CO_2 amount: (a) measured by gas analyser, (b) captured by LF slag

Carbonation reaction under different pressure 1.0, 1.5 and 2.0 bar indicated that, there was slight effect of the pressure on the carbonation yield. The most significant parameter observed was the time needed to reach saturation, where no furthermore amount of CO_2 captured by the slag in the bed. Carbonation reaction under different temperatures; 25, 50 and 75 °C indicated that, the carbonation enhanced in the studied higher temperature.

4.3 Reaction Participants and Products

The differences in the physical and chemical properties of LF slag solution before and after carbonation process is represented in Table 2, which indicates reduction in alkalinity, significant decrease in both electrical conductivity and TDS that can be attributed to the consumption of soluble metal oxides and formation of insoluble carbonates.

The extent of mineral carbonation was determined by thermal gravimetric analysis (TGA) analyses. Figure 4 shows the weight loss before and after the carbonation of LF slag. The decomposition of calcium carbonate indicates the carbonate content of the sample. The percent weight loss of carbonate content before and after carbonation are 0.8 and 6.8%, respectively.

Table 2. Physicochemical properties of LF slag; before and after optimized carbonation

Parameter	Before carbonation	After carbonation
pH	11.6	10.2
Electrical conductivity (μs)	1288	234
TDS (mg/l)	632	112
Loss on ignition (%)	0.8	6.8

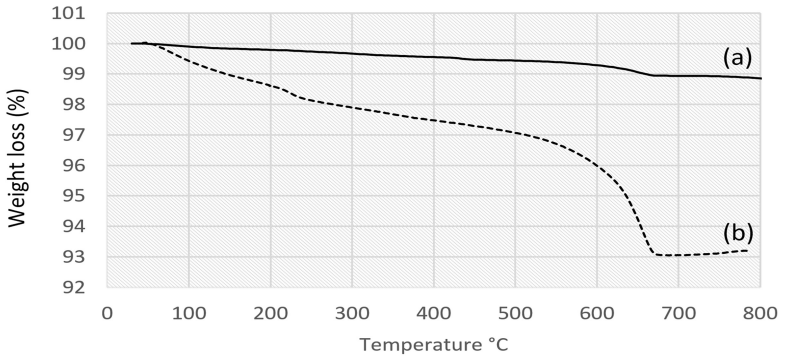

Fig. 4. TG analysis of LF slag (a) before carbonation (b) after carbonation

SEM images characterize the LF slag particles, as shown in Fig. 5. These images disclose that the non-carbonated LF slag enfolds amorphous granules while carbonated LF slag developed compacted aragonite particles with particle size less than 1 μm.

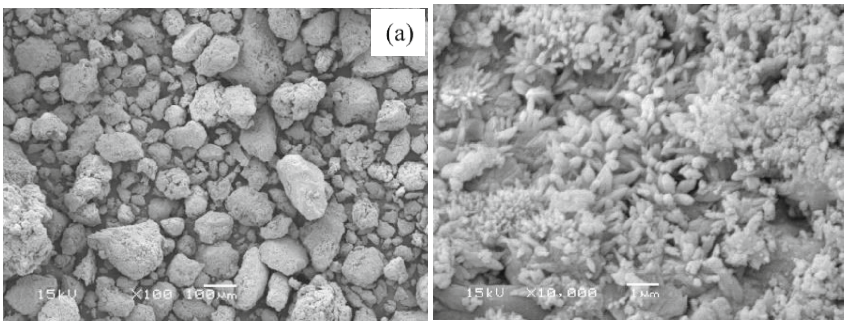

Fig. 5. SEM images of LF slag: (a) before carbonation (b) after carbonation

4.4 Conclusions and Recommendations

From the analytical results, it can be concluded that, the residues of steel-making industries like LF slag are valuable materials for mineral carbonation, where 1 kg of LF slag could capture 0.262 kg of CO_2, based on calcium content. It can also be concluded

that the new designed integrated fluidized bed reactor has many advantages to perform inexpensive mineral carbonation professionally, under different parameters like particle size, flow rate, pressure and temperature. Finally, it is worth to be mentioned that gas analysers have become a powerful tool for calculations of CO_2 captured and then can be employed to monitoring and calculate the carbonation rate.

References

Benson, S.M., Orr, F.M.: Carbon dioxide capture and storage. MRS Bull. **33**(4), 303–305 (2008). https://doi.org/10.1557/mrs2008.63

El-Naas, M.H., El-Gamal, M., Hameedi, S., Mohamed, A.-M.: CO_2 sequestration using accelerated gas-solid carbonation of pre-treated EAF steel-making bag house dust. J. Environ. Manag. **156**, 218–224 (2015). https://doi.org/10.1016/j.jenvman.2015.03.040

EmiratesSteel: Emirates steel website (2018). https://www.emiratessteel.com/index.php/en/who-we-are/about-emirates-steel

Fogler, H.S.: Chemical Reactors, vol. 168. American Chemical Society, Washington (1981)

Huijgen, W.J.J., Comans, R.N.J.: Carbon dioxide sequestration by mineral carbonation Literature Review update 2003–2004, Netherlands (2005)

Huijgen, W., Witkamp, G.-J., Comans, R.: Mineral CO_2 sequestration in alkaline solid residues. Greenh. Gas Control Technol. **7**, 2415–2418 (2005)

Lackner, Klaus S., Christopher, H.W., Darryl, P.B., Edward, L.J., David, H.S.: Carbon dioxide disposal in carbonate minerals. Energy **20**(11), 1153–1170 (1995). https://doi.org/10.1016/0360-5442(95)00071-N

Olajire, A.A.: A review of mineral carbonation technology in sequestration of CO_2. J. Pet. Sci. Eng. **109**, 364–392 (2013). https://doi.org/10.1016/j.petrol.2013.03.013

Deep Fracture Zone Reactivation During CO_2 Storage at In Salah (Algeria) – A Review of Recent Modeling Studies

Antonio P. Rinaldi[1,2(✉)], Jonny Rutqvist[2], and Victor Vilarrasa[2,3,4]

[1] Swiss Seismological Service, Swiss Federal Institute of Technology, ETH, Zurich, Switzerland
antoniopio.rinaldi@sed.ethz.ch
[2] Energy Geoscience Division, Lawrence Berkeley National Laboratory, Berkeley, CA, USA
[3] Institute of Environmental Assessment and Water Research, Spanish National Research Council (IDAEA-CSIC), Barcelona, Spain
[4] Associated Unit: Hydrogeology Group (UPC – CSIC), Barcelona, Spain

Abstract. We present a review of numerical studies aimed at understanding the conditions leading to the reactivation of a deep fracture zone, as well as thermal effects, at the In Salah CO_2 Storage Project. Numerical simulations carried out with the TOUGH-FLAC coupled fluid flow and geomechanics simulator show that a deep fracture opening can explain the observed deformation at the ground surface. Accounting for a fractured reservoir with stress-dependent permeability allows for a better match of the recorded wellhead pressure. Simulation results including thermal effects show that cooling becomes more significant for long-term storage, causing a decrease in fracture stability.

1 Introduction

Despite most modeling studies suggest that a proper pressure management may lead to a safe CO_2 storage, i.e., without inducing earthquakes and without causing CO_2 leakage, demonstration projects are required to turn Geological Carbon Sequestration (GCS) storage into a reality. The In Salah CO_2 Storage Project, Algeria, was an industrial scale GCS demonstration project that permitted to test the geomechanical response of the subsurface to CO_2 injection at relatively high injection pressure (White et al. 2014). About 4 million tons of CO_2 were injected from 2004 to 2011 through three horizontal wells directly into a relatively low-permeable 20 m-thick saline formation, with 900 m-thick caprock preventing the CO_2 to escape (Ringrose et al. 2013). The injected CO_2 reached the storage formation at a temperature around 45 °C colder than the rock.

Being the first on-shore demonstration project, In Salah is well known for the wide-ranging monitoring, which included, among other things, pressure monitoring and satellite InSAR data of ground-surface deformation (Mathieson et al. 2010). This latter showed a ground surface uplift of 5–10 mm per year during the injection phase (Fig. 1a). Such uplift was initially associated to the vertical expansion within the

A. Ferrari and L. Laloui (Eds.): SEG 2018, SSGG, pp. 394–401, 2019.
https://doi.org/10.1007/978-3-319-99670-7_49

reservoir (Vasco et al. 2008; Rutqvist et al. 2010), with a particularly good representation at two of the injection wells (KB-501, KB-503). However, as the injection continued and the InSAR dataset improved, a particular double-lobe uplift was observed nearby the KB-502 injection wells (Fig. 1b). Such a feature has been interpreted as caused by a deep fracture opening, and demonstrated by semi analytical and numerical modeling (Vasco et al. 2010; Rutqvist et al. 2011; Rinaldi and Rutqvist 2013). The presence of this feature at reservoir depth was also confirmed by seismic characterization (Zhang et al. 2015). Furthermore, recent inverse semi-analytical and numerical studies have further demonstrated that the reactivation of a deep fracture zone could have occurred at all the three wells (Rucci et al. 2013; Rinaldi and Rutqvist 2017; Rinaldi et al. 2017).

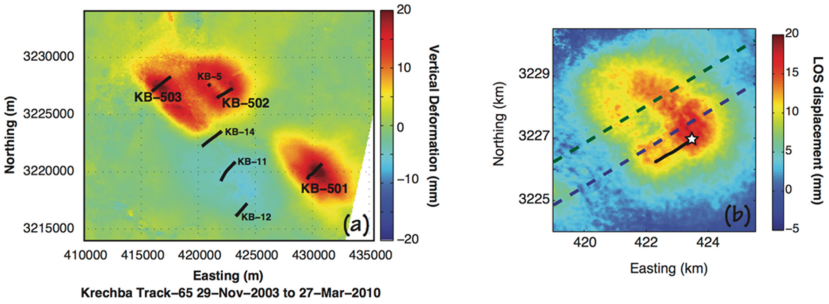

Fig. 1. (a) Observed ground deformation at In Salah in the period 2003–2010. (b) Double-lobe uplift observed at KB-502 injection well. (Figure modified after Rinaldi et al. 2017)

In this paper, we summarize and review the results of numerical modeling aimed at understanding the physical processes leading to the observed ground deformation. The model simulations were conducted using the TOUGH-FLAC simulator (Rutqvist 2011), linking the multiphase fluid flow TOUGH2 (Pruess et al. 2012) and the geomechanical simulator FLAC3D (Itasca 2011).

2 Preliminary Modeling at KB-501 and K-B503

Rutqvist et al. (2010) first attempted to reproduce the observed ground deformation at In Salah by using coupled fluid flow and geomechanics simulation. Their analysis showed that most of the observed uplift magnitude could be related to poro-elastic expansion induced by the CO_2 injection in a thin reservoir (20 m). The model setup accounted for a layered model, including a 900 m-thick caprock, with a variable permeability in the range 10^{-21} to 10^{-19} m^2. Results showed that a constant injection rate over a period of 3 years, with an overpressure in the reservoir in the order of 10 MPa (Fig. 2b), could result in a ground surface uplift of 1.2 cm (Fig. 2a).

Rutqvist et al. (2010) also found that some pressure-induced deformations within a 100-m-thick zone of the lower caprock could play a significant role in the observed ground uplift. Indeed, by setting a lower permeability for the caprock region, the

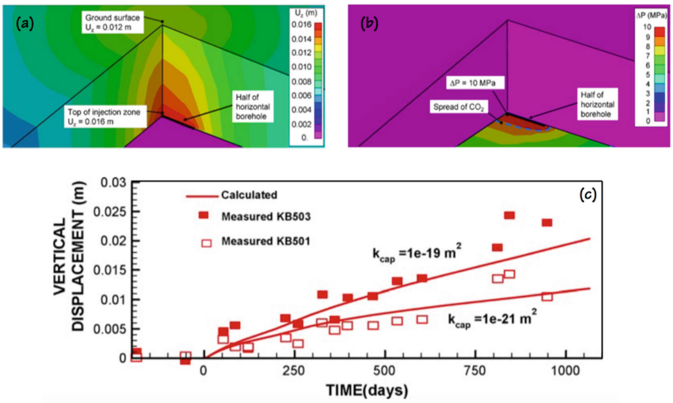

Fig. 2. First coupled geomechanical analysis at In Salah after Rutqvist et al. (2010). (a) Modeled deformation within caprock and at ground surface, and (b) pore pressure changes. (c) Comparison with data at KB501 and KB503 for varying caprock permeability.

deformation is fully explained by the expansion of the reservoir, and satisfactorily reproduces data at KB-501 (Fig. 2c). On the other hand, a high permeability in the caprock allows for a pressurization of the region right above the reservoir, resulting in larger ground uplift as observed at KB-503 injection well (Fig. 2c).

3 Deep Fracture Zone Reactivation at KB-502

Studies by Ringrose et al. (2009) indicated that the pressure distribution at the injection well KB-502 and the occurrence of CO_2 leakage at a monitoring well (KB-5) could have been strongly influenced by pre-existing minor faults and fractures, and, to explain the particular complex observed surface uplift (Fig. 1b), the reactivation of a deep fracture zone in tensile mode was hypothesized (Vasco et al. 2010).

Rutqvist et al. (2011) tried to reproduce a double lobe uplift by using a model grid with a 50 m-wide fracture zone with strongly anisotropic elastic modulus that intersects the injection well and extends about 200 m above the injection zone. Their results showed a maximum uplift of 2 cm after 2 years of injection, with a surface pattern featuring two parallel lobes spaced about 1.5 km (Fig. 3). They also analyzed the simulation results in terms of reservoir stress evolution and the potential for injection-induced micro-seismicity at Krechba. Results highlighted that the combined effect of increased pressure and cooling could rise the potential for induced micro-seismicity, especially close to the cooled injection well, but given the strike-slip stress regime at Krechba such potential was still estimated to be relatively low.

The preliminary results by Rutqvist et al. (2011) were qualitatively in agreement with the observation at KB-502, and motivated a more comprehensive modeling of the deep fracture zone reactivation presented by Rinaldi and Rutqvist (2013). In their study, they simulated a fracture zone with high permeability and low mechanical stiffness. In order to correctly reproduce the transient evolution of displacement and

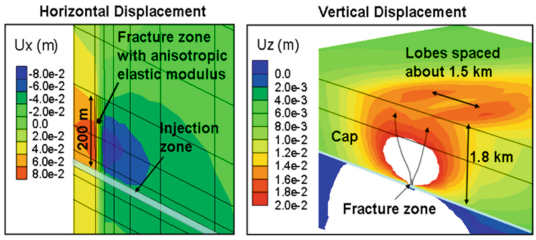

Fig. 3. Preliminary forward coupled numerical modeling of CO_2 injection with pressure inflation of the vertical fracture zone (Figure from Rutqvist et al. 2011)

pressure, the fracture zone was simulated as reactivating after a few months of injection, causing irreversible changes in permeability. The computational model closely followed previous formulations (Fig. 4a), and the fracture zone was simulated as a highly permeable zone, 80 m wide and cross cutting the 1 km–long horizontal injection well (Fig. 4b). The 3500 m length and 350 m extent of the fracture zone within the caprock were determined by model calibration. In order to match the bottomhole pressure (Fig. 4c), the model included a time-step function permeability, in agreement with a stress-dependent formulation (Liu and Rutqvist 2013). This formulation allowed for a detailed representation of both transient evolution of the displacement and pattern of deformation. Figure 5 shows that the resulting displacement calculated in the satellite's Line Of Sight is in good agreement with the measured uplift. The shape of deformation is similar, with two asymmetric lobes (Fig. 5a and b), and a more detailed comparison along two arbitrary profiles shows a very good match between data and simulation, particularly in the double lobe region and with only minor differences in the far field (Fig. 5c and d, red line for the simulation results and green dashed line for the InSAR data). The transient evolution of the uplift was also compared to InSAR data above the injection well (Fig. 5e), with a good agreement between data and simulation during the uplift phase, while differences arise after shut in.

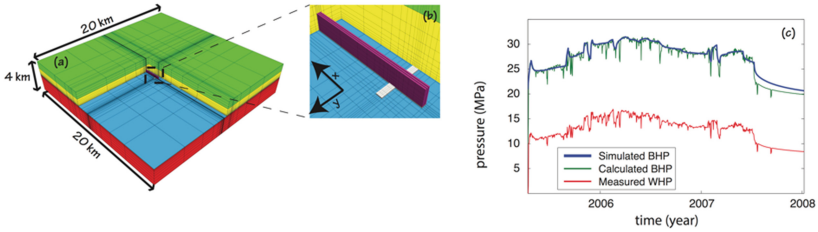

Fig. 4. Detailed modeling of deep fracture zone modeling at KB-502 (figure after Rinaldi and Rutqvist 2013). (a) Computational mesh. (b) Simulated and measured pressures.

Overall the analysis by Rinaldi and Rutqvist (2013) supported the notion of a fracture zone confined within the caprock. A sensitivity analysis confirmed that only a fracture zone confined within the caprock could allow matching of all available field

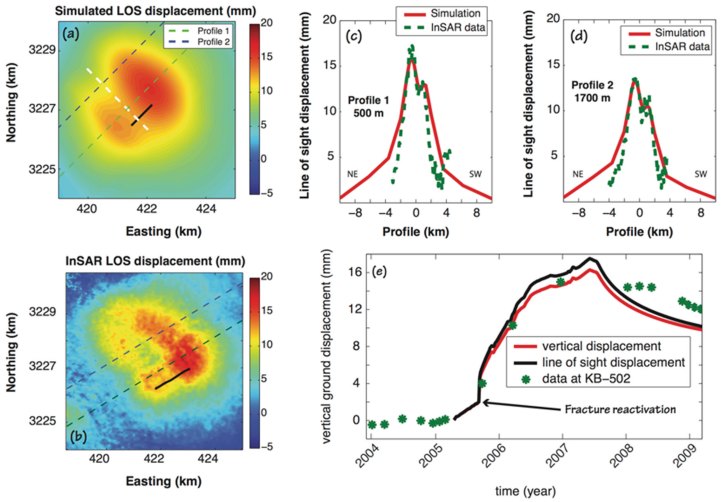

Fig. 5. (a, b) Modeled and InSAR LOS at KB-502 after about 2 years of injection. (c, d) Comparison between data and simulation at two arbitrary profiles located at 500 m and 1700 m from the injection well. (e) Transient evolution of ground surface uplift and comparison with InSAR data. (Figures after Rinaldi and Rutqvist 2013)

information, including time evolution of pressure and deformation, and the 3D seismic indication of a CO_2 saturated fracture zone extending for some thousand meters laterally.

4 Inverse Modeling Approach and Permeability Variation

A recent work by Rinaldi et al. (2017) further improved the formulation of the coupled analysis of pressure and ground deformation by employing an inverse modeling approach with iTOUGH2-PEST and TOUGH-FLAC. The forward model was improved by accounting for a Mohr-Coulomb criterion to determine the time of reactivation of the fracture zone and onset of permeability changes, which followed a more rigorous stress-dependent formulation (Liu and Rutqvist 2013; Rinaldi et al. 2014).

Such an improved formulation allowed to extend the study of deep fracture zone reactivation also at KB-501 and KB-503, as already hypothesized by semi-analytical models (Rucci et al. 2013). On the one hand, the results confirmed the previous formulation for KB-502, by using a more rigorous approach (Fig. 6c and d). On the other hand, results also showed that the opening of a deep fracture zone could explain the observed transient evolution of pressure and displacement at KB-501 (Fig. 6a and b) and KB-503 (Fig. 6e and f), although a similar good fit could be achieved for the case of an intact caprock without fracture zone opening.

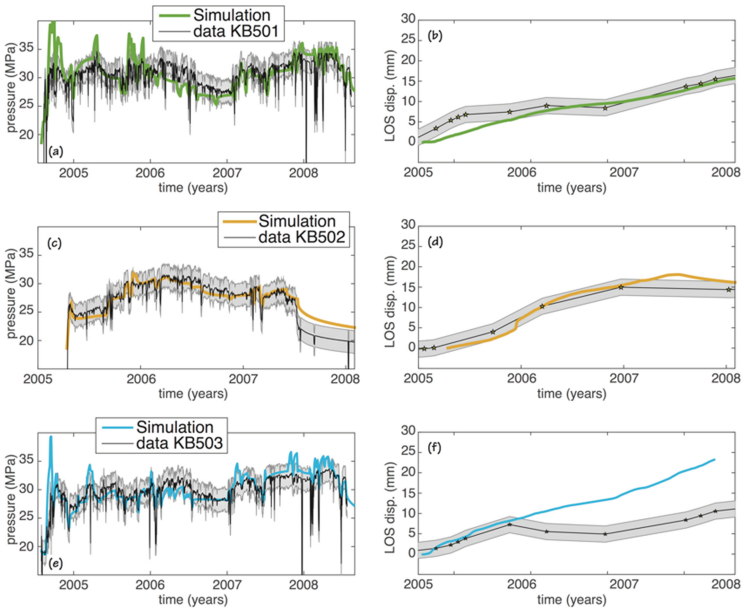

Fig. 6. Inverse modeling of coupled fluid flow and geomechanics with deep fracture zone reactivation at (a, b) KB-501, (c, d) KB-502, and (e, f) KB-503. (Figures modified after Rinaldi et al. 2017 and Rinaldi and Rutqvist 2017)

5 Thermal Effects

Recently, Vilarrasa et al. (2017), evaluated the thermal effects on fracture reactivation at the KB-502 injection well. By using a 2D model, and by employing the inverse modeling formulation (Rinaldi et al. 2017), they were able to reproduce the evolution of the CO_2 plume, including indication of early CO_2 arrival at the location of the leaky well KB-5. The proposed model showed that the temperature changes may have extended within the fracture zone, but their effect in terms of injectivity changes was probably much smaller if compared to the changes induced by pressure. However, they also demonstrated that in a hypothetical scenario with low pressure (e.g., larger reservoir permeability), thermal stress may increase the permeability in fracture zones resulting in pressure drop (Fig. 7a). As also highlighted by Rutqvist et al. (2011) and Vilarrasa et al. (2015), the thermal stress changes (Fig. 7b) may cause a decrease in fracture stability in the long term, which may induce microseismicity. Cooling, which advances much behind the CO_2 plume, causes contraction of the rock matrix, opening up existing fractures, and thus, leading to an increase in injectivity.

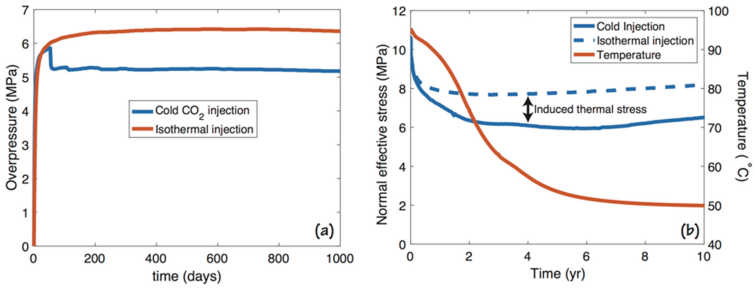

Fig. 7. Long term effect of thermal changes in a scenario similar to In Salah with low pressure injection. (a) Pressure changes highlight changes in injectivity. (b) Induced thermal stress changes that may result in microseismicity (Figures after Vilarrasa et al. 2017).

6 Conclusion

In this paper, we presented recent numerical modeling results obtained with the simulator TOUGH-FLAC to study the coupled CO_2 injection and ground surface uplift at the In Salah storage site. Results were presented from the preliminary works, which attributed most of the deformation to inflation of the injection reservoir, up to very recent results, demonstrating the role of fracture zone reactivation in the framework of CO_2 sequestration as well as thermal effect decreasing fracture stability in the long term. The present review highlights the importance of complex coupled fluid flow and geomechanical modeling to properly assess the physical processes occurring at depth during underground exploitation.

Acknowledgements. This work was supported by the Assistant Secretary for Fossil Energy, Office of Natural Gas and Petroleum Technology, through the National Energy Technology Laboratory, under the U.S. Department of Energy Contract No. DE-AC02-05CH11231. V. Vilarrasa acknowledges financial support from the "TRUST" project (FP7, n. 309607) and from "FracRisk" project (H2020, n. 640979). A.P. Rinaldi is currently funded by Swiss National Science Foundation (SNSF) Ambizione Energy grant (PZENP2_160555). The authors would like to thank the In Salah JIP and their partners BP, Statoil, and Sonatrach for providing field data and technical input over the past 10 years as well as for financial support during LBNL's participation in the In Salah JIP, 2011–2013.

References

Itasca: FLAC3d v5.0, Fast Lagrangian Analysis of Continua in 3 Dimensions, User's Guide (2011)

Liu, H.-H., Rutqvist, J.: Coupled hydro-mechanical processes associated with multiphase flow in a dual-continuum system: formulations and an application. Rock Mech. Rock Eng. **46**, 1103–1112 (2013)

Mathieson, A.S., Midgley, J., Dodds, K., Wright, I.W., Ringrose, P., Saoul, N.: CO_2 sequestration monitoring and verification technologies applied at Krechba, Algeria. Lead. Edge **29**, 216–222 (2010)

Pruess, K., Oldenburg, C., Moridic, G.: TOUGH2 User's Guide Version 2.1, Report LBNL-43134, Lawrence Berkeley National Laboratory, Berkeley, CA, USA (2012)

Rinaldi, A.P., Rutqvist, J.: Modeling of deep fracture zone opening and transient ground surface uplift at KB-502 CO_2 injection well, In Salah, Algeria. Int. J. Greenh. Gas Control **12**, 155–167 (2013)

Rinaldi, A.P., Rutqvist, J.: Modeling ground surface uplift during CO_2 sequestration: the case of in Salah, Algeria. Energy Proc. **114**, 3247–3256 (2017)

Rinaldi, A.P., Rutqvist, J., Finsterle, S., Liu, H.-H.: Forward and inverse modeling of ground surface uplift at In Salah, Algeria. In: 48th U.S. Rock Mechanics/Geomechanics Symposium (2014)

Rinaldi, A.P., Rutqvist, J., Finsterle, S., Liu, H.-H.: Inverse modeling of ground surface uplift and pressure with iTOUGH-PEST and TOUGH-FLAC: the case of CO_2 injection at In Salah, Algeria. Comput. Geosci. **108**, 98–109 (2017)

Ringrose, P.S., Mathieson, A.S., Wright, I.W., Selama, F., Hansen, O., Bissell, R., Saoula, N., Midgley, J.: The In Salah CO_2 storage project: lessons learned and knowledge transfer. Energy Proc. **37**, 6226–6236 (2013)

Ringrose, P., Atbi, M., Mason, D., Espinassous, M., Myhrer, Ø., Iding, M., Mathieson, A., Wright, I.: Plume development around well KB-502 at the In Salah CO_2 storage site. First Break **27**, 85–89 (2009)

Rucci, A., Vasco, D.W., Novali, F.: Monitoring the geologic storage of carbon dioxide using multicomponent SAR interferometry. Geophys. J. Int. **193**, 197–208 (2013)

Rutqvist, J.: Status of the TOUGH-FLAC simulator and recent applications related to coupled fluid flow and crustal deformations. Comput. Geosci. **37**, 739–750 (2011)

Rutqvist, J., Liu, H., Vasco, D.W., Pan, L., Kappler, K., Majer, E.: Coupled non-isothermal, multiphase fluid flow, and geomechanical modeling of ground surface deformations and potential for induced micro-seismicity at the In Salah CO_2 storage operation. Energy Proc. **4**, 3542–3549 (2011)

Rutqvist, J., Vasco, D.W., Myer, L.: Coupled reservoir-geomechanical analysis of CO_2 injection and ground deformations at In Salah, Algeria. Int. J. Greenh. Gas Control **4**, 225–230 (2010)

Vasco, D.W., Ferretti, A., Novali, F.: Reservoir monitoring and characterization using satellite geodetic data: interferometric synthetic aperture radar observations from the Krechba field, Algeria. Geophysics **73**, WA113–WA122 (2008)

Vasco, D.W., Rucci, A., Ferretti, A., Novali, F., Bissell, R.C., Ringrose, P.S., Mathieson, A.S., Wright, I.W.: Satellite-based measurements of surface deformation reveal fluid flow associated with the geological storage of carbon dioxide. Geophys. Res. Lett. **37**, L03303 (2010)

Vilarrasa, V., Rinaldi, A.P., Rutqvist, J.: Long-term thermal effects on injectivity evolution during CO_2 storage. Int. J. Greenh. Gas Control **64**, 314–322 (2017)

Vilarrasa, V., Rutqvist, J., Rinaldi, A.P.: Thermal and capillary effects on the caprock mechanical stability at In Salah, Algeria. Greenh. Gases Sci. Technol. **5**, 449–461 (2015)

White, J.A., Chiaramonte, L., Ezzedine, S., Foxall, W., Hao, Y., Ramirez, A., McNab, W.: Geomechanical behavior of the reservoir and caprock system at the In Salah CO_2 storage project. Proc. Natl. Acad. Sci. U.S.A. **111**, 8747–8752 (2014)

Zhang, R., Vasco, D., Daley, T.M., Harbert, W.: Characterization of a fracture zone using seismic attributes at the In Salah CO_2 storage project. Interpretation **3**, 37–46 (2015)

Analysis of Modified Cement Paste in the Context of CO_2 Geological Storage

Juan Cruz Barría[1], Christian Martin[2], Teresa Piqué[2], Jean Michel Pereira[3], and Diego Manzanal[1,4(✉)]

[1] Facultad de Ingeniería, UNPSJB - CONICET, Comodoro Rivadavia, Argentina
d.manzanal@upm.es
[2] Facultad de Ingeniería, UBA – CONICET - ITPN, Comodoro Rivadavia, Argentina
[3] École des Ponts ParisTech, Laboratoire Navier (UMR 8205 CNRS-IFSTTAR-ENPC), Paris, France
[4] ETSI de Caminos, Canales y Puertos, Universidad Politécnica de Madrid, Madrid, Spain

Abstract. In the context of CO_2 geological storage in deep saline aquifers, it is important to understand the hydro-chemo-mechanical coupling in rock-cement well interface to assess the safety and efficiency of the storage operation and thus to prevent possible CO_2 leakage. This work concerns a study on the effects of bacterial nanocellulose (BNC) and glass microspheres (GM) on chemo – mechanical behavior of cement paste composites when they are subjected to carbonation. A coupled chemo-poromechanical model implemented in finite element code has been used. A homogenization formulation is introduced to account for the BNC and GM in the cement composite. This study aims to simulate the chemo-poromechanical behavior of a system composed of modified cement well and the caprock during CO_2 injection. Chemical reactions (carbonation-dissolution) occurring in the system produce variation of the transport and mechanical properties. The presence of additives in the cement composite reduces the advancement of the front of carbonation in the short-term period of CO_2 exposure. Comparison between modified and non-modified cement composites has been analyzed in terms of porosity, permeability and pore pressure development. These results justify the importance of the coupled chemo-mechanical numerical analysis for the evaluation of additions to cement composites subjected to acidic pore fluid.

1 Introduction

Deep saline aquifers offer an interesting alternative for reducing CO_2 emissions to the atmosphere, for its advantage of having large volume storage. Furthermore, the rate of attack of CO_2-saturated brine solutions is the least compared to the attack of wet-scCO_2 and CO_2-saturated in fresh water (Rimmele et al. 2009).

One of the storage key factors to assess the sustainability and safety of geological site is the sealing capacity of wellbore system. Cement wellbore annulus or faults/fracture in cap rock could provide leakage paths of supercritical CO_2 (scCO_2) to

A. Ferrari and L. Laloui (Eds.): SEG 2018, SSGG, pp. 402–409, 2019.
https://doi.org/10.1007/978-3-319-99670-7_50

upper environment. The reservoir requires sufficient capacity and high porosity which would allow a good injectivity and a caprock with very low permeability to prevent CO_2 leakage through it. To prevent the escape of gases through the zone near the well damaged due to drilling, the cement used during the completion of the well must reasonably resist to the attack of CO_2 at supercritical state (temperatures greater than 31.6 °C and minimal pressures of 7.3 MPa).

Geochemical studies of cement paste show that the diffusion of carbonic acid through cement paste produce principally the dissolution of portlandite CH (calcium hydroxide – $C_a(OH)_{2(s)}$) and C-S-H (calcium silicate hydrate), and the precipitation of calcium carbonate. The first reaction of carbonation corresponds to that of the dissolution of CH:

$$CH + CO_2 \rightarrow CaCO_3 + H_2O$$

whereas the second reaction describes the carbonation of the C-S-H.

$$0,625C - S - H_{1.6} + CO_2 \rightarrow CaCO_3 + 1.3H_2O + 0.625SiO_2(H_2O)_{0.5}$$

The characteristic times of the chemical reactions are very small relative to the slow diffusion of ions in the in-pore fluid so the reactions can be assumed as instantaneous (Vallin et al. 2013). These chemical reactions will induce changes of porosity and the mineral composition of the solid phase.

The modification of cements to lower the density is a subject of interest in the cementing of wells. The objective is to modify the cement matrix, making it lighter but maintaining a high resistance and low permeability in its hardened state. Preliminary laboratory studies carried out at ITPN Laboratory (CONICET-UBA) by the authors (Martin 2017; Martin et al. 2018) show that an adequate combination of glass microspheres (GM) and bacterial nanocellulose (BNC) appear to achieve the desired objective although a greater number of tests are required for confirmation. In this work, a series of samples is presented on hardening Portland cement class G and modified with bacterial nanocellulose and micro glass spheres subjected to a rich-CO_2 atmosphere for 7 days. The study is complemented with the analysis of the behavior of chemo-mechanics of cement paste modified at laboratory level and in a context of geological storage of CO_2.

2 Preliminary Results on Modified Cement Paste

Laboratory uniaxial tests were carried out on 18 cubic samples (5 cm) and cured during 28 days at 20 °C in water following ANSI/API Specification 10A (Martin 2017). The composition of 6 samples corresponded to the pattern cement class G, 6 samples to 12% b.w.o.c. addition of glass microspheres and 6 samples to 12% b.w.o.c. glass microspheres (GM) addition with 0.1% b.w.o.c addition of bacterial nanocellulose (BNC). Half of the samples from each mixture were carbonated after cured in a rich-CO_2 atmosphere with concentration of 4.08 mol/m^3 at environment temperature and pressure for 7 days, and then, tested.

UCS results show a decrease of uniaxial compressive strength (UCS) around 17% for cement samples (CP) after carbonation (Fig. 1). The modified samples present less reduction on the UCS due to carbonation. Samples with additions of 12% of GM showed 5% reduction of UCS of sample without carbonation while samples with additions of 12% GM and 0.1% BNC reduction of UCS was 9%. Some authors concluded that cement class G is not adequate for storing CO_2 in reservoirs (Rimmelé et al. 2007). New materials are being studied to prevent the cracking of cement and CO_2 leakage.

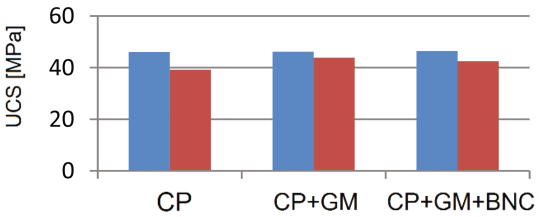

Fig. 1. Compressive strength at 28 days cured for non-carbonated samples (blue) and 28 days cured plus 7 days in CO_2 atmosphere for carbonated samples (red)

In order to evaluate the $Ca(OH)_2$ present in the cement matrix before and after carbonation TGA analyses (Fig. 2) were performed. Table 1 shows, for Non-Carbonated samples, a small variation in the CP-GM with respect to CP. However, we can appreciate an important decrease for CP-GM-BNC, this is due to the delay in the hydration process and the less amount of hydration products generated by the addition of BNC.

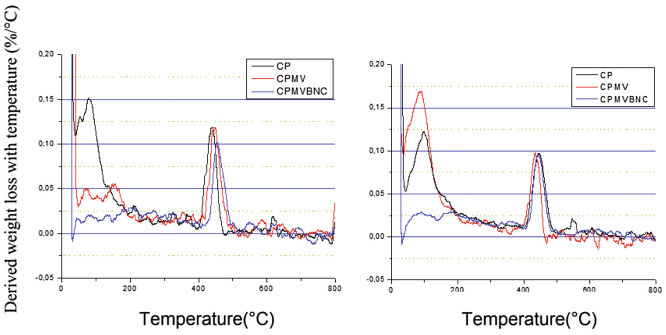

Fig. 2. TGA results for non-carbonated (left) and carbonated (right) cement samples

Table 1. $Ca(OH)_2$ content [%] in samples

Sample type	$Ca(OH)_2$ content [%]		
	CP	CPGM	CPGMBNC
Non-carbonated	15	15.4	12.9
Carbonated	14.8	11.1	12.9

After 7 days of carbonation, the CP sample has lost 1.33% of $Ca(OH)_2$ mass. If the process of carbonation is longer, more $Ca(OH)_2$ will be consumed. On the other hand, the CP-GM sample apparently has leached over 28% of its $Ca(OH)_2$ content, while the CP-GM-BNC shows a good behavior against the CO_2 attack, delaying the leaching process of calcite to zero at 7 days of carbonation.

The mercury intrusion porosimetry (MIP) tests were carried out over non-carbonated and carbonated samples at ENPC (Paris) (Fig. 3).

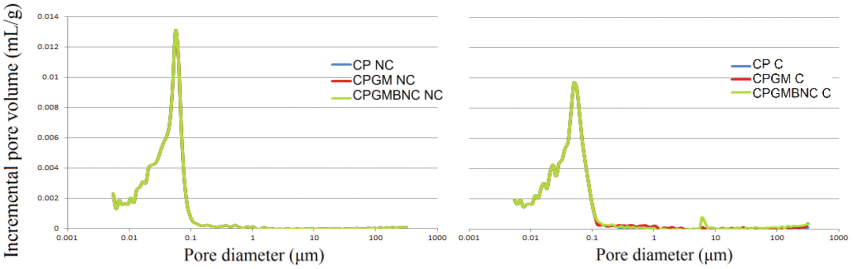

Fig. 3. MIP for non-carbonated (Left) and carbonated (Right) cement samples

The addition of GM and BNC increases the porosity and the average pore size (Table 2). After carbonation, the porosity decreases in all samples and the CPGM sample presents the highest porosity and average pore size for carbonated and non-carbonated samples. The carbonation is slow due to the small concentration of CO_2 in the environment and the short period of carbonation (seven days). In spite of the TGA results, the CPGMBNC samples shows a decrease of porosity and the increase of average pore size. This result would be due to the growth of calcite inside the pores, as a result of CH decomposition. Further tests are required for confirmation.

Table 2. Porosity and average pore size of cement samples

Sample type	Porosity [%]			Average pore size [µm]		
	CP	CPGM	CPGMBNC	CP	CPGM	CPGMBNC
Non-carbonated	11.8	12.8	12.2	1.9	3.58	2.93
Carbonated	11	11.6	11.5	2.15	5.2	3.67

3 Numerical Modelling

A coupled chemo-poromechanical model (Vallin et al. 2013) implemented in BIL 2.3.0 finite element code (Dangla 2017) has been used to simulate the behavior of the laboratory samples in rich-environment of CO_2. Furthermore, a system composed of modified cement well and the caprock during CO_2 injection was considered. Modification on the homogenization formulation has been done to incorporate the BNC and GM in the cement composite following the work of Ghabezloo (2011) and Martin (2017).

The model assumed has 1D axisymmetry under plane strain conditions in the axial direction and C-S-H carbonation does not start until the Portlandite is fully carbonated. Chemical reactions (carbonation-dissolution) occurring in the system produce variation on the transport and mechanical properties in both system, on laboratory samples and well conditions with CO_2 at supercritical state.

The first system was modelled as a cement sample of 1 cm in length at atmospheric conditions for G cement and modified cement samples (12% GM and 0.1% BNC). Tables 3 and 4 summarize the parameters used. The decrease of CH and C-S-H is due to the addition of glass microspheres that substitute part of these components in the cement matrix.

Table 3. Initial parameters for the calibrated model of both cements

d_0 [Diffusion] [$m^2.s^{-1}$]	k_0 [Intrinsic Permeability] [m^2]	η_{vis} [Air viscosity] [MPa.s]	K_F [Air compressibility] [MPa]	R_c [Compressive strength] [MPa]	R_t [Tensile strength] [MPa]
$9.9\ 10^{-10}$	$4.21\ 10^{-20}$	$1.85\ 10^{-11}$	0.142	45	4.5

Molar volumes [cm^3/mol]				
v^S_{CH}	$v^S_{C-S-H_{1.6}}$	$v^S_{CaCO_3}$	$v^S_{SiO_2(H_2O)_{0.5}}$	$v^F_{H_2O}$
33.1	84.7	36.9	31	18.85

Porosity along radius (Fig. 4) and a single point near the exposed surface (Fig. 5) are studied. The $CaCO_3$ quantities are less in the modified cement because of the least amount of $Ca(OH)_2$ and CSH available.

The well-system modelled consisted in a 10 cm cement annulus thickness under downhole condition of supercritical CO_2 with a CO_2 concentration of 1800 mol/m^3. The volumetric proportions assumed for cement paste were: porosity 27.94%, CH 18%, C-S-H 45% and Al 9%. For modified cement paste, following proportions were assumed: porosity 28%, CH 11.07%, C-S-H 26.93%, Al 5%, BNC 0.058% and GM 29% (Sercombe and Galle 2003). Assuming that CO_2 is dissolved in water, water viscosity ($\eta_{vis} = 0.5 \times 10^{-9}$ MPa.s) and water compressibility ($K_F = 1000$ MPa) were adopted.

Table 4. Parameters CP-GM-BN for the calibrated model

Inclusion	Volumetric prop. CP	Volumetric prop. CP-GM-BNC	Bulk modulus [GPa]	Shear modulus [GPa]
Porosity	0.11802	0.12244	–	–
CH	0.15	0.1289	33.00	14.50
C-S-H	0.63198	0.4082	25.00	18.40
Decalcified C-S-H	0.00	0.00	5.10	3.20
Aluminates	0.1	0.05	27.00	9.50
Calcite	0.00	0.00	69.00	37.40
GM	0.00	0.2895	30.00	20.00
BNC	0.00	0.00096	27.778	9.259

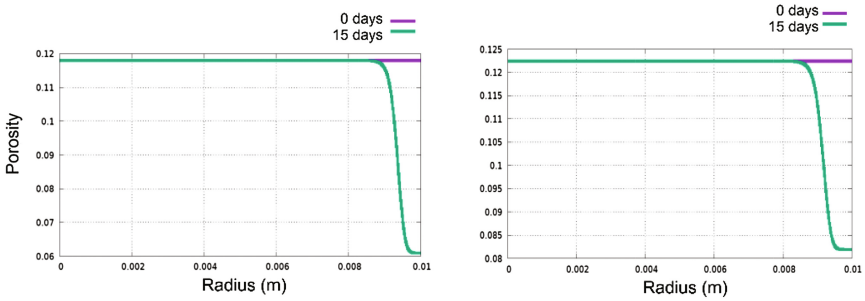

Fig. 4. Porosity for CP (Left) and CPGMBNC (Right) in atmospheric conditions

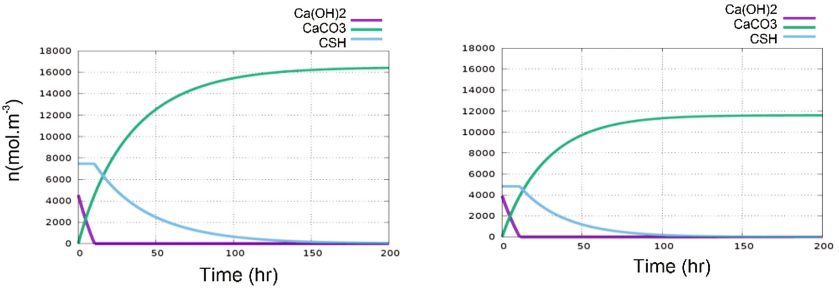

Fig. 5. Molar quantities for CP (Left) and CPGMBNC (Right) in atmospheric conditions

Porosity decreases, and therefore, permeability will decrease (Figs. 6 and 7). In this case, the carbonation diffuses faster in the cement due to the high CO_2 molar concentration (Fig. 8).

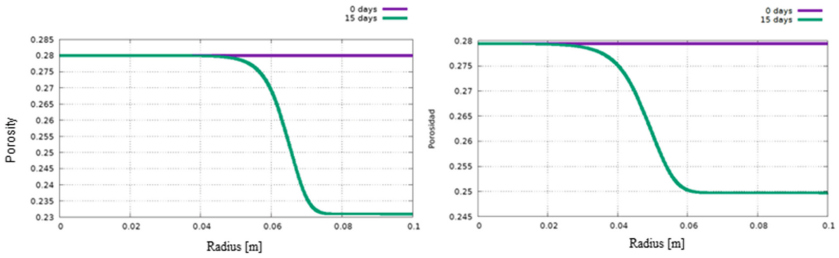

Fig. 6. Porosity for CP (Left) and CP-GM-BNC (Right) in downhole conditions

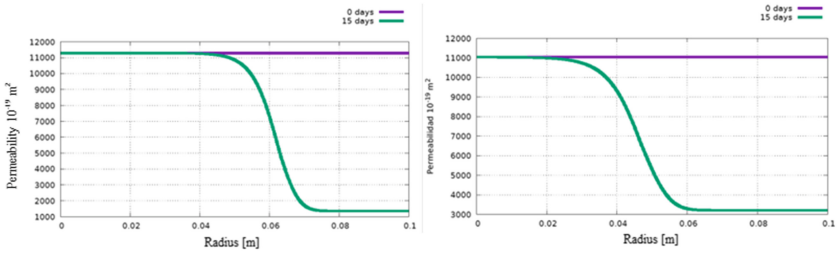

Fig. 7. Permeability for CP (Left) and CP-GM-BNC (Right) in downhole conditions

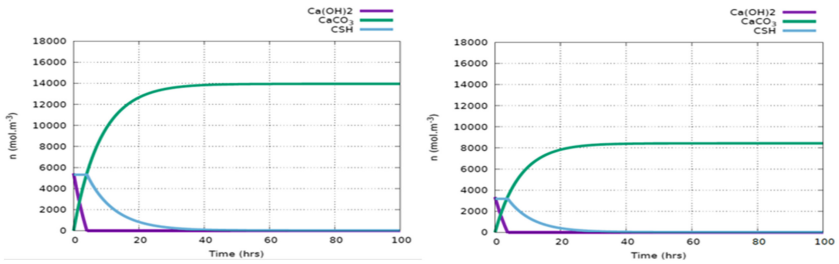

Fig. 8. Molar quantities for CP (Left) and CP-GM-BNC (Right) in downhole conditions

4 Conclusion

This work introduces preliminary laboratory study, carried out at ITPN Laboratory (CONICET-UBA), on the effects of bacterial nanocellulose (BNC) and glass microspheres (GM) on chemo–mechanical behavior cement pastes composites when they are subjected to carbonation processes. Short period of gas carbonation does not show clear trend on the result. The same process was study with a coupled chemo-poromechanical model implemented in finite element code and modification on the homogenization formulation is introduced to incorporate the BNC and GM in the cement composite.

A numerical model of the behavior under downhole in the context of CO_2 geological storage in deep saline aquifers is presented to understand the hydro-chemo-mechanical coupling in rock-cement well interface. Comparison between modified and

non-modified cement composite has been analyzed in terms of porosity, permeability and molar quantities development. Chemical reactions occurring in the system produce variation on the transport and mechanical properties. The addition of BNC reduces significantly the $Ca(OH)_2$ leaching for a relative similar initial porosity and shows higher compressive strength compared to the CP. In the simulations with modified cement, the carbonation front is slightly ahead due to fewer initial amounts of CH and CSH, resulting in a less amount of carbonated products.

More detailed mechanical and chemical tests of the composite with different percentage of BNC and different carbonation conditions are needed to study the BNC addition on cement in the CO_2 context.

Acknowledgements. The first author gratefully acknowledges the fellowship granted by CONICET (National Scientific and Technical Research Council – Argentina). The authors gratefully acknowledge the economic support provided by FONCYT (Argentina) through the project PICT-2016-4543 Design of light slurries for oil wells using biopolymers and nanotechnology and by University of Buenos Aires through the project UBACYT 20020160100055BA. The authors also acknowledge the technical staff from Laboratoire Navier (ENPC, Paris) for the MIP tests performed.

References

Dangla, P.: Bil-2.4, a modeling platform based on finite/element methods (2017). https://doi.org/10.5281/zenodo.1039729

Rimmelé, G., Goffé, B., Porcherie, O.: Well technologies for CO_2 geological storage: CO_2-resistant cement. Oil Gas Sci. Technol. Revue de l'IFP **62**(3), 325–334 (2007)

Rimmele, G., Porcherie, O., Quisel, N., Desroches, J.: A solution against well cement degradation under CO_2 geological storage environment. Int. J Greenh. Gas Control **3**, 206–216 (2009)

Sercombe, J., Galle, C.: Rehydration and microstructure of cement paste after heating at temperatures up to 300 °C. Cement Concr. Res. **33**, 1047–1056 (2003)

Vallin, V., Pereira, J.M., Fabbri, A., Wong, H.: Numerical modelling of the hydro-chemo-mechanical behaviour of geomaterials in the context of CO_2 injection. Int. J. Numer. Anal. Methods Geomech. **37**(17), 3052–3069 (2013)

Ghabezloo, S.: Effect of the variations of clinker composition on the poroelastic properties of hardened class G cement paste. Cement Concr. Res. **41**(8), 920–922 (2011). https://doi.org/10.1016/j.cemconres.2011.03.022. ISSN 0008-8846

Martin: Relation between structures and properties in additions of polymers in cement (Spanish). Graduate Thesis of Civil Engineering. Universidad de Buenos Aires (2017)

Martin, Z., Cerrutti, V., Manzanal, P.: Oil well cement modified with Bacterial Nanocelluloce. In: Taha, M. (ed.) International Congress on Polymers in Concrete (ICPIC 2018). Polymers for Resilient and Sustainable Concrete Infrastructure, Chap. 89, p. 697. Springer, Cham (2018)

Numerical Simulation of Liquid Patch Formation and Retention in Porous Media

Mingrui Dong, Yanyao Bao, and Yixiang Gan(✉)

School of Civil Engineering, The University of Sydney, Sydney, Australia
yixiang.gan@sydney.edu.au

Abstract. Liquid retention and patch formation during drainage processes in porous media are important phenomena in energy geotechnics. These behaviours are governed by drainage conditions, properties of different constituents, and topological structure of pore space. In this study, gravity-driven drainage processes in porous media are simulated using a modified Smoothed Particle Hydrodynamics (SPH) method. An inter-particle interaction force is applied to the liquid-liquid and liquid-solid SPH particles for simulating surface tension and wettability. The influence of Bond number, characterising gravity and surface tension, and surface wettability, represented by the contact angle, on liquid patch formation and retention are investigated. Under a given combination of Bond number and contact angle, the corresponding residual saturation and morphological feature of liquid patches are recorded. During drainage, the formation and evolution of liquid patches and bridges can be observed within the pore space. The van Genuchten equation and stretched exponential function are used to capture the dependencies on the Bond number and contact angle, respectively. The combination of these two theoretical models can lead to quantitative predictions of liquid retention and its relative change under any given Bond number and contact angle.

1 Introduction

Multiphase flow problems in porous media are of great significance in many industrial applications, such as mining (Silva et al. 2013), waste management (Herminghaus 2005), oil recovery (Bautista et al. 2014), and carbon geo-sequestration (Bandara et al. 2011). Understanding such phenomena is the key to optimise applications of porous media involved in energy geotechnics, where the gravity can play an important role for the processes of heat and mass transfer. In particular, during gravity-driven drainage processes, the effective behaviour of porous media depends on the characterisation of liquid retention and patch formation at the pore scale. These behaviours are generally affected by gravitation, surface tension and wettability, density and viscous differences between multiple phases, and topological structure of the pore space.

In this paper, we investigate the relative importance of gravity and surface tension, represented by the Bond number (Bo) (Edwards et al. 1998), and the contribution of surface wettability on the liquid retention behaviour during the gravity-driven drainage. Wettability describes the energy potential at the three-phase contact line, e.g., gas,

A. Ferrari and L. Laloui (Eds.): SEG 2018, SSGG, pp. 410–417, 2019.
https://doi.org/10.1007/978-3-319-99670-7_51

liquid and solid, and it can be quantitatively represented by the contact angle (θ), formed at the contact line.

The simulation of gravity drainage processes is established in a two-dimensional model composed of mono-disperse grains. A modified Smoothed Particle Hydrodynamics (SPH) (Li et al. 2018; Bao et al. 2018) is applied to model the interactions among multiple phases base on an open-source platform PySPH (Ramachandran 2016). Previous studies on the solid-liquid interactions across multiple scales have been validated using SPH (Monaghan 2005; Tartakovsky and Panchenko 2016). Here, we focus on drainage processes under various Bond number and wettability, and propose a qualitative model to capture the retention behaviour.

2 Numerical Modelling

The SPH method is based on discretising a continuous field function, $A(\boldsymbol{r})$, at position $\boldsymbol{r}_i$ and representing the field by a convolution integral with the smoothing function, $W(\boldsymbol{r}-\boldsymbol{r}', h)$, allowing the value of any function to be obtained at a given point with neighbouring particles, see Tartakovsky and Meakin (2005), as:

$$\mathrm{A}(\boldsymbol{r}) = \int A(\boldsymbol{r}')W(\boldsymbol{r}-\boldsymbol{r}', h)d\boldsymbol{r}', \tag{1}$$

where h is the smoothing length.

By discretising the Navier–Stokes equations, the momentum equation controlling the motion of each particles can be obtained. The artificial viscosity developed by Monaghan (1992) is adopted in this work, and the form of momentum equation is shown as:

$$\frac{d\boldsymbol{v}_a}{dt} = -\sum\nolimits_{b=1}^{N} m_b\left(\frac{P_a}{\rho_a^2} + \frac{P_b}{\rho_b^2} + \Pi_{ab}\right)\nabla W_{ab} + \boldsymbol{g}, \tag{2}$$

where $\boldsymbol{v}_a$ is the velocity vector of the a-th particle, m_b is the mass, P_a and P_b are the pressure, ρ_a and ρ_b are the estimated density, Π_{ab} is the artificial viscosity, W_{ab} is the smoothing function, and $\boldsymbol{g}$ is the gravity.

In the gravity-driven drainage model, we consider gas phase as the intruding non-wetting phase. Since the differences in density and compressibility are significantly large, the gas phase is ignored in the SPH model. Both liquid and solid phases are represented by SPH particles, see Fig. 1. An inter-particle interaction force (IIF) with short distance repulsive force and long distance attractive force (Li et al. 2018; Bao et al. 2018) is imposed in this SPH model. In practice, the surface tension of liquids is a physical resultant force at the liquid-gas interface, here modelled by this IIF formulation. The realisation of contact angle is based on Young equation shown as:

$$\gamma_{sg} = \gamma_{sl} + \gamma_{lg}\cos\theta, \tag{3}$$

where γ_{sv} is the solid-gas surface tension, γ_{sl} is the solid-liquid surface tension, γ_{lg} is the liquid-gas surface tension, and θ is the contact angle. The short distance repulsive

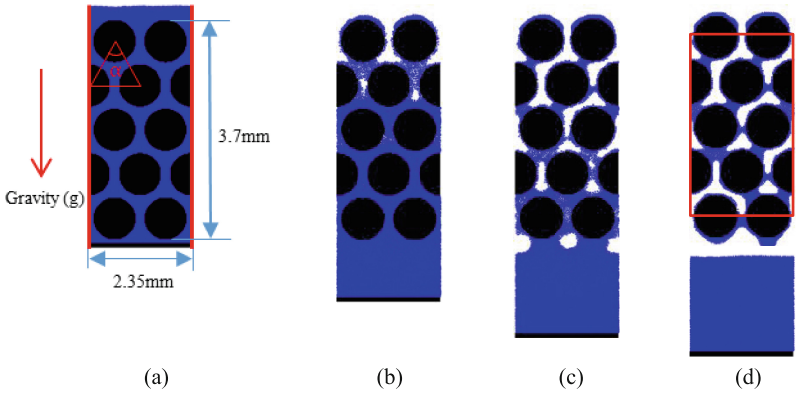

Fig. 1. The simulated gravity-driven drainage process.

force is implemented at liquid-solid interface to avoid penetration of liquid and solid particles.

In Fig. 1(a), a 2D porous media is modelled by mono-sized grains (black circles) in a hexagonal packing. The pore space (consisting of pore and throat) is initially filled with the liquid. Periodic boundary conditions are imposed along the horizontal axis, perpendicular to the gravity. The dimensions of the simulation domain are 3.7 mm in height and 2.35 mm in width. The grain radius is 0.36 mm, and the throat size is 0.14 mm. Note that these dimensions are later normalised by Bond number and porosity (ϕ = 37.95%).

In Fig. 1(b), the bottom plate is moving downwards with a constant velocity of 0.05 m/s and the liquid particles in the pore space are flowing down under gravity. The velocity 0.05 m/s results in a considerable low Capillary number of 2.7×10^{-3}, indicating a negligible contribution of viscosity as compared to the one of the capillary interactions. With the existence of long distance attractive force among liquid particles (representing the surface tension), part of the liquid particles is trapped in the throat (in the form of liquid bridges) or pore (as liquid patches), as shown in Fig. 1(c). Towards the end of drainage process, the degree of saturation will be calculated based on the rectangular area shown in Fig. 1(d).

3 Results and Discussion

To investigate the influence of Bo and wettability on liquid patch formation and retention, 63 drainage simulations have been conducted. Here, Bo is defined by $\Delta\rho g L^2/\gamma$, where the density difference $\Delta\rho$ = 997 kg/m^3, the characteristic length is taken as the throat size as L = 0.14 mm, and surface tension γ = 0.073 N/m. In the following simulations, the gravitational acceleration g is controlled to vary the Bo number from the range between 3.26×10^{-3} and 5.21×10^{-2}. Contact angles of grain surface θ are set from 10° (hydrophilic) to 151° (super-hydrophobic), or 0.17 to 2.64 in

radian, for varying wettability. The results of liquid patches formation are shown in Fig. 2 in which θ increases horizontally from left to right and a rise of Bo can be found vertically from top to bottom.

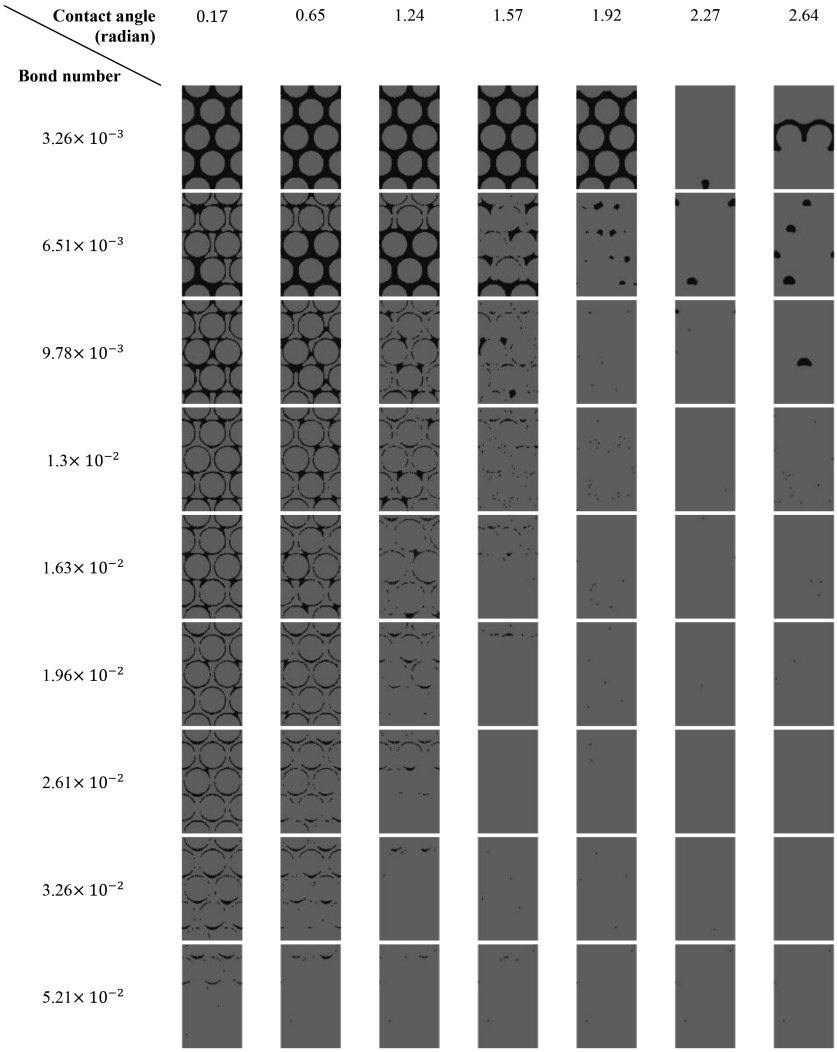

Fig. 2. Pattern diagram for liquid patches under variable wettability and Bo number.

At final drainage stages in Fig. 2, liquid patch patterns can be classified as pendular (continuous gas and discontinuous liquid phases), funicular (both continuous gas and liquid phases), capillary (continuous liquid and discontinuous gas phases), droplet (fully saturated) regimes (Gan et al. 2013). In Fig. 2, the droplet regime can be found when Bo is 3.26×10^{-3} and θ ranging from 0.17 to 1.57. The capillary regime can be

found at Bond number 3.26×10^{-3} with θ equalling 1.92 and 2.64, respectively. When Bond number is 5.61×10^{-3} and θ ranging from 0.17 to 1.57, the funicular regime can be observed. The residual liquid content continues the downward trend as increasing the Bond number from 9.78×10^{-3} to 2.61×10^{-2}. Correspondingly, residual liquid can be found in pendular region at Bo 9.78×10^{-3}, and almost no liquid bridge exists (the adsorption regime) after Bo reaches 2.61×10^{-2}.

For small Bo ranging from 3.26×10^{-3} to 9.78×10^{-3} and θ larger than 2.27, part of liquid phase is entrapped in the pore showing a rebound for the overall liquid retention. In simulations, this phenomenon can be interpreted from two perspectives: (1) the compressibility of the SPH liquid phase, and (2) the SPH mesh of the solid surface, whereby introducing an artificial frictional contact. However, this phenomenon is consistent with the experimental results reported by Hu et al. (2017), where liquid drops can be retained inside the pore space in super-hydrophobic conditions.

The quantitative analysis of Bond number and θ is presented in Fig. 3(a) and (b), respectively. Here, the degree of saturation Sr is defined by the ratio of liquid volume and pore volume. The four inserts in Fig. 3 represent specific drainage conditions corresponding to Fig. 2.

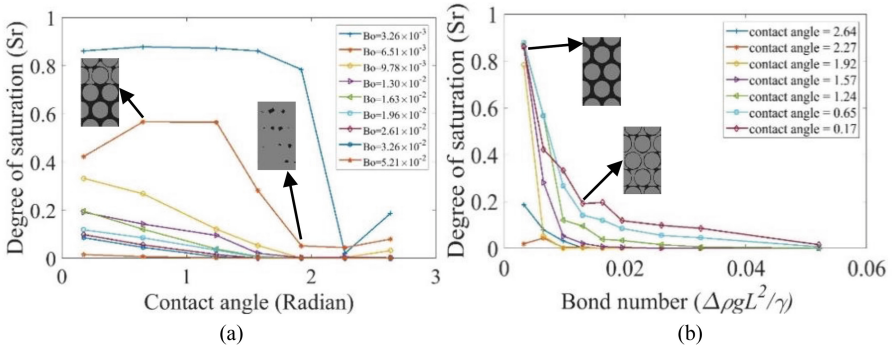

Fig. 3. Degree of saturation vs (a) θ and (b) Bo number.

The effect of wettability (θ) on Sr varies with different Bo. It can be observed in the Fig. 3(a), for Bo 3.26×10^{-3}, the resulting Sr remains constant from θ varying from 0.17 to around 1.5. In comparison, cases with Bo from 9.78×10^{-3} to 5.21×10^{-2} demonstrate downward trend for Sr with the increase of θ. For Sr at large θ, the rebound at the hydrophobic regime becomes less significant as Bo increases and residual water patches were observed for Bo larger than 9.78×10^{-3}. In general, a small Bond number can lead to higher liquid retention for given θ.

In Fig. 3(b), it can be found that the increase of Bond number can lead to a decline trend of Sr with almost all θ cases. Particularly, with the increase of Bo, the absolute decrease of Sr is steeper for θ ranging from 0.17 to 1.92, and the decline trend is less significant for Bo larger than 0.01. However, the relative changes respect to the Bo number are similar. In addition, it is obvious that smaller θ can result in higher Sr, for a given value of Bo.

To capture the dependency of liquid retention on the Bo and θ, we use the formats of the van Genuchten equation (Van Genuchten 1980) and stretched exponential function (Zeng and Xu 2017), respectively. The residual saturation is then achieved by combining the contributions of Bo and θ as:

$$Sr(\mathrm{Bo},\theta) = G(Bo)E(\theta) = \left[(1+(d\mathrm{Bo})^{n})^{-\left(1-\frac{1}{n}\right)}\right]e^{-b\theta^{c}}, \tag{4}$$

Where $Sr(\mathrm{Bo},\theta)$ is the function of degree of saturation based on variables Bo and θ; $G(Bo)$ is the van Genuchten equation; $E(\theta)$ is the stretched exponential function; d, n, b and c are fitting parameters. Note that the original van Genuchten equation for the soil-water retention curve uses the suction term $\psi = \rho gh$, where h is the head (m), instead of Bo number used here. Nevertheless, varying Bo number in any given system indicates different potential states of the porous media, i.e., changing the value of g. With this proposed empirical model, the simulation results are visualized in a three-dimensional plot, see Fig. 4(a). The fitting results is verified by goodness of fitting measures, including the adjusted R-square and sum of squared errors (SSE), which equals to 0.9718 and 0.1057, respectively, and generally show a good prediction.

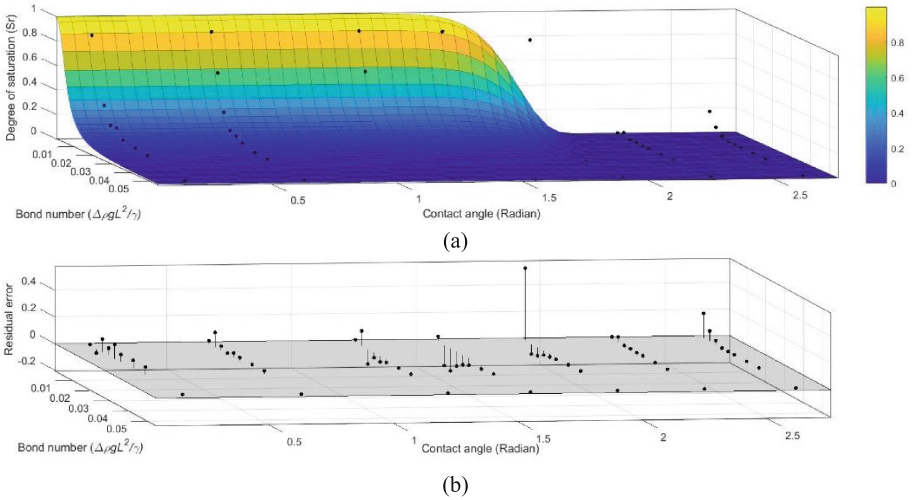

Fig. 4. (a) Comparison between the predictions of theoretical model and simulation results. The fitting parameters in the model are b = 1 × 10^{-5}, c = 18, d = 200, and n = 3. (b) The residual errors of theoretical predictions.

The residual error plot is also depicted in Fig. 4(b) for describing the relative error between simulation results and the predictions of the proposed theoretical model. It can be found that for small Bo (around 0.01) and large θ (around 2 and 2.5), the error is relatively large compared with other cases. This error may imply that the combination

of these two models are not suitable for some extreme conditions, e.g. scenarios with small Bo numbers in porous media with super-hydrophobic surfaces.

4 Conclusions

The gravity-driven drainage processes in a model porous medium composed of monodisperse grains have been simulated using the modified SPH method. The competition between surface tension and gravity has been investigated by varying the Bond number, under different wettability conditions. Based on the results, it can be concluded that the liquid retention can be raised by decreasing the Bond number and θ of solid surface (or increase wettability), which is consistent with the experimental results reported by Kulkarni (2005). Through the parametrical study, a diagram for the residual retention has been constructed. An empirical model by combining the van Genuchten equation and stretched exponential function has been proposed and is shown to be effective to capture the dependencies of liquid retention on various drainage and wettability conditions, i.e., Bo and θ, although minor deviations for super-hydrophobic conditions are observed. This study provides beneficial insights into many applications in the field of energy geotechnics. Typical examples include gas-assisted gravity drainage (GAGD) oil recovery and CO_2 movement during geo-sequestration, where the gravity-driven drainage process plays a key role. The preliminary results presented here warrant future studies on gravity-driven multiphase flow using larger geometrical domains and including microstructural randomness to better represent natural porous media.

References

Bandara, U.C., Tartakovsky, A.M., Palmer, B.J.: Pore-scale study of capillary trapping mechanism during CO2 injection in geological formations. Int. J. Greenh. Gas Control **5**(6), 1566–1577 (2011)

Bao, Y., Li, L., Shen, L., Lei, C., Gan, Y.: A modified smoothed particle hydrodynamics approach for modelling dynamic contact angle hysteresis. arXiv preprint arXiv:1804.02770 (2018)

Bautista, E.V., Barillas, J.L.M., Dutra, T.V., da Mata, W.: Capillary, viscous and gravity forces in gas-assisted gravity drainage. J. Pet. Sci. Eng. **122**, 754–760 (2014)

Edwards, J., Honarpour, M., Hazlett, R., Cohen, M., Membere, A., Pebdani, F., Clayton, C., Al-Hussainy, R.: Validation of gravity-dominated relative permeability and residual oil saturation in a giant oil reservoir. Paper SCA-9903, presented at the 1998 SPE annual technical conference and exhibition (1998)

Gan, Y., Maggi, F., Buscarnera, G., Einav, I.: A particle-water based model for water retention hysteresis. Geotech. Lett. **3**, 152–161 (2013)

Herminghaus, S.: Dynamics of wet granular matter. Adv. Phys. **54**(3), 221–261 (2005)

Hu, H., Lai, Z.L., Ding, G., Zhuang, D., Weng, X.: Experimental investigation on water drainage characteristics of open-cell metal foams with different wettabilities. Int. J. Refrig. **79**, 101–113 (2017)

Kulkarni, M.M.: Multiphase mechanism and fluid dynamics in gas injection EOR processes. Ph.D. thesis (2005)

Li, L., Shen, L., Nguyen, G.D., El-Zein, A., Maggi, F.: A smoothed particle hydrodynamics framework for modelling multiphase interactions at meso-scale. Comput. Mech., pp.1–15 (2018)

Monaghan, J.J.: Smoothed particle hydrodynamics. Annu. Rev. Astron. Astrophys. **30**(1), 543–574 (1992)

Monaghan, J.J.: Smoothed particle hydrodynamics. Rep. Prog. Phys. **68**(8), 1703 (2005)

Ramachandran, P.: PySPH: a reproducible and high-performance framework for smoothed particle hydrodynamics. In: Proceedings of the 15th Python in Science Conference, pp. 127–135 (2016)

Silva, L.F.O., Fdez-Ortiz de Vallejuelo, S., Martinez-Arkarazo, I., Castro, K., Oliveira, M.L.S., Sampaio, C.H., de Brum, I.A.S., de Leão, F.B., Taffarel, S.R., Madariaga, J.M.: Study of environmental pollution and mineralogical characterization of sediment rivers from Brazilian coal mining acid drainage. Sci. Total Environ. **447**, 169–178 (2013)

Tartakovsky, A., Meakin, P.: Modeling of surface tension and contact angles with smoothed particle hydrodynamics. Phys. Rev. E **72**(2), 026301 (2005)

Tartakovsky, A.M., Panchenko, A.: Pairwise force smoothed particle hydrodynamics model for multiphase flow: surface tension and contact line dynamics. J. Comput. Phys. **305**, 1119–1146 (2016)

Van Genuchten, M.T.: A closed-form equation for predicting the hydraulic conductivity of unsaturated soils. Soil Sci. Soc. Am. J. **44**(5), 892–898 (1980)

Zeng, Q., Xu, S.: A two-parameter stretched exponential function for dynamic water vapor sorption of cement-based porous materials. Mater. Struct. **50**(2), 1–13 (2017)

Hydro-Mechanical Modelling of the Boom Clay Excavation, Convergence and Contact with Concrete Lining

Bertrand François[1(✉)], Jérome Nève[1], Séverine Levasseur[2], Arnaud Dizier[3], and Pierre Gerard[1]

[1] BATir Department, Université libre de Bruxelles (ULB), Brussels, Belgium
Bertrand.Francois@ulb.ac.be
[2] ONDRAF/NIRAS, Brussels, Belgium
[3] EURIDICE, Mol, Belgium

Abstract. The Boom Clay is considered as one of the potential host rock formation in Belgium for radioactive waste repository in deep geological layers. Gallery excavations will induce large hydro-mechanical disturbances around disposal system that need to be well understood and characterised. This study discusses particularly the role of interactions between the lining of the galleries and the host formation in the numerical characterisation of excavations in Boom Clay. The excavation and the convergence of the connecting gallery of the HADES underground research facility in Mol is modelled in a hydro-mechanical framework. Zero-thickness interface elements are used to manage numerically the contact between the host rock and the lining. Numerical predictions are compared with strains measurements recorded within the concrete segments of the lining in the underground research laboratory in Mol. The study highlights the impact of the anisotropic behavior of the host rock on the response of the model.

1 Introduction

Repository in deep geological layers is one solution to deal with high level nuclear wastes. In the Belgian concept for underground nuclear waste storage, the Boom Clay is studied as one potential host formation. This material is highly plastic and requires the installation of a lining just after the excavation of the gallery in order to limit the convergence of the rock. Interactions between the Boom Clay and the lining influence the stresses redistribution in the clay, the stresses in the lining and the convergence of the gallery. This clay-lining interaction is time-dependent because of the hydro-mechanical couplings occurring in the clay and is also highly non-axisymmetric around the gallery due to different sources of the Boom Clay anisotropy (in-situ stress state, hydraulic conductivity and elastic stiffness).

The behavior of the lining it-self is also an important factor for the stresses redistribution in the rock. In particular, the geometry of the discontinuous lining (made of rectangular and trapezoidal concrete blocks) creates a pre-stressing after the installation of the key block that strongly impacts the clay-lining interaction. Also, the

A. Ferrari and L. Laloui (Eds.): SEG 2018, SSGG, pp. 418–425, 2019.
https://doi.org/10.1007/978-3-319-99670-7_52

time spent between the excavation and the lining installation controls the convergence of the rock before the contact occurrence between the rock and the lining, which in turn has an impact on the stresses redistribution in the rock and the lining.

Salehnia et al. (2015) investigated the role of the lining on the time-dependent extension of the excavation damaged zone around a gallery in Boom Clay by means of the modelling of strain localization in shear bands through a finite element second gradient approach. They concluded that the lining plays a significant role in decreasing the extension of damaged zone around a gallery. In the present study, strain localization is disregarded but the attention is focused on the role of Boom Clay anisotropy on the clay-lining interactions.

Based on long-term in-situ measurements of strains in the concrete lining during more than 10 years after the excavation of the connecting gallery in HADES underground laboratory in Mol (Belgium), this study aims at assessing the ability of the current available hydro-mechanical models to reproduce the complex time-dependent deformation of the concrete lining and so at explaining the highly coupled hydro-mechanical mechanisms of stresses redistribution in the Boom Clay. To do so, the three sources of the Boom Clay anisotropy are integrated in a unified hydro-mechanical finite element framework, including also the modelling of clay-lining contact through hydro-mechanical zero-thickness interface elements (Cerfontaine et al. 2015).

2 Experimental Data

The connecting gallery in HADES underground laboratory in Mol (Belgium) was constructed using a tunnel boring machine (Bastiaens et al. 2003; Bernier et al. 2003). The lining is made of a succession of rings. Each of these rings has a width of 1 m in the longitudinal direction of the gallery and is composed of 10 rectangular concrete blocks and 2 trapezoidal concrete key blocks. By pushing these key elements, all the blocks enter in compression and induce a pre-stressing in the lining (Bernier et al. 2007).

Four rings of the connecting gallery have been monitored with strain gauges to measure the orthoradial strains in the concrete blocks. The gauges are located at the inner (Intrados) and outer (Extrados) faces of the block. The magnitude of strains slightly differs from one ring to another, but globally the same trend of deformation is observed in each ring (Bernier et al. 2003). In this paper, all the analysis is based on the strain measurements of ring 50.

The measured orthoradial strains are compressive strains all around the gallery. That is characteristic of a global convergence of the lining. However, for some blocks, the intrados deformation is higher than the extrados deformation and inversely. Globally, the lateral segments have a higher orthoradial strain at the intrados than at the extrados. This corresponds to a reduction of the radius of curvature of the gallery. At the opposite, for the top segments, the external strains are higher than the internal ones which means that the radius of curvature is increasing. For the bottom segment, the difference between intrados and extrados strain is tight. Those observations indicate that the lining is submitted to a horizontal ovalisation. This non-axisymmetric deformation is essentially due to the Boom Clay anisotropic behavior (Fig. 1).

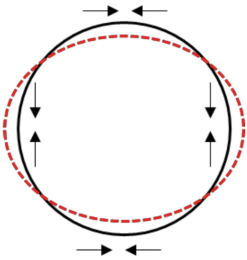

Fig. 1. Horizontal ovalisation of the lining with the main compression forces

3 Boundary Value Problem

2D plane strain and hydro-mechanical modelling of the host rock convergence after excavation and contact with the lining have been performed with the finite element code Lagamine (Collin et al. 2002). For symmetry reasons, only a quarter of the tunnel is modelled. A 2 m long inner radius for the cavity and a 40 cm thick concrete lining are considered. Owing to over-excavation induced by the digging technique, a 4.5 cm gap between the lining and the host rock is introduced in the model.

An initial pore water pressure of 2.25 MPa is considered for the host rock, corresponding to the 225 m deep underground research laboratory in Mol. The initial stress state will be discussed later.

The excavation is modelled by decreasing in 1 day the total radial stress at the host rock wall from its initial value to the atmospheric pressure. A drained condition is applied simultaneously at the host rock wall (at the interface between lining and host rock). Because of the rapid installation of the lining after the excavation, possible desaturation of the host rock due to gallery ventilation is not considered.

The normal contact between the host rock and the lining is modelled through zero-thickness interface elements using penalty method (Cerfontaine et al. 2015). This method allows a limited interpenetration of the two bodies in contact. The corresponding penalty coefficient should be chosen as high as possible to minimize this interpenetration as to ensure the numerical convergence of the simulations. The frictional contact between the two bodies is treated as an elastoplastic problem. A slipping condition is activated at the interface between the two bodies when a Coulomb criterion is reached.

4 Constitutive Laws and Parameters

The mechanical behaviour of the Boom Clay is modelled through an elastoplastic approach, expressed in Terzaghi's effective stress and using a Drucker-Prager yield limit. Hardening of the friction angle (depending on the equivalent plastic strains) is considered (Collin et al. 2002). An initial friction angle of 5° is assumed, while the final friction angle is equal to 18°, as suggested by Dizier (2011). An elastic cross-anisotropy has been also integrated to the mechanical model of the Boom Clay due to

the horizontal bedding planes of the host rock (François et al. 2014). The water transfers within the host rock are controlled by a generalized Darcy's law for saturated conditions. A linear elastic behavior of the concrete is assumed.

The mechanical and hydraulic parameters of the host rock and the concrete lining for the different cases are presented in Table 1.

Table 1. Mechanical and hydraulic parameters of the Boom Clay (Bernier et al. 2007; François et al. 2014; Dizier 2011; Timodaz 2010; Bastiaens et al. 2003) and the concrete.

BOOM CLAY	
Isotropic elastic modulus	300 MPa
Cross-anisotropic elasticity (horizontal/vertical Young modulus)	400 MPa/200 MPa
Poisson ratio	0.125
Cohesion	300 kPa
Initial/Final friction angle	5°/18°
Isotropic hydraulic conductivity	$4\ 10^{-12}$ m/s
Anisotropic hydraulic conductivity (horizontal/vertical)	$4\ 10^{-12}$ m/s/$2\ 10^{-12}$ m/s
Initial porosity	0.39
CONCRETE	
Elastic modulus	50 GPa
Poisson ratio	0.2

5 Numerical Results

First a simplified monolithic concrete lining is assumed, made up of only one circular concrete segment. An anisotropic initial stress state is considered. In the following, the model is progressively upgraded by implementing successively the hydraulic anisotropy (anisotropic hydraulic conductivity) and the elastic cross-anisotropy characterizing the Boom Clay. At the end, a more realistic discontinuous concrete lining is considered, made up of 12 concrete segments all around the tunnel (as described hereabove and shown on Fig. 2). The results presented in this paper focus on the numerical prediction of the orthoradial strains in the upper concrete segments of ring 50, compared with experimental measurements.

5.1 Continuous Concrete Lining - Anisotropic Initial Stress State

Bernier et al. (2007) show that the initial vertical effective stress σ'_V in the underground laboratory in Mol is equal to 2.25 MPa, while the initial horizontal one σ'_H corresponds to 1.58 MPa. This anisotropic initial stress state leads to a vertical ovalisation of the gallery and so of the lining (Fig. 3(a)). This is due to the earlier entry in plasticity along the horizontal axis, because the deviatoric stress at the cavity wall increases directly during excavation. Along the vertical axis, the deviatoric stress at the cavity wall decreases first before an increase. The numerical strains in the lining shows a time-

(a) (b)

Fig. 2. (a) Monolithic and (b) discontinuous lining

dependent evolution, but the long term prediction does not allow reproducing the horizontal ovalisation of the concrete lining observed in-situ. It is worth to mention that the contact of the lining with the host rock is reached after less than 1 day of convergence, and a limited numerical interpenetration between the lining and the Boom Clay is produced.

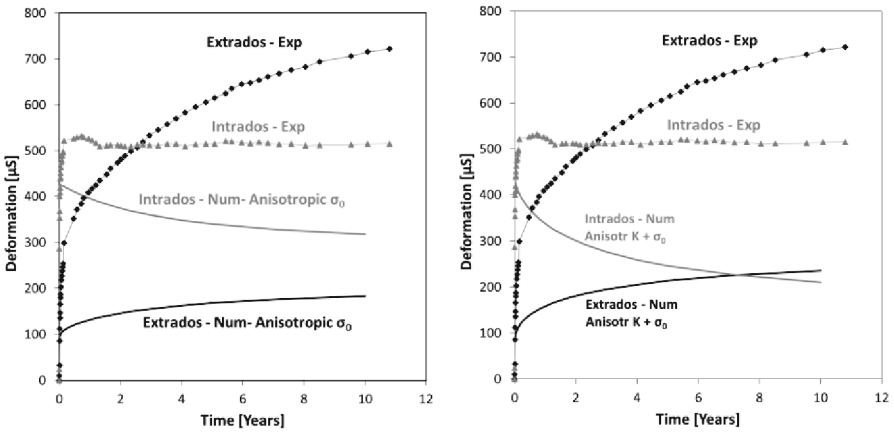

(a) (b)

Fig. 3. Comparison between experimental and numerical orthoradial strains for a monolithic lining (a) for anisotropic initial stress state and for (b) anisotropic initial stress state and anisotropic hydraulic conductivity

5.2 Continuous Concrete Lining - Anisotropic Initial Stress State and Hydraulic Conductivity

The Boom Clay is a sedimentary clay layer with horizontal bedding planes that induces an anisotropic behaviour of the hydraulic conductivity. This anisotropy is introduced in the model and combined with the initial anisotropic stress state. The calibration of numerical model on field measured (see for instance TIMODAZ (2010)) have shown that the horizontal hydraulic conductivity $K_{w,H}$ is equal to $4\ 10^{-12}$ m/s, while the vertical one $K_{w,V}$ is equal to $2\ 10^{-12}$ m/s. That leads to a lower drainage capability along the

vertical axis, and in turn a higher convergence at the top of the tunnel. A horizontal ovalisation of the lining is therefore obtained after 7 days. However, experimental observations show a much faster ovalisation in-situ. Also, the magnitude of the strains predicted numerically remains lower than the experimental data (Fig. 3(b)).

5.3 Continuous Concrete Lining - Anisotropic Initial Stress State, Hydraulic Conductivity and Elastic Cross-Anisotropy

The presence of horizontal bedding planes in the clay justifies also the use of an elastic cross-anisotropy model, with a higher horizontal stiffness than the vertical one. As suggested by François et al. (2014) we use horizontal and vertical elastic moduli of 400 MPa and 200 MPa, respectively. This elastic anisotropy accentuates the horizontal ovalisation of the gallery, now observed after 2 years, as in the experimental data (Fig. 4(a)). However, the modelling still underestimates the strains.

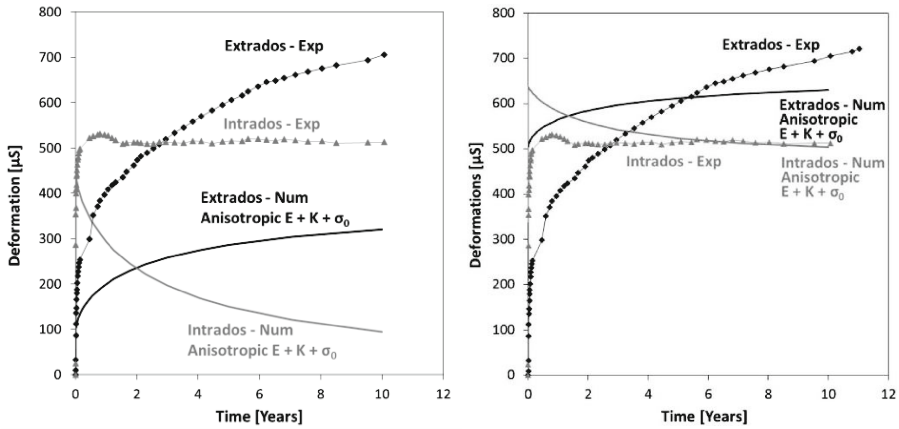

Fig. 4. Comparison between experimental and numerical orthoradial strains for anisotropic initial stress state and anisotropic hydraulic conductivity and elastic cross-anisotropy for (a) a monolithic lining and (b) a discontinuous lining

5.4 Discontinuous Concrete Lining - Anisotropic Initial Stress State, Hydraulic Conductivity and Elastic Cross-Anisotropy

A more realistic geometry of the lining, made of several concrete blocks, can lead to a better reproduction of the strains in the lining. Zero-thickness interface elements are now used both for the host rock – lining contact and the segment – segment contact.

While a technical gap of 4.5 cm is still considered between the lining and the host rock, the initial condition at the contact between the concrete segments is a real issue. The installation of the last trapezoidal key segment produces a pre-stressing in the lining that has to be considered by the model. Due to the lack of information on the

magnitude and the distribution of this pre-stressing, a constant and homogeneous initial normal pressure between all the segments of 20 MPa was considered in the model. It allows obtaining the best calibration between numerical and experimental results.

Considering all the sources of anisotropy presented above (initial stress state, hydraulic conductivity and elastic stiffness), the hydro-mechanical model provides a relatively good agreement with the experimental strains in the lining (Fig. 4(b)). The magnitude of the lining deformation is now consistent with experimental observations. However, the time evolution of those deformations differs slightly. This could be attributed to a series of simplification of the constitutive behaviours of clay and concrete. In particular, strain softening of Boom Clay (inducing strain localization), anisotropy of its plastic behaviour as well as creep behaviour of Boom Clay and concrete lining could play a significant role in the clay-lining interaction.

6 Conclusions

The lining plays an important role in the stresses redistribution in the Boom Clay due to the excavation of the gallery. The problem is complex because it involves different sources of Boom Clay anisotropy as well as the contact behaviour between lining and clay and between the lining segments. Numerical modelling allows to highlight and to understand the impact of those various features.

From a hydro-mechanical finite element approach including interface elements, we were able to reproduce the horizontal ovalisation of the gallery observed a few years after the excavation if anisotropy of the hydraulic conductivity and the elastic stiffness is considered. The time-dependent response is due to the consolidation process occurring in the clay produced on one hand by the drainage effect of the gallery and on the other hand by the stress release induced by the excavation. In order to reproduce the good magnitude of deformation in the lining, it is required to take into account the pre-stress induced by the installation of the key blocks.

However, only the results in the upper segments of ring 50 have been analysed up to now. When strains in lateral segments are investigated, it is observed that the extrados deformation is under-estimated by the numerical model. As a perspective, the creep effect in concrete lining and in Boom Clay could be considered to improve the prediction of the model.

References

Bastiaens, W., Bernier, F., Buyens, M., Demarche, M., Li, X., Linotte, J., Verstricht, J.: 2003 - EURIDICE - The Connecting Gallery - The Extension of the HADES Underground Research Facility at Mol, Belgium. 03-294. EURIDICE (2003)

Bernier, F., Li, X., Bastiaens, W.: Twenty-five years' geotechnical observation and testing in the Tertiary Boom Clay formation. Géotechnique **57**(2), 229–237 (2007)

Bernier, F., Li, X., Verstricht, J., Barnichon, J., Labiouse V., et al.:. CLIPEX: Clay Instrumentation Programme for the Extension of an Underground Research Laboratory. Nuclear Science and Technology, EUR 20619EN. Luxembourg: EURATOM (2003)

Cerfontaine, B., Dieudonné, A.C., Radu, J.P., Collin, F., Charlier, R.: 3D zero-thickness coupled interface finite element: formulation and application. Comput. Geotech. **69**, 124–140 (2015)

Collin, F., Li, X., Radu, J.P., Charlier, R.: Thermo-hydro-mechanical coupling in clay barriers. Eng. Geol. **64**, 179–193 (2002)

Dizier, A.: Caractérisation des effets de température dans la zone endommagée autour de tunnels de stockage de déchets nucléaires dans des roches argileuses. Univ. Liège, Belgium (2011)

François, B., Labiouse, V., Dizier, A., Marinelli, F., Charlier, R., Collin, F.: Hollow cylinder tests on Boom Clay: modelling of strain localization in the anisotropic excavation damaged zone. Rock Mech. Rock Eng. **47**, 71–86 (2014)

Salehnia, F., Collin, F., Li, X.L., Dizier, A., Sillen, X., Charlier, R.: Coupled modeling of excavation damaged zone in Boom Clay: strain localization in rock and distribution of contact pressure on the gallery's lining. Comput. Geotech. **69**, 396–410 (2015)

TIMODAZ: Deliverable D13 – Simulation of Lab and In Situ Tests. European commission (2010)

The Residual Shear Strength of the Shaly and Sandy Facies of the Opalinus Clay

Marco Rosone[1(✉)], Alessio Ferrari[1], Maurizio Ziccarelli[1], and Silvio B. Giger[2]

[1] Department of Civil Environmental, Aerospace, Materials Engineering (DICAM), Università degli Studi di Palermo, Palermo, Italy
marco.rosone@unipa.it
[2] National Cooperative for the Disposal of Radioactive Waste (NAGRA), Wettingen, Switzerland

Abstract. The paper presents a comprehensive laboratory campaign carried out with the aim to asses the residual strength of the Opalinus Clay. Ring shear tests with vertical effective stress up to 1 MPa were performed on remoulded samples of two different facies of the Opalinus Clay. Test results show that the «Shaly» facies is characterized by a low range of variation of residual strength while the strength of the «Sandy» facies is very sensitive to the variation of grain size distribution. Microstructural analyses (SEM) suggest that the difference in the observed mechanical behavior of the two facies can be related to different particles arrangements along the shear surfaces.

1 Introduction

Opalinus Clay shale formation is being considered as potential host geomaterial for geological repository for long-term radioactive waste disposal in Switzerland due to its favourable thermo-hydro-mechanical properties (Favero et al. 2016), self-sealing capacity of fractures (Gautschi 2017) and the aptitude to prevent the migration of radionuclides (Bossart et al. 2017). Opalinus Clay is deeply investigated at the Mont Terri Underground Research Laboratory (Canton Jura, Switzerland). In this deep formation three different facies can be distinguished (Bossart and Thury 2008): a Shaly facies consisting of mica-bearing marly shales with nodular zones or mm-thick layers including quartzous silty fraction; a Carbonate-rich Sandy facies characterised by quartz-bearing calcareous biodetritic layers up to 10 cm thick; and a Sandy facies which is a light-grey calcareous silty claystone with lenses of laminated silt and bioclastic material. The residual shear strength characterization takes on particular importance in consideration of the fact that a large tectonic fault zone, known as the "Main Fault", was observed in the centre of the Opalinus Clay formation at the Mont Terri site. Due to the geo-material complexity, the difficulties in sampling (fragile in nature) and shearing in the direction in which shear stress had occurred along the shear surface in the field (Stark and Hussain 2013), remoulded samples prepared in laboratory can be preferred for laboratory residual shear strength testing (Rosone et al. 2018b). Clearly, the fundamental role of the microstructure in the mechanical

A. Ferrari and L. Laloui (Eds.): SEG 2018, SSGG, pp. 426–433, 2019.
https://doi.org/10.1007/978-3-319-99670-7_53

behaviour of soils, both in saturated and unsaturated conditions, should also be taken into account (Leroueil and Vaughan 1990; Valore and Ziccarelli 2009; Burland 1990; Celauro et al. 2014; Mandaglio et al. 2016; Rosone et al. 2016, 2018a).

In this contribution, the drained residual shear strength parameters of two different facies of Opalinus Clay (Shaly and Sandy facies) obtained by means of Bromhead ring shear tests with vertical effective stress up to 1 MPa are reported. Furthermore, particular attention is paid on the microstructural arrangements of the material along the shear surface and on their influence on the residual shear resistance. To this regard, SEM observations are carried out on samples coming from the ring shear tests.

2 Tested Material

Opalinus Clay formation was formed as a marine sediment deposited in marine environments during the Jurassic period (Ziegler 1990). Opalinus Clay Shale presents different facies (Shaly, Sandy and Carbonate-rich Sandy facies) and is characterised by a multi-scale heterogeneous composition, typical fissile structure with well-defined bedding plane and intrinsic anisotropic behaviour (Ferrari et al. 2016; Favero et al. 2018). The samples used for the preparation of remoulded specimens are from the Mont Terri Underground Laboratory (Switzerland), which is located at depth of approximately 300 m, belong both to Shaly and Sandy facies. Some samples were stored in black PVC tubes filled with resin while other samples were coated with melted paraffin or even simply wrapped in transparent plastic films. Core sample storage in PVC tubes presented good condition while other samples were partially air-dried.

The main geotechnical properties and the classification (ASTM D2487) of intact samples belonging to different facies are reported in Table 1.

Table 1. Index properties and classification (ASTM D2487) of tested samples

Sample	G_s (–)	w_l (%)	w_p (%)	PI (%)	A (–)	Grain size fraction (%)				Class
						Gravel	Sand	Silt	Clay	
Shaly 1	2.76	45	24	21	0.60	0	4	61	35	CL
Shaly 2	2.68	38	24	14	0.24	0	11	32	57	CL
Sandy 1	2.75	32	20	13	1.07	49	21	18	12	GC
Sandy 2	2.71	25	15	10	0.50	25	19	37	19	CL

3 Experimental Procedures

Ad hoc procedures have been developed to prepare remoulded specimens since no international standards are available and no protocols have been so far developed and systematically applied for their preparation. Literature studies on remoulded clay samples (Burland 1990; Favero et al. 2016) were taken as a reference for the formulation of the preparation technique. Due to the reduced dimensions of the shear test box, the fraction passing a 0.425 mm sieve was selected for shaly materials while for

the preparation of remoulded samples of Sandy facies, both the fraction passing through 0.425 mm and 1.18 mm was considered. Hence, the slurry, having water content between the liquid limit (w_l) and $1.5w_l$, was prepared by mixing the soil with distilled water and strongly working with a metallic spatula on a glass sheet. The slurry was placed in the test box with the aid of a metallic spatula, and small portions of material were progressively disposed to avoid air trapping as much as possible. Ring shear tests were carried out by means of a ring shear apparatus, based on the original design developed by Bromhead (1979). The cell had an inside diameter of 7 cm, an outside diameter of 10 cm and an height equal to 0.5 cm. The vertical effective stress applied on the tested samples was in the range $\sigma'_v = 100 \div 1000$ kPa. Failure stages were carried out according to the ASTM standard method (D6467-13), which provides a pre-shear stage at high strain rate (3°/min corresponding to 2.2 mm/min) to rapidly accumulate large displacements (about 250 mm) on the shear surface and a second failure stage at low strain rate (0.024°/min corresponding to 0.018 mm/min), carried out with the aim to measure the residual strength in drained condition. In order to verify that the displacement rate was appropriate to ensure the drained conditions, some preliminary experimental checks were carried out. The failure stage was halted for 24 h in order to allow dissipation of excess of water pressure, if any. Then, the test started again with the same rate verifying that the shear strength did not increase. After the tests the samples were dried at 105÷110 °C for 20 min in order to simplify its extraction from the ring shear test box. For each facies analyzed, two different SEM (Scanning Electron Microscope) investigations on the same remoulded sample were carried out. In the first investigation the face of the shear surface was observed while in the second investigation the section of the same sample, containing the track of the shear surface was observed. Hence, microstructure analysis was carried out on samples coming from the ring shear tests. Energy dispersive X-ray analysis was carried out in order to identify the mineral composition of elements present along the fractured shear surface.

4 Results and Discussion

In order to highlight the mechanical behaviour of remoulded samples when large shear strains are accumulated along the shear surface, Fig. 1 reports the ratio between shear stress and vertical effective stress, τ/σ'_v, and the vertical displacement δ_v as a function of the horizontal displacement δ_h for tests carried out on shaly remoulded samples according to the ASTM test method. The stress-displacement curves of these specimens are characterized by a perfectly plastic evolution with nil or negligible volumetric variations, although horizontal displacements in the order of 250 mm were accumulated already during the pre-shear stage. Figure 1 also reports a test on a shaly specimen carried out with a unique failure stage at low strain rate (0.024°/min). In this way, peak and post-peak conditions are recognizable and after a slow reduction of shear strength and a contractive volumetric behaviour, mainly due to soil extrusion, the residual condition is clearly reached for horizontal displacements higher than 100 mm.

The comparison between tests carried out on specimens of Shaly facies applying the two different failure methods proves substantially the equality of test methods in terms of shear stress at residual condition. Figure 2 reports the result of ring shear tests on sandy remoulded samples in terms of ratio between shear stress and vertical effective stress as a function of the horizontal displacement. The comparison between test results shows that the residual shear strength of Sandy facies is strongly affected by the considerable variability of its grain size distribution. The Shaly facies is characterized by a low range of variation in τ/σ'_v. In fact, the ratio of shear stress to vertical effective stress varies between 0.154 and 0.192 and the corresponding value of the shear strength angle, for nil cohesion intercept, is $\varphi'_r = 8.8° \div 10.9°$. Instead, the shear strength of the sandy material is very sensitive to the variation of the grain size distribution, which characterizes this facies (see Table 1). In this case, the stress ratio τ/σ'_v ranges from about 0.31 to 0.53 when the selected fraction of specimen subjected to ring shear tests varies from passing to diameter 0.425 mm to passing to diameter 1.18 mm respectively (Fig. 2). For the material passing through sieve 1.18 mm the range of variation of the stress ratio at residual condition may be constrained between 0.40 and 0.53 (Fig. 2). To support this result, sandy remoulded specimens were subjected to grain size analysis by wet sieving after the ring shear tests. Results show that the higher ratio of shear stress may be justified by the higher content in sandy fraction rather than by a vertical effective stress effect. In fact, for the Sandy facies only the results of the tests carried

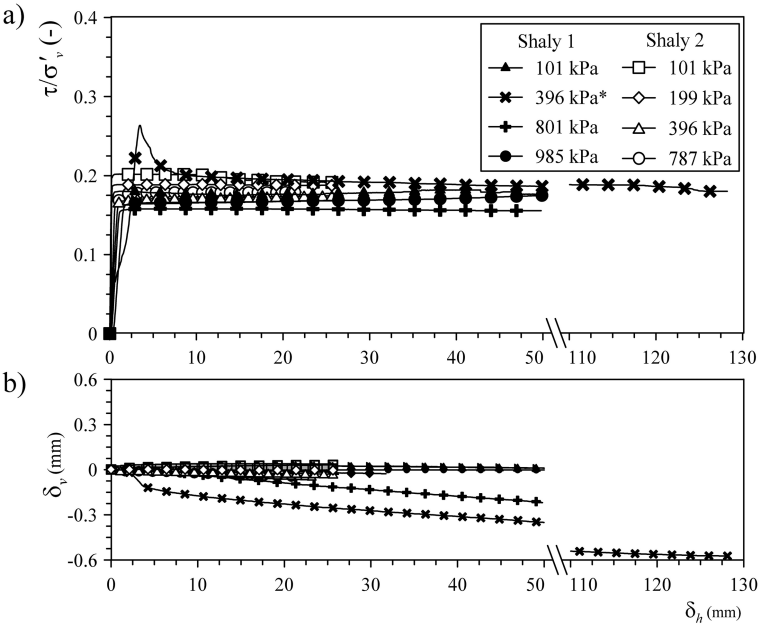

Fig. 1. Results of ring shear tests carried out on shaly remoulded samples (*test carried out according to traditional method): ratio between shear stress and vertical effective stress, τ/σ'_v, (a) and vertical displacement, δ_v, (b) in function of horizontal displacement, δ_h

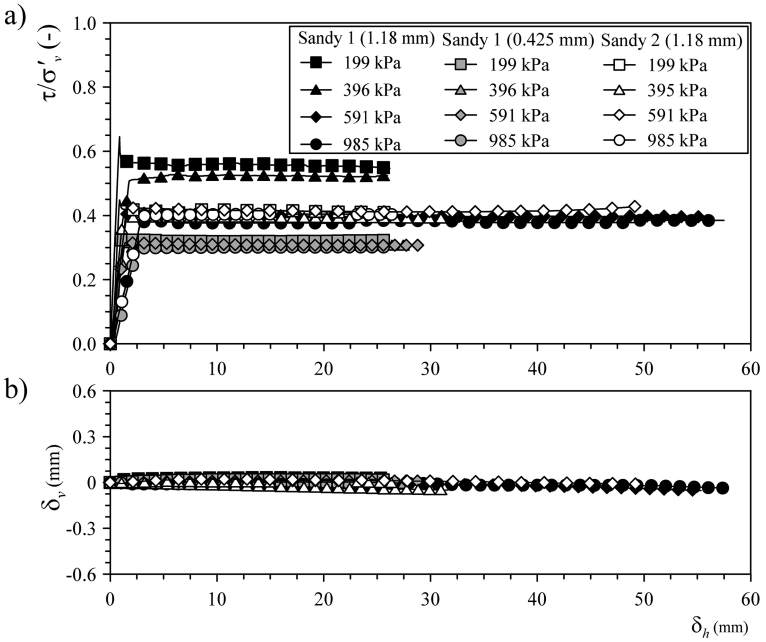

Fig. 2. Results of ring shear tests carried out on sandy remoulded samples: ratio between shear stress and vertical effective stress, τ/σ'_v, (a) and vertical displacement, δ_v, (b) in function of horizontal displacement, δ_h.

out on selected material passing through sieve 1.18 should be considered. In conclusion, the residual shear strength angle, for nil cohesion intercept, to be considered for the Sandy facies is $\varphi'_r = 21.8° \div 27.8°$.

The SEM observation of shaly sample at 50× (Fig. 3a) shows a slickensided surface caused by frictional displacements between the two sides of specimen during the ring shear test. In fact, the surface is clearly striated in direction of the movement (Fig. 3b). Very high magnification shows that on the shear surface flattened clay particles are iso-oriented (Fig. 3c), although some rounded silty grains of quartz are visible. The SEM observations of the section of the same sample reported in Fig. 3d shows preferential planes (shear band), having thickness of about 20–100 μm, along which several stacks of iso-oriented clay particles slided. Instead, a stepped surface opposite to the direction of the shear displacement is showed in Fig. 4a where a SEM observation at 100× of remoulded sandy sample is reported. Higher magnification (500× in Fig. 4b) shows the presence on the shear surface of partly rounded edged dark grey particles, having dimensions of sand and silt, made of some minerals which are not of clayey nature, i.e. Ca-rich Siderite, Pyrite and Quartz. SEM observations at 5000× (Fig. 4c) show that a well-defined and always continuous shear surface is not

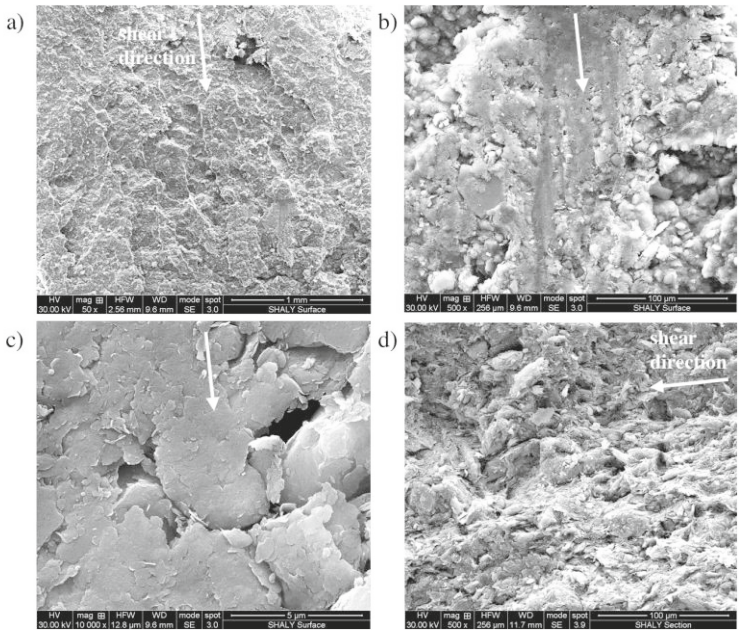

Fig. 3. SEM observations of remoulded shaly sample: a view of the slickenside shear surface at 50× (a) and 500× (b); iso-oriented flattened clay particles with rounded silty grains are visible at 10000× (c). SEM observation of the section of remoulded shaly sample shows preferential planes (shear bands) along which clay particles slided (d).

discernible but also pores having dimension up to 20 μm are visible. Also in the section (Fig. 4d), a zone having higher porosity is clearly evident at magnification of 250×. The microstructure of specimens at the end of ring shear tests is different from those of intact samples (Houben et al. 2013) due to the intense remoulded process applied for the specimen preparation and the shearing action along the failure surface during the tests. Furthermore, the SEM image analyses confirm that the mechanism of sliding mode (Lupini et al. 1981; Skempton 1985) develops on the shear surface in Shaly facies.

Observations of shear zone in sandy specimens indicate that the shear surface involve discontinuous sliding shear surfaces and pockets of soil behaving in the turbulent mode. This transitional shear behaviour, as shown in Fig. 2, is able to sustain a lower reduction of strength at residual condition as reported by Lupini et al. (1981) and Skempton (1985).

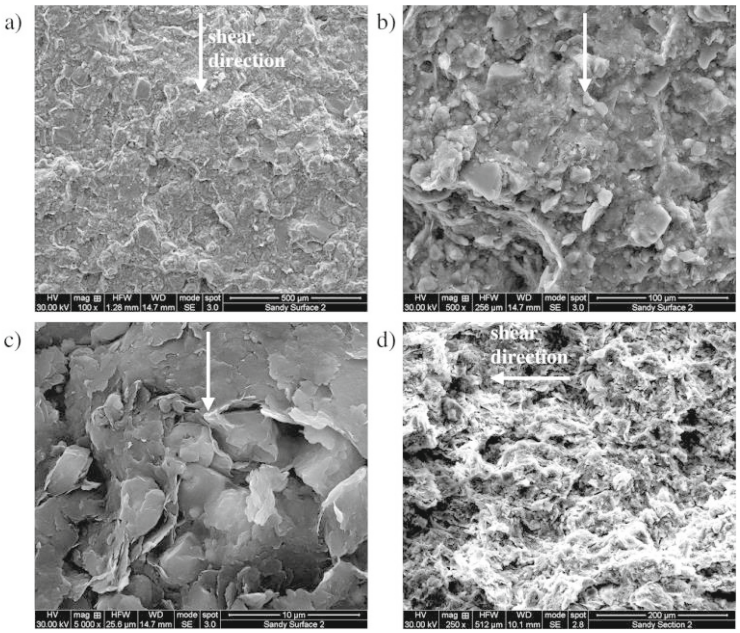

Fig. 4. SEM observations of remoulded sandy sample: a stepped surface opposite to the direction of shear displacement is clearly visible at 100× (a); higher magnifications (500× in b) show the presence on the shear surface of partly rounded edged dark grey grains, with dimensions of sand and silt, made of some minerals which are not of clayey nature; SEM observations at 5000× of remoulded sandy sample do not show a well-defined and always continuous shear surface (c) but also in section (d) at 250× zones having higher porosity are visible.

5 Conclusions

The paper pointed out the effects of the large cumulated shear strains on the residual shear strength of the Shaly and Sandy facies of the Opalinus Clay. The Shaly facies is characterized by a low variation in residual strength, while the strength of the sandy material is very sensitive to the variation of grain size distribution, which, by the way, is a peculiarity of this facies. The microstructural analyses prove that different arrangements of the material along the shear surface mark the two facies. A slickenside surface, made of several stacks of iso-oriented clay particles, was observed in the Shaly facies. Instead, a stepped surface opposite to the direction of shear displacement was observed in remoulded samples of the Sandy facies. This shear zone was also characterized by heterogeneous particles rearranged in a high porosity system and discontinuous shear surface.

References

Bossart, P., Bernier, F., Birkholzer, J., Bruggeman, C., Connolly, P., Dewonck, S., Fukaya, M., Herfort, M., Jensen, M., Matray, J.-M., Mayor, J.C., Moeri, A., Oyama, T., Schuster, K., Shigeta, N., Vietor, T., Wieczorek, K.: Mont Terri rock laboratory, 20 years of research: introduction, site characteristics and overview of experiments. Swiss J. Geosci. **110**(1), 3–22 (2017)

Bossart, P., Thury, M.: Mont Terri Rock Laboratory. Project, programme 1996 to 2007 and results. Wabern: Reports of the Swiss Geological Survey no. 3 (2008)

Bromhead, E.: A simple ring shear apparatus. Ground Eng. **12**(5), 40–44 (1979)

Burland, J.B.: On the compressibility and shear strength of natural clays. Géotechnique **40**(3), 329–378 (1990)

Celauro, C., Ziccarelli, M., Parla, G., Valore, C.: An automated procedure for computing the packing properties of dense and locked sands by image analysis of thin sections. Granul. Matter **16**(6), 867–880 (2014)

Favero, V., Ferrari, A., Laloui, L.: On the hydro-mechanical behaviour of remoulded and natural Opalinus Clay shale. Eng. Geol. **208**, 128–135 (2016)

Favero, V., Ferrari, A., Laloui, L.: Anisotropic behaviour of Opalinus Clay through consolidated and drained triaxial testing in saturated conditions. Rock Mech. Rock Eng. **51**(5), 1305–1319 (2018)

Ferrari, A., Favero, V., Laloui, L.: One-dimensional compression and consolidation of shales. Int. J. Rock Mech. Min. Sci. **88**, 286–300 (2016)

Gautschi, A.: Safety-relevant hydrogeological properties of the claystone barrier of a Swiss radioactive waste repository: an evaluation using multiple lines of evidence. Grundwasser **22**(3), 221–233 (2017)

Houben, M.E., Desbois, G., Urai, J.L.: Pore morphology and distribution in the Shaly facies of Opalinus Clay (Mont Terri, Switzerland): Insights from representative 2D BIB–SEM investigations on mm to nm scale. Appl. Clay Sci. 71, 82–97 (2013)

Leroueil, S., Vaughan, P.R.: The general and congruent effects of structure in natural soils and weak rocks. Géotechnique **40**(3), 467–488 (1990)

Lupini, J.F., Skinner, A.E., Vaughan, P.R.: The drained residual strength of cohesive soils. Géotechnique **31**(2), 181–213 (1981)

Mandaglio, M.C., Moraci, N., Rosone, M., Farulla, C.A.: Experimental study of a naturally weathered stiff clay. Can. Geotech. J. **53**(12), 2047–2057 (2016)

Rosone, M., Farulla, C.A., Ferrari, A.: Shear strength of a compacted scaly clay in variable saturation conditions. Acta Geotech. **11**(1), 37–50 (2016)

Rosone, M., Ferrari, A., Celauro, C.: On the hydro-mechanical behaviour of a lime-treated embankment during wetting and drying cycles. Geomech. Energy Environ. **14**, 48–60 (2018a)

Rosone, M., Ziccarelli, M., Ferrari, A., Farulla, C.A.: On the reactivation of a large landslide induced by rainfall in highly fissured clays. Eng. Geol. **235**, 20–38 (2018b)

Skempton, A.W.: Residual strength of clays in landslides, folded strata and the laboratory. Géotechnique **35**(1), 3–18 (1985)

Stark, T.D., Hussain, M.: Empirical correlations: drained shear strength for slope stability analyses. J. Geotech. Geoenviron. Eng. **139**(6), 853–862 (2013)

Valore, C., Ziccarelli, M.: The evolution of grain-size distribution of sands under 1-D compression. In: Hamza, M., et al. (eds.) Proceedings 17th ICSMGE—Alexandria, October 2009, vol. 1, pp. 84–88. IOS Press, Amsterdam (2009)

Ziegler, P.A.: Geological Atlas of Western and Central Europe. Shell Internationale Petroleum Maatschappij, The Hague (1990)

Experimental Investigation of Gas Transport in the Shaly Facies of Opalinus Clay

María Victoria Villar(✉), Francisco Javier Romero, Pedro Luis Martín, Vanesa Gutiérrez-Rodrigo, and José Miguel Barcala

CIEMAT, Madrid, Spain
mv.villar@ciemat.es

Abstract. An experimental setup was designed to measure gas permeability and gas breakthrough pressures in Opalinus clay samples. The confining pressures applied were higher than the maximum in situ stress, and the tests were performed by slowly increasing the injection pressure whereas backpressure was kept atmospheric and the outflow was measured. The breakthrough pressure perpendicular to bedding was generally higher than 18 MPa, which is consistent with the air entry values deduced from mercury intrusion porosimetry tests for this material, which was between 19 and 36 MPa. In samples with degrees of saturation lower than 70% flow occurred for lower gas injection pressures, and the effective gas permeability measured was in the range from $8 \cdot 10^{-21}$ to $4 \cdot 10^{-23}$ m^2, decreasing with confining pressure. The gas transport mechanism in those cases was probably 2-phase flow.

1 Introduction

The multiple-barrier concept for underground disposal of radioactive wastes invokes a series of barriers, both engineered and natural, between the waste and the surface. In the quantitative assessment of repositories it is necessary, among others, to understand gas generation and migration in the barrier system. Gas will be generated within the repository by several mechanisms, such as the anaerobic corrosion of metals, the microbial degradation of organic wastes and the radiolysis of water. It is expected that the maximum gas pressure builds up around the container and once gas arrives at the interface between the engineered barrier and the host rock it will flow along this interface into the backfill material that closes the galleries, whose gas permeability is higher. Gas transport along this interface would be guaranteed by the very low permeability values of clay host rocks, but this has to be checked and assessed.

The research presented here was conducted in the framework of the European Commission FORGE project with the aim of providing information on the gas transport characteristics of the shaly facies of the Opalinus clay, a plastic clay chosen as potential host rock in Switzerland.

A. Ferrari and L. Laloui (Eds.): SEG 2018, SSGG, pp. 434–441, 2019.
https://doi.org/10.1007/978-3-319-99670-7_54

2 Material

The material used in the tests came from a borehole drilled in the Opalinus Clay Mesozoic formation at the Mont Terri Underground Research Laboratory (URL) in the Folded Jura mountains (http://www.mont-terri.ch). This formation is a mainly marly claystone with differing proportions of sand and carbonates around 180 million years old (Aalenian). At the URL, the Opalinus Clay has a layer thickness of around 140 m.

From a mineralogical point of view the Opalinus Clay consists of 40–80% clay minerals (including mixed layers of illite and swelling smectite), 10–40% quartz, 5–40% calcite and smaller proportions of siderite, pyrite and organic carbon. The dry density range is between 2.20 and 2.41 g/cm^3, the water content between 5.0 and 8.9% and the hydraulic conductivity between $2 \cdot 10^{-14}$ and $1 \cdot 10^{-12}$ m/s (Marschall et al. 2004).

Of the three facies of Opalinus Clay, the materials used in this investigation belong to the shaly one, which is a homogeneous, barely visible laminated claystone with low sand content. For the gas permeability tests a core from borehole BDR-1 was used. The total suction of this core was measured at laboratory temperature (21 °C) with two capacitive sensors inserted in a suitable perforated hole. The equilibrium value was found to be 31.3 ± 0.1 MPa for a dry density of 2.33 g/cm^3 and water content of 6.4% (determined in samples drilled from the same core). The measured grain density for this sample was 2.71 g/cm^3.

The water retention curves of samples from cores BHT-1 and BHG-D1, also drilled in the shaly facies of the Opalinus clay, were determined under different conditions (Villar and Romero 2012). Through the fitting of these results to the van Genuchten expression, a capillary strength parameter, P_0, between 6 and 34 MPa was computed.

3 Methodology

A setup was designed to perform steady gas permeability measurements under different gas pressures (Fig. 1). The cylindrical sample was confined in a stainless steel isotropic cell that was filled with water and pressurised to the desired confining pressure. A high-pressure nitrogen source supplied the gas to a 300-cm^3 pressurised vessel (gas buffer), equipped with a pressure transmitter, from which nitrogen was injected on top of the sample. The gas injection pressure could be independently varied and maintained constant during the period of time necessary to get steady gas flow, while the gas backpressure was atmospheric and the outflow was measured. The gas outflow coming out from the bottom of the sample to the atmosphere was measured using a series of three gas-mass flowmeters with different ranges: 1000, 100, 10 or 2 STP cm^3/min, with a turndown of 1:50 (minimum value measured with acceptable accuracy 2% FS). Injection and confining pressures of up to 18 and 33 MPa, respectively, could be applied. The tests were performed at room temperature. Nitrogen was used as the permeating gas because it is relatively inert and has low water solubility.

The samples were drilled from the BDR-1 core in the sense perpendicular to bedding and they were later lathed to smooth the surface and obtain the right diameter as well as to ensure the parallelism of the cylinders' ends. The resulting specimens were

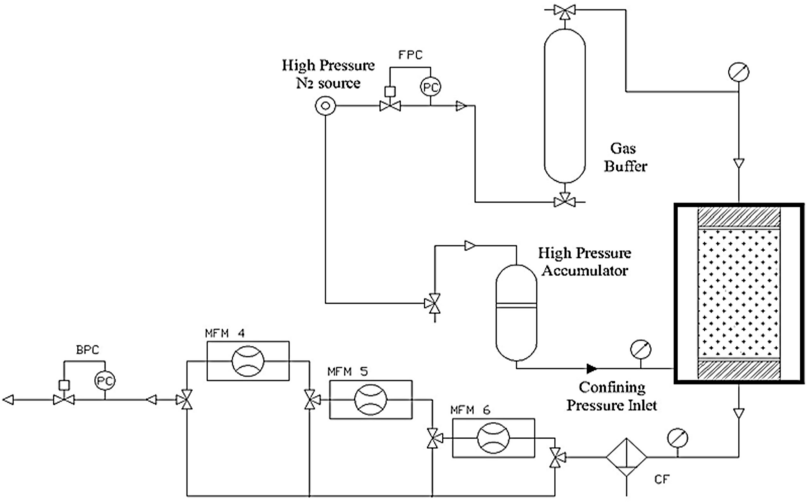

Fig. 1. Experimental setup (CF: coalescing filter, FPC: forward-pressure controller, BPC: back-pressure controller, MFM: mass flow meter)

1.2–3.0 cm in height and 9.2 cm^2 in surface area. Once the isotropic cell was filled with water, it was pressurised to 8 MPa, which is a value slightly higher than the maximum *in situ* stress at the Mont Terri URL (Corkum and Martin 2007), and gas was injected at a pressure of 0.5 MPa through the top of the sample. The pressure was increased by 0.5 MPa every 24 h, until reaching a value of 7 MPa. Then a confining pressure of 15 MPa was applied, either in steps or at a time. The injection pressure was also stepwise increased up to a value of 14 MPa. The process was repeated until reaching maximum confining pressures and injection pressures of 20 and 19 MPa, respectively. The exact pressure path followed differed between samples.

To compute the effective gas permeability, $k_{ig} \cdot k_{rg}$ (with k_{ig} being the intrinsic permeability measured with gas flow and k_{rg} being the relative permeability to gas), the outflow measurements were used, applying the following equation for incompressible media with compressible pore fluids (Scheidegger 1974):

$$k_{ig} \cdot k_{rg} = \frac{Q_m \times \mu_g \times L \times 2P_m}{A \times (P_{up}^2 - P_{dw}^2)} \tag{1}$$

where Q_m is the measured flow (volume of fluid as a function of time), A is the sample cross-sectional area, μ_g is the fluid dynamic viscosity, L is the sample length and P_{up} and P_{dw} are the upstream and downstream pressures applied at the top (inlet) and the bottom (outlet, atmospheric), respectively, of the sample, and P_m is the pressure of the measured flow (atmospheric pressure, because of the measurement conditions of the gas mass flowmeters).

4 Results and Discussion

Nine gas permeability tests were conducted, OPA1 to OPA9 (Villar et al. 2015). The average dry density of the samples was 2.31 ± 0.04 g/cm^3 and the water content of 4.5 ± 1.8% (S_r = 69 ± 22%). Hence although the samples tested were quite homogeneous in terms of dry density, the range of water contents was broad. The samples were not saturated prior to or during gas testing. Although no water was supplied during the tests, the degree of saturation during testing was probably higher than the initial one, because of the increase in density caused by confinement. This increase was checked by final measurement of the sample dimensions, since there was no sample volume control during the tests. Nevertheless the degrees of saturation of the samples were below 100% at the beginning and end of all the tests.

The total duration of the tests was between 400 and 2800 h. In most of them no correctly measurable outflow was detected, because the values were below the turndown value (accurate detection limit) of the flowmeters used. This would mean either that the flow was too low to be detected by the equipment used or that no flow took place because the pressures applied were below the air breakthrough value. In some instances, even if the flow was below the turndown value of the flowmeter, values higher than 0 were recorded. This is probably an indication of non-steady flow. In this sense, the flows recorded could be at least representative of qualitative trends, even if they are not valid to compute correct permeabilities. This is particularly so in those cases in which the measurement of small flow was accompanied by pressure decreases in the upward gas buffer.

In those cases in which correctly measurable flow occurred, the effective gas permeability could be computed and the values shown in Fig. 2 were obtained. The three samples in which flow took place had initial water contents below 4% and degrees of saturation below 70%. The effective gas permeability values were in the range from $8 \cdot 10^{-21}$ to $9 \cdot 10^{-22}$ m^2 and decreased for each sample as the confining pressure was higher. The increase in injection pressure resulted in all cases in an increase in the measured outflow (Q_m), but this did not always translate into an increase in permeability because of the change in other factors affecting the computation of permeability with Eq. 1 (namely the increase in P_{up}, which compensated the increase in Q_m). The final water content and dry density of the samples was systematically checked. Overall, gas testing did not result in major changes in any of these properties. Only in tests OPA6 and OPA9 the water content of the sample decreased during gas testing, which would indicate that some water displacement took place in these instances, but not in the other tests in which no gas flow was measured.

During the test OPA9 the sample consolidated from a dry density of 2.36 to 2.39 g/cm^3. At the end of this test the sample was cut into three parts (upper, from which gas was injected, middle and bottom). Fragments of each part were lyophilised and their pore size distribution was determined by mercury intrusion porosimetry (MIP). Figure 3 shows the pore size distribution determined after gas testing at these levels. Most of the pore sizes were comprised in the range 2–50 nm, i.e. in the mesopore range, with a dominant pore size mode between 8 and 15 nm, which would correspond to air entry values calculated from the Laplace's equation between 19 and

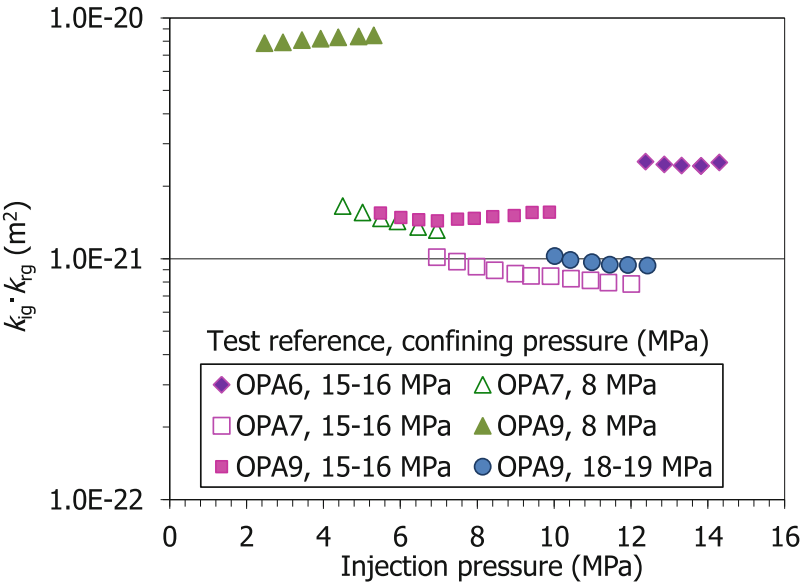

Fig. 2. Gas permeability values obtained in samples of Opalinus clay of borehole BDR-1

36 MPa. Only the uppermost sample, which was the one through which gas was injected, presented a higher percentage of macropores (28%) and these with a larger pore size mode. The Figure shows also the pore size distribution for a sample of Opalinus clay from borehole BHG-D1 (Villar and Romero 2012). This sample had not been submitted to gas testing and its dry density was 2.4 g/cm^3 and water content 3.4% (slightly air-dried). The dominant pore mode (11 nm) would correspond to an air entry value of 28 MPa. The percentage of macropores was clearly higher (37%) than for the sample tested, which could be explained by the confining stress to which the OPA9 sample was submitted during gas testing.

Since all the specimens tested came from the same borehole, had similar initial dry densities and were submitted to similar gas pressure paths, it is remarkable that flow was measured only in a few cases. The possible effect of the size of the specimens on flow was checked (Villar et al. 2015), but it was not possible to clearly relate flow and height of the sample. Hence, except for some experimental artefacts, such as the proper restraining of the sample in the cell or the slight temperature variations, it is concluded that the natural variability of the rock and the existence of features such as calcite veins or cracks, which were observed under a stereomicroscope and could act as preferential pathways, could be the cause of the different behaviour between samples. The variability was particularly significant in terms of initial water content and degree of saturation, and in fact flow was recorded only in those samples with degrees of saturation lower than 70%.

Nevertheless, with the devices available, it was not possible to measure steady flow in most cases, which indicates that the flow was too low to be measured (maybe because it was turbulent) or that the gas breakthrough pressure in the sense

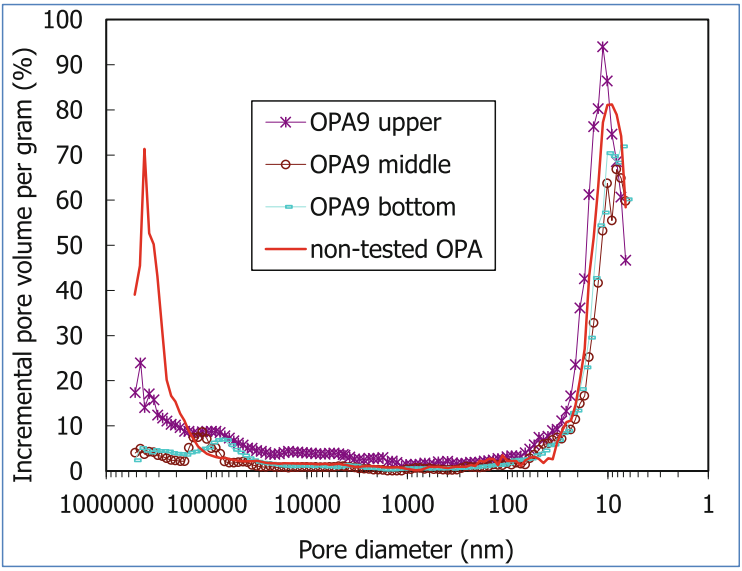

Fig. 3. Final pore size distribution obtained by MIP at three levels along sample OPA9 (after gas testing) and for an Opalinus clay sample from borehole BHG-D1

perpendicular to bedding was higher than 18 MPa, which was the maximum injection pressure applied. In fact, this value is below the air entry value deduced from mercury intrusion porosimetry (Fig. 3), which was between 19 and 36 MPa in the specimen OPA9 analysed at the end of the test and of 28 MPa in an Opalinus clay sample taken from core BHG-D1. The air entry value is the suction above which air is able to enter the pores of the sample, and consequently, above which 2-phase flow can take place in the soil pore structure. Additionally, the capillary strength parameter (P_0) of the van Genuchten expression fitted to results of the water retention curve of samples from boreholes BHG-D1 and BHT-1 was between 6 and 34 MPa, and tended to be higher for the samples tested under 8-MPa stress, in drying paths and when total suction was used (Villar and Romero 2012). This parameter is interpreted as representing the capillary pressure at which a continuous gas path is established and is frequently assimilated to the air entry value. Hence, it seems that the maximum injection pressure applied in the tests presented here was slightly below the air entry value of the material, which could explain why flow was only measured in a few instances.

In test OPA4 the sample was saturated with deionised water after the gas injection test. A hydraulic gradient was then imposed under a confining stress of 1.5 MPa and the hydraulic conductivity was measured in the direction perpendicular to bedding. The hydraulic conductivity obtained under effective stress conditions of 0.8 MPa (void ratio 0.24) was $2.7 \cdot 10^{-14}$ m/s (corresponding to an intrinsic permeability of $2.7 \cdot 10^{-21}$ m^2). Afterwards a gas injection test was carried out again. Although no reliable gas flow was measured before or after saturation (it was too close to the turndown value of the flowmeters), the tentative flow values recorded were consistently and considerably lower after saturation.

In the air-injection tests in the sense normal to bedding performed by Senger et al. (2014) in Opalinus clay samples coming from borehole BHA-8/1, continuous gas flow occurred at an injection pressure of 12 MPa under an isotropic confining stress of 15 MPa. The P_0 van Genuchten parameter for the material used in these tests was 18 MPa (Romero et al. 2012), thus lower than for the material tested here. The different methodology followed by these authors to perform the gas permeability tests could also be the reason for the lower breakthrough pressure found by them. They injected air at fast volumetric-controlled rate and breakthrough took place in less than 10 min. These authors found that during gas injection, expansion and a corresponding increase in void ratio occurred associated with gas migration into the pore space of the core samples and effective stress decrease caused by the pore pressure increase. Gas continued to migrate into the expanding pores prior to the breakthrough response, which suggests that preferential gas paths were developed at increasing injection pressures, resulting in higher gas mobility and a corresponding rapid pressure recovery following gas breakthrough.

5 Conclusions

The gas injection tests reported showed that the breakthrough pressure in the sense perpendicular to bedding of the shaly facies of the Opalinus clay was higher than 18 MPa (for confining pressures of up to 20 MPa), although in a few instances flow occurred. This happened only for samples with degrees of saturation lower than 70% and the effective gas permeability ($k_{ig} \cdot k_{rg}$) measured in those cases was in the range from $8 \cdot 10^{-21}$ to $4 \cdot 10^{-23}$ m^2, decreasing with confining pressure. This would mean that 2-phase flow (without significant deformation of the pore space) was the mechanism for the gas flow observed in the samples with lower degree of saturation (which in fact slightly dried during testing, probably as a result of water displacement), whereas macroscopic fracture formation (fracking, dependent on the local stress state of the material) could be the gas transport mechanism for higher degrees of saturation, this requiring higher gas injection pressures.

The air entry value deduced from mercury intrusion porosimetry tests for this material was between 19 and 36 MPa, and this is consistent with the fact that these tests showed that the breakthrough pressure was higher than 18 MPa. This value is higher than the breakthrough pressure found for saturated Opalinus clay by other authors, which could be due to the natural inhomogeneity of the material or to the particularities of the experimental procedure.

References

Corkum, A.G., Martin, C.D.: Modelling a mine-by test at the Mont Terri rock laboratory, Switzerland. Int. J. Rock Mech. Min. Sci. **44**(6), 846–859 (2007)

Marschall, P., Croisé, J., Schlickenrieder, L., Boisson, J.Y., Vogel, P., Yamamoto, S.: Synthesis of hydrogeological investigations at the Mont Terri site (phases 1 to 5). In: Heitzmann, P. (ed.) Mont Terri Project-Hydrogeological Synthesis, Osmotic Flow. Reports of the Federal Office for Water and Geology, FOWG, Geology Series No. 6 (2004)

Romero, E., Senger, R., Marschall, P., Gómez, R.: Air tests on low permeability claystone formations. Experimental results and simulations. In: Laloui, L., Ferrari, A. (eds.) Multiphysical Testing of Rocks and Shales. Springer Series in Geomechanics and Geoengineering, pp. 69–83. Springer, Berlin (2012)

Scheidegger, A.E.: The Physics of Flow Through Porous Media, 3rd edn. University of Toronto Press, Toronto (1974)

Senger, R., Romero, E., Ferrari, A., Marschall, P.: Characterization of gas flow through low-permeability experiments and two-phase flow analyses. In: Norris, S., Bruno, J., Cathelinau, M., Delage, P., Fairhurst, C., Gaucher, E.C., Höhn, E.H., Kalinichev, A., Lalieux, P., Sellin, P. (eds.) Clays in Natural and Engineered Barriers for Radioactive Waste Confinement, pp. 531–543. Geol Soc Sp Pub 400, London (2014)

Villar, M.V., Romero, F.J.: Water Retention Curves of Opalinus Clay. Informes Técnicos CIEMAT 1262. Octubre 2012. CIEMAT, Madrid (2012)

Villar, M.V., Romero, F.J., Martín, P.L., Gutiérrez-Rodrigo, V., Barcala, J.M.: Gas Transport in Opalinus Clay. Informes Técnicos CIEMAT 1378. Diciembre 2015, p. 40. CIEMAT, Madrid (2015)

Anisotropic Behaviour of Shallow Opalinus Clay

Eleonora Crisci[1(✉)], Alessio Ferrari[1], Silvio B. Giger[2], and Lyesse Laloui[1]

[1] Swiss Federal Institute of Technology, EPFL, Lausanne, Switzerland
eleonora.crisci@epfl.ck
[2] National Cooperative for the Disposal of Radioactive Waste, NAGRA, Wettingen, Switzerland

Abstract. Opalinus Clay shale, the selected host geomaterial of a high-level radioactive waste repository in Switzerland, was sourced at shallow depth in a borehole in the northern part of the country. Pairs of specimens, retrieved from the same depth were prepared to be tested in oedometric conditions, with loading in the direction either parallel or perpendicular to the bedding planes. The results showed a marked anisotropy of the material response in the low effective stress ranges (<10 MPa), with stiffer response in the direction of the bedding planes. The anisotropy reduced markedly at higher effective stress levels ($\geq$ 10 MPa), resulting in similar compressibility in the two loading directions at the highest investigated effective stress level. Similarly, the computed hydraulic conductivity (via the consolidation theory) revealed larger differences in the low stress range, where the hydraulic conductivity is greater in the direction of the bedding planes.

1 Introduction

Opalinus Clay shale is the geological formation that has been selected to be the host geomaterial for the deep geological repository for the high-level radioactive waste in Switzerland. The formation is found all over the northern part of the country, at variable depths (outcropping at the surface and reaching depths of a few kilometres). The current depth variability of the formation is related to the geological history of the area, strongly affected by the forebulge in association of the Alpine orogeny leading to a southern dip of the Mesozoic strata.

The minimum depth for the construction of a radioactive waste repository is selected to meet the required isolation period ($\approx 10^6$ years) from possible geological processes (exhumation and erosion) which could affect barrier integrity.

To investigate the effect of exhumation on the barrier integrity, Opalinus Clay was sourced from a borehole in Northern Switzerland in which the formation is found at a very shallow depth (<100 m below ground). The current depth of the formation in this site is the result of an exhumation phenomenon, driven by glacial erosion, which occurred over the geological timescale, and brought the formation close to the surface from a much greater depth (likely in excess of 1000 m).

A. Ferrari and L. Laloui (Eds.): SEG 2018, SSGG, pp. 442–448, 2019.
https://doi.org/10.1007/978-3-319-99670-7_55

One-dimensional consolidation tests were performed on several specimens obtained from various depths. Two specimens, sourced from approximately the same depth were prepared to be tested in the direction either perpendicular or parallel to the bedding planes, to compare the results from the two directions, and gather information on the anisotropy of the material properties. The main findings regarding the anisotropic behaviour of the Opalinus Clay from shallow depth are discussed in this contribution, and an example of the obtained oedometric curves is reported.

2 Tested Material

The investigated shale is a sedimentary formation, deposited about 180 million years ago, that is mainly composed of clay minerals, carbonates and quartz (Mazurek 1999). The formation is characterized by low porosity, ranging from 0.09 to 0.24 for more superficial specimens, and low hydraulic conductivity, 10^{-10}–10^{-14} m/s (Nussbaum and Bossart 2008). The material is transversely isotropic, with the planes of isotropy corresponding to the sedimentation planes (also referred to as bedding). The anisotropy could be attributed to the reorientation of the clay particles, in the bedding direction, and to the depositional and post depositional phenomena.

A relevant part of the research until now was conducted on cores from the Mont Terri Underground Rock Laboratory (URL), where Opalinus Clay, estimated to have reached a maximum burial depth of approximately 1350 m (Mazurek et al. 2006), is found nowadays at about 300 m depth. Several works, studying the anisotropic features of Opalinus Clay have been conducted, and highlighted the anisotropy in the mechanical behaviour (e.g. Bossart and Thury 2008; Favero et al. 2018) and in the sensitivity to water saturation (Ferrari et al. 2014; Minardi et al. 2016). In particular, the stiffness of the material was found to be greater when loaded in the direction of the bedding planes, rather than in the orthogonal direction.

From the mentioned shallow borehole, several samples were sourced at different depths between 6 and 70 m and part of those were used for a laboratory geomechanical program. Some preliminary results, presented in Crisci et al. (2017), explored the similarities in the behavior of samples sourced at different depths.

Complete geotechnical characterization of the specimens was performed. The obtained geotechnical parameters vary among the specimens in the following ranges: void ratio e = 0.15–0.31; bulk density ρ = 2.31–2.53 Mg/m^3; particle density ρ_s = 2.74–2.79 Mg/m^3; water content w = 5–10%.

Grain size distributions of several samples from various depths were also obtained. The range of grain size distributions obtained via the mentioned procedure is reported in Fig. 1. The grain size distribution of sample L8, later mentioned for the oedometric behavior, is highlighted. The samples showed a higher percentage (70–95%) of particles with sizes in the silt-clay range, coherent with the expected average mineralogical composition. Only a small percentage of sand size grains was detected.

The sample microstructure was investigated using the Mercury Intrusion Porosimetry (MIP) technique on cubic specimens with side of 0.8 cm, showing a single dominant pore size in the range of 15–30 nm of pore throat diameter.

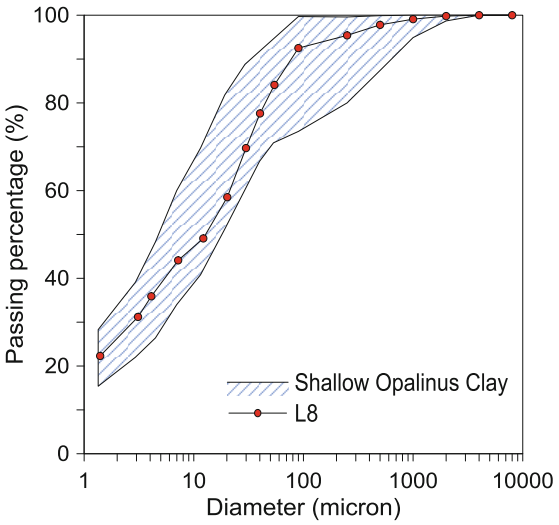

Fig. 1. Grain size distribution range obtained on Opalinus Clay samples from shallow depths; sample L8 curve is highlighted.

3 Testing Methods

The specimens for one-dimensional testing were obtained with a procedure finalized to minimize the damage to the specimens. A slice of thickness approximately double the final specimen height was sawed from the core, before removing the PVC tube and aluminum foil where the core is stored. Then, the slice was cut to obtain a smaller block, whose surface was smoothed and reduced to the desired size by the use of a lathe. The sample was finally inserted in the oedometric ring, made of stainless steel, using a hydraulic press.

A high pressure oedometric cell, designed to perform loading-unloading cycles at high stress levels (Ferrari and Laloui 2013), was used in this experimental program to perform one-dimensional consolidation and permeability test. The cell was designed to hold cylindrical specimens of 35 mm in diameter and 12.5 mm in height. The oedometer ring was inserted into a rigid stainless steel frame.

In this setup, the loading ram is positioned in the lower part of the system and a hydraulic jack connected to a volume/pressure controller applies the vertical load. The maximum applicable vertical total stress to the specimens is about 100 MPa. The volumetric strains are measured by two LVDTs (with a resolution of 1 μm), which are fixed to the frame and are in contact with the loading ram. The tests are performed in incremental loads, and a pore water pressure controller is used to control the pore water pressure at the bottom and top bases of the specimen.

The specimens were first re-saturated inside the oedometric cell at constant-volume condition. To constrain the swelling induced by the saturation, the vertical load was increased in steps to counterbalance axial expansion until equilibrium. Specimen saturation and loading/unloading steps were performed using synthetic water, following

preliminary results of in situ water analysis (complete recipe in Mazurek et al. 2017), in order to reproduce closely the chemical composition of the in situ pore water at different depths. At each loading step, the induced water overpressure was allowed to dissipate from the two end surfaces of the cylindrical specimen and the settlements were recorded.

The results in terms of settlements versus time for each loading/unloading step were interpreted using an analytical solution that extends the one-dimensional consolidation theory to consider the poroelastic behaviour of shales and the non-instantaneous loading condition (Ferrari et al. 2016), that is necessary to apply such high stresses.

4 Results

The tests allow estimating for each specimen the swelling pressure generated upon saturation, the compressibility (C_c) and swelling (C_s) indexes. In addition, from the analysis of the settlement versus time curve for each loading/unloading step, the consolidation coefficient (c_v), the oedometric modulus (E_{oed}) and the hydraulic conductivity (k) were computed.

In Fig. 2, examples of oedometric curves obtained for two specimens, from the same depth, tested in two different loading directions is documented. The results are reported in terms of vertical deformation, attained at the end of the primary consolidation of each loading step, versus the vertical effective stress applied. Similar curves were obtained for all the performed tests. The compression tests began at the and of the saturation phase, therefore the first point corresponds to vertical load needed to constrain the swelling induced by the saturation phase (i.e. the swelling pressure), and was found to be higher for specimens loaded in the direction perpendicular, rather than for those in the direction parallel to the bedding planes.

Generally, the overall vertical deformations obtained for the specimens tested in the direction perpendicular to the bedding was found to be higher compared to the orthogonal direction. A higher rigidity was detected for the specimens loaded in the direction of the bedding planes, in agreement with findings from previous works. Moreover, a transition in the behavior were identified as a change of slope in the semi-log curves (i.e. the apparent pre-consolidation pressure), occurring at a vertical stress ≈2–4 times higher in specimens loaded in the direction parallel to the bedding. Above these stress levels, the differences in rigidity between samples loaded parallel and perpendicular to bedding reduced, leading to comparable compressibility values.

It can be inferred that at high stress levels the cement bonds, attributed to the diagenetic process occurred in the Opalinus Clay (Favero et al. 2016), are weakened, and that the compressibility on which the material behavior relies depends only on the particle properties and arrangement. As the stress increases, the porosity reduces and the material compressibility reduces towards the one of the solid particles.

The consolidation theory was adopted to evaluate the hydraulic conductivity of the tested specimens, in the two loading directions. The obtained results were found to be in line with results from previous works, with ranges of hydraulic conductivity found in

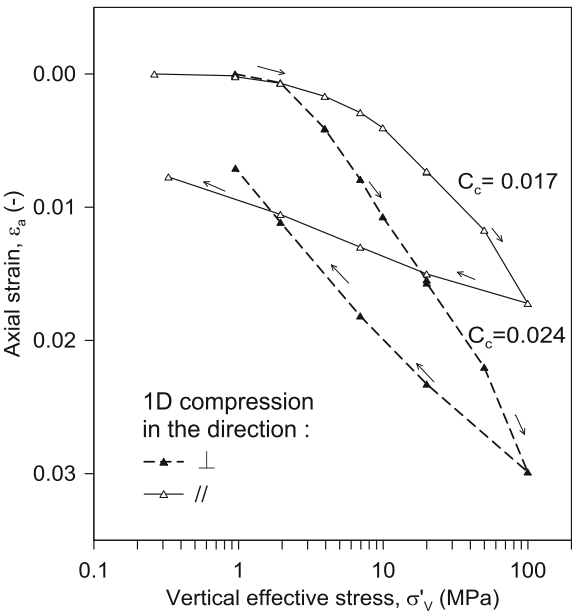

Fig. 2. End of primary consolidation curves of two Opalinus Clay specimens from the same depth tested in the direction perpendicular and parallel to the bedding planes.

the order of 10^{-11}–10^{-14} m/s for all the tested specimens in a vertical effective stress range varying from few MPa to 100 MPa.

Concerning the hydraulic conductivity anisotropy, a trend similar to the compressibility response was found. The results of the hydraulic conductivity (k) were analyzed in terms of ratios of the values obtained for specimens loaded parallel to the bedding and specimens loaded perpendicular to the bedding ($k_{//}/k_{\perp}$). The results for all the pairs of performed oedometric tests are presented in Fig. 3, in form of the ratio $k_{//}/k_{\perp}$ versus the vertical effective stress at the beginning of the steps.

By and large, the ratios are above 1, highlighting the higher hydraulic conductivity measured in the direction of the bedding planes. At low stresses the hydraulic conductivity is ≈2–4 times higher for flows in the direction parallel to the bedding planes compared to the orthogonal direction. Moreover, a high variability in the results is observed, while towards high stresses, the variability reduces and the ratios tend to be closer to the unity. Therefore, the differences among the flow directions are significantly reduced at high compaction levels.

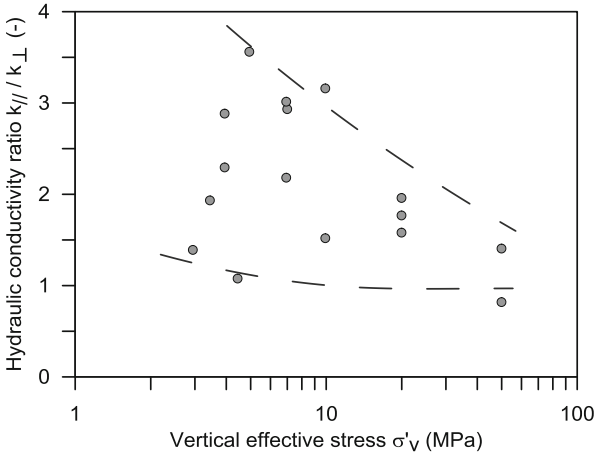

Fig. 3. Ratio of the hydraulic conductivities (in the direction // and ⊥ to the bedding planes) computed via the consolidation theory, on primary loading steps.

5 Concluding Remarks

In this work, results obtained from an experimental programme on shallow Opalinus Clay samples were presented. The investigation focused on the hydro mechanical behaviour of saturated intact shale in one-dimensional loading conditions. Pairs of specimens from the same depth were obtained to be loaded either parallel or perpendicular to the bedding plane and to compare the results.

The main findings revealed that the compressibility of the saturated samples is higher for the direction perpendicular to the bedding, and for those same specimens the change in slope (in the semi-log plane) is detected at lower stress values. Towards high stresses, on the other hand, the differences between the two loading directions reduced, and a similar compressibility was found.

The outcomes regarding the hydraulic conductivity, derived from the results of the primary loading steps, showed similar trends. At low stress level, the differences between the pairs of specimens, loaded in different directions, is higher, and it is shown a higher hydraulic conductivity in the direction of the bedding planes. As stress increases and the porosities reduce, the hydraulic conductivity becomes similar in the two directions.

Therefore, the anisotropic hydro-mechanical behaviour of Opalinus Clay, in particular in terms of one-dimensional compressibility and hydraulic conductivity, is strongly dependent on the range of stress applied, and tends to reduce at very high stresses towards similar responses in the directions perpendicular and parallel to the bedding planes.

Acknowledgements. The support of the Swiss National Cooperative for the Disposal of Radioactive Waste (NAGRA) for this research is acknowledged.

References

Bossart, P., Thury, M.: Mont Terri rock Laboratory. Project, Programme 1996 to 2007 and results. Reports of the Swiss Geological Survey (2008)

Crisci, E., Ferrari, A., Giger, S., Laloui, L.: One dimensional consolidation of Opalinus Clay from shallow depth. In: Advances in Laboratory Testing and Modelling of Soils and Shales (ATMSS). Springer Series in Geomechanics and Geoengineering. Presented at the Advances in Laboratory Testing and Modelling of Soils and Shales, pp. 338–344. Springer, Cham (2017). https://doi.org/10.1007/978-3-319-52773-4_39

Favero, V., Ferrari, A., Laloui, L.: Anisotropic behaviour of Opalinus Clay through consolidated and drained triaxial testing in saturated conditions. Rock Mech. Rock Eng. **51**, 1305–1319 (2018). https://doi.org/10.1007/s00603-017-1398-5

Favero, V., Ferrari, A., Laloui, L.: On the hydro-mechanical behaviour of remoulded and natural Opalinus Clay shale. Eng. Geol. **208**, 128–135 (2016). https://doi.org/10.1016/j.enggeo.2016.04.030

Ferrari, A., Favero, V., Marschall, P., Laloui, L.: Experimental analysis of the water retention behaviour of shales. Int. J. Rock Mech. Min. Sci. **72**, 61–70 (2014). https://doi.org/10.1016/j.ijrmms.2014.08.011

Ferrari, A., Favero, V., Laloui, L.: One-dimensional compression and consolidation of shales. Int. J. Rock Mech. Min. Sci. **88**, 286–300 (2016). https://doi.org/10.1016/j.ijrmms.2016.07.030

Ferrari, A., Laloui, L.: Advances in the testing of the hydro-mechanical behaviour of shales. In: Multiphysical Testing of Soils and Shales, pp. 57–68. Springer (2013)

Mazurek, M.: Mineralogy of the Opalinus Clay. In: Thury, M., Bossart, P. (eds.) Mont Terri Project: Results of the Hydrogeological, Geochemical and Geotechnical Experiments Performed in the Opalinus Clay (1996–1997) (1999)

Mazurek, M., Hurford, A.J., Leu, W.: Unravelling the multi-stage burial history of the Swiss Molasse Basin: integration of apatite fission track, vitrinite reflectance and biomarker isomerisation analysis. Basin Res. **18**, 27–50 (2006)

Mazurek, M., Wersin, P., Hadi, J.: Opalinus Clay in the shallow decompaction zone: geochemical investigations on drill core samples from borehole Lausen KB (No. NAB 16-58) (2017)

Minardi, A., Crisci, E., Ferrari, A., Laloui, L.: Anisotropic volumetric behaviour of Opalinus Clay shale upon suction variation. Géotech. Lett. **6**, 144–148 (2016). https://doi.org/10.1680/jgele.16.00023

Nussbaum, C., Bossart, P.: Geology—Mont Terri rock Laboratory. Project, Programme 1996 to 2007 and results, Bern (2008)

Others Geotechnical Activities Related to the Energy Sector

Dynamic Responses of Jacket Foundation Offshore Wind Turbine Considering the Cyclic Loading Effects

Wenjie Zhou(✉), Zhen Guo, Lizhong Wang, and Shenjie Rui

Zhejiang University, Hangzhou, China
zhouwenjiesd@163.com

Abstract. With increasing of offshore wind turbines (OWTs) in recent years, the supporting structure are needed to suite the cases with water depth greater than 100 m. In such cases, the effects of wind, wave and current become much obvious, and jacket support structure are recommended for the OWTs. During the service period, the soil-pile interaction has a significant effect on the dynamic response of the OWT structure. Thus, this paper aims to first investigate the characteristics of soil-pile interaction under the cyclic loadings, and then study the dynamic responses of the jacket support OWTs. Based on the bounding surface elasto-plastic theory, the cyclic *t-z* curve is proposed, which used to simulate the load-displacement relationships along the pile shaft. Related parameters can be analyzed and calibrated based on the constant normal stiffness cyclic direct shear test of pile-soil interface. The cyclic *t-z* curves are programmed using the software COMSOL, and used in the FEM model for the dynamic simulation of jacket foundation OWT. Under two-way sinusoidal regular load case, the dynamic responses of jacket foundation OWT are simulated and studied. The results show that the API *t-z* curve will underestimate natural frequency, which leads to insecure design for jacket foundation OWTs. And the proposed cyclic *t-z* model can reflect natural frequency degradation under cyclic loading, which can well evaluate the dynamic response than API method.

1 Introduction

The soil-pile interaction has a significant effect on the dynamic response of the OWT structure, including natural frequency degradation, permanent accumulated rotation (Wei et al. 2015; Carswell et al. 2016). The current design methods are based on the elastic theory in the API (2007) and DNV (2013) codes, so, the code methods can't consider the natural frequency change under cyclic loads. Dong (2012) proposed a *p-y* model based on the boundary surface elasto-plastic theory, which can simulate the soil-pile interaction under cyclic loading. McCarron (2016) proposed a boundary surface model for soil resistance to cyclic lateral pile displacement with arbitrary direction.

Compared to monopile, the pile resistance of jacket foundation mainly depend on the tension and pression which results that the *t-z* curve has great effect on the dynamic response of OWTs. This paper aims to first investigate the characteristics of soil-pile

A. Ferrari and L. Laloui (Eds.): SEG 2018, SSGG, pp. 451–458, 2019.
https://doi.org/10.1007/978-3-319-99670-7_56

interaction (t-z curve) under the cyclic loadings, and then study the dynamic responses of the jacket support OWTs. Related parameters in cyclic t-z model can be calibrated by cyclic direct shear test of pile-soil interface. The intention is to develop a new method to evaluate the dynamic response of jacket OWTs.

2 Boundary Surface Model Theoretical Framework

Traditional p-y, t-z curves aren't suitable for cyclic loading and two-way loading. Based on the boundary surface theory, this paper developed a t-z model, which has cyclic weakening effect.

2.1 Elasto-Plastic Cyclic t-z Model

Model Building

The t-z model relating the pile axial displacement z at a certain depth and the pile axial resistance t for unit area. The displacement increment dz caused by the resistance increment dt is decomposed into elastic part and plastic part, which are showed in Fig. 1, and this can be described as:

$$dz = dz^e + dz^p \tag{1}$$

where dz^e, dz^p are the elastic, plastic displacement increment respectively.

$$\text{For elastic resistance factor:} \quad K_e = \frac{dt}{dz^e} \tag{2}$$

$$\text{For plastic resistance factor:} \quad K_p = \frac{dt}{dz^p} \tag{3}$$

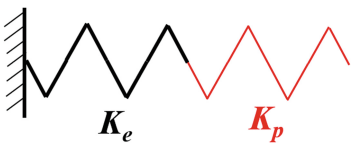

Fig. 1. Constitution of soil-pile interactive spring

The elastic-plastic resistance factor relating the resistance increment dt and the axial displacement increment dz is of the form:

$$K_{ep} = \frac{1}{\frac{1}{K_e} + \frac{1}{K_p}} \tag{4}$$

Firstly, define the boundary,

$$p_{\max} = p_m, \tag{5}$$

$$p_{\min} = -p_m, \tag{6}$$

and the boundary length is

$$\overline{\rho} = 2p_m. \tag{7}$$

In the Eqs. 5–7, p_m is the maximum soil-pile interface friction in a certain depth in history. When $dp > 0$, ρ is the distance between the minimum boundary $-p_m$ and the current p; When $dp < 0$, ρ is the distance between the maximum boundary p_m and the current p. That is to say, when

$$dp \cdot p > 0, \quad \rho = p_m + |p|; \tag{8}$$

when

$$dp \cdot p < 0, \quad \rho = p_m - |p|. \tag{9}$$

Dong (2012) gives the plastic resistance factor K_p expression in p-y model:

$$K_p = hK_e f(y^p)(p_u/p_m \cdot \bar{\rho}/\rho - 1) \tag{10}$$

where h is curve shape parameter, $f(y^p)$ is degradation function:

$$f(y^p) = (\rho/\bar{\rho})^n + e^{-\alpha\frac{\int |dy^p|}{y_r}}[1 - (\rho/\bar{\rho})^n] \tag{11}$$

where n is model parameters, equal to 10 and α is degradation parameter, $\int |dy^p|$ is accumulated plastic displacement of spring, y_r is the reference displacement.

The study found that for the t-z curve in sand, the displacement required for the soil-pile surface ultimate resistance is far less than that of p-y curve, which meas t-z curve in sand degradates slower than p-y curve. So, the degradation function in the reference (Dong 2012) is not suitable for soil-pile surface mechanics in sand under cyclic loading. In addition, parameters in the p-y model can't be calibrated using soil element laboratory tests.

This paper adopt the p-y curve theory framework in reference (Dong 2012) to develop a t-z model in which the parameters can be calibrated using soil element laboratory tests. And then, this paper develops a new t-z curve degradation function in sand, which makes results are in good agreement with the experimental results. The new degradation function is showed in Eq. 12:

$$g(y^p) = \frac{1}{\left(1 + \frac{\int |dy^p|}{y_r}\right)^a} - b \cdot \int |dy^p| \tag{12}$$

where a, b are model parameters.

Model Parameters' Calibration Based on Soil Element Laboratory Tests

In order to fix the parameters in the model at every depth, a certain simplification is needed to deal with the actual problems. The main assumptions are listed as follows:

(1) The same soil at different depth have the same displacement to reach the ultimate resistance.
(2) The same soil at different depth have the same friction angle of soil-pile interface.
(3) The same soil at different depth have the same degradation law in soil-pile surface mechanics.

Based on the three assumptions, model parameters at every depth can be confirmed.

(1) Elastic resistance factor K_e
Elastic resistance factor K_e is the initial tangent modulus for t-z curve, which is a constant in the model. The relationship between shear stress and shear displacement can be obtained by direct shear test of soil-pile interface, which is called τ-z curve. The initial tangent modulus of the τ-z curve is elastic resistance factor K_e.
(2) Capacity p_u
p_u is the ultimate strength of the soil-pile interface, which can be calibrated by direct shear test of soil-pile interface at a certain normal stress. In addition, p_u also can be estimated by Eq. 13:

$$p_u = \sigma \cdot \tan\varphi \cdot K \tag{13}$$

where σ is effective stress at a certain depth, φ is soil-pile surface friction angle, K is coefficient of lateral pressure, equal to 0.8.
(3) Curve shape parameter h
Curve shape parameter h controls the t-z curve's shape for monotonic loading, which can be calibrated through direct shear test of soil-pile interface.
(4) Degraded parameters a, b
Degraded parameter a, b control the stiffness degradation under cyclic loading. The test results found that the strength of the interface is greatly degraded after first cycle, and in the subsequent cycles, the strength degradation of the interface is smaller, as well as the gap between different cycles decreases gradually. Parameter a controls the strength degradation in the first cycle, b controls the strength degradation in the subsequent cycles. Through cyclic direct shear test of the soil-pile surface, parameters a, b can be obtained by fitting date or try method.

In this way, this part explanation can calibrate t-z model parameters based on soil element laboratory tests.

3 Engineering Application

This part is an example of engineering application to calibrate *t-z* model parameters based on the cyclic direct shear test of soil-pile surface results obtained from reference (Shang 2016). After parameters calibration, the cyclic *t-z* curves are programmed using the software COMSOL, and used in the FEM model for the dynamic simulation of jacket foundation OWT.

3.1 Introduction About Cyclic Direct Shear Test of Soil-Pile Surface

From reference (Shang 2016), the cyclic direct shear test of soil-pile surface under constant normal stiffness (CNS) condition has 10 mm shear displacement amplitude and 20 cycles, and the shear speed is 5 mm/min, the normal stress is 90 kPa. The sand used in test is China ISO standard sand, which d_{50} is 0.34 mm, D_r = 90%. The surface of steel plate is treated with polishing, and the roughness of the surface is close to the roughness of the steel pipe pile.

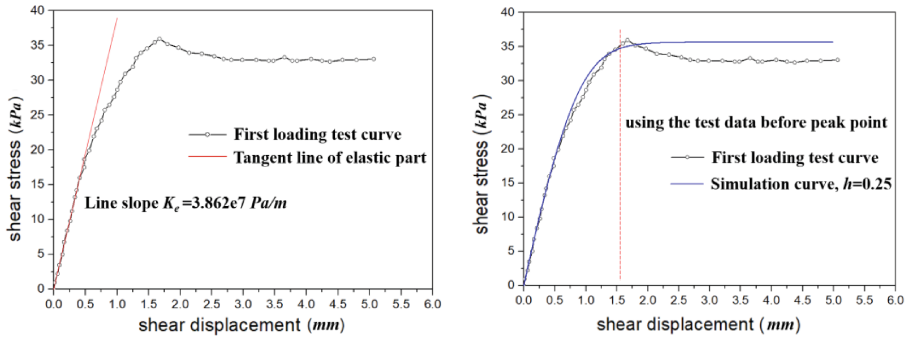

Fig. 2. Calibration of elastic resistance factor K_e (a) and curve shape parameter h (b)

3.2 *t-z* Model Parameters' Calibration

(1) **Elastic Resistance Factor K_e**
From the results of soil-pile surface cyclic direct shear test, the relationship between shear stress and shear displacement in the first loading can be obtained. In Fig. 2(a), it is can be seen that the first few points are approximated to a linear, so, the line's sloop is the elastic resistance factor K_e. In this case, $K_e = 3.862 \times 10^7$ Pa/m.

(2) **Curve Shape Parameter h**
Due to h control the shape of the stress-displacement curve, we can adjust the value of h to make the simulated curve fits in well with the first loading curve (before peak point). Figure 2(b) shows the comparison of simulation curve and test curve when h = 2.5.

(3) **Friction Angle of Soil-Pile Surface φ**
Friction angle of soil-pile surface φ can be obtained using Eq. 14.

$$\varphi = \arctan\left(\frac{\tau_{max}}{\sigma}\right) = \arctan\frac{35.21}{90} = 21.367^{\circ} \tag{14}$$

where τ_{max} is the peak strength in the first loading, σ is normal stress.

(4) **Degraded Parameters *a*, *b***
Due to the test data isn't complete, data fitting can't be carried out to calibrate *a*, *b*. In this case, using try method to calibrate *a*, *b*. Figure 3 shows the comparison between simulation and test date hysteresis loops when $a = 0.05$, $b = 0.55$. It can be seen that the simulation curve coincides with the test curve in general.

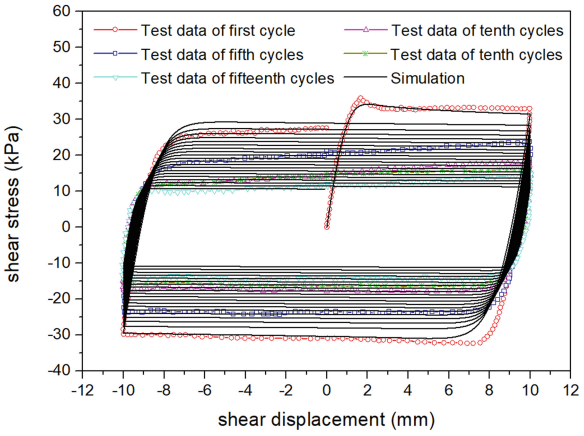

Fig. 3. Calibration of degradative parameters *a*, *b*

3.3 Brief Introduction About the Numerical Model

In this part, using FEM software COMSOL builds a numerical model to study the effect of cyclic degraded *t-z* curve to dynamic response of jacket foundation OWT. Some detail information about the jacket foundation OWT can be found in Table 1. The soil condition is assumed to the homogeneous sand which is the same with the above tested sand. The jacket foundation OWT numerical model is built by using the beam element, and the number of total elements are 224. To study the effect of cyclic *t-z* curve, this numerical model is combined with the API *p-y*, API *Q-z* and the cyclic *t-z*.

In this paper, one load case under two-way deterministic condition is investigated. The load direction is along the diagonal of the jacket structure which is the most dangerous case, and the point load magnitude acted on the hub is showed in Eq. 15.

$$F = 5000 \cdot \sin(2\pi \cdot f \cdot t) \quad [\text{kN}] \tag{15}$$

where f is the load frequency, $f = 0.1$ Hz.

Table 1. Jacket foundation and OWT's parameters

OWT parameters	Value
Rated power (MW)	4
Mass of rotor nacelle assembly (RNA) (t)	243.0
Tower length (m)	73.0
Pile length (m)	54.0
Pile diameter (m)	2.2
Water deep (m)	28.3
Foot distance of jacket bottom (m)	22.0
Foot distance of jacket top (m)	12.0

4 Results and Discussion

The numerical simulation founds that the first order natural frequency has degraded from 0.31942 to 0.31743 Hz after 18 cycles. Table 2 shows the initial natural frequencies, natural frequencies' change after 18 loading cycles and the natural frequencies obtained by using the API *t-z* curve.

The results show that the cyclic *t-z* model can consider natural frequency degradation after loading cycles. So, the method is more accurate to reflect the fact. At the same time, it can be seen that the natural frequencies obtained by using the API *t-z* curve is lower. A main problem in the jacket structure design is the global stiffness over the upper limit, so, using API *t-z* curve will underestimate natural frequencies which leads to insecure design.

Table 2. Comparation of first four order natural frequencies

Cycle number	First order (Hz)	Second order (Hz)	Third order (Hz)	Fourth order (Hz)
0	0.31942	0.31997	1.6133	2.173
18	0.31742	0.31972	1.6133	2.0884
API *t-z*	0.31432	0.31501	1.6133	1.9636

5 Conclusion

This paper developed a cyclic *t-z* model based on the boundary surface theory, and studied the cyclic *t-z* model's effects on the dynamic response of jacket foundation OWTs by using FEM method. The results show that the API *t-z* curve will underestimate natural frequencies, which leads to insecure design. And the proposed cyclic *t-z* model can reflect natural frequencies degradation under cyclic loading, which can better evaluate the dynamic response than API method.

References

American Petroleum Institute (API): Recommended practice for planning, designing and constructing fixed offshore platforms-working stress design. API Recommended Practice 2A-WSD (RP2A-WSD), Errata and Supplement 3, August 2007

Carswell, W., Arwade, S.R., Degroot, D.J., et al.: Natural frequency degradation and permanent accumulated rotation for offshore wind turbine monopiles in clay. Renew. Energy **97**, 319–330 (2016)

DNV, DNV-OS-J101: Design of Offshore Wind Turbine Structure. Det Norske, Vertas AS (2013)

Mccarron, W.O.: Bounding surface model for soil resistance to cyclic lateral pile displacements with arbitrary direction. Comput. Geotech. **71**, 47–55 (2016)

Shang, W.: Study on the Weakening Mechanism of Pile Soil Interface Under Cyclic Loading. Qingdao Technological University, Shandong (2016)

Dong, S.: Elastoplastic p–Y model and incremental finite element method for nonlinear foundation beams. J. Geotech. Eng. **34**(8), 1469–1474 (2012)

Wei, S., Park, H.C., Chung, C.W., et al.: Soil–structure interaction on the response of jacket-type offshore wind turbine. Int. J. Precis. Eng. Manuf. Green Technol. **2**(2), 139–148 (2015)

Numerical Simulation of Open Ended Pile Installation in Saturated Sand

Christian Moormann(✉), Sujith Gowda, and Shreyas Giridharan

Geotechnical Institute, University of Stuttgart, Stuttgart, Germany
christian.moormann@igs.uni-stuttgart.de

Abstract. Open-ended pipe piles have been the preferred choice for various foundation applications, and in particularly for offshore wind turbines. The need to know, well in advance, certain design parameters prior to installation thus arises, and through numerical analyses, ranges for these installation parameters, and the behavior of the sand surrounding the pile can be estimated. Offshore environment poses an additional challenge of taking into account not only the penetration process and effects of dynamic loading of the sand, but also the pore pressure built up in the soil skeleton. This paper presents a novel approach to simulate the dynamic installation process of open-ended piles in saturated soil. Thus, the simulation also provides the basis to predict the pile behavior due to axial or lateral loading considering the installation effects. By coupling the aspects of Lagrangian and Eulerian methods, a particle-based method, called Material Point Method (MPM), more specifically its extension called Convected Particle Domain Interpolation (CPDI) method has been employed in the present work. To simulate saturated media, an extension of CPDI is incorporated in the form of 2-phase formulation, different velocities for soil and water are considered and thus able to capture precisely the saturated-soil behavior. A 2-D axisymmetric model is considered, along with a penalty method formulation to calculate contact forces between pile and soil. This method, when applied in conjunction with the hypoplastic constitutive model, provides a framework which allows us to study detailed effects of pile installation on the surrounding soil.

1 Introduction

Open ended piles are mostly used for the foundations of offshore wind turbines. The ease of installation makes this a good option for the foundations. Various installation methods can be observed such as installation by hammering, vibration or by suction. During the installation process, soil around the pile is heavily distorted. Density of soil changes during the process which can be observed by the change of void ratio in the soil domain. The hypoplastic constitutive model used in the present work, deals with a concept where the soil stress state is related to the void ratio change. So, the bearing capacity of the pile after installation can be determined by analyzing the radial stress development in the soil. By analytical or experimental analysis, the effect of solid pile installation can be studied in a simplified manner. But the complex geometry of open ended pile and the dynamic process of installation poses more challenge for testing. In

A. Ferrari and L. Laloui (Eds.): SEG 2018, SSGG, pp. 459–466, 2019.
https://doi.org/10.1007/978-3-319-99670-7_57

such cases, the numerical procedure is more advantageous to estimate the behavior and understand the effects. Finite Element Method (FEM) which is commonly used in structural engineering, provides a reliable approach to simulate small deformation problems. In case of pile installation, there is need to examine the effects in soil which shows large deformation and material movement. FEM fails to capture this, as the problem of mesh distortion arises by following Lagrangian formulation. Eulerian FEM approaches eliminate the mesh distortion problems but with an additional cost. To overcome this, meshless methods were developed carrying the best features from Eulerian-Lagrangian approaches. In these methods, the particles represent and store the material information and calculations are performed in a mesh (generated by particle connectivity). The continuous mesh generation is replaced with a fixed computational grid (mesh) in Material Point Method (MPM) developed by Sulsky et al. (1994). Here, the particles carrying information move over the fixed mesh. So, the MPM emerges as the best method to simulate large deformation applications.

Material Point Method (MPM) is formulated in a similar way to FEM. The governing equation is written as,

$$M\,a = F_{ext} - F_{int}$$

where M is the lumped mass matrix, a is the acceleration vector, F_{int} and F_{ext} are the total internal and external forces respectively. The difference is with the procedure of solving the governing equation. At the beginning of each computational step, the material information, state variables are mapped to the computational grid from the particles to solve for governing equation. After calculation, the position of particles is updated and then the information is mapped back to the particles. Because of this, only particles can move around over the fixed computational mesh without any problems of mesh distortion.

By using linear shape functions for the interpolations and mapping, numerical problems arise with the basic formulation of MPM. Grid crossing error is one such numerical error observed during the movement of material point from one grid to other. In MPM, the material points are collocated to a point using Dirac-delta functions. This concentration of mass causes instability during the crossover initiating oscillations in the state parameters.

To alleviate this error, there is a requirement of smooth interpolation of information between the grids. This is provided by distributing the particle mass over a finite domain. Many variations are obtained by this approach such as Generalized Interpolation Material Point (GIMP), updated-GIMP (Bardenhagen and Kober 2004) and Convected Particle Domain Interpolation (CPDI) (Sadeghirad et al. 2011). These differ in the shape of the domain considered for the material point. In this paper, a recent variant i.e. CPDI is adopted due to its robust and stable computations. In CPDI, the material point is made of parallelogram shaped domain and the vectors of the parallelogram are updated by the deformation gradient of the particle. As these domains are only the representation of particle which assists in smooth interpolation, the extensive deformation of parallelogram domains are restricted by a desired size (Homel et al. 2014). In the present work, axi-symmetric CPDI formulation is considered (Hamad 2016).

1.1 Two-Phase Formulation for Axi-Symmetric CPDI

Together with the large deformation and material movement during the pile installation, the water present in the soil plays an important role to select the numerical approach. The fully saturated soil is required for the soil domain. MPM or CPDI provides an easy platform to accommodate the effects of water. Depending on the application, the method offers many possibilities to model saturated soil. For the pile installation application, a formulation based on the different velocity field (water and mixture) can be utilised. Here, only a single particle represents the saturated soil. The formulation involves following steps:

- A single CPDI particle accommodates the mass of soil and water based on the porosity value.
- Velocity of water is calculated by solving the governing equation and then the velocity of mixture.
- Using the mixture and water velocities, strain and excess pore pressure are calculated respectively.
- Finally, the internal force is updated based on the total stress and total water pressure.

Detailed formulation of two-phase model is described in the work of Jassim et al. (2013). In the present work, the basic two-phase formulation is extended to CPDI version of MPM and considerations have been made to accommodate axi-symmetry.

2 Numerical Model and Simulation

The open-ended pile is modelled as a 2D axi-symmetric model as shown in the Fig. 1. The dimensions are scaled down with respect to a general offshore pile size. Around the pile surface, more finer particles are considered to have better interaction during the contact. The computational mesh is also varied in size relative to the particle so that the particle density in each computational grid remains same. The computational mesh consists of rectangular mesh as shown in the left picture of Fig. 1 together with the boundary conditions. The particle distribution and the traction load applied on top of the pile is shown in the right picture of Fig. 1.

Hypoplastic constitutive model is used for the sand which can capture the stress change based on the change in void ratio during the installation process. The properties of the hypoplastic sand are given in Table 1. Medium dense sand with initial void ratio of $e_o = 0.55$ is considered. The pile is modelled as a linear elastic body with the material properties: Young's modulus E = 200 GPa, Poisson's ratio $\nu = 0.34$ and density $\rho = 8000$ kg/m^3.

The interaction between pile and soil is modeled by Penalty contact method (Hamad et al. 2017). In this approach, certain additional linear elements define the boundary of the bodies which is differentiated as master and slave surface based on the stiffness of material.

To define the boundaries, 1500 linear elements are considered in the current model. After the contact pair detection, a very little penetration is allowed into the slave

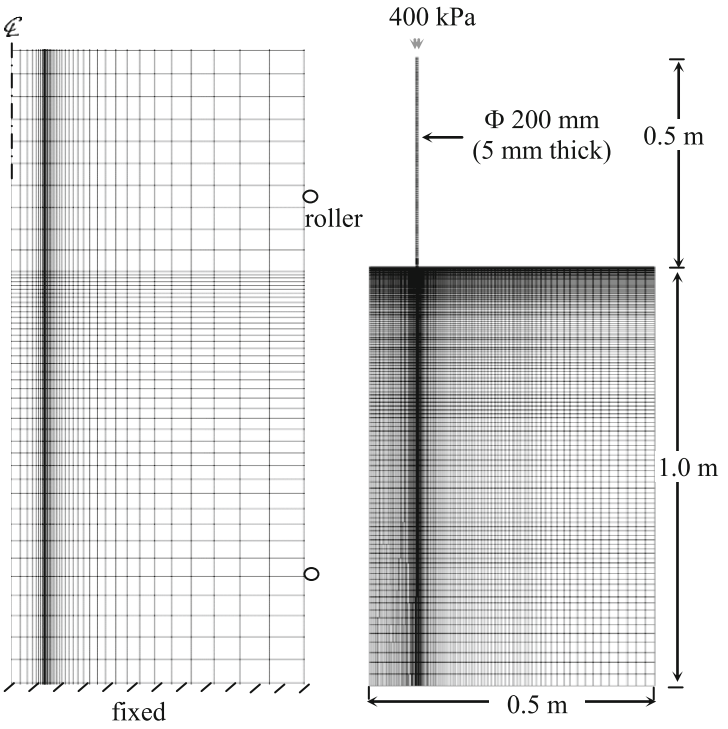

Fig. 1. Initial configuration of the simulation model

Table 1. Hypoplastic parameters used for the soil domain

$\phi(^{o})$	h_s(GPa)	n	e_{d0}	e_{c0}	e_{i0}	α	β	m_R
33	1.6	0.19	0.44	0.85	1	0.25	1	5

m_T	R	β_r	χ	e_o
2	1e-4	0.5	2	0.55

surface and a penalty force is applied to overcome the penetration of the two bodies thereby avoiding the interpenetration. As there exists a frictional interaction between soil and pile, Mohr-Coulomb friction criteria is used to limit the tangential forces. In the present model, friction co-efficient $\mu = 0.25$ is taken.

2.1 Simulation

The simulation is performed to prove the capabilities of the numerical approach by exhibiting the dynamics involved in the process. In the present work pile installation is made from the surface of soil achieving greater depth of penetration undergoing large

deformation in the soil. Sometimes pile is initially embedded into soil to study smaller section of soil (Galavi et al. 2017).

Three steps are followed to simulate the realistic behavior during installation. First, the geostatic stress distribution is achieved in the soil domain from the K_o procedure. Here the total stress at a required height h is calculated according to the equation,

$$\sigma = \rho g h$$

where ρ is the saturated density which is $\rho = (1 - n)\,\rho_s + n\rho_w$, here n is the porosity, ρ_s is the solid density of soil domain and ρ_w is the density of water. According to this equation, for the current simulation maximum total stress at the bottom is found to be 21 kPa.

Then the pile is allowed to penetrate into sand in the action of gravity. This allows pile to penetrate to a certain depth. Then, vibration loading is applied on top of the pile with maximum dynamic force of 1200 N with a frequency of 21 Hz.

3 Result

The soil behavior due to the pile installation is studied by monitoring certain parameters such as void ratio, water pressure, stress states etc.

The penetration curve is shown in the Fig. 2. The installation becomes slower with the depth due to various factors such as skin friction, densification of soil around the pile and higher stresses at greater depths. Void ratio distribution is shown in the Fig. 4 for the pile penetration to a depth of 20 cm. Here, it can be observed that the initial void ratio

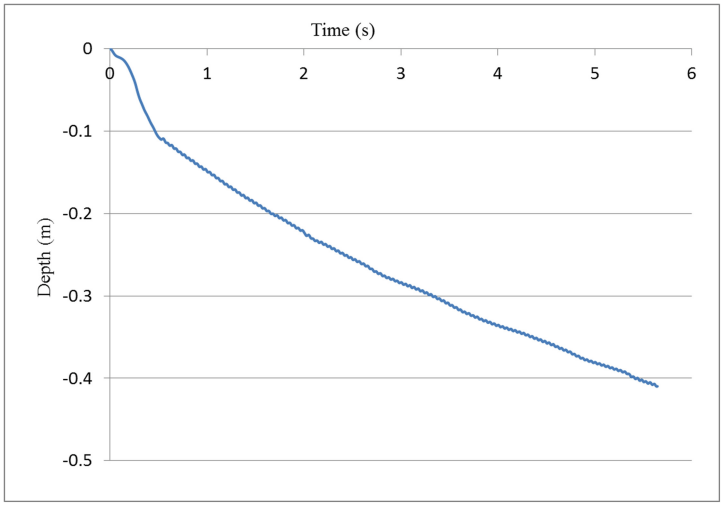

Fig. 2. Pile penetration curve for 6 s of simulation

(i.e. e_o = 0.55) is maintained in the soil region greater than 1D distance (D – diameter of pile). But the void ratio has been increased near the surface of pile (around the distance of pile thickness) to a maximum of e = 0.61. This indicates the loosening or dilation of soil during the penetration. Similar observations have been observed and studied in the work of Rodger (1979).

During the installation, the soil region near the pile shaft fails by the shear forces which lead to loosening. Due to this, void ratio is increased and the hypoplastic model captures the change in void ratio and accommodates it for the stress change in the soil. Liquefaction or fluidized zone increases the pore pressure near the surface of pile (Fig. 3) thereby reducing the effective stresses. This facilitates the motion of pile and allows a faster penetration. Away from the pile shaft, soil densification can be observed with the decrease in void ratio as shown in Fig. 4. This provides the bearing capacity for the pile to withstand the lateral and vertical load after installation.

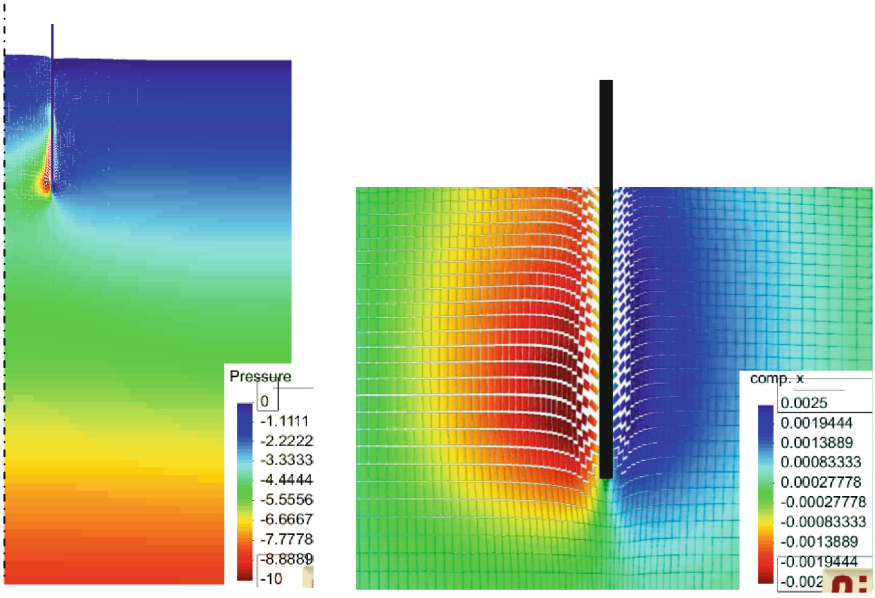

Fig. 3. Pore water pressure increase during penetration (red - maximum and blue – 0 kPa) (left) and the soil displacement around the pile (right)

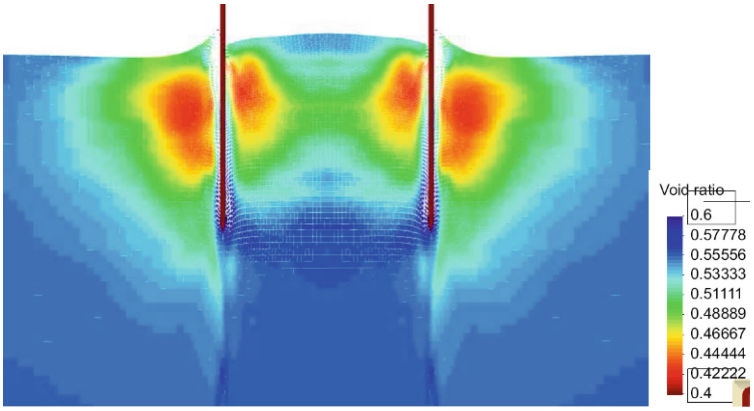

Fig. 4. Void ratio distribution near the pile (red-dense and blue-loose soil)

4 Summary

The paper provides the ability of Material Point Method to simulate large deformation problems. Specifically, geotechnical case i.e. installation of pile has been simulated considering the real conditions of offshore and the dynamic process involved. Two phase CPDI and hypoplastic model clearly captured the soil behavior. Penalty contact approach provided the realistic interaction between the soil and pile particles defining the clear boundary.

Oscillations near the surface and along the pile shaft during liquefaction need to be addressed in future to obtain smoother simulation results. These further optimizations will allow CPDI to simulate various applications to analyze the effects prior to the field test.

References

Bardenhagen, S.G., Kober, E.M.: The generalized interpolation material point method. Comput. Model. Eng. Sci. **5**(6), 477–496 (2004)

Bardenhagen, S.G., Brackbill, J.U., Sulsky, D.: The material-point method for granular materials. Comput. Methods Appl. Mech. Eng. **187**(3–4), 529–541 (2000)

Galavi, V., Beuth, L., Coelho, B.Z., Tehrani, F.S., Hölscher, P., Van Tol, F.: Numerical simulation of pile installation in saturated sand using material point method. Procedia Eng. **175**, 72–79 (2017)

Hamad, F.: Formulation of the axisymmetric CPDI with application to pile driving in sand. Comput. Geotech. **74**, 141–150 (2016)

Hamad, F., Giridharan, S., Moormann, C.: A penalty function method for modelling frictional contact in MPM. Procedia Eng. **175**, 116–123 (2017)

Homel, M.A., Brannon, R.M., Guilkey, J.E.: Simulation of Shaped-Charge Jet Penetration into Drained and Undrained Sandstone Using the Material Point Method with New Approaches for Constitutive Modeling, pp. 676–687. CIMNE, Barcelona (2014)

Jassim, I., Stolle, D., Vermeer, P.: Two-phase dynamic analysis by material point method. Int. J. Numer. Anal. Methods Geomech. **37**(15), 2502–2522 (2013)

Rodger, A.A.: Vibrocompaction of cohensionless soils. Internal report, R.7/79. Cementation Research Limited, Croydon, UK (1979)

Sadeghirad, A., Brannon, R.M., Burghardt, J.: A convected particle domain interpolation technique to extend applicability of the material point method for problems involving massive deformations. Int. J. Numer. Methods Eng. **86**(12), 1435–1456 (2011)

Sulsky, D., Chen, Z., Schreyer, H.L.: A particle method for history-dependent materials. Comput. Methods Appl. Mech. Eng. **118**(1–2), 179–196 (1994)

von Wolffersdorff, P.A.: A hypoplastic relation for granular materials with a predefined limit state surface. Mech. Cohesive-Frict. Mater. **1**(3), 251–271 (1996)

Geotechnical Performance of Suction Caisson Installation in Multi-layered Seabed Profiles

M. Mehravar[1(✉)], O. Harireche[2], and A. Faramarzi[3]

[1] School of Engineering and Applied Science,
Aston University, Birmingham, UK
M.Mehravar@aston.ac.uk
[2] Department of Civil Engineering, Faculty of Engineering,
University of Medina, Medina, Saudi Arabia
[3] Department of Civil Engineering,
University of Birmingham, Birmingham, UK

Abstract. Suction caissons consist of large cylindrical buckets made from steel. In order to serve as foundations for various offshore structures, suction caissons are pushed into the seabed under pressure differential exerted on their lid by an imposed suction. Despite their wide use in the oil and gas industry, there are still some uncertainties regarding their installation process as a result of changes in seabed profiles such as the existence of low permeability layers as well as the variation in soil properties with depth (e.g. permeability decreasing with depth due to an increase in soil density). It is known that seepage conditions play a pivotal role in the installation process, particularly in sand. Indeed, pressure gradients generated by the imposed suction inside the caisson cavity cause an overall reduction in the soil resistance around the caisson wall and at caisson tip, thereby assisting the penetration into the seabed. Successful installation of caisson foundations relies on accurate prediction of soil conditions, in particular soil shear resistance during the installation. Existing knowledge of the prediction of soil conditions and required suction during caisson installation has some limitations which often resulted into rather conservative design methods. Most design procedures used to control suction during caisson installation assume an isotropic and homogenous seabed profile. Moreover, the actual variation of pressure gradient around the caisson wall at different penetration depths is often ignored, although it significantly affects soil resistance. Natural seabed can possess a heterogeneous property where it may comprise of different layers of soils including the presence of layers with low-permeability i.e. clay or silt. In this paper, the effect of seepage on soil conditions during caisson installation is studied within the frame of the presence of a substratum that consists of silt. Suction induced seepage described throughout the installation process and its effects on frictional and tip resistance are considered. For this purpose, a numerical simulation is conducted on a normalised geometry of the suction caisson and surrounding soil, at different penetration depths. The distribution of pressure gradient on both inside and outside of the caisson wall is taken into consideration in both soil shear and tip resistance. Particular conclusions will be drawn on the implications of the presence of a low permeability silt layer on caisson installation.

A. Ferrari and L. Laloui (Eds.): SEG 2018, SSGG, pp. 467–474, 2019.
https://doi.org/10.1007/978-3-319-99670-7_58

1 Introduction

Suction caissons are large upturned bucket structures of cylindrical shape that are typically made from steel. These structures have recently been considered for foundations of offshore wind turbines (Byrne et al. 2002). To install caissons, water will be extracted from the hollow space between the caisson lid and mudline (initial penetration into the seabed is achieved with caisson self-weight). In permeable soils such as sands, seepage occurs as a result of the applied suction which causes an overall reduction in soil resistance and facilitates caisson penetration (Tran et al. 2007; Harireche et al. 2014). The effect of seepage in installation has been well documented for soil profiles with a homogenous nature (Houlsby and Byrne 2005; Harireche et al. 2013, 2014; Mehravar et al. 2017a, b). However, certain soil layer configurations, (e.g. the presence of a low-permeable layer), can have significant impact on the seepage mechanism and thereby the installation process. Nevertheless, design procedures in these particular situations have received less attention (Ibsen and Thilsted 2010). For instance, there are concerns when suction caissons are installed in sand underlain by a low permeability soil such as clay or silt. In such a soil profile the low permeability layer may create a hydraulic barrier in the soil and causes the installation to become very difficult if not impossible (Raines et al. 2005). Few studies have considered suction caisson installation in multi-layered seabed profiles (Allersma et al. 2001; Matusi et al. 2002; Tran et al. 2007; Cotter 2009). It has generally been concluded that a larger suction is required compared to installations in homogeneous sand. In the above works, pressure gradients between seabed and caisson tip was used to predict the hydraulic gradient on both sides of the caisson wall (Houlsby and Byrne 2005; Cotter 2009). Nevertheless, it has been proved that the variation of pressure gradient over the caisson penetration depth affects the whole installation process both in terms of reduction in soil resistance and critical condition for piping (Harireche et al. 2014). Therefore, it is important to investigate the pressure gradient distribution over the penetration depth throughout the whole installation process. In this paper, a finite element procedure is implemented in an in-house finite element (FE) code and used to study the effect of the existence of a low permeability layer on suction caisson installation in sand. A parametric study is performed to investigate the effect of the depth of the low permeability layer on the reduction in soil resistance. The results are compared with those obtained from an installation in homogeneous sand and the difference will be highlighted and discussed.

2 Formulation of the Normalised Seepage Problem

In this study the model problem of a suction caisson of radius R, and height L is considered. Dimensions and values of pressure are normalised with respect to the caisson radius (R) and magnitude of the applied suction respectively. The caisson penetration depth into the seabed and the depth of a silt layer (from the mudline) are denoted as h, and h_s respectively. Therefore, the following normalized variables are adopted:

$$p^* = \frac{p}{\bar{s}} \quad h^* = \frac{h}{R} \quad h_s^* = \frac{h_s}{R} \tag{1}$$

Where p^*, h^* and h_s^* represent normalized excess pore water pressure, caisson penetration depth and depth of silt layer from the mudline, respectively. Figure 1, shows a vertical section of the soil-caisson system. A normalised cylindrical system of coordinates $z^* = \frac{z}{R}$ and $r^* = \frac{r}{R}$ in the meridian plane is adopted where all dimensions were scaled with respect to the caisson radius. Due to the axisymmetric nature of the problem, only half of the caisson is modelled. In order to investigate the effect of the presence and the location of a silt layer on the caisson installation, four different soil profiles designated as Case A ($h_s^* = 0$), B ($h_s^* = 3h^*$), C ($h_s^* = 2h^*$) and D ($h_s^* = h^*$) are considered. The soil profile in Case A corresponds to homogenous sand with permeability, k_{sand}. The other three soil profiles (Case B, C and D) represent a sandy soil profile with a layer of silt that lies at different depths from the caisson tip. The caisson tip touches the top of the silt layer when the installation is complete in Case D ($h_s^* = h^*$).

The permeability of the silt layer (k_{silt}) in the multi-layered cases (Case B, C and D) is considered two order of magnitude lower than that of the sand layer (Tran et al. 2007). The relevant sand and silt properties which are considered in this study have been selected based on the sand and silt sample properties used in the experimental tests conducted by Tran et al. (2007). These properties are shown in Table 1.

Table 1. Soil properties

Soil property	Sand	Silt
Permeability	1.3×10^{-4} m/s	1.3×10^{-6} m/s
Saturated unit weight γsat	21 kN/m^3	20 N/m^3

The porewater seepage is described by Darcy's law: $\boldsymbol{u} = -k\nabla p$ where $\boldsymbol{u}$ is the porewater velocity, k the permeability and ∇p represents the excess porewater pressure gradient. The normalized excess porewater pressure p^* must satisfy Eq. 2:

$$\nabla^{*2} p^* \equiv \frac{\partial^2 p^*}{\partial r^{*2}} + \frac{1}{r^*}\frac{\partial p^*}{\partial r^*} + \frac{\partial^2 p^*}{\partial z^{*2}} = 0 \tag{2}$$

and the boundary conditions $p^* = -1$ on OC$^-$, $p^* = 0$ on C$^+$F, FH, BH and $\frac{\partial_p *}{\partial_r *} = 0$ on CD and OB (Fig. 1).

The finite element procedure has the advantages of taking into account soil loosening inside the caisson cavity ($\Omega 1$) due to applied suction in a much more natural way compared to other numerical methods. The effect of soil loosening inside the caisson is not pronounced at the early stages of caisson penetration ($h^* < 1$). Therefore, a single permeability on both sides of the caisson wall is considered in this study. Of particular interest in this analysis, are the effects of the low permeability silt layer and its location, on soil resistance to caisson penetration. The scaled penetration depth has values: $h^* = 0.2$ (typical of self-weight penetration), $h^* = 0.4$, $h^* = 0.6$, $h^* = 0.8$ and $h^* = 1$.

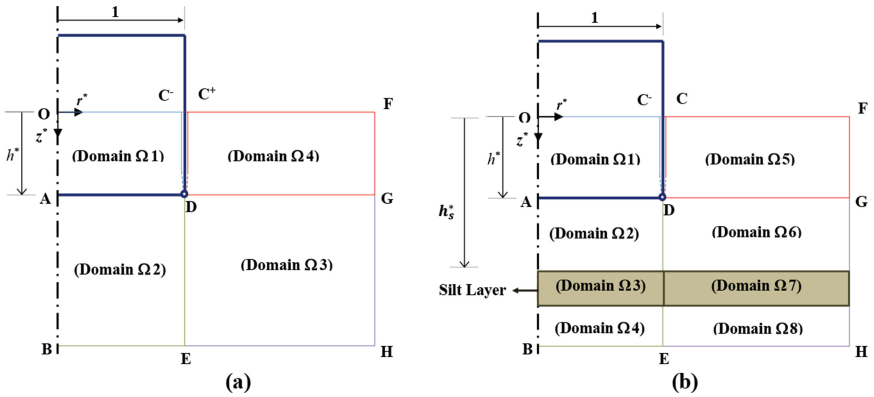

Fig. 1. Normalized geometry; (a) homogenous sand ($h_s^* = 0$), (b) sand overlying a silt layer (zones Ω3 and Ω7)

3 Effect of Silt Layer on the Excess Porewater Pressure Variation

Generally, porewater seepage produced by suction causes a hydraulic gradient which on both sides of the caisson wall varies with depth. The contours of the normalised excess porewater pressure, p^* for $h^* = 1$ are shown in Fig. 2. This figure corresponds to homogenous sand (Fig. 2a), sand with a silt layer located at a depth, $h_s^* = 2h^*$ (Fig. 2b) and a sandy soil profile with a silt layer at $h_s^* = h^*$ (Fig. 2c). These figures clearly indicate that the contours of excess porewater pressure have been affected due the presence of a layer of silt and this consequently has an impact on soil resistance to caisson penetration.

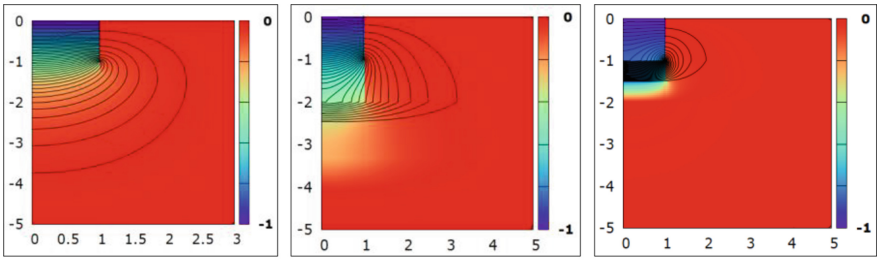

Fig. 2. (a–c): Excess porewater pressure p^* distribution for normalized penetration depth $h^* = 1$ at (a) $h_s^* = 0$ (homogenous sand), (b) $h_s^* = 2h^*$, (c) $h_s^* = h^*$.

The vertical component of the normalized hydraulic gradient ($g^* = \partial p^*/\partial z^*$) on both sides of the caisson wall is represented as a function of the normalized penetration depth, z^* and shown in Fig. 3(a–d). It should be noted that the vertical component of the pressure gradient on the inner and outer side of the caisson wall are given by $g_i(R, \xi)$ and $g_o(R, \xi)$, respectively. Two values of scaled penetration depth, namely: $h^* = 0.4\, and\, 0.8$ have been considered in conjunction with four different seabed profiles defined by $h_s^* = 0, 3h^*, 2h^*\, and\, h^*$ are considered. By comparing the normalized pressure gradient on both sides of the caisson wall (Fig. 3a–d), It can be seen that:

- Regardless of soil seabed profile, pressure gradient at both sides of the caisson wall is higher at shallow penetration depths and the maximum pressure gradient occurs at the caisson tip. The effect of a low permeability silt layer is more noticeable inside the caisson cavity and becomes more pronounced when the caisson tip touches the silt layer ($h_s^* = h^*$).
- There is no significant difference in the gradient magnitude for the first three soil profiles (Case A to C) on both sides of the caisson wall. However, such a difference becomes more noticeable once the caisson tip reaches the silt layer (Case D), and can affect the soil resistance through the increase in soil effective stress.

4 Effect of Silt Layer on Soil Resistance to Caisson Penetration in Layered Soil

In this study, the effect of the presence and location of a silt layer in a sandy soil profile on the soil resistance to caisson penetration is studied. For this aim, the reduction in frictional forces acting on the caisson wall and soil resistance at the caisson tip, due to applied suction, are calculated. Under seepage conditions produced by an applied suction, the lateral effective stress (σ'_h) acting on both sides of the caisson wall at a depth z, is respectively given by:

$$\sigma'_{hi}(R, z) = K\left(\gamma' z - \int_0^z g_i(R, \zeta) d\zeta + \tilde{\sigma}_i(R, z)\right) \tag{3}$$

$$\sigma'_{ho}(R, z) = K\left(\gamma' z - \int_0^z g_o(R, \zeta) d\zeta + \tilde{\sigma}_o(R, z)\right) \tag{4}$$

where the indices i and o indicate the regions inside and outside the caisson, respectively. The parameter K denotes the coefficient of lateral earth pressure, γ' is the effective unit weight of the soil, $\tilde{\sigma}$ is the enhanced effective stress due to the effect of shear resistance which develops on the soil-caisson interface and $g_i(R, \xi)$ and $g_o(R, \xi)$ represent the vertical components of the pressure gradient on the inner and outer side of the caisson wall, respectively.

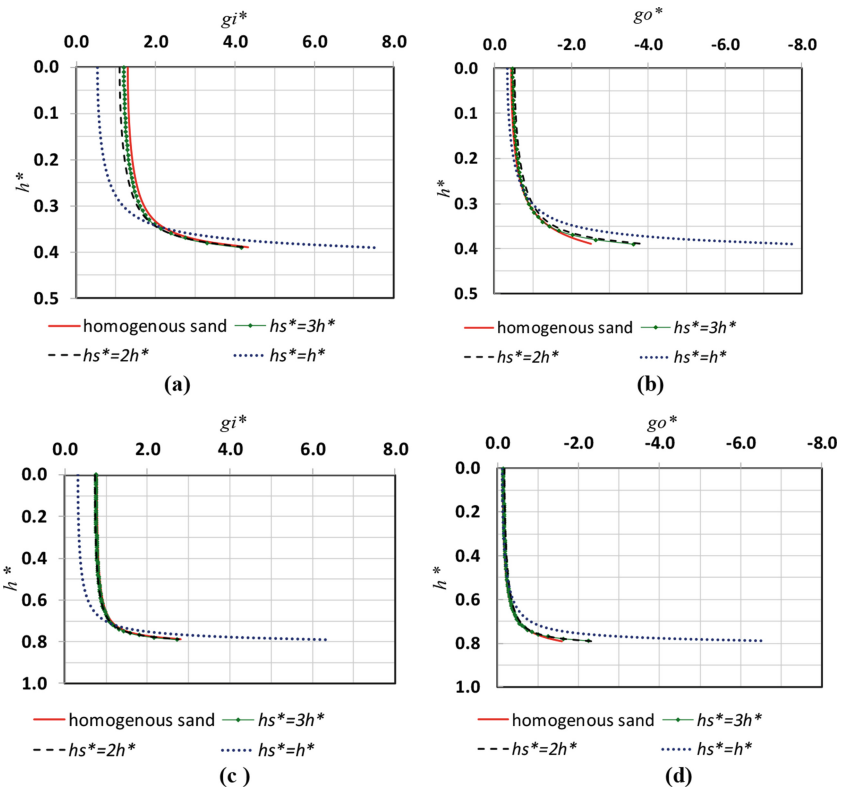

Fig. 3. (a–d): Dimensionless pressure gradient as a function of normalized depth for $h^* = 0.4$ and 0.8, and four different soil seabed profiles

Seepage causes an overall reduction (ΔF_s) in the magnitude of the shear force acting on the caisson wall. This reduction (ΔF_s) can be expressed as a function of the normalized penetration depth h^* as follows:

$$\frac{\Delta F_s}{2\pi R^2 K\,\bar{s}\tan\delta} = \int_0^{h^*} \left[L_i^*(z^*) + L_o^*(z^*)\right] dz^* \tag{5}$$

$$\Delta F_s^* = \frac{\Delta F_s}{(2\pi R^2 K\,\bar{s}\tan\delta)} \tag{6}$$

where

$$L_i^*(z^*) \equiv \int_0^{z^*} g_i^*(1,\zeta^*)d\zeta^* > 0, \quad L_o^*(z^*) \equiv \int_0^{z^*} g_o^*(1,\zeta^*)d\zeta^* < 0 \tag{7}$$

and δ denotes the angle of friction at the interface soil-caisson and the suction magnitude at the mudline inside the caisson cavity is denoted by $\bar{s}$. The normalised

reduction in frictional soil resistance, $\left(\Delta F_s^*\right)$ is calculated for all soil profiles (Case A to D) using the results of the FE model and Eqs. (5–7). In addition, the vertical effective stress at the caisson tip is reduced due to the applied suction, leading to further reduction in the total resisting force. Assuming the enhanced vertical stress at the caisson tip not affected by seepage, the reduction of resisting force at the caisson tip can be calculated by the following equation (Harireche et al. 2014):

$$\Delta F_t^* = \frac{\Delta F_t}{2\pi RtN_q\bar{s}} = \frac{1}{2}\left(L_i^*(h^*) + L_o^*(h^*)\right) \tag{8}$$

Figure 4 shows that in all four soil profile cases, the reduction in both shear and tip resistance forces increases during caisson penetration. This clearly shows that the location of the silt layer plays an important role in the reduction of the overall soil resistance to caisson penetration. The effects of the presence of a low permeability layer are particularly more considerable when the caisson tip gets closer to the silt interface. In other words, the difference in the reduction in soil resistance for the first three soil profiles (i.e. cases A to C) is not considerable. The soil profiles with silt layer located around the caisson tip, correspond to less reduction, and this is more pronounced in case D where the caisson tip is closer to the silt interface (Fig. 4a and b)). It can be observed that, the reduction of shear and tip soil resistance in homogenous sand (Case A) is approximately 2.7 times higher than in case D. As a result, caisson installation in multi-layered seabed profiles, in the vicinity of a silt layer (e.g. Case D), requires a suction magnitude about 2.7 times higher than in homogenous sand (e.g. case A).

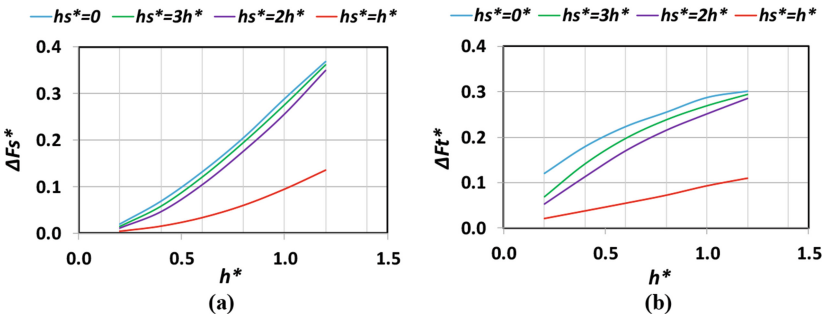

Fig. 4. Magnitude of the reduction in (a) soil shear and (b) tip resistance

5 Conclusion

This study has been motivated by the need for further investigation to predict the effect of suction induced seepage on soil resistance to caisson installation in seabed profiles with low permeability layers. Firstly, the normalised model problem of suction induced seepage around a caisson foundation has been formulated considering the variation of the pressure gradient around the caisson wall. In order to investigate the effects on caisson installation, of the presence of a low permeability layer such as silt, four

different soil profiles were considered. A semi-analytical approach has been developed to calculate the reduction in soil resistance due to applied suction, in each of these soil profiles. The results revealed that the presence of a silt layer at a certain depth in homogenous sand, can affect the reduction in soil resistance to caisson penetration and reduces the benefits of suction induced seepage on caisson installation. Furthermore, the location of the silt layer plays an important role. It was observed that reduction in soil resistance due to suction induced seepage becomes significantly smaller when the caisson tip gets closer to the silt interface, compared to homogenous sand. Finally, this study suggests that the applied suction in seabed profiles where low permeability layers exist at various depths, should be increased by about 60% for the caisson installation in the vicinity of a silt layer to obtain reductions in soil resistance similar to those that can be achieved in homogenous sand. Implications of such an increase in suction on critical soil conditions, such as piping, must be considered for the installation process to be safe. This aspect will be presented in a future publication.

References

Allersma, H.G.B., Hogervorst, J.R., Pimoulle, M.: Centrifuge modelling of suction pile installation in layered soil by percussion method. In: Proceedings of 21st International Conference on Offshore Mechanics and Arctic Engineering (2001)

Byrne, B.W., Houlsby, G.T., Martin, C., Fish, P.: Suction caisson foundations for offshore wind turbines. Wind Eng. **26**, 145–155 (2002)

Cotter, O.: The installation of suction caisson foundations for offshore renewable energy structures. PhD thesis, Oxford University (2009)

Harireche, O., Mehravar, M., Alani, M.A.: Suction caisson installation in sand with isotropic permeability varying with depth. Appl. Ocean Res. **43**, 256–263 (2013)

Harireche, O., Mehravar, M., Alani, M.A.: Soil conditions and bounds to suction during the installation of caisson foundations in sand. Ocean Eng. **88**, 164–173 (2014)

Houlsby, G.T., Byrne, B.W.: Design procedures for installation of suction caissons in sand. In: Proceedings of the Institution of Civil Engineering (ICE), pp. 135–144 (2005)

Ibsen, L.B., Thilsted, C.L.: Numerical study of piping limits for installation of large diameter buckets in layered sand. In: Proceedings of the 7th European Conference on Numerical Methods in Geotechnical Engineering (2010)

Matusi, N., et al.: Review of penetration resistance based on in situ monitoring. In: Proceedings of 12th International Offshore and Polar Engineering Conference, Cupertino, California (2002)

Mehravar, M., Harireche, O., Alani, A.M.: Modelling the variation of suction pressure during caisson installation in sand using FLAC3D. Ships Offshore Struct. **12**(7), 893–899 (2017)

Mehravar, M., Harireche, O., Faramarzi, A., Dirar, S.: Soil condition and piping criteria during suction caisson installation in layered strata. In: Proceedings of the 25th UKACM Conference on the Computational Mechanics, Birmingham (2017)

Raines, R.D., Ugaz, O., Garnier, J.: Centrifuge modelling of suction piles in clay. In: Proceedings of the International Symposium on Frontiers in Offshore Geotechnics, London (2005)

Tran, N.T., Randolph, M.F., Airey, D.W.: Installation of suction caissons in sand with silt layers. J. Geotech. Geoenviron. Eng. ASCE **133**(10), 1183–1191 (2007)

Modeling of Oil Transport in Porous Media Using Multiscale Method with Adaptive Mesh Refinement

Hasan Ghasemzadeh(✉) and Mohammad Sanaye Pasand

Civil Engineering Faculty, K. N. Toosi University of Technology, Tehran, Iran
ghasemzadeh@kntu.ac.ir

Abstract. The porous media of oil reservoirs have different layers with wide range scales which are different in effective scale of fluid flow. To reduce the calculating time of porous reservoirs modeling, each physical effect should be treated separately on its scale and area of influence. It is proposed that, the fluid transport and deformation of solid part of porous media are determined through separate frameworks. The fluid flow equations are solved using multiscale finite volume methods. The finite element method is used for solving the solid equilibriums. The available mesh dimensions is refined for different areas of solid media in each iteration of the analysis, according to the density of data and results. The interactions between solid deformation and multiscale multiphase flow frameworks are instated through iterative coupling. Also, the linear elastic relationship is considered between stress and strain of solid part and the capillary pressures parameters between fluid phases are added on fluid flow equations to increase the accuracy of modeling. Finally, indicative test cases are analyzed and reasonable results are achieved.

Keywords: Adaptive mesh refinement · Multiscale · Geomechanics
Capillary · Porous media

1 Introduction

The behavior of the porous oil reservoirs can be examined by numerical modeling. If an oil reservoir is modeled more accurately in the less time, the production management will be better done. In the past, the production management was carried out only on the vast and important reservoirs due to the time consuming process of studies and simulation of the reservoirs as well as the high cost of that. But nowadays, all of the reservoirs are managed and therefore it is necessary to be simulated and to be modeled. So, it is essential to increase the accuracy of reservoir modeling as well as reducing the time and amount of calculations.

Considering that any physical phenomenon influences in a certain scale, the simulation of oil porous reservoirs includes a wide range of different scales. These scales are between a micron for the pore size and several kilometers for the reservoir dimensions (Aarenes et al. 2007). The geological aspects of oil reservoirs are generally

A. Ferrari and L. Laloui (Eds.): SEG 2018, SSGG, pp. 475–485, 2019.
https://doi.org/10.1007/978-3-319-99670-7_59

provided with networks measuring about 10–50 m in horizontal directions and 0.1–1 m in vertical direction (Wen et al. 2003). In this situation, the number of elements in an oil reservoir will be greater than the number of elements which a computer will be able to model with them. So, the simulation of oil reservoirs with pore scale is impossible. On the other hand, the flow in the oil reservoir is affected by phenomena that are mainly influenced by larger scales. So, the flow analysis with larger scales is sufficient in the oil reservoirs. In the multiscale method, every physical phenomenon is investigated in its scale of influence. So, the computational cost is significantly reduced without decreasing accuracy. Due to the nature conservative solution and the scales studied in the modeling of porous reservoirs, the Multi Scale Finite Volume (MSFV) method for fluid phases is used in the interaction with the finite element method for the solid phase. Multiphase flow and solid deformation are coupled via a nonlinear iteration loop in each time step. An iteratively coupled approach could reach a fully coupled results if a restricted condition is considered for iteration.

According to the fact that the mass is conservative in the MSFV, this method is suitable for modeling the fluid phases of porous oil reservoirs. This method was founded by Jenny et al. (2003). This model at first was presented for a phase, without consideration capillary and solvability in a two-dimensional state. The basis functions were defined in order to account the heterogeneity which is affected by the down-scale analysis. These functions are obtained by solving the elliptic pressure equations on the subbases. Also, this method guarantees the mass conservation on a down scales by defining other basis functions which is very important in solving the flow equations. In this method, the mass equation is divided to two equations of the pressure and the degree of saturation. First, the pressure equation is solved on the coarse grid. Then, the degree of saturation equation is solved after solving the conservative pressures on fine grid with considering the mass balance rule. The proposed model was upgraded to two phases mode by Jenny et al. (2004). Lunati and Jenny (2006) optimized the model by changing the solving method of the conservative pressures. Then Jenny et al. (2006) provided a model for fully implicit solving the mass equation and obtaining the degree of saturation in each phase. Also, Tchelepi et al. (2007) presented a model based on the calculation of basis functions conservatively. Lunati and Jenny (2008) studied the effects of gravity in the mass equation. Lee et al. (2008) upgraded the model to simulate the black oil pattern. Lunati and Jenny (2007) presented a method for boundary condition corrections of high anisotropic environments. Hajibeygi et al. (2008) modified the basic assumptions that were applied locally on the subzones. This method, which was introduced as an iterative-MSFV method, was promoted by Hajibeygi and Jenny (2009) to consider the compressibility of different phases and the parabolic nature of the pressure equation. The proposed model have a good answers for high-heterogeneity and high anisotropy environments. Dehkordi and Manzari (2013), using the idea of border region upscaling, presented a multi-resolution multiscale method. In the model presented by Taheri et al. (2015), deformation of porous media due to the geomechanical effects of the surrounding rock of a reservoir is considered. Recently, attempts have been made to improve the accuracy of the model by using a combined problem solving with central and local coordinates (Tomin and Lunati 2015). To overcome the convergence problems and reduce the computational cost, some of corrections were applied to designing better solvers (Li and Tchelepi 2015). Some researchers improved

the multiscale method to the multilevel multiscale method. In this method, all areas are solved with fine mesh network in first iteration. Next, the mesh network will be coarsen in the areas which do not need a high accuracy in the further iterations (Cusini et al. 2016).

Capillary pressure is the free energy at the levels between phases of a medium, which is a function of surface tension and pore radius. It is one of the important parameters for modeling and simulating the multiphase fluid behavior in porous media. In modeling of oil reservoirs, capillary pressure affects the solid phase stress and changes the stress-strain behavior. There is also a capillary pressure between the fluid phases which can causes a change in the relationship between them.

Gravity and capillary forces play an important role in fractured reservoirs. Because the gravity and the capillary gradients between the cracks and the matrix in fractured reservoirs is much higher than these gradients in homogeneous reservoirs (Monaghan 1985). Capillary forces are more noticeable in finer pores, while gravity forces enhance with increasing the height of the solid part of porous media. So, in the presence of large blocks with coarse pores, gravity forces are more effective and in the presence of small blocks with fine pores, capillary forces are more effective in a porous medium. Also, a significant part of oil reservoirs have low production efficiency due to their high thickness and high pressure gradient. To increase the efficiency of these reservoirs, the artificial fractures are made in these reservoirs using a hydraulic fracture method. After creating an artificial fractures, a lot of fine cracks are created in the vicinity of them and the capillary effect is enhanced.

Most of the equations which were proposed for calculating capillary pressure had two adjustable parameters. One of these parameters indicates the diameter of the pores and determines the curvature of the capillary pressure. Another parameter determines the area below the capillary pressure curve, which is as same as average pressure. In drained conditions, capillary pressure is an obstacle for flow in the porous medium and should be overcome to capillary pressure for flowing. Under injection conditions, capillary pressure is an agree force which absorbs a quantity of wetting fluid into the media. Since measuring the capillary pressure is time consuming and costly, there is always interest to predict this property by other parameters. The amount of capillary pressure obtained in accordance with a difference between the pressure of the two wetting (p_w) and non-wetting (p_{nw}) fluids which are in equilibrium at the contact surface.

$$P_C = p_{nw} - p_w \tag{1}$$

The tradeoff between numerical accuracy and cost is a crucial issue of both fundamental science and practical applications. It is expensive to use fixed fine meshes based on the maximum accuracy which we need for the entire of a problem. Global coarse-scale problem has longer conservation time than the local fine-scale problems. Mesh refinement is required to resolve only the regions that we need more accuracy in where. An adaptive mesh refinement (AMR) method allows for spatially and temporally varying resolution. AMR is commonly used to efficiently resolve the problem in regions which need more accuracy or where resolution is needed. For example, the finer grids are only used in the vicinity of phase interface and coarser grid is used

elsewhere. The efficiency of an AMR method can be improved by allowing variable accuracy along the problem. AMR can be performed at every time-step if necessary. Interpolation of quantities on refined cells is also relatively simple and is achieved conservatively both for momentum and volume fraction (Chen and Yang 2014). Crack propagation in brittle and porous media is currently one of the major research topics in mechanical, energy, and environmental engineering (Lee et al. 2016). The AMR method is able to adaptively mesh a highly fractured porous medium with increasing the mesh density at around the fractures. The AMR method is divided to two categories of structured and unstructured. The type of refined mesh is as same as coarse mesh with fixed refinement ratio for all of refinet elements in structured AMR. But, the type of refined elements and the value of refinement ratio is different in unstructured (Xie et al. 2014). There are some examples for the use of adaptive mesh refinement for structured meshes in Popinet (2009).

The use of AMR for modelling the flow in porous media is depends on the Reynolds number and behavior (hyperbolic–elliptic or hyperbolic–parabolic) of the flow. At first, hierarchical AMR was designed for hyperbolic problems. But, it can also be used for elliptic problems. The standard approach of AMR is to use the grids and grids data of each level in the next level of refined meshes. The important problem in the AMR method is the interface between coarse and fine meshes (Lovett et al. 2015).

The purpose of this article is to upgrade the model of Taheri et al. (2015), considering the capillary pressure in the governing equations of fluid phases and AMR in deformation calculation of solid phase. To assess accuracy and efficiency of the proposed method, an indicative test case is analyzed and concluded.

2 Governing Equations Considering Capillary Pressure

In this work, three nonlinear, compressible and irresolvable fluid flows consists of oil, water and gas with deformable solid skeletons are modeled considering capillary effects between fluid phases. The assumptions which the model equations are based on them are: 1. The solid particle is incompressible. 2. The behavior of the solid skeleton is elastic. 3. The deformations are small. 4. Fluid flow obeys Darcy's law. 5. The effects of temperature will be ignored. So, we have a nonlinear parabolic pressure equation. The governing equation in deformable porous media are mass balance and momentum balance for fluids and solid phases. Substituting the momentum balance of fluid and solid equations in mass balance equation of fluid, we have the following equation.

$$\phi \frac{D^S}{Dt} S_\alpha \rho_\alpha + S_\alpha \rho_\alpha \frac{D^S \phi}{Dt} + \nabla . \left(\rho_\alpha \frac{K k r_\alpha}{\mu_\alpha} . [-\nabla p_\alpha + \rho_\alpha g] \right) + \phi S_\alpha \rho_\alpha \frac{\varepsilon_{VOL}}{\Delta t} = \dot{m}_\alpha \qquad (2)$$

where ϕ is porosity, ρ_α is density of phase, S_α is degree of saturation of phase, K is the absolute permeability tensor, k_{ra} is relative permeability, μ_α is the phase viscosity and $\dot{m}_\alpha$ denotes sink and source terms. For more comprehensive information, the reader could refer to Taheri et al. (2015). Given that the number of unknowns is more than the number of equations in the governing equations, we have some conservation equations

such as the continuity of degree of saturation, porosity and density, the equation between permeability and degree of saturation and relationship between density and pressure. Also, the pressure of fluid phases are related to each other for considering capillary pressure as folowing.

$$p_{c\alpha o} = p_\alpha - p_o \tag{3}$$

The implicit discretization of Eq. (2) with considering the capillary pressure, leads to

$$\varphi^{n+1}\frac{\rho_\alpha^{n+1}.S_\alpha^{n+1}-\rho_\alpha^n.S_\alpha^n}{\Delta t}+\rho_\alpha^n.S_\alpha^n.\frac{\varphi^{n+1}-\varphi^n}{\Delta t}-\nabla.\left(\rho_\alpha^{n+1}.\lambda_\alpha\left(\nabla(p+p_{c\alpha o})^{n+1}-\rho_\alpha^{n+1}.g.\nabla z\right)\right)$$
$$+\left(\varphi^{n+1}.\rho_\alpha^{n+1}.S_\alpha^{n+1}\right).\frac{\varepsilon_v^{n+1}-\varepsilon_v^n}{\Delta t}=\rho_\alpha^{n+1}.q_\alpha \tag{4}$$

where q is a volumetric sink/source term, n and $n + 1$ show two sequential time steps. The above equations have a combination of pressure and volume strain. First, these equations are solved in fluid phases and the pressure is obtained. Next, the volumetric strain is obtained in solid phase based on the pressure. The cycle is iterated till converged. The above equations should be multiplied in α to obtain decoupled pressure. This value is calculated from $\alpha_a = 1/\rho_a^{n+1}$ for different phases. Then, by taking the sum over all phases, the Eq. (5) is obtained.

$$\frac{\phi^{n+1}}{\Delta t}+\frac{-\phi^n}{\Delta t}\left(\sum_{\alpha=1}^{n_p}\alpha_\alpha^{n+1}\rho_\alpha^n S_\alpha^n\right)=RHS \tag{5}$$

After linearization of above equation, the Eq. (6) is obtained.

$$C\frac{(p^{v+1}-p^v)}{\Delta t}-\sum_{i=1}^{n_p}\alpha_i.\nabla.\left(\lambda_i'^v.\nabla p^{v+1}\right)=RHS \tag{6}$$

where $\lambda_O'^v = \rho_O^v.\lambda_O^v$, $\lambda_W'^v = \rho_W^v.\lambda_W^v$ and $\lambda_g'^v = \rho_g^v.\lambda_g^v$. Also, v and $v + 1$ show the pressure in two sequential iterations. The compressibility index (C) and RHS are obtained from below equations.

$$C=\left.\frac{\partial\phi}{\partial p}\right|^v-\phi^n\sum_{i=1}^{n_p}\left.\frac{\partial\alpha_i}{\partial p}\right|^v\rho_i^nS_i^n+\Delta t\sum_{i=1}^{n_p}\left.\frac{\partial\alpha_i q_i}{\partial p}\right|^v \tag{7}$$

$$RHS=-\frac{\phi^v}{\Delta t}+\frac{\phi^n}{\Delta t}\sum_{i=1}^{n_p}\alpha_i\rho_i^nS_i^n+\sum_{i=1}^{n_p}\alpha_i\rho_i^vq_i^v-\sum_{i=1}^{n_p}\alpha_i.\nabla.\left(g\rho_i\lambda_i'^v.\nabla z\right)$$
$$+\alpha_W.\nabla.\left(\lambda_W'.\nabla p_{CWO}\right)^v+\alpha_g.\nabla.\left(\lambda_g'.\nabla p_{CgO}\right)^v-\phi^v\frac{\varepsilon_v^v-\varepsilon_v^n}{\Delta t} \tag{8}$$

3 Multiscale Multiphysic Mixed Geomechanical Model with Adaptive Mesh Refinement

In this work, the pressure of fluid phases is calculated by conservative MSFV method and the deformation of solid phase is obtained by finite element method on coarse grid considering the AMR method. The MSFV framework relies on two imposed grids, namely, the coarse grid (solid line in Fig. 1) and the dual coarse grid (dashed line in Fig. 1). The size of these two grids could be much larger than the underlying fine cells extracted from the geological model.

The MSFV consists of two main operators. The first operator upscales the fine grid geological property with respect to integration fine pressure obtained from two sets of shape functions, that is, basis and correction functions. The second operator also utilizes these two sets to obtain fine-scale pressure and corresponding fine-scale flow over each coarse volume to obtain conservative fine pressure with original resolution. These two functions are the general and particular solutions of Eq. (6) with localized assumptions and reduced boundary conditions on the borders of each dual volume cells. After obtaining the conservative fluid fine pressure, the deformation of solid phase is obtained in adaptive mesh refined coarse cells in terms of fluid pressures. The second term on the right-hand side of the Eq. (9) which is writhed based on finite element method, is obtained by integrating over all fine cells encapsulated in each coarse volume.

$$\left[\int_{\Omega} \mathbf{B}^T \mathbf{D} \mathbf{B}\, d\Omega\right].\hat{\mathbf{u}} = -\int_{\Gamma^N} \mathbf{N}_u^T \bar{t} d\Gamma + \int_{\Omega} \mathbf{B}^T (p\mathbf{m}) d\Omega \tag{9}$$

The coupled procedure of Newton iteration loop is applied to consider interactions between fluid pressures and solid deformation. Moreover, physical properties such as degree of saturation and porosity shall be updated in the iterations.

Inability to obtain the exact amount of solid deformation in some areas of reservoir is one of the reasons for creating the error in the MSFV method. The distribution of the flow pressure and, consequently, the distribution of stress are different in the reservoir zones. Also, the mechanical properties of the solid part of the reservoirs are various

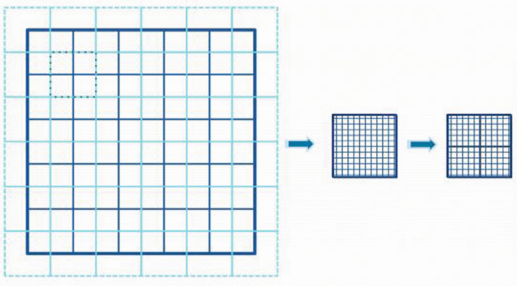

Fig. 1. Illustration of (a) coarse grid (solid line), dual coarse grid (dashed line), (b) fine grid in a coarse cell and (c) fine grid in a refined coarse cell after 1 level refinement

heterogeneously. It can be determined refined meshes for critical stress locations such as injector and producer wells or locations which have inhomogeneity in the permeability. So, the determined hardness matrix can take into account the corresponding deformations. In this regard, we define an error function as following. If the ratio of solid deformation in iteration n+1 to that deformation in iteration n is more than 1.03 or less than 0.97 in a coarse cell, the AMR method will be started.

Special care should be taken at coarse-fine interfaces for maintenance of consistency and convergence of the problem. As shown in Fig. 2, the refinement levels start from level 0 (the coarsest) to level *n* (the finest). The level 0 covers the whole area of a problem. The subsequent AMR levels contains smaller and smaller parts of the area. The refinement ratio between any two AMR levels is fixed. We use a refinement ratio of 2 between AMR levels in this work. The resuls of each AMR level is maintained in the grids and can be used in the next AMR level. Each grid level must be in an area of previous level. The quadratic elements with eight nodes forming a serendipity family is implemented for coarse and refined cells in solid phase.

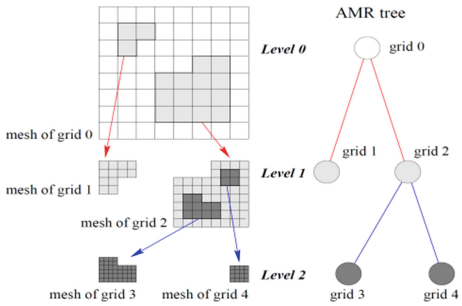

Fig. 2. A 2-dimensional AMR example with 2 levels of refinement (Liao et al. 2002)

4 Numerical Results

A five spot oil reservoir is shown in Fig. 3. The water is injected into the well in the middle of these reservoirs and the oil is extracted from the four wells at the corners of the reservoirs. Due to the symmetric shape of these reservoirs, only one quarter of them is modeled and the results are generalized to other parts. The water is injected into the lower left corner and production occurs in the upper right corner in the analyzed model for a quarter of the reservoir.

Water injection in a homogeneous oil reservoir was studied with numerical simulation to control the accuracy, calculations and efficiency of the proposed model. In this case, a square domain (44 m $\times$ 44 m) is initially saturated with oil. The water is injected into the lower left corner with rate of 1×10^{-4} m^3/s and production occurs in the upper right corner. The parameters of the simulated oil reservoir are shown in Table 1. Each coarse cell contains 11 $\times$ 11 underlying fine cells, so a coarsening factor of 121 is considered. Also, each refined coarse cell contains 5.5 $\times$ 5.5 underlying fine cells after 1 level refinement.

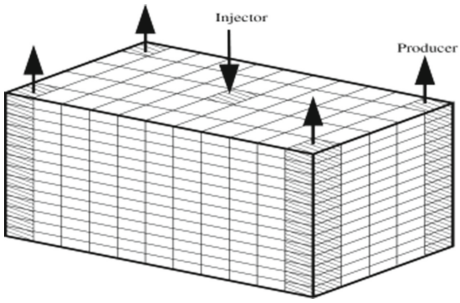

Fig. 3. Five spot oil reservoirs and the injector and producer wells

Table 1. The parameters of modeled oil reservoir

Parameter	Value	Unit
Absolute permeability	2.5×10^{-13}	m^2
Elastic modulus	5	GPa
Poison number	0.2	–
Porosity	0.2	–
Initial oil degree of saturation	1	–
Oil density	950	kg/m^3
Water density	1000	kg/m^3
Gas density	100	kg/m^3
Oil dynamic viscousity	5×10^{-3}	$N.s/m^2$
Water dynamic viscousity	1×10^{-3}	$N.s/m^2$
Gas dynamic viscousity	1×10^{-4}	$N.s/m^2$

To compare the effect of AMR, three simulation types are carried out. In the first simulation, the reservoir was modeled with only fine cells. In the second simulation, the reservoir was modeled with multi scale method and in the third simulation, the reservoir was modeled by multi scale method with AMR. Figures 4 and 5 show the pressure in the reservoir in three simulation cases after 0.01 and 0.1 pore volume injection (PVI), respectively. As expected, pressure will increase around the injection well in each cases. The results of modeling by multi scale method with AMR are almost similar to the results of simulating by fine cells. On the other side, Fig. 6 shows the deformation distribution in the reservoir domain by multi scale method with AMR after 0.01 PVI. It shows that the maximum deformation is rightly occurred on the top of the injection well.

Considering plastic deformations will be occurred in the solid phase modeling after adding AMR especially in critical locations such as injector and producer wells, fractures and heterogeneities. Therefore, it was possible to add elastoplastic strain-stress models to porous media of oil reservoirs, which will be presented in the next paper.

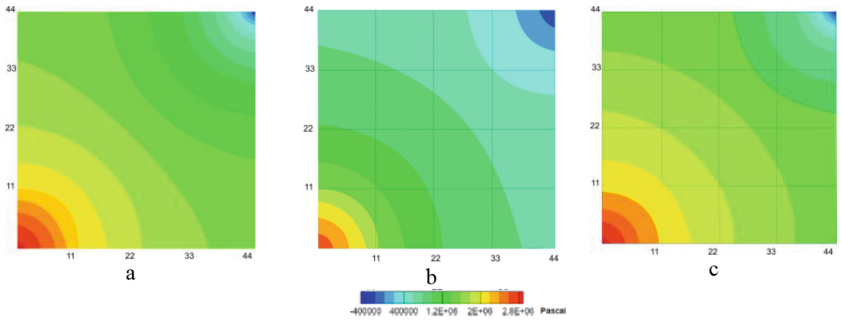

Fig. 4. The pressure distribution in the square domain of the reservoir (44 m × 44 m) after 0.01 PVI in three simulation cases: (a) simulation by fine cells (b) simulation by multi scale method (c) simulation by multi scale with AMR method

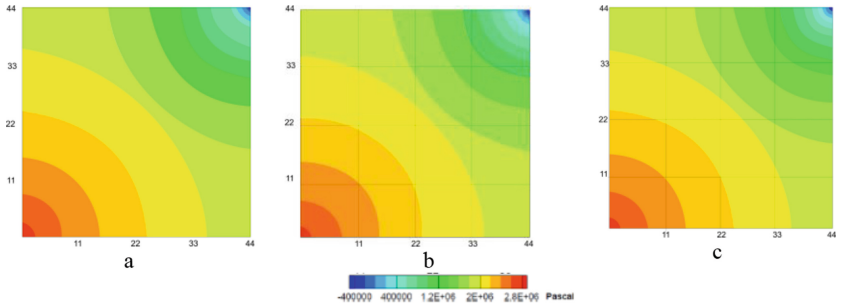

Fig. 5. The pressure distribution in the square domain of the reservoir (44 m × 44 m) after 0.1 PVI in three simulation cases: (a) simulation by fine cells (b) simulation by multi scale method (c) simulation by multi scale with AMR method

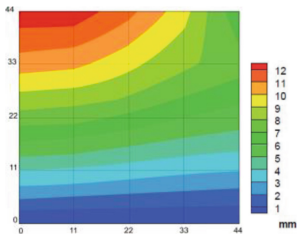

Fig. 6. The deformation distribution in the square domain of the reservoir (44 m × 44 m) by multi scale method with AMR after 0.01 PVI

5 Conclusion

A new model is presented for geomechanical aspects of oil reservoirs. Regarding the multiscale nature of reservoir porous media, flow of liquid phases and deformation of solid phase are simulated in the region of influence. Also, multi scale finite volume and AMR finite element are applied to simulate fluid transport and solid deformation, respectively. Also, capillary pressure was added to model equations. Indicative test case is analyzed and reasonable results with high computational efficiency are achieved. By implementing an AMR method and considering the capillary pressure, the results almost reach to the fine-scale solution.

References

Aarenes, J.E., Kippe, V., Lie, K.A., Rustad, A.B.: Modelling of multiscale structures in flow simulations for petroleum reservoirs. In: Geometrical Modeling, Numerical Simulation and Optimization Applied Mathematics at SINTEF. Springer, Heidelberg (2007)

Chen, X., Yang, V.: Thickness-based adaptive mesh refinement methods for multi-phase flow simulations with thin regions. Comput. Phys. **269**, 22–39 (2014)

Cusini, M., Kruijsdijk, C., Hajibeygi, H.: Algebraic dynamic multilevel (ADM) method for fully implicit simulations of multiphase flow in porous media. Comput. Phys. **314**, 60–79 (2016)

Dehkordi, M.M., Manzari, M.T.: Effects of using altered coarse grids on the implementation and computational cost of the multiscale finite volume method. Adv. Water Resour. **59**, 221–237 (2013)

Hajibeygi, H., Bonfigli, G., Hesse, M.A., Jenny, P.: Iterative multiscale finite-volume method. Comput. Phys. **227**, 8604–8621 (2008)

Hajibeygi, H., Jenny, P.: Multiscale finite-volume method for parabolic problems arising from compressible multiphase flow in porous media. Comput. Phys. **228**, 5129–5147 (2009)

Jenny, P., Lee, S.H., Tchelepi, H.A.: Multi-scale finite-volume method for elliptic problems in subsurface flow simulation. Comput. Phys. **187**, 47–67 (2003)

Jenny, P., Lee, S.H., Tchelepi, H.A.: Adaptive multiscale finite-volume method for multiphase flow and transport in porous media. Multiscale Model Simul. **3**, 50–64 (2004)

Jenny, P., Lee, S.H., Tchelepi, H.A.: Adaptive fully implicit multi-scale finite-volume method for multi-phase flow and transport in heterogeneous porous media. Comput. Phys. **217**(2), 627–641 (2006)

Lee, S.H., Wolfsteiner, C., Tchelep, H.A.: Multiscale finite-volume formulation for multiphase flow in porous media: black oil formulation of compressible, three-phase flow with gravity. Comput. Geosci. **12**, 351–366 (2008)

Lee, S., Wheeler, M.F., Wick, T.: Pressure and fluid-driven fracture propagation in porous media using an adaptive finite element phase field model. Comput. Methods Appl. Mech. Eng. **305**, 111–132 (2016)

Li, B., Tchelepi, H.A.: Nonlinear analysis of multiphase transport in porous media in the presence of viscous, buoyancy, and capillary forces. Comput. Phys. **297**, 104–131 (2015)

Liao, W.K., Liu, Y., Choudhary, A.: A grid-based clustering algorithm using adaptive mesh refinement (2002)

Lovett, S., Nikiforakis, N., Monmont, F.: Adaptive mesh refinement for compressible thermal flow in porous media. Comput. Phys. **280**, 21–36 (2015)

Lunati, I., Jenny, P.: Multiscale finite-volume method for compressible multiphase flow in porous media. Comput. Phys. **216**, 616–636 (2006)

Lunati, I., Jenny, P.: Treating highly anisotropic subsurface flow with the multiscale finite-volume method. Multiscale Model Simul. **6**, 308–318 (2007)

Lunati, I., Jenny, P.: Multiscale finite-volume method for density-driven flow in porous media. Comput. Geosci. **12**, 337–350 (2008)

Monaghan, J.J.: Particle methods for hydrodynamics. Comput. Phys. Rep. **3**(2), 71–124 (1985)

Popinet, S.: An accurate adaptive solver for surface–tension–driven interfacial flows. J. Comput. Phys. **228**, 5838–5866 (2009)

Taheri, E., Sadrnezhad, S.A., Ghasemzadeh, H.: Multiscale geomechanical model for a deformable oil reservoir with surrounding rock effects. Multiscale Comput. Eng. **13**(6), 533–559 (2015)

Tchelepi, H.A., Jenny, P., Lee, S.H., Wolfsteiner, C.: Adaptive multiscale finite volume framework for reservoir simulation. SPE J. **12**, 188–195 (2007)

Tomin, P., Lunati, I.: Local–global splitting for spatiotemporal-adaptive multiscale methods. Comput. Phys. **280**, 214–231 (2015)

Xie, Z., Pavlidis, D., Percival, J.R., Gomes, J.L.M.A., Pain, C.C., Matar, O.K.: Adaptive unstructured mesh modelling of multiphase flows. Multiph. Flow **67**, 104–110 (2014)

Wen, X.H., Durlofsky, L.J., Edwards, M.G.: Use of border regions for improved permeability upscaling. Math. Geol. **35**, 521–547 (2003)

Large Diameter Pile Combined with Micropiles to Improve the Stabilization of Transmission Tower Foundations

Tsung-Po Tsai(✉)

Kaoping Power Supply Branch, Taiwan Power Company, Kaohsiung City, Taiwan (R.O.C.)
smashing671226@gmail.com

Abstract. Taiwan Power Company built power transmission lines all over the island across the mountains decades ago. Recently, due to global warming and extreme climate change, transmission tower foundation safety maintenance is significantly important (Wang et al. 2017). Facing poor conditions, it is difficult to improve the existing tower foundations. The giant drilling machines cannot access the restricted spaces inside the frame. Though deep pile foundations can resist applied loads, the geological instability under the pile foundations must be also studied. In this work a large diameter pile foundation was built and combined with micropiles. The large diameter pile foundation was 3.5 m in diameter and 10 m in depth and connected a group of 7 micropiles, 20 m in depth and 15 cm in diameter, which were made of steel pipe and cement. The micropiles penetrated into the rock layer to increase the stability of the transmission tower. The stability of the tower had been checked by an inclinometer survey for several months through the rain season. It could prevent the small scale of potential landslide underneath the transmission tower foundation and increased the safety factor of the slope.

1 Introduction

To supply stable power for people and industry in Taiwan, where the forest covers 60% of the surface, Taiwan Power Company built power transmission lines mostly crossing the mountains. Taiwan is situated in the Circum-Pacific Seismic Belt and seismic activities occurred frequently, which caused geological instability in the mountains. Transmission tower foundation safety maintenance has been vital. Shallow foundations and grillage foundations were the main type in the early construction of transmission tower foundations in the mountains as shown in Fig. 1. Facing poor conditions, it is difficult to improve the existing foundation. It was not feasible for giant drilling machines in restricted spaces inside the frame. Foundation design had to take into account vertical loads, horizontal loads and seismic loads. The depth of pile was designed by analysis of axial bearing capacity and lateral bearing capacity. Though deep pile foundation can resist the applied loads, the geological instability under the pile foundation must be checked as well. In this practice we built large diameter pile foundation combined with micropiles. The large diameter pile foundation after analysis

A. Ferrari and L. Laloui (Eds.): SEG 2018, SSGG, pp. 486–494, 2019.
https://doi.org/10.1007/978-3-319-99670-7_60

was 3.5 m in diameter and 10 m in depth. This was connected to a group of 7 micropiles with 20 m in depth and 15 cm in diameter, which were made of steel pipe and cement. The micropiles penetrated into the rock layer to increase the stability of the transmission tower and the safety factor of the slope. The stability of the tower was monitored by inclinometer survey during several months through rain and Typhoon season, which prevented the small scale of potential landslide underneath the transmission tower foundation. Building the pile foundation in the mountains was an extremely difficult task expecially the deeper pile. This practice could be considered both beneficial and safety.

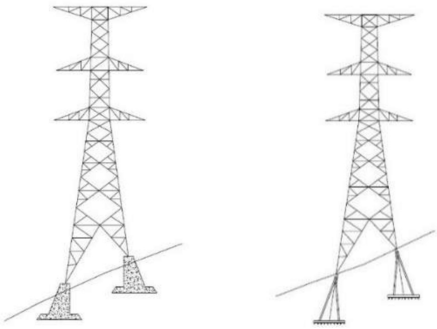

Fig. 1. Shallow foundation and grillage foundation

2 161 kV Kaogang-Nangong #9 Transmission Tower Foundation Improvement

61 kV Kaogang-Nangong #9 transmission tower is located in Xiaogang district, Kaohsiung City, Taiwan (R.O.C.). The tower is about 10 m from the slope. According to the geotechnical investigation report of the tower in November 2014, the subsoil (as shown in Fig. 3) consists of: a brown gravel layer mixed with sand in 7 m below the surface, a brown fine sand layer mixed with clay and sandstone from the depth of 7–17.9 m and the gray mudstone mixed with sandstone on the depth between 17.9 to 30 m. The underground water was at 30 m deep from the surface.

The compression strength (q_u) of the sandstone sampling for uniaxial compression test was 0.87 kgf/cm^2 which is typical of a weak rock. SPT-N value of the fine sand layer mixed with clay was between 17 and 23 and the average value of SPT-N was above 50.

10 inclinometer surveys were performed between the 1st of June 2015 and the 23rd of August 2016 including the Typhoon Soudelor in 2015 and Typhoon Nepartak in 2016. The displacement underneath the tower had been trending to the slope slightly. There was a deformation from 23 m deep as shown in Fig. 2.

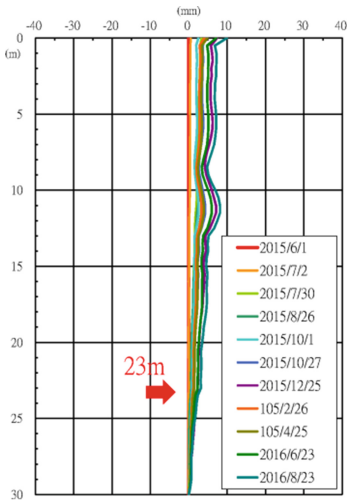

Fig. 2. Displacement from 23 m deep by inclinometer survey

2.1 The Improvement Structure of the Existing Foundation

The existing foundation below the tower type B-1 (12.5 + 4.5/3, 4.5, 3, 3) was a grillage foundation built in 1970s. The applied loads on the tower foundation was as follows: Hx = 14.05 tf; Hy = 23.42 tf; Vz = 41.69 tf; Mx = 430.58 tf-m; My = 161.37 tf-m; Mz = 41.3 tf-m. Considering the displacement underneath the tower and the stability of the tower in the long term, the existing foundation was suggested to be improved. With the contribution of the existing foundation, we applied a 25% reduction in loads. To resist earthquake forces, we used 0.3 W (selfweight) for the seismic load.

The geological situation of the bottom of pile regarding the geotechnical investigation report was not firm enough in this project. Idealy the pile should penetrate through the firm rock layer, but a deeper pile would be more dangerous from the construction point of view.

Due to the deformation from 23 m depth underneath the tower (as shown by inclinometer survey), the improvement structure type of the tower foundation was reinforced with the large diameter pile in 10 m depth and combined with several micropiles in 20 m depth in the bottom of the pile as shown in Fig. 3. The large diameter pile foundation and the existing grillage foundation could bear the applied load and provided the stability of the transmission tower. The micropiles penetrating through the firm rock layer provide more bearing capacity and shear resistance to decrease the possibility of the small scale potential landslide and increase the stabilization of the slope.

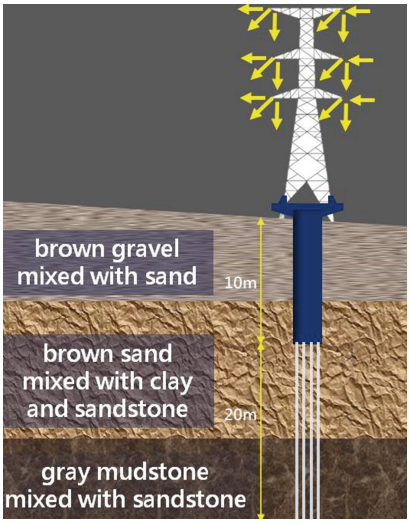

Fig. 3. Large diameter pile combined micropiles foundation.

2.2 The Large Diameter Pile

In this project, the large diameter pile with 3.5 m of diameter and 10 m in depth had to be constructed in restricted space. Taiwan Power Company referred in this case, to the technique of manual excavation of deep piles by steel liner plate that has been used from decades in Japan. Firstly, the cavity from surface to underground was excavated, afterwards, the liner plates until the design depth was assembled. The role of this plates was to resist the lateral earth pressure. The gap between the earth and liner plates was filled by backfill grouting.

2.3 Section of Micropile

Considering the space inside the frame and the kinetic energy of the drilling machine, the diameter of the micropile was chosen as 15 cm. For the main member, we used the pipe of 101.6 mm diameter made of steel compying the requirements of CNS4435 G3102 STK400. The steel pipe was grouted with cement inside as shown in Fig. 4.

According to Building Foundation Design Specification in Taiwan (ROC) (Construction and Planning Agency Ministry of the Interior in Taiwan 2012), the pile center-to-center spacing was not less than the pile diameter plus 1 m. Smaller pile spacing would impact to geotechnical capacity due to group effects and poor construction. In this practice, the micropile spacing was 1.15 m relative to group of 7 micropiles with the pile in 3.5 m diameter as shown in Fig. 5.

2.4 Evaluated Resistance of the Micropiles

Axial bearing capacity of pile was related to skin friction parameter determined with Standard Penetration Tests(SPTs), which in practice for micropiles amounts to f_S = N/8

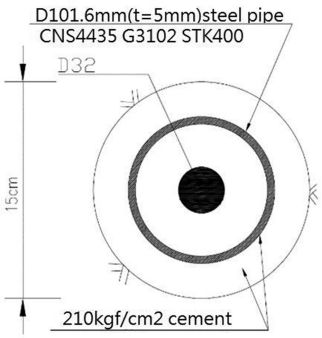

Fig. 4. Section of micropile.

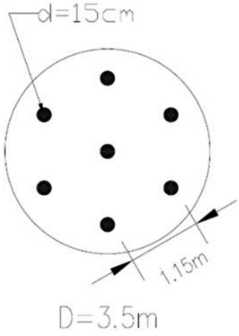

Fig. 5. Micropile spacing.

(Meyerhof 1976). The end bearing capacity was omitted. The evaluated axial bearing capacity per micropile providing extra capacity to support upper frame, was 19.63 tf. The shear resistance per micropile amounting to 12.2 tf was calculated based on the shearing strengthen properties of steel omitting contribution of rebar and cement. The numerical analysis using the software Midas (Fig. 6) reveals that modified foundation was able to bear the upper frame and the applied loads.

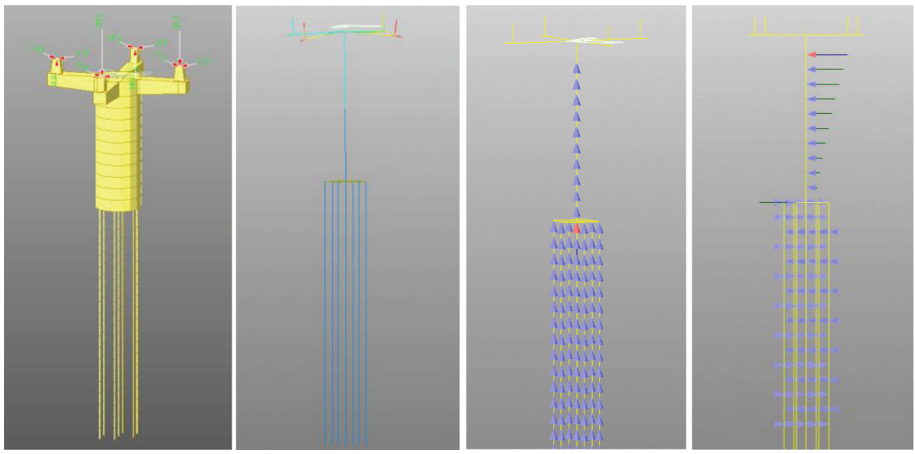

Fig. 6. Large diameter pile combined with micropiles analyzed in Midas.

3 Construction Process

The construction of the large diameter pile combined with micropiles foundation is schematically shown in Fig. 7.

Geological drilling machine, well drilling machine and drill jumbo are in general suitable to work in the restricted area. In this project, the well drilling machine, that had to be slanted to enter inside the tower was chosen (Fig. 8).

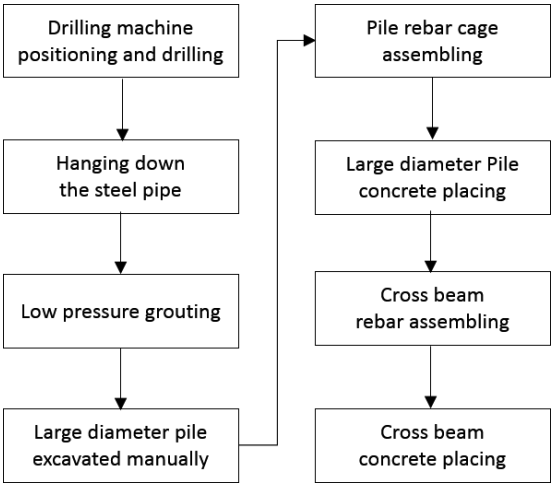

Fig. 7. Construction process.

Fig. 8. Drilling machine positioning and drilling.

As shown in Fig. 9, the steel pipes were hung and spliced by welding down to the designed depth, then grouting with low pressure of 10 kgf/cm^2. The large diameter pile was excavated cavity by manpower from surface to underground and assembled the liner plates to resist the lateral earth pressure until the design depth. The rebar cage of pile was assembled after excavating as shown in Fig. 10.

Concrete was poured into the pile after the rebar cage was assembled and then rebar and formwork of cross beam were arranged. The large diameter pile combined with micropiles foundation was finished after concrete was poured into cross beam as shown in Fig. 11.

Fig. 9. Steel pipe spliced by welding and pile grouting

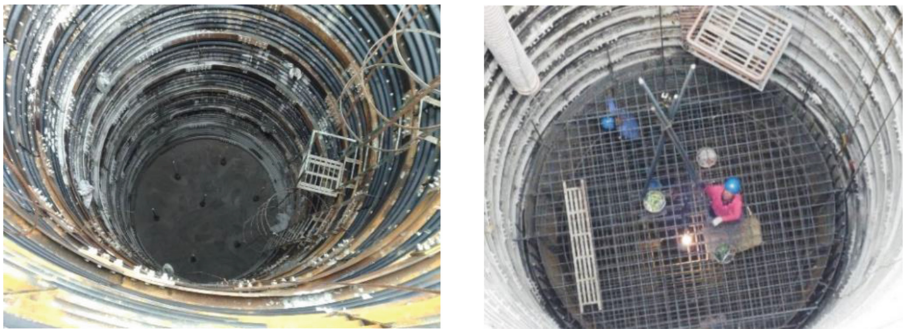

Fig. 10. Pile manual excavation and rebar cage of pile assembling

Fig. 11. Improvement of transmission tower foundation finished

4 Inclinometer Survey

Inclinometer surveying took place from July 2015 to September 2016 before the construction. During this period the range of the rate of movement was about 0.6–1.9 mm per month. After improvement the rate of movement of the slope had significantly decreased as shown in Fig. 12.

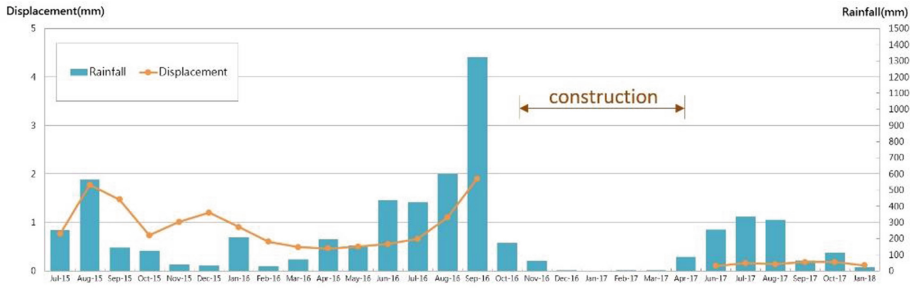

Fig. 12. The rate of movement of the slope decreased after improvement.

5 Conclusion

Since existing transmission towers had been constructed almost forty years ago, some transmission tower in the mountains were considered to be improved. The designed large diameter pile and the existing foundation could bear applied loads from the tower but the depth of the pile could not reach firm rock layer even in colluvium. This might lead to instability of the slope in the long term.

The extension of the length of large diameter pile to penetrate through firm rock layer was dangerous since construction had to be done manually in restricted frame. Moreover, the realization of large diameter pile of more than 20 m depth was costlier with respect to a group of micropiles of the same length. Considering safety of the construction procedure and stability of the slope, a foundation consisting of a large diameter pile combined with 7 micropiles was used in this project. It was shown that this construction was able to bear applied loads while improving the slope stability in the long term.

References

161 kV Kaogang-Nangong #9 Transmission Tower Geotechnical Investigation Report, pp. 5–30 (2013)

Construction and Planning Agency Ministry of the Interior in Taiwan: Building Foundation Design Specification. Pile Foundation, pp. 5-1–5-30 (2012)

Chinese National Standards: Carbon Steel Pipes for General Structure, CNS4435 G3102 STK400 (2013)
Wang, Y.-Z.: Extreme climate test for transmission tower. Taipower J. **657**, 018–019 (2017)
Meyerhof, G.G.: Bearing capacity and settlement of Pile foundation. J Geotech. Eng. Div. ASCE **102**(GT3), 195–227 (1976)

Finite Element Modelling of the Performance of Hybrid Foundation Systems for Offshore Wind Turbines

Koohyar Faizi(✉), Asaad Faramarzi, Samir Dirar, and David Chapman

Department of Civil Engineering, School of Engineering, University of Birmingham, Birmingham, UK
KXF577@bham.ac.uk

Abstract. This paper presents the results of a series of numerical simulations predicting the performance of a novel hybrid suction caisson foundation used for offshore wind turbines under overturning moment. The proposed new winged foundation is a hybrid foundation system that utilises steel plate sections attached to a caisson shaft (also steel), to increase its overturning capacity. In this study, a numerical 3D finite-element model with an elasto-plastic soil constitutive model, is developed to simulate the soil-caisson interaction and evaluate the additional overturning capacity provided by the wings. Results indicate significant contribution of the wings to increases overturning capacity compared to a simple caisson foundation through changes in the failure mechanism. The increase in overturning resistance provided by placing wings on a caisson is illustrated by presenting the results for a suction caisson with aspect ratio (embedment length/diameter) of 1. The effect of shape and size of the wing on overturning capacity is investigated.

1 Introduction

Suction caisson foundation (SCF) is a relatively new design concept used for offshore structures with significant potential to reduce costs of foundations in offshore construction industry. These structures are made of steel in the shape of inverted buckets and are installed into the seabed via the creation of negative pressure within the caisson skirt drawing the caisson into the seabed (Harireche et al. 2013). This method of installation allows for comparatively quick placement and removal making it cheaper than traditional foundations (Lombardi et al. 2011). Suction caisson foundations with a small aspect ratio (length to diameter ratio, L/D), due to their easy installation process, are becoming increasingly viable options for offshore wind turbines (Houlsby et al. 2005).

In general, foundations of offshore wind turbines, including suction caissons, are subjected to various loadings; vertical, horizontal, and moment loads or combinations of horizontal-vertical and moment loads. In particular, they experience large overturning moments due to the significant horizontal wind pressures acting high above the foundation level (Gourvenec and Jensen 2009; Houlsby et al. 2005; Villalobos et al.

A. Ferrari and L. Laloui (Eds.): SEG 2018, SSGG, pp. 495–501, 2019.
https://doi.org/10.1007/978-3-319-99670-7_61

2004). Wind turbine foundations are more critical against lateral loads or moments compared to their vertical load (Kim et al. 2016a). The resistibility of these foundations under overturning moments is the biggest challenge facing designers (Zhu et al. 2014). There is a need to enhance the capacity response of OWTs when bearing capacity is not sufficient for conventional suction caisson to stand stable under overturning moment.

To address the ever-increasing demand on capacity enhancement of OWTs' foundations (Lehane et al. 2010), and in order to improve the static and dynamic performance of offshore wind turbine foundations, a series of novel hybrid systems of caissons have been proposed in recent years (Dimmock et al. 2013; Fu et al. 2014; Kim et al. 2016b; Zhang et al. 2016; Wang et al. 2018). The proposed hybrid foundations include the conventional suction caisson foundation that combined with an external short skirt (Li et al. 2015; Li et al. 2014), reformed with circular mat (Fu et al. 2014; Li et al. 2015), equipped with internal honeycomb, and double or multiple skirt (circular compartment) (Wang et al. 2017; Li et al. 2015; Fu et al. 2014; Mana et al. 2012).

Although the above studies show promising results, these foundations have remained at the concept level and it is unclear how the benefits of hybrid foundation systems can be transferred to the real projects. Given the complexity and challenges associated with uncertainty of the offshore projects, finding novel and practical ways to increase capacity for foundation of offshore wind turbines whilst efficiency, and sustainability are ensured.

This paper attempts to address some of the issues associated with bearing capacity of suction caisson foundation by proposing an innovative design to improve its overturning capacity.

2 A New Foundation for Offshore Wind Turbines

In this research study, a novel foundation is proposed with the potential for use in OWT. The proposed foundation is a caisson with four wings attached to the main shaft in vertical positions at 90° intervals (see Fig. 1). We call this 'winged suction caisson'.

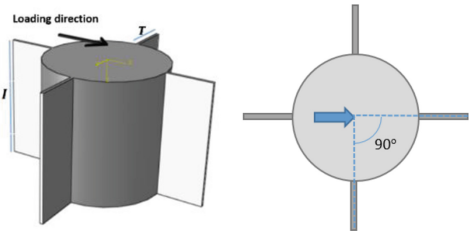

Fig. 1. Problem under study: direction of lateral load applied for winged caisson; T: wing width; l: wing height (left); Cross-sectional of a winged caisson (right)

This paper presents the results of numerical studies performed on the proposed winged suction caisson foundation installed in sand and subjected to overturning moment.

In this paper, a series of numerical models are developed using finite element (FE) method to simulate and predict the behavior of winged suction caissons. The models are used to understand the mechanisms in which the wings and caisson contribute to supporting the overturning moments. In addition, the models are employed to study the advantages and benefits of the winged suction caisson over traditional caisson foundations. To validate the numerical models, a series of experimental tests at normal gravity condition (i.e. 1 g) was conducted on small scale models of the proposed winged suction caissons.

A three-dimensional (3D) finite element (FE) analysis was adopted to model the 3D geometry of both the traditional and winged suction caisson foundations and the appropriate soil–foundation interaction using ABAQUS/Explicit. Figure 2, shows the geometry of half of a typical model that was used in the FE to simulate the 1:70 scale model experiments. The model foundations and the towers were assumed rigid. To simulate the overturning moment, a lateral load was applied at a height of 220 mm above the model surface (e in Fig. 2).

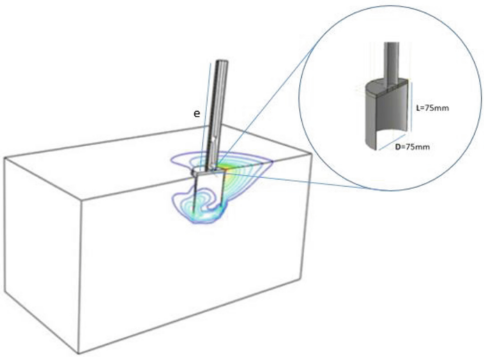

Fig. 2. The geometry of half of a caisson model in FE model: *L*, caisson length; *D*, caisson diameter; *e*: load eccentricity

To model the sand behavior, Drucker-Prager material was used with parameters derived from the Mohr Coulomb model as reported in Ciampi (1997). The soil and the caisson are modelled using the C3D8R solid homogeneous elements available in Abaqus/Explicit element library, which are 8-noded linear brick elements with reduced integration and hourglass control. Taking advantage of the symmetrical nature of the problem, only half of the problem was modelled in the FE model. Figure 3, shows FE mesh of the winged caisson foundation with the ratio of the skirt length (*L*) to the diameter (*D*) equal to 1. In the numerical model, the foundations are "wished in place", assuming that installation effects have a negligible impact on their capacity behavior. Table 1 shows the properties of the soil used in the numerical model.

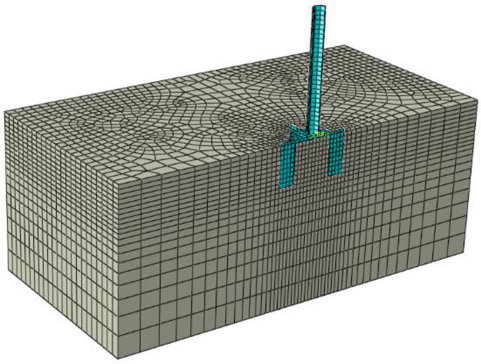

Fig. 3. Finite element model of the soil and winged caisson

Table 1. Physical properties of sand used in the model tests, Redhill 110 (Kelly et al. 2004)

$d_{10}, d_{30}, d_{50}, d_{60}$ (mm)	0.08, 0.10, 0.12, 0.13
Coefficients of uniformity, C_u and curvature C_c	1.63, 0.96
Specific gravity, G_s	2.65
Minimum dry density, γ_{min} (kN/m^3)	12.76
Maximum dry density, γ_{max} (kN/m^3)	16.80
Critical state friction angle, $\varnothing_{cs}$	36°

3 Results and Discussion

The moment-rotation curves ($M - \theta$) obtained from the numerical analysis were compared with the experiment results conducted in 1g condition. Non-dimensional parameters proposed by Houlsby et al. (2005) were used to normalize all the results. Therefore, loads will be proportional to unit weight of the soil (γ) and to 3R, where R is radius of the caisson. Similarly, all the moment-rotation curves in this study were plotted in a space of $M/4\pi R^4\gamma$ against $\theta(\frac{P_a}{2R\gamma})^{0.5}$, where P_a is atmospheric pressure (used as a reference pressure). The results obtained experimentally and through a numerical FEM simulation were compared for traditional as well as winged suction caissons when wing width equals 30% of the caisson's diameter ($T = 0.3D$) (see Fig. 4). As it can be seen from this figure, the numerical results are in good agreement with those of the 1 g experimental moment-rotation results. Winged suction caisson with different wing sizes of 20%, 30% and 40% of the diameter were investigated in this study. The results from the FE analysis indicated that the width of four wings used in the proposed foundation has a significant impact on the overturning capacity improvement. The results showed that the overturning capacity of suction caisson was increased by approximately 20%, 50% and 72% for winged caissons with T of 0.2D, 0.3D and 0.4D, respectively (Fig. 5).

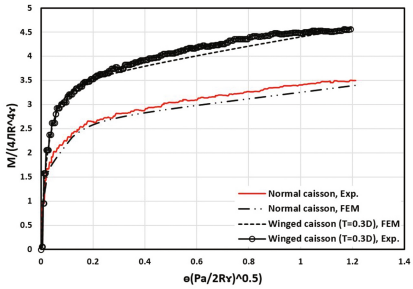

Fig. 4. Comparison of numerical modelling and experimental results for normal and winged caisson

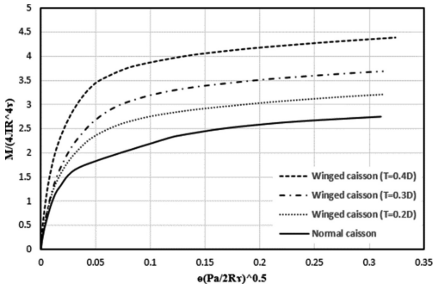

Fig. 5. Moment-rotation curves from FEM for normal and winged caissons

4 Effect of Wing Shape on the Capacity Improvement

A parametric study was conducted to investigate the optimum design of the wings using FE analyses which was developed based on the small-scale models. In particular, the analyses were carried out to study the effects of wing height and shape on the ultimate bearing capacity of the winged caisson with width of 0.4*D*. The wing height effect on the capacity improvement was investigated by selecting full and half height of the wing with respect to the embedment depth of caisson. Different wing shapes were investigated for a suction caisson with aspect ratio of 1. The variation of wing shape used for winged caisson is shown in Fig. 6. In the proposed wing geometries, *I* represents wing height, *T* is the ratio of wing width to the caisson diameter (%*D*), and *t* is the smaller base (the top) in trapezium shape of the wing (see Fig. 6f) which was considered 50% of *T*. The moment-rotation curves for winged caisson modeled in sand, with width of 0.4*D* and various height are presented in Fig. 7. The results clearly indicates that the wings efficiency depends on its height. The maximum efficiency obtained by full height of the wings, and the efficiency drops by almost 50% using half the height of the wing. The capacity enhancement provided by triangular shape is almost similar to those obtained by rectangular wing with half a height. The capacity improvement is not significantly altered by changing the position of the half rectangular wing (top half (c) and bottom half (d) in Fig. 6).

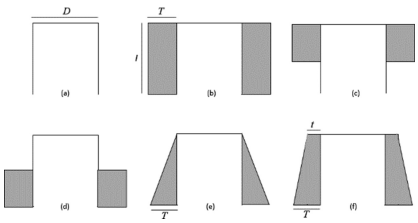

Fig. 6. Schematic dimension of winged caisson with different height and shape

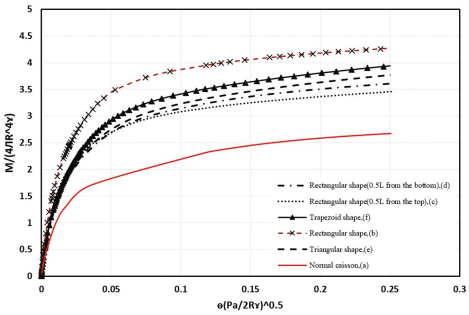

Fig. 7. Moment-rotation curves from numerical modelling for winged caissons

5 Conclusion

The behavior of winged suction caisson subjected to overturning moment in loose sand was investigated through three-dimensional nonlinear FE analysis. The numerical modeling was validated by the results obtained from experimental studies on small scale at 1 g condition. The results showed that a suction caisson reinforced with four wings provides considerably higher overturning capacity compared with a traditional caisson. From the results, it is clear that overturning capacity of winged caisson depends on the wing size and shape. The developed FE models were used to investigate the impact of the wing geometry on the overturning capacity of winged suction caissons. Overturning capacity improvement depends greatly on width of the wings and enhanced with increasing the width, as a ratio of the caisson diameter (%D). The measured enhancement of capacity due to the wing-attachment (T = 20–40%D) is about 20–72% for sand. In addition, overturning capacity improvement depends significantly on height of the wings. For wing width ratio of 0.4D, the maximum improvement achieved with full height of the wing in rectangular shape.

The proposed winged suction caisson can be used as an alternative for offshore foundations thereby saving significant costs associated with conventional foundations such as piles. Winged suction caissons can provide sufficient and reliable overturning and lateral capacity thereby which makes them a desirable option for wind turbine projects.

References

Ciampi, V.: MA Crisfield non-linear finite element analysis of solids and structures. Meccanica **32**, 586–587 (1997)

Dimmock, P., Clukey, E., Randolph, M., Murff, D., Gaudin, C.: Hybrid subsea foundations for subsea equipment. J. Geotech. Geoenviron. Eng. **139**, 2182–2192 (2013)

Fu, D., Bienen, B., Gaudin, C., Cassidy, M.: Undrained capacity of a hybrid subsea skirted mat with caissons under combined loading. Can. Geotech. J. **51**, 934–949 (2014)

Gourvenec, S., Jensen, K.: Effect of embedment and spacing of cojoined skirted foundation systems on undrained limit states under general loading. Int. J. Geomech. **9**, 267–279 (2009)

Harireche, O., Mehravar, M., Alani, A.M.: Suction caisson installation in sand with isotropic permeability varying with depth. Appl. Ocean Res. **43**, 256–263 (2013)

Houlsby, G.T., Ibsen, L.B., Byrne, B.W.: Suction caissons for wind turbines. In: Frontiers in Offshore Geotechnics, pp. 75–93. ISFOG, Perth (2005)

Kelly, R., Byrne, B., Houlsby, G., Martin, C.: Tensile loading of model caisson foundations for structures on sand. In: The Fourteenth International Offshore and Polar Engineering Conference. International Society of Offshore and Polar Engineers (2004)

Kim, D., Choo, Y.W., Park, J.H., Kwak, K.: Review of offshore monopile design for wind turbine towers. Jpn. Geotech. Soc. Spec. Publ. **4**, 158–162 (2016a)

Kim, J.H., Kim, S., Kim, D.S., Youn, J.U., Kim, D.J., Jee, S.H.: Bearing capacity of hybrid suction foundation on sand with loading direction via centrifuge model test. Jpn. Geotech. Soc. Spec. Publ. **2**, 1339–1342 (2016b)

Lehane, B., Powrie, W., Doherty, J.: Centrifuge model tests on piled footings in clay for offshore wind turbines. In: Proceedings of International Conference in Physical Modelling in Geotechnics, ICPMG 2010. Balkema, Rotterdam (2010)

Li, D., Feng, L., Zhang, Y.: Model tests of modified suction caissons in marine sand under monotonic lateral combined loading. Appl. Ocean Res. **48**, 137–147 (2014)

Li, D., Zhang, Y., Feng, L., Gao, Y.: Capacity of modified suction caissons in marine sand under static horizontal loading. Ocean Eng. **102**, 1–16 (2015)

Lombardi, D., Cox, J.A., Bhattacharya, S.: Long-term performance of offshore wind turbines supported on monopiles and suction caissons. Struct. Eng. **89**, 12–13 (2011)

Mana, D.S., Gourvenec, S., Martin, C.M.: Critical skirt spacing for shallow foundations under general loading. J. Geotech. Geoenviron. Eng. **139**, 1554–1566 (2012)

Villalobos, F.A., Houlsby, G.T., Byrne, B.W.: Suction caisson foundations for offshore wind turbines. In: Proceedings of the 5th Chilean Conference of Geotechnics (Congreso Chileno de Geotecnia), Santiago, pp. 24–26 (2004)

Wang, X., Yang, X., Zeng, X.: Lateral response of improved suction bucket foundation for offshore wind turbine in centrifuge modelling. Ocean Eng. **141**, 295–307 (2017)

Wang, X., Zeng, X., Li, J., Yang, X., Wang, H.: A review on recent advancements of substructures for offshore wind turbines. Energy Convers. Manag. **158**, 103–119 (2018)

Zhang, P., Zhang, Z., Liu, Y., Ding, H.: Experimental study on installation of composite bucket foundations for offshore wind turbines in silty sand. J. Offshore Mech. Arct. Eng. **138**, 061901 (2016)

Zhu, B., Zhang, W.-L., Ying, P.-P., Chen, Y.-M.: Deflection-based bearing capacity of suction caisson foundations of offshore wind turbines. J. Geotech. Geoenviron. Eng. **140**, 04014013 (2014)

Calculation Models of Bearing Capacity and Deformation of Soil Foundations with Vertical Elements Reinforced Under Regime Cyclic Loading

Ilizar Mirsayapov(✉) and Irina Koroleva

Kazan State University of Architecture and Engineering,
Kazan, Russian Federation
mirsayapovl@mail.ru

Abstract. A computational model of bearing capacity and deformation of soil foundations of energy buildings with vertical elements reinforced under regime cyclic loading was developed. The bearing capacity of reinforced vertical elements compressive force base in flow resistance consists of a triaxial compression in the middle zone and shear resistance in the boundary zones. Deformation of reinforced vertical elements bases is calculated taking into account the joint deformation of various zones by a summation of layers.

1 Introduction

During the construction of energy buildings and structures, such as buildings of Cogeneration and nuclear power plants, hydroelectric plants, wind power stations, fuel storage tanks, etc., the tendency of cyclic loads to increase at the ground bases and the use of soft ground as a base, contributed to the fact that one of the ways to increase bearing capacity and reduce settlements is the application of ground, that is reinforced by vertical elements, as foundation ground bases.

A reinforced ground base foundation is a combination of ground and reinforcing elements, wherein reinforcing elements change the ground base deformation conditions by limiting the ground deformation and increasing the overall bearing capacity of base in general. Herewith, the question of a cyclic load's influence on the ground base's, which has been reinforced by vertical elements, behavior is not sufficiently investigated.

In the system «foundation - reinforced ground base - reinforcing elements», a regimented cyclic loading jointly deforms materials with different strength and deformation properties. In this case, the deformation of all the system elements occurs in connected conditions.

The authors developed models for calculating the bearing capacity and the deformation (settlement) of the reinforced-by-vertical-elements ground base under regime cyclic loading.

A. Ferrari and L. Laloui (Eds.): SEG 2018, SSGG, pp. 502–507, 2019.
https://doi.org/10.1007/978-3-319-99670-7_62

2 Bearing Capacity Calculation Model

The bearing capacity calculation model of the reinforced-by-vertical-elements ground base was developed on the working hypothesis basis; according to which, the resistance of reinforced, in the compressible layer limits, foundation base, consists of resistance to triaxial compression in the middle zone and shear resistance in the edge zones (Fig. 1a).

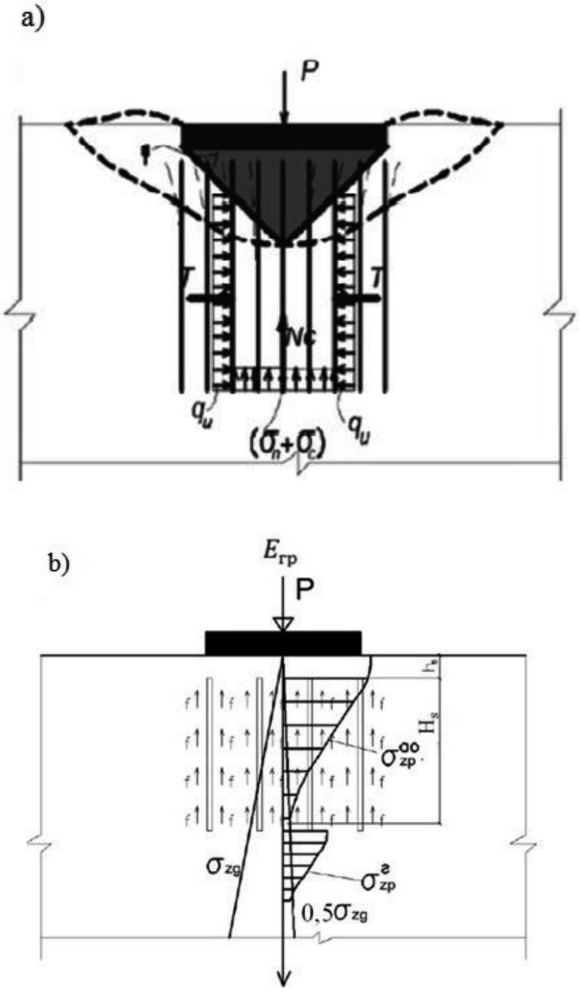

Fig. 1. (a) Design scheme for the reinforced soil base bearing capacity determination, (b) scheme for calculating the vertical deformation of the reinforced base under regime cyclic loading

Based on the proposed hypothesis about the resistance mechanism, the bearing capacity condition of reinforced soil base is written as:

$$P(N^{\max}) \leq ctg\,\varphi(N) \cdot T^{\max}(N) + F_c^{\max}(N),$$

where $T^{max}(N)$ represents the reinforced soil array resistance to the shift in the edge zones; $F_c^{max}(N)$ represents reinforced soil array resistance to compression in the middle zone; φ represents reinforced soil internal friction angle; N represents number of loading blocks.

The shear strength of the reinforced soil array in the edge zones is composed of the bending resistance of the reinforcing elements, the crossing soil glide plane and the soil resistance to compression under the reinforcing elements. In this case, the shear strength of the edge zones is described by the equation:

$$T(N) = R_{ae}(N) + R_{gr}(N)$$

where $R_{ae}(N)$ is the bending resistance of the reinforcing element and R_{gr} (N) the soil compression resistance (compressive strength) under the reinforcing elements.

The reinforcing element bending resistance depends on the joint deformation conditions of this element with the surrounding soil and the strength and deformation characteristics. The deformation of the reinforcing element below the shear line are defined as they would be for a joist on an elastic foundation, for which the deformation properties of the soil base, which change with the reinforcing element length, are very important.

The shear strength calculation of the reinforced soil array in the edge zones is carried out by taking into account the stress and strain changes in the soil and reinforcing elements in the cyclic loading process due to the development of soil vibrocreep strains under the reinforcing elements in the associated conditions. Then current stresses in the reinforced soil base shear zone are represented as:

$$\sigma_{aeT}^{\max}(N) = \sigma_{aeT}^{\max}(N_1) + \Delta\sigma_{aeT}(N);\ \sigma_{grT}^{\max}(N) = \sigma_{grT}^{\max}(N_1) + \Delta\sigma_{grT}(N);$$

where $\sigma_{aeT}^{\max}(N_1), \Delta\sigma_{grT}^{\max}(N_1)$ are the maximum cycle stresses at the first cycle of loading in the reinforcing elements and in the soil respectively; $\Delta\sigma_{aeT}(N)$, $\Delta\sigma_{grT}(N)$ are additional stresses in the reinforced soil base during cyclic loading in the reinforcing elements and in the soil, respectively.

In the determination of the additional (residual) stresses, two variants of ground and reinforcing elements joint deformation are considered: (1^{st}) reinforcing element cohesion with the ground in the shear zone is not violated; (2^{nd}) cohesion is violated.

Limiting bearing capacity of the soil under the reinforcing element can be determined by tensile strength in terms of volume stressed state, because the ground under the reinforcing element is working in cramped conditions, whereby there will be an increase in soil resistance to compression. Based on the destruction schemes and soil stress-strain state zones under triaxial compression proposed in (Mirsayapov and

Koroleva 2011), the soil strength condition under the reinforcing elements at triaxial compression is represented as:

$$4 \cdot [\sigma_V(t,N) \cdot A_{sh} \cdot cos\alpha_1(t,N) + \tau_V(t,N) \cdot A_{sh} \cdot sin\alpha_1(t,N)] \geq \sigma_{grT}^{max}(N) \cdot A_1,$$

where $A_{sh} = b^2/(4cos\alpha_2(t, N))$ represents the surface area of the pyramid side faces; $A_1 = b^2$ represents the side face area of a cube; α_1 represents the equilibrium limit area tilt angle to the time moment t, corresponding to loading cycles N_i; α_2 is the shift area tilt angle to the time moment t, corresponding to loading cycles N_i; $\sigma_v(t, N)$, and $\tau_v(t, N)$ represents normal and shear stresses at the ultimate equilibrium area, considering the influence of dilatant stresses $\sigma_d(t, N)$.

The limit shear force value, perceived by reinforcing elements under cyclic loading, is determined from joint deformation conditions of the soil and the reinforcing element (Mirsayapov and Koroleva 2014, 2015):

$$R_a(N) = 3\frac{M_u}{L_x(N)}n,$$

where M_u is the limiting bending moment, perceived by the reinforcing element, which cross the reinforced array shear plane at the time moment t, corresponding to loading cycles N_i; n is the number of the reinforcing elements crossing the shear plane.

The maximum value of the cyclic load, perceived by the reinforced soil array in the neutral zone, depends on the joint deformation conditions of the soil and the reinforcing elements in the associated conditions, as well as their strength and deformation properties. As a result of this interaction between the elements, an additional stress state and redistribution of forces between the soil and the reinforcing elements at the cyclic loading arises in the reinforced soil base. Then, the current stresses of the reinforced soil base can be represented as

$$\sigma_{ae}^{max}(N) = \sigma_{ae}^{max}(N_1) + \Delta\sigma_{ae}(N), \quad \sigma_{gr}^{max}(N) = \sigma_{gr}^{max}(N_1) - \Delta\sigma_{gr}(N)$$

where $\sigma_{ae}^{max}(N_1)$, $\sigma_{gr}^{max}(N_1)$ are the maximum stress cycle at the first cycle of loading in the reinforcing elements and the soil, respectively; $\Delta\sigma_{ae}(N), \Delta\sigma_{gr}(N)$ are additional stresses, arising in the reinforced soil base during cyclic loading, in the reinforcing elements and in the soil, respectively.

Cramped vibrocreep soil deformation leads to the appearance in the reinforced soil array of more balanced internal stresses. This causes tensile stresses to arise in the soil and compressive stress to arise in the reinforcing elements.

Under the influence of the difference between the free vibrocreep soil deformation $\varepsilon_{pl}^{gr}(N)$ and the cramped vibrocreep reinforced soil deformation $\varepsilon_{pl}^{ae}(N)$:

$$\Delta\varepsilon_{pl}(N) = \Delta\varepsilon_{pl}^{gr}(N) - \Delta\varepsilon_{pl}^{ae}(N)$$

in the soil arise averaged tensile stresses, while compressive stresses arise in reinforcing elements.

The equilibrium of internal forces from the additional stress state symmetrically reinforced soil array has the form

$$\Delta\sigma_{ae}(N) \cdot A_{ae} = \Delta\sigma_{gr}(N) \cdot A_{gr},$$

where A_{ae} is the total cross-sectional area of the reinforcing elements within the foundation soil base area limits; A_{gr} is the foundation soil base area reinforced by vertical elements.

After a number of simplifications, obtained analytical expressions to determine the additional stresses:

– in the soil

$$\Delta\sigma_{gr}(N) = \varepsilon_{pl}^{gr}(N) \cdot E_a \frac{A_{aein}}{A_{gr}} \Big/ \left(1 + \frac{E_{ae}(N)}{E_{gr}(N)} \cdot \frac{A_{ae} \cdot n}{A_r}\right);$$

– in the reinforcing elements

$$\Delta\sigma_{ae}(N) = \varepsilon_{pl}^{gr}(N) \cdot E_{ae} \Big/ \left(1 + \frac{E_{ae}(N)}{E_{gr}(N)} \cdot \frac{A_{ae1} \cdot n}{A_{gr}}\right),$$

where $\varepsilon_{pl}^{gr}(N)$ is the soil vibrocreep deformation; A_{ae1} is the cross sectional area of the one reinforcing element; n is the total number of the reinforcing elements in the soil base compression core.

3 Settlement Calculation Model Under Regime Cyclic Loading

The authors propose a reinforced foundations' engineering settlement calculation method, which is based on the layer summation method, in combination with the stress-strain state of the reinforced soil array. Total reinforced foundation settlement under regime cyclic loading is written as follows (Fig. 1b):

$$S(N) = S_n(N) + S_{ae}(N) + S_y(N),$$

where S_n (N) is the soil cushion settlement; S_{ae} (N) is the settlement within the limits of the reinforced zone; S_y (N) is the settlement below the reinforced zone.

Soil cushion settlement is determined by the layer summation method, taking into account the constraints of a compressible thickness by the soil cushion capacity:

$$S_n(N) = \frac{0.8 \sum_{i=1}^{m} \sigma_{zp,i}^{cp}(N) \cdot \Delta_{n,i}}{E_n(N)}$$

where $\Delta_{n,i}$ is the elementary layer thickness within the soil cushion limits; m is number of elementary layers within the soil cushions limits.

To calculate the soil base deformations, Reinforced soil characteristics should be considered in the reinforcement zone, determined by a previously proposed method (Mirsayapov and Koroleva 2014, 2015), and for the settlement calculation below the soil array reinforcement area – accepted initial soil parameters.

During reinforced array settlement calculating within the reinforced zone the reinforcing element height limits the height of the compressible thickness adopted. The height of the compressible thickness below the reinforcement zone is determined by the condition $\sigma_{zp} = 0.5\sigma_{zg}$ (Fig. 1b). Knowing the vertical stress components at different soil base points, it's possible to determine the average and the intensity of the stress, and then the strain tensor invariants increment: the increment of volumetric strain and strain intensity (Mirsayapov and Koroleva 2011).

4 Conclusions

For the analytical description of non-free deformation system elements, mechanical state equations for the ground and the system "plate – ground cushion – reinforced soil base – reinforcing elements" as well as the efforts equilibrium equations were developed. The simultaneous solution of these equations allows for the calculation of the desired settlement and bearing capacity values of soil base with reinforced vertical elements taking into account the redistribution of forces between the system elements under regime cyclic loads.

The reinforcing elements at the joint deformation, along with the soil, change the condition of soil base deformation, limiting soil deformation, increasing bearing capacity and reducing the deformation of the soil base in general. As a result of joint deformation, redistribution of forces between the reinforced base elements takes place, and the stress with reinforcing elements increases, whereas in soil it decreases under cyclic loads.

References

Mirsayapov, I.T., Koroleva, I.V.: Prediction of deformations of foundation beds with a consideration of long-term nonlinear soil deformation. Soil Mech. Found. Eng. **48**(4), 148–157 (2011). (translated "Osnovaniya, fundamenty i mekhanika gruntov" Journal, 2011, No 4, 16-23)

Mirsayapov, I.T., Koroleva, I.V.: Experimental and theoretical studies of bearing capacity and deformation of reinforced soil foundations under cyclic loading. In: Oka, F., Murakami, A., Uzuoka, R., Kimoto, S. (eds.) Computer Methods and Recent Advances in Geomechanics—Proceedings of the 14th International Conference of International Association for Computer Methods and Recent Advances in Geomechanics, IACMAG 2014, pp. 737–742 (2014)

Mirsayapov, I.T., Koroleva, I.V.: Computational model of the carrying capacity of a reinforced foundation with cyclic loading. Soil Mech. Found. Eng. **52**(4), 198–205 (2015). (translated "Osnovaniya, fundamenty i mekhanika gruntov" Journal, 2015, No 4, 12–17)

Author Index

A. Ferrari and L. Laloui (Eds.): SEG 2018, SSGG, pp. 509–511, 2019.
https://doi.org/10.1007/978-3-319-99670-7